Green Energy and Technology

F.M. Rabiul Islam
Kabir Al Mamun
Maung Than Oo Amanullah *Editors*

Smart Energy Grid Design for Island Countries

Challenges and Opportunities

Springer

Green Energy and Technology

More information about this series at http://www.springer.com/series/8059

F.M. Rabiul Islam · Kabir Al Mamun
Maung Than Oo Amanullah
Editors

Smart Energy Grid Design for Island Countries

Challenges and Opportunities

Springer

Editors
F.M. Rabiul Islam
School of Engineering and Physics
University of the South Pacific
Suva
Fiji

Maung Than Oo Amanullah
School of Engineering
Deakin University
Truganina
Australia

Kabir Al Mamun
School of Engineering and Physics
University of the South Pacific
Suva
Fiji

ISSN 1865-3529 ISSN 1865-3537 (electronic)
Green Energy and Technology
ISBN 978-3-319-50196-3 ISBN 978-3-319-50197-0 (eBook)
DOI 10.1007/978-3-319-50197-0

Library of Congress Control Number: 2017934213

Printed on acid-free paper

This Springer imprint is published by Springer Nature
The registered company is Springer International Publishing AG
The registered company address is: Gewerbestrasse 11, 6330 Cham, Switzerland

Preface

Island countries are extremely vulnerable to the risks of climate changes. These island nations will suffer an uneven share of the global consequences when climate change accelerates. Furthermore island countries are highly reliant on imported fossil fuel (diesel and petroleum), which are not only major contributors to greenhouse gas emissions but are also very expensive. The new concepts and ideas to develop renewable energy (RE) based power grid in Island countries will reduce fossil fuel consumption and assist the transition to a low-carbon economy but to achieve that RE based power grid, a number of issues need to be addressed.

In Island countries, a number of small islands do not enjoy the comfort of trouble-free electrical grid because they are either weakly connected or completely separated from the grid. On the other hand, they need to have access to renewable energies abundant in their surroundings, while keeping their tourism, agriculture, and landscape capital intact. Guidelines for the inclusion of such installation into existing built environments as well as natural contexts are needed.

The obstacles to the fast adoption of renewable energy sources (RES) in such areas are of many types and known since long time and implementation of such technologies are even more complex in Island countries. This book identifies challenges, solution, and opportunities of RES implementation in Island countries and provides guideline for future smart grid.

Chapter "Possibilities and Challenges of Implementing Renewable Energy in the light of PESTLE & SWOT Analyses for Island Countries" of this book discusses two different decision-making techniques: one of them is PESTLE analysis (political, economic, social, technological, legal and environmental) which can be used in energy planning and for business analysis and second, SWOT analysis (strengths, weaknesses, opportunities and threats) which has been utilized to incorporate strategic analysis and for decision-making. The overall chapter presents a holistic idea of prospects and contests of implementing renewable energy in various islands.

Chapter "Utilization and Optimization of Diesel Generation for Maximum Renewable Energy Integration" presents informed consideration of the issues surrounding existing generation, prompting the audience to identify residual value

across these assets, and in return identifies a pathway for improved RES integration. To prevent the increase of carbon emission, the use of quick renewable energy such as PV system and simple solutions considered the clean energy to keep both the population and environment safe are described in Chapter "Optimal Control System of Under Frequency Load Shedding in Microgrid System with Renewable Energy Resources". A comprehensively examination on the commercially available and emerging mitigation methods with a framework that systematically explores the full range of technical methods for PV in distribution network have been explained in Chapter "Power Quality Impacts and Mitigation Measures for High Penetrations of Photovoltaics in Distribution Networks". The strategies of sliding mode control for grid tied and off grid photovoltaic system with multilevel inverters for islanding regions are the main targets of Chapter "Grid-connected and Off-Grid Solar Photovoltaic System". A detailed overview of feasibility design and control strategy of a flywheel energy storage system (FESS) with suitable structure in order to increase reliability and stability of the power in the RES is explained in Chapter "Feasibility Study and Design of a Fly-wheel Energy System in a Micro-grid for Small Village in Pacific Island State Countries". Small-scale energy microgrid with battery-based energy storage system (ESS) enabled with solar–wind hybrid renewable energy system is discussed in Chapter "Energy Storage Systems in Solar-Wind Hybrid Renewable Systems" and the performance has been validated through simulation studies under islanded conditions. The frequency variation issues in presence of PV and wind generation systems have been shown and use of storage systems for dynamic grid support is analyzed in Chapter "Frequency Stability Improvement in Weak Grids by Storage Systems". The specific power converters for storage systems grid interfacing are studied with reference to superconducting magnetic energy storage (SMES), FESS, supercapacitors, and batteries with different case studies also presented in Chapter "Frequency Stability Improvement in Weak Grids by Storage Systems".

Energy trends in an Island and possible cases with solution to that have been presented in Chapter "Identifying Energy Trends in Fiji Islands". Chapter "Energy Grid Management, Optimization and Economic Analysis of Microgrid" proposes a non-dominated sorting genetic algorithm (NSGAII) for the multi-objective optimal operation management (MOOM) for distributed microgrid. Chapter "Energy Management of AC-Isolated Microgrids Based on Distributed Storage Systems and Renewable Energy Sources" presents the frequency and voltage regulation and the energy management strategy for an AC islanded microgrid based on distributed energy storage and RES. To satisfy the load demand of an island Chapter "Optimal Design and Energy Management of a Hybrid Power Generation System Based on Wind/Tidal/PV Sources: Case Study for the Ouessant French Island", focused on a typical hybrid power generation system using wind energy, marine energy (tidal current), and PV in Ouessant French island which has also taken under scope with another set of energy generator combination from hybrid diesel, MCT, and battery system for power supply and power management and presented in Chapter "Hybrid Diesel/MCT/Battery Electricity Power Supply System for Power Management in Small Islanded Sites: Case Study for the Ouessant French Island". An optimal

power flow of battery, wind, and PV in a hybrid system in South Africa has been presented in Chapter "Optimal Power Flow of a Battery/Wind/PV/Grid Hybrid System: Case of South Africa" with reduced operation cost and allows consumers to generate substantial income by selling power to the grid.

The aim of this book is to identify the challenges, solutions, and opportunities of the design and assessment of realistic state-of-the-art smart energy grids (SEG) to store and regulate diversified energy sources such as photovoltaic, wind, ocean energy, and other renewable energy productions in order to meet the electrical energy needs of Island countries.

In summary, this book contains current energy situation of Island countries with technical analysis, weather data analysis, availability of renewable sources, and socioeconomic structure supported by various data table, system structure design, simulation, and case studies.

Suva, Fiji F.M. Rabiul Islam
Suva, Fiji Kabir Al Mamun
Truganina, Australia Maung Than Oo Amanullah

Contents

Editorial Advisory Board

Reviewers

Possibilities and Challenges of Implementing Renewable Energy in the Light of PESTLE & SWOT Analyses for Island Countries

F.R. Islam and K.A. Mamun

Abstract Energy structure redesigning and implementation of renewable energy generation in the distribution grid usually depend upon the availability of resources, socioeconomic structure, political issues, and environmental concern. In this sense a developing Island country faces huge challenges for implementing renewable energy, but those countries are blessed by several opportunities. However, the challenges that prevent developing island countries to reach at a milestone level include capital cost in addition to the devastation caused by natural disaster and the recent trends of decrease in fuel prices which seems to be a cheaper resort for fossil fuel-based generation in terms of expenditure. At present, it seems that the investors, most of the government and various stakeholders are not in a position to take a concrete decision in the field of renewable energy due to the lack of sufficient research on the opportunities and challenges of renewable energy generation in this context. Hence the strategic planning processes of renewable energy implementation for Island countries need a holistic analysis to meet the increasing energy demand from renewable energy sources. In this chapter, major opportunities available for renewable energy generation are explored and analyzed. Two different decision-making techniques are used, namely PESTLE analysis (Political, Economic, Social, Technological, Legal and Environmental) which can be used in energy planning and for business analyses, and SWOT analysis (strengths, weaknesses, opportunities and threats) has been utilized to incorporate strategic analyses and for decision making. This chapter presents an overall idea of prospects and challenges of implementing renewable energy in various Island countries.

Keywords Renewable energy · Challenges · Opportunities · Islands · SWOT · PESTLE

F.R. Islam (✉) · K.A. Mamun
School of Engineering and Physics, The University of the South Pacific, Suva, Fiji
e-mail: islam_f@usp.ac.fj

K.A. Mamun
e-mail: mamun_k@usp.ac.fj

F.M.R. Islam et al. (eds.), *Smart Energy Grid Design for Island Countries*,
Green Energy and Technology, DOI 10.1007/978-3-319-50197-0_1

1 Introduction

For sustainable development and to ensure the symphonic concomitance of life and environment, renewable energy is the ultimate choice for the next generation. Supports from government and nongovernment business organization play a vital role for the implementation of renewable energy.

With the continuous development of society, the demand for energy supply is increasing gradually. Due to the advancement in technology, environmental friendly and availability, renewable energy (RE) has been proved as effective and one of the best choices to guarantee the future development of the world [1]. As most of the Islands countries are developing stage, utilization of renewable energy is essential for their sustainable development [2].

Island countries are the most suitable market place in the world for the standalone renewable energy sources. Due to the geographic location and exclusive dependency on imported fossil fuel for power generation, most of the island countries face the world's uppermost energy costs, with vulnerability in supply chain and interruptions. The average cost of energy in the Caribbean, ranges from US$0.32 to US$0.60 per kWh [3, 4] as shown in Fig. 1, which is almost five times of the mainland U.S. The scenario is even worse in the Pacific Islands, in some countries the tariff exceeds more than US$0.75/kWh [5] as shown in Fig. 2. To meet the essential demand for electricity many governments subsidizing the cost of electricity in spite of weak economic conditions which ultimately cause the high price of food and other essential items, consequently reduces investment for other infrastructures. On an average the Pacific Islands countries, utilize their 40% of total GDP to import petroleum products [6], while for Caribbean Islands it is up to 48% [7].

Information about the present energy scenarios along with opportunities for the future and the potential challenges are the essential elements for the researchers, investors and policymakers to set a trajectory for sustainable energy infrastructures development to ensure green and clean environment.

Strategic planning is a prolonged tool for the development of any country and regional structure which is typically carried out on the basis of participation

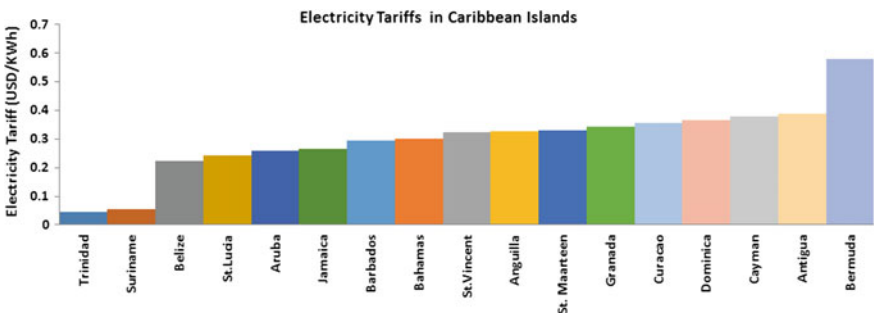

Fig. 1 Electricity tariffs in Caribbean islands

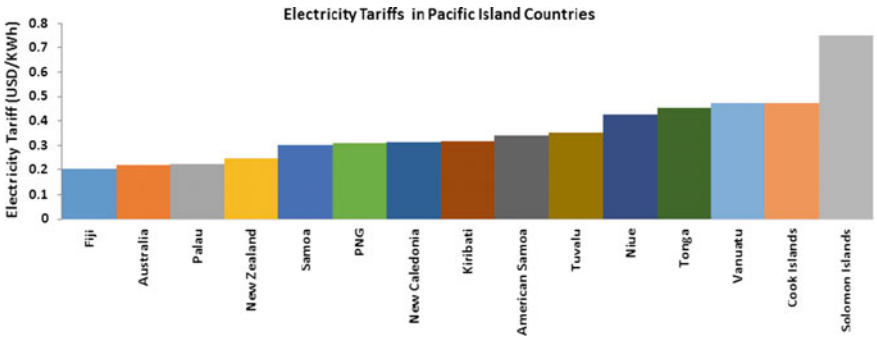

Fig. 2 Electricity tariffs in Pacific island countries

processes. A number of techniques have been used for renewable energy planning around the globe. PESTLE and SWOT analyses are of remarkable ways to address sustainable planning [8–15]. In this chapter, a comprehensive analysis has been conducted on renewable energy implementation in Island countries in the light of PESTLE and SWOT analyses to evaluate the present situations and opportunities with challenges for the integration of renewable energy into the grid. It is anticipated that this chapter will be helpful for the investors and also could be helpful for the government of Island countries to develop the policy for renewable energy sector.

2 PESTLE and SWOT Analyses on Renewable Energy Resources

One of the comprehensive methods for understanding a business environment is PESTLE analysis. It can be explained as a bird's eye view where an organization or individual tries to determine exact trends of the market from a macroeconomic point of view. While PESTLE analysis gives a thorough concept of the external environment where an organization operates; SWOT analysis identifies the internal environment of the organization. Both PESTLE and SWOT are decision-making tools where PESTLE analysis helps the investors to take decision about the investment and SWOT analysis supports the policymaker for further development. PESTLE and SWOT analyses have few similarities in their matrix and in this chapter the similarities in the field of renewable energy in various Islands will be explained with the other characteristics as shown in Fig. 3. Once the fundamentals of the PESTLE have been recognized, they can be utilized to explain in details to accumulation SWOT analysis.

While analyzing the renewable energy integration in most of the Island's power grid, it has been found that they have environmental and political strength; weakness in legal practice and technology; opportunities in the advancement of

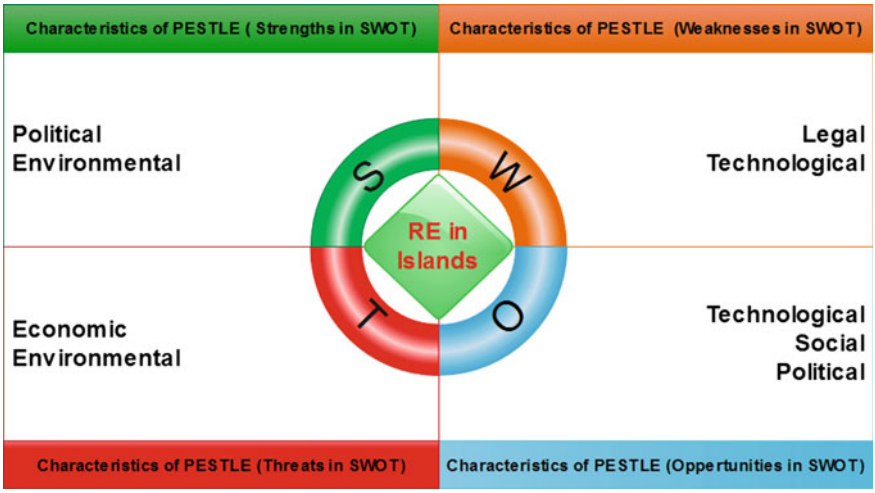

Fig. 3 Relationship between PESTLE and SWOT with respect to RE in island countries

technology; social life and political interest while threats from the environmental disaster and economical situations that represent the matrix of PESTLE and SWOT as shown in Fig. 3.

3 PESTLE Analysis

As discussed in the previous section PESTLE has wider coverage of business and external issues hence from the business organization point of view the PESTLE analysis will be further deliberated in this section. The analyses used in this chapter, consist of investigation that collect evidence and data, produce information that are applicable in renewable energy sector for Island countries. Here a brief description is given below for all the components of PESTLE analysis.

Political issues: Geographical location, regulatory authority, government policies, bureaucracy, international relationship, corruption, and many more are included in political issues.

Economic issues: Employment, gross domestic product (GDP), inflation, economic stability, local, and foreign investments are the major economic factors that influence the development of renewable energy; especially in an Island country along with wages rate, labor force, and division of income.

Social issues: Local energy demand, lifestyles, social cultural structure, business culture, demographics, and few other issues are considerable when PESTLE analysis is carried on renewable energy.

Technological issues: Technological factors are vital when integrating renewable energy to the existing grid or even to design a new grid for the Island countries. Next few chapters of this book will discuss on these issues and their solutions. In this study we will focus on various aspects in technology which should be taken into consideration, such as monitoring and control, network design, tariff system, research facilities in Island countries, and few others.

Environmental issues: *Climate changes*, natural resources, or availability of renewable energy sources and natural disaster will be taken into consideration as the environmental factors.

Legal issues: Policies related to the renewable energy implementation and business organization along with the law and order situation are the main legal issues which has significant impact on the integration of renewable energy sources into the grid of Island countries.

The overall PESTLE analysis can be illustrated in Fig. 4, where all the factors of PESTLE analysis are divided into subfactors for the renewable energy implementation in Island countries and these factors will be explained in details in Sects. 1.3.1–1.3.6.

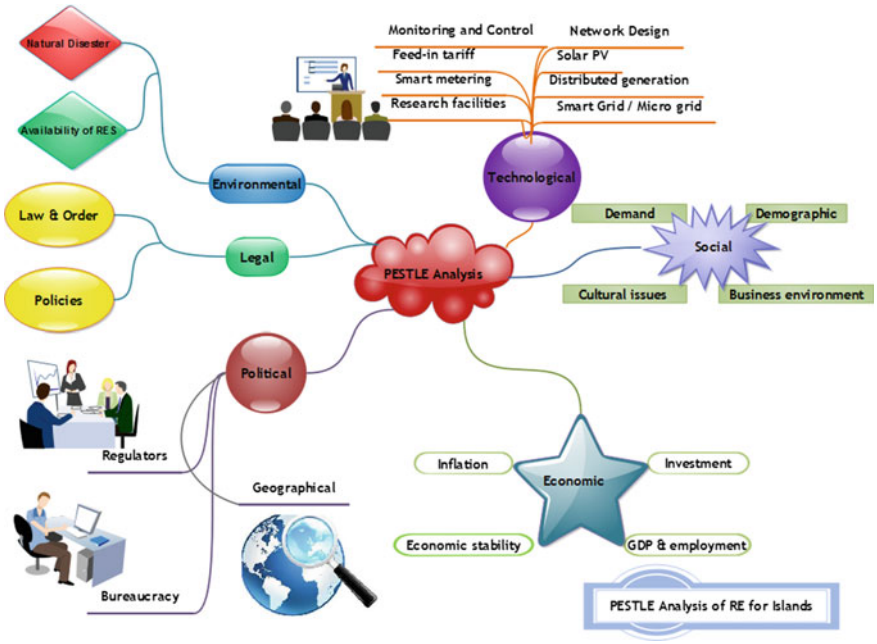

Fig. 4 PESTLE analysis for implementing renewable energy in island countries

3.1 Political

A number of the Caribbean Islands and Pacific Islands were under the rule of British or France for a long time. Currently, most of them are enjoying independence and democracy. The political traditions of these Islands reflect the diverse ways and time [16, 17]. Therefore, the developments in various Island countries are not very similar. Bureaucracy is still a big problem for the development and decision-making while corruption also is a factor which needs to be realized for few countries [18]. As they have a vast geographic area and numbers of islands as shown in Figs. 5 and 6, they are the main victim of climate changes. At present, most of the governments are trying to implement renewable energy sources with attractive policies for the investors to fight against the environmental changes. The target for renewable energy integration in the grid by various Island countries [19, 20] is shown in Table 1.

Table 1 shows that a number of Island countries have a target of achieving renewable energy more than 50% by the 2020 which reflect the interest of the government of that particular country on renewable energy integration. But, when the question comes about the achievement of the target, along with the government interest a number of other issues need to be considered by the government and stockholders. One of those issues is the economic factors which will describe in the next section.

Fig. 5 Geographical location and area of Pacific island countries (Courtesy of the University of Texas Libraries, The University of Texas at Austin)

Fig. 6 Geographical location and area of Pacific island countries (Courtesy of the University of Texas Libraries, The University of Texas at Austin)

Table 1 Comparison of RE target by various island countries

Country	RE target	Target year
Fiji	100%	2030
Australia	23%	2020
Palau	20%	2020
New Zealand	90%	2025
Samoa	100%	2030
PNG	100%	2030
Kiribati	3%	2020
Tuvalu	100%	2020
Niue	100%	2020
Tonga	50%	2015
Vanuatu	100%	2030
Cook islands	50%	2015
Solomon islands	50%	2015
Trinidad	5% peak	2020
Belize	85%	2017
St. Lucia	35%	2020
Barbados	100%	2021
Bahamas	30%	2030
St. Vincent	60%	2020
Antigua	15%	2030

3.2 Economical

The United Nations classifies 52 countries and territories as Small Island Developing States (SIDS) with fifty million people. Forty-three million inhabitants are living in the Caribbean Islands and the Pacific Islands regions. The economical classifications are diversified within these countries as few of them are comparatively rich with developing country standards, such as Singapore and Bahamas, on the other hand a number of them are still in lower income group, including Comoros, Haiti and Kiribati [21].

Table 2 shows selected indicators on the economic framework for the Caribbean and Pacific Islands. Global economic situations have influenced development prospects for both the regions. Island countries economic developments have always been enormously interrupted with a series of external and internal factors such as a number of natural disasters (cyclones, earthquake) and global oil shudders and the global economic crisis.

According to world bank "For the current 2017 fiscal year, low-income economies are defined as those with a GNI per capita, calculated using the World Bank Atlas method, of $1025 or less in 2015; lower middle-income economies are those with a GNI per capita between $1026 and $4035; upper middle-income economies are those with a GNI per capita between $4036 and $12,475; high-income economies are those with a GNI per capita of $12,476 or more" [24].

Table 2 Selected economic indicators of Caribbean and Pacific islands

Country	Total revenue [22] (percentage of GDP average 2012–5)	Gross debt [22] (percentage of GDP average 2012–15)	GDP per capita [23] CIA estimated in 2014 (USD)	Economic class [19, 24]
Fiji	27.3	48.8	8200	Upper middle
Palau	42.5	NA	16300	Upper middle
Samoa	34.5	53.9	5200	Lower middle
Kiribati	99.3	10.1	1700	Lower middle
Tuvalu	114.7	47.6	3300	Upper middle
Tonga	28.1	NA	4900	Lower middle
Vanuatu	24.4	20.6	2600	Lower middle
Solomon	50.1	14.2	1900	Lower middle
Trinidad	32.3	42.6	32100	High income
Belize	27.7	75.4	8200	Upper middle
St. Lucia	25.9	78.7	11600	Upper middle
Barbados	36.1	95.1	16200	High income
Bahamas	17.8	57.8	25000	High income
St. Vincent	26.7	75.2	10800	Upper middle
Antigua	20.1	95.7	22600	High income

The recent economic trends show that island countries have the capability to utilize their financial resources to introduce renewable energy into the grid and people have the purchasing power to enjoy the private renewable energy systems in Island.

3.3 Social

Social cultural structure of a country plays an important role for the faster growth of renewable energy generation. The factors which should be taken under consideration for PESTLE analysis of renewable energy implementation are energy demand, family and community structure, gender legislative responses and demography.

Family structure and the energy demand could be vital for accepting and rejecting of a particular renewable energy technology by the society. Recently, energy engineers and planner of Bangladesh experienced a rejection of family size solar cooking system which was not appropriate for that particular country [25]. While considering the situation of Pacific Island Countries (PICs) the most common structure of families is based on communal values of lifestyle and in a traditional village, people share the responsibilities and rewards in a community managed by a hereditary leader. The extended structure of family ensures the demand for each and every one.

Gender legislation and equity in work force can bring a success in the implementation renewable energy integration which has been recently experienced in India [26]. To ensure the equity in labor force both Caribbean and Pacific Islands countries are improving the situation every year. Figure 7 shows the labor force participation rate with female to male ratio [22].

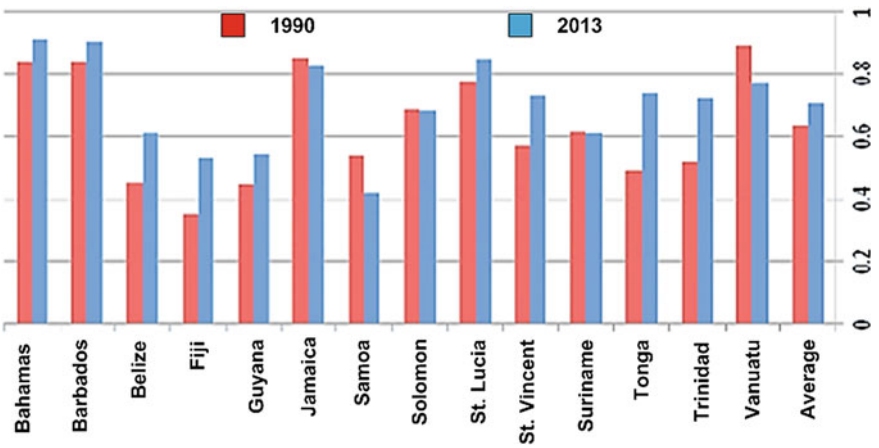

Fig. 7 Labor force participation rates (ages 15–64) with female to male ratios [22]

Most of the Pacific Islands are normally small in size; they are located in extensive distances from the main island and also from each other. As a result, the government is facing huge challenges to electrify these isolated inhabitants. Utility companies are normally supplying electricity only to the main island [27]. The opportunity of small and medium-scale investment in renewable energy sources implementation is enormous in these particular areas due to the social demand and government interest.

3.4 Technological

From the investors point of view Island countries have huge potential for business as most of the technologies required for renewable energy generation need to import from other countries. Most of the Island countries preferred solar photovoltaic (PV) technology for the rural electrification as it decrease system cost and can operate stand-alone mode without any grid connection. For further development on new renewable technologies, few reputed research institute and universities (e.g., The University of the South Pacific, Universidad de Puerto Rico, University of the West Indies, and other universities) have been working based on the local problem associated with renewable energy and they also attracted foreign stockholders for further research in island environments for new technologies. Still the enormous source of ocean energy and geothermal energy sources are unexploded due to the lag of appropriate technologies where government is also interested for foreign invest which is especially true for pacific region [28].

The application of new technologies especially smart grids and microgrids are still very new to these Island countries but few countries already adopted them with the technologies. Implementing more renewable into the grid needs further training on feed in tariff system, smart network design, distributed generation, smart metering, monitoring and control of the grid which indicate a new path way of capacity building, research and investments in renewable energy sector. On the other hand, maintenance and monitoring of these technologies of the existing network is also an issue for the continuous development in energy sector [29]. Table 3 shows the present scenarios of technology support system introduced by various Island countries [19, 20].

3.5 Legal

Confidence of the investors and consumers depend upon the law and order situation of a particular country. Safety and security is a must for the investment and attracts foreign investors. Although most of the governments are trying to ensure a stable law and order situation, but there is still a great concern of security for the investors even today in the Island countries. In recent times, few incidents have been reported

Table 3 Technology support availability in various island countries

Country	Net metering	Feed in tariff
Fiji	x	✓
Australia	✓	✓
Palau	x	x
New Zealand	✓	x
Samoa	✓	✓
PNG	No inf.	No inf.
Kiribati	No inf.	No inf.
Tuvalu	No inf.	No inf.
Niue	No inf.	No inf.
Tonga	No inf.	No inf.
Vanuatu	No inf.	No inf.
Cook islands	No inf.	No inf.
Solomon islands	No inf.	No inf.
Trinidad	x	x
Belize	x	x
St. Lucia	✓	x
Barbados	No inf.	No inf.
Bahamas	No inf.	No inf.
St. Vincent	✓	x
Antigua	No inf.	No inf.

in those countries which indicates lack of respect for the rule of law which caused anxiety and pressures subsequently community problems, including an increasing crime rate and domestic violence. According to United Nation office on Drug and Crime (UNDC), the law and order situation of the Pacific Island countries are in better position with a lower rate in New Zealand (0.9) and highest rate in PNG (10.4) in respect to the murder, while Caribbean Islands are much higher with a lowers rate in Barbados (8.8) and highest rate in Belize (34.4) [30]. Figure 8 shows the comparison of murder rates in various countries of Pacific and Caribbean Islands. Apart from the crime the legal, presence of policies are yet to be finalized in different countries which is not a suitable condition for the potential investors [20].

3.6 Environmental

Renewable sources are readily available in most of the Pacific Island countries [19–21, 31] as well as Caribbean Islands inherited by their geographic location, while the natural disaster like cyclone is a threat for the development and investment in this sector. The environmental impact on RE can be simply explain with frequency of typical cyclone through Pacific and Caribbean Islands as shown in Fig. 9 [32] and Fig. 10 [33], respectively. From Figs. 9 and 10, it is observed that almost every year these island countries are facing tropical cyclone which is a great

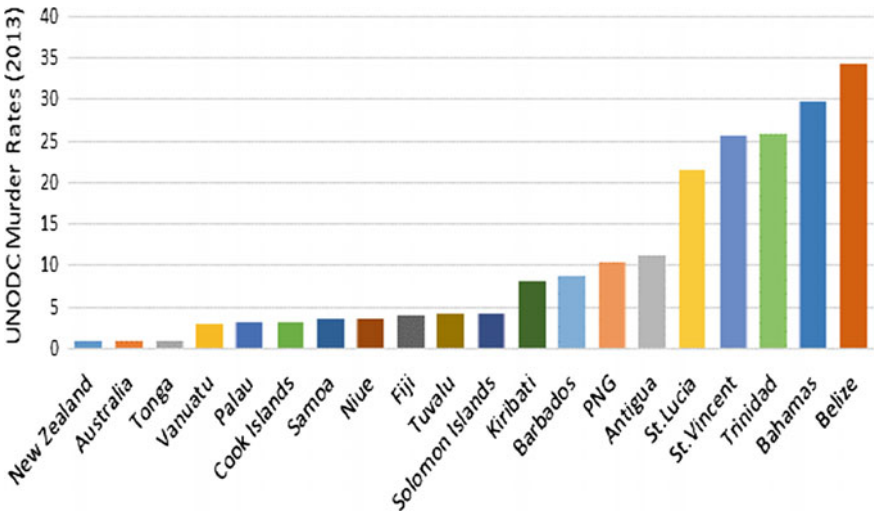

Fig. 8 Comparison of murder rates in various Pacific and Caribbean islands

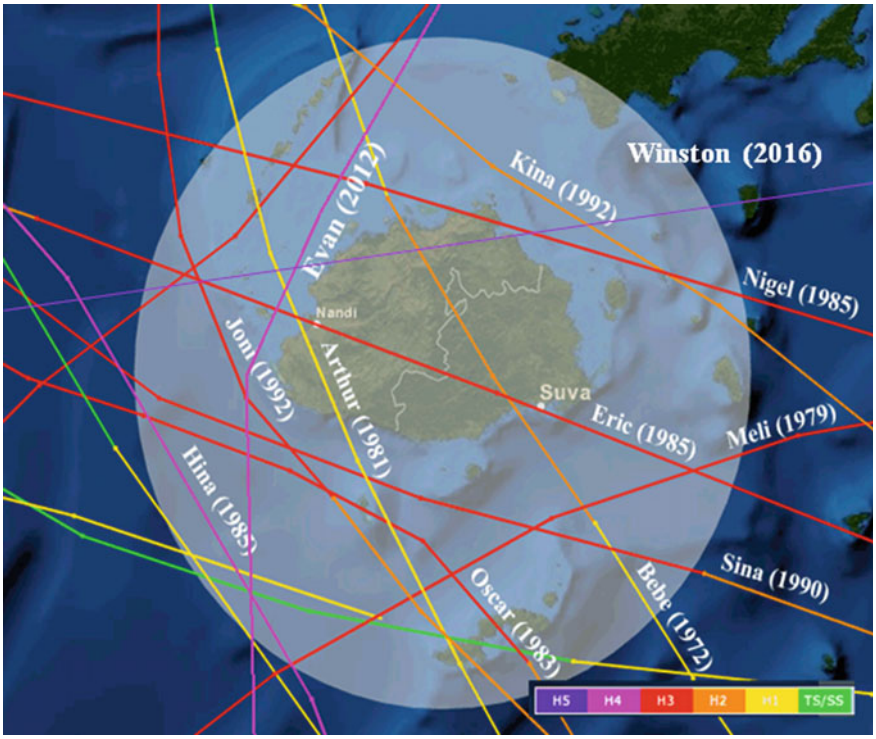

Fig. 9 Tracks of cyclone on record to affect in one of the PICs [32]

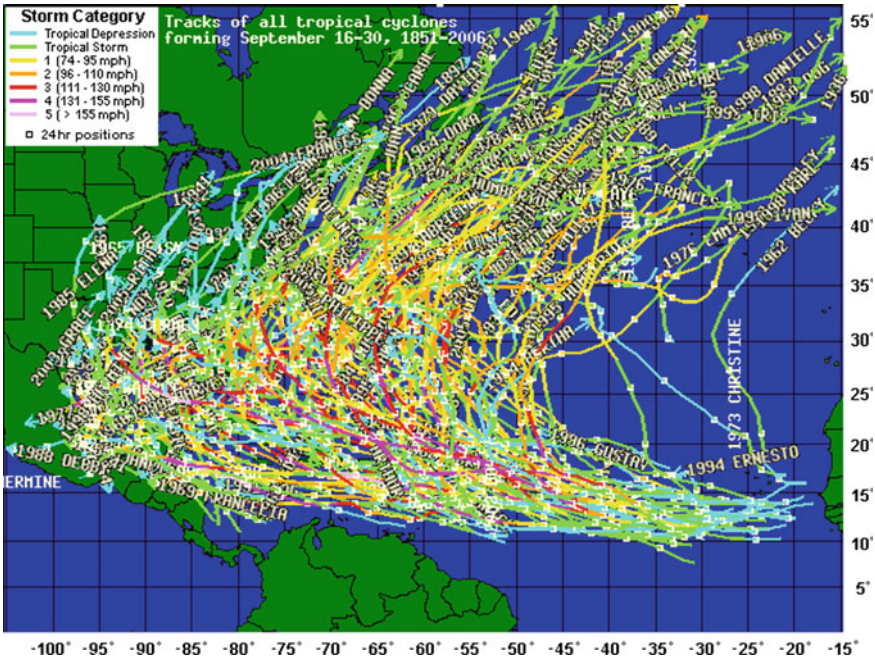

Fig. 10 Tracks of all cyclone on record to affect in Caribbean islands [33]

barrier to the renewable energy integration as few of them become catastrophic even for the whole nation. Recently Fiji and other pacific Island countries experienced such a tropical cyclone TC Winston (category 5) in 2016 which cause an enormous damage to the existing electric network, the intensity of the cyclone is shown in Fig. 11 [34].

4 SWOT Analysis

SWOT is an abbreviation for Strengths (S), Weaknesses (W), Opportunities (O) and Threats (T). To identify the overall strategic position of a business and its environment, SWOT analysis is one of the most popular tools. In SWOT analysis, it is a general assumption that 'O' and 'T' are the external factors with minimum control, on the other hand 'S' and 'W' are the internal factors with essential control for an organization.

The main objectives of SWOT analysis are to determine the strategies for an organization with specific business model considering the organization's resources and abilities suitable for the environment in which the firm will operate.

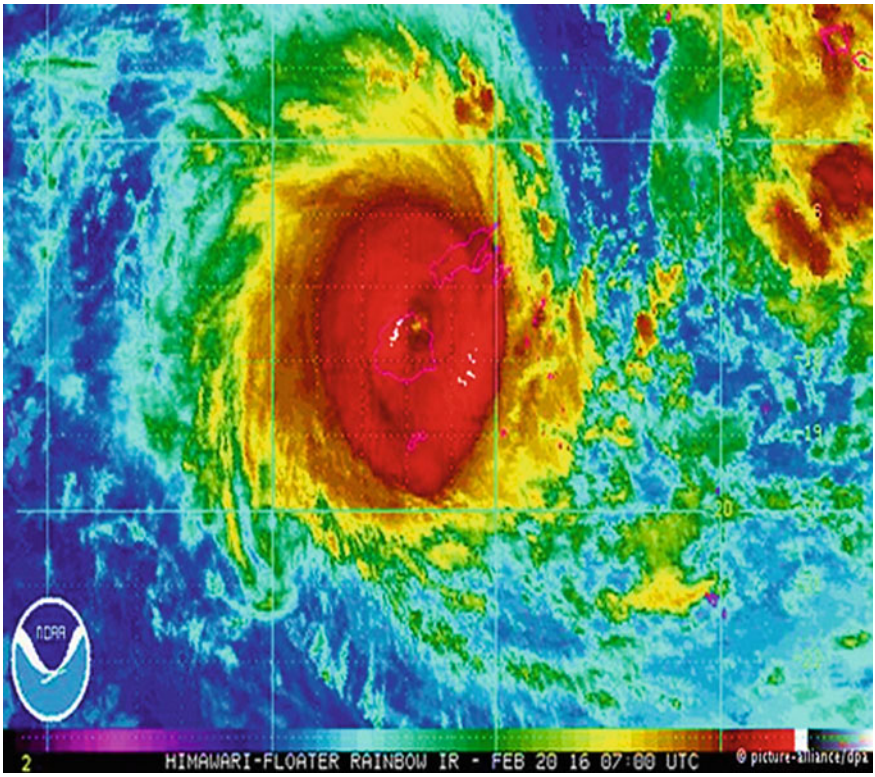

Fig. 11 Fiji in the center of TC Winston 2016 [34]

The renewable energy implementation in various Island countries can be justified using SWOT analysis, where the strength of these countries are the increasing demand for the energy, dependence on the imported fossil fuel, long team financial benefits along with political interest. There are a number of weaknesses in this particular field as most of the island countries have serious problem of infrastructure, especially in the Pacific region. It seems that technologies are lagging behind due to insufficient polices is the major problem associated with the future of RE implementation.

On the other hand, the geographic location with enormous sources of RE are the main opportunity for these countries to become self-sufficient in energy with RE. But unfortunately the natural digester along with the global economy and fuel price always become a threat for the implementation of RE. Figure 12 shows the most common SWOT matrix for renewable energy implementation in those Island countries which may vary a little based on the energy demand, supply and other factors discussed earlier in PESTLE analysis.

Fig. 12 SWOT matrices for renewable energy implementation in island countries

5 Summary

Most of the small island nations faces a lot of barriers and issues that constraint the authorities and investors to promote RE practices toward the sustainable development. Although feasibility studies show potential sites for new projects and such potential attracts expression of interest from different investors. However, the risks and remoteness of the sites and locations give investors second thoughts with hesitations. The factors affecting the initiation, execution, and completion of the potential projects and operation of existing projects can be summarized as:

5.1 Climate

Island countries are prone to at least one or two natural disasters during the cyclone period in every year. Cyclones are accompanied by torrential rain fall which leads to flooding and leads to damages to the existing national grid, and also causes landslides results inaccessibility to the potential sites. It also damages solar farms and wind farms by the strong gust of winds and falling trees or flying objects [35, 36].

Drought is also a major concern to the authorities since the largest renewable generation plants in some Islands countries (i.e., Fiji) are hydro plants. Long spells without rain give authorities no choice but to run thermal generators to meet the demand of electricity [37].

5.2 Financial

In a small developing Island country, it is very difficult to initiate large projects with huge amount of capital investment without any external support. The initial cost to commissioning the project is huge compared to the operating cost of the plants [38, 39]. In order to execute the project, huge loans are taken by companies. To attract funding from investors are not easy as most are hesitant of the past results since only few documentations are made on payback incentive.

5.3 Fuel Shudders

The continuous decrease in fuel price have also discourage renewable energy practice since the thermal generators will be cheaper and will work at higher efficiency upon commission, while renewable energy generation source may not be working as planned out or lead to new problems. However, decreasing fuel prices also gives an implication that a sudden increase is inhabitable since the fuel price trend for many years have portrayed that an increase of fuel price is just in the corner.

The market price of crude oil ($/barrel) fluctuates all year around annually for the past 16 years going from a maximum of about US$150/barrel to a minimum of about US$12/barrel (Fig. 13) [40].

Surprisingly, the increasing demand in the past few years has a drastic decrease in the price of crude oil since each barrel now cost as low as US$60 (Fig. 14) [40].

Since crude prices have decreased drastically promoting renewable energy technologies seem to be a challenge as it is human nature to adopt to cheaper technologies. The reduced price will decrease the generation cost of diesel engines hence increasing profit for the Authorities and will discourage the investors to invest on renewable energy resources due to higher generation cost per kWh.

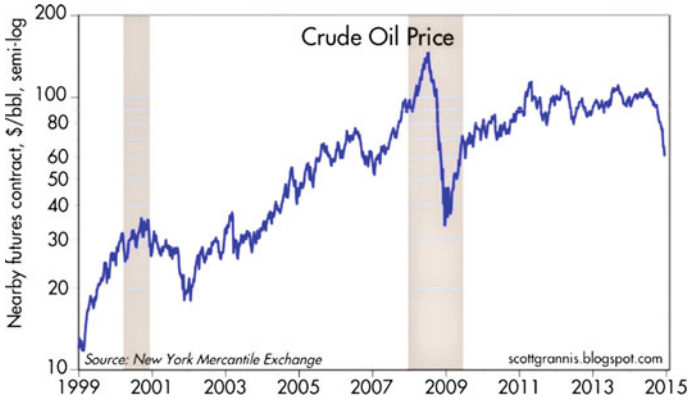

Fig. 13 Historical crude oil prices

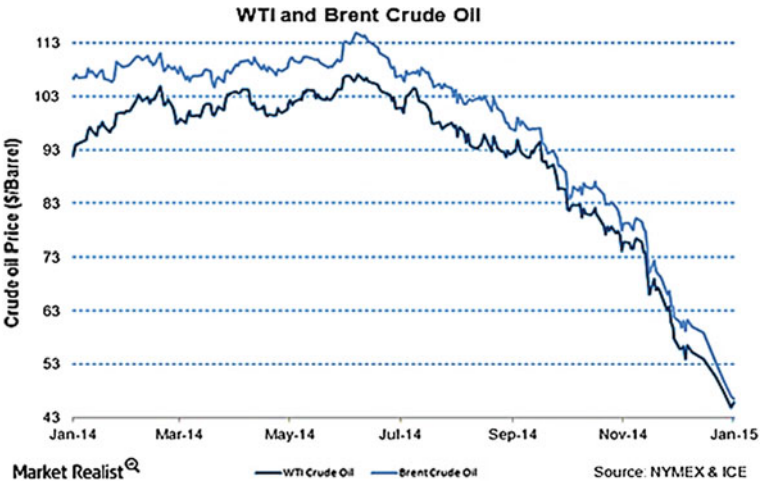

Fig. 14 Falls of crude oil prices during recent months

5.4 Policy

Most of the Island countries have adopted renewable energy policy partially but considering the present situation and the target they set for the year 2020 or 2030 as shown in Table 1, these policies need to be revised or improve. In few countries the energy policies are not yet available or clear, which is actually a major barrier to the implementation of RE.

5.5 Lack of Technical Expertise

It is very natural that Island countries will suffer from the lack of technical expertise to coordinate the renewable energy project independently without external supports. Since most of the Islands are in developing state hence all the major projects on renewable energy resources are done by professionals hired from abroad to carry out the required tasks. A major part of the project fund is paid to external expertise and companies to complete such projects. Also, small island nations pay huge amount of money just to hire expertise on particular field to inspect or consult on potential resources or the existing power plants.

With the enormous opportunities and renewable resources most of the Island countries are below the target level of renewable energy implementation. The overall barriers can be summarized as: capital investment and high cost of access the remote island, climate conditions, sufficient management and technical capacity for management, maintenance and repair of renewable energy systems, socioeconomic structure with small number of population in remote islands. The suggested

pathways to overcome these challenges are attracting national and international investors, building awareness of people for using renewable energy, implementing the energy policy to achieve a secure and sustainable energy network from renewable sources.

References

1. Omer AM (2008) Energy, environment and sustainable development. Renew Sustain Energy Rev 12(9):2265–2300
2. Ghina F (2003) Sustainable development in small island developing states. Environ Dev Sustain 5(1–2):139–165
3. Ernst and Young (2014) Renewable energy review: the island markets. Renewable Energy World Magazine, Dec 2014
4. CARILEC (2010) Tariff survey among member electric utilities (Mid year, June 2010). CARILEC, Castries, St. Lucia
5. FEA (2012) Final determination on electricity tariff rates. Fiji Commerce Commission, Raiwaqa, Suva
6. Fiji Bureau of Statistics (2016) online: http://www.statsfiji.gov.fj/. Accessed on 20 Nov
7. Szczesniak PA, Torres IE (2002) The islands of the caribbean. Miner Yearb 3:119
8. Fertel C, Bahn O, Vaillancourt K, Waaub JP (2013) Canadian energy and climate policies: a SWOT analysis in search of federal/provincial coherence. Energ Policy 63:1139–1150
9. Zalengera C, Blanchard RE, Eames PC, Juma AM, Chitawo ML, Gondwe KT (2014) Overview of the Malawi energy situation and A PESTLE analysis for sustainable development of renewable energy. Renew Sustain Energy Rev 38:335–347
10. Shilei L, Yong W (2009) Target-oriented obstacle analysis by PESTEL modeling of energy efficiency retrofit for existing residential buildings in China's northern heating region. Energ Policy 37(6):2098–2101
11. Terrados J, Almonacid G, Hontoria L (2007) Regional energy planning through SWOT analysis and strategic planning tools: Impact on renewables develbopment. Renew Sustain Energy Rev 11(6):1275–1287
12. Markovska N, Taseska V, Pop-Jordanov J (2009) SWOT analysis of the national energy sector for sustainable energy development. Energy 34(6):752–756
13. Chen WM, Kim H, Yamaguchi H (2014) Renewable energy in eastern Asia: renewable energy policy review and comparative SWOT analysis for promoting renewable energy in Japan, South Korea, and Taiwan. Energ Policy 74:319–329
14. Helms MM, Nixon J (2010) Exploring SWOT analysis-where are we now? A review of academic research from the last decade. J Strat Manage 3(3):215–251
15. Valentin EK (2001) SWOT analysis from a resource-based view. J Mark Theory Pract 9(2):54–69
16. Meditz SW, Hanratty DM (1987) Caribbean islands: a country study. Federal Research Division, Library of Congress
17. Corbett J (2015) Everybody knows everybody: practising politics in the Pacific islands. Democratization 22(1):51–72
18. United State Department of State (2015) Fiji 2015 crime and safety report. Available online: https://www.osac.gov/pages/ContentReportDetails.aspx?cid=17099
19. REN 16, Renewable (2016) Global status report, (Paris: REN21 Secretariat). ISBN 978-3-9818107-0-7. Available online: http://www.ren21.net/wp-content/uploads/2016/06/GSR_2016_Full_Report_REN21.pdf
20. IRENA (International Renewable Energy Agency) (2012) IRENA policy brief: policy challenges for renewable energy deployment in Pacific island countries and territories. IRENA, United Arab Emirates, p 24

21. Naudé W, McGillivray M, Santos-Paulino AU (2010) The challenge of Small island Developing states, United Nations University. Available online: https://www.wider.unu.edu/publication/challenge-small-island-developing-states
22. Christie TAL, Thakur D (2016) Caribbean and Pacific islands: a survey of gender budgeting efforts. IMF Working Paper Research Department and Strategy, Policy, and Review Department
23. CIA (2015) GDP—PER CAPITA (PPP). CIA world factbook. Archived from the original on Sept 19. Online available: https://web.archive.org/web/20150919160323/, https://www.cia.gov/library//publications/the-world-factbook/fields/2004.html#. Access on 20 Nov 2016
24. The World Bank (2016) World bank country and lending groups-current classification by income. Online available: https://datahelpdesk.worldbank.org/knowledgebase/articles/906519 . Accessed on 20 Nov 2016
25. Mondal MAH, Kamp LM, Pachova NI (2010) Drivers, barriers, and strategies for implementation of renewable energy technologies in rural areas in Bangladesh—an innovation system analysis. Energ Policy 38(8):4626–4634
26. Soma Dutta (2015) Women, energy and economic empowerment, boiling point, issue 66. Available online: http://www.energia.org/cms/wp-content/uploads/2015/07/BP66-Women-Energy-and-Economic-Empowerment-.compressed.pdf
27. Annual Report—Fiji Electricity Authority (2014) Online available: www.fea.com.fj/wp-content/uploads/2015/09/FEA-Annual-Report-2014.pdf. Access on 12 June 2016
28. Mohanty M (2012) New renewable energy sources, green energy development and climate change: implications to Pacific Island countries. Manage Environ Qual Int J 23(3):264–274
29. Islam FR, Mamun KA (2016) Reliability evaluation of power network: a case study of Fiji islands. In: Australasian universities power engineering conference (AUPEC-2016), Brisbane, Australia, 25–28 September 2016
30. UNODC report (2013) Global study on Homicide-trends, contexts, data, United Nations Office on drugs and crime, Vienna, Australia. Available online: http://www.unodc.org/documents/gsh/pdfs/2014_GLOBAL_HOMICIDE_BOOK_web.pdf
31. Islam FR, Mamun KA (2016) Opportunities and challenges of implementing renewable energy in Fiji Islands. In: Australasian universities power engineering conference (AUPEC-2016), Brisbane, Australia, 25–28 September 2016
32. Masters J, Henson B (2016) Fiji pounded by its first category 5 storm on record: tropical cyclone Winston, WunderBlog, Feb 19. Available online: https://www.wunderground.com/blog/JeffMasters/fiji-pounded-by-its-first-category-5-storm-on-record-tropical-cyclone
33. Masters J (2008) November Atlantic hurricane season outlook, WunderBlog, Oct 31. Available online: https://www.wunderground.com/blog/JeffMasters/archive.html?year=2008&month=10
34. Thomas A (2016) Fiji: 'total destruction' in island hit by cyclone, Aljazeera, Feb 24. Available online: http://www.aljazeera.com/blogs/asia/2016/02/fiji-total-destruction-island-hit-cyclone-160223125031408.html
35. Yu X, Taplin R (1997) A survey: international aid for renewable energy in the Pacific Islands since the 1970s. Energ Policy 25(5):501–516
36. Ellison AM, Farnsworth EJ (1996) Anthropogenic disturbance of Caribbean mangrove ecosystems: past impacts, present trends, and future predictions. Biotropica:549–565
37. Smith GC, Covich AP, Brasher AM (2003) An ecological perspective on the biodiversity of tropical island streams. Bioscience 53(11):1048–1051
38. Weisser D (2004) On the economics of electricity consumption in small island developing states: a role for renewable energy technologies? Energ Policy 32(1):127–140
39. Timilsina GR, Shah KU (2016) Filling the gaps: policy supports and interventions for scaling up renewable energy development in Small island Developing states. Energ Policy40
40. Macrotrends (2017) Crude Oil Prices − 70 Year Historical Chart, Available online: http://www.macrotrends.net/1369/crude-oil-price-history-chart. Access on 11 Dec 2016

Utilization and Optimization of Diesel Generation for Maximum Renewable Energy Integration

J.M. Hamilton, M. Negnevitsky, X. Wang, A. Tavakoli and M. Mueller-Stoffels

Abstract Globally, the vast majority of generation within off-grid communities is supplied via diesel generation. The extent to which renewable energy source (RES) technologies can be effectively integrated into these systems depends, to a large degree, on the configuration and control of such existing infrastructure. Utilization and optimization of existing diesel generation is accordingly a key consideration for any successful RES proposal. This chapter explores both modern and legacy diesel technology and control, as available to maximize RES penetration within a hybrid diesel islanded network. Diesel generators are relatively inexpensive to purchase, offering a proven, reliable and stable generation source. Diesel generation is also supported via the ease and availability of both supplier engagement and technical expertise, services readily at hand to consumers. Their downside has proven to be the diesel fuel itself, given both volatile commodity pricing and damaging environmental emissions. These issues have created opportunity for alternative generation sources, and as we will seen throughout the proceeding chapters, the advent of both available and cost competitive RES technologies has given remote communities genuine generation alternatives. RES technologies will become increasingly important to island countries as they seek to reduce their emissions and operational costs. How readily RES technologies are adopted, will depend on how effectively these technologies can be integrated into

J.M. Hamilton (✉) · M. Negnevitsky · X. Wang · A. Tavakoli
Centre for Renewable Energy and Power System, School of Engineering,
ICT University of Tasmania, Hobart, TAS 7001, Australia
e-mail: james.hamilton@utas.edu.au

M. Negnevitsky
e-mail: michael.negnevitsky@utas.edu.au

X. Wang
e-mail: xiaolin.wang@utas.edu.au

A. Tavakoli
e-mail: ahmad.tavakoli@utas.edu.au

M. Mueller-Stoffels
Alaskan Centre for Energy and Power (ACEP), Institute of Northern Engineering,
University of Alaska Fairbanks, Fairbanks, AK 99755, USA
e-mail: mmuellerstoffels@alaska.edu

F.M.R. Islam et al. (eds.), *Smart Energy Grid Design for Island Countries*,
Green Energy and Technology, DOI 10.1007/978-3-319-50197-0_2

existing networks, with this chapter advocating a hybrid diesel architecture as one solution to quickly and effectively deliver high RES penetrations. How do islanded countries embrace the challenges and opportunities of emerging RES technologies? Will diesel generators become obsolete within these future power systems structures? This chapter considers these queries, presenting existing generation as part of the recommended transition. In discussing the role of conventional generation, the audience is asked to recognize the residual value within legacy assets, identifying a cost optimized pathway for improved RES integration.

1 Introduction

Globally, diesel accounts for the majority of generation into off-grid and remote power systems [1, 2], with these communities exposed to some of the world's highest power prices [3–6]. Renewable energy source (RES) technologies are becoming increasingly relevant to these consumers, as they seek to not only lower their cost of energy, but also reduce the environmental emissions directly resultant from diesel fuel use [7, 8]. Power systems incorporating both conventional (thermal) and RES generation are termed hybrid power systems (HPS's). Unfortunately while RES technologies can offer cost competitive supply alternatives, their output is unpredictable, and at high levels of RES penetration a potential conflict arises. As RES penetration increases within a HPS, diesel generators constrain RES utilization, unable to lower their output below minimum load settings. These load set points are predetermined to ensure engine efficiency and preserve engine condition. Under high RES penetration, diesel load set points produce surplus generation, which must be absorbed via regulating devices such as dump loads or energy storages systems. Hence systems configured for high RES penetration currently involve increased complexity, expense and waste. Regardless of approach, it is not currently feasible to totally eliminate diesel generation within a HPS. Instead, minimal diesel usage is targeted.

Ancillary technologies available to increase RES penetration include battery, flywheel, dump load and demand management systems. All technologies require significant investment, increasing the possible RES penetration, but also increasing the HPS complexity. Improved access to RES technologies requires architectures offering minimal diesel and ancillary reliance. A key challenge in reducing the dependence on such technologies remains the performance of existing diesel generators, specifically their inability to run sustained at low loads [9, 10].

This chapter presents one approach to achieve a cost optimized level of RES penetration within a HPS. One which provides much of the benefit associated with prior ancillary approaches, yet at a fraction of the expense. Low load diesel is the ability to run diesel infrastructure below legacy load limits, for the acceptance of additional RES contribution. The chapter commences with discussion of the historical context and relevance of diesel generation, before introducing consideration for both the diesel fuel and emissions compliance aspects. The opportunities and

challenges for diesel generation within islanded countries are then presented, ahead of recent developments within advanced diesel technology and control. Operational theory is briefly discussed, before model development and case study methodologies, both adopted to determine the impact of hybrid diesel power system performance under low load diesel application. Given consideration of the economies of low load diesel, the chapter concludes, finding low load diesel application to offer a viable, low cost, low complexity pathway to improved RES utilization.

2 Historical Diesel Perspectives

Rudolf Diesel invented the compression ignition engine in 1892, and since then our understanding, utilization and demand for the internal combustion engine has continued to grow and evolve within our environment. Diesel's first engine found little commercial application; it was not until he replaced the conventional fuel of the day, coal, with a by-product from the recent crude oil boom, that he developed a successful prototype engine. Today, both engine and fuel bear his name, having found application extensively across the transport (automotive, trucking, marine and rail), industrial and mining sectors. Stationary power generation remains only a small subset of this wider diesel engine market. This statement contrast dramatically with the prevalence of the diesel generator within islanded networks, by both installed capacity and total annual generation, diesel remains the largest energy supplier to islanded consumers globally [4, 11]. Diesel generation is accordingly critical for islanded communities, yet represents only a small percentage of any diesel suppliers' order book. It is primarily for this reason, that diesel technology research and development has failed to prioritise stationary power generation applications over the past decade. This is not to say that modern diesel technological and control advances have not been significant, it is simply to point out that they have not been progressed to address any perceived consumer need within islanded power systems. Modern technological and control advances have in reality, been driven by efficiency and compliance initiatives targeting the larger transport and industrial markets, with this technology filtering down into stationary power generation product lines via the economies of generic/commoditised engine platforms (shared engine platforms across markets). The distinction is subtle; however, the resultant technology pass-through presents significant opportunity for islanded networks, should they explore the full range of modern diesel generator capabilities.

How has the diesel generator risen to such prominence within islanded networks? For one very telling reason, the ease and availability of equipment, fuel and technical expertise. Diesel generator and fuel supply networks are well established to practically every corner of the globe [12]. Diesel generators power Antarctic expeditions as readily as they supply nomadic desert tribes, with little need to deviate from stock standard engine architectures. Diesel generation has been demonstrated in such remote applications for decades, representing a low risk

supply approach. Indeed given both the geographic isolation and entrenched operational practices, diesel generators have, in many instances, been seen as the only generation options for islanded communities. Add the short lead times and small capital investment, and you can appreciate why diesel generation now represents the majority of existing and planned generation to islanded consumers [13]. Unfortunately, some significant downsides are associated with large-scale adoption of diesel generators for energy supply, principally diesel price volatility and diesel fuel emissions [14].

3 Diesel Fuel

Consideration of diesel fuel characteristics is always relevant in consideration of diesel generator performance, given the ability to bias performance comparisons via the introduction of non-standard fuel or atmospheric conditions (one reason for diesel test standards). Diesel fuel also represents the largest single contributor to the levelized cost of diesel electricity within islanded countries [15]. Thus, some familiarity of diesel fuel standards and test conventions is essential for the engineer in assessing the role of diesel generation within any power system. The term diesel fuel can refer to any fuel used within a compression ignition engine, however commonly refers to fuels refined for commercial vehicle use (ASTM International grade 2-D for the United States). Importantly such classification and standards set defined limits for the viscosity, volatility, cleanliness, density, acidity, low temperature performance, stability and heating value for various grades of diesel fuel. Such parameters are relevant to the operation of islanded diesel fired generation given their impact on the operability, reliability, cost and cleanliness of the resultant energy provision. Viscosity, the resistance to flow, is critical to successful lubrication where the fuel itself provides a barrier to opposing surfaces. For diesel fired generation this characteristic impacts fuel pump and injector performance, with both components at least partially dependent on the fuel for lubrication. Importantly, fuel cleanliness is also key to successful lubrication, with both inorganic components and organic acids responsible for abrasive and corrosive engine wear at certain levels.

Low temperature operability involves the solidification of wax components under certain temperatures, with the potential to gel the fuel. The quality of fuel available for islanded generation thus has an appreciable impact on engine performance, with any change to fuel quality likely to impact system performance [16]. Such considerations are most commonly encountered when biodiesel blending is contemplated. Biodiesel is the synthesis of vegetable or animal-based diesel fuel, as opposed to a fractional distillate of crude oil. Biodiesel blending, as the name suggests, involves the addition of biodiesel to crude based diesel products, and is considered further, separately in this chapter. Biodiesel blending represents a common approach to reduce diesel emissions, and while the potential to reduce the environmental impact of diesel generation exists, the quality of the fuel must be accessed to fully appreciate the engine and emission impacts.

Diesel fuel comprises of thousands of individual hydrocarbon components, most of which have a carbon number between 10 and 20, as shown in Fig. 1. Most commonly these compounds represent hydrocarbons from the paraffinic, iso-paraffinic, naphthenic or aromatic classes [17]. The impact of hydrocarbon class to fuel properties is summarized in Table 1.

The cetane number of a diesel fuel represents a measure of the combustion speed and ignition quality. It is an inverse of the octane rating, similarly used to define gasoline (petrol) fuel auto ignition tendency. The higher the cetane number, the superior the fuel quality.

Fuel density is conventionally represented as kg/m^3 or g/cm^3, representing the mass per unit volume of the fuel. Relatively density, sometimes referred to as specific gravity, is defined as the ratio of fuel density to the density of water at a reference temperature. Another common measure for fuel density used in the United States is API gravity, expressed as degrees API, Eq. 1 [18].

$$\text{API}^0 = \left(\frac{141.5}{\text{relative density}}\right) - 131.5 \tag{1}$$

The heating value of fuel is the heat energy released upon ignition as represented adopting either a mass or volumetric basis. To convert between one to the other, the density of the fuel is used. Common values for both density and net heating value are shown in Table 2. The heating value of petroleum fuels can be estimated via Eq. 2 [18].

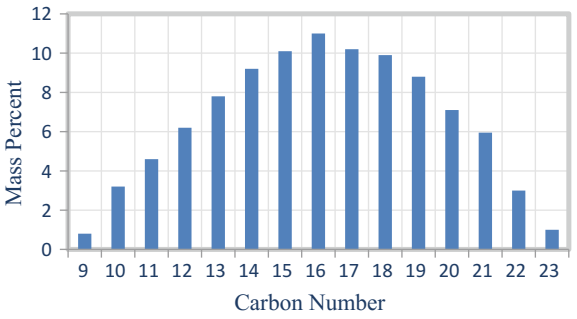

Fig. 1 Diesel fuel generic carbon distribution. *Source* Chevron 2007 [17]

Table 1 Hydrocarbon class fuel performance properties

Fuel property	n-Paraffin	Isoparaffin	Naphthene	Aromatic
Cetane number	++	+/0	+/0	0/−
Low temperature operability	−	+/0	+	+
Heating Value	−	−	0	+

+ positive or beneficial impact on fuel
0 neutral or minimal impact on fuel
− negative or detrimental impact on fuel
Source DieselNet 2013 [18]

Table 2 Density and net heating value of different fuels

Fuel	Density(15 °C) g/cm^3	Net heating value			
		MJ/kg	Btu/lb	MJ/m^3	Btu/gal
Gasoline	0.735	43.33	18,630	31,830	114,200
Premium gasoline	0.755	42.89	18,440	32,390	116,200
Jet fuel	0.795	42.85	18,420	34,060	122,200
Diesel fuel	0.850	42.64	18,330	36,240	130,000

Source DieselNet 2013 [18]

$$\text{Net Heating (MJ/kg)} = \left(46.423 - 8.972\rho^2 + 3.170\rho\right)(1 - (x + y + z)) + 9.420z - 2.499x \quad (2)$$

where

ρ represent the fuel density in g/cm^3 at 15 °C,
x represents the mass fraction of water,
y represents the mass fraction of ash,
z represents the mass fraction of sulfur.

4 Emissions Compliance

Intuitively, the engineer understands the link between engine load and temperature, a heavily loaded engine becoming hot in a very short time. From an emissions perspective, any change in engine and thus exhaust temperature, has a significant impact on exhaust emissions. In part such emissions performance is representative of combustion efficiency, however, thermal deactivation of the after treatment catalysts can also play a significant role. Hybrid diesel architectures place additional requirements on the way diesel engines are loaded and operate, and in doing so, detrimentally impact the emissions performance of the system.

Until recently, emissions compliance was approached via engine redesign, largely targeting combustion refinement. Engines have simply been made more efficient to meet prescribed targets. However, with increasingly stringent emissions limits, the rate of technology development is proving insufficient to deliver the required performance. Engine manufacturers are in addition to efficiency improvement, increasingly forced to adopt post combustion emissions treatment. As a result, most new diesel engines sold into regulated markets, now offer some form of advanced exhaust after treatment. Discussion on this topic is particularly relevant to systems targeting high RES penetration, given the temperature critical nature of many exhaust after treatment approaches (chemical treatments/catalytic reactions, for example), and the notable impact high RES penetration has on engine loading and thus exhaust temperatures.

Diesel engines, as with all combustion engines, produce an exhaust stream, expelling unwanted by products via the combustion process. Under ideal combustion conditions, these emissions would consist of carbon dioxide (CO_2), water vapour (H_2O) and unreacted air charge, Nitrogen (N_2) and Oxygen (O_2). Unfortunately, ideal combustion conditions are almost impossible to recreate, given the complexities of the process, and as such additional pollutants are also exhausted to atmosphere. These pollutants result from any combination of unburnt fuel, the presence of foreign substances (lubrication oil or particles of engine wear), catalytic reactions, or any combination of reactive components exposed to the high temperature and pressures resultant in the cylinder during combustion. Common pollutants include carbon monoxide (CO), various hydrocarbons (H_mC_n), nitrogen oxides (NO_x), sulphur oxides (SO_x) and particulate matter (PM) [19]. It is even possible for exhaust after treatment system to contribute additional components to the exhaust profile, thus any change in engine duty cycle, fuel, control or environment needs to consider the possibility of emission variation and non-compliance.

Diesel emissions become a problem when the unwanted exhaust gases or pollutants exceed threshold quantities. One complexity of exhaust emissions compliance remains the different engine processes responsible for different pollution types. A risk to any engine modification program remains the possibility that measures successful in addressing one specific emission parameter, subsequently impact/increase the levels of other pollutants. A co-ordinated emissions compliance approach is thus a complex undertaking. In addition, increased attention is now being paid to particulate size, with various adverse health impacts linked to not only the type and volume of pollutant, but also the particle sizing. One common approach to classification of diesel exhaust particle matter defines particulates less the 10μm according aerodynamic diameter as follows (diameter of 1 g/cm^3 sphere) [20];

- *PM_{10}*—particles less than 10μm (typically material originating from engine wear)
- *Fine*—particles less than 2.5 μm
- *Ultrafine*—particles less than 0.1 μm (typically heavier hydrocarbons)
- *Nano*—particles less than 0.05 μm (typically lighter hydrocarbons).

A typical PM size distribution is presented in Fig. 2 with two distributions, by number and by mass provided. Of relevance, the reader should note the high percentage of PM content within the nanoparticle range. PM exhaust emissions are thus characterized by a large number of very small, very light particles. These particles are so light that they have essentially no appreciable impact on the total mass of PM, with the tendency to beoverlooked. The distinction is important given increasing concern over the health impacts of small particle exposure (particles which penetrate deeper into organic tissue given their size), with modern engines performance standards evolving to address PM emission by both number and mass.

Carbon dioxide (CO_2) contributes the largest relative concentration of all such pollutant exhaust gases, principally given its role within the ideal combustion cycle; unfortunately, it is also a key contributor to human induced climate change, with

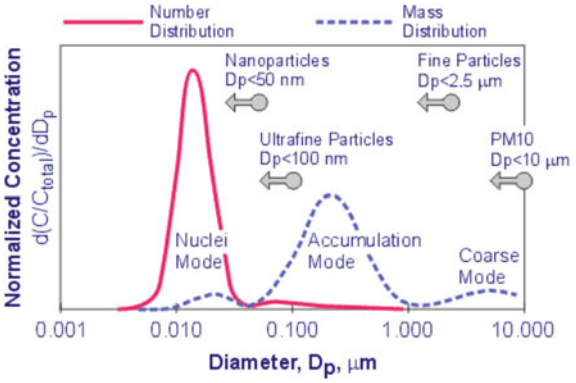

Fig. 2 Diesel particulate size distributions. *Source* DieselNet 2013 [20]

recent increases in the atmospheric levels of CO_2 known to play a role in the adverse warming of the earth's climate. CO_2 emissions are directly correlated to an engine's fuel consumption, and thus improvements in engine fuel efficiency directly result in reduced CO_2 emissions.

Carbon monoxide (CO) is a colourless, odourless gas, which becomes flammable at high concentrations. CO emissions from diesel engines typically range from 10 to 500 ppm [21], although exceedance of these limits can occur during engine transients. The oxidation of CO with O_2 over certain catalysts can release a significant amount of heat, resulting in possible thermal deterioration of various emissions after treatment technologies.

Hydrocarbons (H_nC_m) and particulate matter largely result from unburnt fuel and lubrication oil, with the latter effectively controlled with exhaust particulate filters. The generic formula for hydrocarbons represents n atoms of hydrogen with m atoms of carbon. Hydrocarbon gases may exhibit an irritating odour, and can be carcinogenic. Concentrations of hydrocarbons in diesel exhaust typically range from 20 to 300 ppm [21].

Nitrogen oxides (NO_x) principally consist of Nitric oxide (NO), and Nitrogen dioxide (NO_2), both poisonous and highly reactive gases. Concentrations of NO_x within diesel exhaust emissions are typically between 50 and 1000 ppm [21]. While NO is a colourless, odourless gas, NO_2 is a red/brown gas of unpleasant odour. NO_x have been identified as principal agent in the formation of ozone (smog) on hot summer days. As NO_x formation remains temperature dependent, one effective way to reduce NO_x formation is to lower the cylinder temperature. Selective catalytic reduction (SCR) of NO_x with urea has also proved highly effective at controlling NO_x emissions [22].

Sulphur oxides (SO_x), SO_2 and SO_3 generally originate from sulphur present in diesel fuel and lubricating oils, as a result efforts to limit sulphur oxides have involved the development of low sulphur and sulphur free fuels. For low sulphur fuels, lubrication oil consumption can start to present as a major source of SO_x emissions.

Measurement of diesel exhaust emissions are typically performed on a dynamometer test stand, with the dynamometer responsible for providing resistance to the engine torque via mechanical or electric resistance, Fig. 3. Pollution is typically recorded as grams of pollutant released per kWh of mechanical energy. It is important to note the destination between mechanical and electrical energy, for a diesel generator, engine mechanical output is always higher than the generator's electrical output (considering for losses in the generator). Engine manufacturers will typically use kWh mechanical (kWh_m) as a metric for fuel consumption and emissions reporting, with the reader required to confirm a similar measurement basis for any two test reports prior to comparison. The engine is run through a predetermined test cycle representative of real life operation. It is typical for high ramp rate events, common within a hybrid diesel system under high RES penetration, to represent a large share of any averaged emissions contribution, despite these events representing only a small percentage of total operating hours. Exhaust gas is typically collected by the sampling instrument, Fig. 4, prepared for analysis (including dilution and chilling) and analyzed using any one of electrochemical, infra-red or magnetic response.

Commercially available exhaust gas emissions sensors conveniently package multiple analysis technologies into a single unit, with the user able to operate the instrument without knowledge of the underlying principal. In this regard, emissions performance testing is simplified, however the operator should be aware of the specific instrument accuracy, sampling and response times as these are often insufficient to capture transient response. PM emissions are treated separately from gases exhaust emissions, with analysis typically using either opacity (optical) or

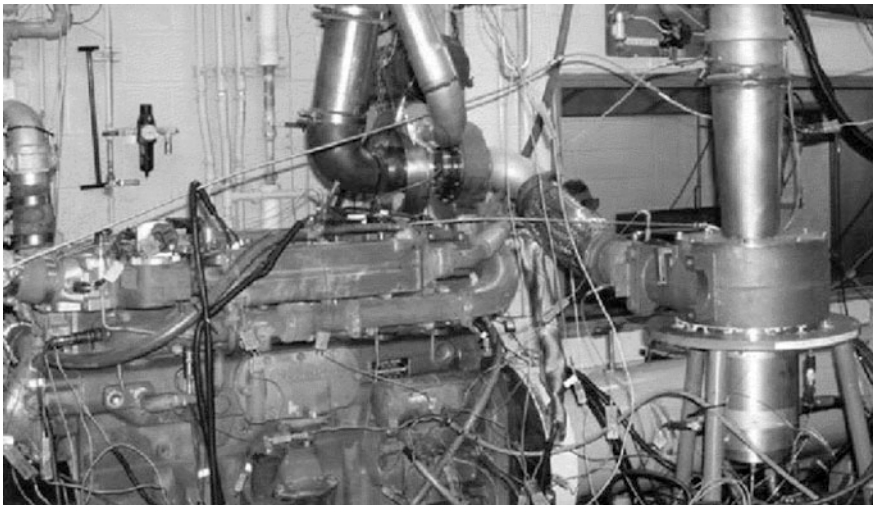

Fig. 3 Diesel engine test bed. *Source* John Deere 2005 [23]

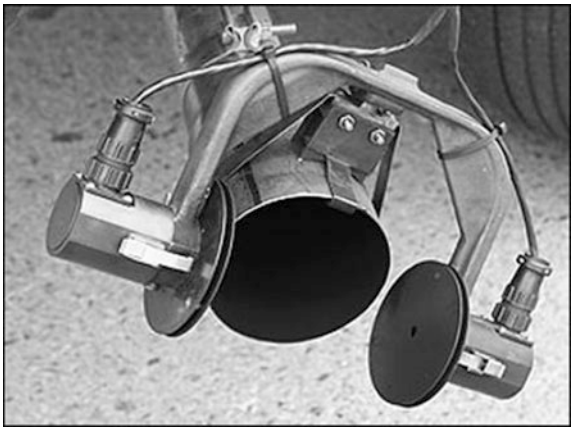

Fig. 4 Exhaust emissions measurement equipment. *Source* DieselNet [24]

gravimetric (weight) assessment of deposited particles to determine the PM mass. Under both of these approaches, comparison across tests can be poor unless the methodology is standardized, hence PM measurements are notoriously hard to correlate across dissimilar test and of most benefit in determining relative variations.

Diesel particulate filters are the most common and cost effective form of post exhaust solid phase emissions treatment, consisting simply of a particulate trap. The filter screens the exhaust flow utilizing a number of possible filtration mechanisms to remove particles from the exhaust stream. Such particles are primarily carbon soot, with the volume of soot sufficient to obstruct flow through the filter in as little as a few hours of operation. Diesel particulate filters subsequently use filter regeneration techniques to extend the service life of the filter indefinitely. In principal, these techniques allow for the supply of heat and air to the embodied carbon for the promotion of oxidation to gaseous CO_2.

Emissions control catalysts are the most common and cost effective form of post exhaust gas phase emissions treatment, consisting simply of passive catalyst system through which the exhaust gas is diverted. Catalytic converters typically adopt a noble metal as the active catalyst, such as platinum (Pt), palladium (Pd) or rhodium (Rh). Diesel oxidation catalysts have been used successfully to control CO, H_mC_n, and organic PM via oxidation of these exhaust gas compounds. Unfortunately, oxidation is also the mechanism for SO_x reaction to sulphuric acid H_2SO_4. Diesel oxidation catalysts are generally not effective at oxidation of NO_x emissions, with SCR catalysts generally adopted for this task. Another disadvantage of this approach is the temperature dependent performance of many catalysts, with reaction conversions increasing with temperature. Accordingly, function at light load and low temperature can present some problems for catalytic conversion systems, Fig. 5. A potential solution to light load applications has been the use of element absorbers to store emission contaminants (washcoat storage), until higher engine

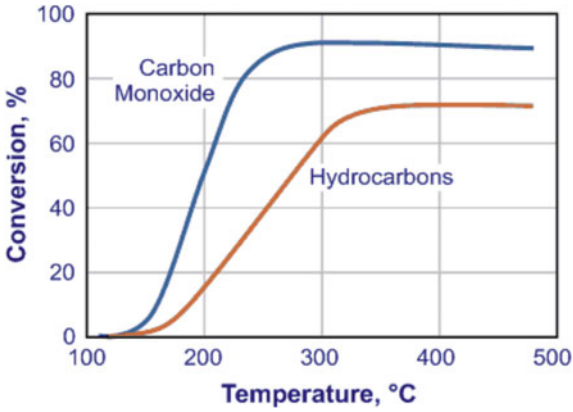

Fig. 5 CO and HC conversion in diesel oxidation catalyst. *Source* DieselNet [25]

loading provides more favourable catalytic temperatures, this approach however also adds further complexity to the emissions process.

The engineer charged with RES integration can start to appreciate the complexities of emissions compliance in addition to the integration and control requirements of any hybrid diesel architecture. In support of this goal, the significant reduction in total kWh generated via diesel supply can be used to demonstrate significant net environmental and health improvements, however should per kWh emissions performance exceed acceptable limits, modification to the after treatment system may be required.

5 Islanded Markets, Challenges and Opportunities

The preceding discussion could quickly lead the reader to form an overwhelming negative view towards existing diesel generation, however in moderation, existing diesel generation presents islanded communities with a supportive platform from which to advance RES integration. Admittedly, diesel fuel is expensive, both as a commodity and considering the environmental impact associated with its extraction, refinement, transportation, storage and eventual consumption [27]. Diesel fuel is however, in amble supply and can safely be stored, providing energy reserves for systems looking to stabilize a stochastic renewable energy supply. The challenge for many islanded countries is thus to, as far as possible, minimize diesel generation, via the introduction of alternative generation, and to limit diesel utilization to the provision of essential services, those unavailable from commercial RES's. The opportunity remains to transition diesel from a base load energy source to an energy storage source, and in doing so provide islanded communities with a pathway to reduced diesel reliance.

Estimates as to the global market capacity of installed diesel generators is in the order of 1000 GW, and growing, to meet the needs of emerging economies and

communities hungry for electrification. This market serves among other communities the more than 10,000 inhabited islands around the world, home to an estimated 750 million islanders [28]. Within Asia, Indonesia itself claims over 1000 habited islands, with a national policy in place to achieve 70–90% electrification over the coming years. The state-owned electricity company, PNL, has an ambitious "1000 islands" program to deliver solar diesel hybrid systems across their portfolio. Within the Pacific Islands and Territories, a community exceeding some 3000 islands, major population centers rely almost exclusively on diesel generation, while at the same time facing the worlds' highest fuel costs [6]. Given a global push for increased electrification, growth in islanded consumption and reducing RES costs, these communities are increasingly turning to RES technologies to provide for their future energy needs. Acknowledgeing that 97% of these communities currently rely exclusively on diesel generation, there is both urgent and expansive opportunity to implement renewable energy systems into this market.

Case studies reviewing the cost of diesel fired generation across the pacific quantify the cost of diesel based electricity supply as between $300 and $400 US per MWh. A similar review of off-grid diesel fired generation costs for mining operations across Australia is presented in Fig. 6. It can be readily appreciated that for both wind and solar technologies returning a cost of generation under $200 US MWh, there exists amble scope for RES integration into these diesel systems. Modelling across the same pacific case studies referenced earlier concluding cost savings of between 12 and 16%, with PV generation contributing between 30 and 40% of the total island generation [5].

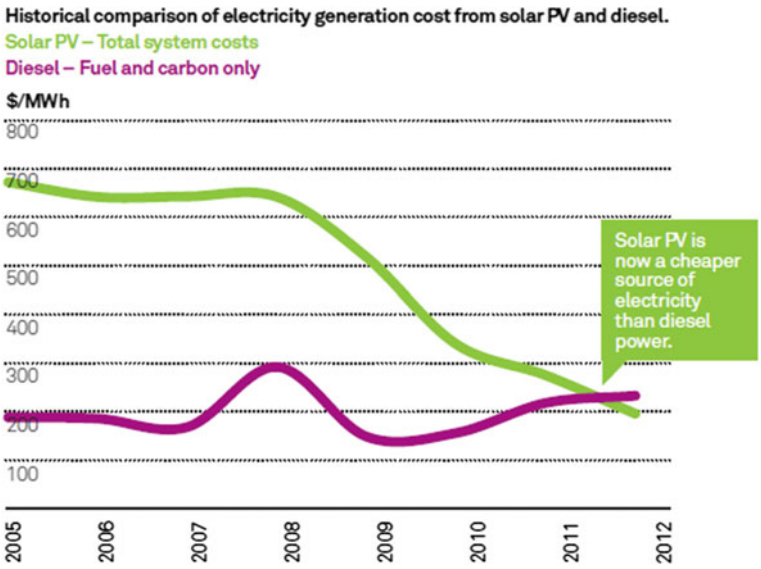

Fig. 6 Solar PV versus diesel generation cost comparison. *Source* AECOM 2012 [26]

While economic and environmental justification for RES integration appears straight forward, there are a number of issues to address. First the economic reality is never clear cut, with the true cost of diesel generation very rarely passed directly onto the consumer. Various government rebates, market subsidy's and tariff structures typically discount the cost of diesel fired generation to remote consumer [29]. The rational for such intervention is often well intentioned, to promote electrification to remote communities and to ensure affordable and accessible electrical supply, however, barriers to renewable integration are introduced, with no single entity able to appreciate the true pass-through cost of diesel generation. Second, diesel generation is most likely the established fuel source to the community, with diesel fuel well established within the commerce and customs of the community. Accordingly, those parties financially dependent on its continued prosperity stand to oppose RES integration. The RES developer is often wise to understand these existing commerce flows prior to finalizing the structure of any project, with one solution to share financial gains widely across the community to foster improved social license.

Unfortunately, the environmental argument is equally complex, with available land and land tenure often impacting RES deployment. A number of RES technologies can require a substantial footprint, as compared to a conventional diesel power station. Whether the proposed development impacts agricultural land, fisheries or possibly airspace, these resources are often limited and high prized within islanded countries, requiring the design and approvals process to carefully manage such considerations. Equally, the ownership model of these resources may involve multiple parties, or even entire villages, with lease and access agreements often difficult to secure in such instances. One solution to these concerns maybe to incorporate RES technologies into community assets, for which the community receives direct value, say in the case of elevating solar PV panels to provide accessible shade and vehicle parking at a community venue.

Technological barriers exist for RES integration given the added complexity additional generators impose into the network. In addition to scheduling and co-ordinating, these additional sources with legacy generation to meet demand, operators have to understand the safe levels of RES penetration given system stability requirements and the inability of common RES designs to allow for reactive power provision and islanded operation. Cultural barriers exist given the significant opposition many communities can have to new and unfamiliar power generation. The systems can be seen as complex, hard to operate and maintain, and unreliable, given human tendency to first blame new and unfamiliar change for any disruption, regardless of the actual fault condition. Many of these barriers are genuine issues for islanded communities. With little established RES expertise available, the operations and maintenance can appear overly complex. Historical development models, reliant on external aid funding and expertise to develop RES projects, do little to establish local ownership and expertise for the asset once the project is operational.

6 Hybrid Diesel Architectures

Off-grid hybrid systems are built to service communities unable to connect to conventional network electricity supply, offering these consumers a comparable level of service and reliability. As we have seen, the majority of these systems adopt diesel generation for their energy supply, however with an increasing justification for RES use, many islanded countries have transitioned to a hybrid diesel architecture. A hybrid diesel architecture is one using both diesel and renewable generation sources. The advantage of this approach is its ability to extract benefit from each generation source, mitigating the downsides inherent to either technology in isolation. Diesel generation is polluting and reliant on an available and affordable diesel supply. Renewable generation is highly variable, with the power system operator left with little control as to when and how much renewable generation will be available to consumers. Hybrid diesel systems use diesel generation to provide system stability and reliability, while integrating RES technologies to reduce emissions and reduce generation costs. As such the approach mitigates many of the risks inherent with RES reliance. The diesel generation system and infrastructure remain in place and available should the operator need to restore historical performance levels, with additional generation sources iteratively introduced to the system as familiarity and confidence regarding their performance is established. Hybrid diesel systems currently represent the default approach for any system upgrade or redevelopment.

Which RES to adopt within a hybrid diesel system is always a site specific consideration. Multiple RES technologies have been presented within this text, with the developer afforded an apparent wide array of possible technologies. In reality almost all systems currently use either wind, solar PV or both, as the mainstay of their renewable portfolio. The reason for the dominance of these two technologies is simply a matter of cost. Some considerations pertinent to either technology are presented below for completeness.

Wind is currently the most cost competitive renewable technology, subject to a suitable wind resource [30]. With the growth of the Chinese wind market, both as a consumer and supplier of technology, the industry has seen technology development move away from high wind speed platforms, to develop a range of moderate to low wind, large rotor solutions. This shift is reflective of the lower wind resource prevalent across much of mainland China, and indeed much of the rest of the world. Accordingly, there is now more choice in wind turbine technology than ever before. Key considerations for islanded countries contemplating RES suitability should not overlook transportation and erection issues. Wind turbine blades alone can span in excess of 70 m. Complex vehicle access can quickly rule out use of such a large rotor, while availability of lifting solutions to install tall tower wind turbines can equally become prohibitive if a crane with sufficient boom extension is not available regionally. Additionally with these large rotor platforms, rated to multi-MW output, the turbines may simply be too large for the local demand. Consideration of multiple smaller platforms may improve the purchasing position of the developer,

with more prospective suppliers interested, however in response a larger number of suitable sites need to be available for development. Sites closer than 1000 m to occupied residences are typically avoided given the potential for audible noise pollution. Finally, wind development needs to consider the site extreme wind speed risk, with many cyclonic regions unsuitable for conventional wind technologies. Custom tilt-down, tilt-up solutions are available to mitigate this risk, but unfortunately limit the developer's technology choice, as few suppliers offer commercial products with this capability.

Solar is increasingly becoming the default option for hybrid diesel integration, while the systems return a higher cost of energy in comparison to wind developments, they have many attractive advantages. Of immediate note solar developments do not require an extensive site resource evaluation. Whereas for a wind project a minimum of 12 months of measured hub height wind data is required to select the appropriate technology and prepare a business case, solar PV projects can be commenced with little to no site monitoring. This ability allows solar projects to commence with substantially less delay and cost in comparison to a wind project. Solar also scales to practically any capacity the consumer may require, simply by adding or subtracting panels. This modular functionality allows solar to be distributed across a network, say on residential rooftops, or centrally located at a large solar farm, one downside to the latter being the large area required for solar projects, typically in the order of 6 acres per MW of installed capacity [31]. Solar is also incapable of providing network frequency and voltage support without inclusion of grid forming inverter technology. Regardless of the RES preference the possible renewable penetration, and thus the effectiveness of the hybrid architecture is significantly influence by the type, control and co-ordination of the generation sources, as discussed further in the next section.

Ancillary technologies commonly integrated within hybrid diesel systems include energy dissipation (dump load, co-generation, tri-generation) and energy storage (battery, flywheel) systems. Energy dissipation systems are essentially used to allow the generation to exceed demand, with the excess generation diverted to serve an artificial (dump load) or supplementary (co-gen, tri-gen) loads. Fast acting demand management of these loads can be used effectively to provide frequency response and control within an islanded power system. For example should the system encounter a dip in renewable output, instead of requiring a response from the online diesel generation, such ancillary loads can simply be curtailed to maintain the supply and demand balance. While dump loads are fairly cost effective, consisting essentially of paired dynamic resistors, the resultant energy throughput serves no useful function. For the higher complexity and higher cost co-gen and tri-gen applications, where waste heat is used to support a heating or cooling application respectively, much of this available heat (up to 70% of the fuels available thermal energy, of which almost half is recoverable) can serve a practical need within the community. Finally energy storage technologies are now available, facilitating storage of the energy for use within the system at a future time. The benefit of storage approaches is enormous, able to extend RES integration to meet

100% of an island countries demand. Unfortunately, such systems are currently cost prohibitive, with standard hybrid diesel architectures preferring to adopting a dump load capability to rationalize required system investment [13].

7 Advanced Diesel Technologies and Control

Advanced diesel technologies and control entail a range of approaches available within a hybrid diesel architecture to achieve cost optimized renewable penetrations. In other words, how to get the greatest value from any renewable capacity available within a hybrid diesel system. Correct selection and control of your generation sources is key to the effective operation of a hybrid diesel system, and to this extent configuration and control is the primary metric impacting on the success of any RES development.

7.1 Low Load Diesel (LLD)

Diesel generator sets are commonly adopted for a variety of reasons, including equipment affordability, availability of fuel supply and access to engineering support. Unfortunately, conventional diesel generators need to operate heavily loaded to ensure efficient and reliable operation, a scenario which leaves limited scope for meaningful renewable generation. Thus, consumers become stranded between the need to run their diesels heavily loaded, to ensure efficient operation, and their increasing awareness of the adverse impacts of climate change, of particular relevance to many islanded communities.

A range of innovative renewable energy technologies are increasingly becoming both available and cost competitive with diesel generation [10]. A hybrid approach coupling renewable generation with diesel generation is rapidly becoming a default solution to both reduce fossil fuel reliance and the cost of energy. As renewable penetration increases within a hybrid diesel system a potential conflict arises, with the diesel generators unable to lower their output below a minimum operating set point. Such load set points are predetermined to ensure engine efficiency and preserve engine condition. Under high renewable penetration, diesel load set points produce surplus generation, which must be absorbed via regulating devices such as dump loads or energy storages systems. Hence, systems configured for high renewable penetration currently involve increased complexity, expense and waste.

Low load diesel technology offers one solution to minimizing surplus generation under high renewable energy penetration, adjusting the way legacy generators are used within an islanded power system. Conventionally, diesel is used for the majority of power supply, with only a small component of renewable generation possible. Under low load application, diesel use is more about energy storage, with

diesel called upon to back up renewable generation, covering periods when renewable generation is unavailable. How effectively communities' transition from diesel to emerging energy storage technologies relies on a systems ability to maximize their current renewable penetration. Low load diesel technologies significantly reduce the cost of high penetrations of renewable energy into remote and off-grid power systems. Removing the barriers to low load diesel operation promises to deliver the lowest cost pathway to reduce remote community reliance on diesel generation. LLD capability is available to both legacy and new diesel generators.

To understand the emergence of low load diesel application, the engineer must understand historical resistance to the practice, particularly as many communities reliant on diesel for their energy maintain these perspectives. Historically, a number of operational issues have been associated with low load operation including wet stacking, slobbering, turbocharger sooting and cylinder glazing or honing [33]:

- Wet Stacking
  Wet stacking is a condition diagnosed via the observation of unburnt fuel condensing within the diesel engines exhaust (otherwise known as the engines "stack"). Wet stacking is essentially a result of low cylinder temperatures, and given the correlation between load and temperature it is easy to understand the connection between low loads and wet stacking. At low loads, insufficient fuel is delivered to the cylinder to maintain the optimal thermal equilibrium. In many cases, constant rate engine cooling can contribute to this thermal imbalance, with the introduction of variable load engine cooling an effective investment. As the cylinder temperature drops, heat is removed from the hot combustion gases at an increasing rate. As a diesel engine relies on these hot combustion gases to provide an optimal combustion environment, a heat deficient leads to incomplete combustion. The fuel condenses in both the exhaust stack, turbocharger and within the lube oil, while soot accumulates on injectors, pistons, cylinder liners. Fuel seepage commonly presents an aesthetic and safety issue. By far the largest engine impact results from soot build-up or carbonization of the engine components, Fig. 7.
  Wet stacking is a positive feedback process, with incomplete combustion further reducing combustion efficiency across subsequent cycles. Sooting of the injectors reduces the accuracy, timing and spray formation of fuel delivery into the cylinder, and subsequently also impacts the combustion efficiency. Injector sooting represents an issue of increasing concern for modern engines, with modern technologies increasingly reliant on precise injector timing and burst performance to meet efficiency and emissions targets, Fig. 8. It is now common practice to adopt multiple injectors per cylinder, with each injector synchronized to a multiple burst pre and post combustion injection schedule, requiring micro second precision.
- Oil Dilution
  Oil dilution results as a symptom of low cylinder temperature and pressure. We have previously discussed the development of low cylinder temperatures, and

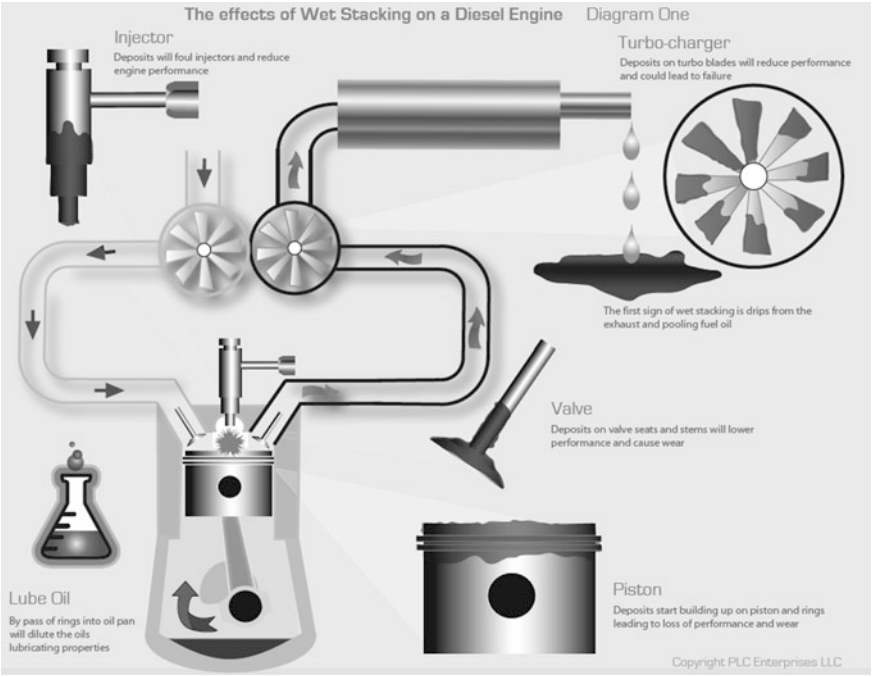

Fig. 7 Wet stacking of a diesel engine. *Source* Clifford Power [32]

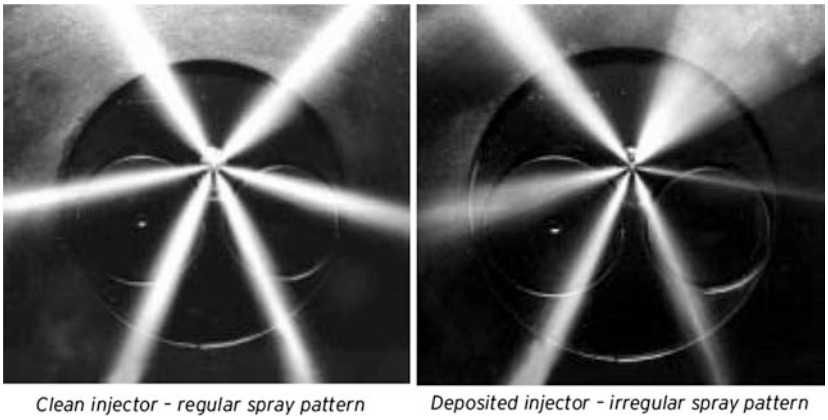

Fig. 8 Sooting of injectors and resultant spray disruption. *Source* Chevron 2007 [17]

equally, low pressures result from a combination of incomplete combustion and low air charge boost pressure. Air charge boost pressure being directly proportional to exhaust gas flow rates. Under these conditions the piston ring provides only a partial seal to the cylinder liner, with the resultant piston flutter

leaving an excessive oil film against the cylinder walls. Oil which has subsequently mixed with fuel and returned to the engine sump exhibits modified properties as a result of additional contaminants, requiring more frequent oil replacement.

- Turbocharger Sooting
  At low loading exhaust volumes drop, to the extent that the turbocharger, Fig. 9, may idle. At idle the gaskets within the turbocharger are unable to maintain an effective seal, and oil passes through to the compressor. Oil ingress to the compressor, in addition to shooting of the turbo impeller blades, results in performance detrition, imbalance and possible turbo failure.
- White smoke
  White smoke is a direct symptom of low temperature combustion, with unburnt fuel leaving the exhaust stack as fuel vapour.
- Blow-by
  Blow-by refers to the phenomenon of exhaust gas blowing past the piston ring and into the crankcase. Some blow-by is unavoidable, however as blow-by increases so does the crank case pressure, placing additional strain on the crankcase seals and oil separator, leading to oil egress from the crankcase.

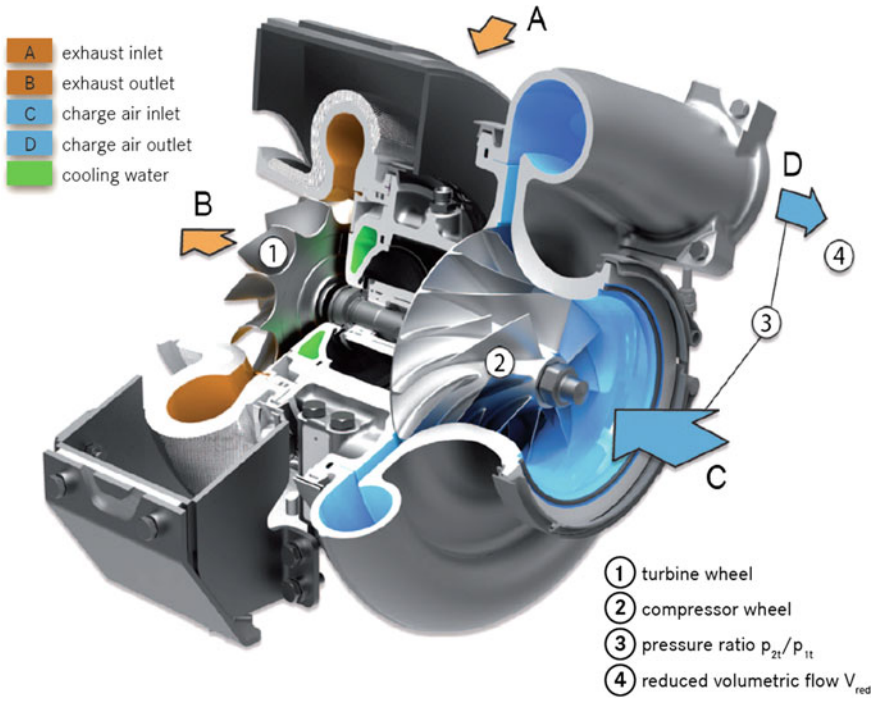

Fig. 9 Turbocharger geometry. *Source* MTU 2014 [34]

- Black smoke
  Black smoke is a direct symptom of low temperature combustion, with carbonized oil and fuel residue leaving the exhaust stack as black carbon particulate matter. Black smoke usually occurs following a period of low load operation, as the engine load is raised sufficiently to dislodge any carbon residue from the piston and cylinders. Most vehicle drivers are familiar with this phenomenon, having observation black exhaust smoke as a diesel truck accelerates. Upon application of the throttle, a thick cloud of black smoke is released to the annoyance of other motorists. While the black smoke presents health concerns, the emissions are beneficial to the engine, as they represents a purge of the engine's carbon accumulation. Black smoking is also only a short term phenomenon, lasting the period required to purge the carbon accumulation from the engine.
- Con rod bearing wear
  Varying cylinder pressures result in a non-uniform load profile across the con rod bearings. Excessive loading leads to increased bearing wear and reduced bearing life.
- Cylinder liner wear
  Cylinder wear can often be misunderstood, as a number of distinct wear mechanisms exist. Additionally, many engineers do not realize that modern engines require no run-in period. Running in an engine was historically required to remove slightly elevated ridges from the cylinder liners surface, effectively matching the piston ring and cylinder tolerances. As modern cylinder liners are produced with the required surface finish, they run efficiently off the shelf. The critical parameter under either scenario remains the surface finish of the liner. Too smooth, or too rough a surface and the liner has reduced capacity to hold the required oil film essential for lubrication. As mentioned, two distinct phenomena exist to reduce the surface roughness below optimal, bore glazing and bore polishing. Bore glazing occurs as fuel and oil derivatives coat the cylinder liner, flash burning to form a smooth glazed coating (similar in concept to glazing ceramics during kiln firing). If left too long without a purge cycle, cylinder glazing can require cylinder replacement or jeopardize the engine condition. Liner polishing is characterized by a mirror finish within the cylinder bore, indicative of local mechanical wear at that surface. The wear is often a result of oil contamination, leading to replacement of both the cylinder liner and oil, the later to restore the correct lubrication characteristics.
- Piston ring carbonization
  Accumulation of carbon on the piston ring can result in polishing. Carbonization results from the same low load mechanism described above, however in this instance a high risk of piston seizure exists.

Thankfully a number of technologies and approaches exist to mitigate the issues historically preventing low load application of diesel generator sets. Essentially, they all seek to improve the thermal characterisation of the engine, with a number of technologies discussed further below.

7.2 Load Variable Cooling

Stationary power diesel generator sets commonly adopt a geared fixed speed cooling fan. If the engine is running the fan is on. Not only is this inefficient, it restricts low load capability given unnecessary air movement and some degree of convective cooling of the engine. Load variable cooling is one easy approach to improve both efficiency and low load diesel capability.

Heat transfer to the coolant system represents between one quarter and one third of the total combustion energy for a conventional diesel engine [35]. This number may surprise some readers, with a substantial amount of heat flowing from the engine. Under normal operation this is actually the purpose of the cooling system, to extract excess heat from the engine to ensure the function and condition of the engine components. With increasing adoption of low load operation (that of increased RES utilization), the thermal proposition is somewhat reversed, requiring the retention of thermal inertia within the engine block (while a similar requirement exists during startup, startup remains a short duration application, whereas low load operation is not). Thermostatic valves are commonly employed to bypass the flow of cooling fluid during startup and low load operation, however as stated, the coolant fans typically remain on. Parasitic loss for cooling fan operation is typically within the order to 2–3% of the engines rated mechanical output. Load variable cooling introduces opportunity to reduce much of this parasitic loss, by as much as 80% [35], typically via the introduction of a hydrostatic or variable speed fan drive. In addition to load variable cooling, redesign of the cooling system for low load application introduces opportunity to incorporate heat recovery mechanisms into the cooling circuit. Such heat recovery systems are common for combined heat and power applications, where the waste thermal energy is used to supply a heat load in parallel (co-generation). Under a load variable cooling application, this same heat energy is efficiently stored within the system to serve as a thermal source when benefit exists in elevated water jacket temperatures. The concept has found limited commercial application, principally via the integration of a dump load element into the engines water jacket, allowing for additional heat to be made available to the diesel engine during periods of high renewable penetration (and consequently low diesel loading). The benefit of which being higher permitted RES utilization via reduced low load level operation and improved diesel engine ramp rate (transient) response characteristics. Cold engine performance is known to delay transient response by 50–100% subject to ramp rate requirements. While variable load cooling has been observed to increase fuel efficiencies by up to 16%.

7.3 Multi-burst Common Rail Injection

While modern diesel engines are essentially all direct injected, injector capability varies significantly across platforms and suppliers. Common rail injection, supported by electronic governor control is essential to ensure the required injector capability, that of accurate metering combined with fast response. Injector research and development has also seen a move to higher and higher injection pressures, primarily to improve fuel delivery and spray formation, a key driver of combustion efficiency. Significant injector development and refinement is ongoing, with advanced materials being incorporated to further improve response times and flow control (for example direct acting piezoelectric injectors are able to provide flow rate shaping via control of the charge stored in the piezoelectric stack). To this extent injection systems now commonly represent over 30% of the entire engines production costs.

Fortunately or not, refinement of inject performance is outside of the control permitted for most diesel operators. However it is imperative in selecting a diesel generating set that the engineer be aware of the injector options given the tuned combustion staging available across a range of load profiles with improved injector control and response.

7.4 Variable Injection Nozzle Geometry

Injector nozzle geometry is typically optimized for conventional loading applications, with variable injector nozzle geometry one recent development, providing the ability to customize nozzle geometry for low load applications. The ability to reduce nozzle geometry at low loads extends to superior fuel delivery pressures, better spray penetration and formation and improved combustion efficiency. Variable injector nozzle geometries are typically achieved via multiple injection holes, with the injector able to select across ports to suit the loading condition.

7.5 Cylinder Switching/Deactivation

Cylinder deactivation, also known as variable displacement, is used effectively to reduce fuel consumption and emissions under low load operation. The principal involves turning off an even number of cylinders during low load operation to allow for a higher fuel and air loading across the remaining cylinders. Cylinder deactivation is achieved by keeping the inlet valves, and in some cases also the exhaust valves closed, while deactivating the injectors to those same cylinders. Deactivated cylinders reduce the air consumption across the air charge system, reducing

pumping loses and allowing for higher cylinder pressures across all remaining active cylinders. The resultant deactive cylinders act as an "air spring" further improving the mechanical efficiency of the engine. As the engines mechanical output remains fixed, simply with fewer cylinders to supply the required torque, fuel loading increases to simulate proportionally higher loaded operation. A number of deactivation combinations are possible to any engine, with the ratio of deactive cylinders proportional to the de-rated capacity of the engine.

For example, an eight cylinder engine rated at 400 kW, deactivated to four cylinders, would be capable of delivering an adjusted 200 kW. The benefit being this load state now represents a higher cylinder loading and therefore efficiency, than that available when the entire engine was active. It is vital that the engine manufacturer select the configuration of cylinders to ensure balanced engine operation under any available state, however this is easily achieved for large displacement multi-cylinder engines. The benefits of cylinder deactivation also extend to exhaust emissions given the temperature dependent nature of much of the pollutant formation.

7.6 Turbocharging

Turbocharging has proven to be so successful in extracting additional energy from the diesel engines exhaust stream that there exists a myriad of different turbocharger designs and applications. One reason for this range of application is that turbochargers have proven to be very effective at achieving peak boost pressures, or operating effectively over a range of speeds, but not both. To recapture some of the engines exhausted energy, as much as 25% of the engines total output, turbochargers exist.

In principal, a turbocharger consists of an exhaust gas turbine rigidly coupled to a compressor turbine. As the exhaust turbine spins in the high velocity exhaust gas stream, it drives the compressor turbine, which in turn provides compressed air to boost air charge density available to the engines cylinders, Fig. 10. Some issues exist with turbocharger performance, principally turbo lag and low load/low exhaust flow performance. Turbo lag represents a time delay post engine governor response, as the exhaust side turbo waits for increased exhaust flow to become available downstream of the cylinders. Of note these conditions have historically been a deterrent to the use of highly turbo reliant [high brake mean effective pressure (BMEP)] diesel engines, however thankfully a number of approaches exist to improve these characteristics. Principally approaches to improve low load turbo performance entail addition of multiple turbocharger elements to limit reliance on a single stage turbocharger, including those discussed below;

- *Superchargers* are any application used to boost air charge pressure, in much the same way as a turbocharger, only without the reliance on exhaust flow. Typically superchargers are engine driven pumps or compressors, although

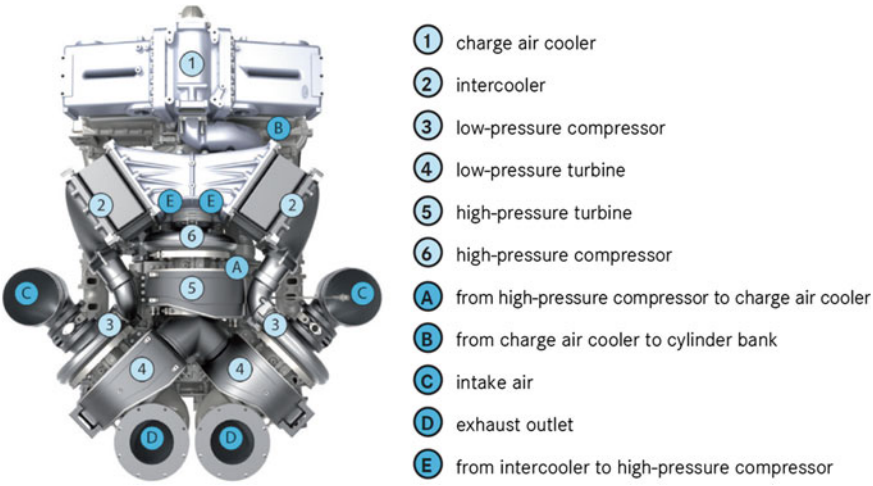

Fig. 10 Air charge passage via sequential turbocharging. *Source* MTU 2014 [34]

dynamic or pulse supercharging is also possible. Dynamic or pulse supercharging uses pressure wave formation as the principal to boost air charge pressure available to the cylinder. Combined supercharger and turbocharger systems offer improved low load engine performance with superchargers experiencing no turbo lag. While superchargers offer many benefits over a turbocharger they often (in the case of engine driven systems) impose an additional fuel penalty on the system, limiting their application to services unavailable to a turbocharger solution.

- *Sequential Turbocharging* (*STC*) involves the use of multiple turbochargers, typically connected in series configuration (multiple stage STC), to provide for precompression of the intake air, followed by further high pressure compression within a subsequent high pressure turbo charger, Fig. 10. Sequential turbocharging can also adopt parallel architectures (single stage STC), operating on much the same principal, with deactivation of turbochargers under either structure possible to tune the engine response. Sequential turbocharging in this manner provides improved dynamic response, a wider operating range and higher boost pressures than that available to single turbo architectures.
- *Variable geometry turbocharging* (VGT) involves either pivoting vanes (Fig. 11), or moving walls to provide flexibility over the pressure ratio/flow relationship, and by extension the torque characteristics of the turbocharger, Fig. 12. The benefit for this additional complexity is improved low load and transient response. VGT can also be used to enhance the function of engine compression braking, via closing of the VGT vanes.
- *Turbo compounding* (*TC*) allows for improved turbocharger recovery, offering improved fuel economy of up to 10% coupled with improved transient response [23]. In principal, the system adds a power turbine to a conventional

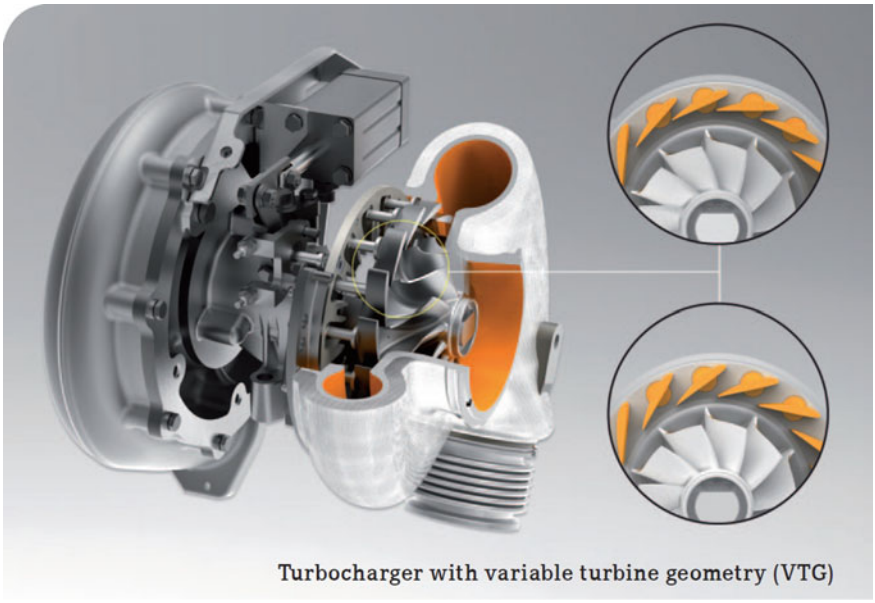

Fig. 11 Variable gate turbo geometry. *Source* MTU: 2014 [34]

Fig. 12 Air charge boost pressure response under VGT. *Source* DieselNet 2013 [36]

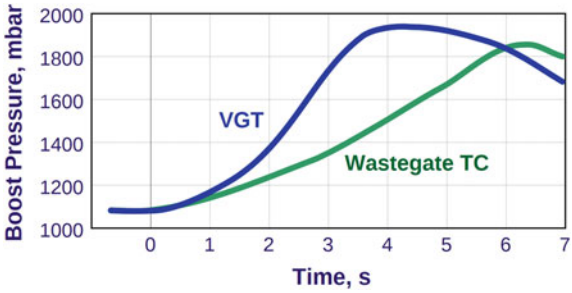

turbocharged system, where the power turbine is connected to either a gear train or a generator (as opposed to the conventional compressor) to provide for an additional source of energy to the diesel engine. In the case of mechanical coupling the power turbo could be connected directly to the engines crankshaft via a gear train, potentially boosting peak engine power output by up to 10%. In the case of electrical coupling, the power turbo provides a source of electrical energy which can be consumed by the engine or stored for future use. Unfortunately TC offers little benefit under low load operation, and may actually be detrimental to low load efficiency, unless the generator can be configure to run as a motor, in which case, the process becomes assisted turbocharging.

- *Assisted turbocharging* is much the same as turbo compounding, only the energy flow is reversed and now flows from the engine to the turbocharger, for the purpose of assisting turbocharger output. Assisted turbocharging can thus provide significant advantage to low load application.

7.7 Reverse Power Acceptance

For vehicle applications, engine braking is essentially reverse power acceptance, using the diesel generator's mechanical friction to offer a dump load capability, aiding to slow down the vehicle without excessive use of brakes. For stationary power applications, the same functionality can be used to allow the diesel generator to provide a load for the system. For example, under high renewable penetration it is advantageous to run you diesel generators as lightly loaded as possible (refer to the earlier discussion of low load diesel application). In such a scenario, should you be able to maintain your diesel engines at no load (zero mechanical output, varies from idle operation, as for the later, shaft speed is allowed to vary) a unique problem arises, that of peaking RES output. As the RES generation varies, you will inevitable overshoot the notional set point, say as the wind gusts around its average value. In this instance where does the additional energy go. Your diesel engines are not actively contributing kW's to the system, as they are at no load, they therefor have no ability to further throttle back to allow for additional RES contribution. One possible solution is to use the engine braking (motoring) capability of the diesel generator to absorb some of this short term transient. This approach has not found practical application with islanded power systems, primarily given operational concerns over motoring generator sets and the risk of mechanical failure quickly leading to engine destruction. Never the less, some permissible motoring of the generator set could assist in elevating engine temperature and providing improved engine response. An approach which has found some commercial applications is that of engine integrating dump load, which allows a separate resistive element to act as a resistive load, the resultant heat being used to increase the engines thermal inertia. In support, it is also possible to maintain mechanical inertia of the alternator via inclusion of a clutch, able to separate the engine and alternator. In doing so the alternator can act as a synchronous condenser, allowing for the diesel engine to be turned off whilst maintaining a fast start capability should the diesel need to be brought online quickly. While the later approach involves significant additional complexity, particularly within the engine control unit, its ability to extend reverse power acceptance beyond the rated capacity of the engine, and eliminate the no load fuel consumption has found favour with niche suppliers.

7.8 Exhaust Gas Recovery (EGR)

EGR is a key technology in emissions compliance for modern diesel generators, involving the recirculation of some exhaust gases back into the air charge volume. This practice reduces NO_x emissions, principally via the reduction in combustion flame temperature. This result is achieved through a combination of reduced oxygen, as exhaust gases displace some O_2, reduced combustion efficiency, given the additional moisture and CO_2 introduced, and modified cylinder gas enthalpy. EGR is not directly related to low load application, however as the practice involves reduced cylinder temperatures it has an adverse effect on low load capability. As such low load application should seek to eliminate EGR use and seek alternative NO_x reduction approaches.

7.9 Under Frequency Voltage Roll-Off (UFRO)

Temporary voltage relief, to aid improved engine response under large load acceptance scenarios, is one easy mechanism to improve power security within islanded power systems under high RES penetration. The application allows the system voltage to dip temporarily, in proportion to the frequency dip, reducing the load on the engine. UFRO is a common application within many automatic voltage regulators and assists in the application of low load response.

7.10 Variable Speed Diesel (VSD)

Engine mechanical losses are proportional to engine speed, independent of load. Hence as the load decreases within a constant speed application, the losses remain, becoming an ever increasing percentage of the supplied energy. This is one reason why it is typically undesirable to run an engine lightly loaded. At the same time, diesel generator sets are sized for maximum demand, regardless of how infrequent this demand might present. By definition, these units spend much of their life partially loaded. Variable speed diesel concepts allow the diesel engine to move away from fixed speed operation, typically lowering shaft speed at low loads, to capture fuel efficiency and improved responsiveness associated with variable speed operation. VSD concepts also add significantly benefit to any LLD application, with low load VSD able to maintain combustion temperatures comparable to conventional operation.

VSD application can adopt one of two approaches, with mechanical or electrical solutions possible. The mechanical solution involves the integration of a variable

speed coupling, typically a gearbox as commercialized by CVT corp [37], Fig. 13. Regardless of the coupling mechanism, mechanical solutions add significant complexity to the drivetrain, typically requiring an increased maintenance obligation. For this reason, electrical solutions appear to offer increased reliability and suitability within islanded applications.

Electrical solutions essentially entail replacement of the synchronous alternator with either a DFIG or permanent magnet generator (common technologies for wind turbine application) [38, 39]. Electrical VSD concepts require a frequency converter to meet the constant frequency requirement of the grid, and while the increased cost and complexity of power converters have been a barrier, a number of electrical VSD concepts are now commercialized, particularly in the small generator set market [40]. Of relevance for hybrid diesel architectures it is possible for multiple generators, say wind, energy storage and diesel to share a common power converter, further reducing cost [41].

Theoretical fuel savings resultant from VSD application have been suggested up to 50% [42], Fig. 14, although some deterioration in full load fuel efficiency is observed given the losses inherent to the power converter. In addition, a VSD application is able to extract a higher resultant torque than a conventional fixed speed engine [43]. While power converter costs remain prohibitively high for VSD adoption, as we see the cost of power converter technology reduce the benefits of low load VSD technology are anticipated to be realized across a range of market applications and generator set sizes.

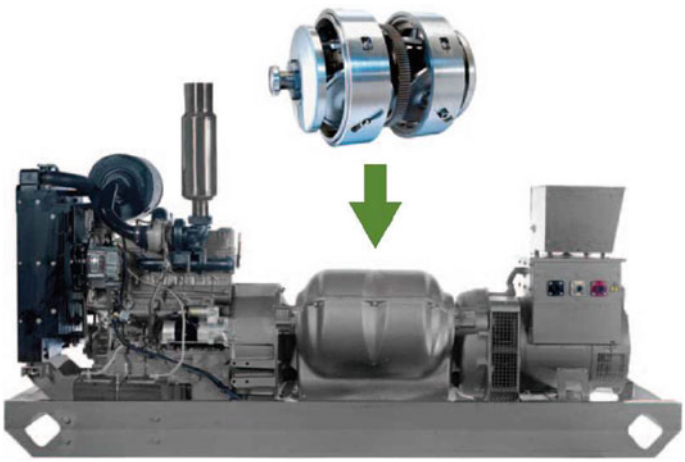

Fig. 13 CVT corp variable speed transmission concept for variable speed generation. *Source* CVT Corp 2016 [37]

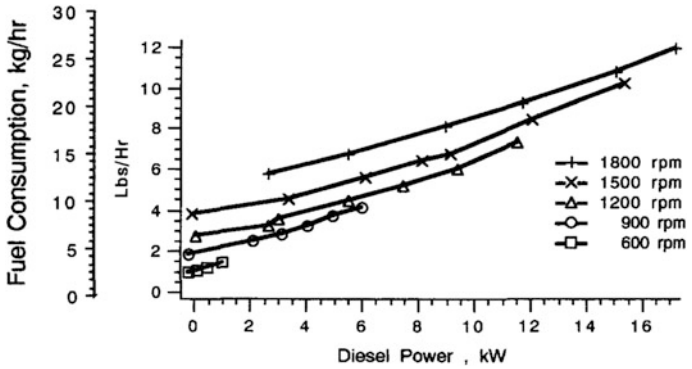

Fig. 14 Fuel consumption for VSD application [38]

7.11 DC Diesel (DCD) Hybrids

As RES technologies reduce in price, emerging energy storage and battery technologies are commercialized, and wind turbines move towards full power conversion platforms, increased justification presents for islanded applications to implement direct current networks. Upon historical review, AC networks have largely evolved from a requirement for efficient transmission of power, generated within large central power stations, to consumers located across the vast geography of the network. For islanded applications these requirements commonly do not apply, with small community loads located in close proximity to available renewable resources. In addition renewable and ancillary technologies such as solar PV and battery storage work on direct current and are commonly distributed across a network at both domestic and industrial levels. Further, with discussion of variable speed wind and diesel generation, direct current output of these generation sources also becomes viable. DCD acknowledges this technology shift in identifying the optimal location and sizing for AC/DC power conversion, allowing for a dedicated central DC bus or transmission system. AC conversion is only undertaken, if at all, prior to consumption of AC within a residence or facility.

7.12 Biodiesel Blending

A brief discussion of biodiesel blending is presented given its increasing relevance to hybrid diesel power systems and its direct impact on the engine thermal profile. In principle, biodiesel presents an opportunity to utilize available on-island waste products as a blended diesel derivative, thus reducing reliance on costly imported fuels. However a number of issues require careful consideration, including

technical, economic and social impacts. Common queries include, what blending ration is optimal, and what impact will the blended fuel have on engine performance and emissions compliance? Is the available biodiesel feedstock reliably available in sufficient quantities to support ongoing viability? Will biodiesel use modify conventional agricultural practice and productivity (introducing competing demand with food production)? Such concerns complicate the technical viability of producing a biologically derived fuel from vegetable oils or animal fats. Suitable sources of which include soybean, palm, coconut, used frying oil or algae. Even when these feed stocks can be obtained at subsidized, or no cost, their refinement typically adds a price premium to that of pure diesel, especially when considering the small scale of operation typical of an islanded economy.

As such, biodiesel blends typically use any waste oil derivatives in small quantities, far below the 7% blending limit currently imposed by equipment suppliers [45]. Such limits are typically driven by engine warranty provisions and the potential of biodiesels to foul piston rings and injectors above certain levels. Of note standard provisions assume ever increasing biodiesel capability (*Bxx* limits) from engine technologies.

Biodiesels blends can be characterized by the follow generic traits, although some variation specific to feed stock does exists:

- Lower heating value;
- Higher cetane value;
- Higher viscosity (restricting use in cold climates);
- Higher freezing temperature (restricting use in cold climates);
- Lower toxicity;
- Increased combustion odour;
- Biodegradable (impacts storage life and water absorption);
- Modified corrosive properties.

In regards to emissions compliance, the general trends presented in Table 3 can be expected, although these are subject to a number of parameters including the biodiesel source and quality, engine configuration, test cycle and environmental conditions. The general trend is for reduced resultant pollutant emissions linked to biodiesel combustion.

Biodiesel blending is considerably more complex an undertaking than initially apparent, it impacts on almost every aspect of the engine performance from injector timing, combustion rate, compression ratio, flame propagation, oxygenation and exhaust temperature. Some of these benefits are positive, while others are negative, for both engine performance and longevity. In addition, biodiesel blending has implications for LLD, VSD and DCD application, with careful consideration of these impacts recommended prior to any widespread adoption. As a minimum practice, biodiesel introduction should work iteratively up to targeted blend ratios with the exercise more suited to a lab research environment than that of an operating islanded power system.

Table 3 Effects of biodiesel fuel on exhaust emissions

Emission	**Effect of biodiesel**
Regulated emissions	
Carbon monoxide	↓
Hydrocarbons	↓
Nitrogen oxides	↑
Total particulate matter (TPM)	↑ OR ↓
Unregulated emissions	
Carbon particulates	↓
Organic particulates (SOF)	↑
Sulfate particulates	↓
Visible smoke	↓
PAH, nitro-PAH	↓
Aldehydes	↑ OR ↓
Legend: ↑ biodiesel increases emissions (relative to standard diesel)	
↓ biodiesel decreases emissions (relative to standard diesel)	

Source Diesel Net 2009 [44]

8 Operational Theory

Diesel generators remain the backbone for the majority of deployed island country networks. To understand how a diesel generator works, a basic understanding of the diesel engine and generator component architectures and interaction is required. A diesel generator consists of a diesel engine, controlled by the engine governor and a synchronous alternator controlled by the automatic voltage regulator (AVR). Both of these systems are co-ordinated by the Engine Control Unit (ECU). Operation of the engine and alternator is considered separately in this text to reduce system complexity for the reader, with the coordination of the two required to define a conventional diesel generator. We start our discussion with consideration for the diesel engine, often referred to as the prime mover, given its role in the conversion of chemical energy to mechanical rotation. At its simplest level, the diesel engine comprises of an engine block, cylinder head, cylinders, running gear, pistons, fuel system, valve and injection systems, air charge system, cooling and exhaust systems. These component groupings in turn consist of a number of common components and subsystems, the function of which is briefly presented below.

The structural foundation of the engine is provided by the engine block, to which the cylinder head is mechanically fastened. In this manner, the block can be considered the body of the engine. The function of the head is to provide a pressurized seal for each cylinder environment, with the head commonly consisting of either a single casting or multiple heads to cover respective cylinder groupings, subject to the size of the engine. The cylinder head houses the injectors, intake and exhaust values, in addition to the valve guides and seats. Within the cylinder head, porting allows for the flow of coolant around the engine for dissipation of heat from the cylinder walls. Gaskets, seal rings and grommets are commonly used to provide a seal between the block and head given any irregularity which may exist between the two surfaces.

The bore, defining the engine cylinder may be machined directly within the engine block, however, it is preferable and common practice to insert a pressed cylinder liner, given both exacting piston to cylinder tolerances and the ability to replace liners should they exhibit excessive wear. Liners must be able to withstand the extreme heat and pressure developed during combustion while maintaining alignment of the piston and piston rings. To assist in lubricating, honing grooves within the liner assist to retain a film of lubrication oil.

The running gear, responsible for torque transfer from the cylinders, consists of any number of, con rods, bearings and crankshaft. The fuel system comprises of fuel pump and injectors. The valve system in turn comprises of inlet and exhaust valves, with a number of auxiliary components to support sequencing under correct operation, Fig. 15. The air charge system commonly comprises a turbo, Fig. 10, and intercooler. The function of the air charge system is to supply clean air to the cylinders at an appropriate density to ensure efficient combustion. The air charge manifold and ducting should be kept as short as possible with minimal obstructions to ensure acceptable pressure losses. A turbocharger is used to boost the air pressure, while an intercooler is used to reduce the temperature of this high pressure

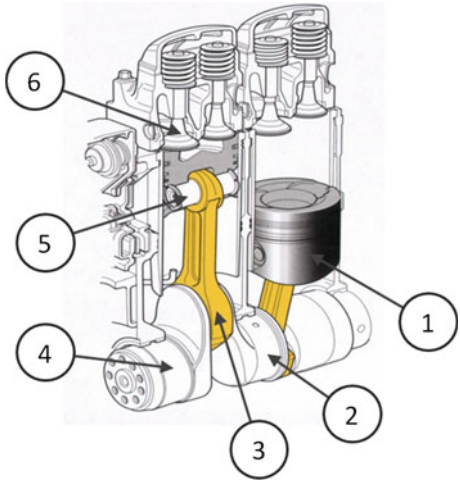

Fig. 15 Running gear cross section incorporating the piston (*1*), crankshaft (*2*), con rod (*3*), bearing (*4*), cross head (*5*), and valve (*6*). Image reproduced with permission from MTU Friedrichshafen

charge. Air filters are essential to any air charge system given the impact of dust and debris on accelerating engine wear, although again pressure drop over such a filter should be kept to a minimum.

The cooling system is essentially a heat exchanger working on either an air-cooled or water-cooled principal. The basis for adopting either system is commonly engine size, with smaller engines adopting air-cooled systems and larger engines reliant on water-cooled systems. For water-cooled systems the quality of the water is vital to ensure reliable operation, with untreated river or sea water unsuitable for use given the presence of minerals and salts, and the potential for solidification of these elements (scaling). For this reason closed cooling systems are common practice, eliminating any exposure of the treated coolant to the environment.

Diesel engines are conventional classified by fuel type, speed, application or rated capacity. Speed is by far the most common grouping with speed indicative of both the weight, cost and by inference the life of the engine. For stationary power applications, both high speed (>1000 rpm) and medium speed (400–1000 rpm) solutions are common. For AC diesel generator sets, the speed of the engine is set to the network frequency according to Eq. 3, [46].

$$n = f\frac{60}{p} \tag{3}$$

where

n is the speed of the machine in rpm;
f is the required network frequency; and
p is the number of pole pares in the alternator.

Both two stroke and four stroke working cycles are common diesel engine configurations. Two stroke engines having twice the power strokes of a four stroke engine given a common rpm reference. It is however incorrect to assume that a two stroke engine develops twice the power of a four stroke engine, in part because of inefficiencies in combining the intake and exhaust functions with the compression and combustion process respectively. The four stroke engine has many advantages over its two stroke counterpart, including improved ramp rate and transient performance and increased low load capability, both key selection criteria for any islanded application.

The power output of a diesel engine is often referred to as brake power, simply referring to the act of measuring this output against some form of mechanical resistance or brake. Brake power is always lower than the theoretical power (indicated power) of an engine given the presence of internal engine friction. The mechanical efficiency of the engine can be defined as the ratio of brake to indicated power. The brake power of an engine is calculated according to Eq. 4 [47], defining the relationship between cylinder pressure and shaft torque.

$$P = \frac{p.l.A.w.N}{k} = 2\pi\omega T \tag{4}$$

where

p is the brake mean effective pressure (average pressure acting on the piston as applied throughout the entire stroke),
l is the stroke of the engine piston,
A is the piston area,
w is the number of working strokes per unit of time,
N is the number of active cylinders in the engine,
k is a constant dependent on units selected (typically k = 1000 for SI units), and,
ω is the shaft rotational speed, and,
T is the shaft torque.

The role of the engine is to accept fuel and air, providing an optimal ignition environment for the conversion of cylinder pressure to mechanical torque. Torque is delivered through the engine via the running gear. It is the resultant output shaft speed which provides the feedback loop to the governor, facilitating speed control. The diesel engine and governor model, Fig. 16, describes the conversion of fuel, supplied to the engine in response to actuator control, to cylinder pressure then crank torque, and finally rotational shaft velocity. The role of the governor is to regulate the output shaft speed (ω) via control of the fuelling rate. Inherent to the governor operation are governor and actuator delay ($\tau 2$ and $\tau 3$) [49]. Governor delay representing the response time of the governor within the ECU. Actuator delay is inclusive of any mechanical response delay, prior to injector response (shaft speed change prior to fuel injection, thus introducing additional set point error).

In Fig. 16, p_i and p_f represent the indicated cylinder pressure and the engines mechanical losses represented as an equivalent pressure drop. Diesel engine delay

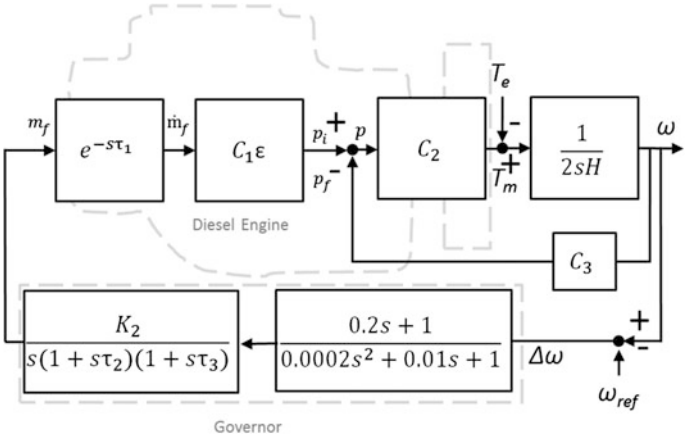

Fig. 16 Diesel engine governor and engine model [48]

($\tau 1$) results from both crank angle delay, the engines inability to accept a predetermined fuel load due to the crank angle position, and an ignition delay, determined by the cylinder environment. Crank angle delay is a function of cycle timing, with a four stroke engine having to complete combustion and exhaust stokes prior to any subsequent intake. Ignition delay represents a function of cylinder temperature, pressure, fuel stoichiometry and environmental factors. Cylinder effective pressure is developed according to Eq. 5, [48].

$$p = C_1 \dot{m}_f \varepsilon_t \tag{5}$$

where C_1 is the proportionality constant, $\dot{m}_f$ is the fuel consumption rate (m_f representing the fuel delivery rate) and ε_t is the thermal efficiency (the thermal efficiency, defined as the brake power divided by the thermal energy of the consumed fuel, is not to be confused with the mechanical efficiency). Mechanical torque is developed according to Eq. 6 [48].

$$T_m = \frac{P}{2\pi\omega} = C_2 p \tag{6}$$

where

C_2	is a proportionality constant
$p = p_i - p_f$	as defined earlier, and
$T = T_m - T_e$, with T_e	representing electromechanical torque.

Shaft speed is defined considering H, the generator sets combined mechanical inertia.

The alternator essentially consists of two parts, the stator, which carries the armature winding, in which emf is induced, and the rotor, which carries the field winding, and is supplied via dc current. From an engine perspective, any change in load must be met by a response from the governor, adjusting the fuel load to the engine for constant speed output. Equally any change in load must be met by a response in alternator excitation, which regulates the field current to maintain stable terminal voltage. In this manner, the governor controls the system frequency and the AVR controls the system voltage. The efficiency of the alternator is defined as the ratio of realized power to that of supplied power. Typically, alternator efficiency will increases with unit size, with an efficiency range of 0.92–0.95 characteristic for commonly sized stationary diesel generators sets (100 kW to 1 MW in size).

The dynamic model of the synchronous generator is represented by a sixth-order state-space model used in Simulink [49]. The internal impedance of the machine is implemented via phase specific voltage sources in series with RL impedance. The equivalence circuit is represented in q-axis and d-axis rotor reference frames, as shown in Figs. 17 and 18. The subscripts used are defined as follows:

d/*q* represent the *d*- and *q*-axis quantity, respectively;
R/*s* represent the rotor and stator quantity, respectively;
l/*m* represent leakage and magnetizing inductance, respectively;
f/*k* represent field and damper winding quantity, respectively;

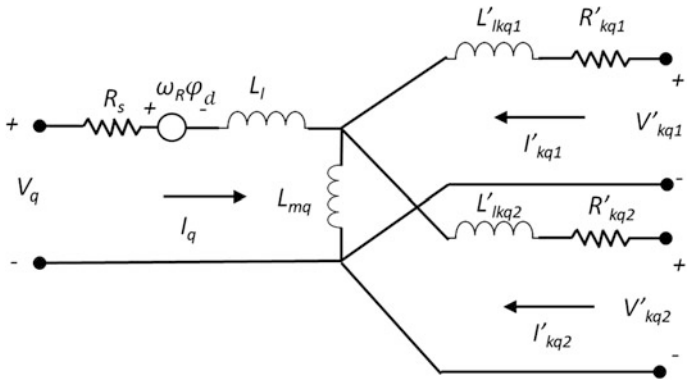

Fig. 17 Equivalent circuit model of electrical system of synchronous machine in *q*-axis frame of Ref. [49]

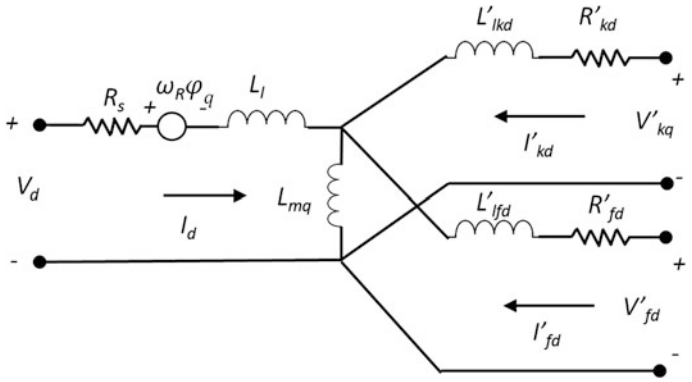

Fig. 18 Equivalent circuit model of electrical system of synchronous machine in *d*-axis frame of Ref. [49]

Electrical system response is defined by Eqs. 7–12, [50]

$$V_d = R_s i_d + \frac{\mathrm{d}}{\mathrm{d}t}(\varphi_d) - \omega_R \varphi_q \tag{7}$$

$$V_q = R_s i_q + \frac{\mathrm{d}}{\mathrm{d}t}(\varphi_q) - \omega_R \varphi_d \tag{8}$$

$$V'_{fd} = R'_{fd} i'_{fd} + \frac{\mathrm{d}}{\mathrm{d}t}\left(\varphi'_{fd}\right) \tag{9}$$

$$V'_d = R'_{kd} i'_{kd} + \frac{\mathrm{d}}{\mathrm{d}t}\left(\varphi'_{kd}\right) \tag{10}$$

$$V'_{kq1} = R'_{kq1} i'_{kq1} + \frac{\mathrm{d}}{\mathrm{d}t}\left(\varphi'_{kq1}\right) \tag{11}$$

$$V'_{kq2} = R'_{kq2} i'_{kq2} + \frac{\mathrm{d}}{\mathrm{d}t}\left(\varphi'_{kq2}\right) \tag{12}$$

where

$$\begin{aligned}
\varphi_d &= L_d i_d + L_{md}\left(i'_{fd} + i'_{kd}\right)\\
\varphi_q &= L_q i_q + L_{mq} i'_{kq}\\
\varphi'_{fd} &= L'_{fd} i'_{fd} + L_{md}\left(i_d + i'_{kd}\right)\\
\varphi'_{kd} &= L'_{kd} i'_{fd} + L_{md}\left(i_d + i'_{fd}\right)\\
\varphi'_{kq1} &= L'_{kq1} i'_{kq1} + L_{mq} i_q\\
\varphi'_{kq2} &= L'_{kq2} i'_{kq2} + L_{mq} i_q
\end{aligned}$$

The equations for the mechanical system are below, Eqs. 13 and 14, [49];

$$\omega(t) = \Delta\omega(t) + \omega_o \tag{13}$$

$$\Delta\omega(t) = \frac{1}{2H}\int_0^1 (T_m - T_e)\mathrm{d}t - D\Delta\omega(t) \tag{14}$$

where

D is the damping factor representing the effect of damper windings,
$\omega(t)$ is the rotor speed,
$\omega(o)$ is the operational speed,

The standard parameters of a synchronous generator are found either by test, as in IEEE Std115-1983 (R1991) or IEEE Std 115A-1987, or supplied directly via the manufacturer. Model specific detail data, specific direct and quadrature axis model structures, with their associated element values, to transient and sub-transient reactances and time constants is presented in Table 4.

The excitation system consists of an exciter, autonomic voltage regulator (AVR), measuring elements, power system stabilizer and limiters and protective circuits as shown in Fig. 19. The exciter provides dc power to the synchronous machine field winding. The exciter is controlled by the AVR in steady state operation, although during disturbances, due to field current changes in the generator, it also impacts on the damping of power transients. The power system stabilizer provides an input signal (based on rotor speed variation, accelerating power, and frequency deviation) to the regulator, to dampen power system oscillation. Measuring elements obtain excitation system input values such as generator armature voltage, armature current, and the excitation current and voltage. A limitation and protection unit provides

Table 4 Standard parameters of a synchronous generator

Parameter	Description	Manufacturer's value	Units
Ra	Stator resistance	0.033	pu
Xd	D-axis synchronous reactance	3.13	pu
Xq	Q-axis synchronous reactance	1.6	pu
Xl	Leakage reactance	0.074	pu
X'd	D-axis transient reactance	0.184	pu
X'q	Q-axis transient reactance	1.6	pu
X"d	D-axis sub-transient reactance	0.148	pu
X"q	Q-axis sub-transient reactance	0.161	pu
T'do	D-axis O.C. transient time constant	2.11	s
T'qo	Q-axis O.C. transient time constant	0.012	s
T"do	D-axis O.C. sub-transient time constant	0.012	s
T"qo	Q-axis O.C. sub-transient time constant	0.089	s
Sbase	MVA upon which above data is provided	830	kVA

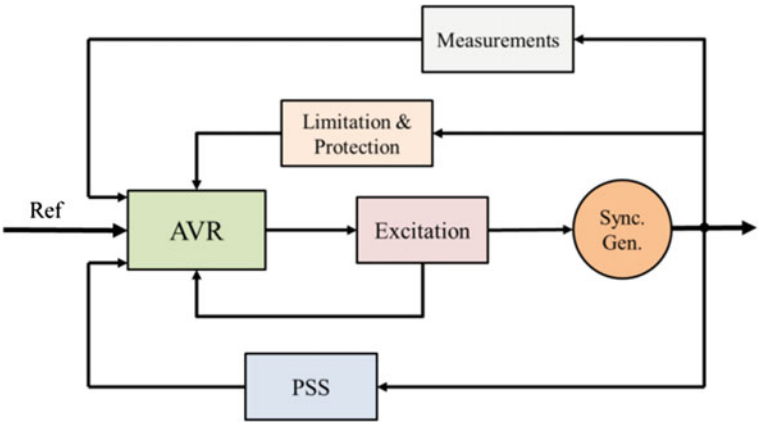

Fig. 19 Excitation system of synchronous generators

proper control and protective functions to ensure that capability limits of the exciter and synchronous generator are not exceeded.

Excitation systems can be divided into three main categories [50]: DC excitation system (type DC), AC excitation system (type AC) and static excitation system (type ST). Type DC utilizes direct current generation with a commutator as the system's source. Type AC uses an alternator and either a stationary or rotating rectifier to produce a direct current to the field winding of a synchronous generator. Type ST utilizes a transformer or auxiliary generator windings and rectifiers as a power source. A model for the AVR and exciter can be sourced either from [51, 52] or may be supplied directly by the manufacturer. A typical model for the AVR and exciter has been provided by Stamford, and is presented in Fig. 20 (Table 5).

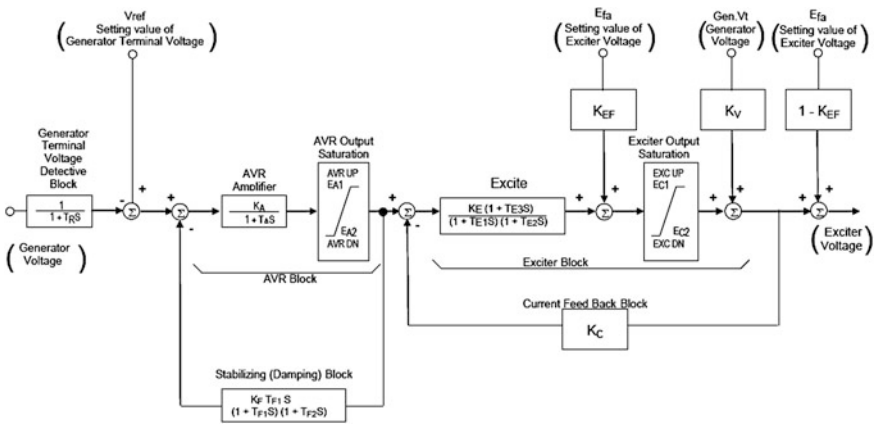

Fig. 20 Modified to IEEE2 Exciter (Stamford AVR's), courtesy of Stamford AvK

Table 5 Generator and AVR data for modelling, courtesy of Stamford AvK

Parameter	Model reference	Value
Regulator forward gain	(KA)	500
Feedback gain	(KF)	0.04 > 0.01
Input filter constant	(TR)	0.01 s
Amplifier time constant	(TA)	0.1 s
Feedback time constant	(TF1)	0.7 s
Feedback time constant	(TF2)	0.05 s
Minimum AVR output	(EA2)	0
Maximum AVR output	(EA1)	8
Maximum rate of change	(DM)	2500
Exciter gain	(KE)	1
Exciter voltage offsets	(KEF)	0
Exciter voltage offsets	(KV)	0
Exciter current F/B gain	(KC)	0
Exciter time constant	(TE1)	See below
Exciter time constant	(TE2)	0
Exciter time constant	(TE3)	0
Maximum exciter output	(EC1)	3
Minimum exciter output	(EC2)	0
Exciter saturation @ 75%	(SE1)	110%
Exciter saturation @ 100%	(SE2)	190%
Exciter time constant	(TE1)	0.22–0.91

9 Diesel Modelling Simulation (Conventional/D-UPS and LLD)

System and technology simulation allows for rapid system prototyping and evaluation. Under such a methodology we examine three common diesel engine configurations, as evaluated via simulation to determine the merits of the each specific topology, case studies 1–3:

- Case 1: Two conventional diesel generators (CDG's) paired.
- Case 2: One CDG and one Diesel UPS with large inertia flywheel.
- Case 3: One CDG and one low load diesel (LLD).

All modelled diesel generator units have identical capacities (1 p.u.) with a constant 0.6 p.u. system load assumed. As, a CDG operating at 60% rated capacity is close to its optimal efficiency loading, it would seem practical to run CDG one at 0.6 p.u. with CDG two turned off. In considering this mode of operation, we need to examine the systems reserve requirements. Power systems are required to demonstrate sufficient reserve to maintain consumer supply under a variety of contingencies. One such contingency is loss of any single generator, should the generator trip off-line for any reasons. This is exactly the scenario modelled for discussion below, Fig. 21.

In Case 1, the second CDG unit is off to limit fuel consumption and preserve engine condition. If both CDG's were on, they would both be required to operate at a conventional low load limit (30% of rated capacity). In Case 2 and 3, the secondary unit is replaced by either a Diesel UPS (UPS-D) with large inertia, or low load diesel (LLD), which are considered On, but in idle mode. For the Diesel UPS this entails decoupling of the engine and alternator/flywheel via a mechanical clutch. For the LLD this entails operating the diesel generator set at no load.

In all case studies a simulated fault, leading to loss of the primary CDG, results in the primary CDG being disconnected and at $t = 4$ s, Fig. 21. At this time the system needs to respond to maintain supply to a constant consumer load. The system behaves as follows:

The results of the simulation are presented in Fig. 22, demonstrating the frequency response for different system configurations. In Case 1, CDG two is unable to start in sufficient time to prevent an excessive drop in frequency, with the cold reserve CDG engine unable to ramp sufficiently to avoid an under frequency power system blackout. In Case 2, the inertia available in the grid is large (thanks to the addition of the flywheel spinning reserve), the drop in frequency is subsequently moderated (2% dip) when the 0.6 p.u. load is picked up by the Diesel UPS. The system is critically damped, and the frequency is eventually returned to stable operation after 10 s (a representative time for the reserve engine to be brought online via closure of the mechanical clutch). In Case 3, the system frequency again drops at a similar rate to that observed under conventional diesel operation, Case 1,

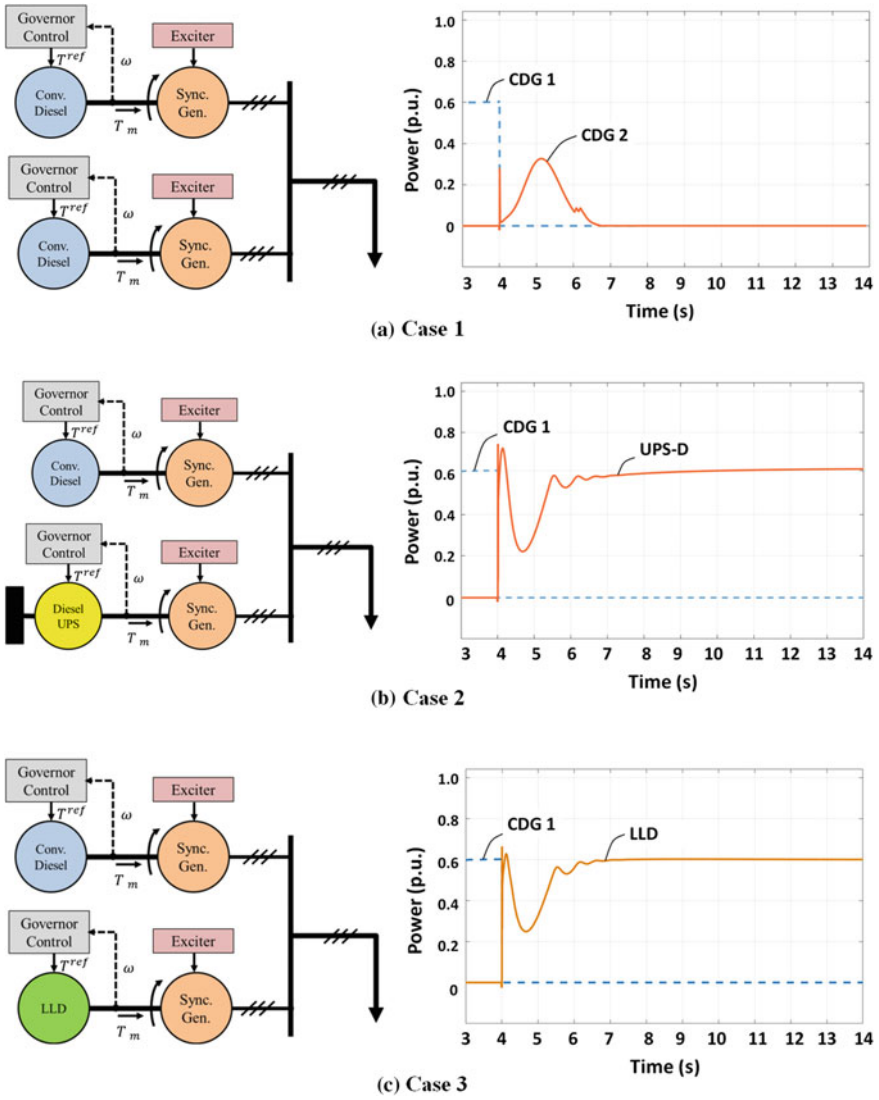

Fig. 21 Different case configurations and loading represented under $N - 1$ simulation

(6% dip), although in this instance the LLD remains online, with the low load diesel offering improved ramp rate response, to that of a cold start diesel. Figure 22 also shows larger frequency transient under Case 3, although the settling time is short, and supply is maintained.

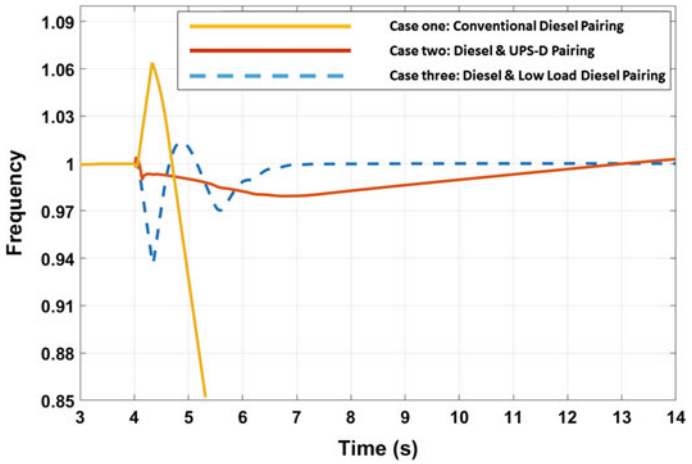

Fig. 22 Frequency response for different types of configurations

Review of the provided simulation provides useful insight into the real world operation of diesel engines, their capabilities and constraints. We can appreciate that power system security may often require more than one diesel engine to be in operation, despite the ability of one diesel to readily meet the apparent load. The need to have two diesel engines running pushes both into a load share arrangement, where they are run inefficiently and lightly loaded. Accordingly system reserve requirements often results in increased system fuel usage and engine wear. One acceptable solution to this issue is to introduce spinning reserve into the system, typically via the introduction of a flywheel (although a battery may alternatively be used to provide synthetic inertia). System inertia provides a dampening effect, affording the reserve diesel unit time to start, thus eliminating the need to have the reserve unit in operation. While this approach ensures engine condition and saves fuel, it unfortunately adds significant cost and complexity to the system design. In Case 3, LLD application achieves functionally adequate spinning reserve via operation of a low load diesel. For Case 3, LLD application achieves much of the fuel reductions afforded under Diesel UPS application, with both approaches permitting the primary diesel to run optimally loaded. (It is important to appreciate the parasitic losses required to motor the flywheel when operational as a synchronous condenser. These losses are approximately equivalent to no load LLD operation). LLD application in principal permits a diesel engine to be run at low load for the provision of security reserve. While LLD application consumes fuel to maintain a no load state, it saves fuel in comparison to a twin CDG architecture, Case 1 (typically 2–3%). Both UPS-D and LLD approaches are thus able to offer the required system security while both returning moderate fuel savings and improving system flexibility. Within hybrid diesel systems, those utilizing RES generation, such improved flexibility can deliver dramatically greater benefit. It is thus within hybrid diesel architectures where LLD finds commercial application.

Accordingly, discussion of the prior case studies can be extended to hybrid diesel systems, inclusive of RES technologies. Within hybrid diesel networks, spinning reserve is increasingly in demand to address RES variability. LLD offers hybrid diesel architectures maximum RES utilization, while providing the additional spinning reserve requirements of such systems. LLD applications accordingly offer optimal savings when paired with high penetration RES generation. In Fig. 23, hybrid system performance is assessed, adopting both a conventional (30%) and LLD (10%) low load constraint. The figure presents the average January daily load profile, with RES generation and demand identical across simulations. Of note, the system energy spillage is significantly reduced under LLD application. Over the course of a year, LLD is modelled to return diesel fuel savings of 10%, with a 16% reduction in fuel consumption possible under a no load limit (0%) [8]. LLD achieves this additional efficiency in partnership with RES generation, given its ability to accept maximum renewable energy content (with the engines able to run lightly loaded at high RES penetration). Within HPS LLD improves renewable penetration, reducing fuel consumption, while maintaining system security without the need for additional energy storage [9]. Accordingly under both diesel and diesel hybrid architectures, LLD has a valuable role to play in maintain system security, reducing fuel consumption, reducing system complexity and minimizing system cost.

10 Economics of Diesel Generation

Diesel generation has historically been presented as the ideal solution to remote and islanded consumers seeking improved electrification. Diesel generators remains a low risk, readily available, well supported and demonstrated technology. However, in recent years we have observed a reliance on diesel generation to expose such communities to volatile commodity and thus energy pricing (terminal gate diesel fuel price). Pricing which is many times higher than in established markets given the premium paid for remote area transport and storage. Diesel prices paid by many

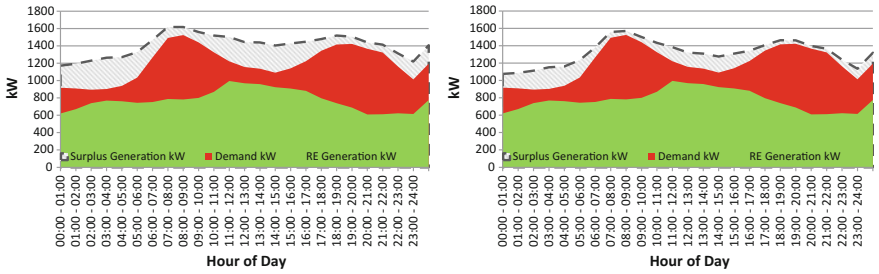

Fig. 23 Load, RES generation and energy spillage under conventional (*left*) and LLD application (*right*)

islanded nations are among the highest paid globally, often 3 or 4 times the price paid for conventional supply [6]. Society has also increasingly come to understand the negative health and environmental impacts linked to diesel emissions.

A number of alternative technologies exist to reduce diesel reliance, with these technologies capable of achieving cost parody with diesel generation [5]. While it is difficult for any reference text to make comment on the cost competitiveness of various RES technologies, given the pace of developments across this sector, it is anticipated these technologies will decrease in cost as they achieve improved economies of scale. The following case studies are provided to demonstrate the current cost competitiveness of RES architectures, with an anticipation that future RES costs will fall below the cost of diesel generation for many islanded countries. As the following cases studies illustrate RES integration can achieve both economic and environmental benefits for islanded communities, with the scale of such benefit dependent on the geography, natural resource, population density, location and seasonality of the application. As the case studies below will illustrate RES integration can be used to reduce energy costs, restructure an underperforming and unreliable power system, or to remove diesel generation entirely from a network, with both the costs and benefits scaling proportional to the intended application.

10.1 Viti Levu Island, Fiji, Pacific

Fiji is a Melanesian island nation in the South Pacific, consisting of 110 permanently inhabited islands, home to over 880,000 islanders. Fiji has developed a diverse mix of renewable technologies including hydro, wind and biomass, the installed capacity of which exceeds 62% of total generation capacity [53]. Over 60% of generation is supplied via renewable technologies, delivering Fiji both the lowest oil dependency and the lowest cost of energy among all the islands of the Pacific [29]. Fiji is home to emerging economic activity, inclusive of mining, manufacturing and construction industries, which expansion of RES integration, including geothermal and solar, envisaged to meet 99% of demand across all sectors by 2030.

Viti Levu, the main island within Fiji, Fig. 24, represents the majority of RES capacity within Fiji, as serviced by a central 132 kV transmission backbone. As such, RES penetration on Viti Levu is significantly higher than the national average, Table 6.

10.2 Cabo Verde, Atlantic Ocean

Cabo Verde is a volcanic archipelago of 10 islands sitting of the western coast of Africa. Given its climate and resources, it imports most of its food and relies on desalination for most of its drinking water. The economy is heavily reliant on

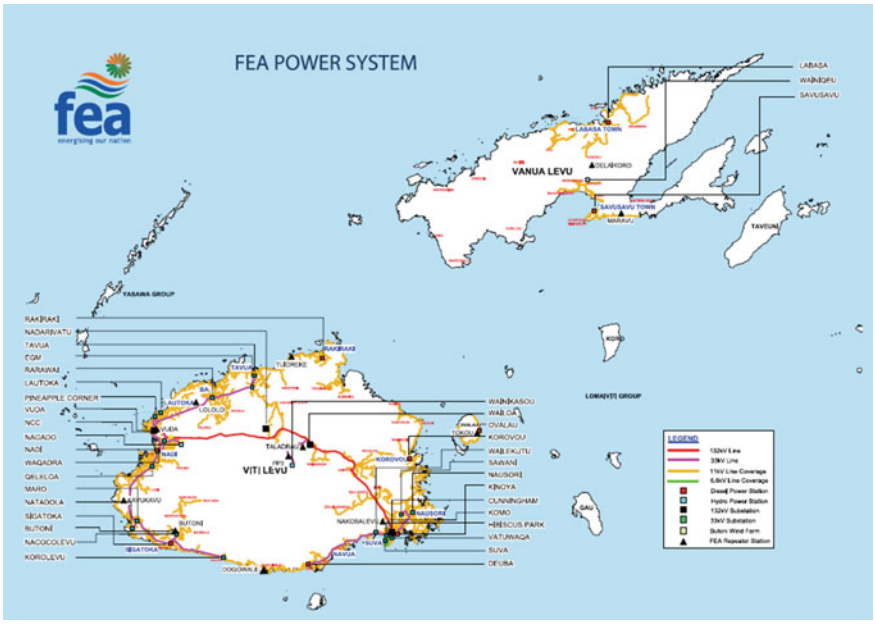

Fig. 24 FEA service supply network, Fiji. *Source* FEA

Table 6 Fiji Energy market metrics

Electricity access (2012)		92%
Installed capacity (2012)	263 MW	
Renewable capacity combined (2012)	164 MW	62%
Renewable capacity hydro (2012)	129 MW	49%
Renewable capacity wind (2012)	10 MW	4%
Renewable capacity solar (2012)	Unknown	n.a.
Renewable capacity biomass (2012)	25 MW	9%
Total generation (2012)	823 GWh	
Renewable generation combined (2012)	493	60%
Renewable capacity hydro (2012)	452	55%
Renewable capacity wind (2012)	33	4%
Renewable generation solar (2012)	Unknown	n.a.
Renewable generation biomass (2012)	8	1%
Electricity tariff (subsidized)	8 c/kWh	
Electricity tariff (unsubsidized)	17 c/kWh	

Source IRENA 2014 [29, 53]

tourism and fishing. With a high dependence on diesel generation and unaffordable electricity tariffs, the Cabo Verde's utility became insolvent, requiring administration by the government. As a result of subsequent modernisation, a quarter of the countries energy supply is now met via renewable generation, Table 7, with the

Table 7 Cabo Verde energy market metrics

Electricity access (2012)		99%
Installed capacity (2012)	140.5 MW	
Renewable capacity combined (2012)	33.9 MW	24%
Renewable capacity hydro (2012)	n.a.	n.a.
Renewable capacity wind (2012)	26.4 MW	19%
Renewable capacity solar (2012)	7.5 MW	5%
Renewable capacity biomass (2012)	n.a.	n.a.
Total generation (2012)	330 GWh	
Renewable generation combined (2012)	68.7	21%
Renewable capacity hydro (2012)	n.a.	n.a.
Renewable capacity wind (2012)	61.3 MW	19%
Renewable generation solar (2012)	7.4 MW	2%
Renewable generation biomass (2012)	n.a.	n.a.
Electricity tariff (subsidized)	38 c/kWh	

Source IRENA 2014 [29]

government setting a target to reach 50% over the next few years. Cabo Verde endures one of the highest electricity tariffs in the world, creating a market attractive to Independent Power Producers (IPPs), with the government keen to reprivatize the utility and reach its RES targets purely via private investment, unsupported by any feed in tariff or alternative subsidy.

11 100% Renewable Energy System Design

We have talked of increasing diesel fuel prices and falling RES prices. As these price trajectories extend past the commercialisation of battery storage systems, many market participants anticipate a rapid transition to 100% RES architectures. While this end point appears to be the logical progression of higher and higher RES penetration, indeed King Island in Tasmania is already able to run 100% diesel off, both the timing and the costs associated with this transition are unknown. While the commercialisation of energy storage will no doubt be advanced via the adoption of partner technologies, such as electric vehicles (electric vehicle uptake creates an ideal supply stream of repurposed batteries for the stationary power storage market) Unfortunately cost parody for these systems is expected to be at least a decade away. With this in mind, the prospects for any imminent energy storage revolution should not be used as an excuse for delay or inaction by islanded countries. Many cost effective steps are available to transition existing power systems in preparation for an eventual 100% RES capacity. These include configuring a power system to be modular and expandable, maximising the costs effective level of RES integration, and updating or reconfiguring diesel generation to allow for maximum RES

utilization. It is also important for all stakeholders to acknowledge diesel generation as an essential component to the operability of islanded country power systems, irrespective of energy storage. 100% RES configurations remain reliant on some form of scheduled generation reserve for occasions when renewable supply and storage is unable to meet demand. Diesel generation is ideally placed to meet this requirement given the infrastructure is already in place. Thus, the end game appears to be one of reduced reliance on diesel, acknowledging the residual value these technologies can plan in transitioning communities to the power systems of the future. This chapter has presented a few such opportunities, with the audience reminded that for many islanded countries, electrification is an essential pathway to improve the living standards and opportunities for their communities. How effectively we meet this need remains reliant on our ability to communicate the embodied challenges and opportunities available to existing generation infrastructure.

12 Conclusion

It can be easy to identify opportunity for RES integration within islanded countries solely reliant on diesel fuel for electricity generation. In response, the default approach to system design and development is increasingly to adopt hybrid diesel architectures. Less apparent are the societal challenges inherent in moving these communities away from an established and reliable technology. As the level of RES integration increases additional technical challenges also present around maintaining robust and secure power systems.

This chapter presents possible solutions, advocating a step-by-step transitional approach to the promotion of increased RES utilization. The main advantage of this approach has been to extract maximum value from the existing generation footprint. We have seen how diesel generator operability, often considered as a simple but inflexible supply solution, is in fact a complex and adaptable technology, able, if configured correctly, to run in cooperation with various RES technologies. Indeed multiple approaches exist to configure and control legacy diesel generator as a means to integrate greater levels of renewable penetration. As systems transition from diesel dependence to greater RES utilization, the degree to which value is returned depends heavily on an understanding of the opportunities and challenges presented in this chapter. Principally opportunity to move away from legacy load limit constraints, to capture significantly improved RES value under LLD application.

Preliminary modelling has demonstrated how LLD approaches offer improved system flexibility, given either a diesel, or diesel hybrid architecture. Under a hybrid scenario, diesel assets are required to perform in parallel to a variable RES, and hence the requirement for flexibility is greatest. While spinning reserve or energy storage can be integrated into a system to improve RES integration, a simpler and more cost effective approach is to run your diesel generator sets at low load. As the

technical barriers to low load operation are addressed, LLD presents as both an improved system security and improved RES penetration enabler, accessible to all diesel power systems.

Acknowledgements The authors would like to thank the Office of Navy Research Global (ONRG), Hydro Tasmania and the Australian Research Council (ARC) for funding contributed towards research of utilization and optimization of diesel generation sources for maximum renewable integration.

References

1. Nayar C (2012) Innovative remote micro-grid systems. Int J Environ Sustain 1(3):53–65
2. Frischknecht I (2014) Increasing renewable energy off the grid. Paper presented at the 1st Australian Remote Area Power Supply Conference, Perth, 17 Mar 2014
3. Nikolic D, Negnevitsky M, de Groot M et al (2014) Fast demand response as an enabling technology for high renewable energy penetration in isolated power systems. Paper presented at IEEE PES General Meeting, Washington, DC, 27–31 Jul 2014
4. Hamilton J, Negnevitsky M, Wang W (2015) Low load diesel perceptions and practices within remote area power systems. Paper presented at IEEE International Symposium on Smart Electric Distribution Systems and Technologies (EDST) CIGRE SC C6 Colloquium, Vienna, Austria, 8–11 Sept 2015
5. Al-Hammad H, Becker T, Bode A et al (2015) Renewable energy in hybrid mini-grids and isolated grids: economic benefits and business cases, Frankfurt School—UNEP Collaborating Centre for Climate and Sustainable Energy Finance
6. Mofor L, Isaka M, Wade H et al (2013) Pacific lighthouses: renewable energy roadmapping for islands, the International Renewable Energy Agency (IRENA)
7. Haruni AMO, Negnevitsky M, Haque ME et al (2013) A novel operation and control strategy for a standalone hybrid renewable power system. IEEE Trans Sustain Energy 4:402–413
8. Mendis N, Muttaqi KM, Perera S et al (2015) An effective power management strategy for a wind-diesel-hydrogen-based remote area power supply system to meet fluctuating demands under generation uncertainty. IEEE Trans Ind Appl 51:1228–1238
9. Hamilton J, Negnevitsky M, Wang X et al (2016) No load diesel application to maximise renewable energy penetration in offgrid hybrid systems. Paper presented at CIGRE Biennial Session 46 (C6 PS3), Paris, 21–26 Aug 2016
10. Hamilton J, Negnevitsky M, Wang X et al (2016) Investigation of no load diesel technology. Paper presented at IEEE PES General Meeting, Boston, 17–21 Jul 2016
11. Wang DH, Nayar CV, Wang C (2010) Modelling of stand-alone variable speed diesel generator using doubly-fed induction generator. In: 2nd International Symposium on Power Electronics for Distributed Generation Systems, PEDG, 16–18 June 2010, Hefei, China, pp 1–6
12. Cooper AR, Morrow DJ, Chambers KDR (2010) Performance modelling of generator sets during load acceptance In: 45th international universities power engineering conference (UPEC), pp 1–5
13. Glassmire J, Komor P (2012) Electricity storage and renewables for island power: a guide for decision makers, the International Renewable Energy Agency (IRENA)
14. Maruf-ul-Karim M, Iqbal MT (2010) Dynamic modelling and simulation of a remote wind-diesel-hydrogen hybrid power system, In: 4th IEEE electrical power and energy conference: "Sustainable Energy for an Intelligent Grid", EPEC, 25–27 Aug 2010
15. Green N, Mueller-Stoffels M, Whitney E (2016) Diesel generator report, Alaska Affordable Energy Strategy, Alaska Center for Energy and Power, Fairbanks, AK

16. Lee R, Pedley J, Hobbs C (1998) Fuel quality impact on heavy duty diesel emissions:-a literature review. SAE Technical Paper 0148-7191
17. Bacha J, Freel J, Gibbs A et al (2007) Diesel fuels technical review, chevron global marketing. Available via https://www.chevron.com/-/media/chevron/operations/documents/diesel-fuel-tech-review.pdf. Accessed 04 June 2016
18. Jaaskelainen H, Majewski A (2013) What is diesel fuel [online]. Available: https://www.dieselnet.com/tech/fuel_diesel.php. Accessed 06 June 2016
19. Majewski A (2012). What are diesel emissions [online]. Available: https://www.dieselnet.com/tech/emi_intro.php. Accessed 12 June 2016
20. Majewski A (2013) Diesel particulate matter [online]. Available: https://www.dieselnet.com/tech/dpm.php. Accessed 06 Jul 2016
21. Various (2010). Gaseous emissions [online]. Available: https://www.dieselnet.com/tech/emi_gas.php. Accessed 06 Jul 2016
22. Sluder CS, Storey JME et al (2005) Low temperature urea decomposition and SCR performance. SAE paper, 2005-01-18582
23. Vuk CT (2005) Turbo compounding: a technology who's time has come. John Deere Moline Technical Center. Available at http://energy.gov/sites/prod/files/2014/03/f9/2005_deer_vuk.pdf. Accessed 24 Jul 2016
24. Jaaskelainen H, Majewski A (2013) Smoke opacity [online]. Available: https://www.dieselnet.com/tech/measure_opacity.php. Accessed 12 Jul 2016
25. Majewski A (2012) Diesel oxidation catalyst [online]. Available: https://www.dieselnet.com/tech/cat_doc.php. Accessed 16 June 2016
26. Riesz J (2012) Off-grid solar in the mining sector, AECOM [online]. Available: http://jenny.riesz.com.au/wp-content/uploads/2013/06/Off-grid-Solar-in-the-Mining-Sector.pdf. Accessed 12 Jul 2016
27. Mofor L, Journeay-Kaler P (2013) Pacific lighthouses: hybrid power systems, the International Renewable Energy Agency (IRENA) [online]. Available: http://irena.org
28. Kempener R, Lavagne d'Ortigue O, Saygin D et al (2015) Off-grid renewable energy systems: status and methodological issues, the International Renewable Energy Agency (IRENA) [online]. Available: http://irena.org
29. Various (2014) Renewable Islands: settings for success, global renewable energy islands network, International Renewable Energy Agency [online]. Available: http://irena.org
30. Wiser R, Bolinger M (2016) 2014 wind technologies market report. US Department of Energy [online]. Available: http://www.energy.gov/
31. Ong S, Campbell C, Denholm P et al (2013) Land-use requirements for solar power plants in the United States, National Renewable Energy Laboratory [online]. Available: http://www.nrel.gov/
32. Wet Stacking of Generator Sets and How to Avoid It (2012) [online]. Available: http://www.cliffordpower.com/stuff/contentmgr/files/0/971a5485c1088e9230413aa3d1189ef7/misc/is_09_wet_stacking.pdf. Accessed 15 July 2016
33. Nikolic D, Negnevitsky M, Groot MD (2015) Effect of the diesel engine delay on stability of isolated power systems with high levels of renewable energy penetration. Presented at IEEE International Symposium on Smart Electric Distribution Systems and Technologies (EDST) CIGRE SC C6 Colloquium, Vienna, Austria, 8–11 Sept 2015
34. Kech J, Hegner R, Mannle T (2014) Turbocharging: key technology for high-performance engines. MTU Engine Technology White Paper, 2014
35. Parra CAF (2008) Heat transfer investigations in a modern diesel engine. University of Bath, PhD thesis, Feb 2008, pp 6–7
36. Jaaskelainen H (2013) Variable geometry turbochargers [online]. Available: https://www.dieselnet.com/tech/air_turbo_vgt.php. Accessed 04 Dec 2015
37. Fetters A (2013) Discussion of low load diesel options. Presented at the Alaska Wind Diesel Workshop, Seward, Alaska, 14–15 Feb 2013
38. Manwell J, Stein W, Rogers A et al (1992) An investigation of variable speed operation of diesel generators in hybrid energy systems. Renew Energy 2:563–571

39. Mathews SV, Rajakaruna S, Nayar CV (2013) Design and implementation of an offgrid hybrid power supply with reduced battery energy storage. Paper presented at 2013 Australasian Universities Power Engineering Conference, AUPEC 2013, 29 Sept–3 Oct 2013, Hobart, TAS, Australia
40. Fan Y, Rimali V, Tang M et al (2012) Design and implementation of stand-alone smart grid employing renewable energy resources on Pulau Ubin Island of Singapore. Paper presented at Asia-Pacific Symposium on Electromagnetic Compatibility, APEMC, 21–24 May 2012, Singapore, pp 441–444
41. Stott PA, Mueller MA (2006) Modelling fully variable speed hybrid wind diesel systems. Paper presented at 41st International Universities Power Engineering Conference, UPEC, 6–8 Sept, Newcastle upon Tyne, UK, pp 212–216
42. Dengler P, Geimer M, Zahoransky R (2011) Potential of reduced fuel consumption of diesel-electric APUs at variable speed in mobile applications. Paper presented at 10th International Conference on Engines and Vehicles, ICE, 11–15 Sept 2011, Naples, Italy
43. Koczara W, Iwanski G, Kaminski B et al (2008) Power distribution in RES-diesel autonomous power system with doubly fed induction generator for reduction of fuel consumption. Paper presented at 11th International Conference on Optimization of Electrical and Electronic Equipment, OPTIM, 22–24 May 2008, Brasov, Romania, pp 339–344
44. Majewski A, Jaaskelainen H (2009) Biodiesel—Mono Alkyl Esters [online]. Available: https://www.dieselnet.com/tech/fuel_biodiesel.php. Accessed 14 Mar 2016
45. European Committee FOR Standardization, EN 590. Automotive fuels—diesel—requirements and test methods (2013)
46. Mahon LLJ (2003) Diesel generator handbook. Butterworth Heinemann, Great Britain, p 3
47. Heywood JB (1988) Internal combustion engine fundamentals. McGraw-Hill, Singapore, p 46
48. Stavrakakis G, Kariniotakis G (1995) A general simulation algorithm for the accurate assessment of isolated diesel-wind turbines systems interaction a general multimachine power system model. Energy Convers IEEE Trans 10:577–583
49. Rajasekaran V, Merabet A, Ibrahim H (2012) Modelling, simulation and development of supervision control system for hybrid wind diesel system supplying an isolated load. Wind Energy Techno-Centre Report, Saint Mary's University
50. Kundur P, Balu NJ, Lauby MG (1994) Power system stability and control, vol 7. McGraw-Hill, New York
51. IEEE (2006) Recommended practice for excitation system models for power system stability studies, vol. Std 421.5
52. IEEE (1987) Procedures for obtaining synchronous machine parameters by standstill frequency response testing . In IEEE guide: test procedures for synchronous machines, vol. Std 115
53. Various (2015) Fiji renewables readiness assessment, International Renewable Energy Agency, 2015 [online]. Available: http://irena.org

Optimal Control System of Under Frequency Load Shedding in Microgrid System with Renewable Energy Resources

T. Madiba, R.C. Bansal, J.J. Justo and K. Kusakana

Abstract Nowadays many of the power systems are facing serious problems because of the lack of know-how to utilize the available renewable energy resources (RER) so as to balance between the power supply and demand sides. As the consequence of the power unbalancing into their distribution networks, under frequency load shedding (UFLS) which leads to life span reduction of various expensive equipment and deteriorating production in general are of much concerns. Thus, proper control system for the load flow in a system like microgrids (MG) with RER in general is the first thing to carry out the assessment with the aim to solve the power balancing problem within the power system networks. Actually, the major problems which many utilities are facing all over the world are how to utilize the available and future energy resource reserves in order to balance between the supply and demand sides within their power distribution networks. Moreover, because of the quick, improvised and unforeseen increasing number of consumers' power demands and lack of additional macro energy resources plants which can favorably respond to the instantaneous consumer requirements, optimal control strategy (OCS) is inevitable. The OCS is required to maintain the steady-state operations and ensure the reliability of the entire distribution system over a long period. For that case, the OCS is required to principally stabilize parameters such as voltage, frequency, and limit the injection of reactive power into the MG system under stress. Therefore, in this chapter, the OCS is proposed as an approach to be

T. Madiba (✉) · R.C. Bansal · J.J. Justo
Department of Electrical, Electronics and Computer Engineering,
University of Pretoria, Pretoria, South Africa
e-mail: symphomadiba@gmail.com

R.C. Bansal
e-mail: rcbansal@ieee.org

J.J. Justo
e-mail: jackjusto2009@gmail.com

K. Kusakana
Department of Electrical, Electronics and Computer Engineering,
Central University of Technology, Bloemfontein, South Africa
e-mail: kkusakana@cut.ac.za

F.M.R. Islam et al. (eds.), *Smart Energy Grid Design for Island Countries*,
Green Energy and Technology, DOI 10.1007/978-3-319-50197-0_3

applied in an intelligent way to solve the UFLS and blackout problems (BP) in a typical MG with RER. The proposed control solution is analyzed using emergency power supply reserves integrated with RER. These typical energy resources can be wind and photovoltaic (solar PV) systems associated with the battery energy storage system (BESS), hydro pump storage, biomass power plant and fuel cell systems.

Keywords Optimal control system (OCS) · Microgrid (MG) · Under frequency load shedding (UFLS) · Wind turbine · PV system · Batteries energy storage systems (BESS) · Renewable energy resources (RER)

1 Introduction

Energy industry has been the major driving force for the technological development of mankind through the famous biological theme of "survival of the fittest." Actually, the world population grows in arithmetic progress with the demand for energy. The conventional power generating systems utilize fossil fuel (i.e., coal, gas and oil) as their primary input sources to the boiler for combustion. Now, the by-products of the combustion system (such as CO, NO_x, and SO_x) are the major causes of environmental pollution which is detrimental to both human and animal health. In fact, the carbon dioxide (CO_2) emitted during combustion has been identified as the main cause of global warming which result in undesirable climate change. Thus, to eliminate the dependent on fossil fuels as the primary source of energy and mitigate their environmental consequences, renewable energy resources (RER) like photovoltaic (PV), biomass and wind energy are the promising solutions [1].

More specifically, a small-scale power generating system close to the customers is considered as a microgrid (MG) system. Technically, small capacity power generating units such as those using RERs can be integrated in the MG system. Some of the advantages of adopting the concept of the MG system include reduction of line losses, network congestion and line costs by increasing the energy efficiency [2]. On the other hand, there are challenges which hinder the direct implementation of the RERs in the form of MG system into the existing power networks. These challenges are voltage and frequency control, intelligent energy management systems, power converters control systems which link various power generating units in the MG system, and investment cost practical implementation as well as the social acceptability. However, the higher level of flexibility and reliability provided by the MG system when run both in grid-connected and islanded modes of operations outweigh the above-mentioned challenges when observing from the grid perspectives. In that case, the MG system and its components may physically be close to customers and distributed geographically depending with their energy resource allocation [3].

The concept of the MG is that many micro generators are connected to grid with the objective to reduce the need of the network distribution system [4]. However, the MG can be integrated with the network system but this can produce a problem to the safety and reliability of the grid due to the net loss of line flow, voltage and power quality [5]. Generally, the MG operates in two modes which are islanded and grid-connected. For single MG, different control strategies are used to stabilize the output which utilizes *P-f* and *Q-V* control modes for grid-connected and isolated mode [6]. The combination of a series of control strategies are utilized to enable stable operation of the MG in each mode and switch smoothly between the two modes [7]. A blackout in a power system refers to the absence of power supply in a given area/community for a short or long period. These power blackouts can occur due to natural disasters or technical reasons. The stable operation of a power system requires frequency and voltage to be constant [8]. When power grid fails to supply sufficient power [9], the appliances of under frequency load shedding (UFLS) models could improve the system frequency dynamic response and enhance the stability of power grid and in the past many researchers have focused on this subject [10]. The UFLS models describe the detailed procedures of how many steps should be taken and how much load should be shedded at each step [11]. Load shedding scheme based on frequency alone has several disadvantages, among which are the load may be tripped unnecessarily at low import level and too much load tripped at high import level [12]. The traditional or conventional load shedding approach does not provide optimum load shedding solution and cannot deal efficiently with modern and complex power systems [13, 14].

To address these problems, the application of half-adapted and adapted methods UFLS with less amount of loads being shed compare to the conventional systems have been presented [15]. Although, nonlinear optimization model can solve this problem more accurately, this method is very lengthy, that is, it increases computational complexity when practical results are of interests as it takes longer time [16]. Alternatively, computational intelligence techniques which have robust and flexible properties when dealing with complex nonlinear systems could be an option in addressing this problem [17]. The limitation of computational intelligence techniques restricts their applications in load shedding in real time [18]. Because of this reason, this chapter discusses a solution regarding load shedding and blackout problems into the MG power system, and proposes a method of controlling the voltage and frequency within the MG system when operating in grid-connected mode as well as in islanded mode.

The chapter is organized as follows: the general introduction about the chapter which includes the problem statement, literature review on MG concept and control methods is provided in Sect. 1. In Sect. 2, the general configuration of the MG system is prevailed with brief description of its various components including renewable and nonrenewable energy technologies while Sect. 3 presents their detail operating characteristics. The contribution of renewable and nonrenewable resources into the MG system is explained in this section by highlighting the

problem statement, objective function, system constraints and later on simulation studies are presented. The conclusion and technical challenges to further improve the performance of the MG systems are briefly explained in Sect. 4.

2 General Configuration of the MG System

The main work with electric utilities is to design and implement Community MGs that utilize local renewable energy resources to provide a reliable and cost-effective foundation for a modern grid. The operation principles the MG system technologies is based on the number of its main components applied at supply and customer sides [19]. The fundamental of realizations activities for different types of renewable energy technologies and others sources of energy include the major points listed as follows: land clearing for site preparation and access routes; excavation, blasting, and filling; logistic aspect of materials and fuels; construction of foundations involving excavations and placement of concrete; operating cranes for unloading and installation of equipment; construction and installation of associated infrastructure [20], construction and reticulation plans of power cables; and closeout and decommissioning activities may include removal of project infrastructure and site rehabilitation [21]. The next subsections present the details characteristics of a MG system containing various renewable energy technologies which can be used in the MG system.

2.1 MG System General Model

This section explains an overview of the MG with various renewable energy technologies (RETs) looking on the principles of their operating characteristics and limitation. Their configuration when operating as MG system with power electronics interfaces is also briefly highlighted in the Fig. 1 The MG shown is containing RETs such as diesel generator, micro-hydropower, hydro pump storage, wind turbine generator, PV system, inverters, bidirectional converter and a battery storage system in case of power shortage when there is no power from any of the supply sources. From the demand side, there are a certain number of loads to be feed with power during the specified period of the day according to the daily consumption needs.

As said before, the subsections of the Sect. 2.1 give the brief descriptions and the operating principles of some of the RETs to be applied into the MG system with the objective to keep the power system operating continuously.

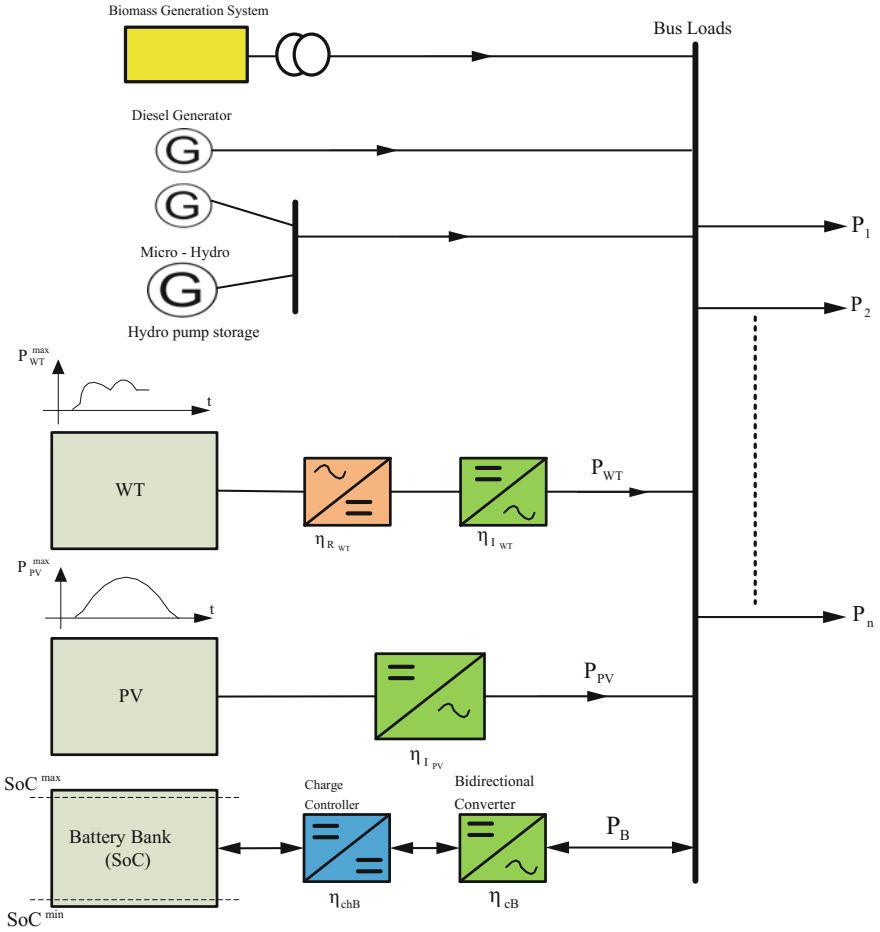

Fig. 1 Representation of a MG system general model

2.1.1 Micro-Hydropower System

The micro-hydropower requires water from the river to be channeled through a basin where sediment which may damage the turbine is removed. The water is then passed to a tank before flowing downhill through a pipe called a penstock. A turbine is located at the bottom of the penstock and is driven by the force of the falling water to produce electricity [22]. The communities should be made to participate fully from the beginning in order to own the project and maintain it through its lifetime. Once the system is in operation, the local people pay a small charge to use the electricity, which is used to cover maintenance and the eventual cost of replacement. The locals are also involved in the construction which will enable them to maintain the facility [23]. Today, small hydropower projects offer

emissions-free power solutions for many remote communities throughout the world such as those in Nepal, India, China, and Peru as well as for highly industrialized countries, like the United States. The energy head in the water flowing in a closed conduit of circular cross section, under a certain pressure, is given by Bernoulli's equation [24]:

$$H_1 = h_1 + \frac{P_1}{\gamma} + \frac{V_1^2}{2g} \tag{1}$$

where H_1 is the total energy head, h_1 is the elevation above some specified datum plane, P_1 the pressure γ the specific weight of water, V_1 the velocity of the water, and g the gravitational acceleration. The total energy head at point 1 is then the algebraic sum of the potential energy h_1, the pressure energy P_1/γ, and the kinetic energy $V_1^2/2g$, commonly known as the "Velocity head." For an open channel, the same equation applies, but with the term P_1/γ replaced by d_1, the water depth [25].

2.1.2 Photovoltaic System

PV technology system seems to be the simple and desired method because of its easier method of maintenance, installation process, which is highly important in a small, remote island nation with limited technical expertise or access to replacement parts. It can be developed as a distributed system of small-sized systems, which can spread benefits widely and has the potential for widespread replication. The flexibility of the grid stability and grid management is increased by the predictable PV system. The major opportunities to develop PV technology is significant in private sectors where the systems seems to be economical and competitive compared with other options and the government expects it to become more so in the near to mid-term [26]. Figure 2 represents a diagram of PV system supplying the AC load via inverter and the DC load via a controller.

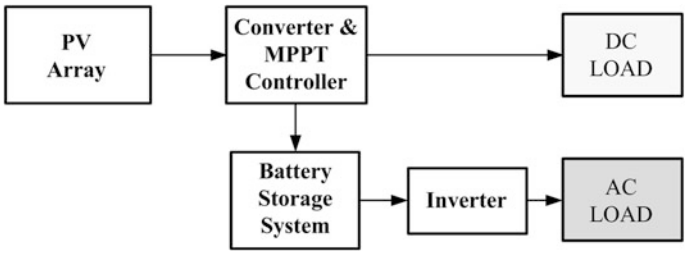

Fig. 2 PV generator system diagram layout

2.1.3 Biomass System

The value of a particular type of biomass depends on the chemical and physical properties of the large molecules from the source [27]. More recently, fossil biomass has been exploited as coal and oil. However, since it takes millions of years to convert biomass into fossil fuels, these are not renewable within a time-scale mankind can use [28]. Burning fossil fuels uses "old" biomass and converts it into "new" CO_2; which contributes to the "greenhouse" effect and depletes a nonrenewable resource [29]. Burning new biomass contributes no new carbon dioxide to the atmosphere, because replanting harvested biomass ensures that CO_2 is absorbed and returned for a cycle of new growth [30]. One of the dilemmas facing the developed world is the need to recognize this time delay and take appropriate action to mitigate against the lag period [31]. Biomass can be converted into three main types of products such as electrical or heat energy, transport fuel, and chemical feedstock but of particular interest in this study, the main purpose here is the generation of electricity [32]. The biomass system typical plant diagram layout is presented in Fig. 3 As this can be seen in the diagram, the biomass heat system is characterized by the input parameter Q_{in} and outputs such as the energy from the turbine W_t, cooling water Q_{out}, and the pump W_p. The design of a biomass plant technology is based on these four main factors as shown in the Fig. 3 [31, 32].

2.1.4 Battery Bank System Characteristics

Without batteries to store energy, it would only be possible to have power when renewable energy sources are available or the diesel generator running [33–36]. It must also be decided how many days' worth of energy must be stored in the battery bank. Generally, system designs allow for an autonomy range of 2–5 days. In the case of the example, an autonomy capacity of 2 days will be taken into account. The total battery energy of a certain number of kW is multiplied by two and results

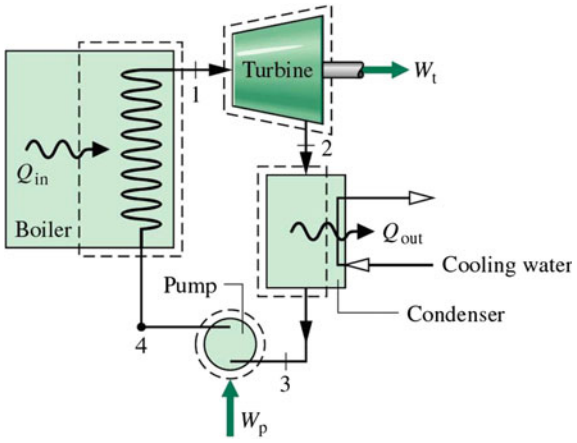

Fig. 3 Biomass system plant layout

in kWh, which then gives system autonomy of 2 days [37–39]. When designing MG system, solar power generation systems, the designer must pay specific attention to the selection of PV modules, batteries, inverters, and installation material and labor expenses, and specifically be mindful of the financial costs of the overall project. The designer must also assume responsibility to assist the end user with rebate procurement documentation [40]. Figure 4 shows how a storage battery system unit is installed into the grid system with the objective to compensate with power in case of shortage of energy for the household system.

2.1.5 Wind Turbine Generator Characteristics

Many rural areas have an ideal situation for developing community sized wind projects on their reservations. Frequency control requires real-time balance between generation and load, with system frequency deviation maintained within a certain range and for a large interconnected system, frequency control performance is important because of reliability concerns [41]. Figure 5 shows the wind turbine generator system with the objective to give the idea of the operating principle of this technology.

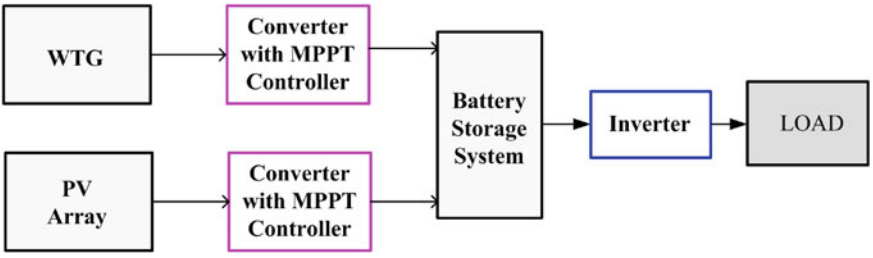

Fig. 4 Storage batteries diagram system interfacing DER

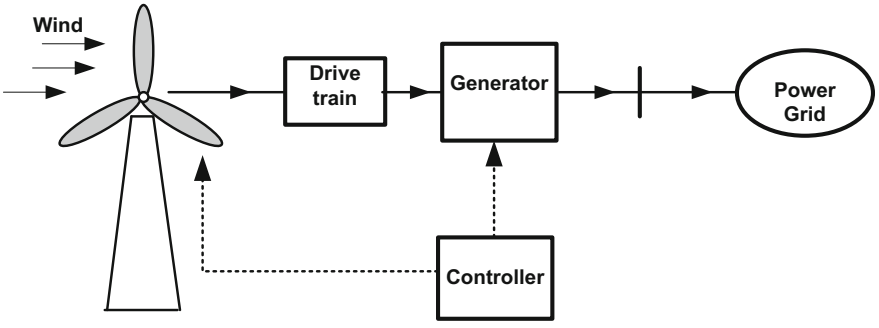

Fig. 5 Wind turbine generator system layout [41]

The operation of wind system requires adequate knowledge of average wind conditions as well as the information on the turbulent nature of the wind [42]. The knowledge of wind turbulence of a given site is necessary for cost optimization of modern large wind turbines and it is crucial in the designing of the supporting structures for wind turbines [43]. It also helps in the design of appropriate control system that can mitigate the impact of structural loading on wind turbine resulting from the turbulent wind [44].

One of the most important criteria for determining the feasibility of a wind project is the level of wind resource available. The amount of energy that can be harnessed from the wind is greatly dependent on the wind speed. Small to medium size wind turbines generally need at least a class two wind resource, which averages 4.1–4.9 m per second. To easily explain the wind turbine design and its aerodynamic characteristics, first consider the speed of wind as a random variable. The Weibull distribution function with two parameters is commonly used to describe a wind speed data [45]. It provides a convenient representation of the wind speed data for wind energy calculation purposes. The general representation of the Weibull distribution is given by:

$$F(V_{\text{wind}}) = (\eta/c)(V_{\text{wind}}/c)^{\eta-1} \exp(-(V_{\text{wind}}/c)^{\eta}) \tag{2}$$

where V_{wind} is the wind speed (m/s), c is the scale factor of the Weibull distribution with unit of speed, and η is the shape factor of the Weibull distribution, which is dimensionless. There are several methods for calculating the parameters of the Weibull wind speed distribution for wind energy analysis. Generally, we can calculate the two parameters using the following expression:

$$\eta = (\sigma_{\text{w}}/V_{\text{mean}})^{-1.086} \text{ and } c = \frac{V_{\text{mean}}}{\gamma(1+1/\eta)}, \tag{3}$$

where the γ is the gamma function, V_{mean} is the average value of wind speed data, and σ_{w} is the standard deviation of the wind speed data.

The mechanical part of the wind turbine consists of a yaw system, a pitch system, blades, a tower, and a gearbox in which the extracted wind power from air moving mass is transmitted to electrical system, i.e., generator for electric power generation. The extracted power can be expressed as [46, 47]:

$$\begin{cases} P_{\text{m}} = \frac{\rho}{2} A_r V_{\text{wind}}^3 C_{\text{p}}(\lambda, \beta) \\ \lambda = R_T \times \omega_T / V_{\text{wind}} \end{cases}, \tag{4}$$

where P_{m} is the mechanical active power in watts, ρ is the air density in kg/m^3, A_r represents the surface area swept by the blade in m^2, V_{w} stands for the wind velocity in m/s, and C_{p} (λ, β) is the power coefficient which is a function of the tip speed ratio (i.e., λ) of the turbine blade and its pitch angle (i.e., β) in degree. Also, R_T represents the radius of the rotor in meter while ω_T is the mechanical speed of the rotor in rad/s.

Based on (4), the torque output by the wind turbine can be expressed as [48]:

$$T = \rho\pi R^3 C_{\mathrm{p}}(\lambda,\ \beta) V_{\mathrm{wind}}^2 / 2\lambda. \tag{5}$$

Therefore, referring to (4) above, the rotor speed can be regulated to maintain λ at its optimum value λ_{opt} and C_{p} at its maximum designed value C_{pmax}. In this case, the maximum power captured by the wind turbine is given by [49]:

$$P_{\max} = \rho\pi R^5 C_{\mathrm{p\,max}} \omega_{\mathrm{opt}}^3 / 2\lambda_{\mathrm{opt}}^3 = k_{\mathrm{opt}} \omega_{\mathrm{opt}}^3 \tag{6}$$

and the maximum torque is

$$T_{\max} = \rho\pi R^5 C_{\mathrm{p\,max}} \omega_{\mathrm{opt}}^2 / 2\lambda_{\mathrm{opt}}^2 = k_{\mathrm{opt}} \omega_{\mathrm{opt}}^3 \tag{7}$$

where k_{opt} is the constant which is determined by the wind characteristics. The coefficient C_{p} can be approximated using the wind turbine characteristics [48, 49]:

$$\begin{cases} C_{\mathrm{p}}(\lambda,\ \beta) k_1 \left(\frac{k_2}{\lambda_1} - k_3\beta - k_4\right) e^{\frac{-k_5}{\lambda_1}} + k_6\lambda \\ \frac{1}{\lambda_1} = \frac{1}{\lambda + 0.08\beta} - \frac{0.035}{\beta^3 + 1} \end{cases}, \tag{8}$$

where the coefficients k_1–k_6 depend on the wind turbine design characteristics which are given by $k_1 = 0.5176$, $k_2 = 116$, $k_3 = 0.4$, $k_5 = 21$, and $k_6 = 0.0068$ [50].

Therefore, it is important to install the turbine where the wind resource is at high speeds. It should also be noted that wind speed increases with elevation. The wind shear is a variable that describes how much the speed differs with elevation. Data collection of wind speeds and direction will need to be conducted for a minimum of 1 year [49–51].

2.1.6 Fuel Cell

A fuel cell consists of two electrodes, the anode and the cathode, separated by an electrolyte [52]. Thin layer of platinum or other metals, depending on the type of the fuel cell, is coated on each electrode to activate the reaction between oxygen and hydrogen when they pass through the electrodes. The overall reaction is shown by the equation below [53]:

$$\mathrm{H_2\,(g)} + \frac{1}{2}\mathrm{O_2(g)} \rightarrow \mathrm{H_2O(1)} \quad \Delta\mathrm{H} = -287\mathrm{kJ\ mol^{-1}}. \tag{9}$$

There are five major types of fuel cells generally available in the market. All of them have the same basic design as mentioned, but with different chemicals used as the electrolyte [54]. These fuel cells are the following: Alkaline Fuel Cell (AFC), Phosphoric Acid Fuel Cell (PAFC), Molten Carbonate Fuel Cell (MCFC),

Solid Oxide Fuel Cell (SOFC), and Proton Exchange Membrane Fuel Cell (PEMFC). These fuel cells require fairly pure hydrogen fuel to run. However, large amount of hydrogen gas is difficult to transport and store [55].

2.1.7 Gas-Fired Power Stations

Gas-fired power stations generate electricity by burning natural gas. A distinction must be made between gas turbine power stations and gas-fired steam power stations. Quick-start plants of this nature are used especially when power fluctuations or grid outages have to be made up for in short order and more electricity has to be made available extremely quickly [56]. What is special about gas-fired power stations is that they are among the few types of power station that are peak load-capable. In other words, gas-fired power stations can be run up from stationary to peak capacity in a matter of minutes. Quick-start plants of this nature are used especially when power fluctuations or grid outages have to be made up for in short order and more electricity has to be made available extremely quickly [57].

2.1.8 Diesel Generators

A standby generator consists of an engine-driven generator that is used to provide auxiliary power during solar blackouts or when the battery power discharge reaches a minimum level. The output of the diesel generator is connected to the auxiliary input of the inverter and engines that drive the motors operate with gasoline, diesel, natural gas, propane, or any type of fuel [58]. As an option, the diesel generators can be equipped with remote monitoring and annunciation panels that indicate power generation data log and monitors the functional and dynamic parameters of the engine, such as coolant temperature, oil pressure, and malfunctions [59]. Engines also incorporate special electronic circuitry to regulate the generator output frequency, voltage, and power under specified load conditions [60]. The diesel Generators are best used for backup power during long periods of little or no wind. Under these circumstances the diesel generator runs just long enough to provide the batteries with their bulk stage charge and for a portion of the absorption charging stage [61, 62].

2.2 Comparison of Production Energies Options

Apart from its own merits, PV technology system is considered the best option for many projects because of the potential state of development of other RETs in the most of the countries. PV power is estimated to be the most expensive RET option and micro-hydro is attractive on a cost basis [63]. Table 1 provides a summary of

Table 1 Comparison of various energy production options [64]

Factors	PV	Fossil fuels	Wind turbines	Micro-hydro	Municipal solid waste/biomass
Stakeholder interest Leadership and/or investment—government	High	Not applicable	High	Medium	High
Stakeholder interest Private sector and general public	High	Not applicable	Medium	Low	High (5 companies, 3 foreign, 2 local, have participated in tender)
Cost Overall cost per unit of electricity	High (but costs are steadily decreasing)	Medium (with risk of significant cost increases)	High	Low	Low
Cost Up-front capital costs	High	Medium	High	High	High
Cost Availability of financing	Low	Medium (Govt. subsidies to end)	High (grant)	Low	High (financing in place)
Technical feasibility Complexity of technology	High (simple, proven technology)	High (already exists)	Medium (complex, new to country)	High	Low
Technical feasibility Grid compatibility	High	Very high (already exists)	Medium	expensive	average
Technical Feasibility Site suitability	High (many sites can be used)	Very high (already exists)	Low (few sites possible)	Low (very few sites)	High (existing landfill)
Technical feasibility Reliability of supply	High	High (although risk exists of supply disruptions)	Low (winds are highly seasonal)	Low (rainfall is highly seasonal)	Medium
Social benefits Job creation	High	Medium	Low	high	high
Social benefits Human health (air quality)	High	Low	High	High	Medium
Social benefits National energy security	High (if there is widespread adoption)	Low (vulnerable to price fluctuations; supply disruptions)	High	Low (total potential is 1.8 MW)	Medium

the strengths and weaknesses of the various RETs in comparison to one another, and to the existing fossil fuel-based energy production system.

This is with regard to the financial costs of solar PV and other renewable energy technologies (RETs) as compared to the existing fossil fuel-based energy production in many developed countries. PV systems are currently a competitive option for energy production in many of the countries in the world.

3 Contribution of Renewable and Nonrenewable Resources into the Microgrid System

In this section of this chapter, a microgrid system has been considered as a case of study with the objective to show how the voltage and the frequency can be controlled when there are disturbances with the plan to keep the system running properly.

3.1 Microgrid System Configuration

Figure 6 presents the typical MG system to be taken into consideration during performance evaluation. The main components of the MG system are the Wind, PV, diesel systems, batteries energy storage system (BESS) and loads. The BESS is entitled to supply power to the system when there is lake of power from both diesel generator and PV systems.

3.2 Problem Formulation

3.2.1 System Description

The MG used in this work is presented in Fig. 6. The system is composed of three energy sources namely, a diesel generator, PV system, and their associated battery storage systems. Additionally, from the consumer's side, there are two identical loads which are noncritical P_{L1} and $P^{c}_{L_2}$. The power from the diesel generator system is considered to be produced at lowest cost and to keep its value as long as the MG is operating. The aim is to meet the demand with the capacity of power delivery and the control of voltage and frequency to the hybrid system. The modeling of the MG under frequency load shedding (UFLS) scheme can be done according to the logical method of solving this kind of problem.

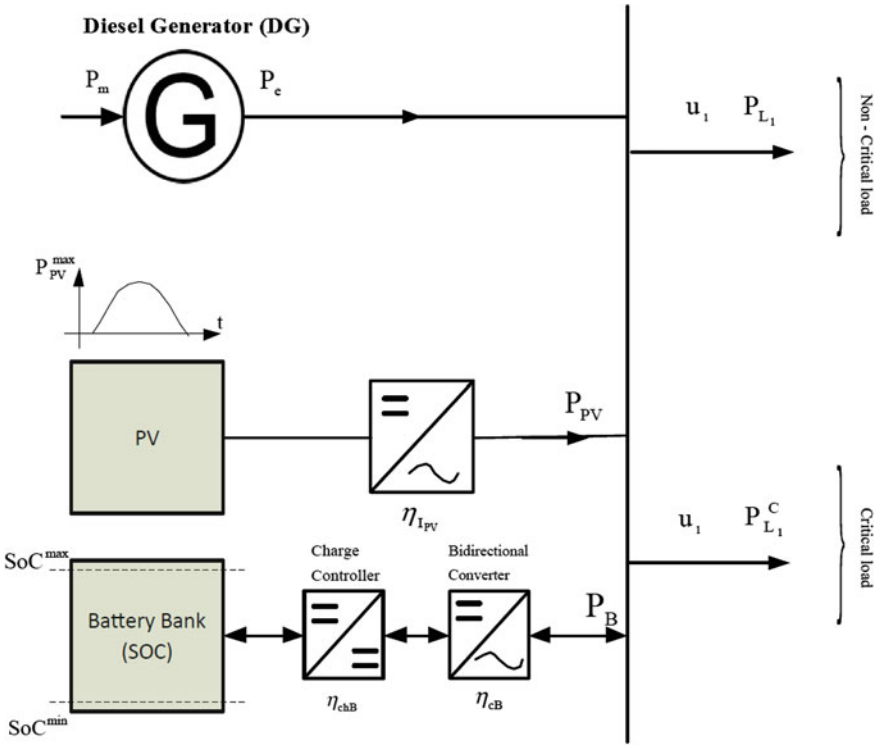

Fig. 6 Typical configuration of microgrid system with renewable energy resources

3.2.2 Objective Function

The objective of this work is to minimize the cost of the fuel and the noncritical power consumption by incorporating switches as control devices to the model operating on ON/OFF. Both switches are applied to the number of variables in accordance with number of samples N_s during the operation period of the hybrid system. Mathematically, this can be written as optimal control problem where the control objective is the minimization of the cost of the total daily energy produced by the diesel generator to the loads. This problem can be characterized by the Eq. (10) as follow:

Objective function:

$$\min C_f \sum_{i=1}^{N_s} [aP_{DG}^2(j) + bP_{DG}(j) + c] \times \Delta t, \quad (1 \le i \le N_s), \tag{10}$$

where C_f is the cost of the fuel used to run the DG; a, b, and c are respective factors applied to the fuel properties; Δt is the variation of time during what the hybrid system will be operating daily; P_{DG} is the output power from the diesel generator

system to the hybrid system; i is the number of horizon, and N_s is the number of samples considered for the optimization study of the hybrid system.

3.2.3 Constraints

The constraints equations of the system are characterized by the main expressions which are power balance, frequency constraint, state of charge of the battery bank, and boundary constraints of the control variables considered for this study into the MG system.

(a) *Power balance equation*

The power balance generated at the common point of the connections should be greater or equal to the total power demand at the same point. We can write the Eq. (11) as follows:

$$P_e(k) + P_{PV}(k) \pm P_B(k) \geq \sum_{i=1}^{n^{Load}} P_L \times u_i, \quad \left\{ \begin{array}{l} 1 \leq i \leq n^{Load} \\ 1 \leq k \leq N_s \end{array} \right\} \tag{11}$$

where $P_L(t)$ is the power demand of the ith critical load at time t; $P_e(k)$ is the electrical power from the diesel generator, $P_{PV}(k)$ is the output power from the PV system, $P_B(k)$ is the output power from the battery system, u_i is the switch applied to each load, and n^{Load} is the number of loads to be supplied into the hybrid system.

(b) *Frequency constraint*

The speed of the diesel generator in the MG power system changes in direct proportion to frequency. As frequency drops in the system, the selected diesel generator will turn slower and supply less energy. The accelerated power of the small hydropower generator is written by the expression (12) as follows [60]:

$$\left\{ \begin{array}{l} P_a = M \frac{d\omega_d}{dt} = P_m - P_e \\ M = \frac{GH}{\pi f_s} \\ \omega_d = \omega_e - \omega_s \end{array} \right. , \tag{12}$$

where G is the machine rating (base) expressed in MVA; H is the inertia constant in MJ/MVA; f_s is the synchronous frequency expressed in Hz, and the considered value is (60 or 50 Hz); M is the moment of inertia in MJ/MJ/rad/s; ω_d is the electrical rotor speed displacement from synchronously rotating reference frame; ω_s is the synchronous speed of the synchronous machine; ω_e is the electrical rotor speed of the machine.

The motion Eq. (12) of the generator can also be expressed in the discrete-time domain and is written as the expression (13):

$$M\frac{\omega(k)-\omega(k-1)}{\Delta t}=P(k-1)-P(k-1), \tag{13}$$

In another form, Eq. (13) can be rewritten as (14) below:

$$\omega_{\mathrm{d}}(k)=\omega_{\mathrm{d}}(k-1)+\frac{\Delta t}{M}[P_{\mathrm{m}}(k-1)-P_{\mathrm{e}}(k-1)]. \tag{14}$$

By recurrence manipulation, the displacement speed ω_{d} (k) can be expressed in terms of its initial value, ω_{d} (0) as follows:

$$\omega_{\mathrm{d}}(k)=\omega_{\mathrm{d}}(0)+\frac{\Delta t}{M}\sum_{\tau=1}^{k}P_{\mathrm{m}}(\tau)-\frac{\Delta t}{M}\sum_{\tau=1}^{k}P_{\mathrm{e}}(\tau). \tag{15}$$

The boundary constraints of the frequency constraints are therefore written as follows:

$$\omega_{\mathrm{d}}^{\min}(k)\le\omega_{\mathrm{d}}(0)+\frac{\Delta t}{M}\sum_{\tau=1}^{k}P_{\mathrm{m}}(\tau)-\frac{\Delta t}{M}\sum_{\tau=1}^{k}P_{\mathrm{e}}(\tau)\le\omega_{\mathrm{d}}^{\max}(k). \tag{16}$$

(c) *State of charge of battery bank*

The state of charge of the battery bank as shown in Fig. 6 can be expressed in discrete-time domain, by the following equation:

$$\mathrm{SoC}(k)=\mathrm{SoC}(k-1)-\frac{\Delta t}{C_{\mathrm{n}}}P_{\mathrm{B}}(k-1), \tag{17}$$

where C_{n} is the nominal capacity of the battery bank. The state of charge (SoC) can be expressed in terms of its initial value, SoC(0) by the following expression:

$$\mathrm{SoC}(k)=\mathrm{SoC}(0)-\frac{\Delta t}{C_{\mathrm{n}}}\sum_{\tau=1}^{k}P_{\mathrm{B}}(\tau). \tag{18}$$

The lower and upper limits on the state of charge of the battery bank are expressed as:

$$\mathrm{SoC}^{\min}(k)\le\mathrm{SoC}(0)-\frac{\Delta t}{C_{\mathrm{n}}}\sum_{\tau=1}^{k}P_{\mathrm{B}}(\tau)\le\mathrm{SoC}^{\max}(k). \tag{19}$$

(d) *Boundary constraints of control variables*

The boundary constraints of the considered variable parameters into the MG system under frequency load shedding scheme are explained and written by their appropriated from Eqs. (20)–(23) as follows:

The active power of the DG is defined as the real part of the complex variable of the apparent power. This quantity is physically limited in the selected generator. The lower and upper generator active power limits are expressed by Eq. (20) as follows:

$$P_{\mathrm{e}}^{\min} \leq P_{\mathrm{e}}(k) \leq P_{\mathrm{e}}^{\max} \quad (1 \leq k \leq N_{\mathrm{s}}). \tag{20}$$

The power generated by PV system is defined to be the real variable. This quantity is physically limited in the selected PV plant. Thus, the lower and upper boundaries of PV active power limits are expressed as in Eq. (21):

$$P_{\mathrm{PV}}^{\min}(k) \leq P_{\mathrm{PV}}(k) \leq P_{\mathrm{PV}}^{\max}(k), \quad (1 \leq k \leq N_{\mathrm{s}}). \tag{21}$$

The output power of the battery bank is also defined as the real-active power. This quantity is physically limited in the selected batteries. The lower and upper capacities limits are expressed by the Eq. (22) as follows:

$$P_{\mathrm{B}}^{\min}(k) \leq P_{\mathrm{B}}(k) \leq P_{\mathrm{B}}^{\max}(k), \quad (1 \leq k \leq N_{\mathrm{s}}). \tag{22}$$

The variations of the network frequency and voltage variables must be maintained under certain limits. These quantities are physically limited for the selected equipment into the MG system. In this case, the lower and upper limits of frequency and voltage can be expressed by taking the system nominal frequency and voltage as in Eq. (23) with the following structure:

$$\begin{cases} f^{\min}(k) \leq f_{\mathrm{nom}}(k) \leq f^{\max}(k) \\ V^{\min}(k) \leq V_{\mathrm{nom}}(k) \leq V^{\max}(k), \quad (1 \leq k \leq N_{\mathrm{s}}) \end{cases} \tag{23}$$

3.3 Simulation Results

For the adequate study, additional load data need to be provided in order to complete the design of power supply resources. The main the objective is that the supply side must meet the demand side capacities. Finally, the simulation results of the MG model under frequency load shedding scheme are presented in this section.

3.3.1 Optimization Algorithm

Several optimization methods of algorithm can be applied for the resolution of the concerns defined in this work. The mathematical modeling of the problem of the MG power system is a nonlinear objective function and there are some assumptions to be taken into account. The fmincon function in MATLAB is proposed to find the minimum of a constrained nonlinear multi-variable function. Otherwise fmincon finds a constrained minimum of a function of several variables. Because of these reasons, the fmincon function of MATLAB R2015 Optimization Toolbox is implemented to solve all the issues of this problem. The equation can be solved by this function is expressed as:

$$\min f(X) \tag{24}$$

subject to

$$\begin{cases} AX \leq b \,(\text{linear inequality constraint}), \\ A_{\text{eq}}X = b_{\text{eq}} (\text{linear equality constraint}), \\ C(X) \leq 0 \,(\text{nonlinear inequality constraint}), \\ C_{\text{eq}}(X) \leq 0 \,(\text{nonlinear equality constraint}), \\ L_{\text{b}} \leq X \leq U_{\text{b}} \,(\text{lower and upper bounds}). \end{cases} \tag{25}$$

For the optimal control equation, the vector X contains the feeders speed for all sampling intervals. The linear inequality constraints are integrated into A and b. The lower and upper boundary constraints Eqs. (20)–(23) are incorporated into L_{b} and U_{b}. The MATLAB code implemented to solve this problem has been applied using closed loop control system.

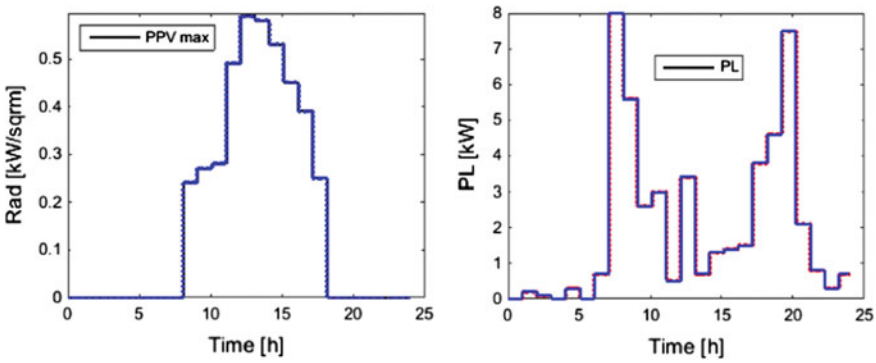

Fig. 7 Daily variations of global radiation and total load profile

Table 2 Simulation parameters [65, 66]

Item No	Parameter	Value
1	Diesel Generator	6 kW
2	Sampling time	1 h
3	Battery nominal capacity Battery maximum SOC Battery minimum SOC Battery discharging efficiency Battery charging efficiency	4 kWh or 84 Ah or 1 kW 95% 40% 100% 80%
4	Accepted Frequency Accepted Voltage	(50 ± 1.5) Hz (1 ± 0.05) pu
5	Diesel fuel price	1.4 $/l
6	Diesel Generator parameters	a = 0.246, b = 0.0815
7	PV system	0.7 kWmax

3.3.2 Typical Application

The total variation of the typical daily load profile *PL* [kW] of the consumers and the variation of the global radiation per square meter Rad [kW/sqm] for solar are given of in the Fig. 7.

Additionally, for doing the study of the MG system described in Fig. 6 presented under Sect. 3, it is required to have other parameters to be applied into the simulation of the power system that are given in the Table 2.

3.4 Results and Discussions

After simulating the MG system described in Fig. 6 of Sect. 3 with consideration of all the supply sources are operating at their full supply capacity, the results of the variation of the energy resources are given in the Fig. 8. From the results shown in Fig. 8, it seems that system is operating normal. We can also note that there is no need to shed any of the load as the system is running at full capacity with the main power supply from the diesel generator, PV unit compensated by battery system, making the system run without any problem. Additionally, the saving on the fuel is evaluated to 30% of the daily total consumption of the nominal consumption of the diesel generator. As the effect of variation of frequency and the voltage of the hybrid system are good and this can be seen from the Fig. 9. The results are characterized by two types of legends. The dashed red lines mean the maximum values while the black lines mean the normal values of parameters.

When the deliverable capacities of the supply system are not meeting their maximum capacities because of some of the disturbances such as default of the radiation, storage capacity problem, and malfunctioning of the diesel generator set for some reasons, these have impact on the frequency and voltage as shown in Fig. 10.

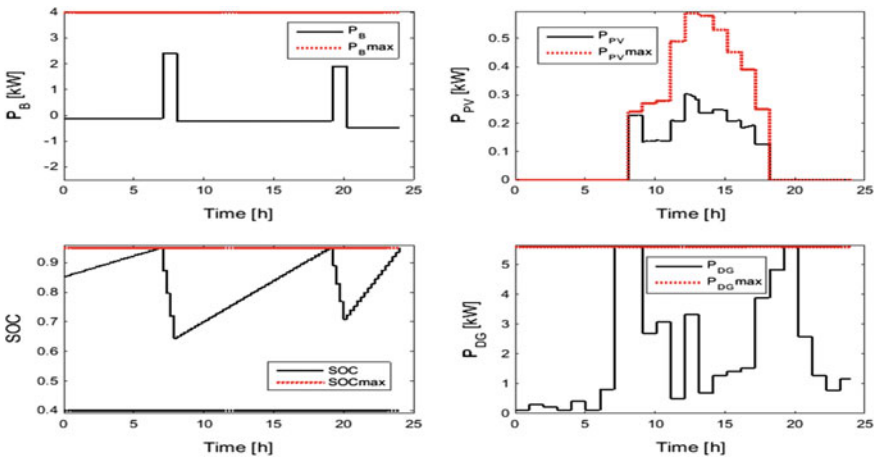

Fig. 8 Variation of the supply capacities of the hybrid system at full capacity

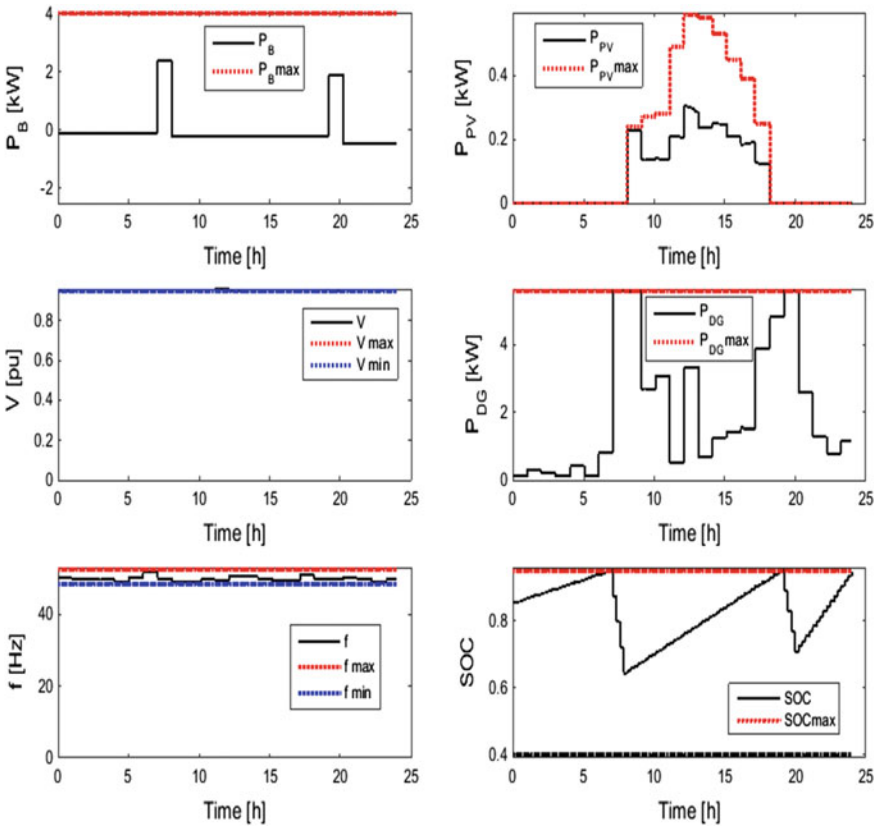

Fig. 9 Variation of the all the parameters of the hybrid system

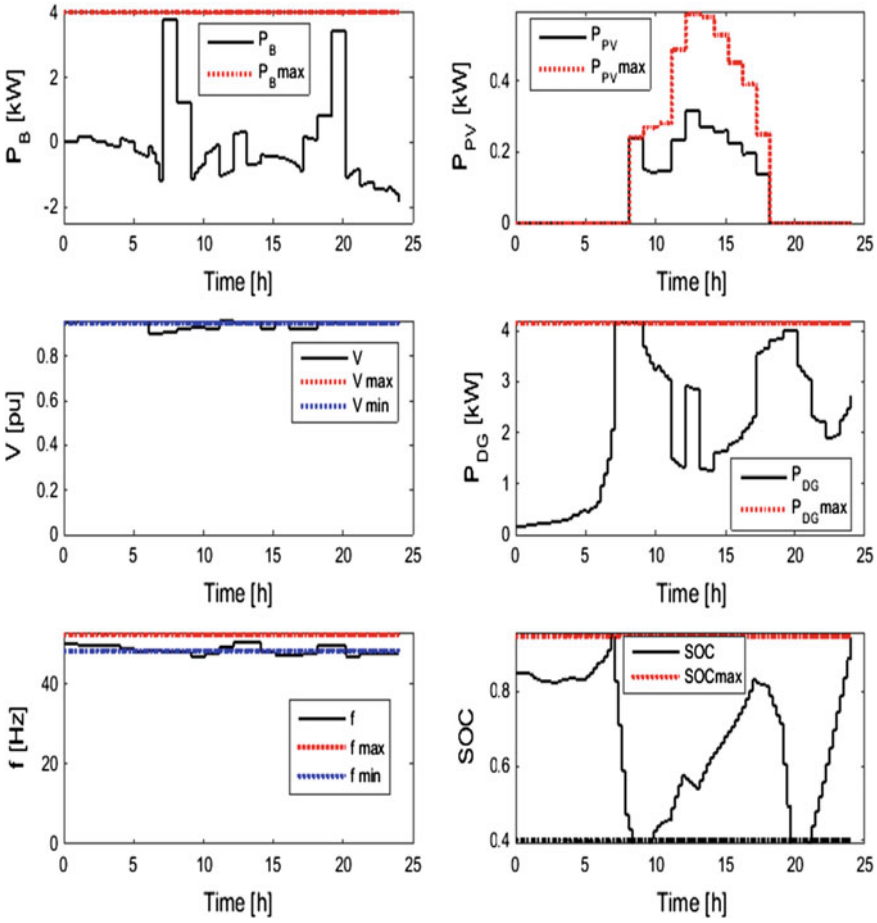

Fig. 10 Variation of parameters of the hybrid system when the DG set and the PV are not running at its full capacity

The disturbance is caused especially when both the diesel generator and PV systems are running at 80% of their installed capacities and both loads are still connected to the bus. As consequence, the variations voltage and the frequency of the hybrid system are under the lower boundaries limits which is very dangerous for the system and this has effect on the shedding of one of the load.

As this can be seen in the Fig. 10, the variations of voltage, frequency and the State of Charge are not following the rules because of lack of power as both suppliers are not running at their full capacities. For that, the need to equilibrate the system is necessary. Therefore, the system is running under frequency load shedding and the only way to solve the problem is to compensate the supply side in such a way it still be at its required capacity for to balance the MG system.

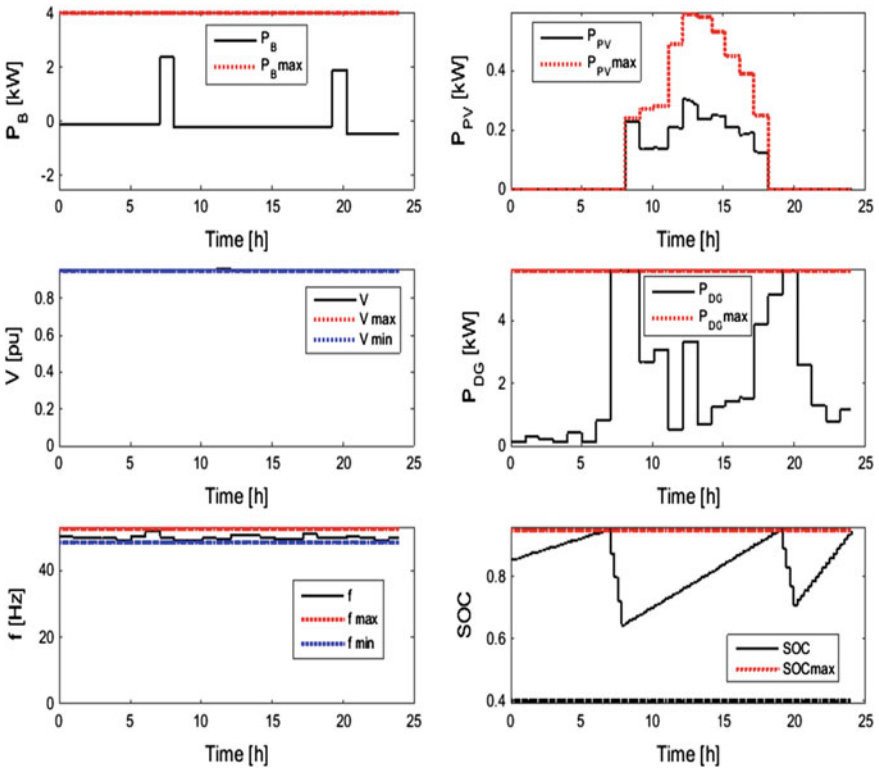

Fig. 11 Adjustment of the supply capacities to correct the voltage, the frequency and the state of charge of the hybrid system

After adjustment of the power from diesel generator set as shown in Fig. 11, the frequency and the voltage variations parameters have become normal which mean both parameters ranging between the average percentage limits of the nominal required values. In other words, no load shedding simply because the supply capacity has met the demand and it is concluded that the hybrid system is running under balancing condition.

4 Conclusion and Technical Challenges

The hybrid power system needs to be appropriately controlled with the objective to keep the system operating continuously. Especially when the main power supply is considered to be provided from the diesel generator, the reliability of the system is highly recommended in for the success of the both supplier and consumers. The fluctuations of the both frequency and the voltage into the microgrid system affect

the productivity of the system. When there is no additional source of power to compensate the existing sources of energy, this implies the elimination of one of the loads to avoid the unbalancing of the microgrid power system. In case of both critical and noncritical loads are still connected with supply side operating at its less required capacity, the consequence of this is the under voltage which automatically implies under frequency problem into the distribution system. The good way to solve the variation of the frequency and voltage into the microgrid system when there is unbalancing between the supply side capacity and demand side is to carefully control the system in such a way that in case of disturbance at the generator side as main supply capacity, the renewable energy need to compensate with additional power to keep very small the variation of the voltage and frequency. During the daytime, it always preferable to have the diesel generator set and PV running at their full capacities so that when nighttime will come the battery can still be able to supply the based load in the microgrid system. The effect of this, will keep the variation of both frequency and voltage very low and there will be no need to shed the load. The fluctuation of both frequency and voltage in the hybrid systems are not a factor to consider because this aspect has bad effect on the lifespan equipment used in term of maintenance and operating costs. Additionally, after this problem is well solved, also the productivity and the rentability of the hybrid system are achieved. As future recommendations for both off-grid and grid-connected microgrid systems, it is always preferable to provide a reserve renewable source of energy which may be efficient in price such as solar PV system to compensate the existing suppliers and to save the operating cost of the diesel generator. A second generator unit as a spare supplier source of energy is not preferable because of the increase of the operating cost of the system which will affect the rentability of the power system and the pollution of the atmosphere. Finally, to prevent the increase of carbon emission, the use of quick renewable energy such as PV system is the best and simple solution to be applied as described in this chapter which is considered as clean energy to keep both the population and environment safe.

References

1. Ochoa LF, Harrison GP (2011) Minimizing energy losses: optimal accommodation and smart operation of renewable distributed generation. IEEE Trans Power Syst J 26(1):198–205
2. Frias P, Gomez T, Cossent R, Rivier J (2009) Improvement in current European network regulation to facilitate the integration of distributed generation. Electr Power Energy Syst J 31:445–451
3. Zobaa AF, Bansal RC (eds) (2011) Handbook of renewable energy technology. World Scientific Publishers, Singapore
4. Chowdhury AA, Agarwal SK, Koval DO (2003) Reliability modelling of distributed generation in conventional distribution systems planning and analysis. IEEE Trans Ind Appl J 39(5):1493–1501
5. Zobaa AF, Cantelli M, Bansal RC (eds) (2011) Power quality-monitoring, analysis and enhancement. INTECH-Open Access Publishers

6. Tsikalakis AG, Hatziargyriou ND (2008) Centralized control for optimizing microgrids operation. IEEE Trans Energy Convers J 23(1):241–248
7. Sao CK, Lehn PW (2008) Control and power management of converter fed microgrids. IEEE Trans Power Syst J 23(3):1088–1098
8. Bansal RC, Bhatti TS (2008) Small signal analysis of isolated hybrid power systems: reactive power and frequency control analysis. Alpha Science International, Oxford, U.K
9. Gil HA, Joos G (2008) Models for quantifying the economic benefits of distributed generation. IEEE Trans Power Syst J 23(2):327–335
10. Hung DQ, Mithulananthan N, Bansal RC (2013) A combined approach of DG, capacitor placement and reconfiguration for loss reduction in distribution networks. Appl Energy J 105:75–85
11. Qiang L, Lin Z, Ke G (2011) Review on the dynamic characteristics of micro grids system. In: IEEE conference on industrial electronics and applications, Singapore, 18–20 July 2011
12. Andersson G, Donalek P, Farmer R et al (2005) Causes of the 2003 major grid blackouts in North America and Europe, and recommended means to improve System Dynamic Performance. IEEE Trans Power Syst J 20(4):1922–1928
13. Nagliero A, Mastromauro RA, Monopoli VG, Liserre M, Dell'Aquila A (2010) Analysis of a universal inverter working in grid-connect, stand alone and microgrid. In: IEEE international symposium on industrial electronics, Bari, 4–7 July 2010
14. Mazheruddin HS, Zeineldin HH, El Moursi MS (2013) Grid code violation during fault triggered islanding of hybrid micro-grid. In: IEEE PES international conference on innovative smart grid technologies, Washington DC, 26–27 Feb 2013
15. Radzi NH, Bansal RC, Dong ZY, Hassan MY, Wong KP (2013) An efficient distribution factors enhanced transmission pricing method for Australian NEM transmission charging scheme. Renew Energy J 53:319–328
16. Pan QK, Wang L, Qian B (2009) Review on operation of micro grids and virtual power plants in the power markets. In: IEEE international conference on adaptive science and technology, Ghana, 14–16 Jan 2009
17. Wang J, Wang Z, Xu L, Wang Z (2012) A summary of application of D-FACTS on microgrid. In: IEEE international conference on Asia Pacific power and energy engineering, Shanghai
18. Gidwani L, Tiwari H, Bansal RC (2013), Improving power quality of wind energy conversion system with unconventional power electronic interface. Electr Power Energy Syst J 44(1): 445–453
19. Xue-Song Z, Li-qiang C, You-jie M (2011) Research on control of microgrid. In: Third IEEE international conference on measuring technology and mechatronics automation, Shanghai, 6–7 Jan 2011
20. Laghari JA, Mokhlis H, Bakar AH, Mohamad H (2013) Application of computational intelligence techniques for load shedding in power systems: review. Energy Convers Manage J 75:130–140
21. Mahat P, Zhe C, Bak-Jensen B (2010) Under frequency load shedding for islanded distribution system with distributed generators. IEEE Trans Power Deliv J 10(25):911–918
22. Rudez U, Mihalic R (2009) Analysis of under frequency load shedding using a frequency gradient. IEEE Trans Power Deliv J 26(2):565–575
23. Bhatti TS, Bansal RC, Kothari DP (eds) (2004) Small hydro power systems. Dhanpat Rai & Sons, India
24. Katiraei F, Iravani R, Hatziargyriou N, Dimeas A (2008) Microgrids management. IEEE Power Energy Manage J 6(3):54–65
25. Bernhard S, Marland G (1997) The role of forest and bioenergy strategies in the global carbon cycle. Biomass Bioenergy 10(5–6):275–300
26. Bansal RC (2013) Renewable energy systems. In: Beaty HW (ed) Standard handbook for electrical engineers, 16th edn. McGraw-Hill, pp 11-5–11-10
27. Bernde G, Monique H, Richard VDB (2003) The contribution of biomass in the future global energy supply: a review of 17 studies. Biomass Bioenergy J 25(1):1–28

28. Levron Y, Guerrero JM, Beck Y (2013) Optimal power flow in microgrids with energy storage. IEEE Trans Power Syst J 28(3):3226–3234
29. Sigrist L, Egido I, Rouco L (2013) Principles of a centralized UFLS scheme for small isolated power systems. IEEE Trans Power Syst J 28(2):1779–1786
30. Song Z, Liu J, Liu1 Y, Bazargan M (2013) A method for the design of UFLS scheme with dynamic correction. Energy Power Eng J 5:442–447
31. Rao YS, Laxmi AJ, Kazemineha M (2012) Modeling and control of hybrid photovoltaic conversion system. Int J Adv Eng Technol J, 2231–1963
32. Valenciaga F, Puleston PF (2005) Supervisor control for a stand-alone hybrid generation system using wind and photovoltaic energy. IEEE Trans Energy Convers J 20(2):398–405
33. Kim XJ, Guerrero JM, Rodriguez P, Teodorescu R, Nam K (2011) Mode adaptive droop control with virtual output impedances for an inverter-based flexible AC microgrid. IEEE Trans Power Electron J 26(3):689–701
34. Rostamirad S, Wang K, Marti JR (2011) Power management in disasters: application of load shedding and wind turbine controllers. In: IEEE Canadian conference on electrical and computer engineering, connecting engineering applications and disaster management workshop, Niagara Falls, Ontario
35. Lu X, Guerrero JM, Sun K, Vasquez JC (2014) An Improved droop control method for DC microgrids based on low bandwidth communication with DC bus voltage restoration and enhanced current sharing accuracy. IEEE Trans Power Electron J 29(4):1800–1812
36. Biswas MM, Kamol KD, Baqee IA, Mohammad AH, Farhad HMS (2011) Prospects of renewable energy and energy storage systems in Bangladesh and developing economics. Glob J Res Eng J 11
37. Islam MS, Mondal T (2013) Potentiality of biomass energy for electricity generation in Bangladesh. Asian J Appl Sci Eng 2(2):2305–2915
38. Mamun MRA, Kabir MS, Alam MM, Islam MM (2009) Utilization pattern of biomass for rural energy supply in Bangladesh. Sustain Crop Prod J 4(1):62–71
39. Gonzalez-Espin F, Chang N, Valdivia-Guerrero V, Foley R (2013) Configuration, modelling and control of a microgrid for commercial buildings application. In: 15th European conference, power electronics and applications (EPE), Lille, 2–6 Sept 2013
40. Antar B, Hassen B, Babes B, Afghoul H (2015) Fractional order PI controller for grid connected wind energy conversion system. In: 4th international conference, electrical engineering (ICEE), Boumerdes, 13–15 Dec 2015
41. Majumder P, Ghosh A, Ledwich G, Zare F (2011) Power management and power flow control with back-to-back converters in a utility connected microgrid. IEEE Trans Power Syst J 25(2)
42. Govindaraj T, Hemalatha D (2014) Dynamic reactive power control of islanded microgrid using IPFC. Innov Res Electr Electron Instrum Control Eng J 2(1)
43. Zhang Y, Ruan J, Zhan T (2012) Electromagnetic force analysis of a driving coil. In: 16th international symposium on electromagnetic launch technology (EML), Beijing, 15–19 May 2012
44. Peng Q (2010) Harmonic coil design, fabrication and commissioning for European XFEL linear accelerator superconducting magnets field measurements. IEEE Trans Appl Supercond J 20(3):2015–2018
45. Polak M (2006) Properties of a YBCO pancake coil operating with AC current at frequencies up to 1000. IEEE Trans on Appl Supercond J 16(2):1423–1426
46. Jardini JA, Tahan CMV, Gouvea MR, Ahn SU, Figueiredo FM (2000) Daily load profiles for residential, commercial and industrial low voltage consumers. IEEE Trans Power Deliv J 15(1):375–380
47. Mohideen R (2012) The implications of clean and renewable energy development for gender equality in poor communities in South Asia. In: IEEE conference on technology and society in Asia, Singapore, 27–29 Oct 2012
48. Pfluger B, Wietschel W (2012) Impact of renewable energies on conventional power generation technologies and infrastructures from a long-term least-cost perspective. In: 9th international conference on the European energy market, Florence, 10–12 May 2012

49. Mehrizi-Sani A, Iravani R (2010) Potential-function based control of a microgrid in islanded and grid-connected modes. IEEE Trans Power Syst J 25(4):1883–1891
50. Lamberti T, Sorce A, Di Fresco L, Barberis S (2015) Smart port: exploiting renewable energy and storage potential of moored boats. In: IEEE conference OCEANS, Geneva, 18–21 May 2015
51. Lopes VS, Borges CLT (2015) Impact of the combined integration of wind generation and small hydropower plants on the system reliability. IEEE Trans Sustain Energy J 6(3): 1169–1177
52. Ammar M, Joos G (2013) Impact of distributed wind generators reactive power behavior on flicker severity. IEEE Trans Energy Convers J 28(2):425–433
53. Borkowski D, Węgiel T (2013) small hydropower plant with integrated turbine-generators working at variable speed. IEEE Trans Energy Convers J 28(2):452–459
54. Gallego JD, Franco CJ, Zapata S (2015) Policies for the utilization of hydropower potential in Colombia using small plants. IEEE Trans Latin America J 13(12):3844–3850
55. Li YH, Rajakaruna S, Choi S (2007) control of a solid oxide fuel cell power plant in a grid-connected system. IEEE Trans Energy Convers J 22(2):405–413
56. Tsourapas V, Sun J, Stefanopoulou A (2009) Incremental step reference governor for load conditioning of hybrid fuel cell and gas turbine power plants. IEEE Trans Control Syst Technol J 17(4):756–767
57. Hawkes AD, Leach MA (2009) Modelling high level system design and unit commitment for a microgrid. Appl Energy J 86(7–8):1253–1265
58. Niwas R, Singh B, Goel S, Jain C (2015) Unity power factor operation and neutral current compensation of diesel generator set feeding three-phase four-wire loads. IET Gener Transm Distrib J 9(13):1738–1746
59. Yang WH, Zhao SN, Wang KH, Li W, Ma JY (2009) Greenhouse effect reduction in biomass power plant: a case study. In: 3rd international conference on bioinformatics and biomedical engineering, Beijing, 11–13 June 2009
60. Chakraborty S, Weiss MD, Simoes MG (2007) Distributed intelligent energy management system for a single-phase high-frequency AC microgrid. IEEE Trans Ind Electron J 54(1):97–109
61. Jalilnezhad Z (2010) Feasibility study of anaerobic digester for biogas plant in FEKA dairy farm. A report prepared by the FEKA dairy farm
62. Hunter R, Elliot G (eds) (1994) Wind-diesel systems: a guide to the technology and its implementation. Cambridge University Press
63. Pouresmaeil E, Montesinos-Miracle D, Gomis-Bellmunt O (2012) Control scheme of three-level NPC inverter for integration of renewable energy resources into AC grid. IEEE Syst J 6(2):242–253
64. Kamiev K, Nerg J, Pyrhönen J, Zaboin V, Tapia T (2014) Feasibility of an armature-reaction-compensated permanent-magnet synchronous generator in island operation. IEEE Trans Ind Electron J 61(9):5075–5085
65. Barklund E, Pogaku N, Prodanovic M, Hernandez-Aramburo C, Green TC (2007) Energy management system with stability constraints for stand-alone autonomous microgrid. In: IEEE international conference on system of systems engineering, San Antonio, TX, pp 1–6
66. Chen C, Duan S, Cai T, Liu B, Hu G (2011) Smart energy management system for optimal microgrid economic operation. IET-Renew Power Gener J 5(3):258–267

Power Quality Impacts and Mitigation Measures for High Penetrations of Photovoltaics in Distribution Networks

Peter Wolfs, M. Mejbaul Haque and Sawkat Ali

Abstract Island power systems often have high costs of generation in comparison to most large-scale continental power systems due to a high reliance on diesel generation. Many island systems are small with many being sub-megawatt in size. Apart from the issues of the economies of scale, the costs in island systems are increased by the difficulties of remoteness in terms of fuel delivery and access for maintenance. Island systems often have access to good renewable resources such as wind, biomass and solar resources. These have been successfully harnessed in many systems to reduce the reliance on diesel generation. Island power systems often have very high fractions of renewable energy. Many renewable technologies are now mature and reliable and the costs of solar systems have continued to reduce. The economics of the situation drive increasing interest and usage of PV systems. Some technical challenges emerge once a considerable fraction of the consumer energy is to be supplied from renewable sources. These key issues are intermittency and voltage control. Intermittency is reduced with a technology diversified and a spatially diversified portfolio of generation sources. Highly responsive backup generation, load demand control and storage are often used to compensate for the intermittent generation of renewables. Voltage can be easily controlled in new systems that are specifically designed to work with renewables. Older systems may need modifications such as partial reconstruction or the retrofitting of regulation devices.

Keywords Photovoltaics · Renewable energy · Distribution networks · Energy storage

P. Wolfs (✉) · M. Mejbaul Haque · S. Ali
Central Queensland University, Rockhampton, QLD 4702, Australia
e-mail: p.wolfs@cqu.edu.au

F.M.R. Islam et al. (eds.), *Smart Energy Grid Design for Island Countries*,
Green Energy and Technology, DOI 10.1007/978-3-319-50197-0_4

1 Introduction

Solar energy is often included in the generation mix for island communities [1–5]. Island generation systems often are based on diesel fuel and this can result in a significant economic burden. As an example the Pacific Island states spend on average 14.77% of GDP on fuel and have high electricity tariffs [6]. These average 0.35 USD/kWh and can reach as high as 1.50 USD/kWh in outlying islands [6]. In 2014, a power purchase agreement (PPA) was struck for a 100 MW solar plant in Dubai where energy was delivered for 58.5 USD/MWh [7, 8]. This is a wholesale price of 0.0585 USD/kWh. A retail price may be three or four times higher but even allowing for these multipliers, solar energy is often cheaper than diesel-fired energy. Clearly, photovoltaics can potentially displace fossil fuels and provide an economic advantage in an island power system. Island power systems can often tap a range of renewable resources such as wind and biomass. In this case the diversity of sources has an additional benefit [9, 10]. These sources are intermittent and the power system reliability impacts do need careful consideration [11, 12].

Photovoltaics are a mature technology and now enjoy global annual installation rates of approximately 40 GWp and prices have reduced to well below 1 USD/Wp [7, 8]. For many island power systems PV can be readily installed as an effective means of displacing diesel generation. Some PV might be connected in centralised solar farms connected to a medium-voltage (MV) system. PV is frequently installed by private customers as "behind the meter" commercial or residential systems [5].

These will reduce the energy demand and may be encouraged in several ways. These may include tariff structures or financial incentives [8]. Small commercial and residential PV systems will often achieve price parity with a public grid in an island system [8–12]. It is possible that home owners will have a significant economic motivation to install systems if the local regulations allow. Residential PV is generally connected by single-phase inverters to low-voltage (LV) networks and may produce an impact in these systems.

This chapter focuses on the management of island power systems with high levels of PV penetration. Two impacts arise:

- Generation ramp rate impacts;
- Voltage impacts.

1.1 Generation Ramp Rate Impacts

Solar generation is directly affected by cloud cover as shown in Fig. 1. This figure is the output power over one day from a 6 kWp rooftop solar installed at Rockhampton, Australia, latitude 23.37° South. Rapid power reductions from 5 to 1 kW can occur several times each day. This is more than 65% of the array nominal rating. These changes in generation can occur in a few seconds. Forty seconds of

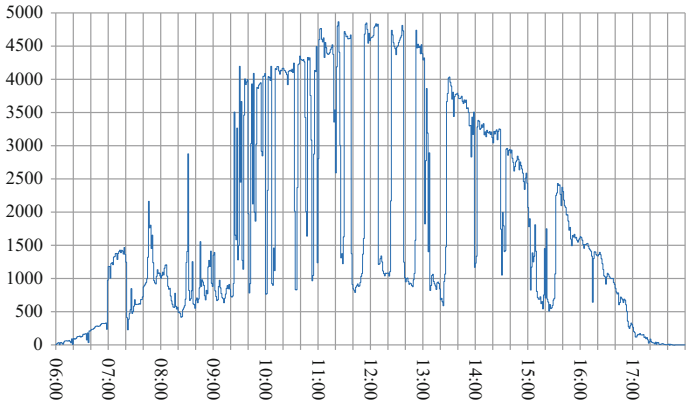

Fig. 1 Real power output (W) from a 6 kWp rooftop solar array

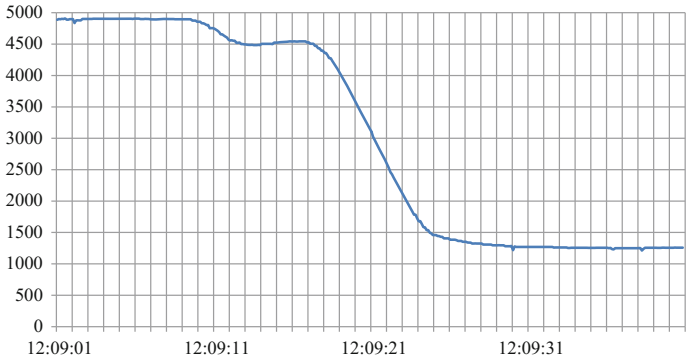

Fig. 2 Fast reduction in output power (W) due to shading

data are shown in Fig. 2. In this case, the largest generation reduction rate is 480 Ws^{-1} or 8% of the array rating per second.

The time for the generation to fall is determined by the cloud velocity and the array dimensions. Larger arrays require longer times to shadow [13]. The total generation from a group of distributed arrays will show less variability as the impacts of a specific cloud will occur at different times on each array. When arrays are sufficiently separated, the peaks and throughs due to passing clouds become uncorrelated. This effect is termed in-plant spatial smoothing [13].

These cloud-induced generation changes do have adverse effects in small power systems where a significant reduction in solar generation may force the remaining generation to rapidly increase its output. Small grids with diesel generation are particularly vulnerable as these cannot rapidly increase their output [13–15]. Utilities may force the solar plant to install energy storage devices to limit the rate of change of the solar generation to ten or twenty percent per minute. It is possible

to limit increases in the output of a solar system electronically by moving the solar module operating point away from the maximum power point. The limitation of the rate of decrease requires energy storage. Given the ramp down times will be five to ten minutes batteries are the common choice [14], but some installations may use a flywheel [17].

As the cost of solar generation reduces it becomes optimum in economic terms to install larger amounts of solar generation. This might frequently exceed the load requirements. While this appears wasteful, it is common in small wind and micro-hydro systems to use dump resistors to regulate the system by spilling excess generation. The King Island power system in the Australian Bass Strait has a wind, solar, diesel hybrid power system. This uses a combination of demand response, a battery, a flywheel and a fast responding energy dump resistor to balance the real power within a microgrid [16, 17]. If the renewable resource is plentiful and may be harnessed at a reasonable cost then a guarantee of high levels of diesel fuel replacement offsets the increased capital cost.

For an island power system there is clear economic pressure to include a large renewable fraction of energy production. This forces island power systems towards very high penetration levels. The island power system designer will need to take every advantage, such as renewable source diversity or spatial smoothing to reduce the costs of fast responding generation or the costs of energy storage.

1.2 Voltage Impacts

Many island power systems will not require a power transmission system. Unless the power system exceeds tens of megawatts or the distances are hundreds of kilometres the transmission voltage levels are not warranted. If a transmission system exists it will include the traditional mechanisms for voltage control such as tap changing or reactive power control. The PV impacts are much more visible in the medium-voltage (MV < 35 kV) and low-voltage (LV < 1000 V) networks. The traditional MV systems will have active control devices such as on-load tap changing transformers (OLTCs) and voltage regulators.

LV networks traditionally rely on passive designs to limit voltage variations. LV distribution networks are generally radial. They can be unbalanced with respect to loads and feeder structures and have high resistance to inductive impedance (R/X) ratios. Nations that have a British or European heritage, and this includes many island states, have a 400/230 Vac four-wire three-phase LV distribution system. These have an extensive LV network when compared to a 234/117 V three-wire split-phase North American-based systems. In 400/230 Vac systems, the LV network typically produces more than half of network voltage drops.

The large-scale deployment of PV in distribution networks is limited by voltage quality issues. These are most frequently over voltages and occasionally voltage unbalance. In addition to utility scale solar farms, residential customers often install rooftop domestic systems. The larger scale solar farms are less problematic in that

dedicated transformers and regulation devices are often used. In the larger continental power systems, PV penetration levels are rapidly increasing in the LV distribution networks. Given that many customers can connect at a shared point of common coupling (PCC) the effects of voltage rise produced by one customer can affect others.

For high penetrations, mitigation techniques are essential to effectively and efficiently manage the voltage impacts for both the MV and especially the LV distribution networks. Distribution networks will have an operational life of several decades. Only a small fraction of the network will be replaced or constructed in any year. The possibility of significant amounts of PV in the LV distribution networks was not considered when older networks were designed. High levels of PV in LV distribution networks may alter the normal operational behaviour. The usual design assumption was that power flows from the upstream high-voltage networks to the downstream low-voltage networks. In this case it is sensible to set the voltages at the head of a feeder at the upper end of the allowable voltage range. With high levels of PV generation the demand reduces. At some times of the day the customer loads may be low while their generation is high. In this case a customer's excess energy may be exported to the public network. If many customers exhibit this behaviour the feeder flow may reverse. It would be very unusual for the reverse flows to exceed the equipment current ratings. However, if solar generation causes a reversal of power flow the feeder voltage profile rises [18, 19]. Given that the voltage at the head of a feeder may be set close to the upper voltage limits the end sections of the feeder can quickly exceed those voltage limits.

Voltage unbalance will exist in the network due to unbalanced distribution of consumer loads and unbalanced impedances in the distribution networks which are not normally transposed. The increased dynamic load range resulting from the addition of PV will generally increase the voltage unbalance. Network impedance unbalance in combination with a strong reverse power flow can result in two phase voltages rising while the remaining phase voltage drops.

Higher negative sequence voltages can result in equipment damage [20]. High voltages produced by excessive solar generation may cause inverters to trip on overvoltage. This results in the loss of that generation. Customers at the ends of feeders with voltage rise problems might be routinely prevented from producing solar energy and this becomes an issue of fairness.

Overvoltage may encourage the network operator to impose limits on the amount of renewable generation within a specific LV distribution network. Once a network reaches a technical limit, often expressed as a percentage of the rating of the distribution transformer to which PV arrays connect, further connections may be refused. A network operator may avoid voltage rise problems by limiting the amount of energy that a customer may export. For a commercial customer that wishes to install an array of tens kilowatts or a few hundred kilowatts energy export maybe forbidden. This often results in commercial arrays standing idle on weekends. If an island power system operator wishes to displace diesel generation it is unfavourable for PV systems to be prevented from generating because of voltage issues.

A review of recent papers shows a strong interest on the voltage quality issues caused by PV in LV distribution networks [21, 22]. A number of techniques exist to alleviate these problems. This chapter provides an extensive review of the impacts and technical approaches to increase PV penetration in both European- and North American-inspired island networks.

2 The Growth of PV Installations

The growth in energy consumption occurs unevenly across the globe. In Western nations the growth is low or even negative while in the developing world growth rates are high. The populations of island nations often have relatively limited access to electric power and are frequently in the high growth camp [23]. PV is one of the most accessible forms of distributed renewable energy [24], and is predicted to become the biggest contributor to electricity generation among all renewable energy candidates by 2040 [25].

2.1 The Global Scenario

PV exceeded wind power as the largest renewable source after hydropower in 2014 [7]. Figure 3 shows the progress of cumulative installed PV capacity in the world over the period 2000–2014. A more than 40% of the total PV capacity is integrated with LV distribution networks in the form of rooftop domestic systems [7, 8].

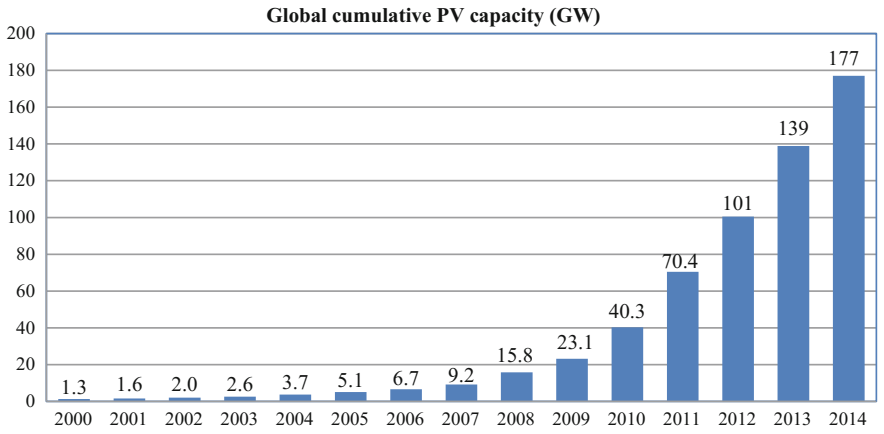

Fig. 3 Global cumulative installed PV capacity (2000–2014) [7]

Table 1 Global PV cumulative installed capacity to 2014 [8]

Region	2011 (GWp)	2012 (GWp)	2013 (GWp)	2014 (GWp)
Americas	4.587	8.296	13.639	21.025
Asia-Pacific	11.127	18.674	39.713	63.542
Europe	53.486	70.999	82.003	89.015
Middle East and Africa	0.212	0.277	0.734	1.792

Table 1 presents numerical data for actual cumulative PV installed capacity by region. The Asia-Pacific region, including China, has the highest growth rates and should represent a major share of PV installations in the coming years.

2.2 PV Applications in Island States

Island states represent a relatively small part of the global PV installations and the available data is scattered and incomplete. Good data sets are generally available for the larger island power systems with examples being Hawaii [26] and Fiji [10]. These power systems have capacities of hundreds of megawatts. For example, the Oahu and Maui grids are 1822 and 264 MW, respectively [26]. These highly sophisticated and large power systems will follow renewable energy trajectories that are similar to the rest of the developed world. As an example Hawaii has a Clean Energy Initiative which aims to meet 40% of its current needs from renewable sources by 2030 and has recently completed a major solar energy integration study [26].

There are tens of publications describing small island power systems which include PV and other renewables in their generation mix. There is strong evidence that the smaller island power systems are embracing growing amounts of PV. Grid-connected PV (GCPV) has become a regular feature of Pacific Island Communities (PICs) [5]. Table 2 lists some key installations in selected PICs. Fiji is included but this is not a small system. The vast majority of these installations have occurred in the past ten years and most projects are less than five years old.

While many of these are small by international standards these arrays have a large local impact. As an example Tokelau has 90% of its energy supplied by PV and coconut biodiesel is used for backup power. This allows Tokelau to claim which is a 100% renewably powered nation.

Table 2 Installations in Pacific island communities 2014 [5]

Nation	Selected installations
Cook Islands	667 kWp of GCPV in 2012. A 950 kWp peak system is in the installation phase
Fiji	1278 kWp has been installed in projects ranging from 45 to 600 kWp
Micronesia	52.5 kWp in five systems
Kiribati	Finance has been approved for a 400 kWp project
Marshal Islands	557 kWp in four systems ranging from 12 to 279 kWp
Nauru	70 kWp in two systems
Niue	252 kWp in three systems ranging from 2 to 200 kWp
Palau	614 kWp in more than 10 installations
Samoa	4.2 MWp including a 2.2 MWp systems which is claimed, at the time of publication, to be the largest in the Pacific
Tokelau	891 kWp in multiple PV clusters
Tonga	4.05 MWp in solar farms ranging from 500 kWp to 1.3 MWp
Tuvalu	448 kWp in six installations
Vanuatu	80 kWp in four systems

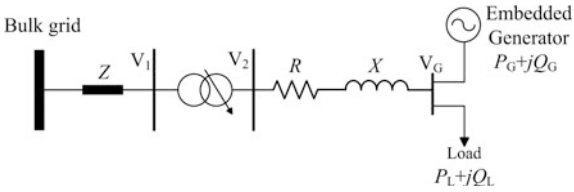

Fig. 4 Single-line diagram of a distribution network [27]

3 Impacts of High Levels of PV Penetration in LV Distribution Networks

A single-line diagram of a radial LV distribution network [27] is shown in Fig. 4. An embedded generator, which can be PV, is connected at the load. In Fig. 4, V_2 is the substation MV bus voltage and X and R are the feeder reactance and resistance, respectively. LV distribution networks have high R/X ratios and are not normally transposed which gives some differences in the phase impedances. These networks are designed to have unidirectional power flow. A hand calculation of the voltage at the generator bus, V_G, will show that voltage unbalance will result from asymmetry in both the load currents and the feeder impedances. High levels of PV installations will further increase the unbalance voltages if the range of the feeder current unbalance is increased.

The voltage impact of integration of PV and other forms of distributed generation in LV distribution networks has been extensively reported [18–21, 28–36]. Overvoltage is the most frequent voltage quality issues that arise when several consumers share a PCC which is most often formed when customers share a

distribution transformer. Solar PV impacts on LV three-phase distribution networks were investigated using a comprehensive assessment tool in [18]. PV output may have a major impact at midday on week days in residential feeders. A combination of high generation and lighter loads may significantly change the power flow resulting in voltage rise and voltage unbalance. Feeder voltage profiles may improve at heavily loaded phases, but there is still the risk of voltage rise and reverse power flow on lightly loaded phases [18–21].

More frequent voltage variations cause additional operations of on-load tap changers (OLTCs), line voltage regulators (VRs) and voltage-controlled capacitor banks. This may reduce life time and increase the maintenance requirements. The degree of voltage unbalance (VU) factor depends on how the solar PVs and loads are distributed across the phases of the LV distribution feeder [18–21].

Significant efforts may be required to militate against such voltage variations. Many voltage regulation devices may lack the appropriate operating range. To deal with the conventional issues of voltage drop under peak loads, most devices provide stronger boost ability in comparison to their voltage reduction or buck capability. Voltage unbalance cannot be corrected with conventionally switched LTC and capacitor banks and these may now require an ability to operative each phase independently.

3.1 Voltage Regulation

A utility operator will be required to maintain the network voltages within a standardised range. The dominant standards are IEC 60038 [37] for British and European heritage systems and ANSI C84.1 [38] for North American-inspired systems. The permissible IEC standard voltages are shown in Table 3. Some nations utilising the IEC standard will define a preferred voltage range that is substantially narrower than the permissible range. The ANSI C84.1 standard specifies the normal and emergency ranges for 120 V power systems. The service and utilisation voltage limits are shown in Table 4. The service voltage is the voltage at the PCC where the consumer connects to the public network. The utilisation voltage is measured at the point of usage within the consumer premises and will be lower due to voltage drops within the customer's installation.

Table 3 IEC 60038 voltage range for 230 V systems [37]

	Service		Utilisation	
	Minimum	Maximum	Minimum	Maximum
Permissible range (V)	207	253	196	253

Table 4 ANSI C84.1 voltage range for 120 V systems [38]

	Service		Utilisation	
	Minimum	Maximum	Minimum	Maximum
Range A (normal) (V)	114	126	108	126
Range B (emergency) (V)	110	127	104	127

3.2 Voltage Unbalance

The voltage unbalance factor (VUF) is defined as the ratio of negative sequence to positive sequence voltage components and is expressed in percentage terms [39]. Voltage unbalance has a significant impact on the operation of three-phase motors [40], and voltage unbalance can result in overheating and de-rating of all induction motor loads. Voltage unbalance has several causes including unbalanced loading, unbalanced solar generation and unequal system impedances [41]. Voltage unbalance also depends on the location and rating of distributed PV. At the beginning of a distribution feeder the impedances are low and significant load or generation unbalance can be tolerated. At more distant locations the feeder impedances are more significant and the unbalance problems increase [41].

4 Mitigation Methods

The traditional approaches used to solve voltage regulation or unbalance problems are network upgrading; online tap changing (OLTC) transformers; fixed or switched capacitors and the curtailment of PV generation. Additionally, there are new or emerging techniques which include inverter-based reactive power control; the use of energy storage and flexible AC transmission system (FACTS)-based controllers. These are now examined.

4.1 Traditional Mitigation Methods

4.1.1 Reconfiguration Reconstruction and Reconductoring

Distribution networks are routinely reconfigured to improve the voltage profile. In British and European distribution systems the LV network can be a few hundred metres long. A long LV section can be split and a new distribution transformer can be added. Another option is reconductoring. The cross section of conductors is increased to achieve lower impedances and this will reduce the voltage drop along

the feeder. Resistance is often important in the distribution network and larger cross sections reduce this directly. Larger cross section conductors have a higher *X*/*R* ratio which will make capacitive voltage regulation methods much more effective. Although upgrading the feeders is very effective for reducing the voltage drop and unbalance it can be an expensive approach.

In North American distribution systems the LV network is relatively short and the voltage drops due to the LV conductors are more limited. In these systems the transformer rating may be increased to reduce the transformer impedance. In these cases the MV conductor impedances are more significant and network is often reconductored.

In either distribution system type, the MV network can be reconfigured to reduce the length of the MV feeders. This can be done, at considerable expense, by the provision of a new point of MV supply. As power systems grow, new zone substations may be added between older stations to add additional capacity.

4.1.2 Transformer Tap Changers and Regulators

Online tap changing is widely used to regulate the bus voltages at distribution substations. The majority of the distribution voltage quality problems occur in the MV and LV distribution feeders which are traditionally purely passive. In very long distribution feeders a pole-mounted voltage regulator based on an OLTC autotransformer maybe applied is shown in Fig. 5 [27]. The tap changing mechanism may be based on mechanical contacts or power electronic switches [41–43]. A variation on the OLTC in Fig. 5 is shown in Fig. 6. In this figure a compensating transformer introduces the boost or buck voltages. The switches do not carry the full load current and this is reduced by the compensating transformer turns ratio. If the voltage issues to be addressed are voltage rises it is important to select regulators with an adequate buck range. Older regulators may not be capable of buck operations.

Two limitations on OLTCs with mechanical switches are the slow response which ranges between 100 ms and several seconds and the need to limit the

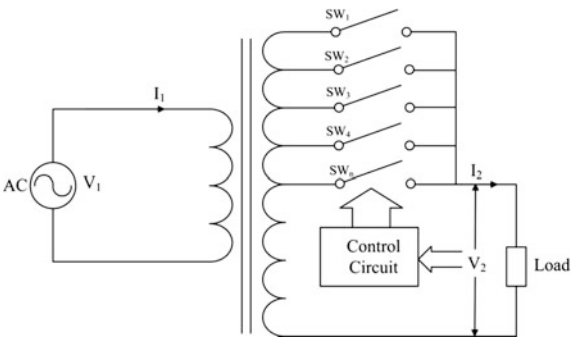

Fig. 5 Schematic of a typical on-load tap changing transformer construction [27]

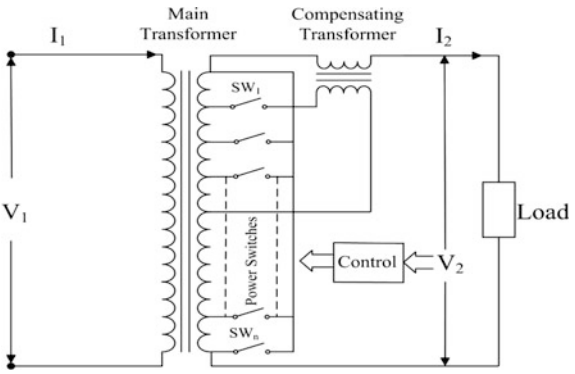

Fig. 6 Schematic of a fast on-load tap changing transformer construction [27]

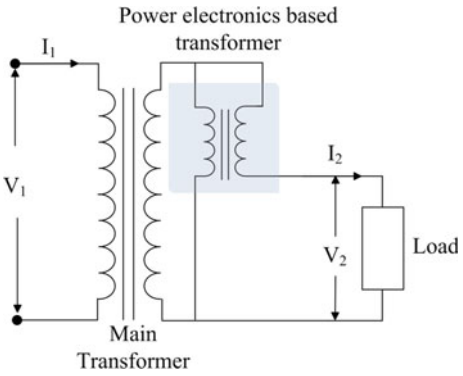

Fig. 7 Schematic of a fast and continuous on-load voltage regulator based on EPT [27]

numbers of operations to manage the maintenance cost. Frequent voltage variations produced by high penetrations of PV may reduce the service life of an OLTC. Power electronics-based OLTCs offer improved performance and reduced maintenance costs due to the replacement of the mechanical tap changing contacts with power electronic switches. These OLTCs can act as fast voltage regulators and in principle cycle-by-cycle switching is possible. Potentially it is possible to respond to rapid events such as sags and flicker. The insulated gate bipolar transistor (IGBT) often forms switch device.

All tap changing devices have one limitation. A voltage discontinuity is caused by their tap changes. The number of switches is limited so that the step size is finite. An on-load voltage regulator (OLVR) based on electronic power transformer (EPT) offers continuous voltage regulation. A schematic of this device is shown in Fig. 7 [43]. The EPT provides a variable compensation voltage and a range of power electronic solutions exist. The EPT may use a conventional compensation transformer that is driven by a power electronic converter. The converter can be an AC chopper, back-to-back bridge converters or a matrix converter. There are also EPT topologies that utilise high-frequency transformers in an effort to reduce size and cost.

In applications with high PV penetrations and OLTCs voltage instability may arise during cloud-induced voltage fluctuations [44]. This can become severe when cloud-induced voltage fluctuations develop faster than the action of voltage regulators, and this may upset the operation of voltage regulation devices [45].

4.1.3 Switched Capacitors

The connection of a capacitor to a distribution feeder with a significant inductive reactance will generally cause the voltage to rise. This statement is qualified as capacitors are more effective in systems with high *X*/*R* ratios. Care must be exercised in a distribution network where the ratio may be low. However, even in a distribution network where resistances dominate a capacitor can still provide a voltage benefit through power factor correction. Power factor correction will reduce the line currents and voltage drops. An optimum capacitor size exists and overcompensation can reduce voltages further.

4.2 Emerging Mitigation Methods

4.2.1 VAR Control of PV Inverters

An inverter based on the bridge configuration is able to transfer both real and reactive power. This technical feature is the basis of static compensators (STATCOMs) [46] and distribution-level static compensators (DSTATCOMs). Figure 8 shows the technical range of real and reactive power for a bridge inverter. The inverter will have an apparent power rating S. If the inverter is required to

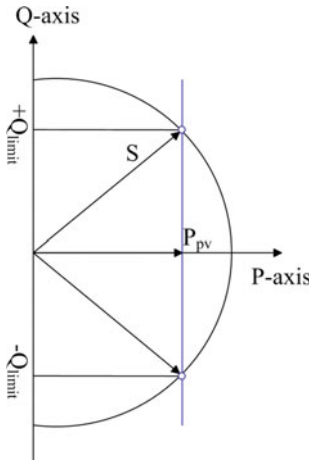

Fig. 8 Reactive power control capabilities of grid-connected PV inverters [51]

export a certain amount of real power P then there will be an upper and lower bound placed on the reactive power import and export. If the inverter is only partially loaded with real power, that is P is less than S, then some reactive capability exists. This feature can be technically exploited in inverters connected to battery storages or to PV arrays. If spare capacity exists these devices can perform STATCOM-like functions.

For PV inverters, a range of national standards exist. These include IEEE 1547 [47], AS 4777 [48] and VDE-AR-N4105 [49]. These will require the inverters to operate within a specified power factor range. The inverters are often required to operate at close to unity power factor. For example IEEE 1547 does not allow PV inverters to provide reactive power. The German inverter standard, VDE-AR-N4105, requires inverters to provide reactive power, in proportion to their generation, to assist in voltage regulation but in an open-loop fashion. STATCOMs can perform both voltage regulation and voltage balance functions. If the regulatory restrictions are set aside and only the technical ability considered then PV inverters can perform this function. The utilisation of a PV inverter's reactive power capability to control the phase balance in LV distribution networks with high PV penetrations has been widely published [50–53]. Phase balancing is most easily accomplished with three-phase inverters but can be achieved with single-phase inverters.

4.2.2 Energy Storage Systems

Energy storage (ES) systems can be used to increase the penetration of renewable energy in any power system. Batteries provide two major abilities:

- An ability to deal with intermittency;
- An ability to improve voltage regulation at the point of connection.

These are of benefit in any power system but in an islanded system where very high penetration levels may be required an ES becomes more critical [54]. An energy storage system can be centralised or distributed. Both can provide energy buffering to reduce the impact of intermittency. A distributed system can potentially provide the additional benefit of voltage regulation at many points of connection [55, 56]. In a distribution feeder with high levels of PV, energy storages may absorb excess PV generation and prevent the reversal of power flow. These storages can discharge at times of high load to support the load voltages. If a distributed ES system is to be used both to address an intermittency issue and to simultaneously provide voltage regulation then a suitable communications and control infrastructure is required. The requirement to control the voltage implies there are significant constraints on the free flow of electric power imposed by the power network

For PV systems batteries will normally be the most appropriate device for dealing with intermittency within the power network. Some larger island projects include [54]:

- Kaua'i—1.5 MW 15 min advanced lead acid battery to mitigate intermittency of a 3 MW PV array—commissioned December 2011;
- Pearl Harbour Hickham Air Force base—125 kW Zn–Br flow battery incorporated with 2400 kW of diesel, 150 kWp of solar and 50 kW of wind power—commissioned December 2012;
- Sana Rita Jail Microgrid 1.2 MW PV, 1 MW fuel cell, 1.2 MW diesel and 11.5 kW wind, 2 MW, 4 MWh lithium ion battery, commissioned March 2012.

These are all relatively large installations operated by a utility or microgrid owner. Energy storages can be installed by individual customers [57]. These are described as being installed on the customer side of the metre or "behind the meter". An individual customer may have a number of motivations. In a large power system the tariffs for energy supplied to the grid may be low. In a smaller or fragile system the export of excess solar energy to the grid may be forbidden to avoid voltage rise issues. In a very small and fragile power system the reliability of the network may be low. In this case, a customer may install an energy storage that is integrated with a PV inverter that can provide an uninterruptible power supply function. For a customer in an island power system several of these scenarios may apply.

Cost remains the major factor in deciding upon the practicality of installing energy storages. A key concept is the levelized cost of energy (LCOE) or the cost of storing and retrieving a kilowatt hour or megawatt hour of energy. This depends strongly upon the capital cost and the cycle life of the battery. For lithium-ion batteries in 2013, the LCOE varied between 100 and 350 USD/MWh for renewable energy integration operations [58]. This corresponds to 0.10 USD to 0.35 USD/kWh. In a large-scale continental power system batteries are still expensive and consequently batteries are not yet widely deployed.

The current costs are more tolerable in higher cost electrical grids as are often found in island applications. In these cases batteries may make more economic sense but price reductions are still desirable. It is anticipated that the rapid growth in electric vehicle production will drive down the cost of larger format lithium batteries. The investment in battery research for electric vehicles has driven the price of lithium batteries well below that of other battery types [59]. In 2014 the cost of lithium batteries to the automotive industry was 325 USD/kWh of usable storage [59]. The industry target cost for 2022 is 125 USD/kWh [59].

An interesting concept is the repurposing of batteries removed from electric vehicles that have reached the end of their working life. At retirement these batteries still have 80% of their name plate. Ampere hour rating and potentially have significant remaining life. These batteries have a scrap value and a value dictated by any "second-life" use. This has the potential to provide large amounts of economically priced batteries that are suitable for network storage applications [60].

4.2.3 Dynamic Shifting of Customer Phase Connections

Much of the phase unbalance in the distribution network is due to unbalanced loading. When networks are constructed, some effort is made to allocate customers evenly across the phases. Over time, the allocations of customers can become unbalanced due to new construction or changes in the utilisation of land. Customers may install rooftop PV systems and these will be randomly distributed across the phases. Customer loads will fluctuate on short- and long-time scales and a reasonably balanced arrangement may be unbalanced in the future. Utility operators will occasionally inspect distribution transformers and if significant current unbalance is present this may be corrected by transferring some customer connections from one phase to another. Emerging research areas include

- The identification of the phase connection of customers using smart metre data [61], for the purposes of identifying cases where action is required;
- The automation of consumer phase changes, using pole-mounted switching systems, to maintain balance [62, 63].

Automated systems that allow customers to be shifted can significantly improve the phase balance. Typically only 10 or 20% of customers need to be connected to phase shifting device at a few locations along the feeder length.

4.2.4 Coordinated Control Between Utility Equipment and PV Inverter

The introduction of any new voltage control methods, such as control PV inverters or ES systems, will require coordination with any pre-existing utility equipment. The coordinated control of a distributed ES with an OLTC has been proposed as shown in Fig. 9 [64].

The major objectives are to limit the PV-induced voltage rises, reduce the numbers of OLTC operations, limit the network peak load and reduce distribution resistive power. A central controller coordinates the distributed ES to charge the battery storage at times of high PV generation to prevent reverse power flow. During the peak hours, the central controller initiates an ES discharge to support the peak load. Simulation confirmed this approach reduces the number of OLTC operations and reduces the resistive losses. Many other examples of the coordination of voltage regulation equipment exist in the literature:

- OLTCs and SVCs coordination for an unbalanced radial distribution system with PV generation [65];
- Network voltage regulators, switched capacitors and PV plants that undertake voltage control at the PCC [66];
- OLTC, distribution feeder voltage regulators and distributed PV [67].

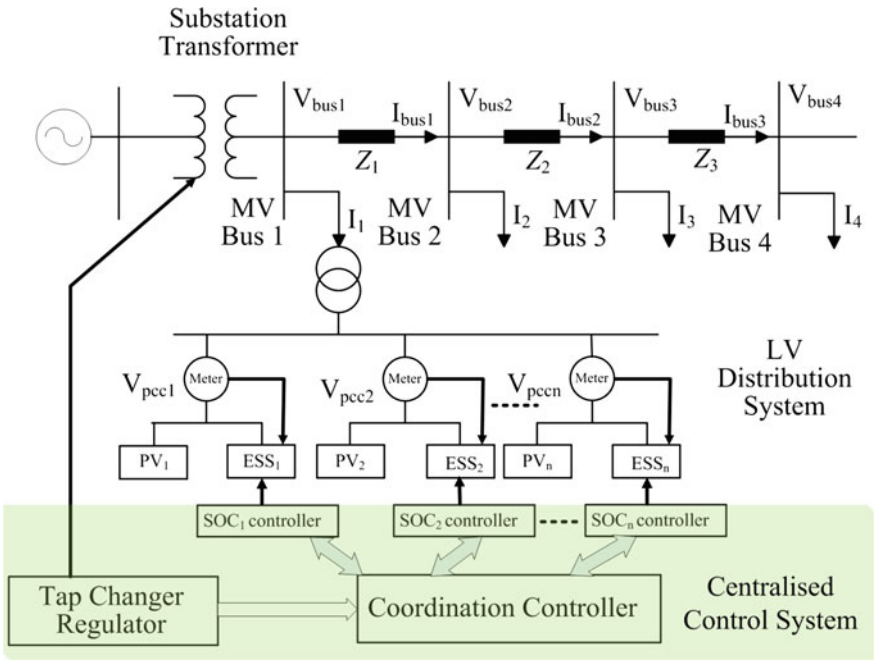

Fig. 9 Coordinated control of distributed ESS with tap changer transformers for voltage rise mitigation [64]

A feature of any ES is the need to manage the battery state of charge (SoC) across a daily operation cycle. A battery must be prepared by charging to support a peak load. Conversely, a battery must be prepared by an earlier discharge to have the capacity to absorb a reverse power flow caused by excessive generation. Battery management systems that have a predictive or forecasting capability are more capable of managing the battery SoC profile in comparison to systems that charge and discharge at fixed times each day. If the demands on the storage system can be forecast for the coming day of operation, it is possible to limit the amount battery usage to optimally satisfy the requirements for that day. This will reduce the cyclic wear cost by avoiding unnecessary charging and discharging and extend the battery calendar life [55, 56].

4.2.5 Dynamic Voltage Restorers

A dynamic voltage restorer (DVR) is a power electronic converter-based series compensator [68]. As shown in Fig. 10, a DVR can be realised with a voltage source inverter (VSI) and a series compensation transformer. The DVR has limited energy storage at the DC bus and cannot make a long-term contribution to real power. The traditional application for the DVR is the compensation of sags and

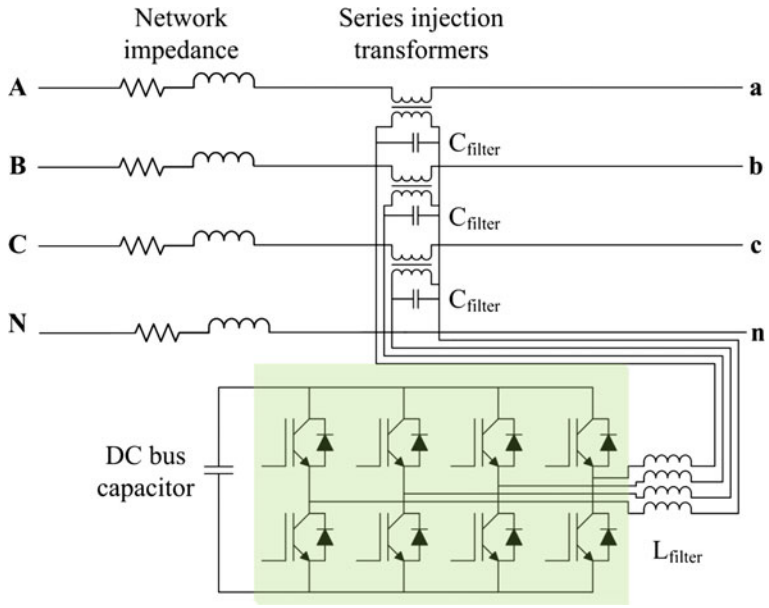

Fig. 10 Schematic of a DVR connected to a distribution network [27]

swells to protect critical loads. These events last a few mains cycles and the energy storage is limited. The normal storage choice is DC capacitors but super capacitors or superconducting magnet energy storages (SMES) can be applied [68].

Figure 10 shows a four-wire variant of the DVR [69], as opposed to a three-wire DVR which is more common in MV applications. This is more suitable for three-phase, four-wire distribution systems where a voltage correction may require positive, negative and zero sequence components. A DVR topology converter can undertake functions in addition to the mitigation of sags and swells. Phase voltage balancing can be performed by adding a negative or zero sequence voltage. These voltages effectively cause a transfer of power between the phases but do not cause a net real power flow [70]. The application of a DVR for compensation in a LV residential feeder with rooftop PVs has recently been proposed [71].

4.2.6 Distribution-Level Static Compensator DSTATCOM

The DSTATCOM is power electronics-based current source connected in parallel to the PCC of a distribution system [44]. A four-wire variant of the DSTATCOM is shown in Fig. 11 [72]. The DSTATCOM inverter is typically supported by energy stored in a DC capacitor. As such the device cannot provide a long-term real power flow. The typical duties include the generation and absorption of reactive power for voltage regulation at the PCC. A DSTATCOM can provide phase current balancing

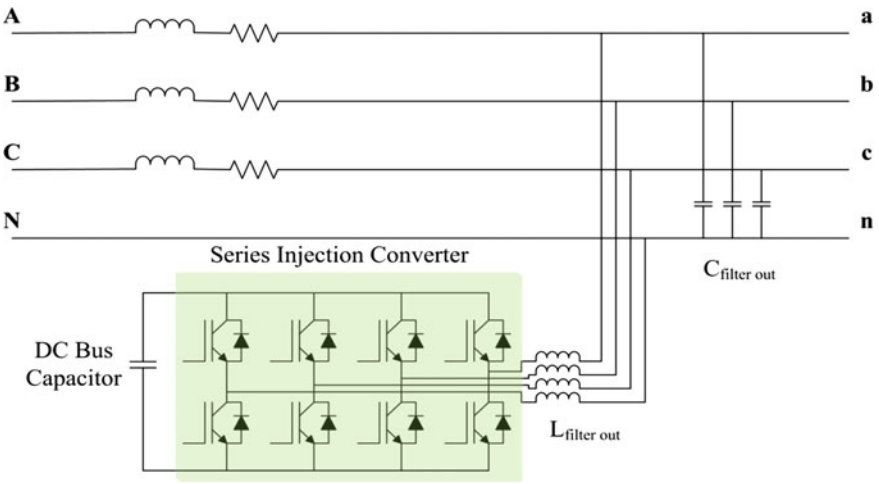

Fig. 11 Schematic of a DSTATCOM connected to a distribution network [72]

by injecting a negative or zero sequence current. It is permissible to transfer real and reactive power between phases so long as the net real power flow is zero. This allows a DSTATCOM to perfectly balance the phase currents upstream of the point of connection.

A DSTATCOM has been used for reactive power compensation in order to increase the PV hosting capacity of a distribution feeder [73]. A DSTATCOM was proposed for voltage profile and unbalance improvement a residential LV feeder with unbalanced distribution of rooftop PV systems [74]. Pole top mounting of DSTATCOMs is an attractive option for treating LV distribution feeders which may reach or exceed their voltage limits with higher PV penetration. Some recent research has focused on using longer life but lower capacitance film capacitors for the DC bus capacitors [75]. The bus capacitor carries significant current at twice the grid frequency, typically 100 or 120 Hz, during phase balancing operations. Film capacitors have very high current capabilities but the capacitance is limited. This gives rise to higher peak bus voltages. The higher voltages can be dealt with using higher voltage rating devices, such as silicon-carbide devices or carefully controlling the STATCOM so that the bus voltage peaks are minimised [72].

A general recommendation is that a DSTATCOM should be installed at 2/3rd of the feeder length to give the best voltage unbalance reduction along the feeder length. A DSTATCOM with sufficient rating can force the current unbalance to zero at the point of connection by measuring the phase currents and calculating a compensating current. An alternative operational method is to measure the unbalance voltage and inject currents to force the unbalance voltage to zero. A DSTATCOM operated in this sense can be considered to be a zero and negative sequence short circuit.

4.2.7 Unified Power Flow Controller

A UPFC consists of a series voltage injection element and a parallel current source element operated that share a common DC link and DC storage capacitor [76, 77]. A four-wire variant of this arrangement is shown schematically in Fig. 12 [78]. The two UPFC elements act as an ideal AC to AC power converter. Real power can freely flow in either direction between the AC terminals of the two inverters. Each inverter can generate or absorb reactive power at its own AC output terminals.

One function of the shunt inverter is to supply or absorb the real power to regulate the voltage on the common DC link. The series converter can absorb or inject real power and is capable of performing the long-term regulation of the line voltage. Additionally the series converter can control the voltage unbalance at the output terminals. The shunt inverter can perform a range of DSTATCOM functions such as phase current balancing and reactive compensation. The rating of the parallel element is a design choice. In a "heavy" design a full range of shunt compensation may be offered. In a "light" design the shunt converter may be limited to supporting the DC bus and satisfying the real power demands of the series element. A UPFC for pole top applications with reduced DC bus capacitance is proposed to mitigate voltage quality problems in LV distribution networks with high levels of PV [78, 79].

4.2.8 AC Chopper and Matrix Converter-Based Voltage Regulators

The UPFC requires two back-to-back inverters with a common DC bus. The application of these converters in reducing the influence of PV on the distribution

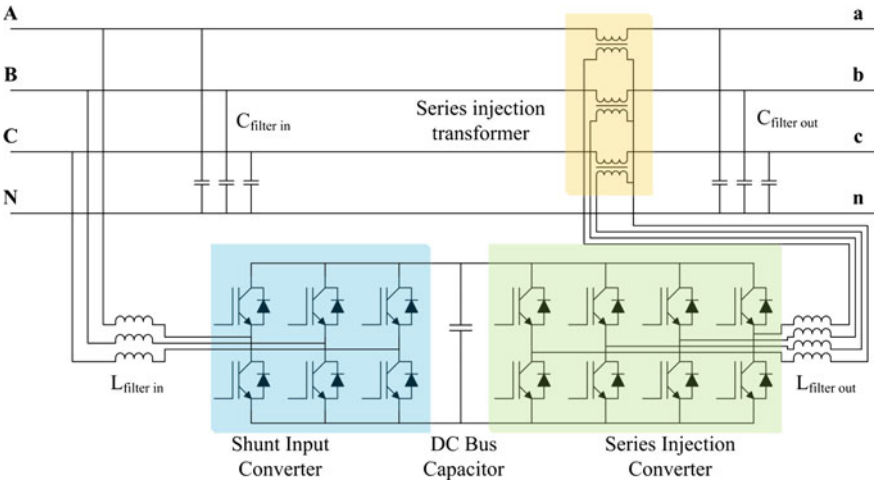

Fig. 12 Schematic of a UPFC connected to a distribution network [78]

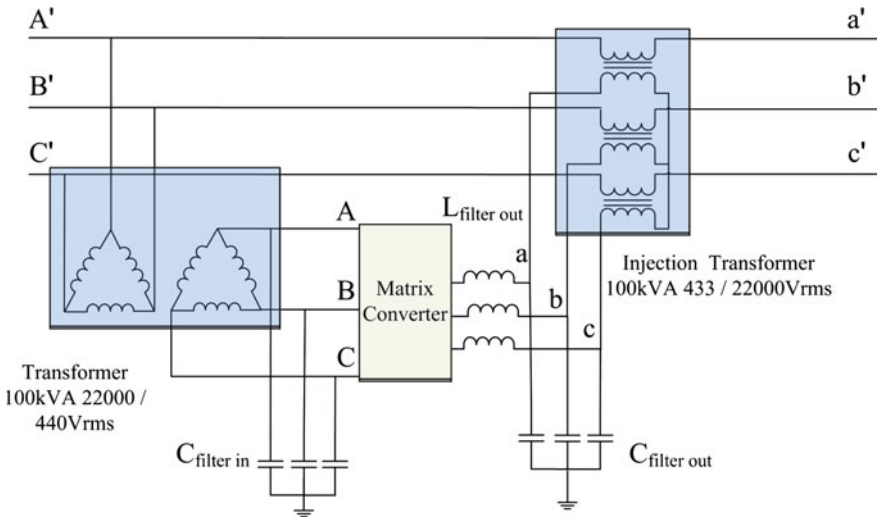

Fig. 13 Schematic of a MC-UPFC connected to a MV distribution network [80]

voltage profile has driven an interest in robust pole-mounted equipment. The DC bus capacitor is a point of concern from a cost and reliability perspective. A matrix converter offers a capacitor-free solution to AC–AC power conversion and a matrix converter-based UPFC (MC-UPFC) has been proposed [80], and is shown in Fig. 13. The matrix converter has one important restriction in that the input and output power must instantaneously balance given the lack of any internal energy storage.

The current MC-UPFCs are capable of voltage regulation and phase voltage balancing. The current devices do not offer a generalised DSTATCOM performance as the control possibilities for the input terminal currents are limited by the lack of internal energy storage.

A simple, capacitor-free alternative are regulators based on AC choppers [81]. These devices can generally only provide an in-phase voltage boost or buck ability. While there is less flexibility than found with an MC-UPFC or an inverter-based UPFC, these devices are relatively inexpensive and single-phase regulators are commercially available [82]. Three units may be combined to provide three-phase voltage regulation ability.

5 Inverter-Dominated Grids

In very small island power supplies, especially those of a few hundred kilowatts or less, there may be an absence of synchronous generation. In these cases, the power grid is dominated by inverter sources. A grid-forming inverter (GFI) is required to

regulate the power system frequency and voltage [83]. In their basic form, the large grid-forming inverter is equipped with a significant battery. This inverter sets the voltage and frequency at a central bus bar. In power system terms, this is a swing bus. The inverter supplies real and reactive power as required to maintain the swing bus voltage and frequency. If diesel generation is present it is normally run in a constant power mode. The diesel is loaded at its maximum fuel efficiency point. Solar generation can be connected to the AC power system but is often connected via maximum power point trackers to the battery of the GFI. The GFI is fast responding and has sufficient capacity to compensate for any intermittency in the renewable generation.

The GFI can be a large centralised unit or a number of units that are controlled in a coordinated fashion. In a physically small power system a single centralised inverter or inverter group may be sufficient. The small physical size limits the physical length of feeders and as a consequence few issues arise with voltage regulation. For a larger inverter-based system it may be necessary to have a few controlled voltage buses. These need to be coordinated by a control system. A range of centralised and decentralised control choices are available. A centralised control solution requires a centralised controller and reliable communications linkages with the bulk of the inverter capacity. In a distributed solution the inverters will have some local controls such as frequency and voltage droop schemes. A control network may be imposed to provide secondary controls such as frequency adjustment and load sharing.

6 Conclusions—The Future for PV in Island Power Systems

Island power systems are relatively small and have high costs of generation in comparison to most large-scale power systems. The high costs of electrical generation are often due to a reliance on diesel generation. Experience with remote power systems, including continentally based systems that reach tens of megawatts, has shown diesel generation is expensive at any scale. Many island systems are sub-megawatt in size. The costs in island systems are increased by the difficulties of remoteness in terms of fuel delivery and access for maintenance.

Luckily many island systems have access to good renewable resources such as wind, biomass and solar resources. These have been successfully harnessed in many systems to reduce, or even eliminate, the reliance on diesel generation. There are very strong economic reasons to operate island power systems with very high fractions of renewable energy. Many technologies are now mature and reliable. The costs of renewable energy systems have continued to reduce. This is especially true for solar generation. It seems inevitable that the economics of the situation must drive increasing interest and usage of PV systems.

The technical challenges emerge once a considerable fraction of the consumer energy, say more than 20%, is to be supplied from renewable sources. The key issues for an island power supply operator with a very high renewable fraction are intermittency and voltage control.

6.1 Intermittency

Intermittency, in any power system, can only be addressed providing mechanisms to maintain the balance between generation and load. The technical options in an approximate order of preference are

- Reduce the intermittency through a technology diversified and a spatially diversified portfolio of generation sources;
- Have some loads that are deferrable or rapidly adjustable which can respond to any renewable generation changes;
- Install highly responsive backup generation that can rapidly replace any sudden loss in renewable generation;
- Provide energy storage to act as a buffer;
- To provide extremely high levels of renewable generation and "spill" the excess capacity.

The first three options are well understood and widely practised in many modern power systems. In island power systems the degree of diversity will be generally lower than in large continental power systems. This is a consequence of size which is reflected in the numbers of generating units and loads. The first three solutions are effective in large power systems. For a small power system, energy storage may become a larger part of solutions which are required to maintain power balance.

Battery storage is the current emerging technology and provides workable solution to the technical problem. Some mature technologies exist and large-scale battery systems have been deployed. A number of manufacturers are producing off the shelf products at a residential and commercial scale. The battery cyclic costs are currently a challenge but large-scale investments in the electric vehicle industry are forcing the costs lower.

The final option seems inherently wasteful but this becomes economically sensible if the generation source cost is low. In recent years the cost of PV has reduced enormously and as a consequence the proportion of PV in hybrid energy designs has increased significantly.

6.2 Voltage Control

The economics of island systems encourage high degrees of renewable penetration. These will have an impact on the voltage profile in the distribution networks.

If a new island power system is to be constructed or new extensions are to be added, it is completely possible and highly desirable to design a power system that is inherently able to absorb the bidirectional power flows that might result from distributed renewable generation. If bidirectional flow is to be allowed or encouraged, the networks can be designed with voltage profiles that lie centrally within the allowable minimum and maximum voltage ranges. This requires that the voltages at the head of feeders are set closer to the nominal voltage. This allows more voltage rise to occur before the upper voltage limits are exceeded. It does reduce the allowable voltage drop at peak load times. This requires either larger conductor cross sections or shorter distribution circuit lengths. This will result in a modest increase in the capital cost of the power system but this is very likely to be the best technical and most economical solution.

If distributed solar generation is to be installed within an existing distribution system then additional efforts will be required to regulate voltage profiles once a critical level of penetration is reached. The exact level will depend on the voltage profile and conductor impedances of the existing network. In general terms, a high-quality network will be able to host more generation. This chapter has explored the full range of traditional and emerging technology approaches that can be applied. These range from the reconstruction of weak feeders to the deployment of storage and distributed power electronics-based devices.

References

1. Cabellero F, Sauma E, Yanine Y (2013) Business optimal design of a grid connected hybrid PV (photovoltaic) wind energy system without energy storage for an Easter Island block. Energy 61:248–261
2. Kuang Y, Zhang Y, Zhou B et al (2016) A review of renewable energy utilisation in islands. Renew Sustain Energy Rev 59:504–513
3. Moharil RM, Kulkarni PS (2009) A case study of solar photovoltaic power system at Sagardeep Island, India. Renew Sustain Energy Rev 13(3):673–681
4. Khan MRB, Jidin R, Pasupuleti J, Shaaya SA (2015) Optimal combination of solar, wind, micro-hydro and diesel systems based on actual seasonal load profiles for a resort island in the South China Sea. Energy 82:80–97
5. Raturi A, Singh A, Prasad RD (2016) Grid-connected PV systems in the Pacific Island Countries. Renew Sustain Energy Rev 58:419–428
6. Betzold C (2016) Fuelling the Pacific: aid for renewable energy across Pacific Island countries. Renew Sustain Energy Rev 58:311–318
7. IEA (2014) Snapshot of global PV markets (Online). http://www.iea-pvps.org/fileadmin/dam/public/report/technical/PVPS_report_-_A_Snapshot_of_Global_PV_-_1992-2014.pdf. Accessed 19 July 2016

8. IEA (2015) Trends 2015 in photovoltaic applications. International Energy Agency Report IEA-PVPS T1-17:2015 http://www.iea-pvps.org/fileadmin/dam/public/report/national/IEA-PVPS_-_Trends_2015_-_MedRes.pdf. Accessed 19 July 2016
9. Neves D, Silva C, Connors S (2014) Design and implementation of hybrid renewable energy systems on micro-communities: a review on case studies. Renew Sustain Energy Rev 31: 935–946
10. Dornan M, Jotzo F (2015) Renewable technologies and risk mitigation in small island developing states: Fiji's electricity sector. Renew Sustain Energy Rev 48:35–48
11. Drouineau M, Assoumou E, Mazauric V et al (2015) Increasing shares of intermittent sources in Reunion Island: impacts on the future reliability of power supply. Renew Sustain Energy Rev 46:120–128
12. Fokaides P, Kylili A (2014) Towards grid parity in insular energy systems: the case of photovoltaics in Cyprus. Energy Policy 65:223–228
13. Lave M, Kleissel J, Ellis A et al (2013) Simulated PV power plant variability: impact of utility –imposed ramp limitation in Puerto Rico. In: Proceedings of the IEEE 39th photovoltaic specialists conference, Tampa Florida, 16–21 June 2013, pp 1817–1821
14. Jinanasombat B, Premrudeepreechacharn S (2015) Optimal analysis of battery energy storage for reduction of power fluctuation from PV system in Mae Hong Son province. In: Proceedings of the IEEE international youth conference on energy, Pisa, Italy, 27–30 May 2015
15. Horizon Power (2016) Technical requirements for renewable energy systems connected to the low voltage (LV) network via inverters. http://horizonpower.com.au/media/1121/technical-requirements-for-renewable-energy-systems-connected-to-the-low-voltage-lv-network-via-inverters.pdf. Accessed 19 July 2016
16. de Groot M, Forbes J (2013) Demand response in isolated power systems. In: Proceedings of the Australasian universities power engineering conference, AUPEC, University of Tasmania, Hobart Australia, 29 Sept–3 Oct 2013
17. Hydro Tasmania King Island Renewable Energy Integration Project. Available at http://www.kingislandrenewableenergy.com.au/. Accessed 19 July 2016
18. Alam M, Muttaqi K, Sutanto D (2012) A comprehensive assessment tool for solar PV impacts on low voltage three phase distribution networks. In: Proceedings of the second international conference on developments in renewable energy technology (ICDRET), Dhaka, Bangladesh, 5–7 Jan 2012
19. Walling R, Saint R, Dugan R et al (2008) Summary of distributed resources impact on power delivery systems. IEEE Trans Power Deliv 23:1636–1644
20. Yan R, Saha TK (2012) Voltage variation sensitivity analysis for unbalanced distribution networks due to photovoltaic power fluctuations. IEEE Trans Power Syst 27(2):1078–1089
21. Wong J, Lim YS, Tang JH, Morris E (2014) Grid-connected photovoltaic system in Malaysia: a review on voltage issues. Renew Sustain Energy Rev 29:535–545
22. Salas V, Olías E (2011) Overview of the state of technique for PV inverters used in low voltage grid-connected PV systems: inverters above 10 kW. Renew Sustain Energy Rev 15(2):1250–1257
23. Eltawil MA, Zhao Z (2010) Grid-connected photovoltaic power systems: technical and potential problems—a review. Renew Sustain Energy Rev 14(1):112–129
24. Dornan M (2014) Access to electricity in small Island developing states of the Pacific: issues and challenges. Renew Sustain Energy Rev 31:726–735
25. Ackermann T, Andersson G, Söder L (2001) Distributed generation: a definition. Electr Power Syst Res 57(3):195–204
26. Eber K, Corbus D (2013) Hawaii solar integration study: executive summary. National Renewable Energy Laboratory
27. Haque MM, Wolfs P (2016) A review of high PV penetrations in LV distribution networks: present status, impacts and mitigation measures. Renew Sustain Energy Rev 62:1195–1208

28. Katiraei F, Aguero JR (2011) Solar PV integration challenges. IEEE Power Energ Mag 9(3): 62–71
29. Baran ME, Hooshyar H, Shen Z, Huang A (2012) Accommodating high PV penetration on distribution feeders. IEEE Trans Smart Grid 3(2):1039–1046
30. Hoke A, Butler R, Hambrick J, Kroposki B (2013) Steady-state analysis of maximum photovoltaic penetration levels on typical distribution feeders. IEEE Trans Sustain Energy 4 (2):350–357
31. Shayani RA, de Oliveira MAG (2011) Photovoltaic generation penetration limits in radial distribution systems. IEEE Trans Power Syst 26(3):1625–1631
32. Solanki SK, Ramachandran V, Solanki J (2012) Steady state analysis of high penetration PV on utility distribution feeder. In: IEEE PES Transmission and distribution conference and exposition (T&D), pp 1–6
33. Tonkoski R, Turcotte D, El-Fouly TH (2012) Impact of high PV penetration on voltage profiles in residential neighborhoods. IEEE Trans Sustain Energy 3(3):518–527
34. Mitra P, Heydt GT, Vittal V (2012) The impact of distributed photovoltaic generation on residential distribution systems. In: North American power symposium (NAPS), IEEE, pp 1–6
35. Agüero JR, Steffel SJ (2011) Integration challenges of photovoltaic distributed generation on power distribution systems. In: 2011 IEEE power and energy society general meeting, IEEE, pp 1–6
36. Schoene J, Zheglov V, Houseman D, Smith JC, Ellis A (2013) Photovoltaics in distribution systems—integration issues and simulation challenges. In: 2013 IEEE power and energy society general meeting, IEEE, pp 1–5
37. IEC (2007) IEC Standard Voltages (IEC 60038), 2002-07, International Electrotechnical Commission. IEEE (2003), IEEE Standard 1547, standard for interconnecting distributed resources with electric power systems, IEEE
38. ANSI (2011) American National Standard for electric power systems and equipment—voltage ratings-60 Hz (ANSI C84.1-2011)
39. Pillay P, Manyage M (2001) Definitions of voltage unbalance. IEEE Power Eng Rev 21: 49–51
40. Ching-Yin L (1999) Effects of unbalanced voltage on the operation performance of a three-phase induction motor. IEEE Trans Energy Convers 14:202–208
41. Shahnia F, Majumder R, Ghosh A et al (2010) Sensitivity analysis of voltage imbalance in distribution networks with rooftop PVs. In: Proceedings of the 2010 IEEE power and energy society general meeting, Minneapolis, Minnesota, 25–29 July 2010
42. Faiz J, Siahkolah B (2006) Differences between conventional and electronic tap-changers and modifications of controller. IEEE Trans Power Deliv 21:1342–1349
43. Jiawei Y, Chengxiong M, Dan W et al (2013) Fast and continuous on-load voltage regulator based on electronic power transformer. IET Electr Power Appl 7(6):499–508
44. Yan R, Saha TK (2012) Investigation of voltage stability for residential customers due to high photovoltaic penetrations. IEEE Trans Power Syst 27(2):651–662
45. Ari GK, Baghzouz Y (2011) Impact of high PV penetration on voltage regulation in electrical distribution systems. In: 2011 international conference on clean electrical power (ICCEP), IEEE, pp 744–748
46. Ghosh A, Ledwich G (2012) Power quality enhancement using custom power devices. Springer Science & Business Media
47. IEEE (2003) IEEE Standard 1547, standard for interconnecting distributed resources with electric power systems, IEEE
48. Standards Australia (2005) Australian Standard AS4777.1-2005, Grid connection of energy systems via inverters, Standards Australia
49. VDE (2011) Erzeugungsanlagen am Niederspannungsnetz - Technische Mindestanforderungen fur Anschluss und Parallelbetrieb von Erzeugungsanlagen am Niederspannungsnetz (Generators connected to the low-voltage distribution network—

technical requirements for the connection to and parallel operation with low-voltage distribution networks), VDE-AR-N4105, Aug 2011
50. Su X, Masoum MA, Wolfs P (2014) Comprehensive optimal photovoltaic inverter control strategy in unbalanced three-phase four-wire low voltage distribution networks. IET Gener Transm Distrib 8(11):1848–1859
51. Su X, Masoum MA, Wolfs PJ (2014) Optimal PV inverter reactive power control and real power curtailment to improve performance of unbalanced four-wire LV distribution networks. IEEE Trans Sustain Energy 5(3):967–977
52. Su X, Masoum MA, Wolfs PJ (2015) Multi-objective hierarchical control of unbalanced distribution networks to accommodate more renewable connections in the smart grid era
53. Su X, Masoum MA, Wolfs P (2014) PSO based multi-objective optimization of unbalanced lv distribution network by PV inverter control. In: 2014 China international conference on electricity distribution (CICED), IEEE, pp 1744–1748
54. Rodrigues EMG, Godina R, Santos SF, Bizuayehu AW, Contreras J, Catalão JPS (2014) Energy storage systems supporting increased penetration of renewables in islanded systems. Energy 75:265–280
55. Jayasekara N, Masoum MA, Wolfs PJ (2016) Optimal operation of distributed energy storage systems to improve distribution network load and generation hosting capability. IEEE Trans Sustain Energy 7(1):250–261
56. Jayasekara N, Masoum M, Wolfs P (2014) An optimal management strategy for distributed storages in distribution networks with high penetrations of PV. Electr Power Syst Res 116:147–157
57. Tesla Motors (2015) Power wall tesla home battery-2015. http://www.teslamotors.com/powerwall. Accessed on 19 July 2016
58. Akhil A, Huff G, Currier A et al (2013) DOE/EPRI 2013 electricity storage handbook in collaboration with NRECRA, Sandia National Laboratories, SAND2013-15131, July 2013
59. DOE (2014) EV everywhere grand challenge, US Department of Energy, Jan 2014, DOE/EE-1024
60. Wolfs P (2010) An economic assessment of "second use" lithium-ion batteries for grid support. In: Proceedings of the Australasian Universities power engineering conference, (AUPEC), Christchurch, New Zealand, 5–8 Dec 2010
61. Pezeshki H, Wolfs P (2012) Consumer phase identification in a three phase unbalanced LV distribution network. In: Proceedings of the IEEE power and energy society innovative smart grid technologies conference, ISGT Europe, Berlin, 14–17 Oct 2012
62. Shahnia F, Wolfs P, Ghosh A (2014) Voltage unbalance reduction in low voltage feeders by dynamic switching of residential customers among three phases. IEEE Trans Smart Grid 5(3):1318–1327
63. Shahnia F, Wolfs P, Ghosh A (2014) Smart inter-phase switching of residential loads in low voltage distribution feeders. Stud Comput Intell 540:329–354
64. Xiaohu L, Aichhorn A, Liming L (2012) Coordinated control of distributed energy storage system with tap changer transformers for voltage rise mitigation under high photovoltaic penetration. IEEE Trans Smart Grid 3:897–906
65. Daratha N, Das B, Sharma J (2014) Coordination between OLTC and SVC for voltage regulation in unbalanced distribution system distributed generation. IEEE Trans Power Syst 29:289–299
66. Ravindra H, Faruque M, Schoder K et al (2012) Dynamic interactions between distribution network voltage regulators for large and distributed PV plants. In: 2012 IEEE PES transmission and distribution conference and exposition (T&D), pp 1–8
67. Muttaqi M, Le A, Negnevitsky M et al (2013) A coordinated voltage control approach for coordination of OLTC, voltage regulator and DG to regulate voltage in a distribution feeder. In: Proceedings of the 2013 IEEE industry applications society annual meeting, Lake Buena Vista, Florida, 6–11 Oct 2013
68. Nielsen J, Blaabjerg F (2005) A detailed comparison of system topologies for dynamic voltage restorers. IEEE Trans Ind Appl 41:1272–1280

69. Changjiang Z, Arulampalam A, Jenkins N (2003) Four-wire dynamic voltage restorer based on a three-dimensional voltage space vector PWM algorithm. IEEE Trans Power Electron 18:1093–1102
70. Ghosh A, Ledwich G (2002) Compensation of distribution system voltage using DVR. IEEE Trans Power Deliv 17:1030–1036
71. Shahnia F, Ghosh A, Ledwich G et al (2014) Voltage unbalance improvement in low voltage residential feeders with rooftop PVs using custom power devices. Int J Electr Power Energy Syst 55:362–377
72. Wolfs P, Yang F, Han Q (2014) Distribution level SiC FACTS devices with reduced DC bus capacitance for improved load capability and solar integration. In: IEEE international symposium on industrial electronics, Istanbul, Turkey, 1–4 June 2014
73. Chao-Shun C, Chia-Hung L, Wei-Lin H et al (2013) Enhancement of PV penetration with DSTATCOM in Taipower distribution system. IEEE Trans Power Syst 28:1560–1567
74. Shahnia F, Ghosh A, Ledwich G et al (2014) Voltage unbalance improvement in low voltage residential feeders with rooftop PVs using custom power devices. Int J Electr Power Energy Syst 55:362–377
75. Wolfs P, Oo A (2013) Improvements to LV distribution system PV penetration limits using a dSTATCOM with reduced DC bus capacitance. In: Proceedings of the 2013 IEEE power and energy society general meeting (PES), Vancouver, Canada, 21–25 July 2013
76. Gyugyi L, Schauder C, Williams S et al (1995) The unified power flow controller: a new approach to power transmission control. IEEE Trans Power Deliv 10:1085–1097
77. Dixon J, Moran L, Rodriguez J et al (2005) Reactive power compensation technologies: state-of-the-art review. Proc IEEE 93:2144–2164
78. Wolfs P (2012) A UPFC with reduced DC bus capacitance for LV distribution networks with high PV penetrations. In: Proceedings of the 22nd Australasian Universities power engineering conference (AUPEC), Bali, Indonesia, 26–29 Sept 2012
79. Haque M, Wolfs P (2015) A reduced capacitance UPFC with active filtering capability for high PV penetration applications. In: Proceedings of the IEEE PES Asia-Pacific power and energy conference, Brisbane, Australia, 25–28 Oct 2015
80. Ali S, Wolfs P (2014) A matrix converter based voltage regulator for MV rural feeders. In: Proceedings of the IEEE power and energy society general meeting, Washington, 27–31 July 2014
81. Park C, Kwon J, Kwon B (2012) Automatic voltage regulator based on a series voltage compensation with an AC chopper. IET Power Electron 5(6):719–725
82. Mircroplanet (2016) Renewable integration. http://www.microplanet.com/products/renewable-integration. Accessed on 19 July 2016
83. Chae WK, Lee HJ, Won JN, Park JS, Kim JE (2015) Design and field tests of an inverted based remote microgrid on a Korean Island. Energies 8(8):8193–8210

Grid-Connected and Off-Grid Solar Photovoltaic System

V. Karthikeyan, S. Rajasekar, Vipin Das, P. Karuppanan and Asheesh Kumar Singh

Abstract PV systems are widely operated in grid-connected and a stand-alone mode of operations. Power fluctuation is the nature phenomena in the solar PV based energy generation system. When solar PV system operates in off-grid to meet remote load demand alternate energy sources can be identified, such as hybrid grid-tied or battery storage system for stable power supply. In the grid-connected condition when solar radiation is insufficient and unable to meet load demand, the energy is accessed from grid via net meter which makes more reliability in the consumer ends. Power quality is a major concern, while injecting PV to the grid and mitigating the effects of load harmonics and reactive power in the distribution system is the challenging area. Off-grid solar PV system is independent of the grid and provides freedom from power quality issues and electricity billing. The excess energy can be accumulated in the battery storage units through superior control. The main research challenges in off-grid are to provide support to load when sudden changes happened in a closed network of the load. This chapter deals with the operational behavior of solar PV system in grid-tied and off-grid system. It includes the issues and research challenges during power unbalancing and environmental (solar irradiation) and load conditions, etc. This chapter contains the control strategies of sliding mode control for grid-tied and off-grid system. The simulations have been performed for solar PV fed multilevel inverters for grid-tied and off the

V. Karthikeyan (✉) · V. Das · P. Karuppanan · A.K. Singh
M.N. National Institute of Technology Allahabad, Allahabad, Uttarpradesh 211004, India
e-mail: karthi13546@gmail.com

V. Das
e-mail: vipindas504@gmail.com

P. Karuppanan
e-mail: karuppanan1982@gmail.com

A.K. Singh
e-mail: asheeshkrs@gmail.com

S. Rajasekar
NEC Laboratories Singapore, NEC Asia Pacific Pte. Ltd., Singapore, Singapore
e-mail: rajasekar_s@nec.com.sg

F.M.R. Islam et al. (eds.), *Smart Energy Grid Design for Island Countries*,
Green Energy and Technology, DOI 10.1007/978-3-319-50197-0_5

grid in islanding regions. Furthermore, the simulations are carried out for load compensation by mitigating the effects of load harmonics and reactive power in the distribution. The results are also presented to provide better insight to reader for understanding grid-connected and off-grid solar PV system.

Keywords Solar PV system · Grid-tied · Off-grid · Load compensation

1 Introduction

Microgrids are the frameworks that incorporate distributed generation (DG) units, energy storage systems (ESS) and loads, controllable burdens on a low voltage system which can work in either stand-alone mode or grid-connected mode [1, 2]. In grid-connected mode, the microgrid alters power equalization of free market activity by obtaining power from the main network or offering energy to the grid to boost operational advantages. In the stand-alone mode, the microgrid is isolated from the upstream distribution network, and the objective is to keep a continuous power supply to clients utilizing DG offers [3]. To reduce the power oscillations of non-dispatchable DG units, different control schemes are utilized as a part of the microgrid, including power balance of each dispatchable DG unit, charging and releasing of ESS, and load shedding [4]. The control techniques used inside a microgrid can be a network operated based voltage-sourced converter (VSC) [5–9] or a network framing control procedure [10, 11]. A microgrid typically requires a power balancing technique—allotting dynamic, reference of reactive power, and guaranteeing collaboration between the controllable units to accomplish steady and economic operation [12–14]. The main block diagram of the solar photovoltaic system integrated with the micro grid is shown in Fig. 1.

The PV inverter systems are widely operated in stand-alone and grid-connected modes of operation. The stand-alone systems are beneficial in remote areas that are isolated from the power distribution network. For remote areas where the AC mains are not available, the stand-alone PV system provides power to the local users behaving as an AC voltage source. Because of the unpredictive nature of the PV source, a chargeable battery or backup supply is necessary to store the excess energy during the high solar irradiation period and supply to the load when the PV energy is not available. Fluctuating voltage and power are of major concern in the stand-alone mode of PV generation systems. To address these problems, a control strategy for voltage control using voltage source inverter in the voltage control mode is used. In the grid-connected mode of application, the PV supported inverter is considered as the controller. The inverter is configured as shunt controller, which not only supplies the PV power to the grid but also performs the load compensation by mitigating the effects of load harmonics and reactive power in the distribution system. This chapter deals with integration of solar photovoltaic system to microgrid and operates in grid-connected and off-grid mode [14, 15].

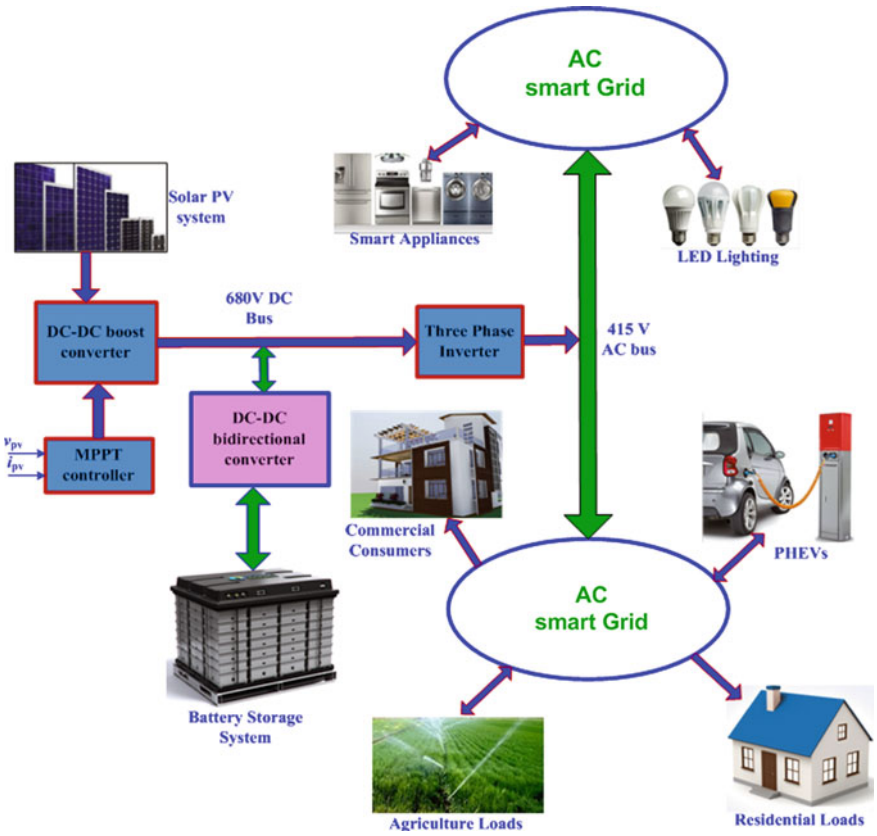

Fig. 1 Main block diagram of solar photovoltaic system integrated with micro grid

1.1 Energy Storage System

The solar energy is fluctuating in nature and to maintain stability of power network supporting energy sources are required. It is usually an energy storage system and it provides supplementary or backup power when it is needed. The energy storage system (ESS) can give a rich range of advantages to the electric framework, to power end-clients, and to society overall [16, 17]. The variety of ESS can be assembled into six wide application/use classifications:

- Charging and discharging cycle based on time,
- Operated with grid integration,
- Reduction of grid infrastructure,
- Benefits to clients,
- Integration with renewable energy generation, and others.

1.1.1 Charging and Discharging Cycle Based on Time

The two power supply profits by capacity are maybe the most commonplace: electric vitality time movement and electric supply limit. The daily curve of ESS is shown in Fig. 2. Energy stored time-shift includes:

i. Capacity of electric vitality when its quality and/or cost are low.
ii. Utilization of the stored energy when the quality and/or cost are high.

These are alluded to as "purchase low–sell high" exchanges. The advantage determined is the contrast between:

i. The praise paid for energy that is stored and
ii. The "high" cost while selling except net losses occurrence while charging and discharging.

For example, at night there is usually limited need for electricity and there is often more supply than there is need. At those times, the cost to generate electricity and the price for that electricity are relatively low.

Conversely, during weekdays, especially summer weekdays, electric energy use is high and as are the cost to produce and the price to purchase the electric energy.

The second electric supply benefit—electric supply capacity—is related to a reduced need for electricity generation equipment (i.e., capacity). Quite simply, if storage use reduces the need to install generation capacity then the benefit from storage is the avoided or reduced cost associated with building and owning that generation equipment.

In the evening, there is normally restricted requirement for power and there is regularly more supply than need. At those times, the expense to produce power and the generation cost are generally low. On the other hand, during weekdays, particularly summer weekdays, the utilization of electrical energy is high and the generation cost and the cost to buy the electric energy are high [18–22].

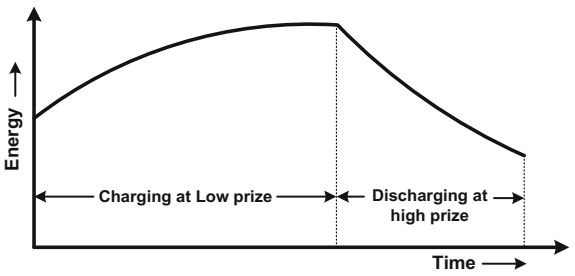

Fig. 2 Daily curve of energy storage system

1.1.2 Operated with Grid Integration

There are a few services required to maintain the effective and reliable electric grid operations which are as follows:

1. Stores or retrieves the energy.
2. Instantly or hour basis compromise of energy to balance out the grid.
3. Voltage regulation that is required while demand changes periodically or rapidly.

Capacity is to some degree or even much preferred as subordinate administrations resources over the traditional fossil-energized approach. There are two key reasons. To start with, The ESS starts up instantly and it can be shifted quickly. Thus, they are more responsive and adaptable as subordinate administrations. Second, the life of ESS and wear are to some degree or even substantially less delicate to yield variability.

The advantage is reduction of cost with respect to generation-based subordinate administrations including decreased requirement for electricity storage equipments, and power generation cost, for fuel and wear. Furthermore, energy storage can give the greater part of the subordinate administrations and the same energy storage unit can be utilized for other purposes [22–25].

1.1.3 Reduction of Grid Infrastructure

Simply, network infrastructure advantages are identified with energy storage use to enhance the effectiveness, productivity, and cost adequacy of the power system transmission and distribution (T&D) and/or to reduce the requirement for T&D components.

To enhance T&D equipment execution, energy storage is associated with the T&D equipment and it diminishes the peak demand [24–26].

1.1.4 Benefits to Clients

There are two subcategories of end-client advantages:

1. Electricity prize administration and
2. Reduction in losses because of electric administration quality and blackouts.

Electricity praise administration includes energy storage use to minimize the end-client's expense to buy power. The bill administration advantage may include:

1. Reduced expense for and utilization of electric energy or
2. Reduced use of electric demand.

In addition, two categories are compared, however the advantages for decreased from money related a misfortune leads blackouts. The first could be alluded to as a power quality (PQ) related advantage. The second subcategory—which could be alluded to as an unwavering quality advantage—is like the PQ advantage. It collects if the capacity is utilized to diminish from expenses connected with electric administration disturbances—"blackouts."

1.1.5 Integration with Renewable Energy Generation

The energy storage is ready to assume a key part in the incorporation of renewable energy (RE) based power generation into the electricity grid. The main block diagram for integration of renewable energy resources to grid is represented in Fig. 3. Exceptionally compelling is the utilization of energy storage to help with the successful and dependable reconciliation of RE-based generation whose yield is variable, essentially wind and sun powered and conceivably including sea wave and tidal energy generation. A few main key terms include

1. Output variability,
2. A transient (time-related) befuddle among generation and power requirement and
3. Undesirable electrical impacts created by RE-based generation.

Yield variability can be either short-term or for long duration. Brief term variability—enduring a few moments to numerous minutes—is brought about by changes in wind speed, in some cases including noteworthy minute-to-minute varieties, and quick vacillations of sun-based energy because of mists. Long haul variability happens from year to year, season to season, and every day and in

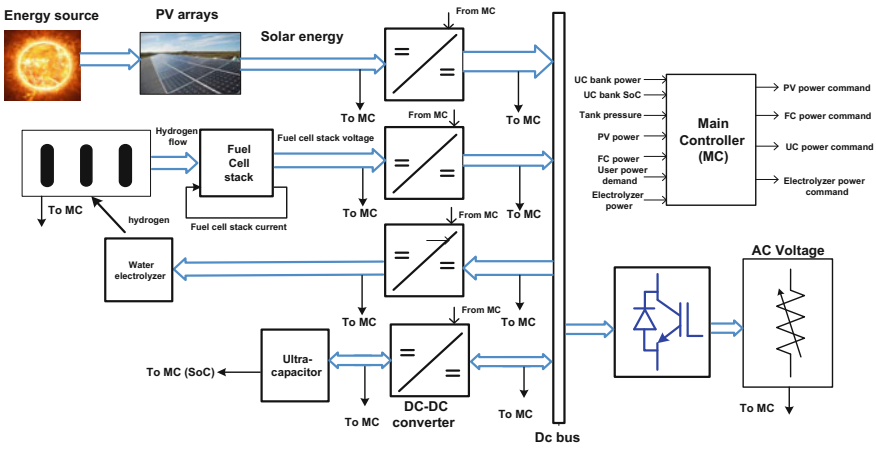

Fig. 3 Integration of renewable energy resources to grid

particular, consistently. Electric storage can be utilized to address both brief span and long-term variability.

To address short-term variability, energy storage yield vacillates in a manner that it counterbalances the RE-based generation's variable yield. For example, if wind generation yield drops because of lower wind speed, then energy storage yield are expanded by the quantity expected to compensate. To address longer length variability consistently, energy storage releases to "fill-in" when the RE is not generating full power. The impact of energy storage utilized as a part of working together with variable RE to address everyday variability is what is now and then called "firming"—implying that the outcome is steady power yield, particularly in peak demand conditions [27–30].

1.1.6 Others

Other energy storage advantages are those:

- No cost and/or
- No settled business sector and/or.

A vital advantage of other storage units is that ESS expands the use of GT&D resource: GT&D base is utilized more in the evening since that is when storage units are charging, so the energy generation and consumption would be more with same GT&D equipment.

1.2 Stand-Alone PV Inverter Systems

Solar PV based stand-alone systems used in islanding regions are generally designed as shown in Fig. 4 which requires some additional attention [31, 32]. The standard voltage level of such applications generally in the range of 220–250 V AC. As a result, the voltage level of the DC link of the DC–AC inverter that feeds these loads needs to be maintained around 360–400 V. One possibility to achieve such a high DC voltage is to use DC–DC boost converter to boost up the PV voltage. The voltage levels of the PV modules that are available commercially are generally in the range of 12–35 V. Therefore, to form a DC bus of around 360–400 V several PV modules are to be connected in series to form PV string. However, with such an arrangement, the system exhibits multiple local maximum power points under nonuniform solar irradiation levels. Use of maximum power point tracking (MPPT) using DC–DC converter varies the output DC voltage due to varying MPP voltage because of varying PV cell temperature and solar irradiance [33]. Variable DC link voltage across the PV inverter can affect the sensitive loads

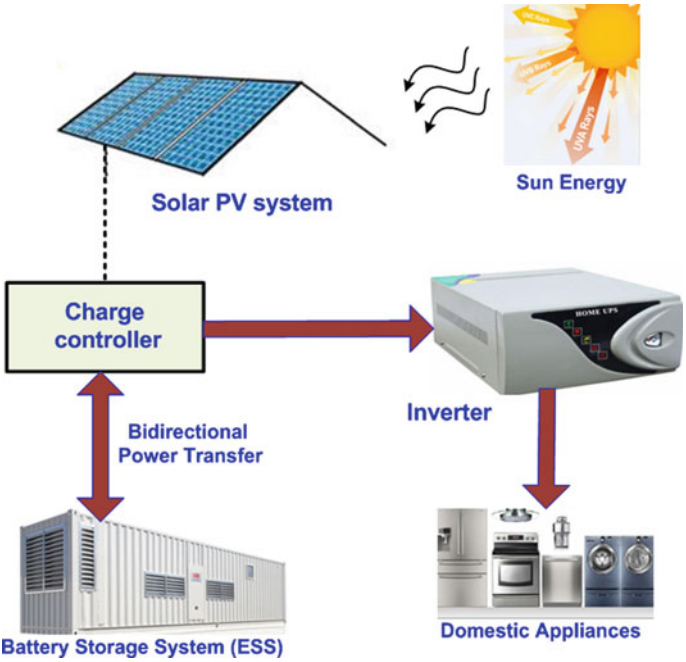

Fig. 4 Block diagram of stand-alone PV system

supplied. As there is no grid in a stand-alone system, the output voltage has to be controlled in terms of amplitude and frequency. The stand-alone control is featured with output voltage and frequency controller capable of handling variable loads.

1.3 Stand-Alone PV System Configuration

1.3.1 PV System Connected Through Single-Phase H-Bridge Inverter for Low Power PV System

Figure 5 represents the PV-interfaced H-bridge inverter for stand-alone power PV system. It consists of PV array system, DC–DC converter, conventional H-bridge inverter and load, through filter network. The PV arrays are connected to the inverter via a DC–DC boost converter used in MPPT or to increase the voltage level. In order to extract the maximum power from solar PV, several MPPT algorithms are being used in DC–DC converter. P&O algorithm is a common approach to extract the maximum power from solar PV.

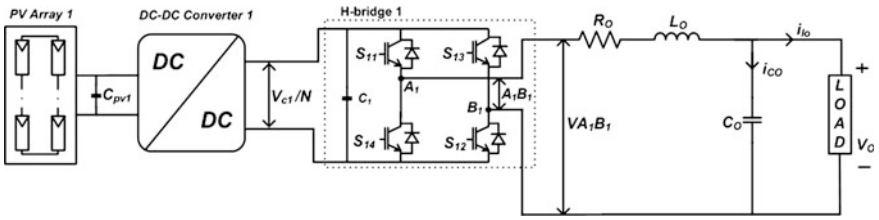

Fig. 5 PV array interfaced single-phase H-bridge inverter

1.3.2 Generalized PV System Connected Through Cascaded H-Bridge Multilevel Inverter for High-Power PV System

In this section, the configuration of generalized *N*-cell PV system connected to a cascaded H-bridge inverter for stand-alone system is shown in Fig. 6. The system consists of *N* number of PV array systems. Each array consists of series/parallel connection of PV modules. The array output is connected to a DC–DC converter, i.e., boost converter for MPPT. The capacitors C_{pv1}, C_{pv2}, …, $C_{\text{pv}n}$ are the input capacitors connected to the boost converters. The output of each DC–DC converter is fed to the *N*-H-bridges of the cascaded multilevel inverter.

The DC link voltages of each H-bridge are isolated as they are supplied from separate PV system. The cascaded H-bridge inverter is able to produce *n*-level output voltage, where $n = (N - 1)/2$. The capacitors C_1, C_2, …, C_n are the DC link capacitors connected across the H-bridges. The switches S_{i1}, S_{i2}, S_{i3}, and S_{i4} ($i = 1, 2, \ldots, N$) are the power semiconductor switches of the H-bridges. The terminals A_i

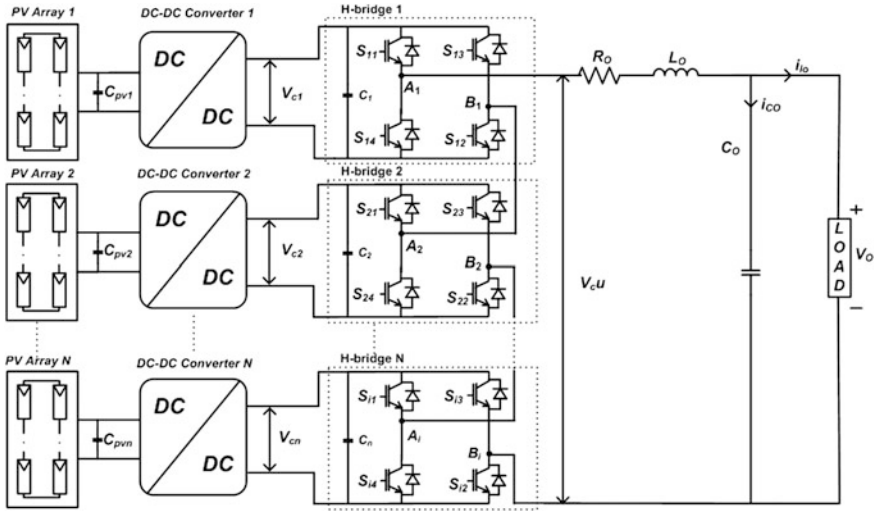

Fig. 6 PV array interfaced cascaded H-bridge multilevel inverter operated in voltage control mode

and B_i generate three different voltage levels $+V_{ci}$, 0 and $-V_{ci}$. This individual three-level output of the H-bridges generates a total n-level output, $+NV_c$, $+(N-1)V_c$, …, $+V_c$, 0, $-V_c$, …, $-(N-1)V_c$, $-NV_c$; assuming equal voltage across each H-bridge, i.e., $V_{ci} = V_c$. The inverter output uV_c, through the filter network consisting of series inductor (L_o, R_o) and parallel capacitor C_o, feeds the load. It is preferred to control the output voltage of series-connected H-bridge inverter such that the load terminal voltage v_o is regulated to a constant value for stand-alone applications. This is called the operation of cascaded H-bridge inverter in voltage control mode [34].

1.3.3 Modeling of Cascaded Multilevel Inverter

For analysis, the equivalent circuit of PV supported n-level cascaded multilevel inverter is shown in Fig. 7. Where Q_1 corresponds to the n-level cascaded multilevel inverter switch and u is the control signal that belongs to the n-discrete values between $+N$ and $-N$. The value will be integer $+N$, $+(N-1)$, …, $+1$, 0, -1, …, $-(N-1)$, $-N$; if all the PV arrays are at the same environmental condition such that all the DC link voltages are equal or else it will assume any real value between $+N$ and $-N$, but belong to the n-discrete set.

Let us consider the state variable as capacitor voltage v_o and its derivative $\dot{v}_o$, the system shown in Fig. 7 is represented by state-space representation as given in Eqs. (1)–(4).

$$\dot{z} = Az + B_1 u + B_2 \gamma \tag{1}$$

$$v_o = cz, \tag{2}$$

where

$$A = \begin{bmatrix} -\frac{R_o}{L_o} & -\frac{1}{L_o} \\ 1 & 0 \end{bmatrix}; B_1 = \begin{bmatrix} \frac{V_c}{L_o C_o} \\ 0 \end{bmatrix}; B_2 = \begin{bmatrix} -\frac{1}{L_o C_o} \\ 0 \end{bmatrix}; C = [0 \quad 1]$$

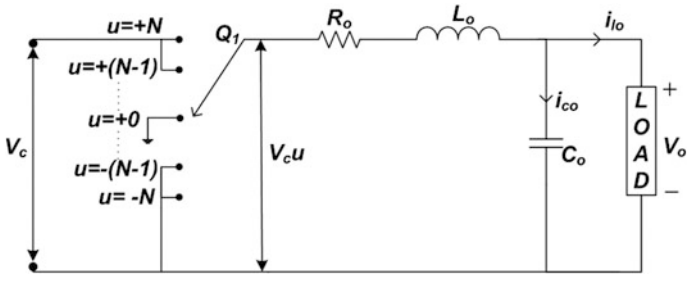

Fig. 7 Equivalent circuit of n-level cascaded multilevel inverter

The state vector is defined by Eq. (3)

$$z = \begin{bmatrix} \dot{v}_o \\ v_o \end{bmatrix} \tag{3}$$

where γ is the disturbance, which is dependent on the load current and its derivative as shown in Eq. (4).

$$\gamma = R_o i_{lo} + L_o \frac{di_{lo}}{dt} \tag{4}$$

The state variable v_o and its derivative $\dot{v}_o$ should track corresponding references so as to feed constant sinusoidal voltage to the load irrespective of the variations in the input DC voltage and load conditions, reflected respectively in V_c and γ. The variation of environmental condition, i.e., changes in solar irradiation and cell temperature, will cause the different output PV voltages in the DC link of the H-bridges [35]. For sinusoidal reference voltage, the state-space realization of reference model is given in Eqs. (5) and (6).

$$\dot{z}_m = F_m z_r + G_m h \tag{5}$$

$$z = \begin{bmatrix} z_{m1} \\ z_{m2} \end{bmatrix} = \begin{bmatrix} R_m \omega_o \cos(\omega_o t) \\ R_m \sin(\omega_o t) \end{bmatrix} \tag{6}$$

where, $z = \begin{bmatrix} z_{m1} \\ z_{m2} \end{bmatrix}$ = model reference state vector, $h = R_m \omega_o \delta(t)$ = input quantity;

$F = \begin{bmatrix} 0 & -\omega_o^2 \\ 1 & 0 \end{bmatrix}$; $G = \begin{bmatrix} 1 \\ 0 \end{bmatrix}$;

R_m amplitude of sinusoidal reference signal,
ω_o angular frequency of sinusoidal reference signal, and
$\delta(t)$ dirac delta function.

The state error vector is defined in Eq. (7)

$$z_e = z_m - z \tag{7}$$

The sliding mode control is used to regulate the load terminal voltage. The switching function for the sliding mode control is defined in Eq. (8).

$$s(z_e) = \beta_e z_e = \beta_1 (z_{m1} - \dot{v}_o) + \beta_2 (z_{m2} - v_o) \tag{8}$$

β_1 and β_2 are the positive gains, e is the voltage tracking error, z_{m1} and z_{m2} are the reference of the state vector denotes the required reference voltage. It is shown that under ideal condition of sliding mode control implementation, the variable structure of control law is given by Eqs. (9) and (10) [4].

$$u = +N, \text{ for } s(z_e) > 0 \tag{9}$$

$$u = -N, \text{ for } s(z_e) < 0 \tag{10}$$

The switching surface defined by Eq. (8) remains stable as long as the eigenvalue lies on left side of the s-plane, i.e., $\lambda = -(\beta_2/\beta_1)$, e.g., $\beta_2 = 1$ and $\beta_1 = 0.001$, lead to $\lambda = -1000$. It is worth noting that to implement control law (Eqs. 9 and 10), the state vector requires derivative of the load terminal voltage. This can be easily measured from the filter capacitor current i_{co} and dividing it by the capacitance C_o. Hence there is no need of external differentiator circuit. The solution provided by Eqs. (9) and (10) produces bipolar AC output voltage, which introduces large harmonic content near switching frequency and introduces higher ripples in the output voltage. The multilevel inverter control scheme used, attains reduced ripples in the output voltage and the harmonic contents are shifted to the higher frequency region, i.e., integer multiple of the switching frequency. With multilevel inverter sliding mode control, the control input u assumes n-discrete integer values between $+N$ and $-N$, leading to nonideal sliding mode control which is equally asymptotically stable as shown in [36].

1.4 Bidirectional Converter Integrated with Solar PV System

Essential DC–DC converters, for example, buck- and boost-type converters (and their derived topologies) do not have power transmission ability in a bidirectional way. This limitation is because of the diodes in their structure, which avoids the current in opposite direction. It is true in all type of unidirectional DC–DC converter and in order to overcome this drawback, diode has to be replaced with controllable switch with antiparallel diode. Such a common configuration is called as bidirectional buck–boost-type converter. The basic circuit diagram of bidirectional DC–DC converter is shown in Fig. 8. There are two terminals, which can be

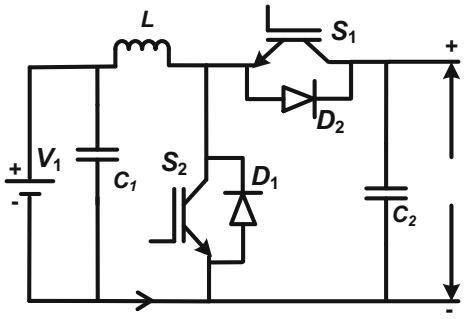

Fig. 8 Bidirectional DC–DC converter

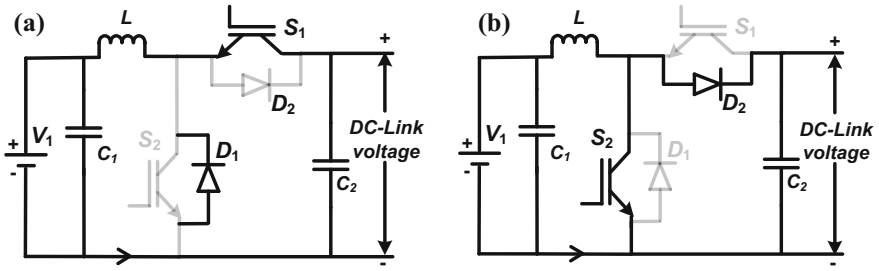

Fig. 9 Equivalent circuit of bidirectional DC–DC converter **a** buck mode, **b** boost mode

connected into battery storage unit and other end is connected to DC link voltage. To exchange the power transmission in a bidirectional way, switches S_1 and S_2 are to be controlled.

When the power mismatches between solar PV (P_{pv}) and load power (P_{load}), the controller enables the bidirectional DC–DC converter to balance the power. When the error power ($P_{pv} - P_{load}$) becomes positive; the bidirectional converter operates in buck mode to store the energy. If error power becomes negative, the bidirectional converter operates in boost mode to discharge the energy. In charging mode, pulse width modulation (PWM) is applied to S_1, the converter operates similar to buck-type converter and the equivalent circuit is presented in Fig. 9a. Inductor stores the energy when S_1 is on and during S_1 is off, the inductor helps to the current to be continuous to battery for charging. In discharging mode, PWM is applied to S_2, therefore, the converter operates similar to boost-type converter as shown in Fig. 9b. When S_2 is on, the inductor stores the energy and when S_2 is off, the inductor voltage plus input voltage are added together to supply the battery power via DC link. By adjusting the PWM of S_1 and S_2, the power can be controlled in a bidirectional way. Commonly a closed loop current controlled technique is preferred to control the power. The average current controller is used to control the power.

1.5 Simulation Results

In this section, simulation is performed to verify the function of PV-interfaced voltage source inverter topologies operating under voltage control mode. The system parameters are given in Table 1. The electrical parameters for the solar PV module are given in Table 2. For simulation study, the performance of two-level and seven-level system configuration is tested with single H-bridge and three H-bridges, respectively, for stand-alone PV system application.

Table 1 System parameters

Parameter	Rating
PV array	9 kW
Input capacitor (C_{pv})	100 μF
Inductor (L)	12 mH
DC link capacitor (C_1)	2200 μF
Switching frequency of boost converter	20 kHz
Switching carrier frequency of H-bridge inverter, f_c	1.5 kHz
Reference voltage state vector, Z_{m2}	250 $\sqrt{2}$ sin (2.π.50.t)
Filter inductance, L_o	2 mH
Filter capacitance, C_o	10 μF
Rated output power, P_o	7.5 KVA

Table 2 Electrical parameters of solar PV module

Maximum power (P_{MAX})	250 W	Temperature = 25 °C Solar irradiation, G = 1000 W/m^2 (standard test condition)
Voltage at MPP (V_{MPP})	30.43 V	
Current at MPPT (I_{MPP})	8.22 A	
Open circuit voltage (V_{OC})	37.70 V	
Short circuit voltage (I_{SC})	8.69 A	

1.5.1 PV-Interfaced Single-Phase H-Bridge Inverter

The 3.0 kW stand-alone PV systems are implemented by connecting DC–DC converter with embedded GMPPT, chargeable battery, single-phase H-bridge inverter, and AC load. The PV array unit is configured in the fashion of thirteen series- and one parallel-connected PV modules. Figure 10a shows the DC link voltage of the single-phase H-bridge inverter with V_{c1} = 450 V and Fig. 10b represents three-level inverter output voltage with the peak V_c = 450 V. It is assumed that the PV system is operating with the balance between the PV power generated and consumed in AC load with suitable energy support at DC side. The energy support at the DC side sinks the power if the power extracted from the AC side is less than the PV generated power, and it supplies the power if AC side extracts more power then generated by PV.

The sliding mode control is used for the cascaded multilevel inverter to control the peak output voltage, V_o = 350 V, across the load terminal as shown in Fig. 10c. The corresponding peak load current i_{lo} = 18 A is shown in Fig. 10d. In this case, a uniform solar irradiation level G = 1000 W/m^2 is considered for all the PV modules in the PV array unit.

The performance of the sliding mode control for single H-bridge three-level inverter is tested under dynamic change in environmental condition. If the solar PV array receives the changing solar irradiation, the effect is reflected in terms of the varying DC link voltage. Figure 11a shows the dynamic response of the DC link

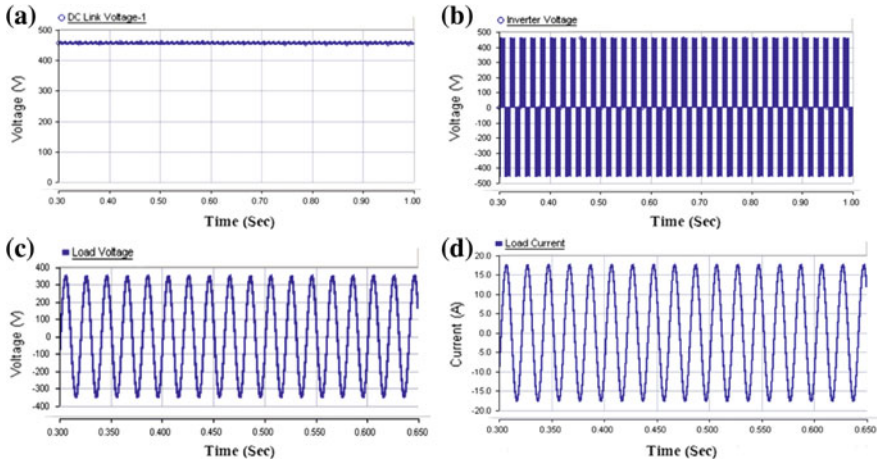

Fig. 10 Under uniform solar irradiation, **a** DC link voltage of single-phase H-bridge inverter, **b** three-level inverter output voltage, **c** controlled load voltage and **d** load current

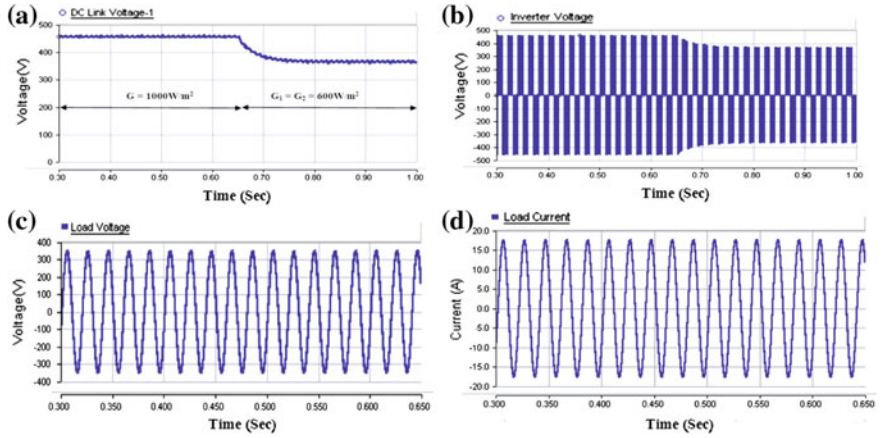

Fig. 11 Varying solar irradiation **a** DC link voltage of single-phase H-bridge inverter, **b** three-level inverter output voltage, **c** load voltage and **d** load current

voltage of the single-phase H-bridge inverter. At the instant $t = 0.65$ s, solar irradiations get lowered to $G_1 = 600$ W/m^2, and it leads to lowering of the DC-link voltages to $V_{c1} = 380$ V. This is due to the fact that the MPP voltage gets lowered at reduced solar irradiation level. Figure 11b shows the variation in AC output inverter voltage. Figure 11c shows the controlled load voltage, showing that the load terminal voltage is maintained constant under dynamic change in the environmental conditions. Figure 11d, shows the load current plot.

Now the simulation is carried without energy support at the DC side of the inverter. At t = 0–0.65 s, the system is working with balance of power. Suddenly the load on AC side is reduced at t = 0.65 s. Due to this, the voltage at the DC link raises continuously due to less power drawn at DC side as shown in Fig. 12a. If energy support is connected at the DC side, it draws the excess power and maintains the DC voltage constant as shown in Fig. 12b. In other case, if the AC load is increased suddenly, then without DC energy support, the voltage at DC side gets collapsed as shown in Fig. 12c. With the DC energy support, the short of power is supplied from the DC storage and voltage is maintained constant as shown in Fig. 12d. Aforementioned theory, when the error power ($P_{pv} - P_{load}$) becomes positive, bidirectional converter stores the energy in battery. Therefore, the state of charge (SOC) increases from its nominal value as shown in Fig. 12e. Similarly when the error power becomes negative, variation of SOC is shown in Fig. 12f.

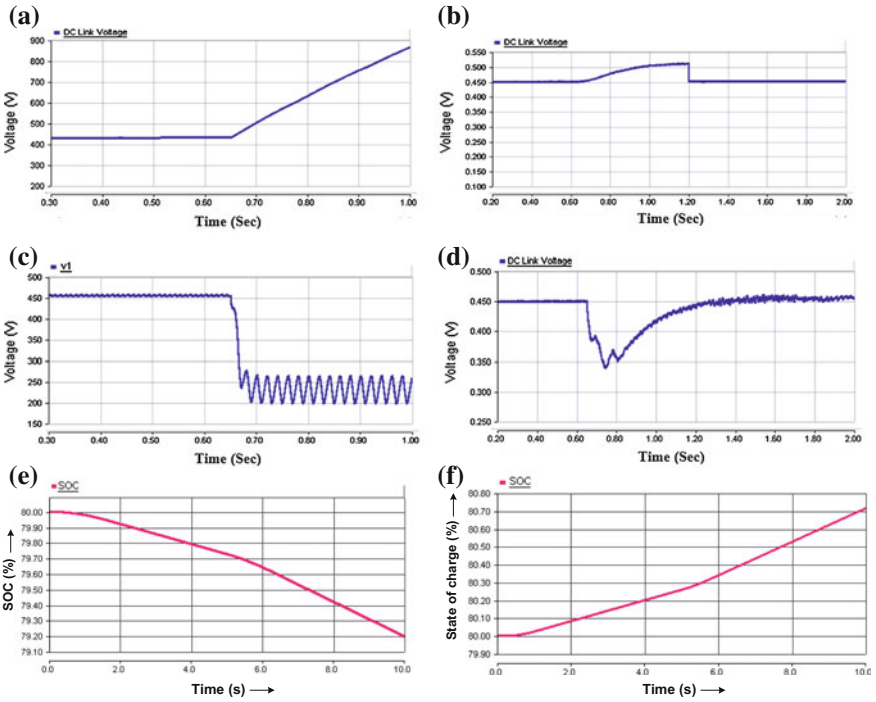

Fig. 12 Varying load condition **a** DC link voltage without DC energy support at light load **b** DC link voltage with energy support at light load **c** DC link voltage without energy support at high load, and **d** DC link voltage with energy support at heavy load, **e** variation of SOC at positive error power, **f** variation of SOC at negative error power

1.5.2 PV Interfaced Seven-Level Cascaded Multilevel H-Bridge Inverter

In this section, the simulation is performed to verify the function of the PV system compatible seven-level cascaded multilevel inverter operating in voltage control mode. It is assumed that the suitable energy support is provided at DC side of each H-bridge to maintain the power balance. The system parameters are given in Table 1. The electrical parameter for the solar PV module is given in Table 2. For simulation study, PV interface seven-level cascaded multilevel inverter for stand-alone application is considered. A 9.0 kW stand-alone PV system is designed by connecting three single-phase series-connected H-bridge inverters. Each single-phase H-bridge inverter is supplied from 3.0 kW PV array with embedded DC–DC converter for MPPT. The outputs of all the H-bridges are connected in series to form seven-level cascaded multilevel inverter. Each PV array unit is configured in the fashion of three series- and four parallel-connected PV modules. Figure 13a shows the DC link voltage of the three single-phase H-bridge inverter with $V_{c1} = V_{c2} = V_{c3} = 150$ V and Fig. 13b represents the seven-level cascaded multilevel inverter output voltage with the peak $V_{cp} = 450$ V. The sliding mode control is used for the cascaded multilevel inverter to control the peak output voltage, $V_{op} = 350$ V, across the load terminal as shown in Fig. 13c. The corresponding peak load current $i_{lop} = 42$ A is shown in Fig. 13d. A uniform solar irradiation level $G = 1000$ W/m^2 is considered for each PV array unit. A phase-shifted multicarrier unipolar modulation based voltage control method is used in [37, 38].

In order to demonstrate the performance of the sliding mode control, the seven-level cascaded multilevel inverter is tested under dynamic change in environmental condition. Consider three PV array units delivering power to the load. If the solar PV arrays do not receive uniform solar irradiation, the effect is reflected in

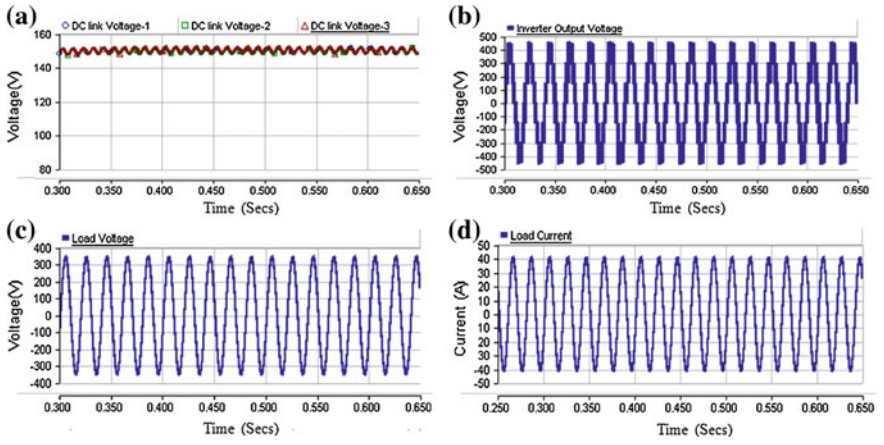

Fig. 13 Under uniform solar irradiation, **a** DC link voltages of three H-bridges of the inverter, **b** seven-level inverter output voltage, **c** controlled load voltage and **d** load current

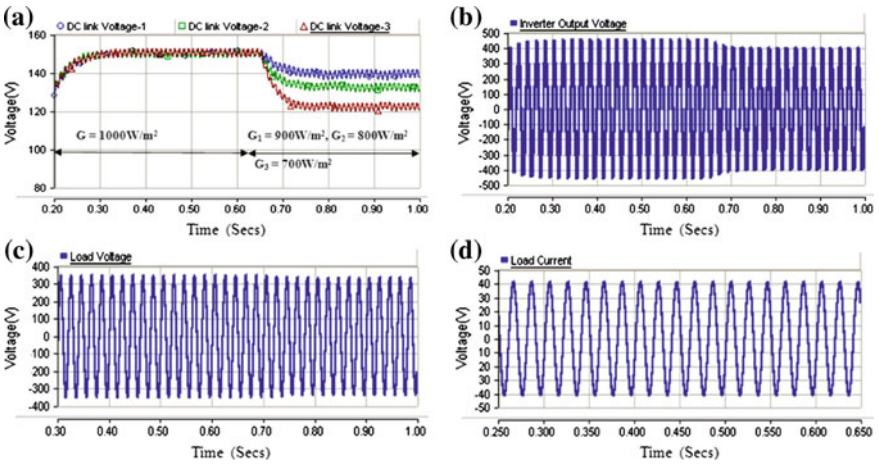

Fig. 14 Performance under nonuniform change in solar irradiation **a** DC link voltages of three H-bridges of the inverter, **b** seven-level inverter output voltage, **c** controlled load voltage and **d** load current

terms of difference in the DC link voltages. Figure 14a shows the dynamic response of the DC link voltage of three single-phase H-bridge inverters. At the instant $t = 0.65$ s, the solar irradiations get lowered and become nonuniform in all three PV array units due to shading, with solar radiation levels, $G_1 = 900$ W/m^2 for PV array unit-1, solar irradiation level $G_2 = 800$ W/m^2 for PV array unit-2 $G_3 = 700$ W/m^2 for PV array unit-3, and it leads to the lowering of DC link voltages as $V_{c1} = 145$ V, $V_{c2} = 135$ V and $V_{c3} = 125$ V, respectively. Figure 14b shows the plot of the seven-level cascaded multilevel inverter output voltage. It follows the DC link input voltage of series-connected H-bridge inverter, i.e., at $t = 0$–0.65, $V_{A1B3} = 450$ V and at $t = 0.65$–1 the inverter voltage is reduced to $V_{A1B3} = 405$ V. Figure 14c shows the controlled load terminal voltage of the seven-level cascaded multilevel inverter, showing that the load terminal voltage is maintained constant under dynamic change in environmental conditions and Fig. 14d shows the respective load current.

In another case at $t = 0.65$ s, the solar irradiations get lowered and nonuniform in the three PV array units due to shading with PV array unit-1 and unit-2 having solar radiation level $G_1 = G_2 = 800$ W/m^2, and PV array unit-3 has solar radiation level of $G_3 = 400$ W/m^2, and it leads to lowering of the DC link voltages to $V_{c1} = 135$ V, $V_{c2} = 135$ V and $V_{c3} = 95$ V, respectively, as shown in Fig. 15a. We can observe that the inverter output voltage follows the PV array input voltage, whereas sliding mode control forces the terminal load voltage to remain constant under dynamic change in input voltage as depicted in Fig. 15b, c, respectively. Moreover Fig. 15d presents the load current. This protects the sensitive load connected to the PV system under varying environmental conditions. In order to show the performance under dynamic changes in the load, a sudden change in load is

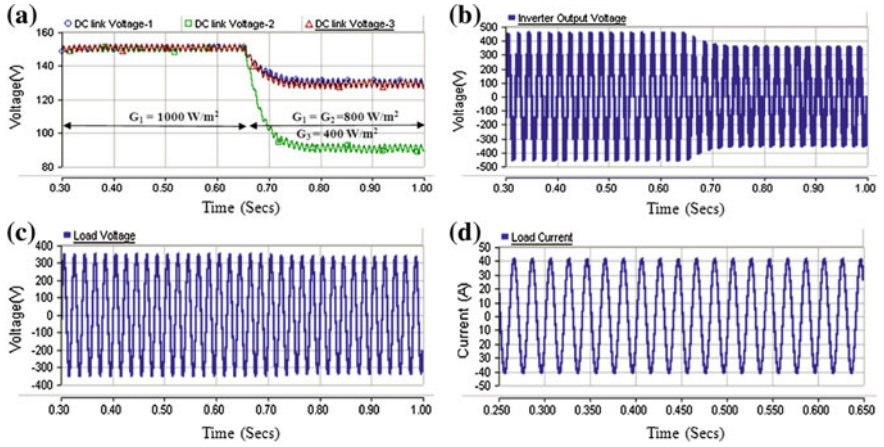

Fig. 15 Performance under nonuniform solar irradiation, **a** DC link voltages of three H-bridges of the inverter, **b** seven-level inverter output voltage, **c** controlled load voltage and **d** load current

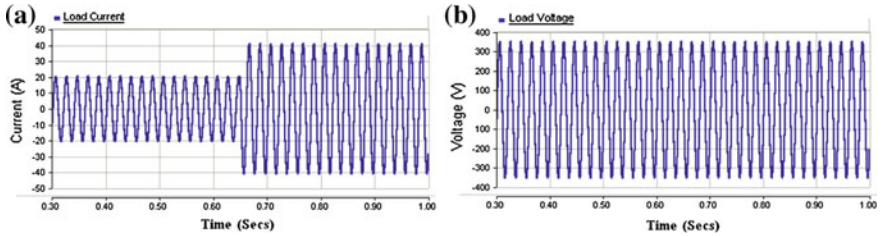

Fig. 16 Performance during sudden change in load, **a** load current, **b** controlled load voltage

created as shown in Fig. 16. The light load is connected initially, and it is suddenly increased at the instant 0.65 s. The load current increases correspondingly with variation in the load but the load voltage is maintained constant.

1.6 Grid-Connected PV Inverter System with Load Compensation

The grid normally refers to the power distribution systems, which receives its input power from substation at 440 V (l-l) and 220–250 V single-phase AC, at 50 Hz. Usually power stations have very large capacity and providing power in megawatts. But individual consumer can utilize the power in the range of 10–15 kW. The block diagram of the common grid-connected PV system is shown in Fig. 17. The main component in grid-connected PV system is the inverter. It converts available DC

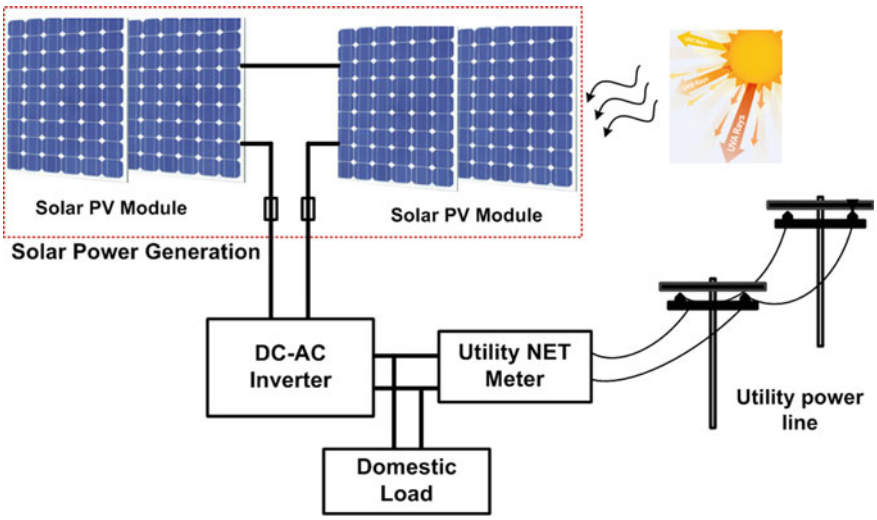

Fig. 17 Grid-connected PV system

power from the PV array into usable AC power consistent with voltage and power quality requirements of the grid utility. A bidirectional interface is made between the PV system AC output terminals and the grid utility network. This enables PV system to supply power to the local loads or feed to the supply, when PV power is greater than load demand power. At night or during high load demands, the power required by load is greater than the PV generated power [39]. The excess power required by the load is received from the grid utility. This safety feature is required in all grid-connected PV systems, and ensures that the PV system will not continue to operate and feed back into the utility grid when the grid is down for service or repair.

1.6.1 PV-Supported Cascaded Multilevel Inverter for Power Conditioning

In order to increase the utilization of grid-connected PV inverter, the PV system can be designed to provide the function of load compensation in addition to power distribution. The designed PV generation system performs the operation of active power filter (APF) to provide the power factor correction, load balancing, harmonic elimination, and reactive power compensation and simultaneously inject the maximum power available from the PV array into the distribution system. When the solar irradiation is available, the system can supply power to the load and simultaneously solve growing problems of harmonics, unbalanced loads, and poor power factor problems in the distribution system.

The PV array is interfaced into the grid via DC–DC boost converters and a two series-connected H-bridge DC–AC converter as shown in Fig. 18. The DC voltage

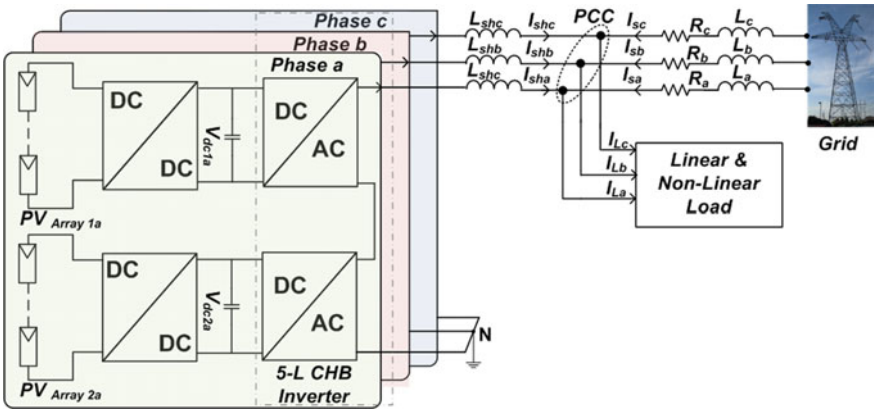

Fig. 18 Grid-connected PV system and using five-level cascaded multilevel inverter as controller

generated by a PV array varies widely and is low in magnitude. Therefore, the DC–DC boost converter generates the boosted DC voltage as desired by the converter. The inverter acts as a controller and exchange real power with the grid and performs load compensation [40].

Generally, the grid-connected PV systems extract maximum power from the PV arrays. The MPPT technique is usually associated with a DC–DC converter. The system can improve power quality in the distribution system by compensating current harmonics in the source side, reactive power compensation, and can also inject real power in the distribution system depending upon the PV generation and load requirement. The AC output of each H-bridge is connected in series such that the synthesized output voltage waveform is the sum of all the individual H-bridges and produces five-level output. Figure 19 shows the ideal active and reactive power flow of the grid-connected PV system.

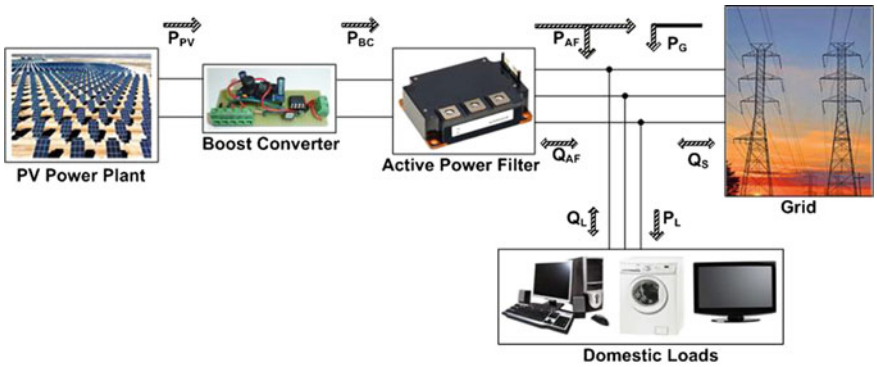

Fig. 19 Ideal active and reactive power flow of grid-connected PV system

1.6.2 Power Flow Control Using Instantaneous Reactive Power Theory

The instantaneous reactive power theory is based on the transformation of three-phase quantities to the two phase quantities in α–β frame. The instantaneous active and reactive powers are calculated in this frame. Figure 20 shows the block diagram of the implementation strategy [41]. The mathematical derivation is explained below using Eqs. (11)–(13). Consider the three-phase grid supply voltages as below.

$$v_{sa} = v_m \sin(\omega t) \tag{11}$$

$$v_{sb} = v_m \sin(\omega t - 120) \tag{12}$$

$$v_{sc} = v_m \sin(\omega t - 240) \tag{13}$$

The respective load currents are given below using Eqs. (14)–(16).

$$i_{La} = \sum I_{Lan} \sin\{n(\omega t) - \theta_{an}\} \tag{14}$$

$$i_{Lb} = \sum I_{Lbn} \sin\{n(\omega t - 120) - \theta_{bn}\} \tag{15}$$

$$i_{Lc} = \sum I_{Lcn} \sin\{n(\omega t - 240) - \theta_{cn}\} \tag{16}$$

In *abc* coordinates, *a*-, *b*-, and *c*-axes are fixed on the same plane and are phase displaced by 120°. The instantaneous space vectors, v_{sa} and i_{La} are set on to the *a*-axis and their amplitude varies in positive and negative directions at the same time.

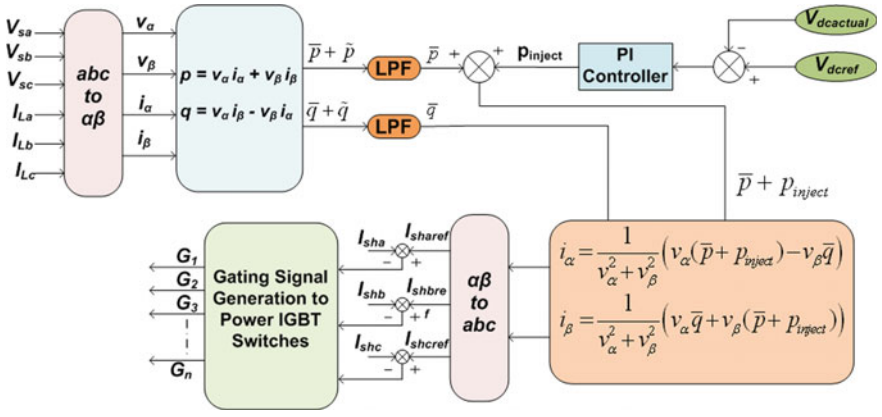

Fig. 20 Block diagram of the reference current generation scheme

This is true for other phases also. These phasors can easily be transformed into α–β coordinates as follows (Eqs. 17 and 18).

$$\begin{bmatrix} v_\alpha \\ v_\beta \end{bmatrix} = \sqrt{\frac{2}{3}} \begin{pmatrix} 1 & -1/2 & -1/2 \\ 0 & \sqrt{3}/2 & -\sqrt{3}/2 \end{pmatrix} \begin{bmatrix} v_{sa} \\ v_{sb} \\ v_{sc} \end{bmatrix} \tag{17}$$

$$\begin{bmatrix} i_\alpha \\ i_\beta \end{bmatrix} = \sqrt{\frac{2}{3}} \begin{pmatrix} 1 & -1/2 & -1/2 \\ 0 & \sqrt{3}/2 & -\sqrt{3}/2 \end{pmatrix} \begin{bmatrix} i_{La} \\ i_{Lb} \\ i_{Lc} \end{bmatrix} \tag{18}$$

where α and β axes are the orthogonal coordinates. The instantaneous power p for the three-phase circuit can be defined as in Eq. (19).

$$p = v_\alpha i_\alpha + v_\beta i_\beta \tag{19}$$

Similarly, the instantaneous reactive power q is defined as in Eq. (20).

$$q = -v_\beta i_\alpha + v_\alpha i_\beta \tag{20}$$

Therefore, in the matrix form the instantaneous real and reactive power are given as in Eq. (21).

$$\begin{bmatrix} p \\ q \end{bmatrix} = \begin{bmatrix} v_\alpha & v_\beta \\ -v_\beta & v_\alpha \end{bmatrix} \begin{bmatrix} i_\alpha \\ i_\beta \end{bmatrix} \tag{21}$$

The α–β currents can be obtained using Eq. (22).

$$\begin{bmatrix} i_\alpha \\ i_\beta \end{bmatrix} = \frac{1}{\Delta} \begin{bmatrix} v_\alpha & -v_\beta \\ v_\beta & v_\alpha \end{bmatrix} \begin{bmatrix} p \\ q \end{bmatrix} \tag{22}$$

where $\Delta = v_\alpha^2 + v_\beta^2$

The instantaneous active and reactive power p and q can be decomposed into the average and an oscillatory component using Eqs. (23) and (24).

$$p = \bar{p} + \tilde{p} \tag{23}$$

$$q = \bar{q} + \tilde{q} \tag{24}$$

where $\bar{p}$ and $\bar{q}$ are the average parts and $\tilde{p}$ and $\tilde{q}$ are the oscillatory parts of the real and reactive instantaneous powers, respectively. The compensating currents can be calculated to compensate the instantaneous reactive and the oscillatory component of the instantaneous active power. In this case, the source transmits only the non-oscillating component of active power. It is assumed that there is no battery storage system connected to the DC bus. Therefore, the total energy delivered by

the PV units may overcharge the DC capacitor. This energy should be injected into the AC source/locally by controlling the signal p_{inject} appropriately. However, the DC bus voltage regulator determines the power p_{inject}. The DC bus voltage passes through a PI controller and its error is added to generate net average power p. The energy exchange between the DC capacitor and the AC utility grid can control the DC bus capacitor. The value of $\bar{p}$, p_{inject} and $\bar{q}$ are used to calculate the reference current in α–β coordinate from Eq. (25) as below [41–44].

$$\begin{bmatrix} i_{\text{sh}\alpha} \\ i_{\text{sh}\beta} \end{bmatrix} = \frac{1}{v_\alpha^2 + v_\beta^2} \begin{bmatrix} v_\alpha & -v_\beta \\ v_\beta & v_\alpha \end{bmatrix} \begin{bmatrix} \bar{p} + p_{\text{inject}} \\ \bar{q} \end{bmatrix} \tag{25}$$

The reference current generated in α–β coordinate is converted back into the *abc* coordinate with the help of Eq. (26).

$$\begin{bmatrix} i_{\text{shrefa}} \\ i_{\text{shrefb}} \\ i_{\text{shrefc}} \end{bmatrix} = \sqrt{\frac{2}{3}} \begin{bmatrix} 1 & 0 \\ -\frac{1}{2} & \frac{\sqrt{3}}{2} \\ -\frac{1}{2} & -\frac{\sqrt{3}}{2} \end{bmatrix} \begin{bmatrix} i_{\text{sh}\alpha} \\ i_{\text{sh}\beta} \end{bmatrix} \tag{26}$$

The error is obtained by subtracting the reference current from the measured shunt active filter current as given in Eq. (27).

$$\text{e}_\text{k} = i_{\text{shrefk}} - i_{\text{shk}} \tag{27}$$

where $k = a, b, c$. The error e_k is used to control the switching of the converter. The switching logic for the cascaded H-bridge multilevel inverter using phase shifted multicarrier modulation for current control has been already discussed in Sect. 1.5.2.

1.7 Simulation Results

The functionality of the combined operation of APF with five-level grid-connected PV generation system and the control system with load compensation has been tested. A five-level cascaded H-bridge inverter is used as a voltage source inverter for the shunt active power filter. The two H-bridges are connected to the DC–DC converter with embedded MPPT controller to serve it as energy storage elements to supply real power difference between the demanded load, and transfers maximum available power from the PV system to the grid. Table 3 shows the system parameters used in the simulation.

Table 3 System parameters

Parameters	Value
Three-phase source voltage	440 V
System frequency	50 Hz
Feeder impedance	R_s = 0.01 Ω, L_s = 0.0005H
DC link capacitor	4400 μF
PV unit	15 kW
Load	Linear 10.0 Ω, 0.01027H, Nonlinear 500 μF, 20 Ω

1.7.1 Performance Without Shunt Controller

The three-phase grid voltage is sinusoidal of 440 V (peak) as shown in Fig. 21. In normal operating condition when the shunt controller is not connected in the distribution system. The harmonic distortion of grid current also increases due to connection of the nonlinear load. Figure 22 shows the load current waveform, which also flows in the grid current, when shunt controller is not connected. The total harmonic distortion of the grid current contains dominant lower order harmonic content as shown in Fig. 23. It is observed that without shunt controller, the grid current gets distorted significantly and it also leads to poor performance of the system.

1.7.2 Performance with Shunt Controller

The performance of the PV supported five-level cascaded multilevel inverter shunt controller is studied in this section. The PV supported shunt controller is connected to the grid supplying nonlinear load. Figure 24 shows the response of the grid

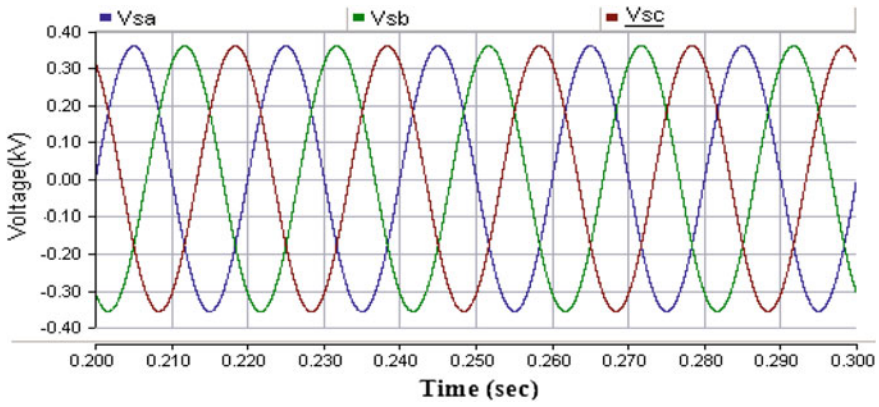

Fig. 21 Three-phase grid voltage

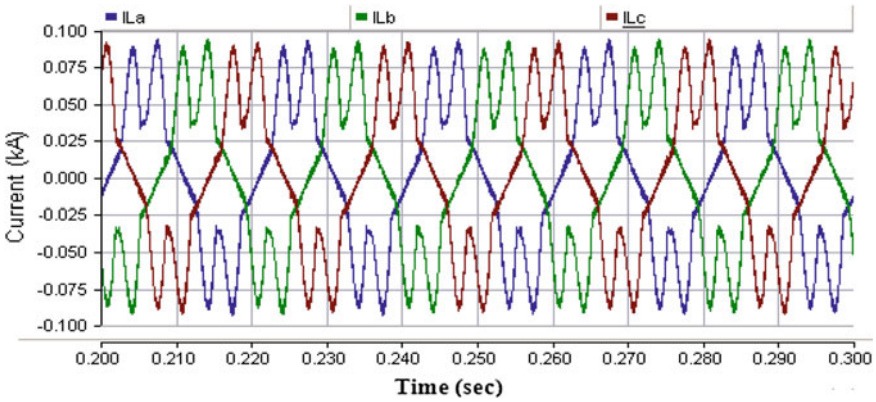

Fig. 22 Three-phase load current

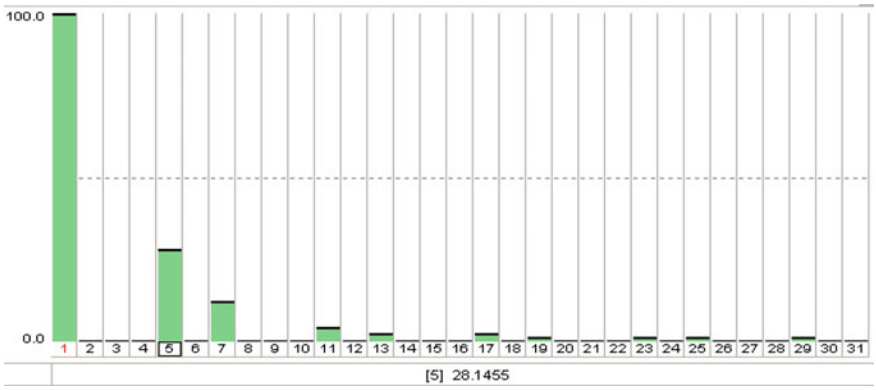

Fig. 23 Harmonic spectrum of grid current

current after compensation using five-level PV-supported inverter connected in shunt with the distribution system. The five-level shunt controller is able to produce grid current close to sinusoidal wave shape and free from harmonics as shown in Fig. 24. Figure 25 represents the compensation current injected by the shunt controller to compensate the current harmonics in the distribution system. The harmonic spectrum of the grid current obtained through the PV supported five-level shunt controller is shown in Fig. 26. Table 4 shows the individual harmonic spectrum produced by the five-level shunt controller. It is clearly evident, that the five-level shunt controller is able to produce reduced harmonic distortions.

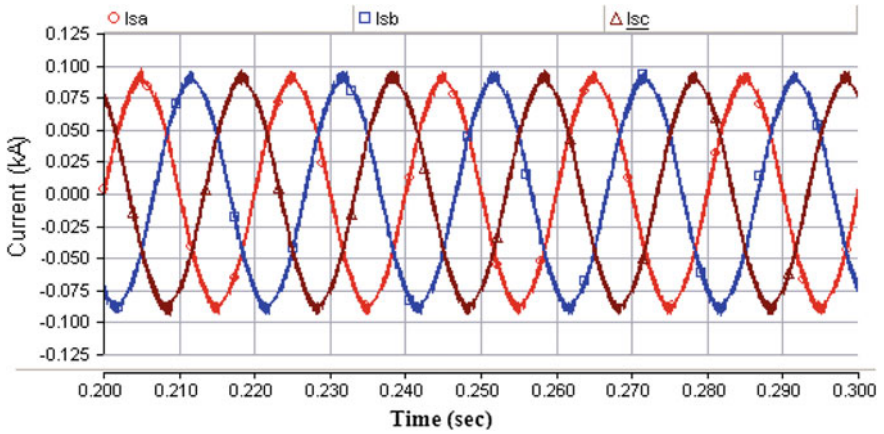

Fig. 24 Three-phase grid current using five-level shunt controller

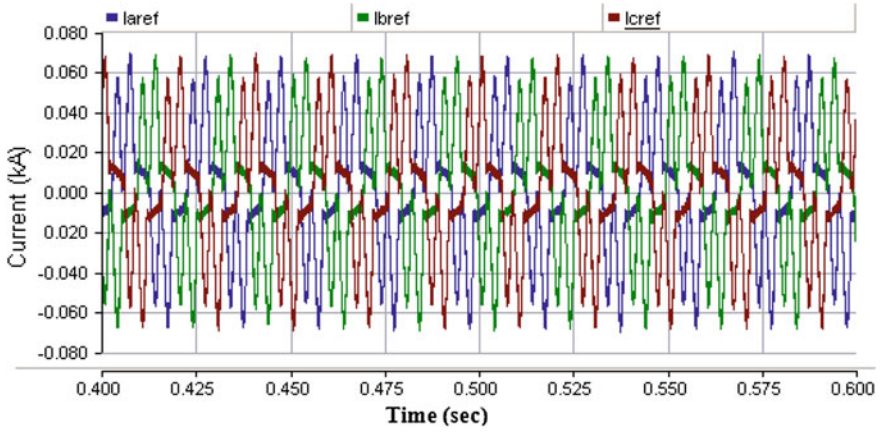

Fig. 25 Three-phase compensation current

1.7.3 Performance of Shunt Controller with Environmental Changes

In this section, the characteristic of the grid-connected PV system under dynamic change in solar irradiation condition has been studied. It is observed that to supply 15 kW of load power, the 5 kW power is supplied from AC grid and around 10 kW is injected by the PV generation system during high solar irradiation period. Figure 27 shows the regulation of the DC link voltage of the single-phase H-bridge inverter. According to this figure, the real power extracted from the PV power plant can pass through the grid. As it can be seen, the DC bus voltage experiences a swell while the PV generated power has increased and returns to the nominal DC voltage.

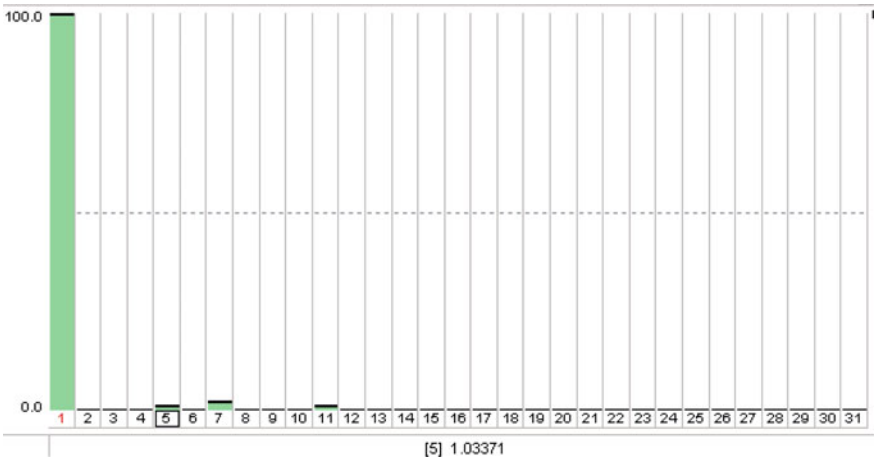

Fig. 26 Total harmonic distortion of grid current

Table 4 Individual harmonic spectrums

Topology	Harmonic distortion in %	1	5	7	11	13
PV-based five-level cascaded multilevel inverter	Before compensation	100	28.14	12.47	6.52	4.72
	After compensation	100	1.03	2.47	0.20	0.19

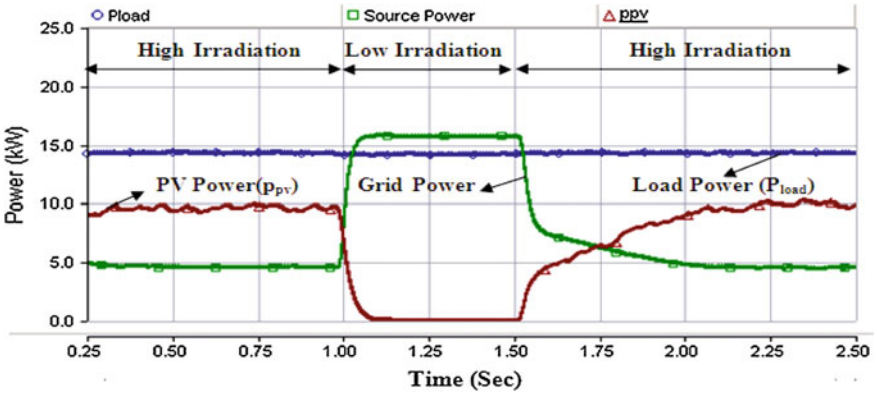

Fig. 27 Power injection during high and low solar irradiation

It is also clear that when the PV generated power has decreased, the DC network voltage experiences the sag phenomena. However, Fig. 28 shows the power transfer during charging and discharging periods of the DC capacitors.

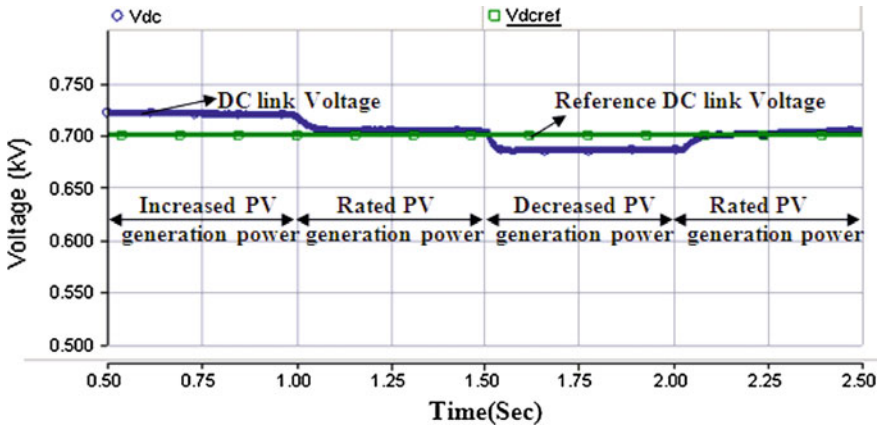

Fig. 28 DC link voltage of single H-bridge inverter

1.7.4 Performance of Shunt Controller with Load Variation

In this section, the effect of load changes on grid-connected PV generation system has been studied. In interval 0.25 s < t < 1.0 s, the required load demand is 15 kW in which grid supply 5 kW and PV generates 10 kW power constantly. As the load demand increases after the interval 1.0 *s*, the grid supplies extra power as per the load requirement, shown in Fig. 29. Figure 30 shows the grid current under dynamic change in load condition at low solar irradiation. Figure 31 shows the grid current under dynamic change in load condition at high solar irradiation. In this case the load is continued increased at t = 0.5 s.

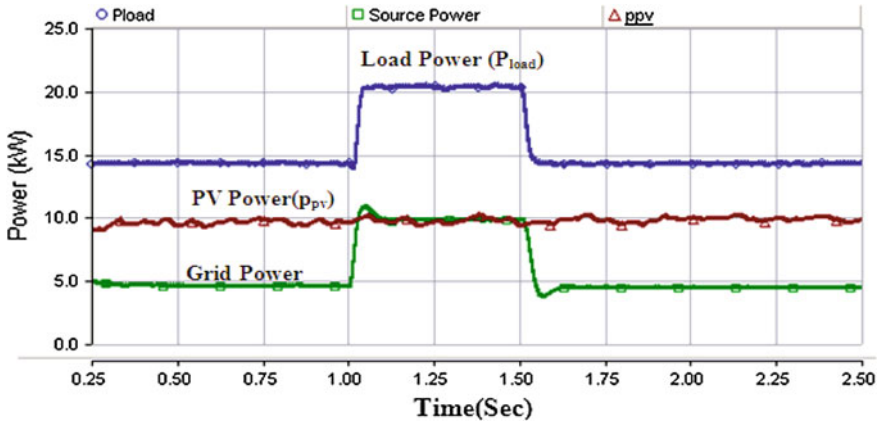

Fig. 29 Power injection during load variation

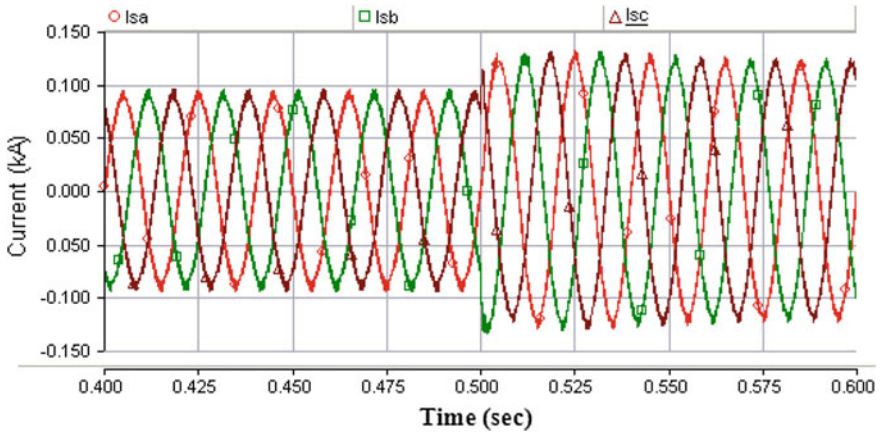

Fig. 30 Source current during load variation at low solar irradiation

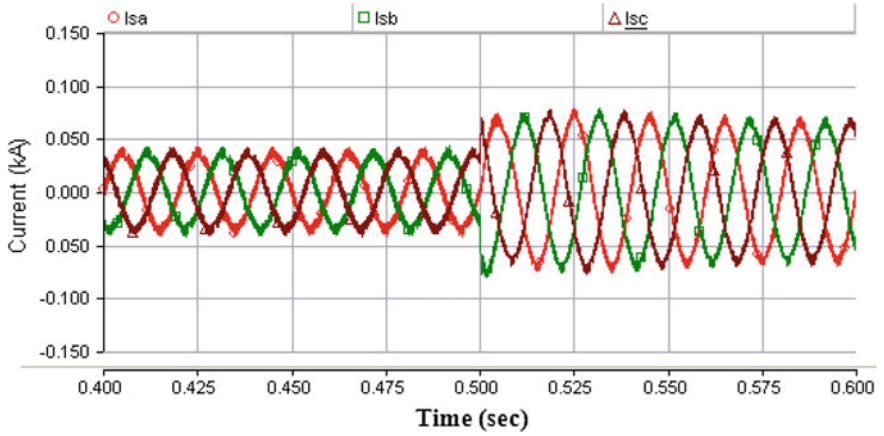

Fig. 31 Source current during load variation at high solar irradiation

2 Conclusion

The sliding mode control based load voltage control for PV-supported cascaded H-bridge multilevel inverter is demonstrated for stand-alone applications. The isolated DC supplies for the H-bridges of the cascaded multilevel inverter are derived from the PV array with, DC–DC converter used for MPPT. The sliding mode control regulates the net output AC voltage across the loads irrespective of the different DC link voltages across the H-bridges due to varying environmental conditions at each set of PV modules. The power balancing has been considered at the DC bus of the H-bridges using EES system. The performance of the higher rated

PV system with maximum power point tracking (MPPT) and voltage control through the cascaded H-bridges has been verified using the simulation studies. For grid-connected mode of application, the PV supported inverter is considered as controller. The inverter is configured as shunt controller which not only supplies the PV power to the grid but also performs the load compensation by mitigating the effects of load harmonics and reactive power in the distribution system.

References

1. Katiraei F, Iravani R, Hatziargyriou N, Dimeas A (2008) Microgrids management. IEEE Power Energy Mag 6(3):54–65
2. Dimeas AL, Hatziargyriou ND (2005) Operation of a multiagent system for microgrid control. IEEE Trans Power Syst 20:1447–1455
3. Tsikalakis AG, Hatziargyriou ND (2008) Centralized control for optimizing microgrids operation. IEEE Trans Energy Convers 23:241–248
4. Lopes JAP, Moreira CL, Madureira AG (2006) Defining control strategies for microgrids islanded operation. IEEE Trans Power Syst 21:916–924
5. Katiraei F, Iravani MR (2006) Power management strategies for a microgrid with multiple distributed generation units. IEEE Trans Power Syst 21:1821–1831
6. Sao CK, Lehn PW (2008) Control and power management of converter fed microgrids. IEEE Trans Power Syst 23:1088–1098
7. Karimi H, Davison EJ, Iravani R (2010) Multivariable servomechanism controller for autonomous operation of a distributed generation unit: design and performance evaluation. IEEE Trans Power Syst 25:853–865
8. Majumder R, Ghosh A, Ledwich G, Zare F (2010) Power management and power flow control with back-to-back converters in a utility connected microgrid. IEEE Trans Power Syst 25:821–834
9. Mehrizi-Sani A, Iravani R (2010) Potential-function based control of a microgrid in islanded and grid-connected modes. IEEE Trans Power Syst 25:1883–1891
10. Moreira CL, Resende FO, Lopes JAP (2010) Using low voltage microgrids for service restoration. IEEE Trans Power Syst 22:395–403
11. Diaz G, Gonzalez-Moran C, Gomez-Aleixandre J, Diez A (2010) Scheduling of droop coefficients for frequency and voltage regulation in isolated microgrids. IEEE Trans Power Syst 25:489–496
12. Ilic MD (2007) From hierarchical to open access electric power systems. Proc IEEE 95:1060–1084
13. Winkelman JR, Chow JH, Allemong JJ, Kokotovic PV (1980) Multi-time-scale analysis of a power system. Automatica 16:35–43
14. Wai RJ, Wang W, Lin C (2008) High-performance stand-alone photovoltaic generation system. IEEE Trans Ind Electron 55:240–250
15. Vachtsevanos G, Kalaitzakis K (1987) A hybrid photovoltaic simulator for utility interactive studies. IEEE Trans Energy Convers 2:227–231
16. Jiang Q, Xue M, Geng G (2013) Energy management of microgrid in grid-connected and stand-alone modes. IEEE Trans Power Syst 28:3380–3389
17. Zhang L, Liu Y, Crow ML (2005) Coordination of UFLS and UFGC by application of D-SMES. Paper presented at the IEEE power engineering society general meeting, 2005
18. Guo Y, Pan M, Fang Y (2012) Optimal power management of residential customers in the smart grid. IEEE Trans Parallel Distrib Syst 23:1593

19. Zhong Y, Zhang J, Li G, Liu A (2006) Research on energy efficiency of super capacitor energy storage system. Paper presented at the international conference on power system technology, 22 Oct 2006
20. Strunz K, Louie H (2009) Cache energy control for storage: power system integration and education based on analogies derived from computer engineering. IEEE Trans Power Syst 24:12–19
21. Elbuluk M, Idris NRN (2008) The role power electronics in future energy systems and green industrialization. Paper presented at the IEEE 2nd international conference on power and energy, 1 Dec 2008
22. Xie L, Thatte AA, Gu Y (2011) Multi-time-scale modeling and analysis of energy storage in power system operations. Paper presented at the IEEE conference on energy tech, 25 May 2011
23. Lukic SM, Cao J, Bansal RC, Rodriguez F, Emadi A (2008) Energy storage systems for automotive applications. IEEE Trans Ind Electron 55:2258–2267
24. Hug-Glanzmann G (2010) Coordination of intermittent generation with storage, demand control and conventional energy sources. Paper presented at the symposium on bulk power system dynamics and control, 1 Aug 2010
25. Nehrir MH, Wang C, Strunz K, Aki H, Ramakumar R, Bing J, Miao Z, Salameh Z (2011) A review of hybrid renewable/alternative energy systems for electric power generation: configurations, control, and applications. IEEE Trans Sustain Energy 2:392–403
26. Kleinberg M, Mirhosseini NS, Farzan F, Hansell J, Abrams A, Katzenstein W, Harrison J, Jafari MA (2014) Energy storage valuation under different storage forms and functions in transmission and distribution applications. Proc IEEE 102:1073–1083
27. Zhang Y et al (2011) Overview of the practice of renewable generation integration and transmission planning in North America. Chin J Energy Technol Econ 23:1–7
28. Zhou X, Lin Y, Ma Y (2015) The overview of energy storage technology. Paper presented at the IEEE international conference on mechatronics and automation (ICMA), 2 Aug 2015
29. Yun L, Huanhai X, Zhen W, Taicheng Y (2014) Power control strategy for photovoltaic system based on the Newton quadratic interpolation. IET Renew Power Gener 8:611–620
30. Komor P, Glassmire J (2012) Electricity storage and renewable for Island power. A guide for decision makers. IRENA, May 2012
31. Islam FR, Mamun KA (2016) Opportunities and challenges of implementing renewable energy in Fiji Islands. In: Australasian universities power engineering conference (AUPEC-2016), Brisbane, Australia, 25–28 Sept 2016
32. Islam FR, Mamun KA (2016) Reliability evaluation of power network: a case study of Fiji Islands. In: Australasian universities power engineering conference (AUPEC-2016), Brisbane, Australia, 25–28 Sept 2016
33. Walker GR, Sernia PC (2004) Cascaded DC–DC converter connection of photovoltaic modules. IEEE Trans Power Electron 19:1130–1139
34. Mishra MK, Ghosh A, Joshi A (2003) Operation of a DSTATCOM in voltage control mode. IEEE Trans Power Delivery 18:258–264
35. Carpita M, Farina P, Tenconi S (1993) A single phase, sliding mode controlled inverter with three levels output voltage for UPS or power conditioning application. Paper presented in the proceedings of the 5th European conference on the power electronics applications, 13–16 Sept 1993
36. Gonzalez R, Lopez J, Sanchis P, Marroyo L (2007) Transformer less inverter for single-phase photovoltaic systems. IEEE Trans Power Electron 22:693–697
37. Nicolas B, Fadel M, Cheron Y (1996) Fixed-frequency sliding mode control of a single-phase voltage source inverter with input filter. Paper presented in the IEEE international symposium on industrial electronics, 17–20 June 1996
38. Selvaraj J, Rahim NA (2009) Multilevel inverter for grid-connected PV system employing digital PI controller. IEEE Trans Ind Electron 56:149–158
39. Oriti G, Julian AL (2011) Three-phase VSI with FPGA-based multisampled space vector modulation. IEEE Trans Ind Appl 47:1813–1820

40. Dhople V, Dominguez-Garcia A (2012) Estimation of photovoltaic system reliability and performance metrics. IEEE Trans Power Syst 27:554–563
41. Rivera S, Kouro S, Wu B, Leon JI, Rodriguez J, Franquelo LG (2011) Cascaded H-bridge multilevel converter multistring topology for large scale photovoltaic systems. Paper presented at the IEEE international symposium on industrial electronics, June 2011
42. Ghosh A, Ledwich G (2002) Power quality enhancement using custom power devices. Kluwer Academic Publisher, Boston, MA 2002
43. Malinowski M, Gopakumar K, Rodriguez J, Perez MA (2010) A survey on cascaded multilevel inverters. IEEE Trans Ind Electron 57:470–475
44. Ribeiro PF (2002) Power electronics conditioners: configurations, performance, power quality and cost issues Paper presented at the 10th international conference on harmonics and quality of power, 6–9 Oct 2002

Feasibility Study and Design of a Flywheel Energy System in a Microgrid for Small Village in Pacific Island State Countries

D. Aitchison, M. Cirrincione, G. Cirrincione, A. Mohammadi and M. Pucci

Abstract In Pacific Island Countries (PICs), energy supplies depend on fossil fuel (FF), with few exceptions. However, since the associated populations are often scattered among different settlements in remote locations, renewable energy sources (RES) are increasingly meeting their electrical production power demands. Contrary to FF generated power, RES vary with season, time and weather conditions. Consequently, to maintain stability, reliability and power quality, energy storage is a key consideration for a viable RES set-up. Despite, there being many different kinds of energy storage system, a flywheel energy storage system (FESS) appears to be highly suitable for the microgrid (MG), because of their minimal environmental impact (green energy storage) and high cycle life when compared with other storage energy devices such as batteries. This chapter presents a detailed overview of the feasibility, design and control strategy of a FESS for MG applications. The fundamental developments are as follows: first, to design a suitable flywheel in order to increase reliability and stability of the power in the RES. Second to design a control technique for the FESS based on a nonlinear observer integrated with total least squares (TLS).

Keywords Microgrid · Renewable energy sources · Flywheel energy storage system · Total least squares (TLS) · Nonlinear observer

D. Aitchison (✉) · M. Cirrincione · G. Cirrincione · A. Mohammadi · M. Pucci
School of Engineering & Physics, The University of the South Pacific (USP), Suva, Fiji
e-mail: david.aitchison@usp.ac.fj

M. Cirrincione
e-mail: maurizio.cirrincione@usp.ac.fj

G. Cirrincione
e-mail: exin@u-picardie.fr

A. Mohammadi
e-mail: ali.mohammadi@usp.ac.fj

M. Pucci
e-mail: pucci@pa.issia.cnr.it

F.M.R. Islam et al. (eds.), *Smart Energy Grid Design for Island Countries*,
Green Energy and Technology, DOI 10.1007/978-3-319-50197-0_6

List of acronyms

DG	Distributed generation
DTC	Direct torque control
ESS	Energy storage system
FESS	Flywheel energy storage system
FF	Fossil fuel
FOC	Field orient control
IGBT	Insulated-gate bipolar transistor
IM	Induction machine
IMPM	Interior mounted permanent magnets
MG	Microgrid
PCC	Points of common coupling
PICs	Pacific island countries
PMSM	Permanent magnet synchronous motor
RES	Renewable energy sources
RES	Renewable energy sources (RES)
SV-PWM	Space vector pulse width modulation
TLS	Total least square
VOC	Voltage oriented control
VSI	Voltage source inverters

1 Introduction

Fossil fuels (FFs) are dominant in providing the world's high electric energy demands. The most well-known forms of FFs are coal, gas and oil; in general, they are easily found and have a high energy density, which results in the capacity of generating huge quantities of electrical energy. On the other side, FFs have disadvantages among which are their depletion rates, the emissions of CO_2 into the air as well as the generation of pollutants that represent a serious threat for human health and the environment. Actually, pollution, global warming and CO_2 emissions are three major disadvantages of FFs and their reduction is of global concern [1].

One way to achieve this goal is the use of renewable energy sources (RES) and many countries around the world are trying to increase the share of energy coming from RES. The introduction of these sources into the existing grid, however, pose some problems. Unlike FF-based generating units, RES units can be built close to the loads and the energy produced can be supplied at distribution or transmission voltage levels. In general, a small network or microgrid (MG) made up of local loads, RES sources and energy storage systems are connected to the main grid at different points (PCC = Points of Common Coupling), which gives rise to distributed generation (DG) [2].

In Pacific Island Countries (PICs), and specifically in some Fiji Islands, the dependence on FFs is a major issue, both for the impact on the environment and for their high costs [3]. On the other hand, RESs are abundant and easy to access. In addition, some of the smaller communities like little inland towns or small islands do not all enjoy the comfort of trouble-free electrical grids, because they are either weakly connected or completely separated from the grid: they need to have access to complementary RES energies which are abundant in their surroundings, while keeping their tourism, agriculture and landscape capital intact. The obstacles to the fast adoption of RES in such areas are many and have been apparent for some time [4–6]. For example, one technical obstacle consists of providing good service quality in grids that are weak, in spite of the intermittent character of the RES. Such problems are revealed as voltage and frequency instability. One way to overcome this is to use energy storage systems in a MG allowing small-scale distributed energy resources to be more reliable and stable. In these MGs, energy sources such as wind, wave, tidal, and solar can be used along with storage devices (flywheel, batteries) to avoid the need for a complicated and expensive grid infrastructure for these remote areas and contribute to a high quality and reliable power supply.

The prerequisite for stable system frequency is to have an instantaneous balance of demand and generation of active power. Inevitable energy oscillations, due to the presence of intermittent RES in a MG, cause network frequency variations especially in weak microgrids [6]. This situation can have an impact on the power quality or the MG security, such as violations of voltage limits and/or system frequency oscillations, among others [6–8]. This condition is exacerbated by the low inertia present in a typical MG. The necessary solution is the introduction of energy storage systems (ESS) which acts as a buffer and permits a reliable and stable power delivery. In general, the type of energy storage selected for a specific application needs to be analysed according to many criteria such as lifetime, life cycle, efficiency, capital cost, environmental impact, etc. [8]. The most common solution is to use batteries or super capacitors, each acting according to the rapidity of the time response, to compensate for the lack of active power generated by the RES.

Another possibility is the use of a flywheel energy storage system (FESS). FESSs are able to store a high level of energy density with a high rotor angular velocity and large inertial mass. Besides, they are more convenient than electrochemical batteries due to long life (15–20 years), high power density, high efficiency (90–95%), long cycle life (from 10,000 to 100,000 cycles), low maintenance and low environmental impact [9, 10]. Furthermore, they are able to compensate power flow fluctuations in a RES MG [11]: in this case the FESS has the task of contributing frequency/voltage regulation into the RES MG for short time periods [12]. In such applications, high performance of the FESS can be achieved by an advanced control system and design development. In the past decade, the direct torque control (DTC) and field orient control (FOC) have been applied to control FESSs [9, 10] in order to obtain superior control of torque and flux, and therefore of active and reactive power within the MG. Actually over the last few years, FESSs have been ever increasingly employed by the industry for their comparative

performance advantages in the areas of high dynamics, long lifetime and good efficiency: FESSs are therefore well suited for short-term storage systems, which are generally sufficient to improve the electric power quality [13] Because of easy transportation and/or set-up small FESS in the range of kW can be more easily adopted as compared to MW class of FESS. However, large power rating can easily be achieved through the adoption of multiple FESSs which may be controlled in parallel for optimal supply and reliability [13–15].

The goal of this paper is to study and design a FESS to solve the problem of energy storage in small communities of the PICs, to partially or totally replace the installed high-capacity batteries, which present problems of longevity, pollution and low time constant for sudden load peaks [16, 17]. In particular, FESSs will be used to provide continuous energy in spite of the intermittent delivery characteristic of the RES. In such cases, the FESS stores the surplus energy when a torque is applied by excess energy production from the energy sources, and it releases stored energy when the energy source is insufficient to match the load. Under a different mode of operation, they can also be used to supply energy at transfer rates exceeding the abilities of RES in possible conjunction with super capacitors.

In response to the above, this chapter is organized as follows. Section 2 describes the load profile of a typical Fijian village and the associates local weather conditions which in turn leads to a study of the local energy availability. Then on this basis, Sect. 3 describes the microgrid architecture. The flywheel-based electrical energy storage system development is explained in Sect. 4. The flywheel dynamic model is summarized in Sect. 5. Finally, the sensorless control of the FESS is presented in Sect. 6.

2 Energy Needs of a Remote Area in Fiji

In this section, the energy needs and the possible electrical energy storage (EES), to be set-up in the area of Bua in Fiji, are analysed. The province of Bua is in the Northern Division of Fiji (Vanua Levu) and the area of Dama is situated between latitudes −16.76 and longitude 178.56 (Fig. 1). This area has been chosen both because it is weekly connected to the grid and for the availability of data from the Bureau of Statistics of Fiji [18]. The population of Dama Bua is estimated approximately at 620 people and 135 households in 2015. At present, the electrical energy is produced by a 10 KVA diesel generator which supplies only 56.3% of the population, amounting to about 135 W for each household, on average.

On the basis of load profile, weather conditions and installed power, a design of the possible RES-based MG is proposed with the help of HOMER® which is capable of computing an optimized MG structure, where a FESS is integrated for energy buffering and resultant continuous supply.

In this chapter, two different MG designs are presented. First, an array of 16 batteries is used in parallel connection with a bus voltage equal to 6 V. Then this array of batteries has been replaced with a system of flywheels for the reasons

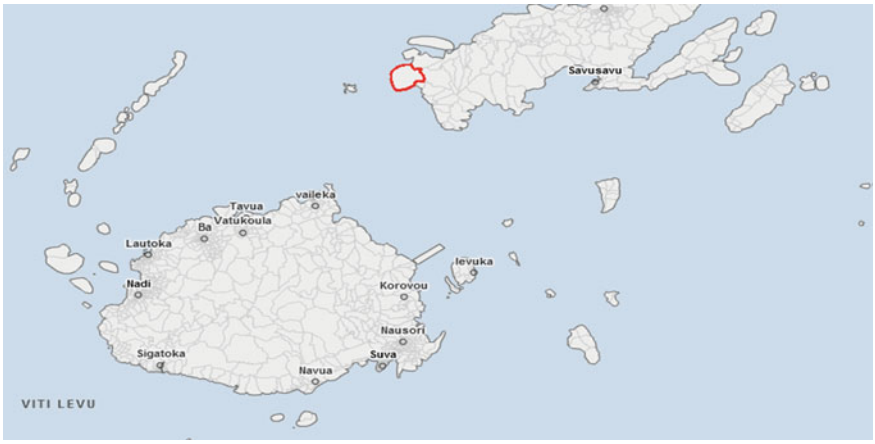

Fig. 1 Location of Dama Bua Fiji

Table 1 Load profile for rural household devices [19]

Consumer	Power (W)	Operation time (h)
Light	9	1–6
Water pump/iron/water heater	400	2–3
Mobile phone	10	3
Radio	40	1–14
Computer	250	2–6
TV	65	3
Fridge	185	4
Fan	40	1–6

explained in the introduction (disposal, pollution, transportation). However, a single flywheel would have a huge volume and weight if designed with the same capacity as the whole battery array, therefore a multiple flywheel array has been proposed, connected in parallel and suitably controlled.

2.1 Load Profile

As is well known, the load profile generally varies according to the user type, the daily time, the season and the temperature. For example, in Fiji for rural areas the average power consumption for different electronic devices is given in Table 1 [19].

This paper assumes that the variation of the load profile over one day for every month is constant during one year. This assumption is made on the basis that the winter and summer seasons are not so different in temperature ranges in Fiji.

The load profile as computed by HOMER® is plotted in Fig. 2, where the maximum power and total consumption during each day are equal to 50 kW and 643.27 kWh (the area under the power curve), respectively. It represents an average hour load profile over one year, as created by HOMER®.

2.2 Solar and Wind Power Calculation

Solar radiation and wind speed patterns are two necessary factors used for calculating the available wind and solar power. Based on the geographical location of the village, the average daily solar radiation in 2015 is plotted in Fig. 3. These values are obtained from the available NASA data for 2015 as created by RETScreen® [20].

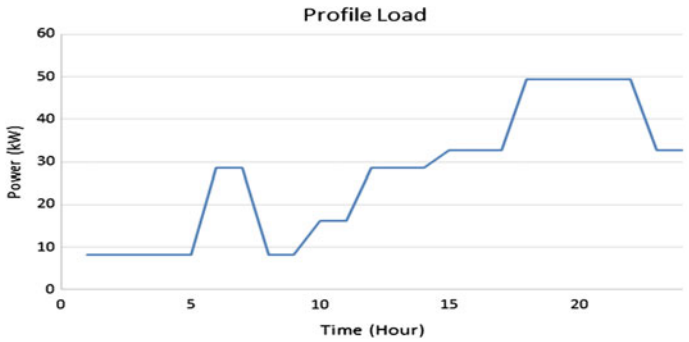

Fig. 2 Load profile distribution per day based on Table 1

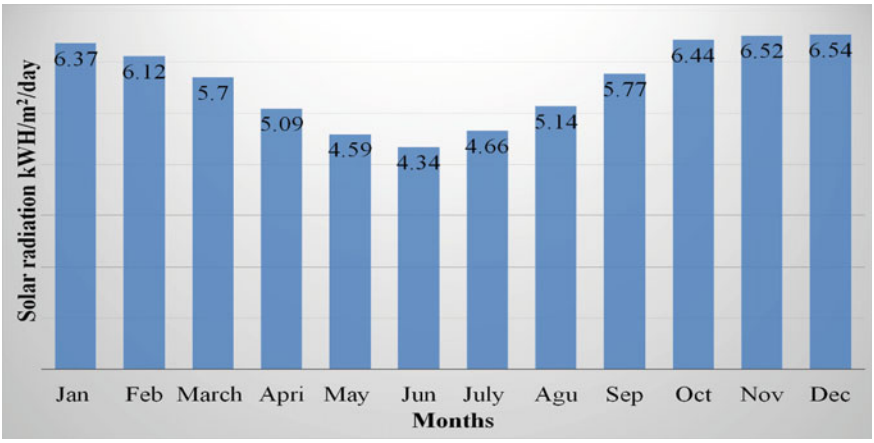

Fig. 3 Average daily solar radiation from January to December in 2015

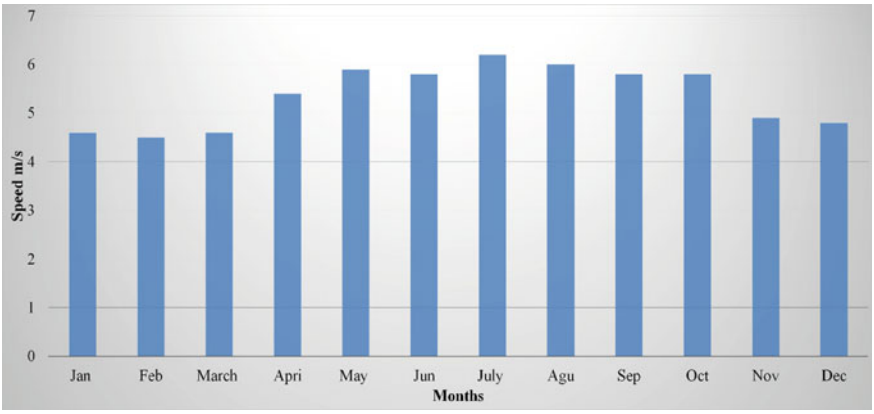

Fig. 4 Average wind speeds from January to December

To estimate the output power of the wind turbine, HOMER® uses the recorded average yearly wind speed (Fig. 4) as well as the well-known logarithmic or power laws to calculate the wind speeds at the turbine hub height and finally the available wind power [21].

3 Microgrid Architecture

On the basis of the load profile and the available energy, HOMER® has been utilized to find a possible optimized MG architecture in order to reduce the actual fuel usage cost. To this end, an optimal blend of the wind and solar energy has been added to the present diesel generator and the necessary EES based on batteries has been designed. Then the possibility of replacing the battery based EES with a FESS has been explored.

3.1 Initial Structure (PV/Wind Turbine with Batteries)

The first structure considered is a blend of wind turbines and PV arrays together with the original diesel generator and batteries for energy storage. A PV array is interconnected with a DC/DC converter (a boost converter in general) to which also a pack of batteries is connected through another boost converter (shown in Fig. 5). The inverter interfaces with the original AC grid which is linked with the original diesel generator, the wind turbine generation system and the AC loads.

The charge–discharge cycle of the batteries is presented in Fig. 6 together with the input energy produced by the process of charging and discharging the energy

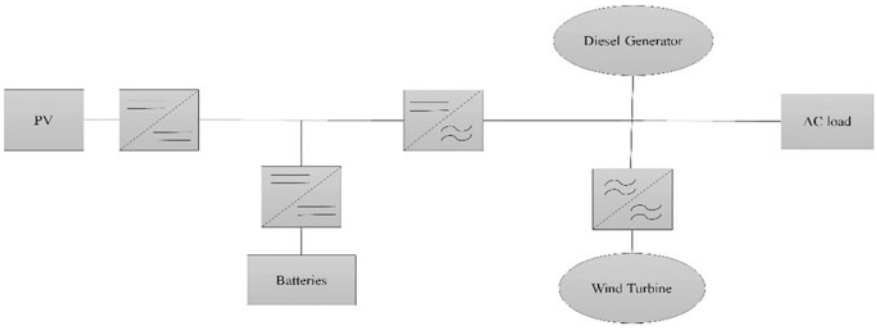

Fig. 5 First structure based on batteries energy storage

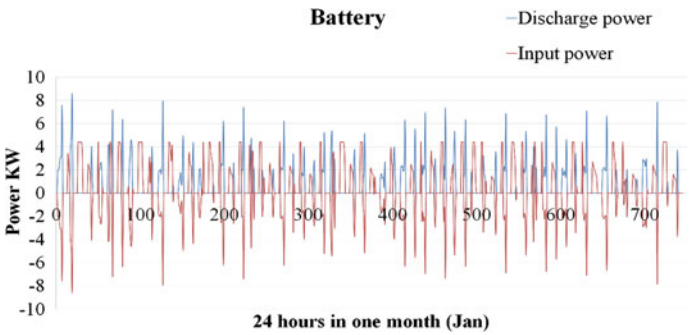

Fig. 6 Charge and discharge power of the batteries pack

Table 2 Wind turbine output power

Wind turbine	Value	Units
Total rated capacity	6	kW
Maximum output	6.00	kW
Mean output	2	kW
Total production	18523	kWh/yr

into a load. In this structure, the charging process of the batteries is obtained from the excess energy of solar power and wind turbine. The average energy obtained during 12 h is equal to 42 kWh (shown in Fig. 6).

The results of the output power of the wind turbine, solar panels and batteries are summarized in the Tables 2, 3, and 4 respectively. The capacity of the wind turbines is equal to 6 kW. Also, the total percentage of energy production in the MG by the wind turbines is near to 26%.

Forty one percentage of energy is supplied by the solar power plant which has the highest power production when compared to other sources of energy generation (shown in Fig. 7). This means that in the target region, solar energy is one of the high yield energy sources. Table 4 shows the total production of solar power per one year.

Table 3 Batteries output information

Batteries	Value	Units
Batteries capacity	110	kWh
Array in parallel	16	
Number of Batteries	16	
Bus voltage	6	
Energy capacity	66	kWh
Number of hours	11	h
Energy input	12288	kWh/yr
Energy output	9853	kWh/yr

Table 4 Solar power output

Solar power plant	Value	Units
Rated capacity power	20	kW
Mean output power	3	kW
Mean output power	80.35	kWh/d
Total production per year	29329	kWh/yr
Maximum output	20.70	kW
Hours of operation	4309	h/yr

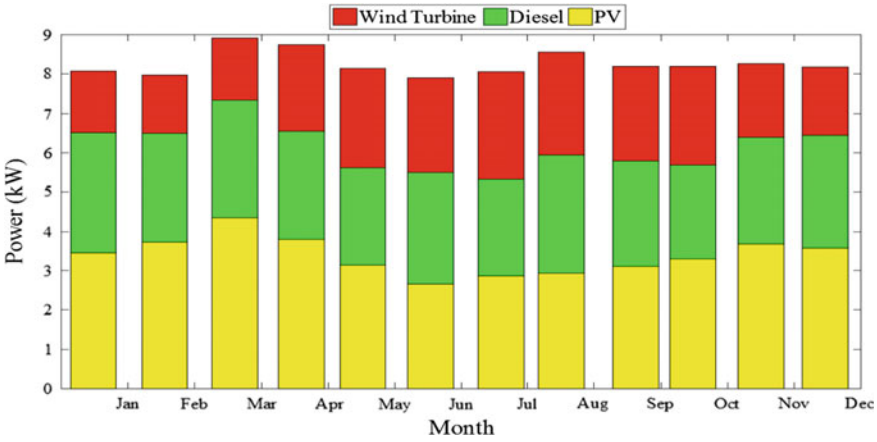

Fig. 7 Contribution power in the first structure

Economics

In the project, total cost minimization can be obtained by economic analysis. Therefore, the economic investment is evaluated in this section. The initial capital costs of different RES are shown in Table 5. The cost of energy in Fiji is

Table 5 Estimation cost of renewable energy sources

	Power	Capital cost	Maintenance
Solar (PV)	10 KW	14097 $ (US dollars)	21 $/year
Battery	1 7 KW/h	1200 (US dollars)	50 $/year
Wind turbine	3 KW	18000 (US dollars)	50 $/year
Diesel	9 KW	6500 (US dollars)	0.2 $/hr
Converter	10 KW	12500 (US dollars)	100 $/year
Total		=71527 (US dollars) 146376 FDJ-Nov 2016	

approximately equal to 32 cents per kWh. Consequently, according to the profile load, the consumption for 135 householders is calculated to equal 643.2 KWh/day. Therefore, $45.74 Fiji dollars per month should be paid by each householder. The total community payment for electricity alone is calculated near to $6175.32 FDJ per month and the total capital cost estimation based on Table 5 is equal to $146376 FDJ ($71527 USD) as of November 2016.

In additional, annual fuel and maintenance costs for the typical diesel generator are calculated in two steps:

First to calculate the fuel cost: the fuel price is assumed to equal to 1.77 Fiji dollars per litre, then a total cost is obtained at 8 $/day (249 $/month). Second, to calculate the maintenance cost for the diesel generator with 10 operating hours per day the value is obtained below:

$$0.2\,\$/\mathrm{h} \times 10\,\mathrm{Hours\,work} \times 365 = 730\,\$/\mathrm{year}$$

Therefore, the total maintenance cost for all devices during five years is equal to $19902.5. Thus, after 5 years, the total potential savings can be obtained and is estimated at $90127.2.

3.2 The Second Structure (PV/Wind Turbine with Flywheel)

The second structure to be considered applies a FESS to a MG which is shown in Fig. 8. This structure has been proposed for PICs with two required development dependencies:

1. First development design of a suitable FESS (more details to follow in Sect. 4).
2. Second, the system will use sensorless control for the induction machine (motor/generator) based on the nonlinear observer (more details to follow in Sect. 5).

In this structure, the batteries are replaced by a FESS as shown in Fig. 8.

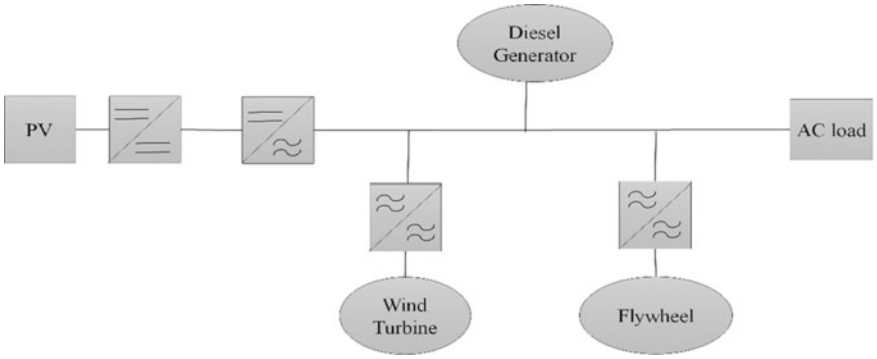

Fig. 8 Second structure based on flywheel energy storage

Fig. 9 Typical flywheel construction

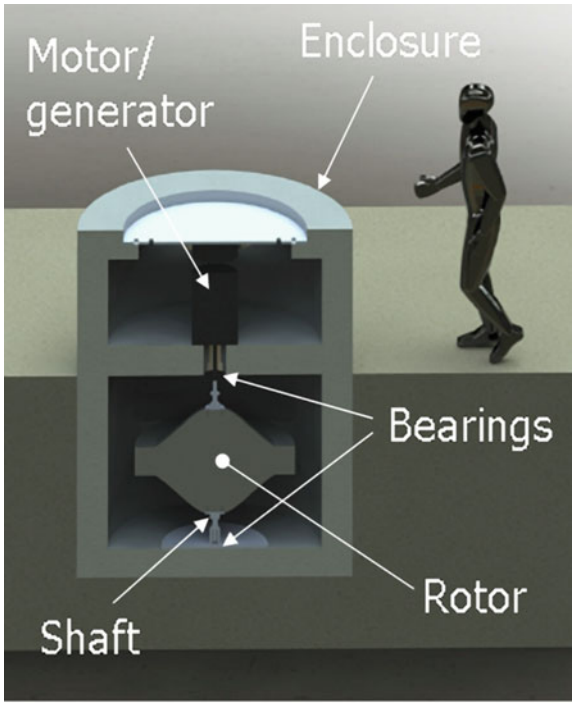

4 Flywheel-Based Electrical Energy Storage System Development

The essential components of a simple flywheel energy storage system are: rotor, shaft, bearings, electric drive motor/electric generator and enclosure/support frame (see Fig. 9). Despite this simplicity, further complexity can be found in developed

and refined commercial flywheel systems. The work reported herein addresses some of the fundamental design decisions and optimizations of a simple flywheel—for the above identified application and deployment situation.

The primary focus is directed at the rotor form and geometry so that it can operate at a high rotational speed (10,000 rpm—considered low speed for some flywheel applications) without exceeding rotor material safe working stress limits. Simplicity of manufacture and construction have been factored into the early design decisions and solution, to ensure ease of producibility, with the available resources in the central Pacific region. Naturally, the objective of having the system developed and maintainable within the business centres of the central Pacific does not and cannot mean that all technological components and/or sub-systems are sourced locally, within this target region. Where possible and practical parts and systems will be developed, made or assembled in the region. Outside of this possibility, parts may be sourced from relevant and qualified sources overseas. The ultimate aim is for a system that can be developed, manufacture (where practicable), assembled and maintained locally.

The associated energy losses are also considered in the development work and viable design solutions are investigated, modelled and optimized for the major contributors, namely the mechanical bearings and the rotor windage losses. Mechanical bearing power losses and severe life limitations are minimized through the introduction of electromagnetic bearings, used in conjunction with mechanical bearings for one investigated scenario. The mechanical load sharing and self-stabilizing characteristics of this combined system make it an ideal solution. In addition, the windage losses, due to the high rotor speed when running in an air atmosphere, are reduced to a workable level through the adoption of a partial vacuum environment, contained by the flywheel enclosure. Various options and working vacuum pressures were investigated in conjunction with the practicality of their implementation. Some of the findings are presented in the later sections of this chapter. The implications and design detailing of the enclosure and shaft have been considered but only at a fundamental level at this preliminary design development stage. While the electrical motor/generator and microgrid elements are introduced and discussed in the concluding technical sub-section which is dedicated to these and allied themes.

4.1 Flywheel Rotor Materials and Configurations

In the design of a flywheel rotor, two notable decisions have to be made, among many others. These decisions relate to the material of construction and shape of the rotor. The shape is important due to the material composition, the limiting working stresses and production processes used to shape it into the final form. Not all of the

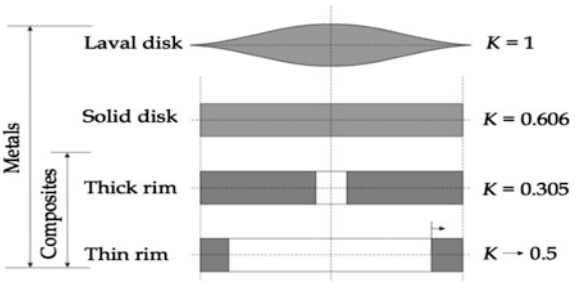

Fig. 10 Shape factor of common flywheel shapes [22]

desired shapes can be made with the selected materials. Four of the most common shapes and their suggested production materials can be seen in Fig. 10. In this figure, the shape factor of each flywheel form is also listed. The factor relates the maximum working strength σ_u (Pa) and the density ρ_v (kg/m^3), to the energy per mass W^{M} (J/kg), as in Eq. (1) below.

$$W = \frac{J\omega^2}{2} \tag{1}$$

During operation, it is suggested that a maximum speed drop in the flywheel rotor should not be greater than 50% [23]. Since the stored energy is related to the square of the rotor angular speed, ω^2, the energy recovered from the rotor, in this case, is 75% of the total stored energy in the flywheel. In order to fulfil the design specifications, the demanded energy should be equal to the (target) energy of 25 kWh, (chosen as an initial estimate). The maximum rotational speed for a low speed flywheel is typically limited to 10,000 rpm [24], which gives a minimum rotational speed of 5000 rpm as per the argument above.

In this approach, three potential candidate materials are initially considered: High tensile Steel AISI 4340, S2-glass and Carbon T1000. The last two materials listed are composites and therefore can be applied to thick rim or a thin rim rotor design solutions, as per Fig. 10. The high tensile steel is more suited to a Laval disk. The solid disk has been removed from the development since the Laval disk has all the advantages of the solid disk and fewer disadvantages. The relevant details of the three materials are listed in Table 6. Here, the maximum allowable working stress σ_u is determined by dividing the yield strength by a safety factor, n. The value of n is material and application specific. For this scenario a typical value of 1.5 has been chosen for the metallic material, however, close attention must be paid to the selection of this value in a commercial design solution. For the composite materials the 'ultimate tensile strength' is divided by a safety factor, n, of 2.0. Normally, composite material safe working limits demand thorough investigations in order to be reliably determined.

Table 6 Material specifications [23, 24]

	Density, ρ (kg/m^3)	Working stress, σ_u (MPa)	Poisson ratio, ν	Unit price ($/kg)
Steel AISI 4340	7830	486	0.29	1.00
S2-glass	1920	735	0.22	24.60
Carbon T1000	1520	975	0.20	101.80

Table 7 Configurations of a thick rim flywheel, W = 25 kWh

	Inner radius, r_1 (m)	Outer radius, r_0 (m)	h (m)	m (kg)
Steel AISI 4340	0.135	0.23	13.10	11920
S2-glass	0.490	0.59	2.29	1488
Carbon T1000	0.440	0.54	3.85	1804

4.1.1 Thick Rim Flywheel

For a thick rim flywheel, there are two stress components that are considered important in the design of the rotor. They are the radial stress, as presented in Eq. (2) and the hoop stress expressed in Eq. (3) [23].

$$\sigma_r(r) = \frac{3+v}{8}\rho\omega^2\left(r_0^2 + r_1^2 - \frac{r_0^2 r_1^2}{r^2} - r^2\right), \tag{2}$$

$$\sigma_\theta(r) = \frac{3+v}{8}\rho\omega^2\left(r_0^2 + r_1^2 + \frac{r_0^2 r_1^2}{r^2} - \frac{1+3v}{3+v}r^2\right), \tag{3}$$

where ρ is the mass density (kg/m^3), ω is the rotational speed (rad/sec), v is the Poisson ratio, r_0 is the outer radius of the rotor (m), r_1 is the inner radius of the rotor (m) and r represents any radius within the rotor (m). It can be seen from simulations that the hoop stress in a thick rim rotor is much higher than the radial stress. Furthermore, the hoop stress is at its maximum at r_1, the inner radius.

Consequently, when designing for the limiting hoop stress at the inner radius the total stored energy W (J) can be calculated by: $W = ½J\omega^2$, where J is the flywheel moment of inertia (kgm^2). In the following investigations, the best rotor configurations are calculated in response to the material specifications. Here the active energy storage is kept to 25 kWh at a maximum rotational speed of 10,000 rpm. Table 7 gives the computed results for the overall dimensions and mass of the flywheels with a thick rim produced in the three targeted materials.

4.1.2 Thin Rim Flywheel

When designing a thin rim flywheel the procedure is similar to the thick rim configuration. The only simplification which is applied is due to the small

Table 8 Configurations of Thin Rim flywheel W = 25 kWh

	Inner radius, r_1	Outer radius, r_0 (m)	h (m)	m (kg)
Steel AISI 4340	0.135	0.23	13.10	11920
S_2-glass	0.490	0.59	2.29	1488
Carbon T1000	0.440	0.54	3.85	1804

cross-sectional area, resulting in a hoop stress that can be taken as constant throughout the rim thickness. Then (3) can be simplified to (4) [22].

$$\sigma_\theta = \rho r_1^2 \omega^2 \tag{4}$$

With this equation, the best configurations of a Thin Rim cylindrical flywheel can be calculated and are shown in Table 8.

4.1.3 Equal Stress Flywheel (Laval Disk)

The equal stressed disk is also known as the Laval disk. As has been shown in Fig. 10, this shape is ideally made from metals. The main reason for using of the Laval disk is the high shape factor K which results in a high energy storage per mass. The shape of an equally stressed disk can be obtained from the known equations of equilibrium and compatibility written in terms of stresses for linear, isotropic materials with constant characteristics [25], as follows.

$$\frac{\mathrm{d}(\sigma_r r h)}{\mathrm{d}r} - \sigma_\theta h + \rho \omega^2 r^2 h = 0 \tag{5}$$

$$\frac{\mathrm{d}(\sigma_r r h)}{\mathrm{d}r} - \sigma_\theta h + \rho \omega^2 r^2 h = 0 \tag{6}$$

If $\sigma_r = \sigma_\theta = \sigma_u$ = constant, then from (5) the profile $h(r)$ (m) can be computed. This profile is given in Eq. (7).

$$h(r) = h_c e^{-B\chi^2} \tag{7}$$

With dimensionless constants $B = \rho\omega^2 r_0/2\sigma_u$ and $\chi = r/r_0$.

The problem with this profile is that the radius goes to infinity. To create a boundary on the infinite profile a rim is needed at the end of the profile [25]. By creating a rim the shape factor is reduced. With $\beta = r_D/r_0$ as the ratio between the inner radius of the rim and the outer radius and $\alpha = h_0/h_D$ as the ratio between the thickness of the rim to the connection point. Both can be seen in Fig. 11. The radial thickness β depends not only on B but also on α [26]. This relation is shown in Eq. (8) and with this the link to the revised shape factor can be determined as shown in Eq. (9).

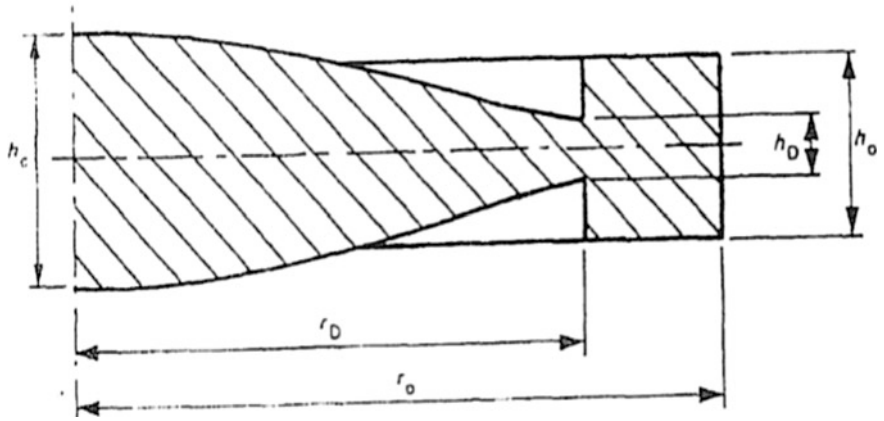

Fig. 11 Constant-stress disk with constant thickness outer rim [25]

$$\beta = \sqrt{\frac{1}{B\alpha}\left[\alpha - 1 + 2\sqrt{\frac{\alpha^2 B(B-1+\nu)}{(1-\nu)^2} + \frac{(\alpha-1)^2}{4}}\right] - \frac{1+\nu}{1-\nu}} \tag{8}$$

$$K = \frac{1 + \left[\frac{\alpha B^2\left(1-\beta^4\right)}{2} - B\beta^2 - 1\right]e^{-B\beta^2}}{1 + \left[\alpha B\left(1-\beta^2\right) - 1\right]e^{-B\beta^2}} \tag{9}$$

In Table 9, the two optimum configurations for a steel, equal stress disk with and without a small rim are given. The resultant profile of the flywheel rotor with a rim can be seen in Fig. 12.

4.2 Flywheel Losses

For a flywheel to be efficient and useful the losses must be determined and the 'high-loss' aspects reduced at the design stage of the flywheel development. In this study, an estimation of the air friction and bearing friction losses were made. In turn, these findings influenced critical design decisions and informed the resultant design solution.

4.2.1 Air Friction

The friction which results from the differential speed between the flywheel rotor and the surrounding atmosphere (windage) typically causes energy losses. The equation that is used to determine the air friction losses of a rotating circular disk in air is

Table 9 Configurations of Laval disk flywheel, W = 25 kWh

Steel flywheel AISI 4340	r_0 (m)	r_D (m)	h_c (m)	h_D (m)	m (kg)
Without rim	1.0	–	0.737	–	1934
With rim	0.525	0.391	0.752	0.195	2140

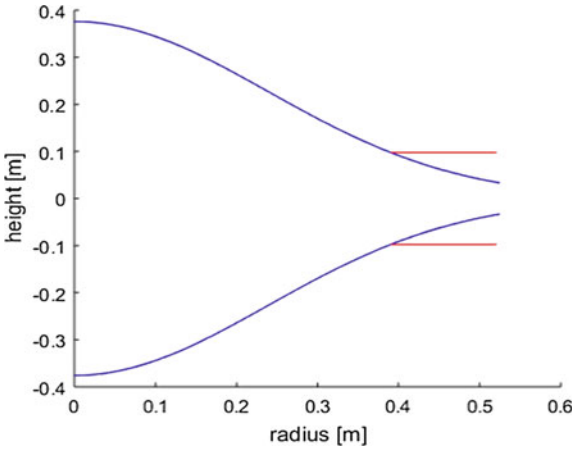

Fig. 12 The profile which results from Eq. (7) and rim added in *red*

given below in Eq. (10) [26]. The flywheel design reported herein is not a circular disk but the suggested approach gives a close first estimate of the anticipated losses. In the equation the terms are as follows: power loss $P_{a,l}$ (W), ρ_a is the gas density (kg/m^3), β_a is the dynamic viscosity of the gas (Pa s), ω the angular speed of the rotor (rad/s), r is the cylindrical flywheel rotor radius (m) and h the thickness (height) of the flywheel (m).

$$P_{a,l} = 0.04\rho_a^{0.8}\beta_a^{0.2}(\omega r)^{2.8}(2r)^{1.8}(\alpha + 0.33), \tag{10}$$

with:

$$\alpha = \frac{h}{2r}. \tag{11}$$

It is commonly understood that the enveloping gas (usually air) friction losses are considerable for flywheel systems, particularly when operated at rotational speeds as high as 10,000 rpm. Consequently, the effects of different 'housing' gases and levels of vacuum were explored. Within the comparative analysis, four different gases were considered and it was assumed that the upper ambient operating temperature expected in the Pacific would be around 50 °C. The four gases under consideration were air, ammonia, helium and hydrogen. These gases were chosen

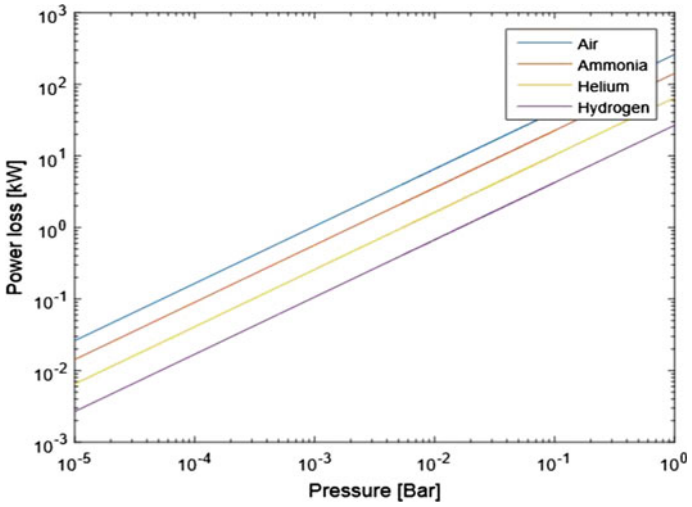

Fig. 13 Power loss due to the gas friction at various pressures

for their low density and low viscosity at 50 °C. In Fig. 13, it can be seen that when the flywheel housing pressure is lowered the enveloping gas frictional losses are decreased. It can also be seen that when the flywheel rotates at atmospheric pressure in air; the power loss will be considerable (261 kW) for the case introduced above. This is over 10 times the storage capacity of the system and clearly illustrates the deficiency of the FESS operated in an air environment at ambient pressure. A combination of other gases and a lower pressure reveals potential solutions to this problem. Under these revised conditions the relative losses are significantly lower.

To further illustrate this point, in Fig. 14 the gas friction is plotted as a function of flywheel rotational speed. In this plot the gas is helium at a pressure of 0.001 bar (100 Pa).

The pressure of 0.001(100 Pa) bar was chosen as it is well within the range of commercially available pumps which can draw vacuums down to 10^{-6} bar (0.1 Pa). It can be concluded from this graph that the flywheel will slow down in 48 h from maximum speed to the minimum speed (6.1 kWh is lost due to gas friction). This is an average of 0.13 kW. Note that hydrogen demonstrates better operational results than helium but the explosive potential when pure hydrogen blends with air is a major safety concern and consequently it is not considered further. In contrast, helium is not as flammable as hydrogen and is for this reason a better option.

4.2.2 Vacuum Generation

As has been discussed above, to reduce the flywheel windage losses the flywheel rotor should be run in a vacuum. With this arrangement the system efficiency and power storage duration can be considerably extended—making the flywheel a more

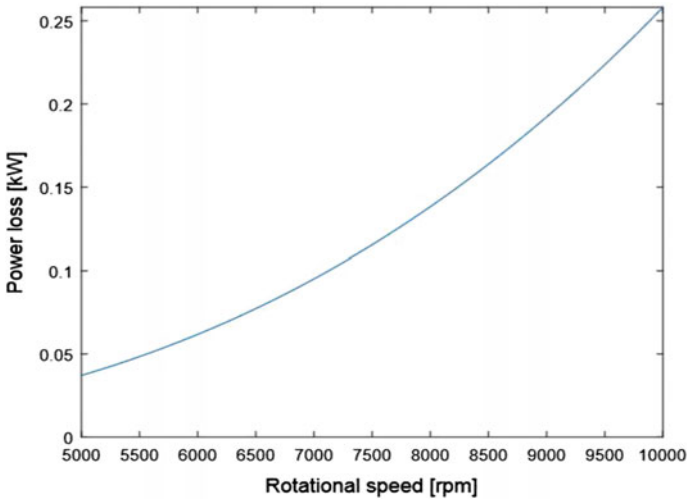

Fig. 14 Enveloping gas friction on flywheel with Helium at 10^{-3} bar (100 Pa)

Table 10 The capability of the pump types

Vacuum state	Typical pump type	Pressure (Pa)	Suitability
Low (Rough) vacuum	Positive displacement	1×10^{5}–3×10^{3}	Yes
Medium (Intermediate) vacuum	Sorption	3×10^{3}–1×10^{-1}	No
High vacuum (HV)	Cryo or turbomolecular	1×10^{-1}–1×10^{-7}	No
Ultra high vacuum (UHV)[a]	Ion or getter	1×10^{-7}–1×10^{-10}	No
Extremely high vacuum (XHV)	Specialized equipment	$<1 \times 10^{-10}$	No
Perfect vacuum	Unachievable	0	N/A

[a]American range definition (European range is 10^{-6}–10^{-10} Pa)

viable and competitive option. Consequently, it was deemed beneficial for this project to develop and hold a partial vacuum in the flywheel rotor chamber. However, this decision presents some technical challenges, especially when it is considered in the context of remote deployment within the Pacific island region. In turn, these technicalities strictly govern the specifications and design of the flywheel chamber and vacuum systems. Some of the pertinent points are introduced below.

Between atmospheric pressure and a perfect vacuum various levels of vacuum exist that have internationally accepted definitions. These levels are loosely defined around the capability of the pump types used to achieve them, as indicated in the Table 10.

Several types of pump may be used in sequence or tandem in order to achieve the desired vacuum level. Typically the pump-down sequence would be initiated with a positive displacement pump which is capable of creating a low or rough

vacuum, down to 3 kPa. To increase the level to a medium (Intermediate) vacuum, potentially down to 10 mPa, a sorption pump would normally be deployed while a high vacuum (down to 1 μPa) would demand multi-stage pumping, typically finishing with a cryopump or turbomolecular pump. High vacuum pumps of this type are widely available but they are well outside of the realms of field deployable equipment for use in remote Pacific Island sites. Medium vacuums can be achieved with single-stage pumping, using sorption pumps, but these pumps are also impractical for the targeted application due to their typical reliance upon liquid nitrogen (or a cryogen) and sensitive hardware. Furthermore, such pumps are unable to operate continuously and cannot effectively pump hydrogen, helium or neon—gases with lower condensation temperature than liquid nitrogen. In light of these points the limiting vacuum that can be expected for practical field applications must at first be considered to fall within the low vacuum range. Consequently, for practical reasons, a positive displacement type pump should be used in the prototype flywheel development.

4.2.3 Bearing Losses

Since, in the previous section, it is concluded that low pressure conditions are needed around the flywheel rotor, the mechanical flywheel bearings must consequently be sealed and isolated from the vacuum in order to prevent the lubrication from outgassing and affecting the quality and condition of the vacuum.

As a consequence, a form of lip seal is needed in order to isolate the bearing lubrication from the vacuum. The frictional losses, in the case of the mechanical bearings, are the rolling friction and hydrodynamic losses in the bearing due to the associated lubrication—particularly in the higher loaded bearing at the base of the flywheel, assuming a vertical rotational axis. These losses comprise a rolling frictional torque M_{rr}, a sliding frictional torque M_{sl}, a seal frictional torque M_{seal}, and the frictional torque due to drag losses M_{drag}. The equations for all these individual losses can be found in the SKF catalogue [27]. Through the related analyses a mechanical bearing was identified with relatively low losses. The calculated total frictional torque amounts to 1.41 Nm. From this value it was determined that the power loss would be 1.4 kW, which would require an increase of 5.6% of the stored energy per hour for compensation purposes. This is a high loss value. Subsequent analyses validated the use of electromagnetic support bearings to carry 87.5% of the weight of the flywheel and therefore reducing the mechanical bearing losses down to 170 W—due to support load reduction. This proposal introduced a reduction of the stored energy losses to 0.68%. Further investigations are due to be conducted on the feasibility of using a bearingless motor.

5 Flywheel Dynamic Model

In previous sections losses are discussed: these are the bearing frictional losses and air frictional losses. For the dynamic model used in this paper, the pressure around the flywheel rotor is chosen to be 1 mbar Helium, while the magnetic support on the bearing is 22 kN. This makes the resulting axial force be reduced from 25 kN down to 3 kN on the bearing. The bearing frictional torque M_b (Nm) is given by data from the catalogue of SKF [11] as follows:

$$M_b = 5.4.10^{-6}\omega + 0.106 = \alpha \cdot \omega + \beta \tag{12}$$

From Eq. (12) the following equation results:

$$T_{\text{air}} = 0.1393\rho_a^{0.8}\beta_a^{0.2}r^{4.6}(\alpha + 0.33)\omega^{1.8} = \gamma\omega^{1.8}, \tag{13}$$

where T_{air} (Nm) is the torque due to the air friction on the flywheel rotor. The resulting mechanical equation then results:

$$J\frac{\mathrm{d}\omega}{\mathrm{d}t} = M(t) - M_b - T_{\text{air}} = M(t) - \alpha\omega - \beta - \gamma\omega^{1.8}, \tag{14}$$

where $M(t)$ (Nm) is the electromagnetic torque of the electrical machine. If $\omega = \mathrm{d}\theta/\mathrm{d}t$, then the following state equations can be written in standard form, which describes the nonlinear dynamical model of the flywheel:

$$\begin{bmatrix} \dot{x}_1 \\ \dot{x}_2 \end{bmatrix} = \begin{bmatrix} \dot{\omega} \\ \dot{\theta} \end{bmatrix} = \begin{bmatrix} \frac{\alpha\omega}{J} - \frac{\beta}{J} - \frac{\gamma\omega}{J}\sqrt[5]{\omega^4} \\ \omega \end{bmatrix} + M(t)\begin{bmatrix} \frac{1}{J} \\ 0 \end{bmatrix}, \tag{15}$$

With the help of Solidworks® the value $J = 219.3$ kg m^2 is obtained for the flywheel rotor.

6 Sensorless Control of the FESS

The FESS which has been conceived is made up of a flywheel connected to an Induction Machine (IM) and of back-to-back bidirectional converters connected to the grid. Since the flywheel can vary in speed and the load on the grid must be supplied at a certain fixed frequency and voltage, the IM is connected to an AC/DC rectifier by a DC link and another DC/AC converter which interfaces with the grid. Each converter must be operated in a bidirectional mode (back-to-back converters), but if no exchange of energy occurs, the FESS is in idle mode and rotates at constant speed (Fig. 15).

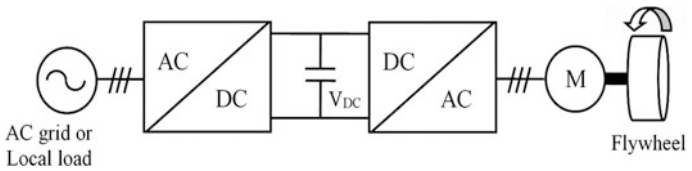

Fig. 15 Block diagram of a FESS

Both converters have been controlled with high performance methods to ensure proper active and reactive power fluxes: the generator has been controlled with a FOC (Field Oriented Control) with a control in speed and flux, while the grid converter has been controlled with a VOC (Voltage Oriented Control).

For the relatively high-speed application like this, an IM has been chosen for its robustness to sudden change of operational mode, and it is operated in field-weakening mode, [16]. As discussed above magnetic bearings should be used to decrease friction losses, at the expense of an increase of the cost of the system and the complexity of the control systems.

One of the challenges for this application would be of course a reliable speed control at high speed. With this respect if a speed sensor were used and embedded in the FESS, there would be problems of cost and downtime due to maintenance. As a consequence, the best viable solution to augment the reliability of the electrical drive is the use of sensorless techniques which however should be able to work in deep field-weakening region. This last circumstance makes use of saliency-based sensorless techniques in FESS not the best choice since the whole DC link voltage should be exploited for proper operation of the drive and moreover the magnetic parameters of the machine vary significantly due to magnetic flux variations. Thus model-based techniques should be used capable of giving a correct flux and speed estimation in the flux-weakening region with the help of a correct nonlinear modelling of the magnetic saturation effects [16] a sensorless technique conceived for an IM FESS based integrated with a total least squares (TLS) speed estimator and the use of a nonlinear model of the IM considering the IM saturation effects. The main idea is to estimate the rotor flux components and the speed of the induction motor system in two steps. In the first, assuming at a certain instant the knowledge of the speed, the state of the model is estimated by means of a nonlinear observer which is based on the nonlinear model of the IM accounting for the magnetic saturation. The second step is then the estimation of the speed by using the magnetizing current components computed in the previous step with the help of the TLS speed estimator. Finally the estimated speed is fed back as input of the observer. See [16] for further details.

A test set-up has been adopted for the experimental application composed of the following items:

- A three-phase induction motor;
- An electronic power converter (three-phase diode rectifier and VSI composed of 3 IGBT modules without any control system) of rated power 7.5 kVA;

- An incremental encoder (model RS 256-499, 2500 pulses per revolution);
- A brushless Interior Mounted Permanent Magnets (IMPM) machine drive for creating an active load.
- A dSPACE card (model DS1103) with a floating point DSP;

The test set-up is organized so that the IM drive can be supplied either by a three-phase diode rectifier (only motoring operation) or by a VSI controlled by a VOC technique (both motoring and generating conditions are allowed). The VSI is driven by an asynchronous space vector pulse width modulation (SVPWM) with switching frequency of 5 kHz. The FESS has been actively emulated by giving proper torque references to a permanent magnet synchronous motor (PMSM) drive, model Emerson Unimotor FM, mechanically coupled to the induction motor under test, behaving as an active load. The electromagnetic torque is measured on the shaft by a torquemeter model Himmelstein 59003 V(4-2)-N-FN-L-K. A photograph of the employed test set-up is shown in Fig. 16, and the parameters of the motor are shown in Table 11.

Fig. 16 Photo of the experimental set-up

Table 11 Rated data of the motor

Rate power	2.2 kW	Rated speed	1425 rpm
Rate voltage	380 V	Rated torque	14.9 Nm
Rate frequency	50 Hz	Pole pairs	2
Cos ϕ	0.75	Inertia moment	0.0067 kg m^2

The proposed TLS-based nonlinear observer has been first tested in numerical simulation. With this regard, the dynamic model of the entire flywheel generation system has been implemented in a MATLAB Simulink environment. As for the flywheel, the model described in Sect. 4 has been adopted. It should be borne in mind that, since the induction machine available in the test set-up presents a rated power of 2.2 kW, while that of the system under study has a rated power of 25 kW, the flywheel inertia has been scaled so to be compatible with that of the induction machine drive available in laboratory. In particular, such a scaling has been performed reducing the inertia proportionally to the rated power reduction of the IM available in the laboratory. As for the dynamic model of the IM, since the generation system is supposed to work in deep field-weakening conditions, a dynamic model taking into consideration the magnetic saturation of the iron core has been adopted.

6.1 Simulation Results

In the simulated test, the proposed sensorless technique has been tested at 1000 rad/s (about seven times the rated speed of the IM), in deep field-weakening working condition. Figure 17 shows the real and estimated speed during the transient from 0 to the steady-state speed. It can be observed that the estimated speed perfectly tracks the real one, both in transient and in steady state. The accuracy of the estimation during the entire duration of the test is quite challenging, since, starting from 0 to 1000 rad/s, not only the rotor flux is variable according to the magnetizing curve, but also the electrical parameters of IM vary accordingly, as the magnetic state of the machine changes. Figure 18 shows the reference and the estimated rotor flux linkage as well as the electromagnetic and the load torque. It should be noted that the rotor flux reference reduces consistently from 0.95 Wb from zero up to 150 rad/s (rated speed) while reducing to 0.2 Wb at 1000 rad/s.

As for the load torque, the torque required by the flywheel at steady state is equal to 0.25 Nm, exactly corresponding to the value in Eq. 14. It should be further noted that then electromagnetic torque remains constant to its maximum value only from 0 to 150 rad/s, after which it starts decreasing with hyperbolic law, according to the rotor flux amplitude reduction. The steady-state final torque is compatible with the limit torque which the IM can provide in such field-weakening conditions.

6.2 Experimental Results

The FESS has been secondly tested experimentally on the test set-up described above, with the brushless motor drive used as active load to emulate the load torque offered by the flywheel, according to Eq. 14. For security reasons, in the experimental test, the sensorless technique has been tested up to a limited speed, equal to 200 rad/s. Figure 19 shows the real and estimated speed during the transient from 0

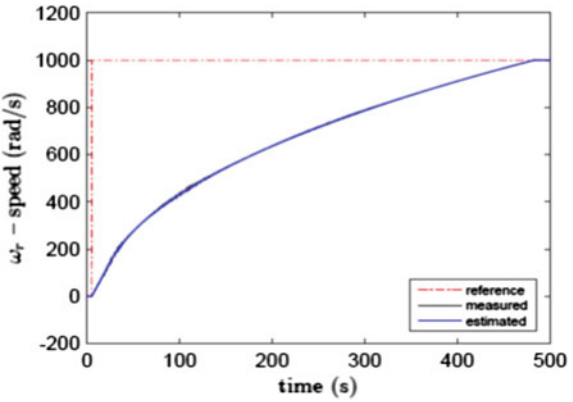

Fig. 17 Measured and estimated rotating speed of IM (sim)

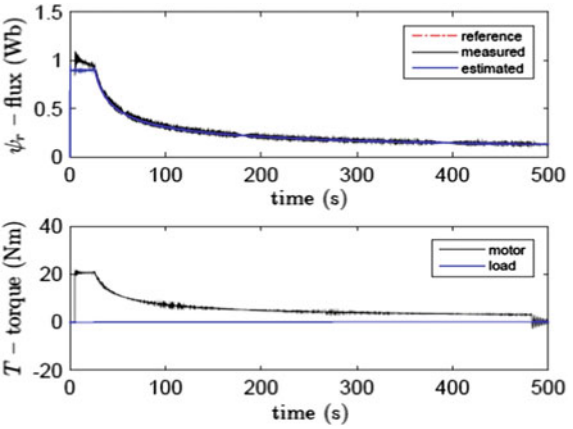

Fig. 18 Reference and estimated flux of the IM (sim)

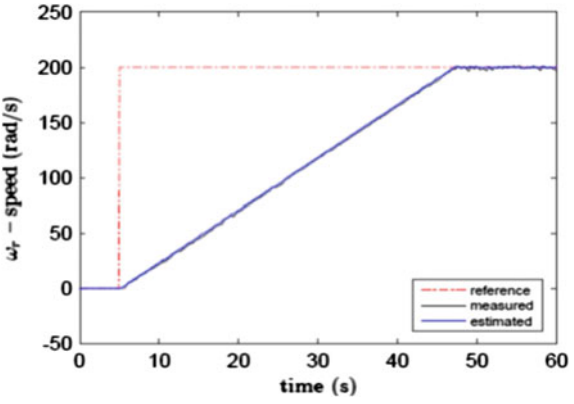

Fig. 19 Measured and estimated rotating speed of IM (exp)

to the steady-state speed. Even in the experimental test, it can be observed that the estimated speed perfectly tracks the real one, both in transient and in steady state. Figure 20 shows the reference and the estimated rotor flux linkage as well as the electromagnetic torque. It should be noted that the rotor flux reference reduces consistently from 0.95 Wb from zero up to 150 rad/s (rated speed) while reducing to 0.8 Wb at 200 rad/s. Moreover, even experimentally, the proposed gain choice for the nonlinear observer permits a stable behaviour of the nonlinear observer, under highly parameters' varying parameter conditions and in presence of the estimated speed as feedback, instead of the real speed. It should be further noted that the electromagnetic torque remains constant to its maximum value only from 0 to 150 rad/s, after which it starts decreasing with hyperbolic law, according to the rotor flux amplitude reduction.

Figure 21 shows the corresponding values of the i_{sx} and i_{sy} current components in the rotor flux oriented reference frame. As expected, i_{sx} remains almost constant from zero to 150 rad/s, after which it starts decreasing. On the contrary, i_{sy} presents

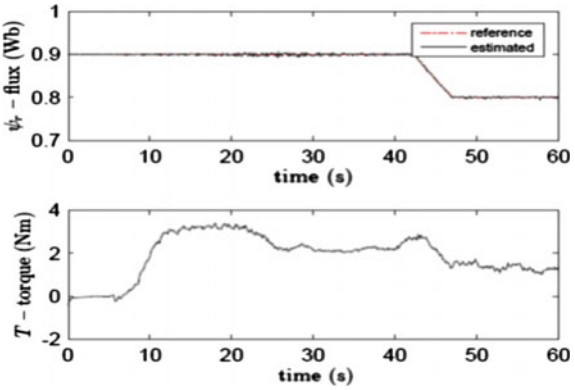

Fig. 20 Reference and estimated flux of the IM (exp)

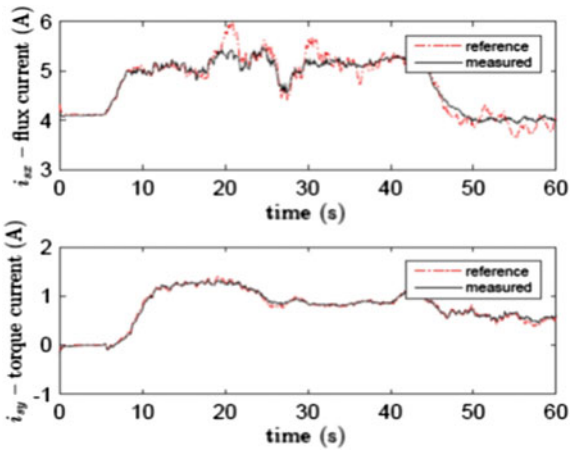

Fig. 21 Direct and quadrature axis components of stator current space vector (exp)

a constant value from 0 up to 200 rad/s, corresponding to the limit value imposed to the i_{sy} by the speed controller of the drive, after which it starts decreasing to its steady-state value.

7 Conclusion

This paper has introduced the concept of interchanging batteries with a flywheel energy storage system (FESS) within a microgrid for use in the Pacific by small communities in island nations.

The energy requirements for a typical small community in the Pacific were investigated, renewable energy source outputs were also determined for the target region and typical power demands evaluated for a chosen community. A typical daily load profile was established through the use of HOMER software. In response to the identified electrical demands, two suitable configurations of microgrid were explored, one with a diesel generator, battery bank and renewable energy generation systems (Solar panels, wind turbine, etc.), the second with a flywheel energy storage device coupled to renewable energy generation devices.

Preliminary design analyses were conducted and the basic form of a suitable flywheel for energy storage was determined for use with the above-mentioned microgrid. Power losses and optimized performance of the rotor were considered alongside the desire for the FESS to be developed, manufacture and serviced (as much as is practically sensible) in the Pacific region. The findings have paved the way for the subsequent development of a small scale, reduced speed prototype flywheel, which will allow a thorough evaluation of the developed models and validation of the design reasoning. The encouraging results obtained so far provide an excellent foundation for further flywheel research and development to be undertaken.

Control strategies for the flywheel were also introduced and the technologies/methods for monitoring the flywheel speed in a sensorless manner were presented. A test-rig for validating and testing a prototype flywheel was also introduced.

Acknowledgements This research has been realized also within the project REFEPICS (Design of a REnewable energy source system with a Flywheel Energy storage system for supplying energy in Pacific Island Countries with weak grid) funded by the French Pacific Fund.

References

1. Farret FA, Simões MG (2006) Integration of alternative sources of energy. IEEE press, pp 112–127
2. Hatziargyriou N (ed) (2013). Microgrids: architectures and control. Wiley
3. Pacific Island Sets Renewable Energy Record (2014) http://www.se4all.org/2014_03_20_pacific-island-sets-renewable-energy-record. Available: NEXIS Library: LEXPAT File: DESIGN

4. Jensen TL (2000) Renewable energy on small islands. Forum for energy and development. Report in Forum for Energy and Development (FED) Renewable Energy on Small Islands, 2nd edn, p 135
5. Masashi K, Kazuo T, Tomoki Y, Tetsuya U (2012, June) A study of parallel operation of flywheel electric storage with high speed network operation. In: 2012 7th international power electronics and motion control conference (IPEMC), vol 2, pp 968–972. IEEE
6. Skander-Mustapha S, Ghorbal MJB, Arbi J, Slama-Belkhodja I (2009) Comparative analysis of control strategies for DFIG based wind system under small grid faults. Int Rev Electr Eng 4:1273–1282
7. Suvire GO, Mercado PE (2008) Wind farm: dynamic model and impact on a weak power system. In: Transmission and distribution conference and exposition: Latin America, 2008 IEEE/PES. IEEE, pp 1–8
8. Molina M, Suvire G, Ontiveros L, Mercado P (2011) Emerging energy storage technologies in utility power systems: a technical insight. Nova Science, Nova Science Publishers Press, New York, pp 173–250
9. Cimuca G, Breban S, Radulescu MM et al (2010) Design and control strategies of an induction-machine-based flywheel energy storage system associated to a variable-speed wind generator. IEEE Trans Energ Convers 25(2):526–534
10. Cimuca GO, Saudemont C, Robyns B, Radulescu MM (2006) Control and performance evaluation of a flywheel energy-storage system associated to a variable-speed wind generator. IEEE Trans Industr Electron 53(4):1074–1085
11. Lawrence RG, Craven KL, Nichols GD (2003) Flywheel ups. IEEE Ind Appl Mag 9(3):44–50
12. Mathiesen BV, Lund H, Karlsson K (2011) 100% Renewable energy systems, climate mitigation and economic growth. Appl Energy 88(2):488–501
13. Hebner R, Beno J, Walls A (2002) Flywheel batteries come around again. IEEE Spectr 39(4): 46–51
14. Itoh JI, Nagano T, Tanaka K, Orikawa K, Yamada N (2014, September) Development of flywheel energy storage system with multiple parallel drives. In: 2014 IEEE energy conversion congress and exposition (ECCE). IEEE, pp 4568–4575
15. Truong LV, Wolff FJ, Dravid NV (2004, July) Simulation of energy sharing among flywheels in parallel configuration. In: Energy conversion engineering conference, 2002. IECEC'02, 2002 37th Intersociety. IEEE, pp 15–20
16. Accetta A, Aitchison D, Cirrincione G, Cirrincione M, Pucci M, Sferlazza A (2016, June). Sensorless induction machine drive for fly-wheel generation unit based on a TLS-based non-linear observer. In: 2016 IEEE symposium on sensorless control for electrical drives (SLED), pp 1–6. IEEE
17. Aitchison DR, Cirrincione M, Leijtens N (2016, July) Design development of a flywheel energy storage system for isolated Pacific Island communities. In: 2016 IEEE international conference on advanced intelligent mechatronics (AIM), pp 1628–1633. IEEE
18. Fiji Bureau of Statistics (2016)—Fiji Bureau of Statistics. Available: http://www.statsfiji.gov.fj/
19. Norta D, Kopietz S, Hien S, Neshvad S, (2016) Generation of synthetic electrical load profiles for rural communities in developing countries—applied in Fiji. In: International conference on renewable energies and power quality (ICREPQ'16) Madrid (Spain), 4–6 May 2016
20. Natural Resources Canada (2016, Nov): http://www.nrcan.gc.ca/energy/software-tools/7465
21. Homer Energy (Nov 2016) HOMER Pro version 3.6 user manual, p 416
22. Östergård R (2011, Dec) Flywheel energy storage—a conceptual study, Uppsala university, vol 48, pp 1–48, Dec 2011
23. Bolund B, Bernhoff H, Leijon M (2007) Flywheel energy and power storage systems. Renew Sustain Energy Rev 11(2):235–258
24. Joshi D (2013) Energy storage technology application for grid frequency control—an ancillary service. Power Gen Europe 4–6 June, 2013. Vienna, Austria

25. Portnov G, Cruz I, Arias F, Fiffe RP (2003, Dec) Flywheels for low-speed kinetic energy storage systems (No. CIEMAT–1031). Centro de Investigaciones Energeticas Medioambientales y Tecnologicas (CIEMAT)
26. Zhang X, Mi C (2011) Vehicle power management: basic concepts. In: Vehicle power management. Springer, London, pp 13–48
27. SKF (2013) SKF Rolling bearings catalogue, pp 97–114

Energy Storage Systems in Solar-Wind Hybrid Renewable Systems

Abhishek Awasthi, V. Karthikeyan, Vipin Das, S. Rajasekar and Asheesh Kumar Singh

Abstract In island countries, microgrid systems have the ability to provide reliable and improved power quality especially in the vast country with low population density in remote regions. There are two major types of smart grid design in the absence of central grid, namely DC microgrid and AC microgrid. When microgrids are enabled with renewable energy sources, energy storage units increase the reliability in power supply for the load demand on consumer end. The optimized means of extracting power from renewable energy resources like wind, solar, and fuel cell is difficult in islanding mode of operation. Due to occurrence of power imbalance, energy storage units are required which support the energy requirement when power generation cannot meet the load demand. A microgrid is controlled by a supervisory controller that decides which energy storage units are connected to satisfy the load demand. Though the task is simple, appropriate control strategies are required by the microgrid to cope up with disturbances such as sudden changes in environmental and load conditions. An energy storage unit should be designed to fulfill the requirement of fast and dynamic transition of power consumed by loads connected with microgrid. In AC microgrid, the presence of local energy sources and the ability to regulate voltage and frequency can alleviate the burden for conventional generating unit. In DC microgrid, such a problem does not exist; however, the issue of voltage handling is needed to be dealt with. This chapter deals with the integration of energy storage system (ESS) with DC and/or AC microgrid and related energy management control algorithms. It also addresses the research challenges and solutions towards smooth operational behavior of ESS by

A. Awasthi (✉) · V. Das · A.K. Singh
M.N.National Institute of Technology Allahabad, Allahabad, UP 211004, India
e-mail: abhishekawasthi761993@gmail.com

V. Das
e-mail: vipindas504@gmail.com

V. Karthikeyan · S. Rajasekar
NEC Laboratories Singapore, NEC Asia Pacific Pte. Ltd., Singapore, Singapore
e-mail: karthi13546@gmail.com

S. Rajasekar
e-mail: rajasekar_s@nec.com.sg

F.M.R. Islam et al. (eds.), *Smart Energy Grid Design for Island Countries*,
Green Energy and Technology, DOI 10.1007/978-3-319-50197-0_7

integrating microgrid enabled with renewable energy sources. The detailed design specifications of ESS for 500 kW microgrid enabled with solar-wind hybrid renewable energy system (RES) is discussed. Validation through simulation studies is performed to understand the operation of effective and efficient integration of ESS with microgrid operating under islanded conditions.

Keywords Microgrid · Energy storage system (ESS) · Energy management · Renewable energy

1 Introduction

Global electricity production in the year 2015 was estimated to be around 22,433 terawatt-hours (TWh). Energy generated from conventional fossil fuel based power plants was the primary contributor, amounting to 13,659 TWh. On the other hand, renewable energy systems (RESs), excluding hydropower, contributed only 1570.31 TWh [1]. For the purpose of bolstering the renewable energy market, incentives have been offered by the global environmental associations and governments. CO_2 emitted from coal-based generating stations contributes to greenhouse effect which inadvertently leads to global warming. Therefore, shifting towards a clean, nonpolluting renewable energy dominated power system is necessary to counter the hazardous implications of global warming [2]. The breakdown of globally installed RESs is shown in Fig. 1.

Unfortunately, high investment cost and intermittent, inconsistent nature of these sources contribute to the skeptical mind-set of the potential end-users. Electrification of grid unconnected small isolated islands with renewables, then, presents a huge challenge. Still, renewable energy based microgrid setup is considered as a viable solution as extending existing ac grid network is extremely costly due to rough topography and environmental concerns. Use of renewable distributed energy resources (DERs), such as, solar, wind, hydro, to power local loads, thereby removing the local network's dependence on the utility grid is a

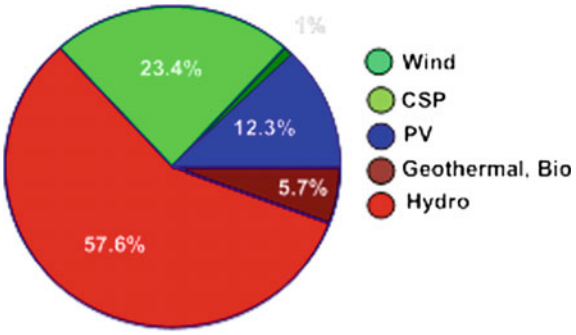

Fig. 1 Installed renewable energy system worldwide

potential future pathway to development of low-cost grid infrastructure. Hence, such islanded microgrids offering resiliency, energy efficiency are a technically feasible option for areas where ac grids might fail [3].

Since, reinforcing the microgrid with an energy storage system (ESS) would assist in tackling the renewable source fluctuations by supplying the excess load power, thereby enhancing the grid's reliability, Sect. 2 is devoted to the study and classification of energy storage technologies with an extensive description of some popular technologies. Specific advantages and applications of different ESSs have been mentioned, and their suitability in relevance to existing grid infrastructure has been discussed. Section 3 deals with issues which arise from the integration of ESSs with renewable based microgrid. Choosing the appropriate energy storage technology for a microgrid is the most important aspect of grid design. Comparison between various ESSs and their configurations has been carried to make the grid design process easier and efficient. Popular renewable DERs include hydro, wind, and solar energy. With increasing demand, the penetration of RESs has also increased which makes it difficult to match the local load profile with available power, especially at peak hours. Also, the variations in the RESs can further decrease the integration and operational activity, thereby rendering the existing grid insufficient to fulfill the real-time demand of customers. Section 4 presents a thorough investigation into the energy management functions based on load forecasting to ensure fulfillment of customers' power demands. Section 5 concerns the energy management of a solar-wind hybrid microgrid with the battery as ESS via coordination control of the microgrid. Solar and wind power are better suited for usage on small, isolated, and ocean/sea surrounded islands with abundant sunlight and wind currents from the oceans. Irregular stochastic energy output from these RESs can be alleviated by combining both solar and wind energy technologies, which has been proved to provide better performance and efficiency overall [4, 5]. Also, mathematical modeling of solar PV panel, wind turbine, and battery has been presented to measure various parameters of these systems and achieve efficient coordination control of converters employed in the hybrid microgrid.

2 Energy Storage Technologies: An Overview

Electrical energy is the most versatile form of energy which can be easily converted into other forms. Research has shown that the transformative capability of electrical energy is 2–4 times greater than energy produced from fossil fuel. Due to large inertia of interconnected components of fossil fuel generating stations, it is not possible to ramp up/down the supply as quickly as the dynamic load profile. ESSs help to satisfy the consumer's demands which fluctuate widely and rapidly within the span of a single day by supplying/storing the excess/deficient energy with a high rate of response and efficiency.

Installations of these storage systems help improve the reliability and effectiveness of the utility supply [6]. These storage systems play a major role in the

development of the future grid. Some of the essential functions which can be addressed with the development of cheaper and superior storage technology include

1. Dynamic energy management
2. Assuaging intermittency of renewable sources
3. Improvement in power reliability and quality
4. Realization of smart grid.

Researchers have contributed to the development and industrialization of energy storage technologies over the past decade. Figure 2 shows the bar graph representing the number of research articles published on the topic (given as heading) in the previous 10 years.

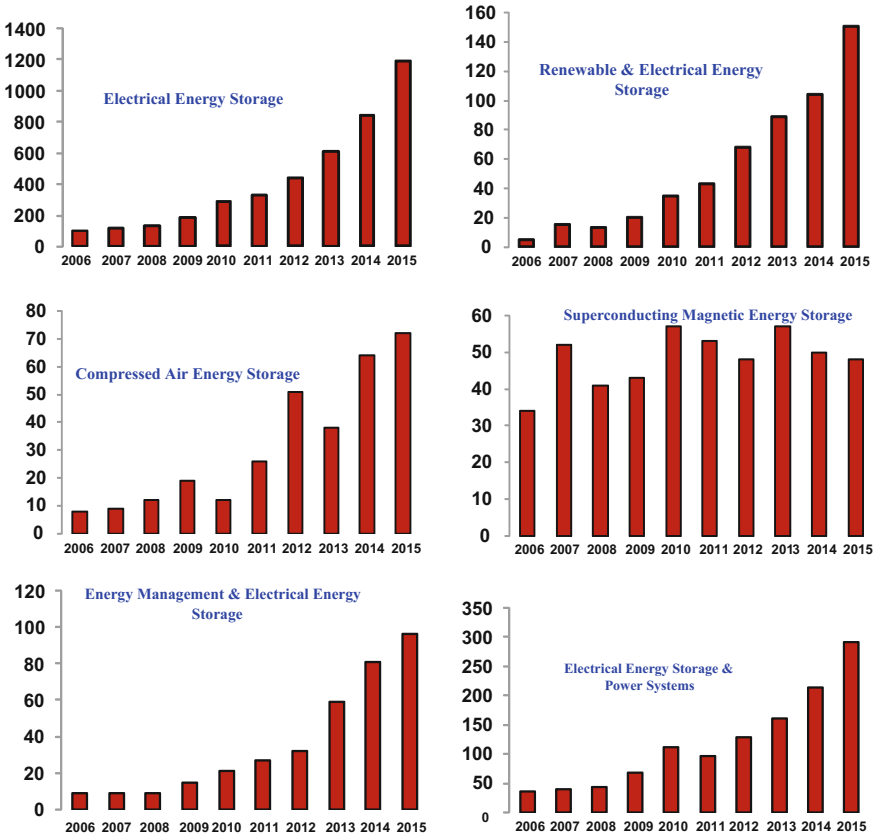

Fig. 2 Recent trends in EES research

2.1 Classification of Existing EES Technology

Various methods have been mentioned in the existing literature based on which the EES technology can be categorized [7–10]. Prominent among these methods are the (i) Response time [7] (ii) Storage duration [8] and (iii) Working function [9]. Categorization is also done on the basis of the form of energy stored in the system [10] as depicted in Fig. 3. Another important classification is based on the criteria of applications, i.e., technologies which can be used for power quality improvement and other technologies designed for energy management as depicted in Fig. 4.

2.2 Electrical-Based Storage Systems

A brief overview of electrical and electrochemical-based storage technologies is presented below.

2.2.1 Capacitor

Capacitors store electrical energy between two or more conducting plates in the dielectric material present, due to the presence of an electrostatic field. They possess shorter charging/discharging time and higher power density storage than the conventional batteries but lower energy density, high dissipation of energy, and limited storage capacity [7, 11, 12, 13].

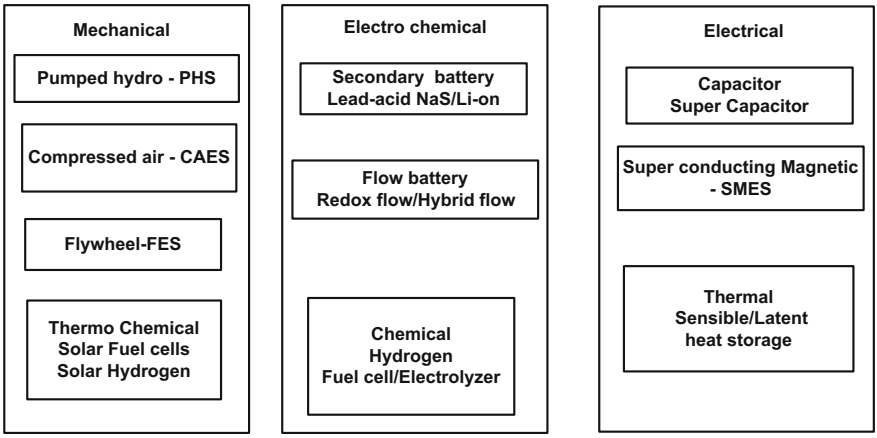

Fig. 3 Classification of energy storage technologies

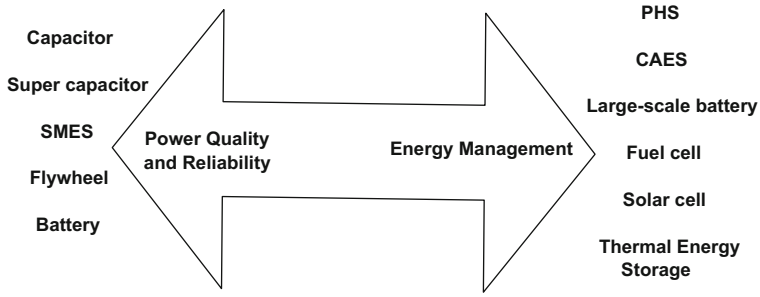

Fig. 4 Various functions of EES systems

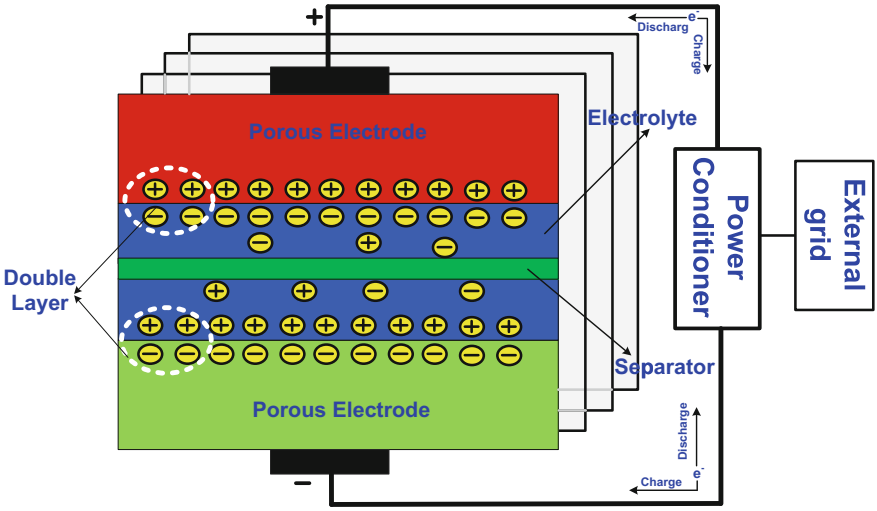

Fig. 5 Schematic diagram of supercapacitor system

2.2.2 Supercapacitor

Figure 5 shows a schematic diagram of supercapacitor system. It is made up of two conducting electrodes, an aqueous electrolyte solution and a porous membrane separator [13]. This structure is responsible for imparting characteristics of both conventional capacitors and electrochemical-based battery to the supercapacitor.

Long cycle duration, reaching approximately 1×10^5 cycles with a high efficiency ranging in between 84 and 97%, are some of its features [7, 14]. The major drawback associated with this storage technology is the high capital cost and high discharge rate varying from 5 to 40% [15–17]. This technology is suited for applications which require high bursts of power for a short term. Large-scale power systems do not prefer employing this technology. Recent developments and active research in this field have vastly improved this technology. Research has been

Table 1 Manufacturing companies of supercapacitors [21–24]

Company name	Manufacturing country	Specifications
TVA company	U.S.	200 kW Imparts starting capability to high power dc machines
Maxwell	U.S.	Single cell structure, 2.2–2.7 V, 1–3000 F UPS applications
Panasonic	Japan	Single cell structure, 2.3–5.5 V, 0.1–2000 F
NEC	Japan	3.5–12 V, 0.01–6.5 F, Power Quality Improvement
Siemens	Germany	21 MJ/5.7 Wh, 2600 F Distribution network of metro
CAP-XX	Australia	Single cell structure, 2.3–2.9 V, up to 2.4 F, 233–358 F

primarily focused on developing new electrode materials for enhancing the efficiency and energy density [18–20]. Table 1 shows a list of supercapacitor manufacturing companies.

2.2.3 Superconducting Magnetic Energy Storage (SMES) System

The distinctive advantage of SMES technology is that it stores electrical energy in the form of electric current directly when a DC is passed through a coiled inductor composed of a superconducting material such that the current circulates with almost zero loss [25]. It can store energy in the form of the magnetic field generated when electric current flows in the inductor. The main requirement for its continuous and hassle free operation is the retention of superconducting properties of the inductor. The coil is immersed in liquid helium contained in a vacuum which preserves its superconducting characteristics. Figure 6 shows a schematic of SMES.

It consists of a power conversion unit, a superconducting unit, and a cryostat system. It demonstrates high storage efficiency of energy reaching 97% with quick response, in milliseconds, but can store energy for a shorter duration of time [7, 26, 27]. Costly features, high self-discharge (10–15%), and degradation to the environment because of the high magnetic field are its drawbacks [7, 26, 28]. Common power rating varies between 1 and 10 MW with a storage time of seconds. Active research is being carried out to develop larger SMES-based systems with a power rating of 10–100 MW and an increased storage time in minutes [29].

2.3 Electrochemical

Battery-based systems have grown popular over the last two decades. These systems can be used at different power levels for a host of applications as shown in

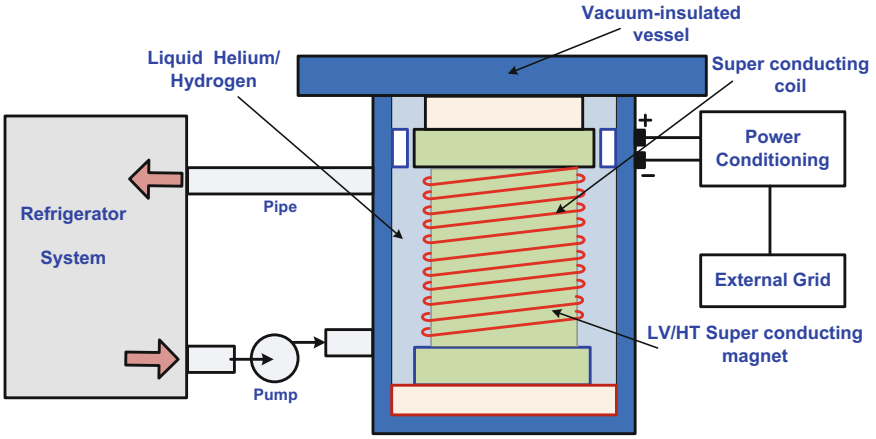

Fig. 6 SMES-based power system

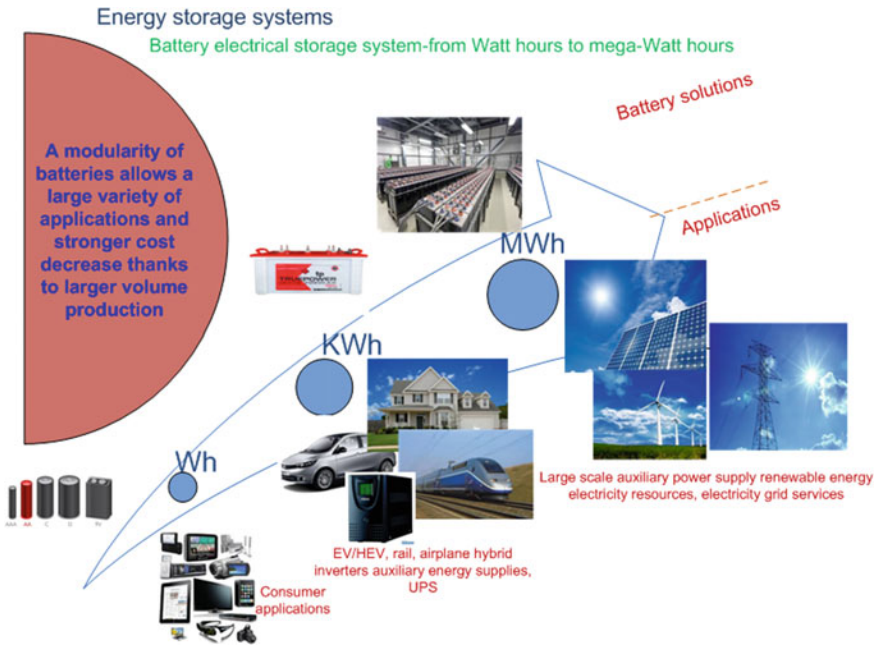

Fig. 7 Applications of battery energy storage systems

Fig. 7. The variability of their usage for such extensive battery-based energy systems (Lead-acid, Li-ion, NaS and NiCd, etc.) are made up of many series or parallel connected electrochemical cells which undergo an electrochemical reaction to produce the desired voltage. The structure consists of two electrodes (positive

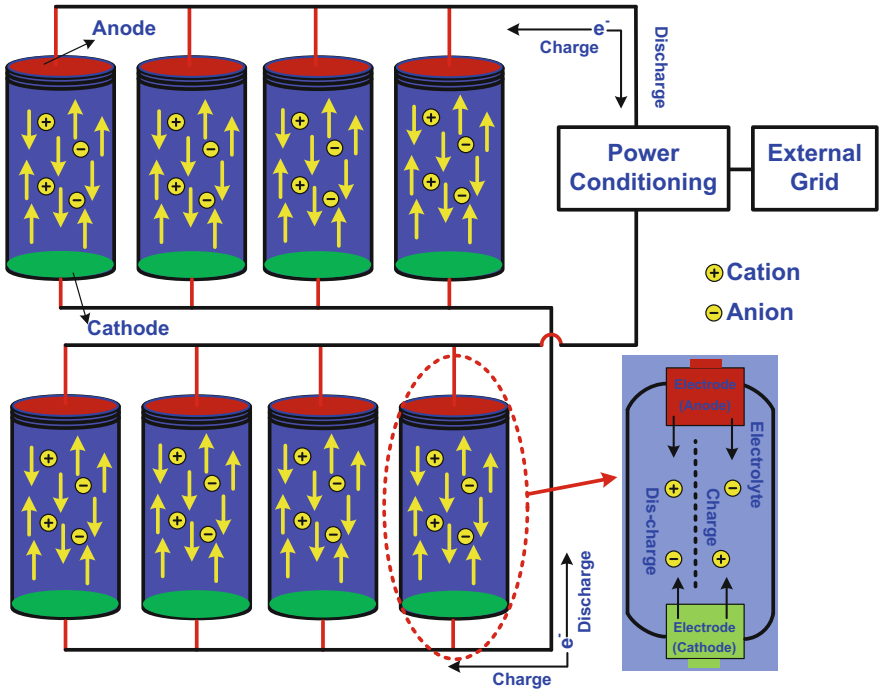

Fig. 8 Internal structure of electrochemical-based EES

potential anode and negative potential cathode) immersed in an electrolyte in the solid, molten, or liquid state as shown in Fig. 8 [30]. The cell allows dual conversion of energy between electrical and chemical form vis-à-vis an electrochemical reaction which takes place at the electrodes.

During charging, electrons are collected at the anode and extracted from the cathode whereas during discharging the reverse reactions take place. The chemical reactions of different types of batteries have been shown in Table 2.

Installation of the ESS in a renewable energy based microgrid requires the agreement of various parameters of the storage technology with the load profile, such as power rating, response time, charging/discharging cycle, capital cost, and energy and power density. Table 3 compares prominent storage technologies by these parameters.

Table 2 Chemical reaction for different batteries [31]

Battery type	Chemical reactions at electrodes	Unit voltage (V)
Lead-acid	$Pb + SO_4^{2-} \Leftrightarrow PbSO_4 + 2e^-$ $PbO_2 + SO_4^{2-} + 4H^+ + 2e^- \Leftrightarrow PbSO_4 + 2H_2O$	2.0
Lithium-ion	$C + nLi^+ + ne^- \Leftrightarrow Li_nC$ $LiXXO_2 \Leftrightarrow Li_{1-n}XXO_2 + nLi^+ + ne^-$	3.7
Sodium-sulfur	$2Na \Leftrightarrow 2Na^+ + 2e^-$ $\lambda S + 2e^- \Leftrightarrow \lambda S^{2-}$	~2.08
Nickel-cadmium	$Cd + 2OH^- \Leftrightarrow Cd(OH)_2 + 2e^-$ $2NiOOH + 2H_2O + 2e^- \Leftrightarrow 2Ni(OH)_2 + 2OH^-$	1.0–1.3

3 Integration of EES with Renewable Microgrids

3.1 Integration with DC Microgrid

Renewable energy based microgrids are emerging as a viable solution for isolated rural areas or oceanic islands. The main issue which plagues its development is the variable/intermittent nature of renewable sources, which makes it tough to achieve smooth operation. Such fluctuation may lead to load imbalance, instability, and damage to system components under the influence of varying loads. In such a scenario, EES systems assume significance because of its capability to act as a generator while discharging and as a load, while charging. The popularization of DC loads has shifted the focus to DC microgrids. Figure 9 explains the importance of EES systems, or more particularly, battery-based ESSs in the distribution network with majority DC loads. In any AC microgrid, power from renewable energy based sources should be converted to AC and then back to DC to supply DC loads. DC microgrid prevents multiple conversions between AC and DC and enhances the efficiency of the whole grid.

An ordinary, simple EES system is homogeneous which makes the implementation, operation, control, and maintenance easier. Figure 10 depicts a typical architecture of such a system. The basic architecture consists of an interfacing power converter (connected to a power source, conventional or non-conventional) and a load (AC/DC) supplying output converter which is controlled by a supervisory controller. The operation of the controller is dispatched from an energy management system (EMS).

3.2 Integration with AC Microgrid

AC microgrids are popular in regions where most of the loads require AC power. Depending upon the application, EES system can be installed either at the load end

Table 3 Comparison of energy storage technologies

Storage technology	Energy density (kWh/L)	Power density (kW/L)	Specific energy (Wh/kg)	Specific power (kW/kg)	Power Rating (MW)	Rated energy capacity (MWh)	Lifetime (years)	Cycle efficiency %
PHS	1×10^{-3} to 2×10^{-3} [7]	~1×10^{-3} [8]	0.5–1.5 [7]	–	<4000 [32]	500–8000 [7]	40+ [33], 30+ [34]	87 [35]
Large-scale CAES	2×10^{-3} to 6×10^{-3} [8]	~1×10^{-3} [8]	30–60 [7]	–	1000 [36]	2860 [37]	20–40 [7],	54 [7]
Flywheel	0.02–0.08 [7]	~5 [8]	5–100 [38]	0.4–1.5 [7]	0.1–20 [34]	up to 5 [34]	20 [32]	~90–95 [7]
Lead-acid	0.05–0.09 [36]	0.01–0.40 [7]	30–50 [7]	180 [38]	0.05–10 [39]	0.001–40 [39]	13 [33]	75–80 [7]
Li-ion	0.20–0.50 [7]	1.5–10 [8]	75–200 [7]	0.5–2 [38]	1–100 [40]	~0.004–10 [41]	14–16 [42]	~90–97 [7]
NaS	0.15–0.30 [8]	~0.14–0.18 [8]	150–240 [7], 100 [43]	0.15–0.23 [7]	<34 [7]	0.4–244.8 [44]	12–20 [45]	75–85 [46]
NiCd	0.06–0.15 [7]	0.08–0.60 [8]	50–75 [7]	0.15–0.30 [7]	0–40 [7]	6.75 [38]	15–20 [38]	60–83 [47]
VRB	0.025–0.035 [7]	~<2 × 10^{-3} [8]	10–30 [7]	0.166 [48]	2 [49]	<60 [13]	20 [50]	65–75 [40]
ZnBr	0.03–0.06 [7], ~0.055–0.065 [8]	~<25 × 10^{-3} [8]	30–50 [7], 75 [51]	0.1 [52], 0.045 [51]	0.05–2 [7], 1–10 [40]	0.1–3 [13], 0.005 and 0.5 [45]	5–10 [7]	66–80 [47]
PSB	~0.02–0.03 [7]	~<2 × 10^{-3} [8]	~15–30 [53]	–	1–15 [7]	up to 120 [50]	10–15 [7]	60–75 [7]
Capacitor	2×10^{-3} to 0.01 [7, 54]	>100 [7]	~<0.05 [55, 56]	~100 [7]	0–0.05 [7]	–	~1–10 [57]	>70 [58]
Supercapacitor	0.01–0.03 [7]	>100 [7]	2.5–15 [7]	~10 [56], 0.50–5 [7]	~0.001–0.1 [36]	0.0005 [36]	10–30 [7]	84–95 [59]
SMES	~6×10^{-3} [8]	1–4 [7]	10–75 [60, 61]	0.5–2 [7]	~1–10 [7]	0.0008 [36]	30 [32]	95–98 [59]
Solar fuel	0.50–10 [7]	–	0.8 × 10^3 to 10^5 [7]	–	0–10 [7]	–	–	~20–30 [7]
Hydrogen fuel cell	0.50–3 [7]	>0.5 [7]	0.8–10^4 to 10^5 [7]	>0.5 [7]	58.8 [62]	0.312 [63]	+20 [64]	45–66 [65]
TES	0.20–0.50 [7]	–	80–200 [7]	0.01–0.03 [7]	0.1–300 [7]		30 [66]	~30–60 [7]
Liquid Air Storage	0.012–0.024 [67]	–	214 [68]	–	10–200 [69]	2.5 [70]	>25 [71]	55–80 + [71]

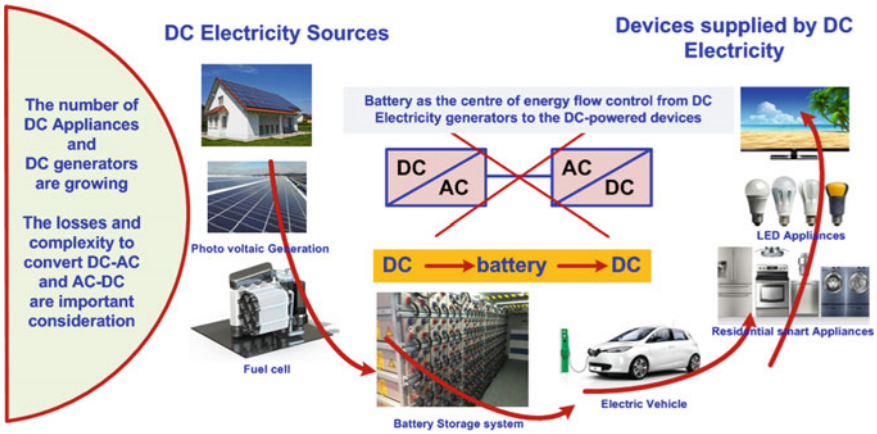

Fig. 9 Distributed microgrid integrated with EES

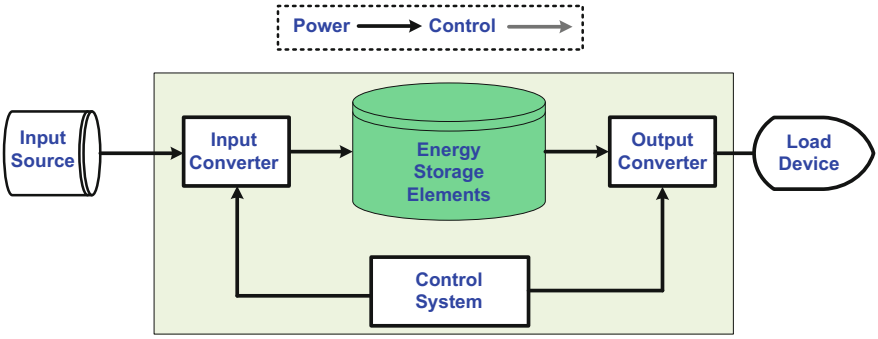

Fig. 10 Typical architecture of EES based system

or source side in AC microgrid. In situations which require smoothening of the load profile and supplying the peak demand, EES is situated at the load side. It performs the function of peak shifting and load leveling whereas it can also mitigate the fluctuations due to renewable generator systems. The configuration of the EES system is also crucial to the systems overall performance. There are mainly two types of configuration for a renewable microgrid

1. Distributed ESS
2. Aggregated ESS

3.2.1 Distributed ESS

Placement of distributed side on the load side or the generator side comes under this particular configuration. Distributed ESS (DESS) on the load side mitigates the load variations and carries out energy management whereas smooth output power is ensured if ESS is installed on the generator side.

Load/Consumer Side DESS

Distributed ESS is smaller in size than an aggregated ESS and hence it can provide less power. Figure 10 illustrates a schematic of load side EES enabled microgrid system. As shown in Fig. 11, the ESS is situated on the consumer side and connected to each local load. ESS is interfaced with a voltage source converter (VSC) which resolves a situation when load suddenly and rapidly changes. The VSC integrates the ESS with the grid network and supplies the necessary power to fulfill the consumer demands. Load leveling technology ensures flattening of load profile which inadvertently decreases the stress on power components (feeder, transformer, etc.).

Generator/Source Side DESS

The primary objective of placing smaller, individual ESS along with each renewable sources/generators is to provide a consistent and smooth flow of power in spite of the variable environmental conditions.

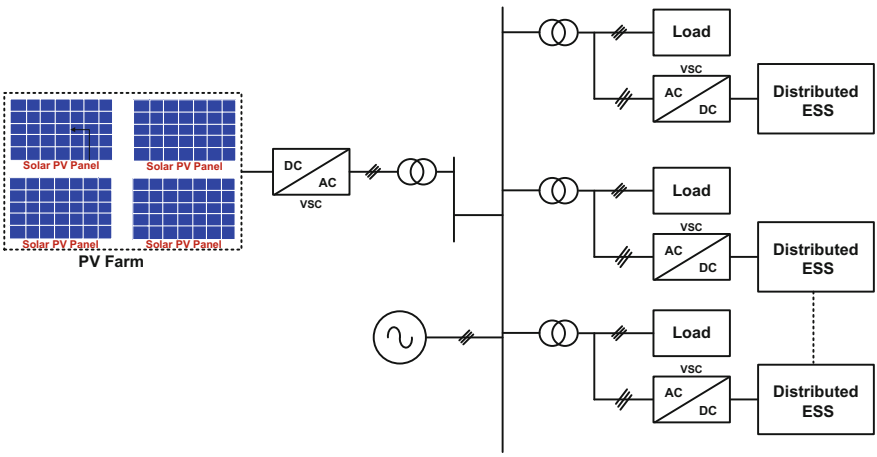

Fig. 11 Typical architecture for load side DESS

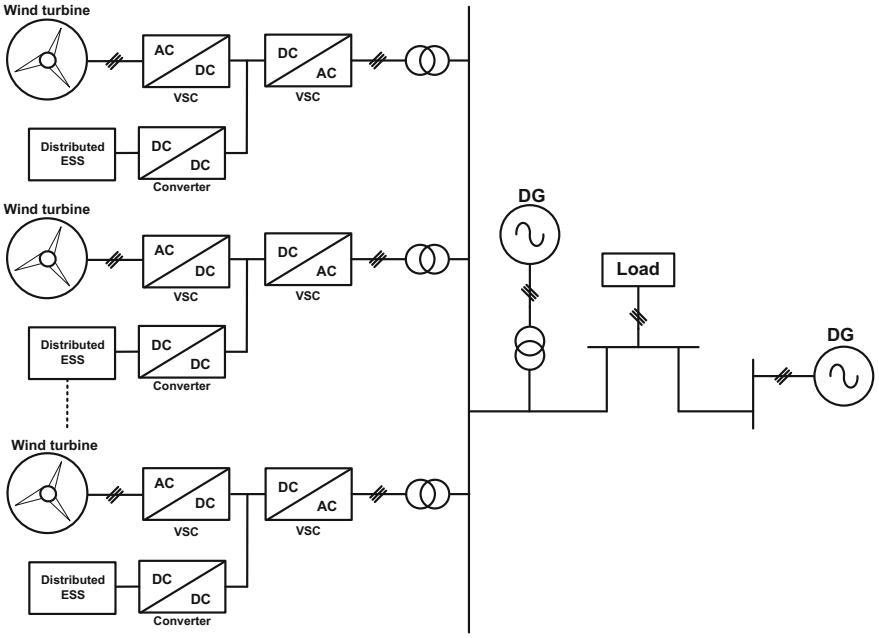

Fig. 12 Typical architecture for generator side DESS

The ESS is connected to the DC link via a dc/dc converter which regulates the voltage and power flow from individual ESS. Such a configuration helps to achieve a constant DC link voltage with less voltage ripple. Improvement in the operation of ac/dc converter is inherent when a stable dc link voltage is attained. Figure 12 shows a general layout of a generator side DESS.

3.2.2 Aggregated ESS

An aggregated ESS is a common feature in many microgrids as it helps in the storage of large amounts of energy dedicated to perform power management and improvement services in the microgrid. It consists of a large number of individual storage units which makes it a reliable source for supplying huge quantities of power. Figure 13 depicts a particular configuration for a solar PV powered microgrid with a battery system as the ESS. Large number of batteries are connected in parallel and interfaced with the grid through a VSC. Such a configuration improves power supply and reliability as the aggregated ESS supplies the excess or deficient power. It was mentioned in [72] that an aggregated ESS is more reliable and economic than a distributed ESS.

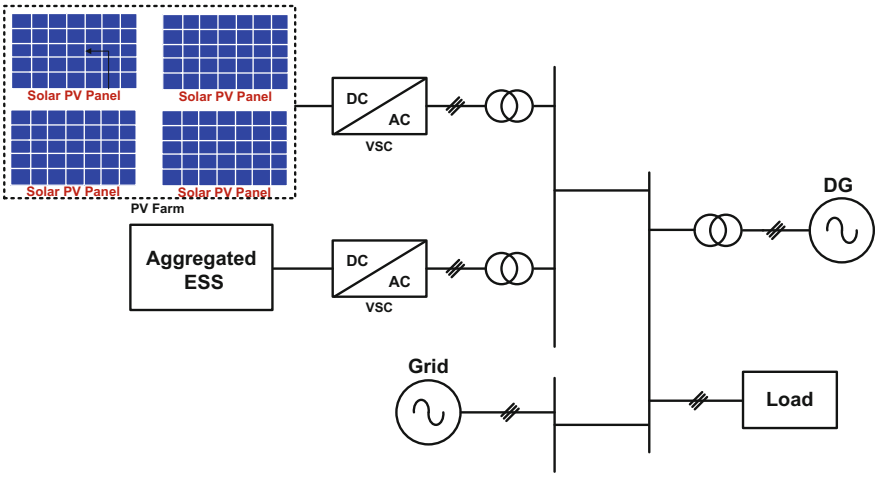

Fig. 13 Typical architecture for aggregated DESS

4 Energy Management Functions

Management of energy is an important aspect of stable and economical operation of a renewable energy based microgrid system. Load leveling and peak shifting are some of the popular energy management functions which help improve power quality and encounter rapid and stochastic load variations. Both peak shifting and load leveling are performed after optimal forecasting of load demand. The major difference between the two lies in the duration of forecasting, i.e., load leveling deals with fluctuations occurring over a short period, whereas, peak shifting is focused on encountering demand variations over a long period, most probably an entire day.

4.1 Peak Shifting

The principle of peaks shifting function is illustrated in Fig. 14. Since the ESS has the capability to act as a load or a generator, therefore a smooth load profile is obtained by filling the valleys (storing energy) and eliminating the peaks (discharging the stored energy).

By long-term forecasting of daily load patterns of a particular region, the EMS provides information to the supervisory controller regarding the required energy during peak hours (18:00–22:00 h). Thus, the ESS stores energy during nonpeak hours (also known as valley period) and provides the stored energy during the peak period.

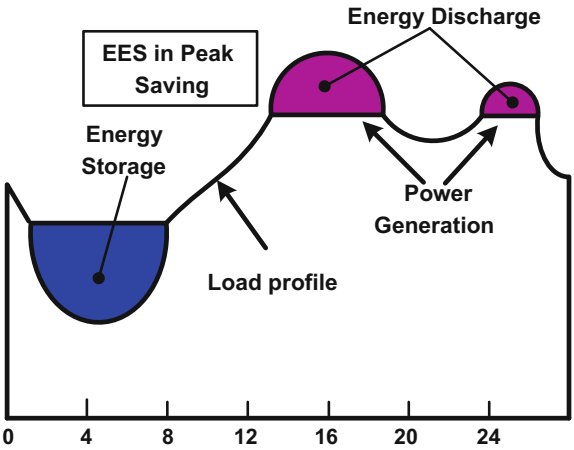

Fig. 14 Concept of peak shaving

Assume that the total power output from power sources during peak time is $P_{S,peak}$ and P_{Si} is the peak power output from the kth generator amongst a total of M sources as shown in Eq. (1).

$$P_{S,peak} = \sum_{k \in M} P_{Si} \tag{1}$$

The total power demand level, P_{load} should be lesser than the combined generated power, $P_{S,peak}$ in order to maintain a generator-load balance. ESS helps reduce the utility load down to the P_{load}. Let us assume that the forecasted load demand for the next day is $P_F(t)$. Subsequently, the energy extracted from the ESS during the peak hours is given by Eq. (2)

$$E_p = \int_{t_{a,p}}^{t_{b,p}} (P_F(t) - P_{load}) dt \tag{2}$$

E_p represents the net energy which should be stored in the ESS during the peak hours. Another way of solving this problem is to find out the net state of charge (SOC) which should be reserved by the ESS before the peak period begins. To calculate the reserved SOC, consider an ESS whose rated energy capacity is E_{rat}, minimum SOC is $SOC_{minimum}$ and reserved state of charge is SOC_{rev}, the following relationship is obtained and shown in Eqs. (3 and 4). The reserved SOC is equal to

$$(SOC_{rev} - SOC_{minimum}).E_{rat} = E_p \tag{3}$$

$$SOC_{rev} = \frac{E_p}{E_{rat}} + SOC_{minimum} \tag{4}$$

It is also necessary that the desired level of load, i.e., P_{load} should follow this particular constraint as shown in Eq. (5).

$$P_{\text{load,max}} - P_{\text{load}} < P_{\text{ESS,max}}, \tag{5}$$

where $P_{\text{load,max}}$ is the maximum power demand on the consumer side whereas $P_{\text{ESS,max}}$ is the maximum power output from ESS.

4.2 Load Leveling

Knowledge of storage capacity and output capabilities of the ESS are precursors to implementing this technique. Let us consider a microgrid which is supplied by M DGs. To calculate the reference power level for ESS, resulting equations of power balance can be written as (neglecting line impedances) shown in Eq. (6).

$$P_{\text{load}} = \sum_{k=1}^{M} P_{\text{DGk}} + P_{\text{O,ESS}} \tag{6}$$

where $\boldsymbol{P_{load}}$ is the actual consumers demand of real power; $P_{\text{O,ESS}}$ is the ESS's output, and P_{DGk} is the generated real power of each DG. To ensure smooth operation of the DG while minimizing economic risks, constant power is extracted from the DGs irrespective of the demand. The reference for the ESS is calculated from Eq. (7).

$$P_{\text{ESSref}} = P_{\text{load}} - P_{\text{Gtotal}} \tag{7}$$

where P_{Gtotal} is the constant power from M DGs. The charging and discharging condition of the ESS can be decided based upon the following conditions:

$$\begin{cases} P_{\text{load}} > P_{\text{Gtotal}}, & \text{Discharging} \\ P_{\text{load}} < P_{\text{Gtotal}}, & \text{Charging} \end{cases} \tag{8}$$

The concept of load leveling has been depicted in Fig. 15 where the variation of load power is illustrated with time with the ESS reference continuously changing as given by Eq. (7).

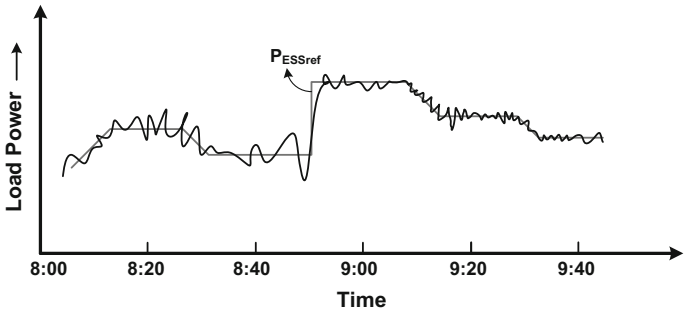

Fig. 15 Concept of load leveling

5 Energy Management via Coordination Control of AC/DC Hybrid Microgrid

Conventional AC power systems have been around for more than 100 years. Efficient and economic transmission of power with full control over the conversion of voltage levels have been its advantage. As discussed in Sect. 1.3, the recent popularization of DC loads such as electric vehicles (EVs) and light-emitting diode (LED) has been integrated into the grid via the ac/dc converter most usually followed by a dc/dc converter. Similarly, for the purpose of reducing CO_2 emissions, renewable energy sources have reemerged as strong contenders for future power sources. Interfacing requires operation and control of dc/dc switched boost converter followed by an inverter (1 or 3 phase). Due to these reasons, DC grids were proposed which eliminates multiple conversions thereby increasing efficiency as explained in depth in Sect. 3.1. These microgrids suffer due to similar reasons when it has to provide power to AC loads. Therefore, it is necessary to develop hybrid microgrids to improve power quality and further enhance the reliability of the grid.

Various AC and DC loads and sources can be connected to the hybrid microgrid reducing multiple conversions. The major concern with hybrid microgrid is the proper operation and control of the grid while ensuring source-load balance. Energy management is attained from coordination control of the various interfacing converters. Coordination control reduces the total power transferred between dc and ac networks, extract maximum power from renewable DERs while maintaining the stability of the grid under dynamic loading conditions and fluctuating supply. The net remaining power of the system, P_{net} is the excessive power which has not been used by the consumers. Development of hybrid microgrid is a step forward to the development of smart grids irrespective of increasing penetration of renewable sources. Figure 16 shows a schematic of a hybrid microgrid. We will deal with the islanded mode of operation of solar PV/wind hybrid microgrid [73] with a battery energy storage system (BESS) since it is the most suitable among all the energy storage technologies discussed in Sect. 2.

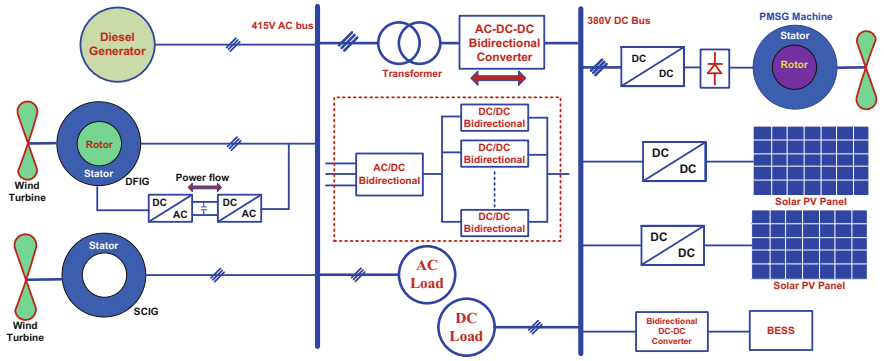

Fig. 16 Generalized block diagram of ac/dc hybrid microgrid

Fig. 17 Equivalent circuit diagram of solar panel [73]

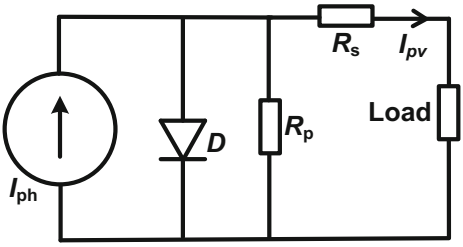

5.1 Grid Configuration

Figure 16 shows the hybrid microgrid and the associated power electronic converters. A wind turbine generator (WTG) such as Double-fed Induction Generator (DFIG) or a Squirrel Cage Induction Motor (SCIG) can be employed. DFIG is connected to the ac bus via ac/dc/ac converter, which supplies power to the rotor side. AC loads are connected to the ac bus of the microgrid. A solar PV module is connected to the dc bus through a dc/dc booster, whereas, the WTG on the dc side is a Permanent Magnet Synchronous Machine (PMSG), which supplies power to the dc bus via a dc/ac converter. A BESS is connected to the dc grid with the help of a bidirectional dc/dc converter which facilitates bidirectional power flow during charging/discharging of the battery. Buck and boost operation are performed during charging and discharging mode respectively. DC loads such as EV are attached to the dc bus. The dc and ac bus are linked together with two, four quadrant ac/dc bidirectional converter.

5.2 Modeling of PV Panel

The equivalent circuit of a PV panel connected with a load is shown in Fig. 17. The current equations are shown in Eqs. (9–11) [74]. Table 4 gives details of the parameters used in these equations.

Table 4 Parameter table for PV panel

Symbol	Description
I_{ph}	Photocurrent
I_{sso}	Short circuit current ($V_o = 0$)
I_{revsat}	Reverse saturation current (at $T = T_r$)
I_{rsatm}	Reverse saturation current of module
A	Ideality factor
q	Charge of an electron
k	Boltzmann constant
R_p	Parallel resistance of PV cell
R_s	Series resistance of PV cell
T_r	Reference temperature
E_{gap}	Band gap energy of silicon
k_{sc}	Temperature coefficient for short circuit current
S	Solar irradiation
T	Cell temperature
n_s	Number of cells connected in series
n_p	Number of cells connected in parallel

$$I_{ph} = (I_{sso} + k_i(T - T_r)).\frac{S}{1000} \tag{9}$$

$$I_{rsatm} = I_{revsat}\left(\frac{T}{T_r}\right)^3 \exp\left(\left(\frac{qE_{gap}}{kA}\right).\left(\frac{1}{T_r} - \frac{1}{T}\right)\right) \tag{10}$$

$$I_{pv} = \left(n_p I_{ph} - n_p I_{rsatm} - \frac{V_{pv}}{R_p}\right) \times \left[\exp\left(\left(\frac{q}{AkT}\right)\left(\frac{V_{pv}}{n_s} + I_{pv}R_s\right)\right) - 1\right] \tag{11}$$

5.3 Modeling of Wind Turbine Generator

The total mechanical power generated from the wind turbine is given by Eq. (12).

$$P_m = 0.5\rho A C_p(\lambda, \beta)v^3 \tag{12}$$

where ρ is the surrounding air density, A is the area swept by the rotor, v is wind velocity, and C_p represents the power coefficient which depends on rotor's pitch angle β and tip speed ratio λ.

The mathematical model of a DFIG is necessary to design a control system. State space model equations for an induction motor in terms of a rotating d-q frame is given in Eqs. (13) and (14).

$$\begin{bmatrix} u_{ds} \\ u_{qs} \\ u_{dr} \\ u_{qr} \end{bmatrix} = \begin{bmatrix} -R_s & 0 & 0 & 0 \\ 0 & -R_s & 0 & 0 \\ 0 & 0 & R_r & 0 \\ 0 & 0 & 0 & R_r \end{bmatrix} \begin{bmatrix} i_{ds} \\ i_{qs} \\ i_{dr} \\ i_{qr} \end{bmatrix} + p \begin{bmatrix} \lambda_{ds} \\ \lambda_{qs} \\ \lambda_{dr} \\ \lambda_{qr} \end{bmatrix} + \begin{bmatrix} -\omega_1 \lambda_{qs} \\ \omega_1 \lambda_{ds} \\ -\omega_2 \lambda_{qr} \\ \omega_2 \lambda_{ds} \end{bmatrix} \tag{13}$$

$$\begin{bmatrix} \lambda_{ds} \\ \lambda_{qs} \\ \lambda_{dr} \\ \lambda_{qr} \end{bmatrix} = \begin{bmatrix} -L_s & 0 & L_m & 0 \\ 0 & -L_s & 0 & L_m \\ -L_m & 0 & L_r & 0 \\ 0 & -L_m & 0 & L_r \end{bmatrix} \begin{bmatrix} i_{ds} \\ i_{qs} \\ i_{dr} \\ i_{qr} \end{bmatrix} \tag{14}$$

DFIG's dynamics for a n_p (No. of poles) pole machine can be expressed by the following Eqs. (15–16)

$$\frac{J}{n_p} \frac{d\omega_r}{dt} = T_{mech} - T_{em} \tag{15}$$

where T_{em} can be expressed by

$$T_{em} = n_p L_m \left(i_{qs} i_{dr} - i_{ds} i_{qr} \right) \tag{16}$$

where subscript q, d, r, and s denote the q-axis, d-axis, rotor, and stator, respectively. L stands for the inductance, λ represents the flux linkage, i and u are the current and voltage, respectively, T_{em} is the electromechanical torque and $\omega_2 = \omega_1 - \omega_r$ where, ω_1 is the angular synchronous speed, ω_r is the rotor speed and ω_2 represents the slip speed. T_{mech} is the mechanical torque. When the synchronous rotating frame is oriented along the direction of the stator voltage vector, it causes the q-axis to align with the reference frame of the stator flux and the d-axis gets aligned with the stator voltage vector. In [75], the following Eq. (17) were derived for such a condition.

$$\begin{aligned} \sigma &= \frac{L_s L_r - L_m^2}{L_s L_r} \\ i_{ds} &= -\frac{L_m}{L_s} i_{dr} \\ u_{qr} &= R_r i_{qr} + \sigma L_r \frac{di_{qr}}{dt} + (\omega_1 - \omega_r)(L_m i_{ds} + L_r i_{dr}) \\ u_{dr} &= R_r i_{dr} + \sigma L_r \frac{di_{dr}}{dt} + (\omega_1 - \omega_r)\left(L_m i_{qs} + L_r i_{qr}\right) \end{aligned} \tag{17}$$

5.4 Modeling of Battery System

The terminal voltage and SOC of a battery can be defined as [76] given below in Eqs. (18, 19)

$$\mathrm{SOC} = 100\left(1 + \frac{\int i_{\mathrm{bat}}\mathrm{d}t}{Q}\right) \tag{18}$$

$$V_{\mathrm{bat}} = V_{\mathrm{oc}} + R_{\mathrm{bat}} i_{\mathrm{bat}} - K\frac{Q}{Q + \int i_{\mathrm{bat}}\mathrm{d}t} + B \cdot \exp\left(A \int i_{\mathrm{bat}}\mathrm{d}t\right) \tag{19}$$

where Q is the capacity of the battery, i_{bat} is the charging current of the battery, V_{oc} is the open circuit voltage of the battery, K is the polarization voltage, A is exponential capacity, and B is exponential voltage.

5.5 Coordination Control of Isolated Hybrid Microgrid

In islanded mode of operation, the main ac/dc bidirectional converter may operate as an inverter to inject active power and maintain the frequency of the grid within operational limits, or it operates as a rectifier to ensure a smooth transfer of power between DC and AC bus. The operation of MPPT control in solar PV and wind energy conversion system is executed by dc–dc converter using P&O algorithm [77]. The ac/dc/ac converter of DFIG and/or dc/dc conventional boost converter may operate in MPPT mode depending on the power balance of the system. Similarly, the bidirectional converter connected to the battery system can operate in discharging or charging mode as per the energy requirement of the system. Power balance equation under the isolated mode of operation of microgrid can be framed as follows shown in Eq. (20)

$$P_{\mathrm{dcL}} + P_{\mathrm{acL}} + P_{\mathrm{loss}} + P_{\mathrm{bat}} = P_{\mathrm{pv}} + P_{\mathrm{wind}} \tag{20}$$

where P_{pv} is PV power, P_{wind} is WTGs power, P_{bat} is the power injected into the battery (during charging), P_{dcL} and P_{acL} are the real power loads which are connected to dc and ac buses respectively, and P_{loss} is the total power loss of grid.

A coordination control scheme based on two levels can be incorporated. The EMS determines the net power of the system, P_{net} and the SOC of battery while following the energy constraints imposed on the system. The system level control is used to determine the operating mode of the converters based on the energy calculations of the EMS whereas, at the local level, each converter is commanded by the EMS. The energy management flowchart is given in Fig. 17. The different cases depicted in the flowchart have been described as follows in Fig. 18.

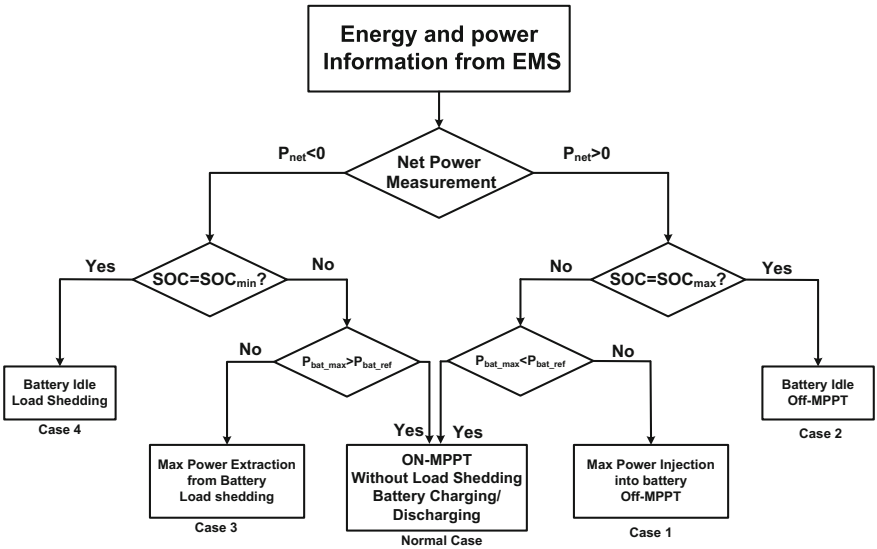

Fig. 18 Flowchart of energy management scheme [73]

Normal Case: The battery converter controls the DC bus voltage in the normal case. BESS can be in charging ($P_{\text{net}} > 0$) or discharging ($P_{\text{net}} < 0$) condition. Solar PV converter operates in MPPT mode to extract maximum power under the operating conditions. There is no load shedding as the generated power is sufficient to satisfy the consumer's needs.

Case 1: In case 1, the battery converter maintains a constant power and misses the DC bus voltage control, which is then regulated by the PV converter in off-MPPT mode.

Case 3: In a condition when net power is below zero, and the battery is discharging at its maximum capacity, the excess load has to be removed. Maximum power extraction from the battery is necessary to bridge the gap between generated and demanded power.

Case 2 and 4: In both the scenarios, the battery converter is idle. In case 2 (off-MPPT mode), the duty ratio of the dc–dc converter is adjusted to regulate DC-link voltage. In case 4, few loads have been disconnected till $P_{\text{net}} \geq 0$.

SOC of the battery is estimated as described in [78] and further, energy constraints are imposed on the battery system as shown in Eq. (21)

$$\text{SOC}_{\min} \leq \text{SOC} \leq \text{SOC}_{\max} \tag{21}$$

i.e., the battery's SOC should not exceed $\text{SOC}_{\max}$ during charging mode and the minimum SOC during discharging should not go below $\text{SOC}_{\min}$. To prevent overheating of the battery, the maximum rate of charging/discharging is shown in Eq. (22).

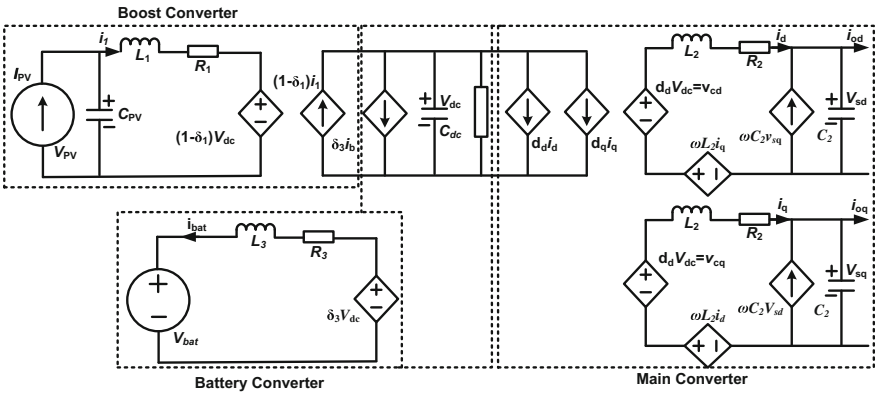

Fig. 19 Time-averaged equivalent circuit of power converters [73]

$$P_{\text{bat}} \leq P_{\text{batmax}} \tag{22}$$

As per the flowchart in Fig. 18, the WTG or PV or both need to operate in off-MPPT mode during Case I or Case II, i.e., when an excess power remains in the grid, $P_{\text{net}} > 0$, then maximum power extraction from either WTG or PV is not required. Tracking of the maximum power point is required when the load requirement cannot be satisfied, and the SOC of the battery is lesser than SOC_{min}. Load shedding is required in the same scenario. Battery converter remains idle in Case 2 and Case 4, operates in charging mode during Case 1, and discharge mode during Case 3. The following conditions shown in Eq. (23) decide the mode of operation:

$$\begin{cases} P_{\text{wind}} - P_{\text{acL}} > 0 & \text{Converter Mode} \\ P_{\text{wind}} - P_{\text{acL}} < 0 & \text{Inverter Mode} \end{cases} \tag{23}$$

Based on the basic circuit theory and principles [79], a time average equivalent circuit of the boost converter, bidirectional battery converter, and main ac/dc bidirectional converter has been presented in Fig. 19. For a rated dc capacitor voltage, V_{dc}, the current (i_{c}) and voltage (V_{D}) dynamics of the dc link capacitor and battery's converter depends on currents exiting from dc (i_{dc}) and ac microgrid (i_{ac}) which can be formulated using Eq. (24).

$$\begin{aligned} V_{\text{D}} - V_{\text{bat}} &= L_3 \cdot \frac{\text{d}i_{\text{bat}}}{\text{d}t} + R_3 i_{\text{bat}} \\ V_{\text{D}} &= V_{\text{dc}} \cdot \delta_3 \\ i_{\text{c}} &= i_1(1-\delta_1) - i_{\text{bat}} \cdot \delta_3 - i_{\text{ac}} - i_{\text{dc}} \\ &= C_{\text{dc}} \cdot \frac{\text{d}V_{\text{dc}}}{\text{d}t} \end{aligned} \tag{24}$$

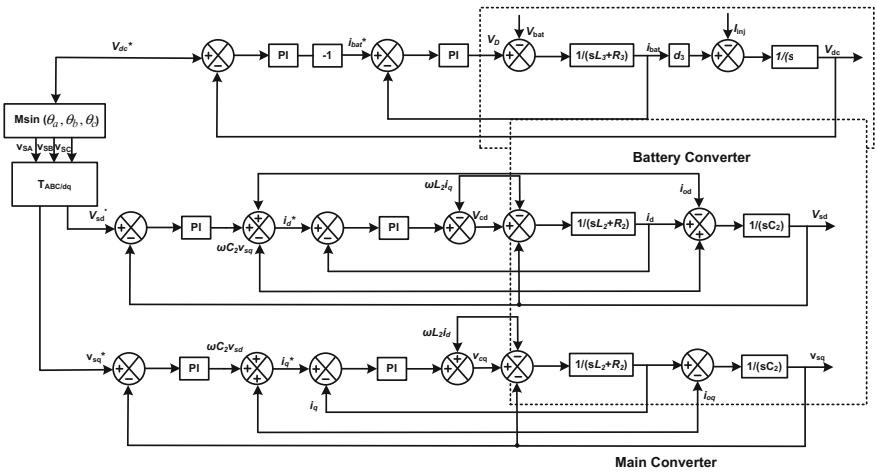

Fig. 20 Control scheme for the normal case [73]

The converter equations for AC side in *d-q* coordinate are given by Eq. (25).

$$C_2 \frac{\mathrm{d}}{\mathrm{d}t} \begin{bmatrix} v_{sd} \\ v_{sq} \end{bmatrix} = \begin{bmatrix} i_d \\ i_q \end{bmatrix} + \begin{bmatrix} 0 & \omega \\ -\omega & 0 \end{bmatrix} \begin{bmatrix} v_{sd} \\ v_{sq} \end{bmatrix} \tag{25}$$

Multi-loop voltage control has been employed for inverter in order to achieve rapid dynamic response without compromising on the power quality of the ac voltage system. The same technique is applied for the control of the main converter when operating in inverter mode. Under the normal conditions, a block diagram of the control technique is shown in Fig. 20. A dual loop control strategy is employed for voltage control of bidirectional battery converter. Battery current, i_{bat}, flowing inside the battery is taken as positive. The current injected into the battery converter is given in Eq. (26).

$$I_{\mathrm{inj}} = i_1(1 - \delta_1) - i_{\mathrm{dc}} - i_{\mathrm{ac}} \tag{26}$$

The output voltage loop is multiplied by −1 so that when V_{dc} decreases due to load transients, the positive error is generated equal to ($V_{\mathrm{dcref}} - V_{\mathrm{dc}}$) which when multiplied by −1 produces a negative battery reference current, i^*_{bat} which leads to discharging of the battery. Similarly, the battery converter transitions into the charging mode.

5.6 Simulation Results

A 500 kWp Solar PV/wind battery storage system enabled three phase AC/DC hybrid microgrid was simulated using PSCAD/EMTDC. The reference voltage for the DC bus was set at 380 V. AC bus was rated at 415 V_{RMS}. Three solar PV panels generated a total of 300 kWp, whereas the WTG system provided 200 kWp. Battery system was rated at 500 kWh, and the maximum power extraction/injection into battery is considered as 300 kWp. Isolated mode of operation was tested using extensive simulation studies. Control strategy block diagram shown in Fig. 19 was implemented for the normal case. The simulation was performed for the normal case, case 1 and case 3. Ideal state operation is also shown in this study, i.e., when $P_{net} = 0$. In-depth analysis of each scenario is discussed below.

5.6.1 Ideal State Operation

Figure 21a shows the threephase voltage waveform at the ac bus. Since the WTG system is the only power source connected to the ac bus, these three-phase voltage waveforms have the same magnitude as the WTG voltage rating, i.e., 415 V_{RMS}. The DC bus voltage is rated for 380 V which is held constant under steady-state condition as exhibited in Fig. 21b. While transferring the power from AC bus to DC bus, the voltage at dc bus must be maintained at 380 V. Figure 21c shows the zoomed view of DC link voltage tracking under steady-state condition.

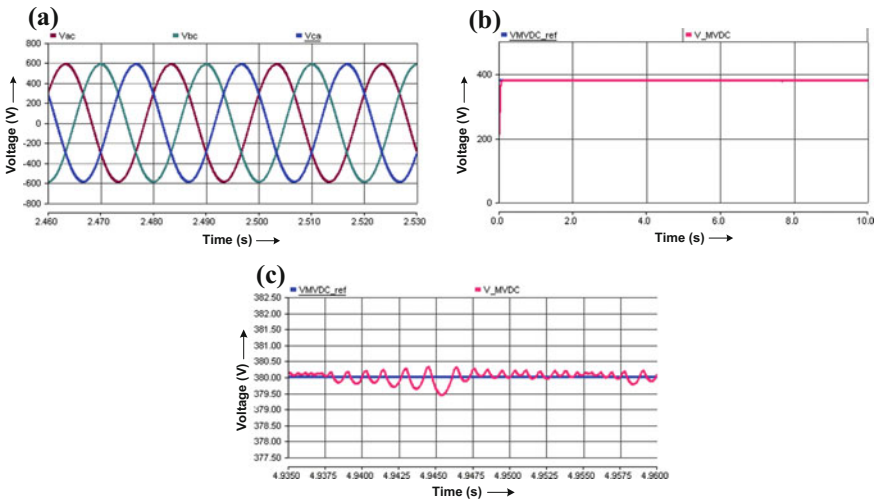

Fig. 21 Simulation results under steady-state operation; **a** 3 phase AC Bus voltage, **b** 380 DC Bus voltage, **c** Zoomed view of DC bus voltage waveform

5.6.2 Normal Case

The normal case represents the situation when there is an excess or deficiency of total power in the system, i.e., either $P_{net} > 0$ or $P_{net} < 0$. In such a case, the battery may either charge (act as a load) or discharge (act as a power generator). Both the scenarios have been taken into consideration. Figure 22a shows the power balance diagram for the condition when generated power is greater than load power. The excess power (net power) is directed to the BESS which starts charging. Since the maximum charging capacity of the battery exceeds the available power, the reference power is set at 220 kW which is effortlessly tracked by the battery. The PV voltage successfully tracks the reference voltage which refers to the power at MPPT as shown in Fig. 22b. The zoomed view of the same has been shown in Fig. 22c.

In the second scenario, when the total load connected to the system is 500 kW and the power generation equals 320 kW only the deficient power is supplied by the battery system as shown in Fig. 22d. Since the maximum power capacity which the battery can discharge exceeds the power requirement, the battery bidirectional converter allows the power to flow to the dc bus of the microgrid. It is to be noted that bidirectional converter plays a major role during the normal case as it stabilizes the dc link voltage whereas the main bidirectional converter which links the ac and dc grid is responsible for regulation of the ac bus voltage.

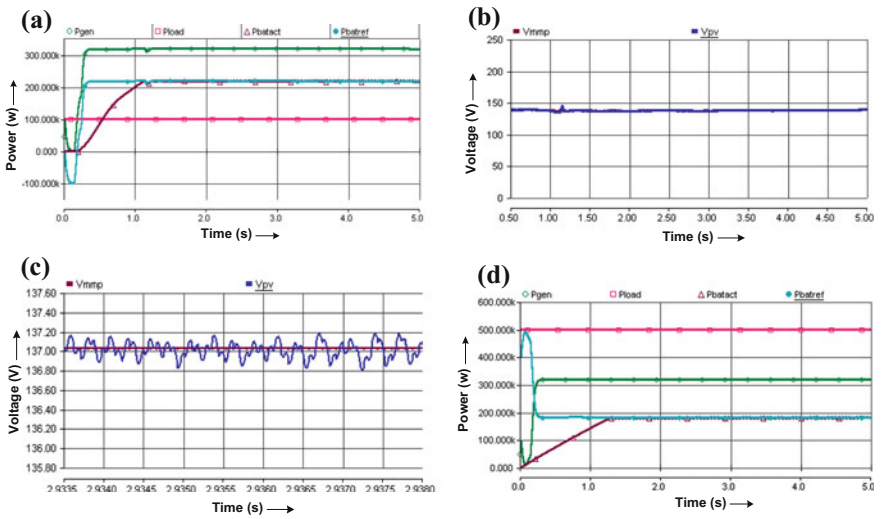

Fig. 22 Simulation results under Normal case; **a** Power graphs of generation, load and EES, **b** Voltage tracking of V_{mmp} and V_{pv}, **c** Zoomed view of voltage tracking of V_{mmp} and V_{pv}, **d** Power graphs of generation, load, and EES

5.6.3 Case 3

In case 3, there an imbalance still exists between the total renewable power generated and load. From Fig. 23a, at $t = 5$ s, the total power suddenly drops from 320 to 180 kW due to environmental conditions. The battery readjusts its output power level to 320 kW, which is the maximum power that can be discharged. Due to this condition, there is insufficient power circulating in the microgrid which causes load shedding as seen in Fig. 23a, when the load power dips to 480 kW. Extending the analysis, there is a slight fluctuation in the wind speed for an extremely short span of time due to which the generated power varies.

In practical systems, there exists a tolerance band between the average rated power capacity and the instantaneous maximum power charged/discharged. This is to prevent users from overloading the battery systems. The same situation is demonstrated in this case where the battery discharges power exceeding the rated capacity by a small amount of 5 kW for a very short span of time. The SOC of the battery is shown in the Fig. 23b. The SOC decreases and the discharging rate increases after $t = 5$ s, which is evident by the slope of the SOC curve which increases suddenly after 5 s.

5.6.4 Case 1

This situation arises when the total power generated becomes greater than the consumers requirements. Figure 24a depicts the case with clarity. The system was operating in the steady-state with total generated power equal to 380 kW. The DC and AC loads consume power equal to 200 kW, and the excess power is utilized to charge the battery system. Suddenly, at $t = 5$ s load is disconnected, and the consumed power decreases to 50 kW. Since the maximum battery charging capacity is 300 kW, an extra 30 kW circulates in the power system. In order to maintain power equilibrium, the on-MPPT operation of solar PV panel is switched to off-MPPT operation. The dc bus voltage is stabilized by the boost converter whereas the main converter supplies the ac bus voltage. Figure 24b shows the SOC which starts increasing. At $t = 5$ s, the rate of charging increases as evident by the increased

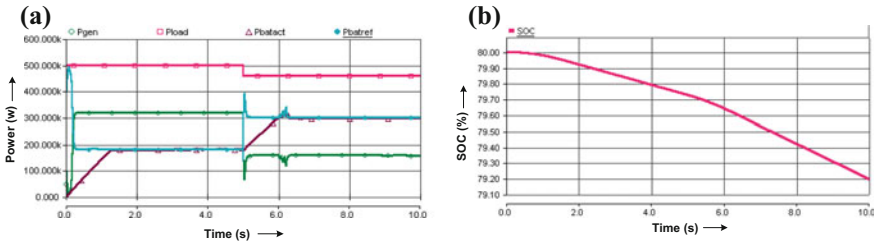

Fig. 23 Simulation results under Case 3; **a** Power graphs of generation, load and EES, **b** SOC graph at case 3

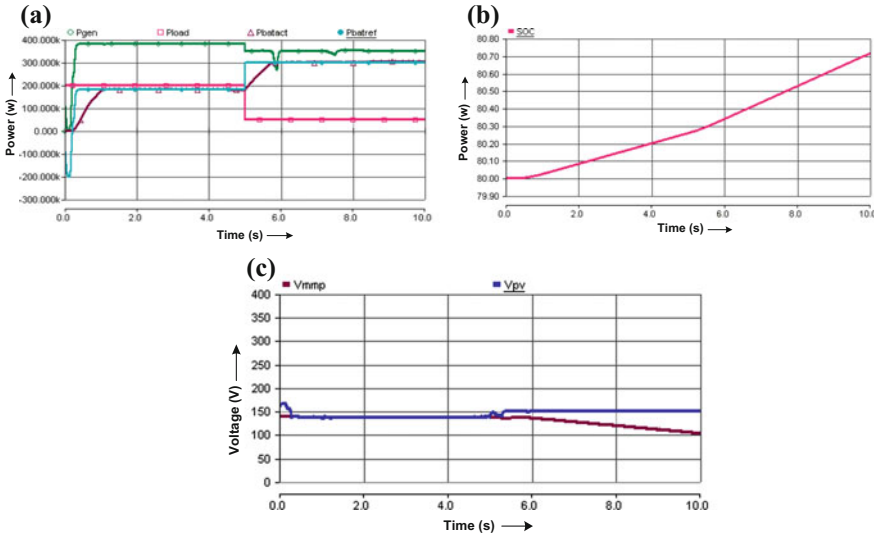

Fig. 24 Simulation results under Case 1; **a** Power graphs of generation, load, and EES, **b** SOC graph at case 2, **c** Voltage tracking of V_{mmp} and V_{pv}

slope of the SOC curve. PV voltage also stops tracking the maximum power point after $t = 5$ s as shown in Fig. 24c.

6 Conclusion

This chapter dealt with the role of electrical energy storage elements in setting up distribution networks in isolated networks, i.e., islands, etc. Various classes of energy storage technologies were described. Merit and demerits of these technologies were discussed, and a comprehensive survey of all the major technologies was discussed. Further, the architectures of ESS, i.e., aggregated ESS and distributed ESS was explained. Aggregated ESS provides better system efficiency as compared to distributed ESS. Various energy management functions such as load leveling and peak shifting were described. Due to an increase of dc loads and to reduce the multiple conversions in a power system to satisfy ac and dc loads, a hybrid microgrid was proposed with DFIG-based wind turbine and solar PV with the battery as the ESS. A 500 kW ac/dc hybrid isolated microgrid was proposed which consisted of a main bidirectional ac/dc convertor which linked the ac and dc bus. AC bus was rated at 415 V while the reference voltage for the dc link capacitor and the dc bus was set at 380 V. Modeling of the PV panel, DFIG system and electrochemical battery was performed. A boost converter was connected to the solar PV panel and operated at MPPT. The DFIG-based WTG system was

integrated with the ac link via ac/dc/ac converter. BESS was connected to the dc bus via a dc/dc bidirectional converter. An energy management control scheme was proposed which ensured proper power balance in the system while coordinating the control of the different converters employed. Different cases were suggested based on the possible scenarios that may arise during operation. Further, a multi-loop voltage control scheme was used to regulate the voltage. Different cases were considered and simulation was performed in PSCAD/EMTDC. The energy management strategy was achieved without compromising on the power quality or reliability of the grid.

References

1. Enerdata (2016) https://yearbook.enerdata.net/world-electricity-production-map-graph-and-data.html. Accessed 15 Aug 2016
2. Nehrir M, Wang C, Strunz K et al (2011) A review of hybrid renewable/alternative energy systems for electric power generation: configurations, control, and applications. IEEE Trans Sustain Energy 2(4):392–403
3. Zubeita LE (2016) Are microgrids the future of energy?: DC microgrids from concept to demonstration to deployment. IEEE Electrif Mag 4(2):37–44
4. Dihrab SS, Sopian K (2010) Electricity generation of hybrid PV/wind systems in Iraq. Renew Energy 35(6):1303–1307
5. Giannakoudis G, Papadopoulos AI, Seferlis P, Voutetakis S (2010) Optimum design and operation under uncertainty of power systems using renewable energy sources and hydrogen storage. Int J Hydrogen Energy 35(3):872–891
6. Islam FR, Mamun KA (2016) Reliability evaluation of power network: a case study of Fiji Islands. In: Australasian Universities power engineering conference (AUPEC-2016), Brisbane, Australia, 25th–28th Sept 2016
7. Chen H, Cong TN, Yang W et al (2009) Progress in electrical energy storage system: a critical review. Prog Nat Sci 19(3):291–312
8. International Electro technical Commission (IEC) (2011) Electrical energy storage: white paper. Technical report. Prepared by electrical energy storage project team. http://www.iec.ch/whitepaper/pdf/iecWP-energystorage-LR-en.pdf. Accessed 15 Aug 2016
9. Molina MG (2010) Dynamic modeling and control design of advanced energy storage for power system applications. In: Brito AV (ed) Dynamic modeling, InTech. Available from: http://www.intechopen.com/books/dynamic-modelling/dynamic-modelling-and-control-design-of-advanced-energy-storage-for-power-system. Accessed 27 Aug 2016
10. Zhao H, Wu Q, Hu S, Xu H, Rasmussen CN (2015) Review of energy storage system for wind power integration support. Appl Energy 137:545–553
11. Farret FA, Simões MG (2006) Integration of alternative sources of energy. Wiley, USA
12. Arepalli S, Fireman H, Huffman C et al (2005) Carbon-nanotube-based electrochemical double-layer capacitor technologies for spaceflight applications. JOM 57:26–31
13. González FD, Sumper A, Bellmunt OG, Robles RV (2012) A review of energy storage technologies for wind power applications. Renew Sustain Energy Rev 16:2154–2171
14. Smith SC, Sen PK, Kroposki B (2008) Advancement of energy storage devices and applications in electrical power system. Paper presented at: 2008 IEEE power energy society general meeting—conversion and delivery of electrical energy in the 21st century, IEEE, 20–24 July 2008
15. Ibrahim H, Ilinca A, Perron J (2008) Energy storage systems—characteristics and comparisons. Renew Sust Energy Rev 12:1221–1250

16. Abbey C, Joos G (2005) Energy management strategies for optimization of energy storage in wind power hybrid system. Paper presented in proceedings of the 36th IEEE power electronics specialists conference, 16 June 2005
17. Kusko A, DeDad J (2005) Short-term, long-term, energy storage methods for standby electric power systems. Paper presented at: fourtieth IAS annual meeting. Conference record of the 2005 industry applications conference, 2005, vol 4, IEEE, New York. 2–6 Oct 2005
18. Zhai Y, Dou Y, Zhao D et al (2011) Carbon materials for chemical capacitive energy storage. Adv Mater 23:4828–4850
19. Xu C, Xu B, Gu Y et al (2013) Graphene-based electrodes for electrochemical energy storage. Energy Environ Sci 6:1388
20. Liu Q, Nayfeh MH, Yau S-T (2010) Supercapacitor electrodes based on polyaniline–silicon nanoparticle composite. J Power Sources 195:3956–3959
21. Sharma P, Bhatti TS (2010) A review on electrochemical double-layer capacitors. Energy Convers Manag 51:2901–2912
22. Zhang W, Qiu M, Lai X (2008) Application of energy storage technologies in power grids. Power Syst Technol 32
23. Maxwell ultracapacitors (2014). Maxwell technologies. http://www.maxwell.com/products/ultracapacitors/docs/uc_overview_flyer.pdf. Accessed 27 Aug 2016
24. CAP-XX supercapacitors product guide 2013. CAP-XX Ltd. [Online]. Available at: http://www.cap-xx.com/products/products.php. Accessed 14 Aug 2014
25. Cheung KYC, Cheung STH, Silva N et al (2007) Large-scale energy storage systems, Imperial College London, ISE2 2002/2003, Available online: http://www.homes.doc.ic.ac.uk/~matti/ise2grp/. Accessed 20 Aug 2016
26. Akhil A, Zaininger H, Hurwitch J, Badin J (1993) Battery energy storage: a preliminary assessment of national benefits. Sandia Report, SAND93-3900, UC-212. Accessed 25 Aug 2016
27. Schainker RB (2004) Executive overview: energy storage options for a sustainable energy future. Paper presented at the IEEE power engineering society general meeting, 6–10 June 2014
28. Beaudin M, Zareipour H, Schellenberglabe A, Rosehart W (2010) Energy storage for mitigating the variability of renewable electricity sources: an updated review. Energy Sustain Dev 14:302–314
29. Koshizuka N, Ishikawa F, Nasu H (2003) Progress of superconducting bearing technologies for flywheel energy storage systems. Phys C 386:444–450
30. Waghorne WE (2001) Viscosities of electrolyte solutions. Philos Trans Roy Soc A Math Phys Eng Sci 359:1529–1543
31. Zhang W, Qiu M, Lai X (2008) Application of energy storage technologies in power grids. Power Syst Technol 32
32. Shoenung SM (2001) Characteristics and technologies for long- vs. short-term energy storage: a study by the DOE energy storage systems program. Technical report. SAND2001-0765. Sandia National Laboratories. United States Department of Energy. Accessed 13 Aug 2016
33. Kondoh J, Ishii I, Yamaguchi H, Murata A et al (2000) Electrical energy storage systems for energy networks. Energy Convers Manag 41:1863–1874
34. International Renewable Energy Agency (2012) Electricity storage: technology brief. Technology Policy Brief, Energy Technology Systems Analysis Programme. http://www.irena.org/DocumentDownloads/Publications/IRENATSAP%20Tech%20Brief%20E18%20Electricity-Storage.pdf. Accessed 28 Aug 2016
35. Hawaiian Electric Company (2016) Clean energy—issues and challenges—energy storage. http://www.heco.com/heco/Clean-Energy/Issues-and-Challenges/Energy-Storage. Accessed 24 Aug 2016
36. Bollen MH , Hassan F (2011) Integration of distributed generation in the power system. IEEE Press Series on Power Engineering, vol 80. Wiley, London
37. Finkenrath M, Pazzi S, Ercole MD' et al (2009) Status and technical challenges of advanced Compressed Air Energy Storage (CAES) technology. In: Int. workshop on environment and

alternative energy. http://www.c3p.org/Workshop%202009/Presentations/Renewable%20and%20Alternative%20Energy%20Systems/Matthias%20Finkenrath_Challenges%20Advanced%20Compressed%20Air%20Energy%20Storage%20Technology.pdf. Accessed 26 Aug 2016
38. Hadjipaschalis I, Poullikkas A, Efthimiou V (2009) Overview of current and future energy storage technologies for electric power applications. Renew Sustain Energy Rev 13:1513–1522
39. McDowall J (2006) Integrating energy storage with wind power in weak electricity grids. J Power Sources 162:959–964
40. Rastler D (2010) Technical report-Electric Power Research Institute (EPRI). Electricity energy storage technology options: a white paper primer on applications, costs, and options. http://large.stanford.edu/courses/2012/ph240/doshay1/docs/EPRI.pdf. Accessed 30 Aug 2016
41. Saft Batteries (2014) Energy storage & renewables overview, solutions and customer case studies. http://www.saftbatteries.com/market-solutions/energy-storage-renewables. Accessed 29 Aug 2016
42. Rydh CJ, Sanden BA (2005) Energy analysis of batteries in photovoltaic systems—part II: energy return factors and overall battery efficiencies. Energy Convers Manage 46:1980–2000
43. Beck F, Rüetschi P (2000) Rechargeable batteries with aqueous electrolytes. Electrochim Acta 45:2467–2482
44. Kawakami N, Iijima Y, Fukuhara M et al (2010) Development and field experiences of stabilization system using 34 MW NAS batteries for a 51 MW wind farm. Paper presented at 2010 IEEE international symposium on industrial electronics, 4–7 July 2010
45. Moghaddam MP, Haghifam MR, Yousefi GR (2009) Electric energy storage systems in a market-based economy: comparison of emerging and traditional technologies. Renew Energy 34:2630–2639
46. Kaldellis JK, Zafirakis D (2007) Optimum energy storage techniques for the improvement of renewable energy sources-based electricity generation economic efficiency. Energy 32:2295–2305
47. Beaudin M, Zareipour H, Schellenberglabe A, Rosehart W (2010) Energy storage for mitigating the variability of renewable electricity sources: an updated review. Energy Sustain Dev 14:302–314
48. Barote L, Weissbach R, Teodorescu R, Marinescu C, Cirstea M (2008) Stand-alone wind system with vanadium redox battery energy storage. Paper presented at 2008 11th IEEE international conference on optimization electrical and electronic equipment, 22–24 May 2008
49. Gonzalez A, Gallachóir B. Ó', McKeogh E, Lynch K (2004) Study of electricity storage technologies and their potential to address wind energy intermittency in Ireland. Final report. http://www.sei.ie/uploadedfiles/FundedProgrammes/REHC03001FinalReport.pdf. Accessed 19 Aug 2016
50. de León CP, Ferrer AF, García JG, Szánto DA, Walsh FC (2006) Redox flow cells for energy conversion. J Power Sources 160:716–732
51. Li P (2008) Energy storage is the core of renewable technologies. IEEE Nanotechnol Mag 2:13–18
52. Pistoia G (2010) Electric and hybrid vehicles: power sources, models, sustainability, infrastructure and the market. Elsevier, The Netherlands
53. Electricity Storage Association (ESA) (2013) Electricity storage technology comparison. http://www.electricitystorage.org/technology/storage_technologies/technology_comparison. Accessed 22 Aug 2016
54. Lin FC, Dai X, Xu ZA, Li J, Zhao ZG (2003) High density capacitors. High Power Laser Part Beams 1:94–96
55. Arepalli S, Fireman H, Huffman C et al (2005) Carbon-nanotube-based electrochemical double-layer capacitor technologies for spaceflight applications. JOM 57:26–31
56. Winter M, Brodd RJ (2004) What are batteries, fuel cells, and supercapacitors? ChemRev 104:4245–4270

57. Emerson network power (2014) Capacitors age and capacitors have an end of life: a white paper from the experts in business-critical continuity. http://www.emersonnetworkpower.com/documentation/enus/brands/liebert/documents/white%20papers/sl-24630.pdf. Accessed 27 Aug 2016
58. R.J. Miller (2010) Capacitors for power grid storage—multi-hour bulk energy storage using capacitors. Technical presentation at: trans-atlantic workshop on storage technologies for power grids, Washington, 19–20 Oct 2010
59. Masaud M, Keun L, Sen PK (2010) An overview of energy storage technologies in electric power systems: what is the future? Paper presented at proceedings of North American power symposium (NAPS), 26–28 Sept 2010
60. Ribeiro PF, Johnson BK, Crow ML, Arsoy A, Liu Y (2001) Energy storage systems for advanced power applications. Proc IEEE 89(12):1744–1756
61. Baxter R (2006) Energy storage: a nontechnical guide. PennWell Books, USA
62. Fuel Cell Energy Inc. (2012). Construction of world's largest fuel cell park expected to commence in 2012. http://www.fuelcelltoday.com/news-archive/2012/october/construction-of-worlds-largest-fuel-cell-power-plant-expected-to-commence-in-2012. Accessed 23 Aug 2016
63. Electric Fuel Ltd (2014) Electric fuel introduces practical, zero-emission transportation. http://www.electric-fuel.com/evtech/ef-tech-brochure.pdf. Accessed 16 Aug 2016
64. Smith W (2000) The role of fuel cells in energy storage. J Power Sources 86:74–83
65. Schaber C, Mazza P, Hammerschlag R (2004) Utility-scale storage of renewable energy. Electr J 17:21–29
66. Andrepont SJ (2012) Energy storage—thermal energy storage coupled with turbine inlet cooling. In: 14th annual electric power conference & exhibition. http://www.turbineinletcooling.org/resources/papers/Andrepont_2012EP.pdf. Accessed 17 Aug 2016
67. U.S. Energy Storage Association (2016) Liquid Air Energy Storage (LAES). http://energystorage.org/energy-storage/technologies/liquid-air-energy-storage-laes. Accessed 30 Aug 2016
68. Liquid air energy network forms in UK: focus on transportation and energy storage (2013) http://www.greencarcongress.com/2013/05/laen-20130509.html. Accessed 30 Aug 2016
69. Taylor P, Bolton R, Stone D et al (2012) Pathways for energy storage in the UK. Technical report. Centre for low carbon futures. http://www.lowcarbonfutures.org/reports/research-reports?page=1. Accessed 22 Aug 2016
70. Gent E (2013) Liquid air energy storage could become £1bn industry. The Institution of Engineering and Technology (IET) Engineering and Technology (E&T) Magazine
71. Highview power storage: secure, clean power. Highview Power; 2011
72. Wei L, Joos G (2007) Performance comparison of aggregated and distributed energy storage systems in a wind farm for wind power fluctuation suppression. Paper presented at Power engineering society general meeting. IEEE, Tampa, FL, USA, 24–28 June 2007
73. Liu X, Wang P, Loh PC (2011) A hybrid AC/DC microgrid and its coordination control. IEEE Trans Smart Grid 2(2):278–286
74. Chao KH, Li CJ, Ho SH (2008) Modeling and fault simulation of photovoltaic generation systems using circuit-based model. Paper presented at proceedings of IEEE international conference on sustainable energy technologies, 24–27 Nov 2008
75. Zhi DW, Xu L (2007) Direct power control of DFIG with constant switching frequency and improved transient performance. IEEE Trans Energy Convers 22(1):110–118
76. Tremblay O, Dessaint LA, Dekkiche AI (2007) A generic battery model for the dynamic simulation of hybrid electric vehicles. Paper presented at proceedings of IEEE vehicle power propulsion conference, 9–12 Sept 2007
77. Kumar AVP, Parimi AM, Rao KU (2015) Implementation of MPPT control using fuzzy logic in solar-wind hybrid power system. Paper presented at IEEE international conference on signal processing, informatics, communication and energy systems (SPICES), Kozhikode, 19–21 Feb 2015

78. Kutluay K, Cadirci Y, Ozkazanc YS, Cadirci I (2005) A new online state-of-charge estimation and monitoring system for sealed lead-acid batteries in telecommunication power supplies. IEEE Trans Ind Electron 52(5):1315–1327
79. Hwan KK, Joo PN, Seok HD (2005) Advanced synchronous reference frame controller for three-phase UPS powering unbalanced and nonlinear loads. Paper presented at 36th IEEE proceedings of power electronics specialists conference, 16 June 2005

Frequency Stability Improvement in Weak Grids by Storage Systems

Gianpaolo Vitale

Abstract This chapter is focused on the improvement of the frequency stability in weak grids by advanced storage systems interfaced with power converters. Weak grids suffer of a reduced inertia of the rotating generators; this increases the variations of the frequency due to large variations of the load. The frequency collapse can be avoided by the automatic load shedding (ALS) disconnecting some loads but it causes consequences on the economic activities and service continuity. Moreover, since the rapid increase of the use of renewable energy systems (RES) with wind and photovoltaic (PV) generation plants connected to the grid reduces the inertial response, in perspective it could represent a potential limit to the maximum penetration of RES and to their inherent benefits in terms of greenhouse and dependence from fossil fuel resources reduction. After a discussion on the frequency variation issues in presence of PV and wind generation systems, the use of storage systems for dynamic grid support is analyzed. Simulations show the frequency drop caused by a reduced inertia and the benefits of the adoption of storage systems to perform a dynamic support. The specific power converters for storage systems grid interfacing are studied with reference to Superconducting Magnetic Energy Storage (SMES), flywheels energy storage (FES), supercapacitors and batteries. Finally some case studies are presented.

Keywords Smart grid · Frequency control · Isolated power systems · Power system dynamic stability · Solar power generation · Wind power generation · Storage systems

List of Acronyms

ALS	Automatic Load Shedding
ASE	Aggregated Swing Equation
BESS	Battery Energy Storage Systems

G. Vitale (✉)
National Research Council of Italy (CNR), Institute of Intelligent Systems for Automation (ISSIA), Via Dante n. 12, 90141 Palermo, Italy
e-mail: gianpaolo.vitale@cnr.it

F.M.R. Islam et al. (eds.), *Smart Energy Grid Design for Island Countries*, Green Energy and Technology, DOI 10.1007/978-3-319-50197-0_8

CSC	Current Source Converter
DESS	Distributed Energy Storage System
DFCS	Dynamic Frequency Control Support
ELDC	Electrochemical Double Layer Capacitors
FESS	Flywheels Energy Storage Systems
KESS	Kinetic Energy Storage Systems
PV	Photovoltaic
RES	Renewable Energy Systems
ROCOF	Rate Of Change Of Frequency
PMSM	Permanent Magnet Synchronous Machine
SVM	Space Vector Modulation
UCTE	Union for the Coordination of the Transmission of Electricity
SCES	Supercapacitors Energy Storage Systems
SHM	Synchronous Homopolar Machines
SRM	Synchronous Reluctance Machines
SMES	Superconducting Magnetic Energy Storage
TSO	Transmission System Operators
VSC	Voltage Source Converter
VSI	Voltage Source Inverter

1 Introduction

In general, in a power electric energy generation-transmission-distribution system in steady-state conditions a balance between the power required by loads and the power supplied by rotating generators occurs. In this case, rotating generators are characterized by constant speed to assure the grid frequency rated value, they supplies a constant torque so that the product torque-speed at the shaft balances the grid losses and the power required by loads. In case of sudden load variation or outage, the imbalance between the power required by loads and the one delivered by rotating generator causes a transient in which its torque is not balanced with a consequent variation of the speed and of the grid frequency [1, 2].

This problem, known as the frequency control, depends strictly from the inertia of the rotating generator. The greater is the inertia the smaller will be the variation of the frequency for given load variation. In other words, the mechanical inertia of the generator represents a reserve of energy that can be used to minimize the variations of the frequency. Obviously, the inertia cannot be arbitrarily large for many reasons including the cost of the plant and the cost of produced energy.

The frequency control problem is a challenge in isolated power systems or in electrical islands where the relatively low inertia can cause very fast changes in rotating speed of the generators after any sudden imbalance between production and

demand [3, 4]. This chapter is focused on the use of advanced storage systems INTERFACED by power converters to improve the frequency stability in weak grids.

In order to restore the power equilibrium, the conventional technologies used for power generation are not always capable of responding so quickly to prevent an unacceptable drop of the grid frequency in such cases when the available amount of frequency control reserve exceeds the power deviation. As a consequence the frequency collapse is avoided by the automatic load shedding (ALS); in this way some loads are disconnected causing consequences, among others, on the economic activities and service continuity.

In this framework, another factor is making critical the frequency stability; as a matter of fact the rapid increase of the use of renewable energy systems (RES) with wind and photovoltaic (PV) generation plants connected to the grid does not provide a sufficient inertial response (even if the inertia of some wind generators could be exploited) and tends to modify the transient of frequency response of the energy system. This could imply a limit to the maximum penetration of RES limiting their inherent benefits in terms of clean energy production [1].

A solution is to provide the grid with supplementary inertia that can be obtained by extra rotating masses or virtually by electronic coupled sources suitably controlled to reproduce the effects of rotational inertia of conventional rotating generators. In this case the virtual inertia is obtained by storage systems which supply a grid connected power converter. The storage systems that can be used providing similar dynamic performance are ultracapacitors or supercapacitors, flywheels and batteries [5]. Figure 1 shows a set of scenarios; in particular, a steady-state situation with a balance between demand and produced power is illustrated in Fig. 1a, the increase of power demand in which the frequency collapse is avoided by the ALS is shown in Fig. 1b, c shows how the frequency collapse is avoided by virtual inertia provided by storage systems, finally in Fig. 1d is sketched a steady state situation in which the energy balance is provided by renewable sources and conventional rotating generators whose reduced mechanical inertia is virtually increased by storage systems connected to the grid.

These systems realize a distributed energy storage system (DESS) able to offer an interesting alternative to improve the frequency control by realizing a dynamic frequency control support (DFCS) with sharing of renewables. Some practical realizations of DFCSs have shown a response time of about tens of milliseconds making the feature of this advanced service very promising to tackle both generation outage and sudden load variation especially in isolated power systems. The virtual inertia provided by DESS appears promising to replace the mechanical inertia of rotating generators in a future in which wind and PV generation will be more and more spread.

The chapter is organised as follows: Sect. 2 deals with the frequency control steps, an analytical study of the frequency transients by the swing equation and its implementation results are given in Sects. 3 and 4 is focused on wind and PV generation issues in weak grids, in Sect. 5 the storage systems for dynamic grid

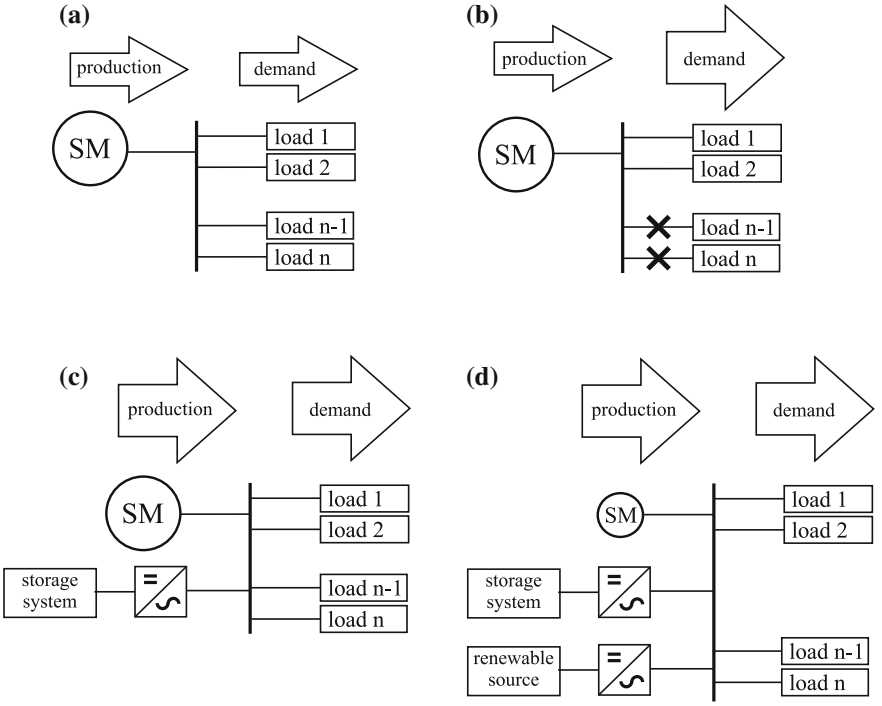

Fig. 1 **a** Steady-state situation with balance between demand and produced power, **b** transient in which the frequency collapse is avoided by the Automatic Load Shedding, **c** transient in which the frequency collapse is avoided by virtual inertia provided by storage systems, **d** steady-state situation in which the energy balance is provided by renewable sources and the reduced mechanical inertia of the rotating generator is virtually increased by storage systems connected to the grid

support are analysed whereas Sect. 6 is devoted to power converters for storage system grid interfacing, finally some practical applications of DESS to support frequency stability in weak grids are described in Sect. 7.

2 Frequency Control Issues

The balance between the active power produced and consumed is crucial for the frequency maintenance. The frequency control is performed by the energy reserve available to lessen the variation of the frequency. This energy is called frequency control reserve. The frequency control reserve is positive if it has to compensate the frequency drop. A negative value of frequency control reserve helps to diminish the frequency.

Three different levels of control are recognizable to assure the balance between the generated energy and the energy required by loads: (a) primary frequency control, (b) secondary frequency control, (c) tertiary frequency control.

2.1 Primary Frequency Control

The primary frequency control is a local automatic control aiming to match the balance of the active power to counteract the frequency deviations. It operates both on the active power supplied by rotating generators and on the consumption of controllable loads. Its role is crucial for the stability of the power system to stabilize the frequency in case of load outage or large generation. All the generators that are located in a synchronous zone are fitted with a speed governor which performs this control automatically. The demand side also participates in this control by the self-regulating effect of frequency-sensitive loads such as induction motors [6, 7] or connecting/disconnecting some load by the action of frequency-sensitive relays set-up with a given frequency threshold.

The action of the primary frequency control is subject to some constraints. First of all, an increase of the delivered energy to face the frequency drop can be maintained only for a relatively short time and must be replaced before it runs out. Secondly it is preferable that this increase of power is distributed across the network to minimize the power transit and to enhance the security of the system in particular for a large generation outage. Finally the uniform repartition helps the stability of islanded systems in case of a power system separation.

2.2 Secondary Frequency Control

The secondary frequency control aims to bring the frequency back to the target value. It is a centralized automatic control as well. Whereas the primary frequency control limits the frequency deviations, the secondary frequency control adjusts the power production of the generating units located in the area of imbalance. Usually the loads do not participate to this control.

The secondary frequency control is not indispensable, some power systems prefer to regulate the frequency by the primary frequency control and the manual tertiary frequency control. Anyway it is adopted in all large interconnected systems since the manual action could be not sufficient to quickly remove overloads.

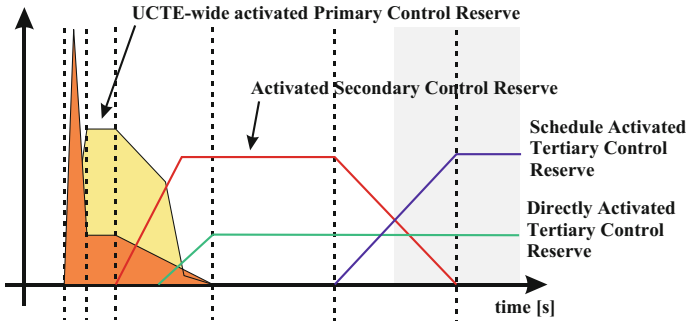

Fig. 2 Scheduling of the control reserve

2.3 Tertiary Frequency Control

The tertiary frequency control is based on manual changes in the dispatching and commitment of generating units. Several tasks can be performed as, for example, the congestions managing in the transmission network and to bring the frequency and the interchanges back to their target value when the secondary control is absent or unable to perform this task [2].

The principle of frequency deviation and subsequent activation of reserves is illustrated in Fig. 2 by a frequency versus time diagram: the primary control action starts within seconds as a joint action of all parties involved; the secondary control replaces primary control over minutes, it is put into action by the responsible parties/transmission system operators (TSOs) only; then the tertiary control partially complements and finally replaces the secondary control by re-scheduling generation, it is put into action by the responsible parties/TSOs [8]. Finally, the global time deviations of the synchronous time is corrected by the time control in the long term as a joint action of all parties/TSOs.

3 Transient Frequency Response of Power Systems

The transient response depends on the kinetic energy stored in the rotating masses, it can be calculated as:

$$E_{\text{kin}} = \frac{1}{2} J(\omega_m)^2 = \frac{1}{2} J(2\pi f_m)^2 \tag{1}$$

where J is the moment of inertia of the synchronous machine and ω_m is the rotating pulsation corresponding to the rotating frequency f_m. On the basis of the kinetic energy, the inertia constant H is defined by the ratio of the kinetic energy and the rated power of the generator S_B.

$$H = \frac{E_{\text{kin}}}{S_B} = \frac{J(2\pi f_m)^2}{2S_B} \tag{2}$$

The inertia constant H gives the time duration during which the machine is able to supply its rated power solely with its stored kinetic energy. Typical values for H are in the range from 2 to 10 s.

The inertial response of the synchronous generator, in terms of variation of rotational frequency f_m due to a power imbalance, is described by the well-known swing equation:

$$\frac{\partial}{\partial t} E_{\text{kin}} = J(2\pi)^2 f_m \frac{\partial}{\partial t} f_m = \frac{2HS_B}{f_m} \frac{\partial}{\partial t} f_m = (P_m - P_e) \tag{3}$$

where P_m is the mechanical power supplied by the generator and P_e is the electric power demand.

Considering that the frequency variations are expected to be small around the reference value f_0, the rotational frequency f_m can be substituted with f_0 and the mechanical power P_m with $P_{m.o}$ corresponding to the set point. Equation (3) becomes:

$$\frac{\partial}{\partial t} f_m = \frac{f_o}{2HS_B} (P_{m.o} - P_e) \tag{4}$$

Finally, defining D_{load} as the frequency-dependent load damping constant (defined alternatively as $k_{\text{load}} = 1/D_{\text{load}}$), Eq. (4) can be completed taking into account a self-stabilizing property of power systems:

$$\frac{\partial}{\partial t} f_m = -\frac{f_o}{2HS_B D_{\text{load}}} + \frac{f_o}{2HS_B} (P_{m.o} - P_e) \tag{5}$$

The higher the inertia constant H, the slower and more benign are frequency dynamics, it correspond to smaller frequency deviations f_m and its derivative for identical load variations.

It must be remarked that the increasing penetration of RES connected to the grid by inverter power units implies two main consequences: (1) the rotational inertia of power systems is gradually reducing; (2) highly time-variant systems shares are fluctuating heavily throughout the year.

In case of energy coming from PV plants the inertia constant is null whereas in case of energy generated by wind plants variable-speed wind turbines could supply synthetic inertia thanks to a supplementary loop in their control system by exploiting the rotating masses which makes this response close to the one of conventional plants [9]. A way to provide a virtual inertia to a PV plant consists in including a sufficient energy stored in the power conversion chain [10, 11]. This is notably a concern for small power networks as island or micro grids in which the expected generation by RES makes frequency stabilization more difficult.

In case of interconnected power systems, in which different aggregated generators and load nodes are connected via tie-lines, Eq. (5) can be rewritten for n generators, j loads and k connected tie-lines giving the Aggregated Swing Equation (ASE) [4]:

$$\frac{\partial}{\partial t} f_m = -\frac{f_o}{2HS_B D_{\text{load}}} + \frac{f_o}{2HS_B}(P_{m.o} - P_e - P_{\text{loss}}) \tag{6}$$

With:

$$\begin{cases} f = \dfrac{\sum_i H_i S_{B,i} f_i}{\sum_i H_i S_{B,i}}; & S_B = \sum_i S_{B,i}; & H = \dfrac{\sum_i H_i S_{B,i}}{S_B}; \\ P_m = \sum_i P_{m,i}; & P_{\text{load}} = \sum_i P_{\text{load},i} & P_{\text{loss}} = \sum_i P_{\text{loss},i}. \end{cases}$$

A simulation of a typical transient of the frequency after a sudden large loss of generation is sketched in Fig. 3. The system is in steady state with frequency equal to f_o until the time t_1 = 1 s. During the time interval between time t_1 and t_2 (of the order of seconds) primary control reserve is activated by the frequency variation and restores the power equilibrium by drawing power from the energy reserve in terms of the rotating masses of the remaining generation units and the frequency drop to the minimum value. After the time t_2 and till the time t_3 a new steady state condition is reached at frequency f_∞. Usually t_3 is of the order of minutes (in Fig. 3 it has been lessened for the sake of clarity).

It can be noted that, in case the primary reserve is not sufficient or if the compensation is too slow, the ALS must be activated. In this case some under-frequency relays placed in HV/MV substations partition the system loads. They are gradually activated when the frequency reaches preset thresholds allowing the power balancing to be restored [1].

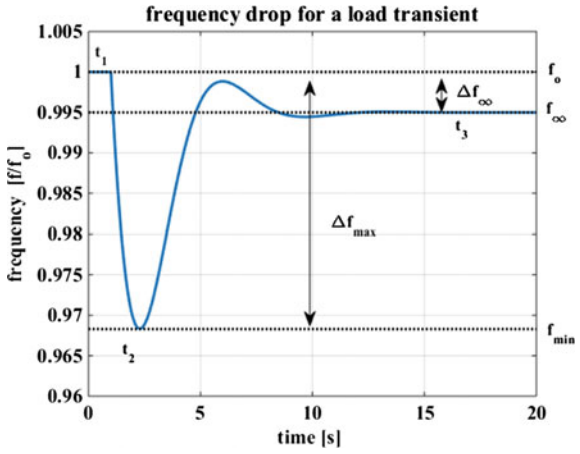

Fig. 3 Transient of the frequency due to a sudden power demand

It can be seen from Fig. 3 that the time derivative of the frequency deviation is crucial since it defines the slope with which the frequency drops to the minimum value. This value can be calculated from Eq. (4) as:

$$\left.\frac{\partial}{\partial t} f_m\right|_{t=t_1} = \frac{f_o}{2H\,S_B}(P_{m.o} - P_e) = \frac{f_o}{2E_{\text{kin}}}(P_{m.o} - P_e) \tag{7}$$

the speed of decrease in the frequency depends on the load variation. The greater is the variation of the load the faster the decrease of the frequency making more critical the system to be controlled. It can be remarked that a weak grid with a low value of E_{kin} will experience larger time derivative of the frequency. Figure 4 shows a simulation with the frequency drop versus time for several load variations. It can be noted that a load variation of 5% would imply a very fast intervention of the control system since the minimum admissible frequency is reached in about 0.1 s.

By Eq. (3) the influence of a reduced value of the inertia constant H due to the use of RES can be evaluated. A simulation of some transients giving the frequency versus time for different inertia constants, maintaining the same load variation, is reproduced in Fig. 5a and a zoom of the minimum of the curves is given in Fig. 5b. It can be noted that the lower is the inertia the higher is the frequency variation Δf_{max} and the lower is the time interval required to the control system to restore the equilibrium. In particular, with a reduction of 50% of the inertia constant, the minimum frequency is reached before the control system is able to successfully operate whereas in a scenario in which almost all the energy is produced by renewables (H = 10%) the minimum frequency is reached in a very short time.

The restoration is performed by involving all the generating units placed in the synchronous area in the first seconds after the loss of generation. In steady-state, the

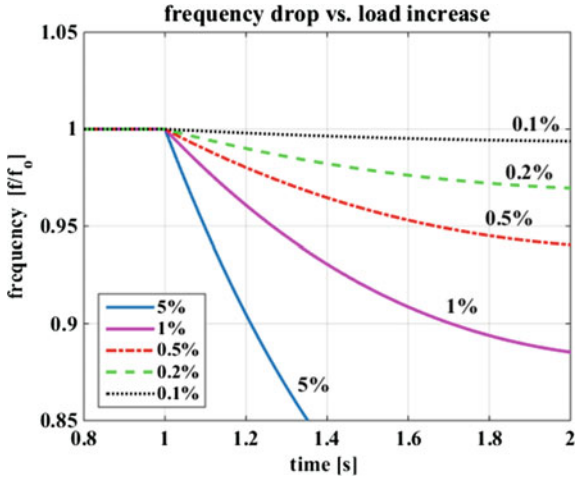

Fig. 4 Frequency drop versus load increase

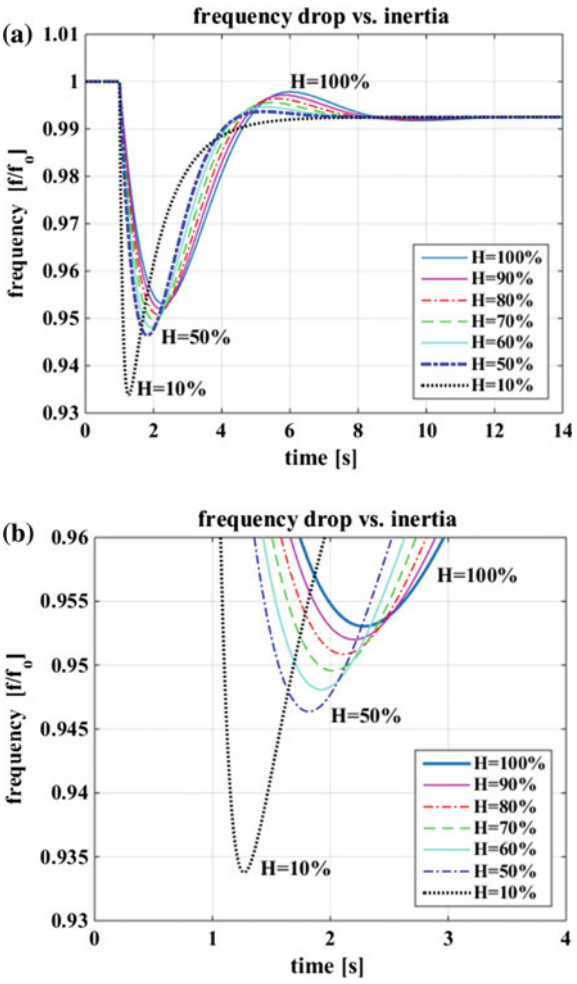

Fig. 5 **a** Frequency drop versus inertia, **b** Zoom of the frequency drop versus inertia

activation of their primary reserve follows a proportional speed-drop characteristic such as:

$$\frac{\Delta P_i(t)}{P_{n,i}} = -\frac{1}{\delta_i}\frac{\Delta f(t)}{f_0} \tag{8}$$

where $\Delta P_i(t)$ is the variation of the power supplied by the generator i provided that its reserve is not completely exploited, $P_{n,i}$ is its rated power and δ_i is a coefficient without dimension representing its permanent drop. On a power system scale, the contributions of the generating units combine with the self-regulating effect of load to restore the balance between generation and demand after a disturbance.

As described by Eq. (8), the rate of change of frequency (ROCOF) is proportional to the magnitude of the overload and inversely proportional to the remaining kinetic energy.

The minimum value reached by the frequency when the primary control reserve is activated depends on many factors among which there are: the amplitude of the imbalance, the system inertia, the dynamic characteristics of loads and the size of generators.

Finally, under the hypothesis that the energy reserve of the plants is able to cover the needs, the frequency will stabilize at a final value f_∞. The quasi-steady-state deviation is proportional to the power variation and inversely proportional to the network power frequency characteristic K. These parameters can be estimated on the basis of the sum of the power frequency characteristics of the generators subject to the primary frequency control with the one corresponding to the self-regulating effect of loads.

$$\Delta f_\infty = \frac{\Delta P_0}{K} \tag{9}$$

$$K = \sum_i P_{n,i} \frac{P_{n,i}}{\delta_i f_0} + \sum_j K_{\text{load},j} \tag{10}$$

The self-regulation of the load in the Union for the Coordination of the Transmission of Electricity (UCTE) synchronous area is assumed to be 1%/Hz that means a load decrease of 1% occurs in case of a frequency drop of 1 Hz [8].

In case the energy reserve of the plants is not able to cover the needs, the ALS must be performed disconnecting the appropriate amount of loads for the restoration of balanced conditions.

A comparison between the former UCTE [8] and the main parameters of Guadeloupe Island [1] is shown in Table 1. In Guadeloupe, the system operator adjusts in real-time the working points of the generators to allocate at least as much reserve as needed and the minimum amount of primary power reserve that must be kept available (about 20 MW) is set; this maintains the risk of activating each stage of ALS under given power quality limits. The ROCOF is over 20 times higher in

Table 1 Comparison of frequency control parameters

	Former UCTE [8]		Guadeloupe [1]	
System load (2009)	Off-peak	Peak	Off-peak	Peak
	250 GW	400 GW	150 MW	250 MW
Refer. incident (MW)	3000		~25	
K (MW/Hz)	15,000	21,000	60	100
f_∞ (Hz)	49.8	49.86	49.58	49.75
M (s)	12		7	9
Δf	−50 MHz/s	−30 MHz/s	−1.2 Hz/s	−0.6 Hz/s
1st level of ALS	49 Hz		48.5 Hz	

Guadeloupe than in former UCTE after occurrence of a reference incident consisting in the loss of the largest infeed. In addition, the f_{∞} value is lower in Guadeloupe as well as the parameter M_{eq} defined as the mechanical starting time of the power system. Finally, a higher value of the time derivative of the frequency deviation at starting time using Eq. (7) is exhibited.

The 1st stage of ALS has a lower threshold since most of the generation technologies used in island grids, including diesel engines and steam turbines, cannot respond fast enough in such cases to prevent a deep frequency drop. From the comparison two main characteristics of the Guadeloupe island grid power system can be deduced: the low inertia constant due to technical reasons and the high ratio of the rated generators power with system load. This is due to economic reasons since any outage results in a considerable overload of the remaining units [1].

4 Wind and PV Generation Issues in Weak Grids

As above cited, the RES with wind and PV generation plants connected to the grid do not provide a relevant inertia and tend to modify the transient frequency response of the energy system. In particular, in small power networks as island or micro grids the expected generation by RES makes frequency stabilization more difficult, implying a limit to the maximum penetration of RES and to their inherent benefits in terms of clean energy production.

As a matter of fact, only fixed-speed wind turbines offer an inertial response (although lower than the one of conventional generators) whereas variable speed turbines or PV plants have a negligible impact on the overall inertia [9].

During operation of RES based plants, as the produced energy increases, synchronous units must be dispatched down or shut down reducing the system inertia. In few words the inertia can vary during the day depending on the energy delivered by RES based plants. The management of the variability and the forecast error could help to avoid sudden variations of the generated energy. In any case, a high amount of energy delivered by renewables implies a higher ROCOF and weakens the ability of isolated power system to manage generation outages.

On the other hand, grid electronically coupled power generation system would be able to remain connected in case of wide frequency excursions (46–52 Hz in the French island grids) [1]. They disconnect usually when the frequency falls below 49.5 Hz to protect distributed synchronous generators and appliances fitted with motors. This threshold jeopardizes the frequency response of the grid especially when it follows the loss of major infeed.

In a power distribution system where the traditional rotating generators are replaced with wind and PV generation systems, Eq. (9) shows that the effect of a decreased number of units involved in primary frequency control results in increased quasi-steady state-deviations as the network power frequency characteristic goes down and the primary reserve is allocated on fewer generators.

In the French islands a maximum penetration limit of renewables to maintain power system security has been imposed, these sources can be temporarily disconnected from the grid when their instantaneous penetration level reaches 30% [12].

A way to provide a virtual inertia consists on the condition that a sufficient energy store is included in RES based plants in their power conversion chain [10, 11, 13].

The virtual inertia provided by DESS appears promising to replace the mechanical inertia of rotating generators in a future in which conventional synchronous units with wind and PV generation will be more and more spread.

5 Storage Systems for Dynamic Grid Support

The rapid advance in storage technology has been allowing such devices to be designed and commissioned successfully aiming at balancing any instantaneous mismatch in active power during abnormal operation of the power grid. For these reasons, storage technologies are expected to give a further significant improvement to the use and to the growth of generation by RES [14]. As a matter of fact, long and medium term storage systems can store energy in off-peaks hours and return it during peak hours. In this way a plant can be operated for a fairly constant load operation below peak demand, reducing the high capital costs of power plants as well as avoiding the drawbacks due to intermittent nature of energy produced by PV and wind generation systems. In addition, short term storage systems can provide a fast-acting generation reserve so that the dynamic security can be significantly enhanced.

Storage systems can be classified on the basis of the time interval in which they are operated as sketched in Fig. 6, transients (microseconds), very short term (cycles of the grid frequency), short term (minutes), medium term (few hours), long term (several hours to days), planning (weeks to months). The storage systems of interest for large-scale system energy management range from hours to days/months [15, 16].

In order to overcome the problems related to the consequences of power flow variations on stability and operation of the electrical grid, short-term storage systems are of great interest. These storage systems, coupled to the grid by an electric power converter, can supply a virtual inertia minimizing the intermittent nature of renewable energy sources with related load-generation imbalances affecting frequency stability. As a matter of fact, RES based distributed systems do not contribute to frequency control by their inertia, they are usually operated in such a way that they generate as much power as possible resulting in a low inertia available by rotating generators [17, 18]. By coupling energy storage systems with power converters to the grid, a power support can be guaranteed as a virtual inertia since they can be rapidly discharged after a disturbance (e.g., a generator tripping) having a constant time lower than the one of rotating mechanical systems. This last feature

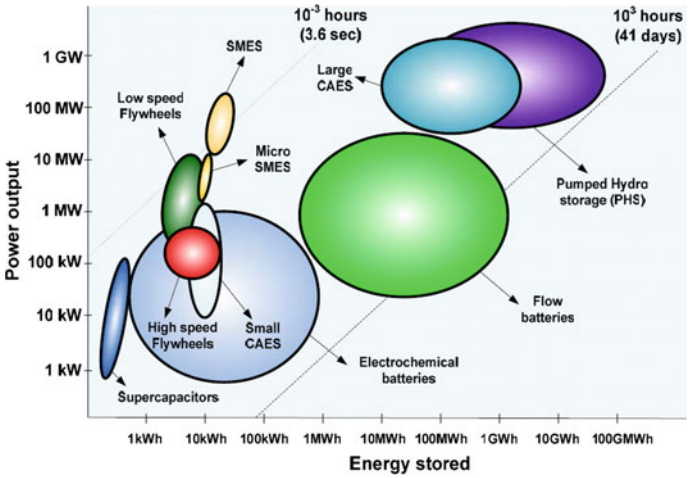

Fig. 6 Classification of storage technologies

fits with increased customer demand for highly reliable electricity and concerns about climate change.

Among storage systems to be used to support the grid frequency stability there are superconducting magnetic energy storage (SMES), flywheels energy storage (FES), supercapacitors energy storage systems (SCES) and battery energy storage systems (BESS) [18, 19].

Several frequency dynamic support based on storage systems have been proposed in literature; for example a magnetic energy storage has been studied in [20], a flywheel energy-storage system associated to a variable-speed wind generator is analyzed in [21] whereas a battery energy storage system for primary frequency control is proposed in [22, 23].

5.1 Superconducting Magnetic Energy Storage

A SMES unit consists of a large superconducting coil, a cryostat provides to maintain a cryogenic temperature. This abates Joule losses into the coil and gives a high efficiency since only the converter losses have to be considered. The energy stored in the coil, E_{SMES}, is given by expression:

$$E_{\mathrm{SMES}} = \frac{1}{2} L i^2 \tag{11}$$

where L is the inductance and i is the current flowing through the coil.

With this technology a very small time response ($\ll$1 s) with high power peaks can be obtained.

5.2 Flywheel Energy Storage

In flywheels (FES) or kinetic energy storage systems (KESS) the electric power is stored as kinetic energy. The maximum stored energy is limited by the tensile strength of the flywheel material. The stored energy is given by:

$$E_{\mathrm{FES}} = \frac{1}{2} J\omega^2 \tag{12}$$

where J is the moment of inertia of the flywheel and ω its angular speed. The energy can be increased by increasing J or ω. On the basis of the material of the rotor, two types of flywheels can be recognized: (1) with an advanced composite rotor, such as graphite or carbon-fiber, which provide high specific energy, (2) with a steel rotor, which allows traditional design (with large diameters, low speed and low power and energy densities) and new high performance flywheels. Flywheels can provide an amount of energy in a relatively short time interval, so they can play an important role in primary frequency regulation. The flywheel is connected to a bidirectional AC electrical machine equipped with a AC/DC converter, in this way a DC voltage is available at its terminals. The operation diagram of a flywheel is shown in Fig. 7 and the whole system including the bearings, the electric machine and the vacuum pump is sketched in Fig. 8.

High speed flywheels are able to be operated up to about 40,000 rpm and low speed flywheels around 7000 rpm. By adopting superconducting magnetic bearings very high overall efficiency, exceeding 90%, is obtained [15, 18].

Stephentown, New York is the site of Beacon Power's first 20 MW plant (40 MW overall range) and provides frequency regulation service to the NYISO. This facility includes 200 flywheels. Initial commercial operation began in January, 2011 and full output was reached in June, 2011. Flywheels perform between 3000 and 5000 full depth-of-discharge cycles a year [24].

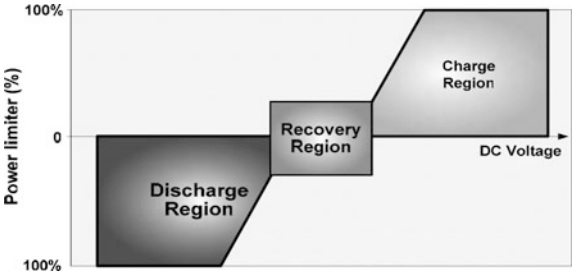

Fig. 7 Operation diagram of a flywheel

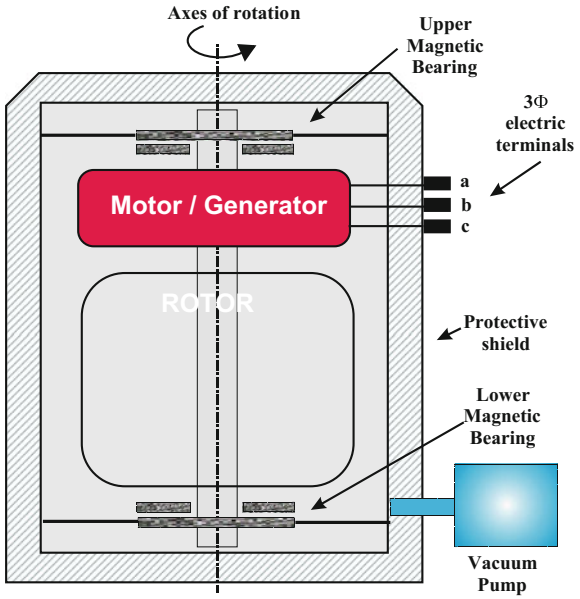

Fig. 8 Flywheel-based system

5.3 *Supercapacitors or Ultracapacitors*

Electrochemical double layer capacitors (EDLC), also called supercapacitors or ultracapacitors, are energy-storage devices able to deliver 100 times the power of batteries and to store 10,000 times more energy than conventional capacitors. They are based on a porous structure of activated carbon for one or both electrodes, they are immersed into an electrolytic solution (typically potassium hydroxide or sulphuric acid) and a separator which prevents physical contact of the electrodes but allows ion transfer between them. In this way two series connected equivalent capacitors are realized and energy is stored as a charge separation in the double layer formed at the interface between the solid electrode material surface and the liquid electrolyte in the micropores of the electrodes. In this way, the effective surface is up to 2500 m^2/g strongly increasing the capacitance. Their volumetric and gravimetric energy density is lower compared with batteries or fuel cells however they become an interesting option when it comes to highly dynamic charging or discharging profiles with high current rates. This is because of their exceptional high power capabilities (specific power densities of several kW/kg) and cycle lives of up to 10^6.

The stored energy is given by:

$$E_{\mathrm{EDLC}} = \frac{1}{2} C V^2 \tag{13}$$

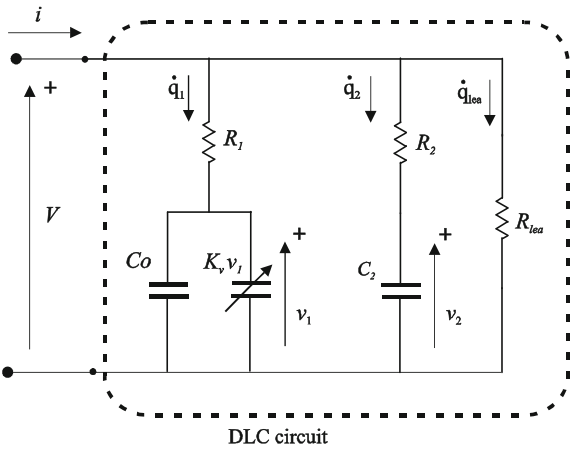

Fig. 9 Equivalent circuit of the supercapacitor

where C is the capacitance and V is the voltage at its terminals. The presence of the double layer implies that the capacitance depends on the voltage and the equivalent model is non-linear. Figure 9 shows the 2-branches model commonly used for power applications, it is composed of a branch with a voltage dependent capacitor that is series connected with a resistor and of a branch with a linear resistor series connected with a linear capacitor. It can be noticed that the voltage dependent capacitor is modelled by a linear capacitor connected in parallel to a linear voltage dependent capacitor. The leakage resistance R_{lea} models the self-discharge.

The capacitor C_1 of the first branch linearly dependent on the voltage follows the law:

$$q_1 = C_0 V_1 + k_c V_1^2 \tag{14}$$

The capacitor of the second branch C_2 is a traditional linear capacitor described by the equation:

$$q_2 = C_2 V_2 \tag{15}$$

Finally the elementary cell of the EDLC has a low rated voltage and high capacitance (e.g. 5000 F/2-3 V), higher operating voltages maintaining high capacitance are achieved by series-parallel connections [17, 25, 26].

5.4 Advanced Batteries Energy Storage Systems

In Advanced Batteries Energy Storage Systems (BESS) the chemical energy is converted into electrical energy by oxidation and reduction of their materials. They consist of a base unit, which is combined with others, in series or parallel, to obtain

the required levels of voltage and current. In principle, batteries are easy to charge; moreover they can be turned on and off very quickly. On the other hand they are expensive both for the material, the production costs and lifetime.

Many types of electrochemical batteries have been developed, which can be used in electric power systems, including: lead acid (flooded type, valve regulated), sodium sulfur, lithium ion, metal air, flow batteries, vanadium redox, zinc bromine, nickel cadmium, etc. [15, 27, 28].

In general, the batteries exhibit a high cycle efficiency (typically 90%) but high cost (typically >$0.1/kWh), probably the most expensive. Recently NiCd, NaS, Li-ion and flow batteries (such as vanadium redox) are drawing attention [22].

6 Power Converters for Storage Systems Grid Interfacing

In addition to the storage systems, new power semiconductor devices and power circuit topologies are allowing the efficiency conversion to be increased. As a consequence, several potential benefits for weak grids are expected.

The overall efficiency exhibited by SMESs and SCESs (higher than 95%) or FESs (about 90%) systems and their fast time response (half millisecond for SMES and SCES devices, up to some milliseconds for FES systems) can provide the potential for energy storage of up to several MWh, this improves the energy management of the grid both in case of large variations in energy requirements and replacement of major generating unit. A certain amount of the short-term generation that must be kept unloaded as spinning reserve can be stored in DESS exploiting excess energy during off-peak periods; in this way the dynamic security of the microgrid is enhanced. The load variations can be followed by DESS so that the conventional generating units can be operated at roughly constant or slowly changing output power. The DESS units are able to damp out low frequency power oscillations and to stabilize the system frequency, compensating the variations of the energy generated by PV or particularly by wind plants, when a transient occurs.

Finally, the features of grid connected converters allow the power factor to be corrected, and the voltage to be regulated as well, since the reactive and the active power can be simultaneously and independently generated [28].

All storage systems need a bi-directional power converter to be interfaced with the grid. The converter must provide to match the different voltage levels and to assure the power exchange on the basis of the reference values of active and reactive power. Moreover, all the above described storage systems give different outputs: the ELDC and the batteries generate a DC voltage, the SMES generates a DC current and the KESS with flywheels is mechanically coupled to an AC electrical machines, for this reason, they need different conversion systems. In general, the dedicated power converter of the storage system gives a DC voltage as output, it is connected by a DC-link to a voltage source converter (VSC) performing the energy exchange with the grid. In any case the conversion chain provides bi-directional power flow capability.

6.1 Power Converters for Ultracapacitors

EDLCs store energy under the form of electric field, hence they can be assumed as voltage sources with a value that depends on the stored charge and varies during the operation. The most common power converter interface used for EDLC is the DC/DC converter topology allowing the operation in buck (step-down) or boost (step-up) mode. The operating voltage of the ELDC can be higher or lower than the voltage level in the connection point, this is obtained by different topologies. The conversion circuit for the output voltage higher than the ELDC voltage is shown in Fig. 10a–c. In particular Fig. 10a shows the buck-boost configuration, Fig. 10b shows the boost operation, in which the ELDC supplies the load, obtained by maintaining in off state the upper device, while in Fig. 10c the buck operation, in which the ELDC is charged, is obtained maintaining the lower device in blocking state [29].

The circuit requires an additional current loop to control the supplied current, it is performed measuring the current flowing through the inductance. On the basis of the error between the reference and measured voltage, a reference current is obtained by a PI voltage regulator. Then a PI current regulator calculates the signal for the PWM modulator calculating of the error between the reference current given by the PI voltage regulator and the measured current. It can be remarked that the current loop must have a higher bandwidth compared with the voltage loop. Figure 11 gives the block diagram of the current control for the buck-boost converter.

The ripple of the current flowing through the EDLC can be minimized by an interleaved structure. In this case the current is shared among n inductors and there are n legs, with two power switches for each leg, connected to the storage device. If the modulator carriers signals have a phase shift of $2\pi/n$, the current ripple through the supercapacitor is minimized. The interleaved structure allows efficiency to be increased since joule losses on inductors are reduced, moreover a further improvement in efficiency is achieved when a reduced number of legs is activated for light loads [30]. A three legs interleaved buck-boost power converter is illustrated in Fig. 12.

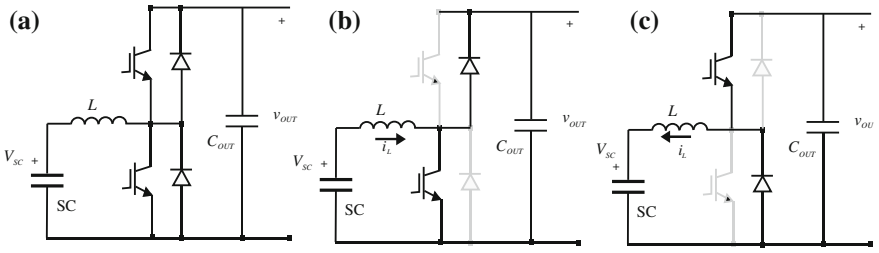

Fig. 10 **a** Buck-boost topology for $V_{sc} < V_{out}$, **b** boost operation, **c** buck operation

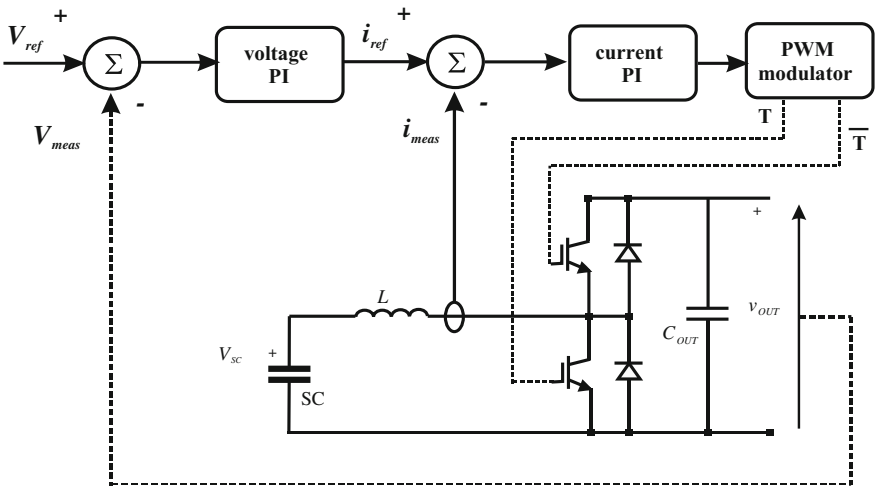

Fig. 11 Block diagram of the current control for the buck-boost converter

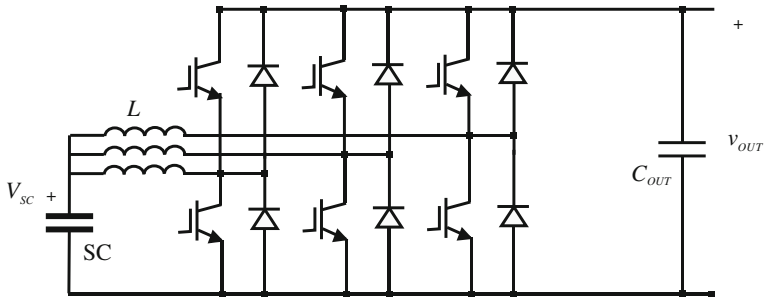

Fig. 12 Interleaved dc–dc buck-boost power converter with three legs

The control strategy is the same for the single leg converter taking into account that each inductor requires a dedicated current loop.

6.2 PWM Converter for Grid Interfacing

The energy exchange with the grid can be performed by a three-phase voltage source PWM converter (also called VSI = Voltage Source Inverter) the corresponding circuit is sketched in Fig. 13. When the energy flows from the DC side to AC side the converter behaves like an inverter, otherwise it behaves like a rectifier. The direction of the energy is imposed by the control of the current supplied by the converter; it is connected to the grid by an inductor so that the current is obtained by the difference

between the grid voltage (imposed by the grid) and the voltage generated by the converter whose amplitude and phase can be controlled. With reference to the single phase representation shown in Fig. 14, it can be noted that, on the basis of the voltage generated by the converter, the resulting current can be injected towards the grid or to the load and the phase can be controlled. It allows a generation with unity power factor or with the management of the reactive power if necessary. The voltage generated by the converter must be synchronous with the grid voltage for which a Phase Looked Loop can be adopted.

Some characteristic situations are sketched in Fig. 15 using a phasor diagram valid in sinusoidal steady-state. Figure 15a shows a generic operating condition in which the grid voltage $\boldsymbol{u}_g$ is obtained as the sum of converter voltage phasor $\boldsymbol{u}_s$, the drop on inductance and the drop on the parasitic resistance. Figure 15b represents a rectification at unity power factor. The current supplied by the converter $\boldsymbol{i}_s$ is positive when flowing from the grid to the converter. Considering the voltage generated by the converter, the sum of the drop on the inductor and of the drop on the parasitic resistor makes the current in phase with the grid voltage. The power flow goes from the grid to the converter representing the behaviour as rectifier. Figure 15c shows the inversion at unity power factor. In this last case the grid voltage phasor and the current phasor are in opposition. It should be borne in mind that the resistive drop has been exaggerated for the sake of clarity since in practise it represents the parasitic resistance of the inductor [31].

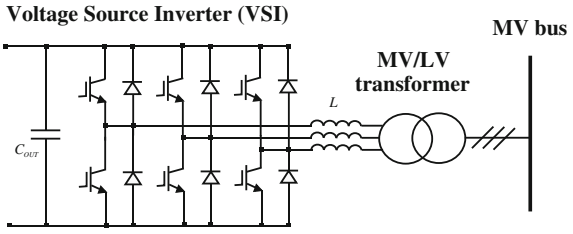

Fig. 13 Voltage source inverter for grid interfacing

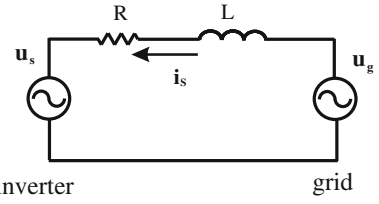

Fig. 14 One phase representation of the scheme of Fig. 11

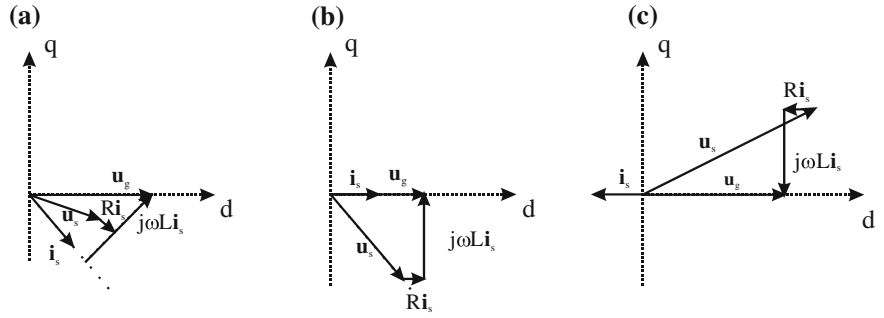

Fig. 15 Operating condition of an active rectifier: **a** generic condition, **b** rectification at unity power factor, **c** inversion at unity power factor

6.3 Power Converters for Superconducting Magnetic Energy Storage Systems

In a superconducting magnetic energy storage system (SMES) the storage is performed by a lossless inductor with inductance L. During the charging phase it is connected to a voltage source V and the current starts with a rate V/L. Once the nominal current is achieved, the inductor is short-circuited by a so-called superconducting switch, the current can flow through the magnet with no losses and the energy is stored in its magnetic field. During the discharging phase the magnet is connected again to the source reversing its polarity. As a consequence it starts to discharge at a rate $-V/L$ until all the energy has been transferred back to the voltage source. It can be remarked that this operation cannot be performed by a traditional inductor with copper conductor since in this last device the losses would lead to a poor efficiency. On the contrary, in a superconducting magnet, in principle, the energy can be stored for an infinitely long time without losses. On the other hand, regardless the type of magnet used in a SMES, the cryogenic aspects and those related to the power electronics converters are crucial.

There are three different topologies that can be used: (a) thyristor-based converter, (b) voltage source converter (VSC), and (c) current source converter (CSC) [32].

The thyristor-based converters were very common in the past thanks to the high voltage and high current rates of GTO (Gate Turn-off Thyristors). The power flow is controlled by the firing angle α. If $\alpha < \pi/2$ the converter behaves like a rectifier and charge the coil, whereas if $\alpha > \pi/2$ the converter behaves like an inverter. The active power is only a function of the angle α since the bridge current I_{smc} is not reversible; for this reason a poor control performance on reactive power is obtained. The Thyristor-based topology for SMES is shown in Fig. 16.

The VSC configuration is composed of a PWM converter as the one described in the previous section and a two-quadrant DC/DC chopper. The VSC gives the possibility to manage both the active and reactive power requirements of the utility.

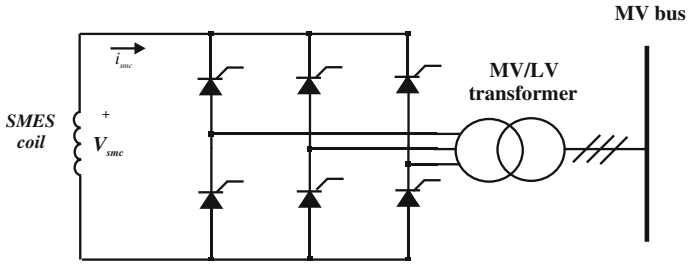

Fig. 16 Thyristor-based topology for SMES

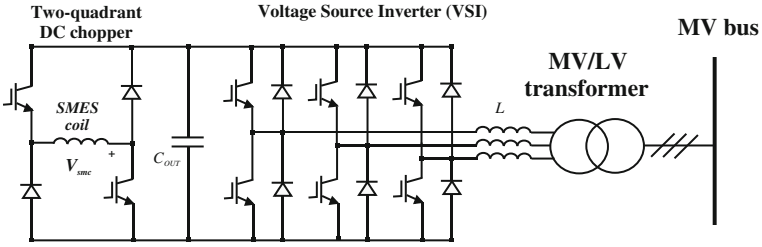

Fig. 17 VSC converter with two-quadrant chopper for SMES

The PWM converter is interfaced to the superconducting coil by the DC/DC two-quadrant chopper, it is connected to the VSC by a DC-link. The voltage V_{smc} applied to the coil is regulated by the duty cycle of the chopper IGBTs. It can be increased or reduced when the duty cycle is larger than ½ or less than ½ respectively. In this way V_{smc} can be increased or reduced, keeping constant the DC-link voltage V_{DC}, and charging or discharging the superconducting coil (increasing or decreasing I_{smc}). The conversion circuit is shown in Fig. 17.

As for the control circuit, a current control allows active and reactive power to be managed. The currents measured on the grid line are processed by the Park transformation to obtain, in a d-q reference frame, the d-axis current i_{sd} component to control the dc-link voltage and the q-axis component i_{sq} to provide the reactive power to control the voltage module at the grid. In particular, two PI regulators give the i_{sd*} and i_{sq*} components on the basis of the error on the DC-link voltage and on the error on the grid voltage respectively. The i_{sd*} and i_{sq*} are then compared with the values measured on the grid line and the PI current controllers give the reference signal for the three phases to the PWM modulator. The control scheme is illustrated in Fig. 18.

The current source converter (CSC) is adopted for DC loads where the current is non-interruptible. The superconducting coil behaves as a current source and it is suitable for this topology in which the current is directly commutated by the coil and the ac side. Firstly GTO devices were adopted but nowadays IGBTs can

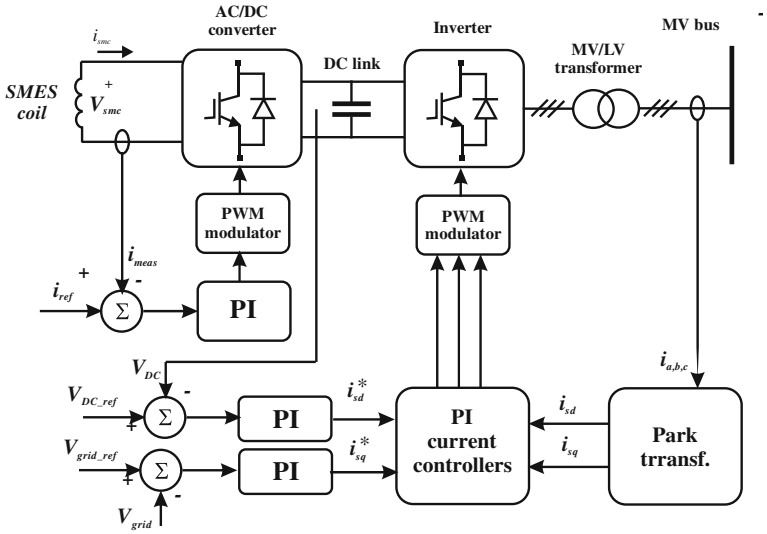

Fig. 18 Control scheme of a VSC and dc chopper for SMES application

manage high currents so they are more commonly used. IGCT modules can be used in case of very high currents.

The CSC topology is shown in Fig. 19. The SMES requires a bypass switch to maintain the current flowing through the coil when null power is exchanged to the electric grid. Finally a quench detector is connected to the SMES coil. The quench phenomena occur when the coil stop being superconducting due to an internal problem with the superconducting material. In this case the coil resistance increases inducing a voltage run up. The quench protection branch dissipates the stored energy by a resistor.

A bank of capacitors at the CSC output buffers the energy stored in all line inductances during the process of ac line current commutation. The simplest control is based on a current control with a current reference and a PI controller which gives

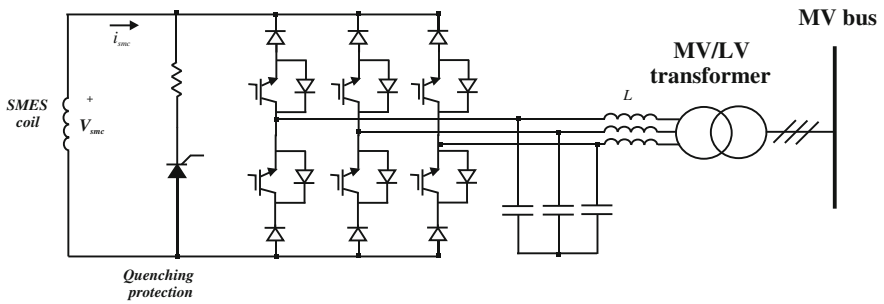

Fig. 19 Current source converter topology for SMES

the modulation index. Anyway the space vector modulation (SVM) is preferred to improve the dynamic behavior, in this case the switching frequency is controlled during the transient of the current and the requirements of the LC filters are reduced. The SVM strategy for a CSC is based on the well-known strategy adopted for VSC [21, 29, 31].

6.4 Power Converters for Kinetic Energy Storage Systems

The source of energy in a kinetic energy storage system (KESS) is represented by the flywheel coupled to an electrical machine. It must be operated as a motor if the kinetic energy has to be increased. In this case the machine exerts a positive torque T to the flywheel increasing its speed at a rate T/J, where J is the moment of inertia, until the maximum speed is reached. After this, only the energy to compensate losses is required. When the stored energy has to be released, the machine must be operated as a generator, it applies a negative torque to the flywheel lessening the speed at a rate $-T/J$, and releasing the energy. The power converter has the aim to control the machine to obtain a behaviour as motor or generator. It is connected to the DC-link and to the machine. This converter is an AC/DC converter as shown in Fig. 20. The DC-link provides the grid connection by a VSI inverter whose operation has been described in Sect. 6.2. The whole topology is known as back-to-back converter, it assures the bidirectional flow of energy. The DC-link voltage can be controlled by one of the two converters.

As for the machines to be used to drive the flywheel, not all the electrical machines are good candidates. As a matter of fact, the machines with wound rotors should be avoided mainly for the presence of the brushes or slip rings not suitable to be operated at high speeds whereas in the squirrel-cage induction machines is difficult to extract the heat generated in the rotor windings.

Actually the preferred electrical machines are Homopolar (SHM), Reluctance (SRM), and Permanent Magnet machines. They can be studied as synchronous

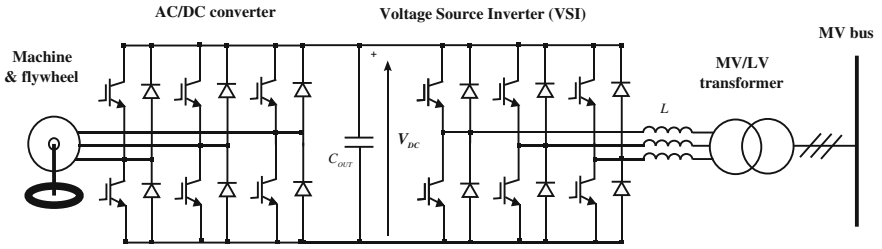

Fig. 20 Connection of a KESS system to the grid by a back-to-back converter

machine with three corresponding windings in the equivalent d-q model: two d-q windings in one side and one D excitation winding (or a permanent magnet as in the case of permanent magnet synchronous machine (PMSM). The main two issues in this type of machine are the magnetic material for the magnets and the topology in which they are arranged.

As regarding the material, Neodymium Iron Boron (NdFeB) and Samarium Cobalt (SmCo) are preferred since their remanence and coercivity are much higher than for any other alternative. The NdFeB magnet exhibits better values than SmCo however its temperature stability is not so good and since rotor heating can be a problem in flywheels, SmCo is usually the preferable option. The PMSM offers high performance with a very good efficiency, the drawbacks are in the cost and availability of the magnets and their potential demagnetization of the magnets due to armature reaction or to temperature increase. In addition, the PMSM suffers of the iron losses when the machine is not exchanging power with the load, since an electromotive force (emf) is always present.

The power electronic converter used as interface between a flywheel and the DC-link is usually a PWM bi-directional converter equipped with insulated-gate bipolar transistor (IGBT). The control depends on the electric machine coupled to the flywheel. The main issue is to provide a constant power during the rotational speed range. To obtain a torque-speed curve with a constant power area, the machine in the range between the rated speed (ω_{rated}) and the maximum speed (ω_{max}) has to be operated in field weakening mode. Since in the PMSM the flux is provided by magnets the i_{sd} component of the current has to be maintained to zero when the ratio $\omega/\omega_{\text{rated}}$ needs to be increased. In this way, this current component produces a flux opposite to the flux generated by permanent magnets. In order to avoid high back emf to preserve the power electronics switches of the converter, a maximum value of the back emf is imposed. The maximum back emf is limited by one half of the DC-link voltage:

$$E_{\max,ph\_n} \leq \frac{V_{\text{dc}}}{2} \tag{16}$$

The same torque-speed characteristic is required in other machine types. In the case of SHM the back emf can be adjusted with the field winding, in SRM the saturation of the magnetic circuit produces a natural behavior in constant power mode once the saturation speed is over passed.

The control circuit of the machine side converter is depicted in Fig. 21. It can be noted that the field weakening control receives the reference torque and the actual speed as input. On the basis of its output the torque command processing obtains the direct and quadrature current components. The two PI controllers provide the direct and quadrature voltage components to the AC/DC converter modulator [29].

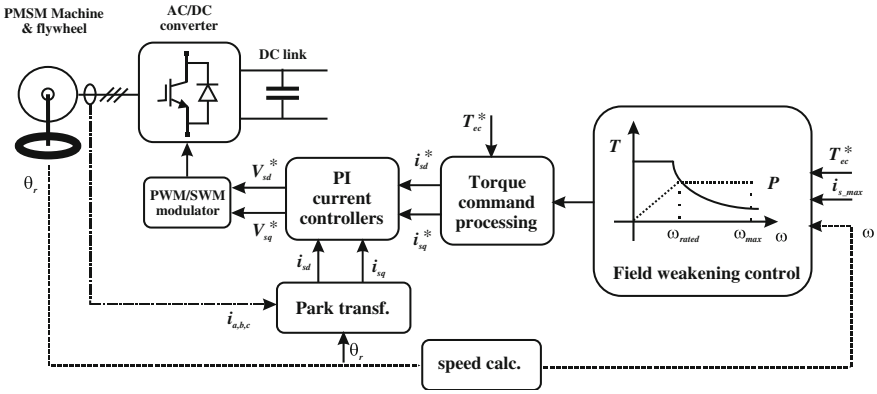

Fig. 21 21 Control scheme of a AC/DC converter connected to a PMSM machine and flywheel

6.5 *Modularity and Integration of Flywheels Energy Storage Systems*

An effective way to support RES integration, especially in weak grids, consists in the introduction of DESSs. As a matter of fact there are some challenges due to RESs as the variability of the available energy and reduced inertia. In particular the effects are recognizable for higher level of RES penetration affecting the frequency regulation reserves needed to maintain the system stability. The DESSs based on flywheel energy storage systems appear advantageous since they provide fast response reducing both the time needed to act and consequently the amount of reserves needed to ensure the system stability. In particular, Flywheels Energy Storage Systems (FESS) can have more number of discharging cycles without affecting the life time of the device and the exact state of charge can be detected easily on the basis of the rotational speed contrarily to batteries requiring more complex systems.

On the other hand, large power machines have not been developed for flywheel application. In order to satisfy applications in which an important amount of power and energy is required, FESSs can be arranged in matrix as described in Fig. 22a. In this case each FESS is equipped with a dedicated AC/DC converter whereas a centralized DC/AC units provides the grid connection so that a single power transformer and electric grid protections for the whole system is adopted. This kind of modularity allows both the total cost to be reduced and FESS units to be assembled with a dedicated power electronic converter.

The FESS with back-to-back converter can be connected in parallel with a PV plant in its point of common coupling (see Fig. 22b), alternatively a FESS equipped with only the converter on the side machine can be connected directly to the DC-link of a RES system. In general, the spreading of more reduced power systems

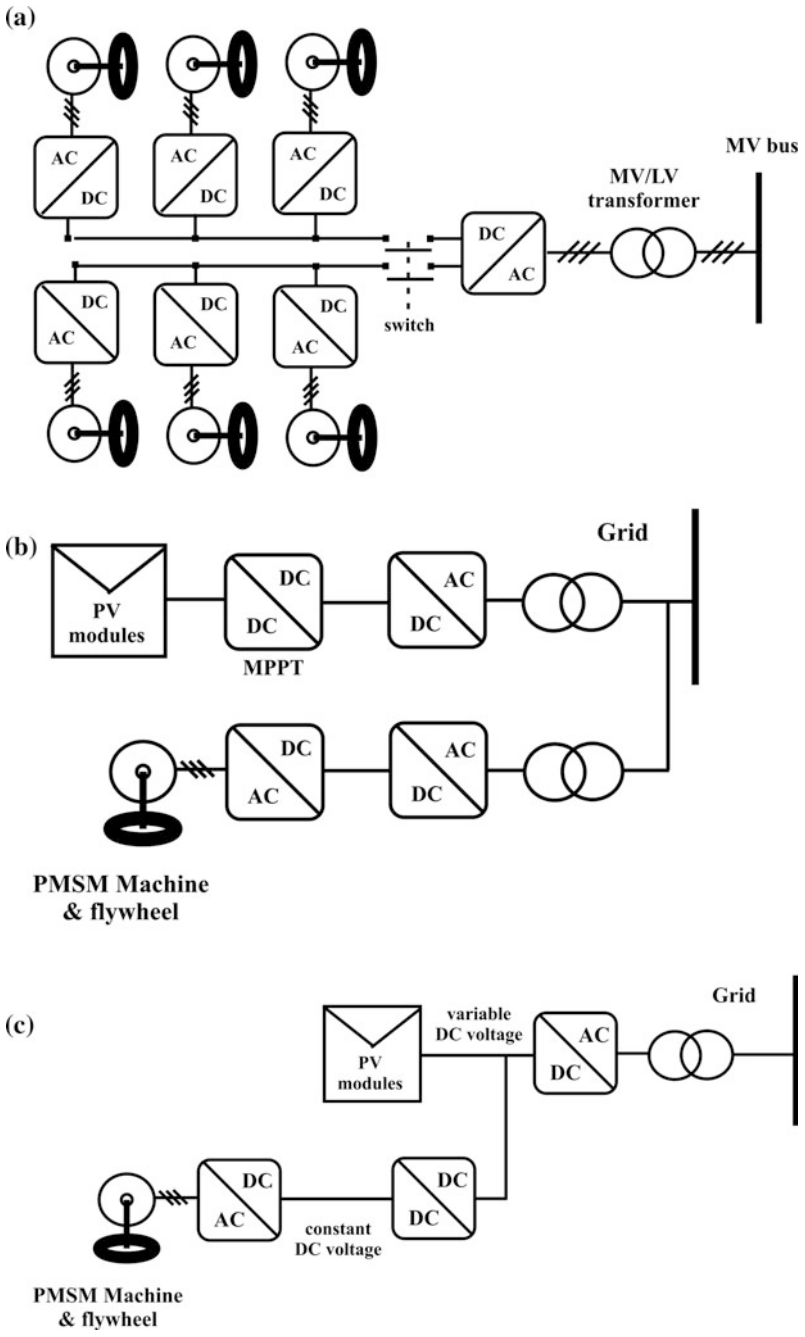

Fig. 22 **a** Matrix connection of FESS, **b** connection of a FESS to the grid in the same PCC of a PV plant, **c** connection of a FESS to the DC-link with variable voltage by an additional DC/DC converter

instead the centralized one increases reliability. It can be remarked however that when the DC-link is operated at variable voltage the flywheel-machine might have variable voltage and an extra dc/dc converter could be required (see Fig. 22c) [29].

6.6 *Simulation Analysis of Storage Systems Integration*

The effectiveness of the use of storage systems in weak grids has been analyzed in simulation. A weak grid in which the inertia has been reduced to 70% due to the introduction of renewables and the same situation in which a storage system has been connected to the grid have been considered.

Figure 23 shows the transient of the frequency before the introduction of renewables corresponding to a value of the inertia constant of 100% and the transient in which the inertia is reduced to 70% corresponding to an increase of power demand equal to 1%. As expected, the lower inertia implies that a lower minimum of the frequency is reached in shorter time. If a storage system is connected to the grid, thanks to its short time of intervention, the frequency transient is characterized by a higher value of the minimum frequency and of a reduced Δf_{max}. After the first transient, the frequency reaches the value f_∞ in a shorter time and with less variations. Figure 24 shows the power supplied by the storage system versus time, it supplies the 0.35% of the increase of the power required by the load in less than 1 s, then this value goes to zero in about 20 s; in the same time the frequency controller is able to restore the equilibrium.

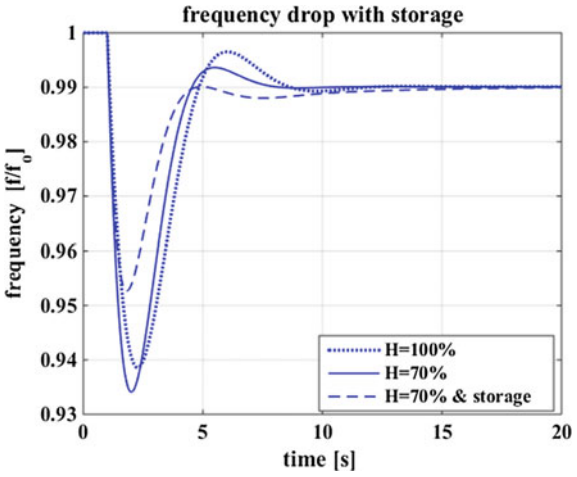

Fig. 23 Transient of the frequency due to a load variation employing a storage system

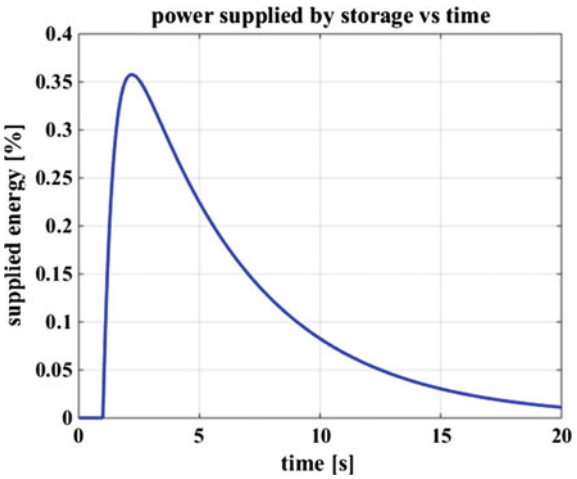

Fig. 24 Power delivered to the grid by the storage system

7 Practical Applications of Storage Systems for Frequency Stability Enhancement

Some practical case studies dealing with the use of storage systems for frequency stability enhancement in small isolated power systems are described in this sections. They have been devised to provide for the lack of inertia causing a higher rate of change of frequency which requires faster and larger primary frequency regulation reserves to prevent frequency being outside +/−2.5 Hz range. All described case studies have been set up in the framework of the demonstration project STORE dealing with small isolated power systems. In particular Spanish Canary Islands are considered. The operation of these small isolated power systems is challenged by frequency stability and control since generation loss due to a generator tripping is generally a great fraction of the total generation. The system collapse is guaranteed by the ALS.

The main features of these systems are summarized in Table 2. The systems described in the following are based on two different short-term and on a medium term energy storage systems. In particular an ultra-capacitor based system in La Palma, a flywheel based system in La Gomera and a Li-ion battery based system in Gran Canaria are described [17, 33].

7.1 Ultra-Capacitor Based System

The energy storage system located in La Palma is equipped with ultracapacitors with rated value equal to 4 MW/20 MWs (5 s). It is connected at 20 kV bus of Guinchos power generating station. The ultra-capacitor bank is connected to the

Table 2 Features of the systems of Spanish Canary Islands

Electric system	Electricity generation (GWh)	Installed capacity (MW)	Peak demand (MW)	Ratio peak dem/capacity (%)
Tenerife	3625	1084.28	593	54.69
Gran Canaria	3653	1111.8	598	53.78
Lanzarote-Fuerteventura	1458.7	377.97	256.5	67.86
La Palma	254.8	105.52	48.4	45.86
La Gomera	66.7	20.1	12.1	60.19
El Hierro	35.7	11.31	7	61.89

MV grid by a power electronic converter and a MV/LV transformer. The capacitance and the voltage of the ultra-capacitor bank are 55.55 F and 1080 V respectively. A power electronic VSC (Voltage Source Converter) with vector control manages the active and reactive power supplied by system to the grid. Figure 25 shows the block diagram representation of La Palma system based on ultracapacitors. The power converter is operated as described in Sect. 6.2. La Palma ultracapacitor has been supplied by Ingeteam [34].

The power converter independently controls active and reactive power as illustrated in Fig. 26. The state of charge of the ultra-capacitor is taken into account as a constraint. There are two controllers devoted to the active and the reactive power respectively. The controller acting on active power delivered to the grid receives the error between the rated frequency and the measured frequency as input whereas the controller acting on reactive power delivered to the grid receives as input the error between the rated voltage and the measured voltage.

As for the active power controller, shown in Fig. 27, the reference power is calculated on the basis of drop and inertia emulation components. The drop component is proportional to the frequency deviation and the inertia emulation H is proportional to the rate of change of frequency. The reference signal is processed by a rate limiter, it takes into account the energy stored in the ultracapacitor since the delivered energy must be decreased gradually before the end of the stored energy.

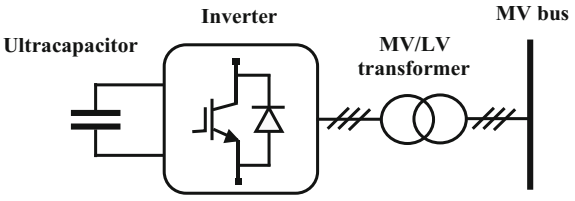

Fig. 25 Block diagram representation of La Palma system based on ultracapacitors

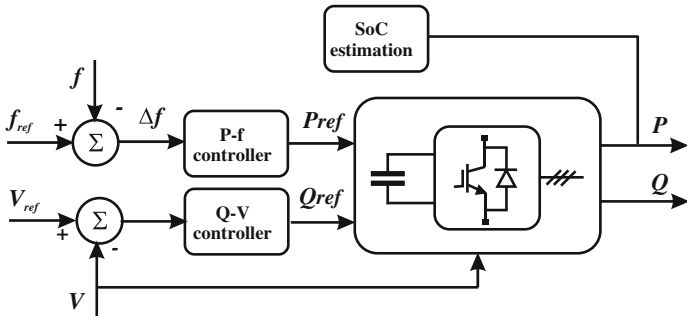

Fig. 26 Block diagram of the high level control model

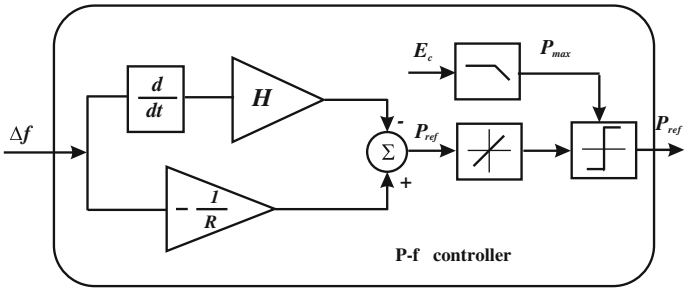

Fig. 27 Block diagram of the active power-frequency controller

7.2 Flywheel Based System

The energy storage system located in La Gomera adopts a flywheel with rated values of 0.5 MW/20 MWs (40 s). The flywheel weighs 3000 kg, it is driven by PMSM at a maximum speed of 3600 rpm. The flywheel has been supplied by ABB-PowerCorp [35]. This installation is connected at Playa de Santiago 20 kV/400 V transformer station which is electrically close to Palmar power generating station. Figure 28 displays the block diagram representation of La Gomera flywheel. The machine is connected to the grid by two power electronic converters (grid side and machine side) coupled by a DC link capacitor. The power electronic converters are of VSC type. The grid side converter controls the reactive power supplied to the grid and the voltage of the DC link capacitor. The machine side converter controls the active power by controlling the speed of the flywheel.

The active power controller transforms the error on the frequency in a direct current reference. This value is limited taking into account the remaining energy of the flywheel, the current, the voltage and the frequency limits. Figure 29 shows the high-level model of the control. The active power-frequency controller calculates the reference power on the basis of drop and inertia emulation components. The

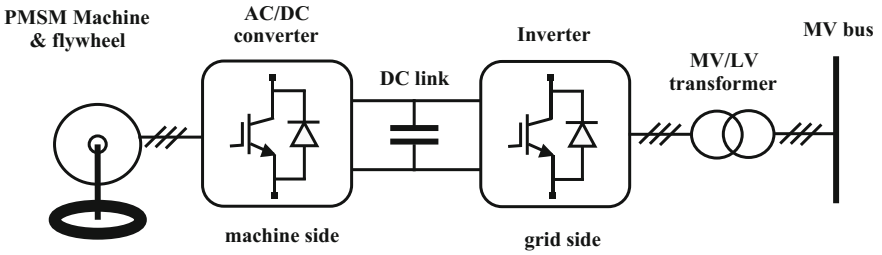

Fig. 28 Block diagram of La Gomera flywheel based system

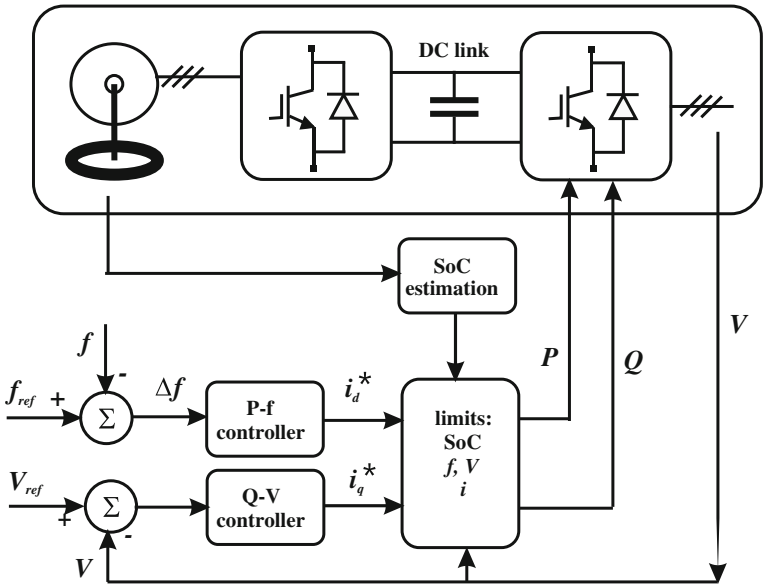

Fig. 29 High-level model of the control of the flywheel based system

drop component is proportional to the frequency deviation and inertia emulation is proportional to the rate of change of frequency. The block diagram of the active power controller is shown in Fig. 30.

7.3 Li-Ion Battery Based System

The energy storage system of Gran Canaria is a medium term energy based on Li-ion batteries with rated value of 1 MW/3 MWh (3 h). It is connected at the end of a 20 kV power line in La Aldea transformer station 20 kV/400 V. The battery

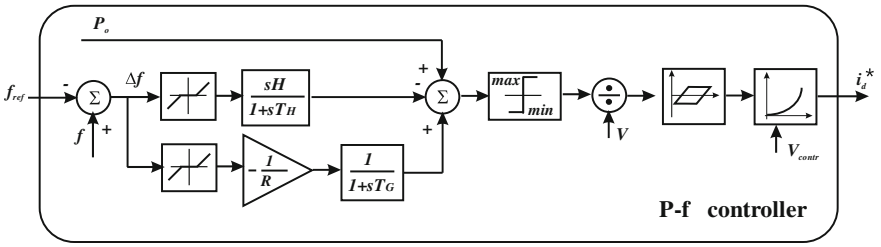

Fig. 30 Particular of the P-f controller of the flywheel based system

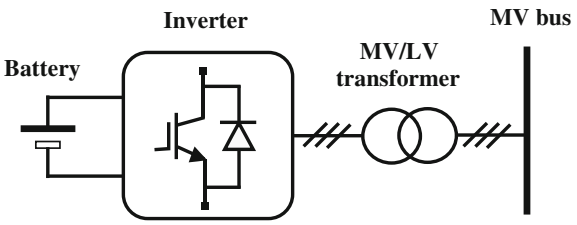

Fig. 31 Block diagram representation of Gran Canaria system based on battery

was supplied by Saft Batteries [36]. The grid connection scheme as well as the controller is similar to the case of ultracapacitor based system. The block diagram of the system is shown in Fig. 31. All the above described plants have allowed the frequency excursion to be reduced and the contribution to the frequency stability to be improved.

8 Conclusions

The consequence of a reduced inertia of rotating generators in weak grids is analyzed in this chapter. The frequency stability in this case could be jeopardized by load variation or outage. The massive use of PV and wind plants offers a viable solution for replacing fossil fuels and abating CO_2 emissions but reduces further the mechanical inertia of rotating generators making crucial the issues.

The use of storage systems have been successfully applied to supply continuity against the intermittent production by solar and wind generation systems. In addition, it has been shown how they can give a virtual inertia and can guarantee fast intervention time to support very well the frequency control if they are interfaced by suitable modern power electronic converters assuring appropriate dynamic performance and a bidirectional flow of energy. The analysis has been supported by simulations.

Finally some case studies using ultra-capacitors, flywheels and Li-ion batteries have been described to show the benefits in terms of frequency stability and control enhancement in weak grids.

References

1. Delille G, François B, Malarange G (2012) Dynamic frequency control support by energy storage to reduce the impact of wind and solar generation on isolated power system's inertia. IEEE Trans Sustain Energy 3(4):931–939
2. Rebours Y-G, Kirschen D-S, Trotignon M, Rossignol S (2007) A survey of frequency and voltage control ancillary services—part I: technical features. IEEE Trans Power Syst 22 (1):350–357
3. Milošević M, Andersson G (2005) Generation control in small isolated power systems. In: Proceedings of the 37th annual North American power symposium, Ames, Iowa, USA, pp 524–529, 23–25 Oct 2005
4. Ulbig A, Borsche T-S, Andersson G (2014) Impact of low rotational inertia on power system stability and operation. Available via https://arxiv.org/pdf/1312.6435. Accessed 28 Oct 2016
5. Delille G, François B (2008) A review of some technical and economic features of energy storage technologies for distribution system integration. In: Proceedings of electrical machines, drives and power systems conference, ELMA, pp 40–48, 11–12 Oct 2008
6. Kundur P (1994) Power system stability and control. McGraw-Hill, New York
7. Wood A-J, Wollenberg B-F (1996) Power generation, operation and control, 2nd edn. Wiley, New York
8. UCTE, Operation Handbook (2010) Available via: https://www.entsoe.eu/publications/system-operations-reports/operation-handbook/Pages/default.aspx. Accessed 28 Oct 2016
9. Yingcheng X, Nengling T (2011) Review of contribution to frequency control through variable speed wind turbine. Renew Energy 36:1671–1677
10. Wesenbeeck M-P-N,. de Hann S-W-H, Varela P, Visscher K (2009) Grid tied converter with virtual kinetic storage. In: Proceedings of IEEE power tech conference, Bucharest, Romania, pp 1–7, 28 June–2 July 2009
11. Driesen J, Visscher K (2008) Virtual synchronous generators. In: Proceedings of power and energy society general meeting—conversion and delivery of electrical energy in the 21st century, Pittsburgh, PA, pp 1–3, 20–24 July 2008
12. French Ministerial order of April 23 2008 (2008) Design and operating requirements for the connection of power generation facilities to MV or LV distribution grids. Ref. DEVE0808815A. Available via: https://www.legifrance.gouv.fr/affichTexte.do?cidTexte=JORFTEXT000018698004. Accessed 28 Oct 2016
13. Liu S, Zhou Y (2015) Wind park power control for improving frequency stability of an integrated power grid. In: Pérez-Donsión M, Vergura S, Vitale G (eds) Renewable energy—selected issues, vol I., Cambridge Scholars PublishingLady Stephenson Library, Newcastle upon Tyne, pp 150–169
14. Bose B-K (2014) Energy, global warming and impact of power electronics in the present century. In: Abu-Rub H, Malinowski M, Al-Haddad K (eds) Power electronics for renewable energy systems, transportation and industrial applications, 1st edn. Wiley, New York, pp 1–26
15. San Martín J-I, Zamora I, San Martín J-J, Aperribay V, Eguía P (2011) Energy storage technologies for electric applications. Renew Energy Power Qual J 1(12):1–6
16. Vitale G (2016) Renewable energies—future perspectives. Renew Energy Environ Sustain 1 (17):1–6
17. Egido I, Sigrist L, Lobato E, Rouco L, Barrado A (2015) An ultra-capacitor for frequency stability enhancement in small-isolated power systems: models, simulation and field tests. Appl Energy 137:670–676
18. Molina M-G (2015) Distributed energy storage systems for applications in future smart grids. In: Proceedings of 6th IEEE/PES transmission and distribution: Latin America conference and exposition (T&D-LA), Montevideo, Uruguay, pp 1–7, 3–5 Sept 2012
19. Egido I, Sigrist L, Lobato E, Rouco L (2015) Energy storage systems for frequency stability enhancement in small-isolated power systems. Renew Energy Power Qual J 1(13):1–6

20. Banerjee S, Chatterjee J-K, Tripathy S-C (1990) Application of magnetic energy storage unit as load-frequency stabilizer. IEEE Trans Energy Convers 5(1):46–51
21. Cimuca G, Saudemont C, Robyns B, Radulescu M-M (2006) Control and performance evaluation of a flywheel energy-storage system associated to a variable-speed wind generator. IEEE Trans Ind Electron 53(4):1074–1085
22. Oudalov A, Chartouni D, Ohler C (2007) Optimizing a battery energy storage system for primary frequency control. IEEE Trans Power Syst 22(3):1259–1266
23. Rouco L, Sigrist L (2013) Active and reactive power control of battery energy storage systems in weak grids. In: Proceedings of IREP symposium-bulk power system dynamics and control —IX (IREP), Rethymnon, Greece, pp 1–6, 25–30 Aug 2013
24. Beacon Power (2011) http://beaconpower.com/stephentown-new-york/. Accessed 28 Oct 2016
25. Vitale G (2016) Supercapacitor modelling by Lagrange's equations. In: International conference on modern electrical power engineering, (ICMEPE-2016), pp 1–6, July 2016
26. Alonge F, Rodonò G, Cirrincione M, Vitale G (2016) Supercapacitor diagnosis using an extended Kalman filtering approach. In: 16th IEEE international conference on environment and electrical engineering (EEEIC), pp 1–6, June 2016
27. Bose B (2013) Global energy scenario and impact of power electronics in 21st century. IEEE Trans Ind Electron 60(7):2638–2651
28. Coppez G (2010) The importance of energy storage in renewable power generation: a review. In: Proceedings of 45th international universities power engineering conference UPEC, Cardiff, Wales, UK, pp 1–5, 31 Aug–3 Sept 2010
29. Chakraborty S, Simões M-G, Kramer W-E (2013) Power electronics for renewable and distributed energy systems. Springer, London
30. Vitale G (2016) Energy saving by power electronics: towards a new concept of renewable source. In: International conference on renewable energies and power quality (ICREPQ'16). Invited Paper, Madrid, Spain, pp 1–10, 4–6 May 2016
31. Cirrincione M, Pucci M, Vitale G (2012) Power converters and AC electrical drives with linear neural networks. CRC PRESS, Boca Raton
32. Ali M-H, Wu B, Dougal R-A (2010) An overview of SMES applications in power and energy systems. IEEE Trans Sustain Energy 1(1):38–47
33. Endesa Press Release (2014) http://www.endesa.com/en/saladeprensa/noticias/energy-storage-plants-STORE-Project. Accessed 28 Oct 2016
34. Ingeteam Brochure, "STORE Guinchos" (2014) http://www.ingeteam.com/Portals/0/Catalogo/Sector/Documento/SSE_1420_Archivo_cs24iptt01-a-pga-store-guinchos.pdf. Accessed 28 Oct 2016
35. PowerCorp (2013) PowerStore: Product Description and Data Sheet. https://library.e.abb.com/public/e13f1d26d87e9167c1257c37002e38bf/9AKK100580A2551_Powerstore_Brochure_EN_HR_(Dic2013).pdf. Accessed 28 Oct 2016
36. Saft Batteries Brochure (2013) Saft Li-ion batteries helps GranCanarias's STORE project to integrate renewable. http://www.saftbatteries.com/sites/default/files/21860–2-0313_CS_Endesa_Protected.pdf. Accessed 28 Oct 2016

Identifying Energy Trends in Fiji Islands

Shamal Selvin Chand, Aamir Iqbal, Maurizio Cirrincione, F.R. Islam, K.A. Mamun and Ajal Kumar

Abstract This chapter intends to simulate the current situation of Fiji Electricity Authority's transmission network of Viti Levu by using the load flow method and investigate the situation of the overall system. The first part of the chapter focuses on finding out the problems faced by Fiji Electricity Authority with the reliability of the network. After inspecting regions vulnerable to faults, different scenarios have been tested in steady state with different loads in various parts of Viti Levu. Reaction of the network was observed to determine the highest load level that the network can support before collapsing. The second part of chapter proposes recommendations to improve the reliability of the network. These recommendations are tested using the ETAP software in the form of scenarios by incorporating different possible choices with the current network, and the results obtained from each scenario are analyzed. This chapter concludes with the listing of recommendations that can be made in order to do further analysis for future expansion of the network through renewable energy sources (RES).

Keywords Transmission network · ETAP · Load flow · Renewable energy sources

S.S. Chand · A. Iqbal · M. Cirrincione (✉) · F.R. Islam · K.A. Mamun · A. Kumar
School of Engineering and Physics, The University of the South Pacific, Suva, Fiji
e-mail: maurizio.cirrincione@usp.ac.fj

S.S. Chand
e-mail: shamalselvin@outlook.com

A. Iqbal
e-mail: aamiriqbal14@hotmail.com

F.R. Islam
e-mail: islam_f@usp.ac.fj

K.A. Mamun
e-mail: mamun_k@usp.ac.fj

A. Kumar
e-mail: kumar_a@usp.ac.fj

F.M.R. Islam et al. (eds.), *Smart Energy Grid Design for Island Countries*,
Green Energy and Technology, DOI 10.1007/978-3-319-50197-0_9

1 Introduction

Fiji is a developing tropical country with abundance of renewable energy source (RES). There is an ever-increasing demand for electrical energy and thus there is a need to harness as many RES as possible to meet the requirements. Presently, majority of the energy is derived from fossil fuel purchased from overseas and costs the government a substantial amount of its annual budget. Thus, a more efficient means of electricity production is necessary, since there is an increasing demand that could eventually increase the fossil fuel imports to an unsustainable level.

The purpose of this chapter is to focus on the vast amount of renewable energy still untapped in Fiji, for instance solar, wind, and hydro and how they can be suitably employed and their impact on the present grid in Fiji. Currently, there are renewable energy generation plants in the form of the three readily available renewable resources, solar, wind, and hydro, which roughly adds up to as much as 40% of the electricity generated throughout the country. Some of these generation plants, however, do not operate at their peak values or are idle [1]. This chapter attempts to explore the possibility to move towards a 100% renewable generation in Fiji and identify the imminent problems associated with it.

According to the Fiji Electricity Authority's (FEA) Annual report, the year 2014 was one of the most difficult times in terms of its economic situation: because of a prolonged dry weather, FEA had to scale down the hydro operation and to increase the diesel generation to meet the demand. This resulted in purchasing containerized diesel plants which cost approximately $16.9M USD with fuel expenses totaling to $67.9M USD, as much as $27.6M USD more than the previous year [1].

On the other hand, Fiji's climate is very suitable for setting up renewable energy plants: currently, the country runs hydro and wind plants for the electrical power generation, while solar is not yet commonly used for large-scale production. Thus, it is possible to further exploit these three sources and get a reasonably higher amount of renewable energy production [1].

At present there are some solar plants on Viti Levu built in the past, but due to some unknown reasons these are not operated to its maximum. Thus, it is important to get such systems back online, considering the abundance of solar energy in Fiji.

In order to carry out the analysis of the transmission network, an electrical power system modeling software, electrical transient, and analysis program (ETAP), has been used in this work. ETAP is well known for the analysis of a power system in terms of modeling, design, optimization, control, operation, and automation. It is very useful for carrying out static analysis of transmission networks, which is very suitable for the requirement of this chapter [2]. In this regard, the chapter has the following targets:

- It will help identify the existing centralized or decentralized power plants in Fiji and estimate their electrical power production per year.
- It will carry out the load flow analysis of the current transmission system of FEA by simulating the condition of the transmission network. This will greatly aid in identifying the weak points in the network, and will also make it easier to find

the cause of power black outs. Particular attention will be paid to analyzing the reliability of the network under different scenarios and possible improvements of the reliability of the existing network will be proposed, with the minimum possible investment.
- Explore the availability of various renewable resources in Fiji to generate electricity and find potential areas to setup renewable energy plants as well as the type of source.
- Propose possible techniques to achieve a 100% renewable energy source electricity generation.

2 Background

The year 2014 was a very challenging for FEA as they struggled to produce sufficient energy. There was a decrease in hydroelectrical energy resulting from a severe drought thus, they had to increase the diesel generator production that eventually led to their all-time record fuel cost of $87.4M USD against a budget of $66.5M USD. This event caused FEA to rethink of finding alternative means of producing electrical energy by using other RES [1].

FEA has just completed the review of its 10-year Power Development Plan ending (2015–2025), which contains the load forecasting and generation planning scenarios up to 2025 for Viti Levu, Vanua Levu and Ovalau power systems. This Plan includes the analysis of the associated network assets to be developed, and the investment plan required to enhance the 132 and 33 kV transmission and sub-transmission of present power networks [1]. The implementation of this Plan would allow FEA to maintain a sustainable demand.

3 Load Flow Analysis of the Fiji Power System

This chapter investigates the present transmission network of FEA by making a steady-state analysis in its normal state by performing Load Flows using the ETAP software. Data were acquired from the FEA's 2014 annual report [1].

The grid map from the FEA's annual report for the year 2014 was used to extract the data needed to design the grid network. Other relevant information was retrieved from a report of KEMA on quantification of power system energy losses and loads in South Pacific utilities from 2012 [3] and the literature [4, 5]. Only the Viti Levu network has been analyzed. To design the network, average load ratings were used and a total of 145 MW of static load was added to the transmission network on different buses. The generation data extracted from the FEA's report showed a total of 217 MW of generation capacity [1]. The general situation is summarized in Table 8 in Appendix, where the total demand is the sum of the load and the transmission losses.

The FEA power grid has three categories of power lines, the high voltage transmission lines with voltage ratings of 132 and of 33 kV, the medium voltage distribution lines with voltage ratings of 11 kV and low voltage distribution lines of 6.6 kV. The FEA report also highlighted the data for all the generating stations across Fiji, which was used in the ETAP network analysis [1].

4 Simulation for the Viti Levu Transmission Network

Network designed using ETAP is a complex diagram, for better understanding of the network each Substation was represented by a composite network block. The network inside these composite blocks are shown in Figs. 3, 4, 5 and 6.

After completing the network of the transmission grid of Viti Levu, the load flow analysis of the network was carried out: Fig. 1 shows the schematic of the Electricity network of FEA in Viti Levu (Fiji Islands). The network in Fig. 2 has a total of 71 buses, of which 14 are PV buses and 56 are PQ buses. The swing bus of the network is placed in Vuda.

Critical buses at Nadarivatu, Wailoa, Korolevu, Rarawai, Tavua, Vatukaula, and Komo Substations are colored pink as shown in Figs. 3a, b, 4b, 5b–d and 6e respectively. A bus becomes critical if it is either under voltage or over voltage. Critical range is from 95 to 98% for under voltage buses and 102–105% for over

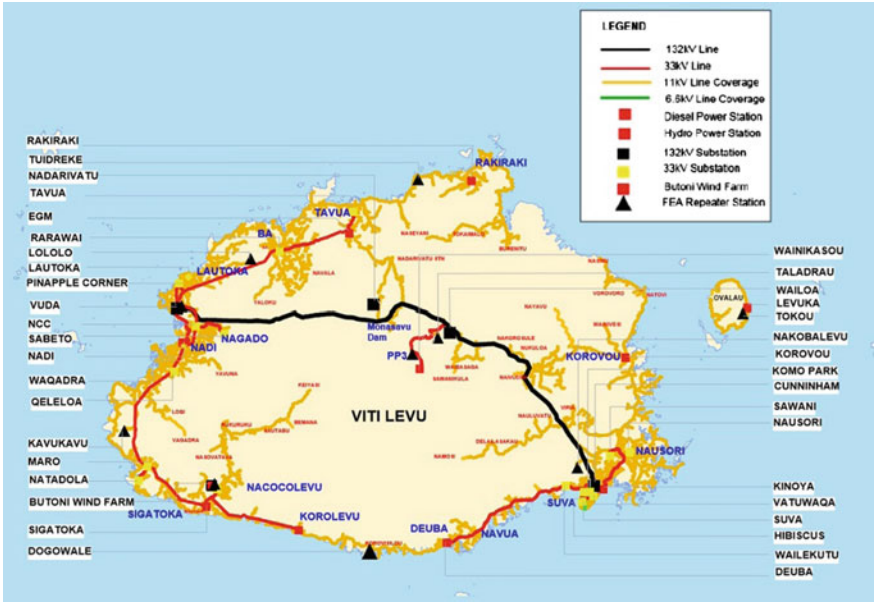

Fig. 1 FEA's map of the power system [1]

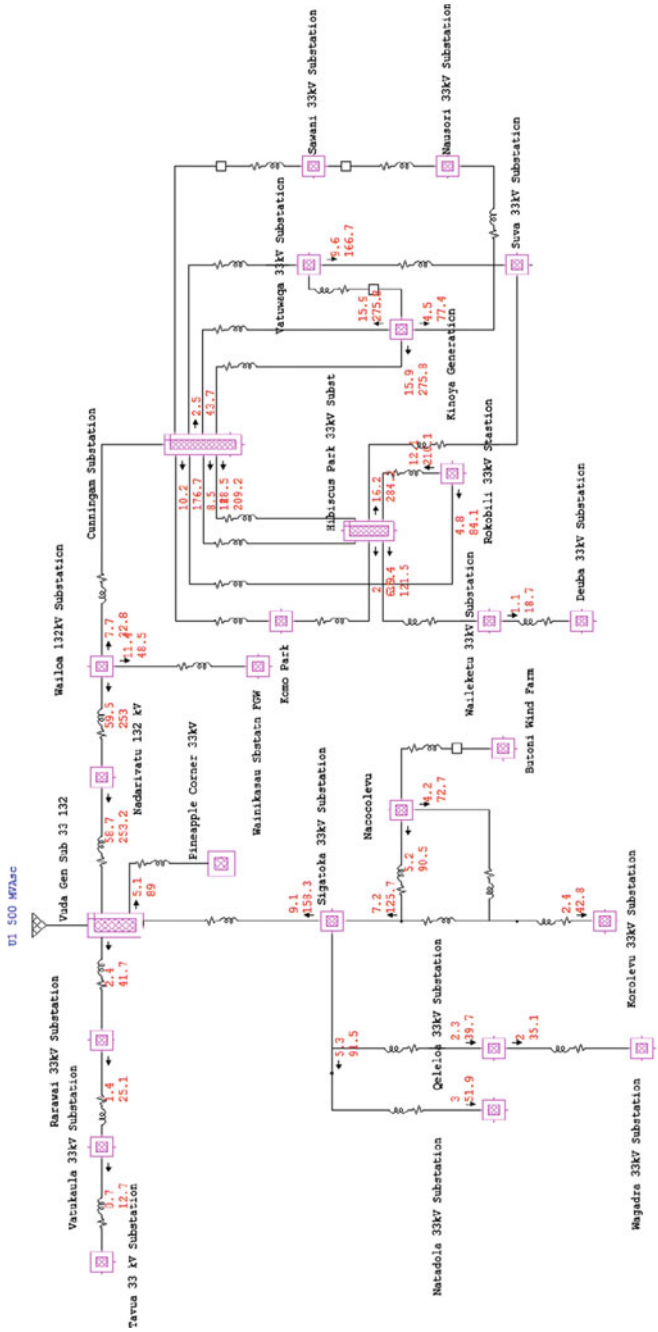

Fig. 2 Schematic of FEA's transmission grid network

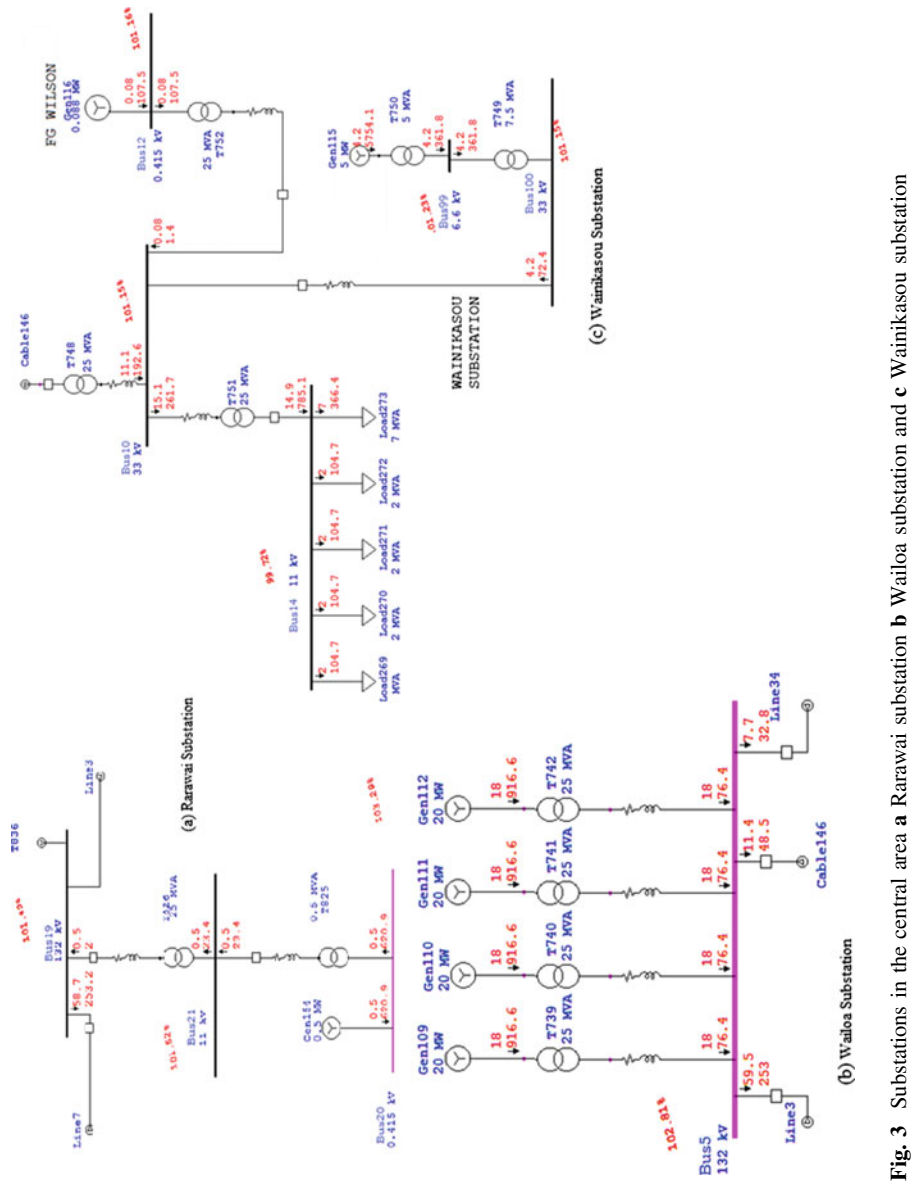

Fig. 3 Substations in the central area **a** Rarawai substation **b** Wailoa substation and **c** Wainikasou substation

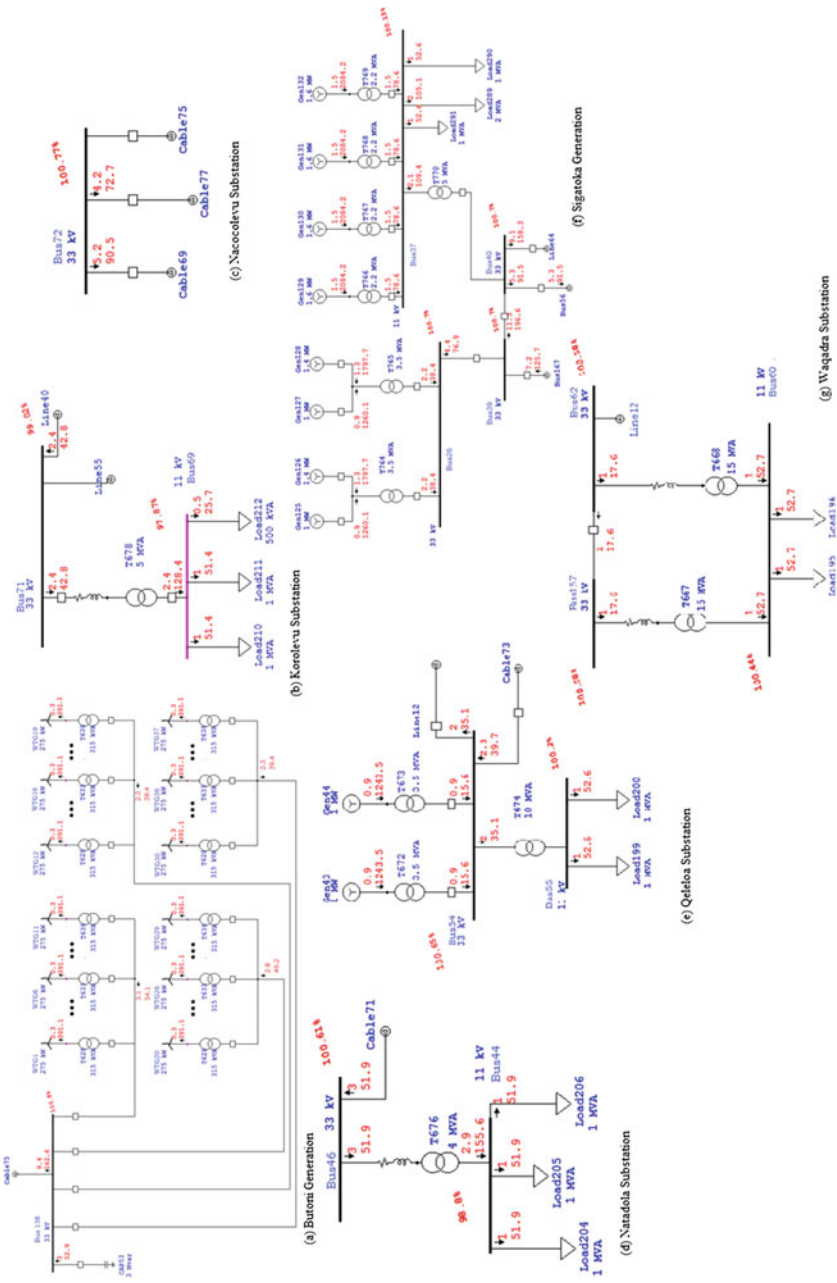

Fig. 4 Substations in the North area **a** Butoni generation **b** Korolevu substation **c** Nacocolevu substation **d** Natadola substation **e** Qeleloa substation **f** Sigatoka generation and **g** Waqadra substation

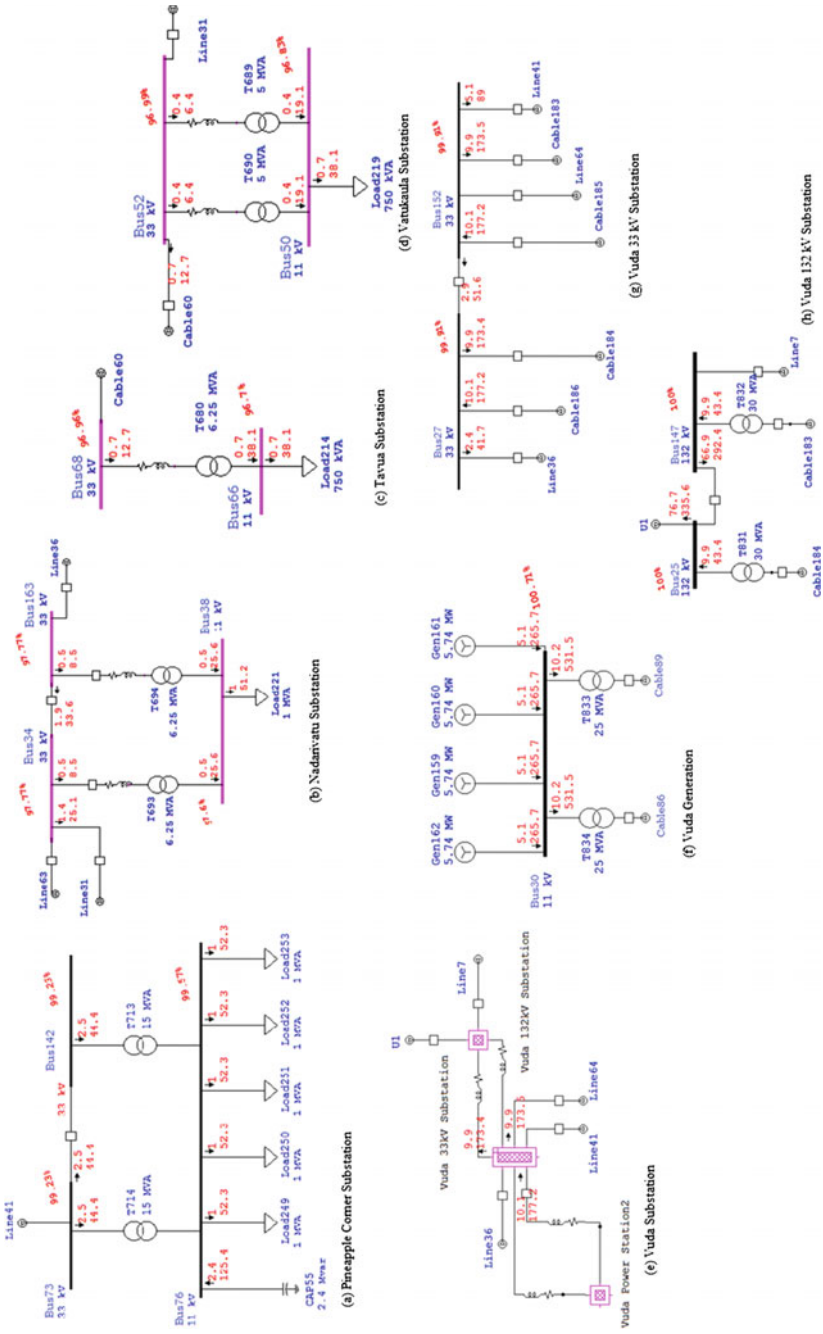

Fig. 5 Substations in the West area **a** Pineapple Corner substation **b** Nadarivatu substation **c** Tavua substation **d** Vatukaula substation **e** Vuda **f** Vuda generation **g** Vuda 33 kV substation and **h** Vuda 132 kV substation

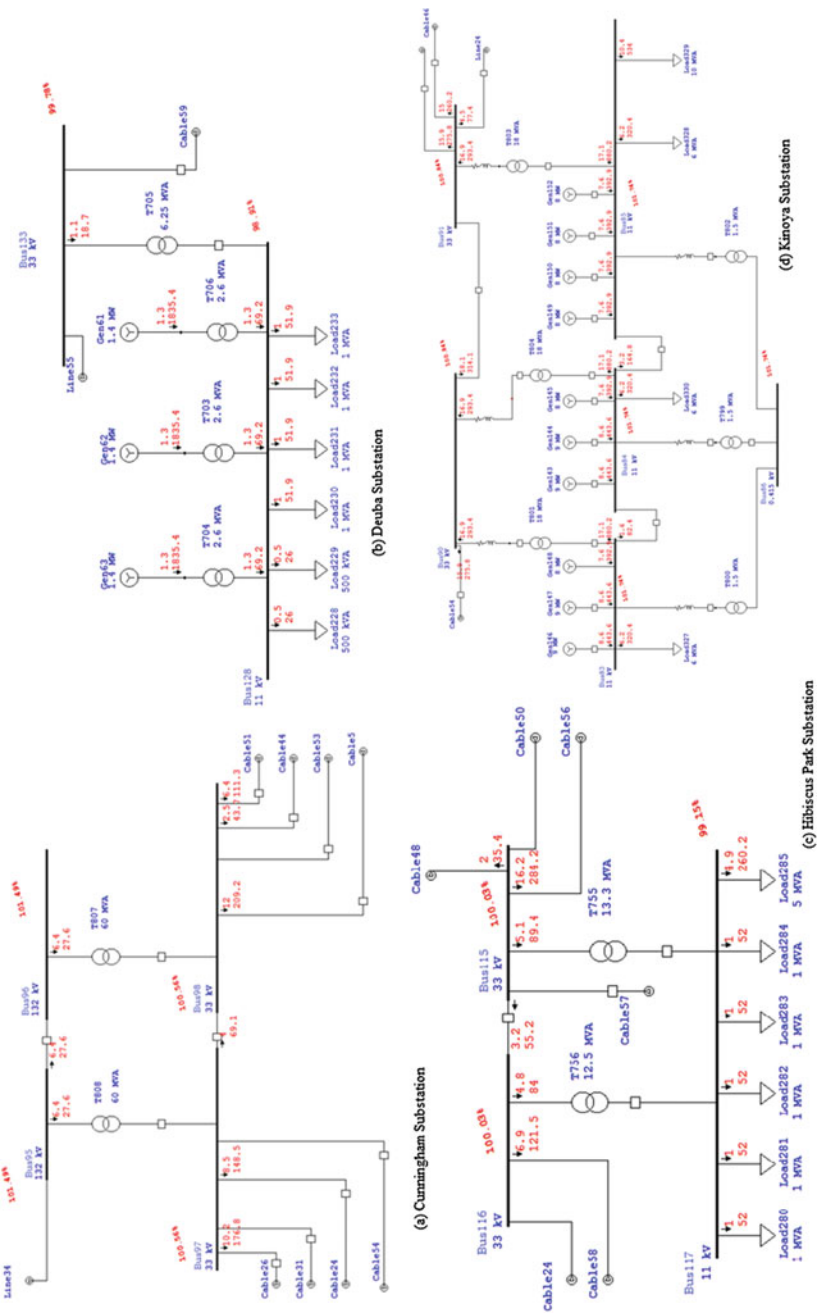

Fig. 6 Substations in the East area **a** Cunningham substation **b** Deuba substation **c** Hibiscus Park substation **d** Kinoya substation **e** Komo Park substation **f** Nausori substation **g** Rokobili generation **h** Sawani substation **i** Suva substation **j** Vatuwaqa substation and **k** Wailiketu substation

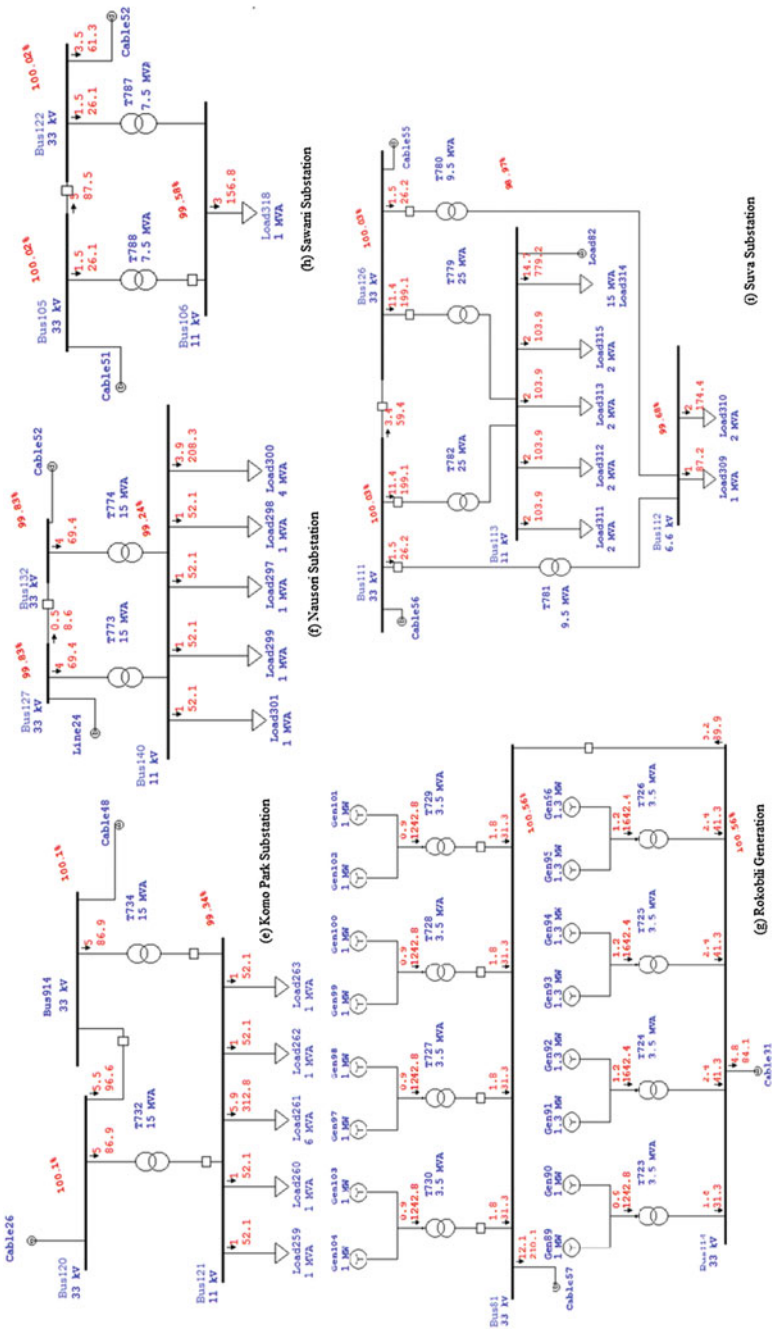

Fig. 6 (continued)

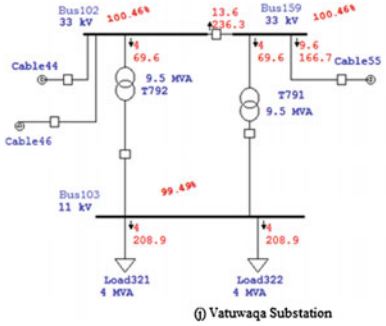

(j) Vatuwaqa Substation

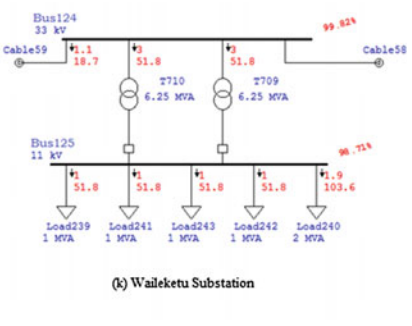

(k) Waileketu Substation

Fig. 6 (continued)

Table 1 Grouping of divisional substations of Viti Levu with their respective bus and figure reference

Group	Substation	Fig.	Bus present
Central	Nadarivatu	Fig.3a	Bus 19, Bus 20, Bus 21
	Wailoa	Fig. 3b	Bus 5
	Wainikasou	Fig. 3c	Bus 10, Bus 12, Bus 14, Bus 99, Bus 100
North	Butoni wind farm	Fig. 4a	Bus 138
	Korolevu	Fig. 4b	Bus 69, Bus 71
	Nacocolevu	Fig. 4c	Bus 72
	Natadola	Fig. 4d	Bus 44, Bus 46
	Qeleloa	Fig. 4e	Bus 54, Bus 55
	Sigatoka	Fig. 4f	Bus 26, Bus 37, Bus 39, Bus 40
	Waqadra	Fig. 4g	Bus 60, Bus 62, Bus 157
West	Pineapple Corner	Fig. 5a	Bus 73, Bus 76, Bus 142
	Rarawai	Fig. 5b	Bus 34, Bus 38, Bus 163
	Tavua	Fig. 5c	Bus 66, Bus 68
	Vatukaula	Fig. 5d	Bus 50, Bus 52
	Vuda	Fig. 5e	
	• Generation	Fig. 5f	Bus 30
	• 33 kV	Fig. 5g	Bus 27, Bus 152
	• 132 kV	Fig. 5h	Bus 25, Bus 147
East	Cunningham	Fig. 6a	Bus 95, Bus 96, Bus 97, Bus 98
	Deuba	Fig. 6b	Bus 133, Bus 128
	Hibiscus Park	Fig. 6c	Bus 115, Bus 116, Bus 117
	Kinoya	Fig. 6d	Bus 83, Bus 84, Bus 85, Bus 86, Bus 90, Bus 91
	Komo Park	Fig. 6e	Bus 120, Bus 121, Bus 914
	Nausori	Fig. 6f	Bus 127, Bus 132, Bus 140
	Rokobili	Fig. 6g	Bus 81, Bus 114
	Sawani	Fig. 6h	Bus 105, Bus 106, Bus 122
	Suva	Fig. 6i	Bus 111, Bus 112, Bus 113, Bus 126
	Vatuwaqa	Fig. 6j	Bus 102, Bus 103, Bus 159
	Waileketu	Fig. 6k	Bus 124, Bus 125

voltage buses. Buses operating under normal conditions are colored black. Buses operating from 98 to 102% fall in the stable range. These values are known as the % operation of the buses.

A composite schematic was created in ETAP to compress the whole network for better understanding and representation. Each composite block represents either a generation or substation. These substations are divided into four groups based on the geographic location as shown in Table 1.

Figure 7 represents the different color codes used in ETAP. The results generated from the load flow showed that the network was in a critical state. The critical Substations include Tavua, Vatukaula, Rarawai, Korolevu, and Komo Park. Presently, addition of any new industrial load to the grid would make the bus voltages go beyond its limits and would force the system in an "alert" and the whole system would go into breakdown with a blackout.

Table 2 illustrates the all the bus that are in critical condition. These bus are located in Nadarivatu, Wailoa, Korolevu, Rarawai, Tavua, Vatukaula, and Komo

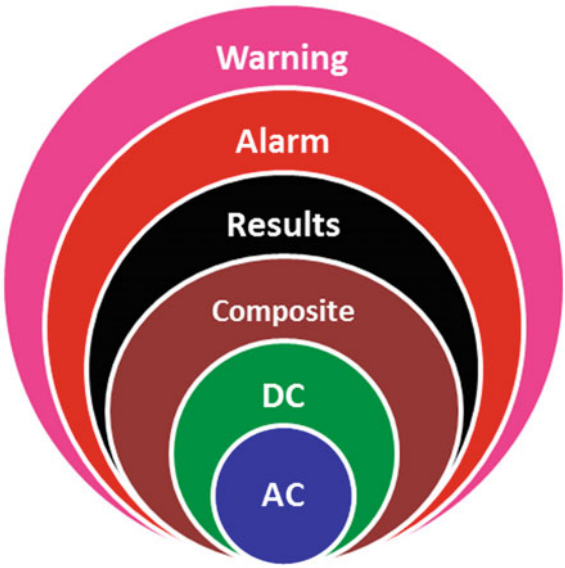

Fig. 7 ETAP color code for load flow analysis

Table 2 Critical bus in the current transmission network with their respective substations

Group	Substation	Fig.	Bus critical
Central	Nadarivatu	Fig. 3a	Bus 20
	Wailoa	Fig. 3b	Bus 5
North	Korolevu	Fig. 4b	Bus 69
West	Rarawai	Fig. 5b	Bus 34, Bus 38, Bus 163
	Tavua	Fig. 5c	Bus 66, Bus 68
	Vatukaula	Fig. 5d	Bus 50, Bus 52
East	Komo Park	Fig. 6e	Bus 121

Park substations and shows the respective figures where aforementioned bus can be found.

Graph in Fig. 8 is a comparison of rated and operation voltages of the critical buses observed from the current network Load Flow. Table 9 in Appendix shows that some of the bus are rated over voltage while other buses are rated under voltage but both fall within a critical range (95–98% for under voltage and 102–105% for over voltage). Over voltage buses are rated critical because those buses are connected to the generators and are known as the voltage control buses (PV buses), where the real power generation is controlled through the prime mover, while the terminal voltage is controlled through the generator excitation. Keeping the input power constant through turbine-governor control and keeping the bus voltage constant using automatic voltage regulator, the PG_i and $|\mathbf{V}_i|$ for these buses are determined thus, these buses are also referred to as PV buses. Hence, these buses are not so vulnerable to faults due to voltage drops and can be neglected [5].

On the other hand, those buses that are rated under voltage operation are a matter of concern because a sudden increase of the load would eventually cause faults in those buses and cause break down of the entire network. There are nine such buses illustrated in Figs. 3a, b, 4b, 5b–d and 6e.

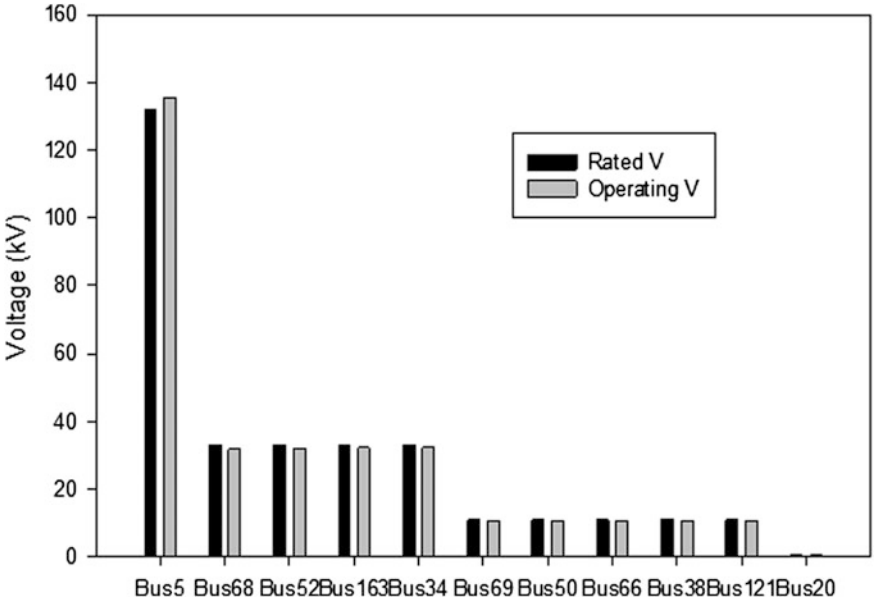

Fig. 8 Voltage comparison of critical bus in the current network load flow

5 Scenario Testing

To understand the reaction of the network to sudden variations in the load, different scenarios were tested, to give a better picture of the network under those circumstances. This allowed for possible configurations to check the network to for "alert" state.

5.1 Case 1 (Adding a Load of 10 MW Load in the Central Division of Viti Levu)

This load is added at the Suva Substation, in the central Viti Levu. This was based on the forecasted increase in population on Viti Levu or addition of new industrial machines.

Table 3 illustrates all the bus those are in critical condition. Bus located in Nadarivatu, Deuba, Suva, Hibiscus Park, Komo Park, Korolevu, Nausori, Rarawai, Sawani, Vatuwaqa, and Waileketu Substations experienced critical situation.

Graph in Fig. 9 is a comparison of rated and operation voltages of the critical buses observed from the current network Load Flow. From this scenario we observe that when a 10 MW load is added in the central division, which is densely populated with large amount of loads, the network buses go beyond their limits and the whole network is in the dangerous state of alert. A total of 29 bus (from Table 10 in Appendix) are now operating at under voltage situation due this load, in comparison to 11 buses in the normal situation.

Table 3 Critical bus in substations after adding a load of 10 MW in the central division of Viti Levu

Group	Substation	Fig.	Critical bus
Central	Nadarivatu	Fig. 3a	Bus 20
North	Korolevu	Fig. 4b	Bus 69
West	Rarawai	Fig. 5b	Bus 34, Bus 38, Bus 163
	Tavua	Fig. 5c	Bus 66, Bus 68
	Vatukaula	Fig. 5d	Bus 50, Bus 52
East	Deuba	Fig. 6b	Bus 133, Bus 128
	Hibiscus Park	Fig. 6c	Bus 115, Bus 116, Bus 117
	Komo Park	Fig. 6e	Bus 120, Bus 121
	Nausori	Fig. 6f	Bus 127, Bus 132, Bus 140
	Sawani	Fig. 6h	Bus 105, Bus 106, Bus 122
	Suva	Fig. 6i	Bus 111, Bus 112, Bus 113, Bus 126
	Vatuwaqa	Fig. 6j	Bus 103
	Waileketu	Fig. 6k	Bus 124, Bus 125

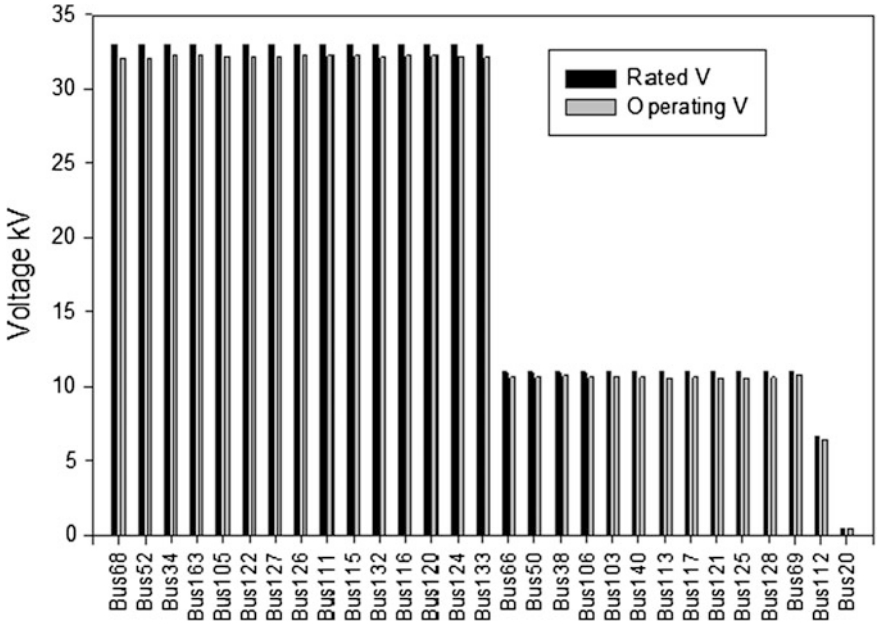

Fig. 9 Voltage comparison of critical buses after adding the 10 MW load in the central division

5.2 Case 2 (Adding a New Transmission Connection Between Deuba and Korolevu with and Without the New Load of 10 MW in East)

This connection is very critical because the current network, which is not meshed adequately, would become interconnected allowing power flows to follow different routes to supply load: this would result in a healthier network, more resilient to load perturbations and to fault: the short-circuit ratio and therefore the stiffness of the network would increase.

5.2.1 Without Load of 10 MW

Table 4 illustrates all the bus those are in critical condition when a new transmission line is added between Deuba and Korolevu, but no new load has been considered in this occasion. In such a situation buses in Nadarivatu, Komo Park, Rarawai, Tavua, Vatukaula, and Wailoa Substations experienced critical situation.

It is evident from Fig. 10 that eight bus are in the critical range; the data of this graph is a comparison of rated and operating voltages from Table 11 in Appendix which is extracted from the ETAP report. In the present state there were a total of 11 bus running under voltage. In this case, the operating mode of the network is more reliable in operating condition than the present one, but still some criticality is present.

Table 4 Critical bus in substations after adding a new transmission line between Deuba and Korolevu without the new load of 10 MW in east

Group	Substation	Fig.	Critical bus
Central	Nadarivatu	Fig. 3a	Bus 20
	Wailoa	Fig. 3b	Bus 5
West	Rarawai	Fig. 5b	Bus 38
	Tavua	Fig. 5c	Bus 66, Bus 68
	Vatukaula	Fig. 5d	Bus 50, Bus 52
East	Komo Park	Fig. 6e	Bus 121

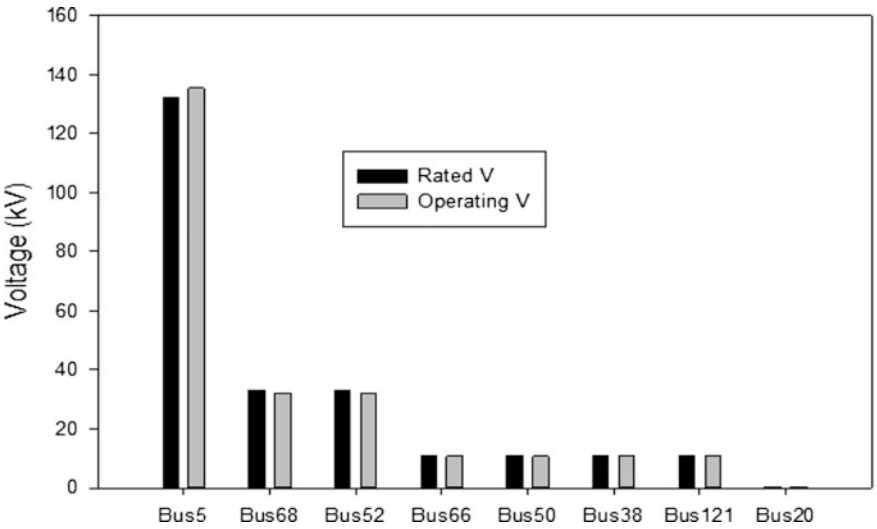

Fig. 10 Voltage comparison of critical buses in the current network with the interconnection between Deuba and Korolevu in place

5.2.2 Case 2 (with 10 MW Load)

Table 5 illustrates all the bus those are in critical condition. Buses in Nadarivatu, Deuba, Hibiscus Park, Komo Park, Korolevu, Nausori, Sawani, Suva, Tavua, Vatukaula, Vatuwaqa, Waileketu and Rarawai substations experienced critical situation.

From Table 12 in Appendix and Fig. 11, it can be noted that when a 10 MW load is added in the east division with the new connection in place, it reduces the number of critical buses by four in comparison to the situation of the current network after adding the same amount of load. The four buses are now well within limits. Stabilizing those buses will vastly improve the stability of the network. Another notable change is the ratio of all the critical buses with respect to all buses: it shows a reduction of the chances of faults in the network.

Table 5 Critical bus in substations after adding a new transmission line between Deuba and Korolevu with a new load of 10 MW in east

Group	Substation	Fig.	Critical bus
Central	Nadarivatu	Fig. 3a	Bus 20
North	Korolevu	Fig. 4b	Bus 69
West	Rarawai	Fig. 5b	Bus 38
	Tavua	Fig. 5c	Bus 66, Bus 68
	Vatukaula	Fig. 5d	Bus 50, Bus 52
East	Deuba	Fig. 6b	Bus 133, Bus 128
	Hibiscus Park	Fig. 6c	Bus 115, Bus 116, Bus 117
	Komo Park	Fig. 6e	Bus 120, Bus 121
	Nausori	Fig. 6f	Bus 127, Bus 132, Bus 140
	Sawani	Fig. 6h	Bus 105, Bus 106
	Suva	Fig. 6i	Bus 111, Bus 112, Bus 113, Bus 126
	Vatuwaqa	Fig. 6j	Bus 103
	Waileketu	Fig. 6k	Bus 124, Bus 125

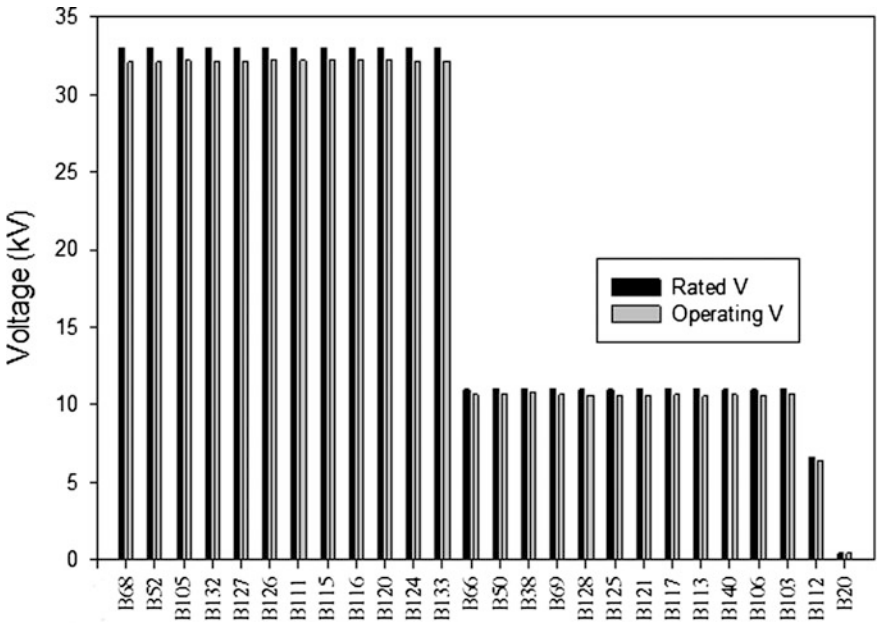

Fig. 11 Voltage comparison of critical buses in the current network with the interconnection between Deuba and Korolevu in place and a load of 10 MW added in east

5.3 *Case 3*

Case 3 is considered; adding a new transmission connection between Deuba and Korolevu and a second transmission network connection from Tavua to Nadarivatu and testing with and without the new load and discussed below.

5.3.1 Without 10 MW Load

Table 6 illustrates all the bus those are in critical condition. Buses in Nadarivatu, Komo Park, Waileketu and Wailoa Substations experienced critical situation.

Figure 12 illustrates that Bus 5, Bus 121, Bus 125, and Bus 20 are now operating at 135.23, 10.76, 10.78, and 0.43 kV, respectively. Table 13 in the Appendix also represents this data.

After making the two connections a noticeable improvement is seen in the bus stability. Now only 4 buses are critical, of which two buses are generation buses, two are load buses, and technically only the two load buses are unreliable. Even these critical buses are operating at almost stable region of % operation. This shows that making these two connections in the network will help greatly in improving the reliability of the network. This will allow the network to be able to support new loads without necessitating an increase in the generation.

5.3.2 With 10 MW Load

Table 7 illustrates all the bus those are in critical condition. Buses in Nadarivatu, Deuba, Hibiscus Park, Komo Park, Korolevu, Nausori, Sawani, Suva, Vatuwaqa, and Waileketu Substations experienced critical situation.

Table 14 in Appendix shows that 22 Bus are critical when 10 MW Load is added to the newly Interconnected Network and is also illustrated in Fig. 13. Earlier in *case 1* 29 buses were in critical region. Through the introduction of the new connections a greater amount of reliable buses can be achieved and it is evident from the statistics. A total of 6 bus fall into the reliable range.

Table 6 Critical bus in substations after adding a new transmission connection between Deuba and Korolevu and a second transmission network connection from Tavua to Nadarivatu

Group	Substation	Fig.	Critical bus
Central	Nadarivatu	Fig. 3a	Bus 20
	Wailoa	Fig. 3b	Bus 5
East	Komo Park	Fig. 6e	Bus 121
	Waileketu	Fig. 6k	Bus 125

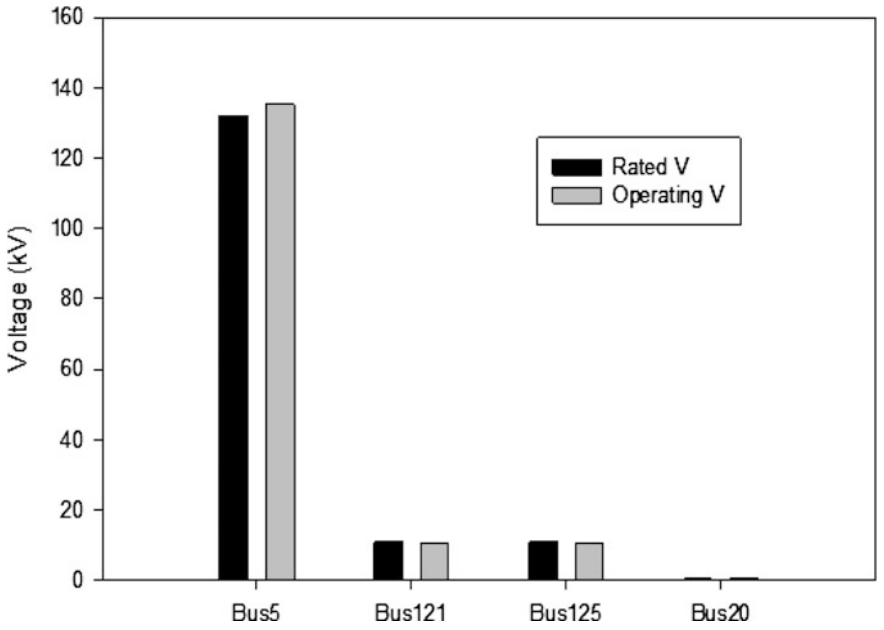

Fig. 12 Voltage comparison of critical buses in the current network with the interconnection between Deuba and Korolevu in place and a second transmission network connection from Tavua to Nadarivatu

Table 7 Critical bus in substations after adding a new transmission connection between Deuba and Korolevu and a second transmission network from Tavua to Nadarivatu with a new load of 10 MW in east

Group	Substation	Fig.	Bus present
Central	Nadarivatu	Fig. 3a	Bus 20
North	Korolevu	Fig. 4b	Bus 69
East	Deuba	Fig. 6b	Bus 133, Bus 128
	Hibiscus Park	Fig. 6c	Bus 115, Bus 116, Bus 117
	Komo Park	Fig. 6e	Bus 120, Bus 121
	Nausori	Fig. 6f	Bus 127, Bus 132, Bus 140
	Sawani	Fig. 6h	Bus 105, Bus 106, Bus 122
	Suva	Fig. 6i	Bus 111, Bus 112, Bus 113, Bus 126
	Vatuwaqa	Fig. 6j	Bus 103
	Waileketu	Fig. 6k	Bus 124, Bus 125

In comparison to the earlier interconnections without load, the number of critical buses have increased. This change is obvious because an increase in load will always deteriorate the bus voltages and in the case of increased load it will always

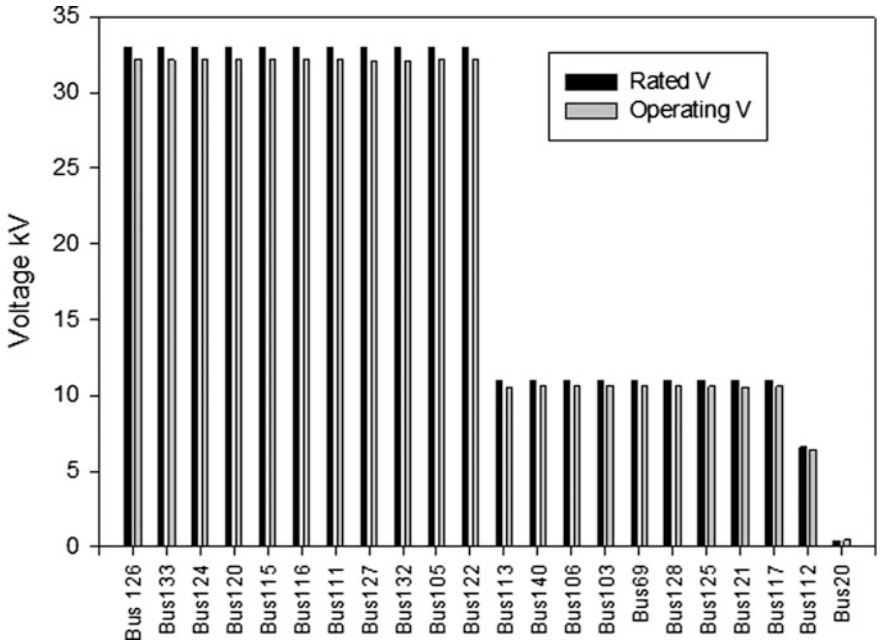

Fig. 13 Voltage comparison of critical buses in the current network with the interconnection between Deuba and Korolevu in place and a second transmission network connection from Tavua to Nadarivatu with a new load of 10 MW in east

drop. When a 10 MW load was introduced in the present network a total of 29 bus are turned critical, while in this case only 22 bus experience critical situation.

5.4 Case 4 (Fault Analysis) Introducing a Three Phase Fault at Vuda 33 kV Substation in the Current Network

Vuda station has been chosen as the location of the fault, since there is a three-way junction at Vuda, making this bus critical and when this fault occurs, a number of substations and loads go offline, making the situation very critical for the grid. These substations include Rarawai, Vatukaula, Tavua, Sigatoka, Waqadra, Natadola, Qeleloa, and Korolevu as illustrated in Fig. 14. The only source left to support these loads is the Butoni wind farm, which is not sufficient at all for its low power rating. However, the other half of the network remains still intact, which includes the east division.

From Table 15 in Appendix, it can be noted that the total load decreases to 126.35 MW from 142.53 MW compared to current network Load. Another notable

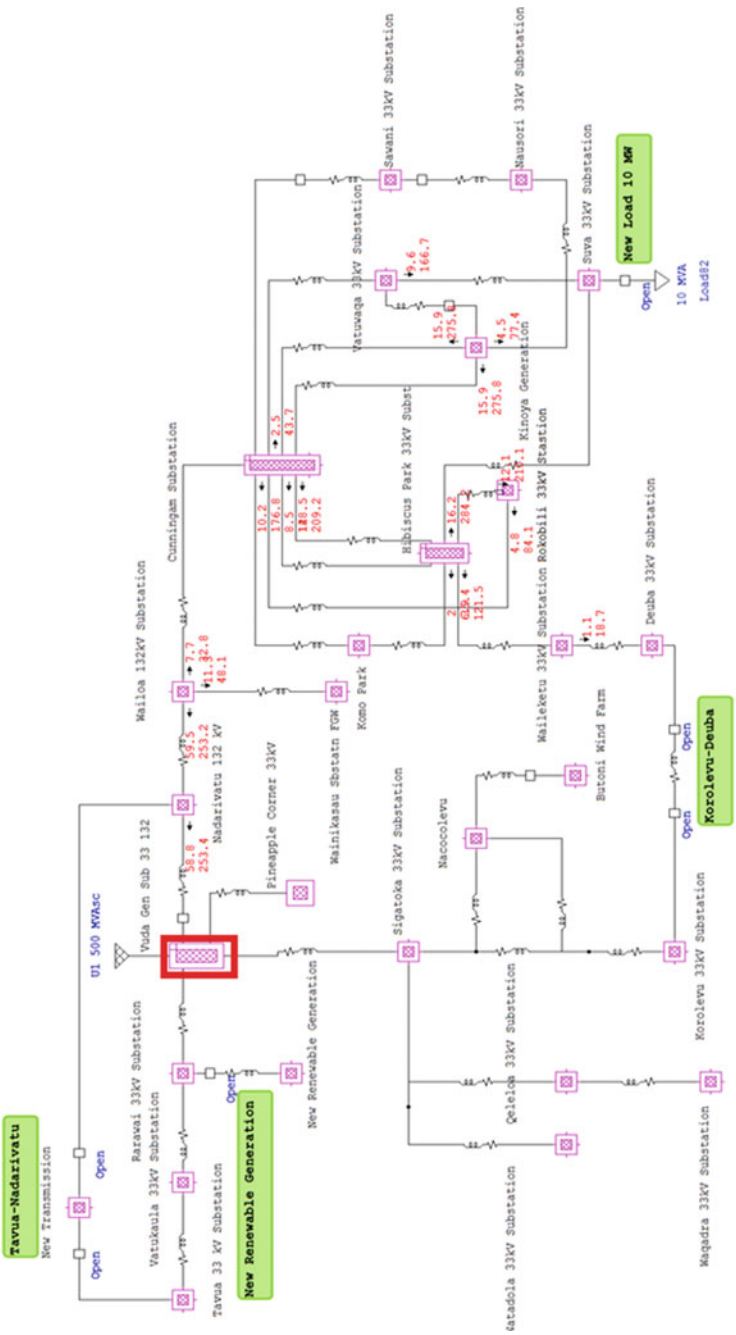

Fig. 14 Schematic of FEA transmission grid network after the introduction of fault at Vuda

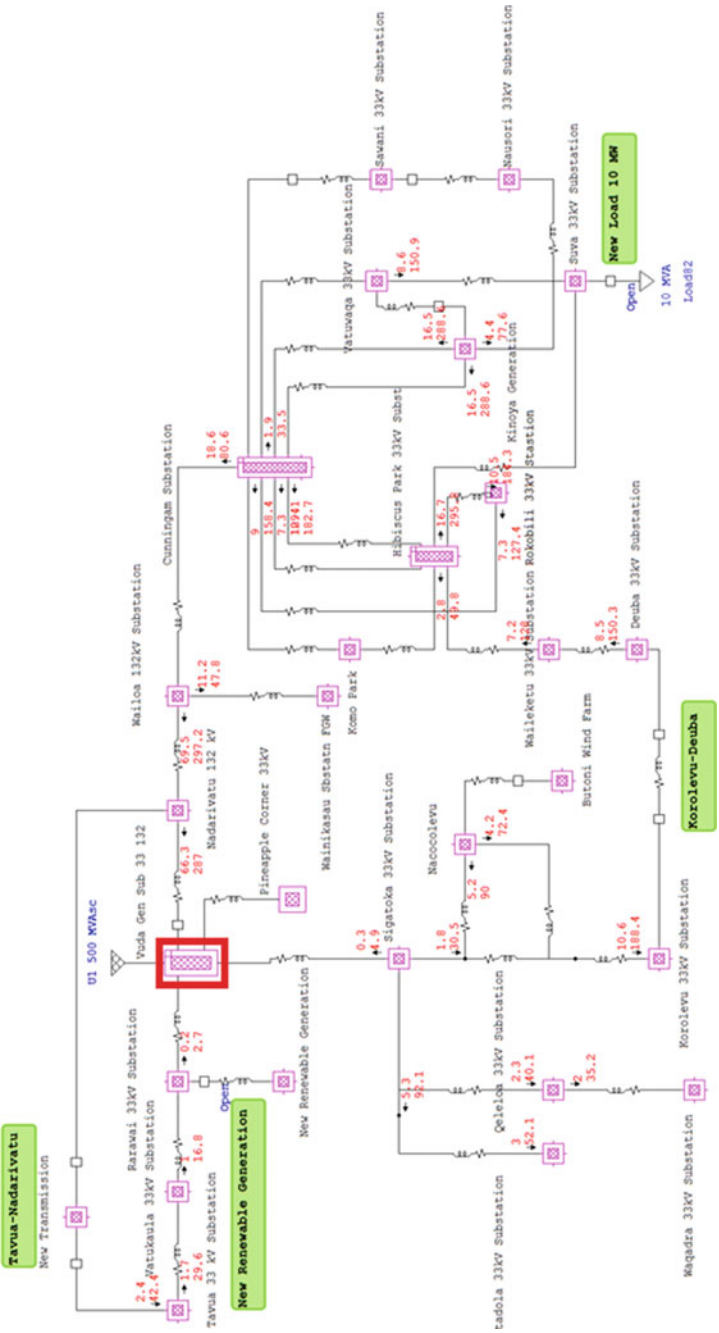

Fig. 15 Schematic of FEA transmission grid network after adding a new transmission connection between Deuba and Korolevu and a second transmission network connection from Tavua to Nadarivatu and then introducing a of fault at Vuda

change is the generation, which drops down to 176.06 MW from 217.42 MW compared to current network generation.

5.5 Case 5 (Fault Analysis) *Occurrence of a Fault at Vuda 33 kV Substation in the Network with the Two New Transmission Connections Are Incorporated*

Figure 15 illustrates that only Vuda area gets affected and the rest of the network remains online. Vuda is around 8% of the total load. This will be very convenient for the restoration of the power, as the fault impacts a small area, with resulting reduction of restoration costs and time.

From Table 16 in Appendix, it can be noted that the total demand increases to 141.81 MW from 126.35 MW compared to Case 4 which was the Introduction of three phase fault at Vuda 33 kV substation in the current network. Another notable change is the generation, which goes up to 197.43 MW from 176.06 MW compared to Case 4.

5.6 *Case 6*

Adding a new renewable source of 12 MW of RES (Wind 6 MW, Solar 2 MW, and Biomass 4 MW), generation units at Rarawai and incorporating it with the network scenario analyzed here as considering case 3.

This scenario is introduced to test if addition of a new RES can further improve the reliability of the system [6]. No additional loads are added in this scenario. Figures 16 and 17 illustrate that Buses in Nadarivatu and Wailoa are in critical condition.

Table 17 in Appendix, shows a total of two buses still remains critical: these are generation buses and are in over voltage condition. It can be concluded from this

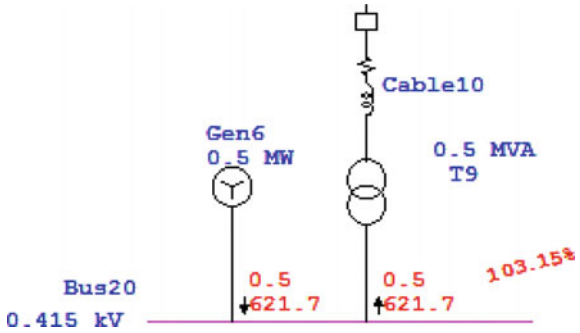

Fig. 16 Backup generation at Nadarivatu

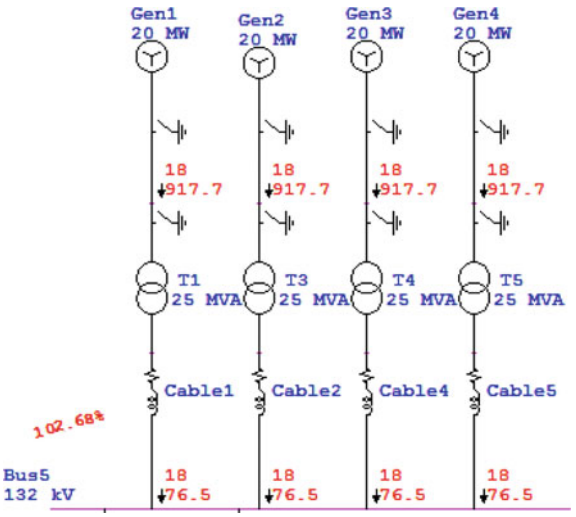

Fig. 17 Wailoa 132 kV substation

scenario that, by adding the new RES, the total system becomes more reliable and it can sustain the present loads without running the risk of encountering faults due to sudden load increase. It also shows that Rarawai is a suitable location for introducing a new RES generation unit and that it is not necessary to add it in the eastern division to make buses more reliable.

6 Conclusions

In this chapter, the FEA's transmission network in Fiji is studied in steady state to understand its weakness and some possible solutions are proposed to increase its reliability, in particular to allow the introduction of new loads without the network getting over stressed or becoming vulnerable to faults.

To determine the impact of new loads, different scenarios have been assumed and tested. Tests were also carried out by adding new RES. Further tests have been carried out with some new proposed transmission network connections. The new connections increase the reliability of the network, make it less vulnerable to faults and blackouts, and gives some added generations boost to support new loads without having to increase generation.

In this respect, some fault testing with different scenarios has also been carried out. Comparing different scenarios shows that if a fault occurs at a substation in Nadi, where there is a three-way junction, more than 50% of the network would collapse in the present network. To overcome this weak point two new transmission network connections have been proposed whereby the effects of the fault would impact the local grid only with reduction of restoration costs.

A number of other scenarios have also been presented and discussed to understand the situation of the present transmission network. The most reliable scenario found is in case 3 where the two connections in the transmission network are proposed: with these connections, the whole network becomes more interconnected with resulting increase of the short-circuit ratio and therefore of its stiffness. The feasibility of this scenario is also clearly shown with comparison to the current scenario: resulting in a significant improvement in the number of reliable buses. This enables 87% of the buses to remain within voltage limits.

Appendix

Tables 8, 9, 10, 11, 12, 13, 14, 15, 16 and 17.

Table 8 Summary of total generation, loading and demand for the current grid network (extracted from KEMA and FEA reports)

	MW	Mvar	MVA	% PF	
Source (swing buses)	−74.886	12.233	75.879	98.69	Leading
Source (non-swing buses)	217.426	18.37	218.2	97.87	Lagging
Total demand	142.539	30.603	145.788	97.77	Lagging
Total load	137.788	22.504	139.614	98.69	Lagging

Table 9 Bus ratings after running load flow on the current network (extracted from ETAP report)

Device ID	Condition	Rating (kV)	Operating (kV)	% operating
Bus 5	Over voltage	132	135.36	102.5
Bus 68	Under voltage	33	32	97
Bus 52	Under voltage	33	32.01	97
Bus 163	Under voltage	33	32.26	97.8
Bus 34	Under voltage	33	32.26	97.8
Bus 69	Under voltage	11	10.77	97.9
Bus 50	Under voltage	11	10.65	96.8
Bus 66	Under voltage	11	10.64	96.7
Bus 38	Under voltage	11	10.74	97.6
Bus 121	Under voltage	11	10.78	98
Bus 20	Over voltage	0.42	0.43	103.1

Table 10 Bus ratings after adding 10 MW load to the current grid network (extracted from ETAP report)

Device ID	Condition	Rating (kV)	Operating (kV)	% operating
Bus 68	Under voltage	33	32	97
Bus 52	Under voltage	33	32.01	97
Bus 34	Under voltage	33	32.26	97.8
Bus 163	Under voltage	33	32.26	97.8
Bus 105	Under voltage	33	32.2	97.6
Bus 122	Under voltage	33	32.2	97.6
Bus 127	Under voltage	33	32.16	97.4
Bus 126	Under voltage	33	32.24	97.7
Bus 111	Under voltage	33	32.24	97.7
Bus 115	Under voltage	33	32.24	97.7
Bus 132	Under voltage	33	32.16	97.4
Bus 116	Under voltage	33	32.24	97.7
Bus 120	Under voltage	33	32.27	97.8
Bus 124	Under voltage	33	32.17	97.5
Bus 133	Under voltage	33	32.16	97.5
Bus 66	Under voltage	11	10.64	96.7
Bus 50	Under voltage	11	10.65	96.8
Bus 38	Under voltage	11	10.74	97.6
Bus 106	Under voltage	11	10.64	96.7
Bus 103	Under voltage	11	10.7	97.2
Bus 140	Under voltage	11	10.65	96.9
Bus 113	Under voltage	11	10.58	96.2
Bus 117	Under voltage	11	10.65	96.8
Bus 121	Under voltage	11	10.59	96.2
Bus 125	Under voltage	11	10.6	96.4
Bus 128	Under voltage	11	10.63	96.6
Bus 69	Under voltage	11	10.77	97.9
Bus 112	Under voltage	6.6	6.42	97.3
Bus 20	Over voltage	0.42	0.43	102.6

Table 11 Bus ratings after making the connection between Deuba and Korolevu without new load (extracted from ETAP report)

Device ID	Condition	Rating (kV)	Operating (kV)	% operating
Bus 5	Over voltage	132	135.31	102.5
Bus 68	Under voltage	33	32.09	97.3
Bus 52	Under voltage	33	32.1	97.3
Bus 66	Under voltage	11	10.67	97
Bus 50	Under voltage	11	10.68	97.1
Bus 38	Under voltage	11	10.77	97.9
Bus 121	Under voltage	11	10.76	97.8
Bus 20	Over voltage	0.42	0.43	103.1

Table 12 Bus ratings after making the connection between Deuba and Korolevu with new load (extracted from ETAP report)

Device ID	Condition	Rating (kV)	Operating (kV)	% operating
Bus 68	Under voltage	33	32.09	97.2
Bus 52	Under voltage	33	32.09	97.3
Bus 105	Under voltage	33	32.19	97.5
Bus 132	Under voltage	33	32.14	97.4
Bus 127	Under voltage	33	32.14	97.4
Bus 126	Under voltage	33	32.22	97.6
Bus 111	Under voltage	33	32.22	97.6
Bus 115	Under voltage	33	32.22	97.6
Bus 116	Under voltage	33	32.22	97.6
Bus 120	Under voltage	33	32.25	97.7
Bus 124	Under voltage	33	32.16	97.5
Bus 133	Under voltage	33	32.16	97.5
Bus 66	Under voltage	11	10.67	97
Bus 50	Under voltage	11	10.68	97.1
Bus 38	Under voltage	11	10.77	97.9
Bus 69	Under voltage	11	10.67	97
Bus 128	Under voltage	11	10.63	96.6
Bus 125	Under voltage	11	10.6	96.4
Bus 121	Under voltage	11	10.58	96.2
Bus 117	Under voltage	11	10.65	96.8
Bus 113	Under voltage	11	10.57	96.1
Bus 140	Under voltage	11	10.65	96.8
Bus 106	Under voltage	11	10.63	96.6
Bus 103	Under voltage	11	10.69	97.2
Bus 112	Under voltage	6.6	6.42	97.3
Bus 20	Over voltage	0.42	0.43	102.6

Table 13 Bus ratings after making the connection between Deuba, Korolevu, and Tavua to Nadarivatu without new load (extracted from ETAP report)

Device ID	Condition	Rating (kV)	Operating (kV)	% operating
Bus 5	Over voltage	132	135.23	102.4
Bus 121	Under voltage	11	10.76	97.8
Bus 125	Under voltage	11	10.78	98
Bus 20	Over voltage	0.42	0.43	103

Table 14 Bus ratings after making the connection between Deuba, Korolevu, and Tavua to Nadarivatu with load (extracted from ETAP report)

Device ID	Condition	Rating (kV)	Operating (kV)	% operating
Bus 126	Under voltage	33	32.21	97.6
Bus 133	Under voltage	33	32.14	97.4
Bus 124	Under voltage	33	32.15	97.4
Bus 120	Under voltage	33	32.24	97.7
Bus 115	Under voltage	33	32.21	97.6
Bus 116	Under voltage	33	32.21	97.6
Bus 111	Under voltage	33	32.21	97.6
Bus 127	Under voltage	33	32.12	97.3
Bus 132	Under voltage	33	32.12	97.3
Bus 105	Under voltage	33	32.17	97.5
Bus 122	Under voltage	33	32.17	97.5
Bus 113	Under voltage	11	10.57	96.1
Bus 140	Under voltage	11	10.64	96.8
Bus 106	Under voltage	11	10.63	96.6
Bus 103	Under voltage	11	10.69	97.2
Bus 69	Under voltage	11	10.66	96.9
Bus 128	Under voltage	11	10.62	96.6
Bus 125	Under voltage	11	10.6	96.3
Bus 121	Under voltage	11	10.58	96.1
Bus 117	Under voltage	11	10.64	96.7
Bus 112	Under voltage	6.6	6.42	96.1
Bus 20	Over voltage	0.42	0.43	102.5

Table 15 Summary of total generation, loading, and demand

	MW	Mvar	MV	% PF	
Source (swing buses)	−49.71	9.98	50.7	98.04	Leading
Source (non-swing buses)	176.06	17.01	176.89	99.54	Lagging
Total demand	126.35	26.99	129.21	97.79	Lagging
Total static load	122.59	22.49	124.64	98.36	Lagging

Table 16 Summary of total generation, loading and demand

	MW	Mvar	MV	% PF	
Source (swing buses)	−55.61	17.33	58.25	95.47	Leading
Source (non-swing buses)	197.43	14.37	197.94	99.74	Lagging
Total demand	141.81	31.7	145.31	97.59	Lagging
Total static load	135.82	22.14	137.62	98.7	Lagging

Table 17 Bus ratings after making the connection between Daube, Korolevu, and Tavua to Nadarivatu with 12 MW of renewable wind generation (extracted from ETAP report)

Device ID	Condition	Rating (kV)	Operating (kV)	% operating
Bus 5	Over voltage	132	135.25	102.5
Bus 20	Over voltage	0.42	0.43	102.5

References

1. Fiji Electricity Authority (2014) Fiji Electricity Authority Report 2014. Fiji Electricity Authority, Suva, Fiji Islands
2. Electrical Power System Analysis & Operation Software, Operation Technology, Inc. Available on: https://etap.com. Accessed 20 Oct 2016
3. KEMA International B.V. (2012) Quantification of the power system energy losses in South Pacific utilities. KEMA International B.V., Netherlands
4. Islam FR, Mamun KA (2016) Reliability evaluation of power network: a case study of Fiji Islands. In: Australasian universities power engineering conference (AUPEC-2016), Brisbane, Australia, 25–28 Sept 2016
5. Islam FR, Mamun KA (2016) Opportunities and challenges of implementing renewable energy in Fiji Islands. In: Australasian universities power engineering conference (AUPEC-2016), Brisbane, Australia, 25–28 Sept 2016
6. Saadat H (1999) Power system analysis. WCB/McGraw–Hill

Energy Grid Management, Optimization and Economic Analysis of Microgrid

Vipin Das, P. Karuppanan, V. Karthikeyan, S. Rajasekar and Asheesh Kumar Singh

Abstract This chapter proposes a non-dominated sorting genetic algorithm (NSGAII) for the multi-objective optimal operation management (MOOM) for distributed microgrid. The main objective of the MOOM is to maximize the safe instantaneous system load, and minimizing the pollutant emission produced by the generating sources. Particle swarm optimization (PSO), genetic algorithm (GA) and NSGAII artificial intelligence techniques are studied and optimized for microgrid. The NSGAII control algorithm projected to maintain the grid voltage and angle stability within the IEEE standards while increased penetration. To construct the microgrid structure, the renewable energy sources such as wind energy, solid oxide fuel cells (SOFC) and solar photo-voltaic (SPV) are considered. The robust NSGAII based optimization algorithm continuously monitors the grid conditions and regulates grid parameters for maximizing the instantaneous safe bus loading. Power system stability indices such as fast voltage stability indices (FVSI), line stability indices (LSI) and line stability factor (LQP).

Keywords NSGA-II · Micro grid · Maximizing loadability · Stability indices · System security · Distributed generators · Islanding operation

V. Das (✉) · P. Karuppanan · V. Karthikeyan · A.K. Singh
M.N. National Institute of Technology, Allahabad, Uttar Pradesh 211004, India
e-mail: vipindas504@gmail.com

P. Karuppanan
e-mail: karuppanan1982@gmail.com

V. Karthikeyan
e-mail: karthi13546@gmail.com

A.K. Singh
e-mail: asheeshkrs@gmail.com

S. Rajasekar
Researcher of NEC Laboratories Singapore, NEC Asia Pacific Pte. Ltd., Singapore, Singapore
e-mail: rajasekar_s@nec.com.sg

F.M.R. Islam et al. (eds.), *Smart Energy Grid Design for Island Countries*,
Green Energy and Technology, DOI 10.1007/978-3-319-50197-0_10

1 Introduction

The advancement in technology, economic and environmental factor influences the electrical power generation, transmission and distribution to change to new scenarios such as microgrid concept. The existing centralized vertical power system structure is actively shifting to distributed structure. In this distributed power system structure, the customer is getting more freedom to choose the distribution companies [1–4]. Figure 1 depicts the typical structure of a centralized and vertical power system.

Microgrid is one of the key advancements in the power system industry. It is basically a dynamic distribution system by combining different DG networks and distinctive loads at distribution voltage level. The sources utilized in the microgrid are normally renewable/non-conventional [5–7]. Power electronics converers are the one of integral part of microgrid [8–10]. Figure 2 shows the typical structure of a microgrid equipped with different sources and security arrangements. In order to improve the reliability and security of the microgrid in the combatting power industry, need to implement highly reliable energy management system (EMS) [11–13]. Real time optimization is incorporated with the microgrid to ensure the optimal utilization of available DGs [14–18].

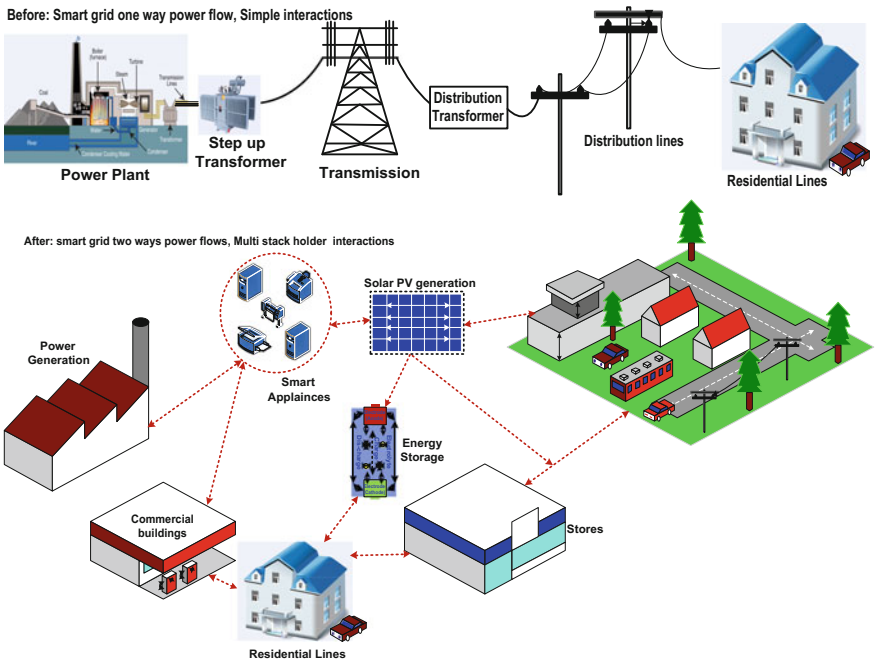

Fig. 1 Centralized and distributed power system architecture

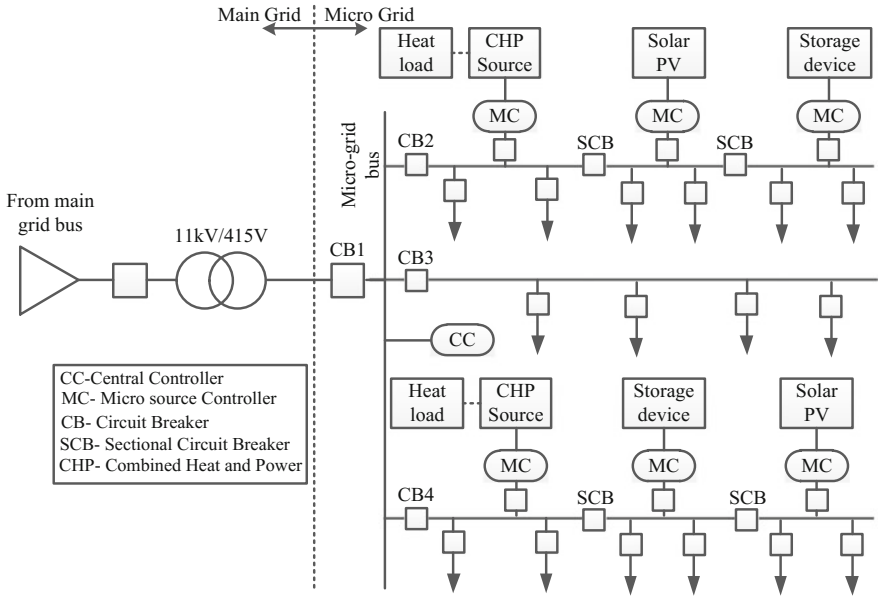

Fig. 2 Microgrid architecture

The microgrid operation has been classified as islanded and grid connected. In grid connected mode of operation, the microgrid is connected to the main grid through a point of common coupling (PCC). Depending on the power exchange through the PCC, the grid connected mode can be divided into two viz power matched and power mismatched operation. In power matched operation, the power exchange through the PCC will be zero. This is most favourable economic operation of the microgrid. In power mismatched operation, the microgrid exchanges power with the distribution network. In islanded mode, the microgrid will operate as an isolated system and it will satisfy its own load requirements from the available DGs.

The islanded mode is most suitable for remote locations [19–22]. The same microgrid can be operated in grid connected or islanded mode depending on the command from the central control system [23–25]. Figure 3 shows the transfer between these two operating mode. When the microgrid is not in operation, it can be converted to grid connected mode by grid connection control or it can work as islanded mode by grid disconnection control. The microgrid can be shutdown at any time using shutdown control for maintenance purposes. The proposed NSGAII controller facilitates transfer operation between the two modes. In grid connected mode the NSGAII measure the power mismatch through the PCC and based on the power mismatch the controller absorb/deliver power to/from the main grid. In case of any emergency condition at the main grid the NSGAII controller sent a control signal for disconnecting the microgrid from the main grid to the control centre. The proposed controller enables the shutdown signal also for scheduled maintenance of

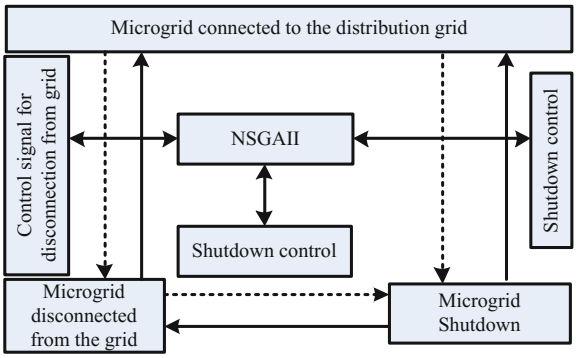

Fig. 3 Transfer between grid connected and islanded mode

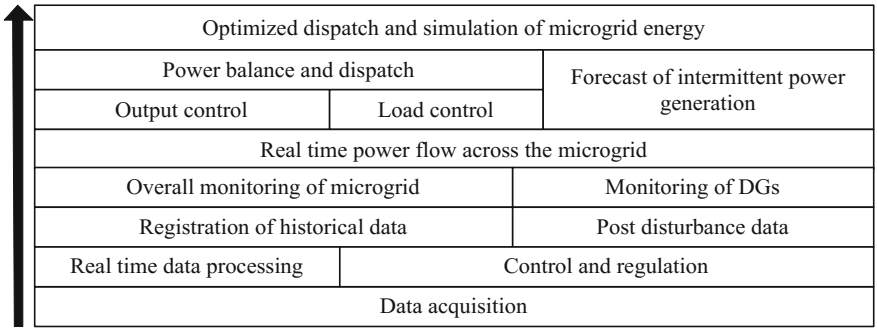

Fig. 4 Functional architecture of EMS and monitoring software for microgrid

the microgrid. The NSGAII optimization technique is illustrated in Sect. 3 for microgrid optimization. The MOOM based microgrid management system is intended to maximize the power penetration from the SOFC. The line flows across distribution network and voltage profile at each bus are tested for the stability analysis.

2 Microgrid Energy Management and Monitoring

The monitoring and management of microgrid serves the observation and utilization of microgrid efficiently. The typical functional architecture of EMS and monitoring software for microgrid is shown in Fig. 4. The monitored data from the DGs, energy storage (ES) and loads is used for analysis and data manipulation purposes. The grid management system is controls the entire grid to ensure the stability and economic operation. The grid management and monitoring system are working together to make the microgrid flexible. Therefore, it is the brain of the microgrid control structure [26–30].

2.1 Microgrid Monitoring

The function of microgrid monitoring system is to collect the data from the remote station and display the collected data on the screen situated at the centralized control centre [31–35]. The main purposes of the monitoring system are listed below,

- Real time monitoring and visualization of supervisory control, distributed generation and the data acquisition system.
- Service management monitoring such as power forecasting, energy storage system and tie line power.
- Optimized dispatch of energy available.

The power flow regulation by the monitoring system depends on the system operation constraints and the energy balance constraints [36–40]. A typical monitoring system consists of PV monitoring system, wind monitoring system and micro turbine monitoring system to monitor the different DG in included in the system [41–46].

2.1.1 PV Monitoring System

The PV monitoring system provides operation information of the PV module. The data provided by the PV monitoring system can be used for comprehensive statistics, analysis and control of PV system. This monitoring system delivers the following functions.

i. Real time monitoring and display of solar PV characteristics, solar power, daily power and total power profile on hourly basis.
ii. Display the inverter parameters such as DC link voltage, DC link power, AC voltage, power and frequency, power factor, total power and instantaneous power.
iii. Monitor the inverter operation and provide alarm indication in case of any component failure.
iv. Control the start and stop of inverter to optimize the power delivery.

2.1.2 Wind Power Monitoring System

Wind power monitoring system monitors the wind power sources connected to the microgrid and provide the data for analysis, efficient control and utilization of wind power sources. The wind power monitoring system mainly intended to fulfill the following functions.

i. Monitor the power generation from the wind power generation station in real time. The power monitoring system displays the total power generated, consumed from the wind power sources, daily power profile and hourly power generation profile.
ii. Observe the wind turbine generator and collect both electrical and mechanical data. The monitoring system displays the AC voltage, frequency, power factor, temperature, speed of turbine and generator for analysis purposes.
iii. Monitor and display the wind speed profile, pitch angle, turbine speed for the efficient operation of Maximum Power Point Tracking (MPPT) controller.
iv. Adjust the power flow and control the start and stop of inverters.

2.1.3 Micro Turbine Monitoring

The operation of micro turbine is monitored in real time and provides alarm indication for any emergency. The data available from the monitoring system can be used for efficient control of the micro turbine based power system by accurate analysis and manipulation of the data. The main functions of the micro turbine monitoring system are as follows.

i. Monitor the major operational data like speed, gas flows, temperature, valve pressures and display these monitored data on the screen for comprehensive statistics and analysis.
ii. Monitor and display the voltage, frequency, power and power factor to ensure the efficient operation of the micro turbine.
iii. Adjust the operational parameter for optimal utilization.

Similar to this manner all the distributed generation sources connected to the microgrid is monitored by the respective monitoring system. Based on these monitored and displayed data, the energy management algorithm controls the operation of the whole DGs in a coordinated manner.

2.1.4 ES Monitoring System

The objective of ES monitoring system is to monitor the energy storage system connected to the microgrid. The data collected by the monitoring system is utilized for the economical and optimal energy storage system management. The main functions handled by the ES monitoring systems are as follows.

i. Monitoring and displaying the charge level, energy that can be charged, current discharge power, total charge stored and total energy discharged in real time fashion.

ii. Communication and protection of the DC-DC bidirectional converter and charge controller by observing the DC voltage level, load condition and generation conditions located at remote locations.
iii. Remote control of battery charging and discharging.

2.1.5 Load Monitoring

Load monitoring is one of the major functions handled by the microgrid monitoring system. The entire operation and management of the microgrid depends on the nature of load that connected to the microgrid. The load monitoring system provides the loading information for comprehensive statistics, analysis and efficient load generation balancing. The main function of load monitoring system is as follows.

i. Monitor the types of load, power consumption, real and reactive power, load voltage and current.
ii. Recording the loading conditions in hourly manner.
iii. Provide warning alarm indication in case of overload, frequency mismatch.

2.2 Microgrid Management

Microgrid management is meant to maintain the operation stability and security of the microgrid. Figure 5 shows the functional block diagram of a microgrid EMS system. The management system improves the efficiency of the system by efficient DG forecasting, load forecasting and energy storage (ES) forecasting. The energy management system (EMS) uses historical as well as real-time data to forecast the DG, ES and loads [47–49].

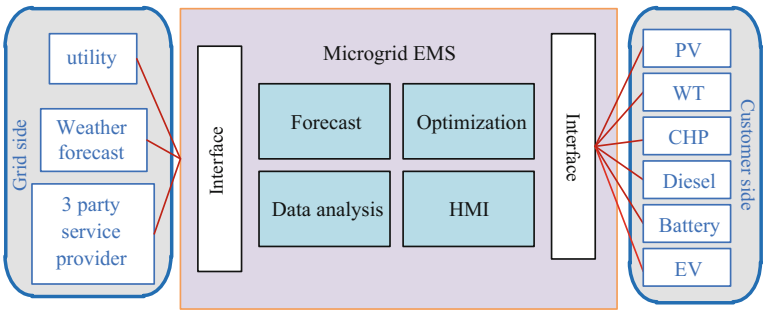

Fig. 5 Illustration of microgrid EMS

2.2.1 Forecasting

The data forecasted by the forecasting system is used for the optimization purpose by the control system; therefore accuracy of forecasting is crucial. The EMS uses historical and real-time environmental operational data for accurate forecasting of DG, ES and loads. Forecasting is one of the challenging problems in microgrid EMS due to the unpredictable nature of DGs (PV and wind) and temporal uncertainties in controllable loads (Electric vehicles). The forecasting system can be divided into DG forecasting, and load forecasting.

DG forecasting is necessary in microgrid management in order to run the microgrid economically as well as eco-friendly. In general, the DG forecasting is intended to predict short term and super short term output of a DG on the basis of optimized energy dispatch. Objective of the DG forecasting is to maximize the utilization of all the DGs connected to the microgrid. In earlier days statistical methods are used to forecast the DG output based on the trend analysis depending on the historical data. Now statistical method is replaced by the soft computing technics like, Fuzzy logic controller, PSO, NSGAII, etc.…

Load forecast is to predict the future load demand, so that the operators can predict the operation status of the network. It is a remarkable for the measure of future operation of electrical microgrid network. Forecasting load plays a major part in control, operation, and planning of the microgrid. Therefore, enhancing the forecast accuracy can play a crucial role in higher security and a superior economy operation of the microgrid. The load forecasting methods can be classified as traditional methods like regression analysis, sequential analysis and modern methods like expert system theory, neural network theory, wavelet analysis, gray system theory, fuzzy theory and combinational method.

2.2.2 Data Analysis

The characteristics of the DGs, loads, and cost effectiveness of the market data should be analysed, which is utilized to adjust the forecast and the optimization models for better performances. It is also useful for the microgrid operator to design control policies for new applications.

2.2.3 Human Machine Interface (HMI)

HMI is a PC-based program for on-demand monitoring and collect system information through microgrid communication network. This program should be capable of visualizing and archiving the collected data and receiving commands and additional information from operators. Some DGs need operator manual interpolations for starting. In this case, the command of supervisory controller should be transferred ahead of time to the HMI to inform operators to manually start the selected DG at the right time. In addition, the operator should be capable of

commanding supervisory controller through HMI to exclude a DG from the microgrid control system for maintenance or include the maintained DG. Another important role of enhanced HMI is in the case of failure of supervisory controller or any special operation. In this case, HMI is used to control the system manually by operator commands.

3 Optimization Techniques in Microgrid

Optimization is meant by solving a problem by mathematical modelling with hard limitations or constraints, generalization and/or simplifications. After modelling, the problem will be solved using arithmetical tools to realize the solution for the problems [50–52]. Optimization is one of the major parts of the EMS; it optimizes the power and economically dispatches the power available from the DGs among the loads connected. Different optimization is performed by the EMS depending on the applications (power management, EV charging and vehicle to grid). The optimization is designed as nonlinear objective functions for different applications. From the optimization point of view, these optimization techniques are broadly classified into three categories [53]. The chapter is focused on mainly GA, PSO and NSGAII optimization techniques for microgrid applications with MATLAB® illustration. These Artificial intelligence based optimization techniques are inspired by the biological phenomenon. These techniques are introduced to the power system optimization area to reduce the complexity that is faced by the conventional techniques. AI techniques optimize the objective function with respect to equality and inequality constraints. Depending on the number of objective functions, AI optimization techniques are classified into single objective and multi objective optimization techniques [54–56].

3.1 Particle Swarm Optimization (PSO)

The PSO is a population based evolutionary computation technique developed by Eberhart and Kennedy in 1995 [57]. It is based on the ideas of social behavior of organisms such as animal flocking and fish schooling. Yoshida et al., proposed a particle swarm optimization (PSO) for reactive power and voltage/var control (VVC) considering voltage security assessment [58–60]. It determines an on-line VVC strategy with continuous and discrete control variables such as AVR operating values of generators, tap positions of OLTC of transformers and the number of reactive power compensation equipment. Park et al. (2005) suggested a modified particle swarm optimization (MPSO) for economic dispatch with non-smooth cost functions [61]. A position adjustment strategy is proposed to provide the solutions satisfying the inequality constraints. The equality constraint is resolved by reducing the dynamic search space. The results obtained from the proposed method are

compared with those obtained by GA, tabu search (TS), evolutionary programming (EP), and numerical methods. It has shown superiority to the conventional methods. Wang et al. presented a modified particle swarm optimization (MPSO) algorithm to solve economic dispatch problem. In this approach, particles not only studies from itself and the best one but also from other individuals [62]. By this enhanced study behavior, the opportunity to find the global optimum is increased and the influence of the initial position of the particles is decreased. The particle also adjusts its velocity according to two extremes. One is the best position of its own and the other is not always the best one of the group, but selected randomly from the group. Vlachogiannis and Lee formulated the multi-objective optimization problem by considering generators power flow contribution in transmission line and calculates using a parallel vector evaluated particle swarm optimization (VEPSO) algorithm. VEPSO accounts for nonlinear characteristics of the generators and lines. The contributions of generators are modeled as positions of agents in swarms. Generator constraints such as prohibited operating zones and line thermal limits are considered. It can obtain precise solutions compared to analytical methods [63].

PSO has its essence in social psychology, artificial life, as well as in computer science and engineering. In PSO, the population is termed as "swarm" and the individual in the swarm is termed as "particle". Each particle is represented by its position, and velocity in n-dimensional search space. The particles fly through the problem hyperspace with some given initial velocities. In each iteration process, the particles' velocities are stochastically adjusted in consideration of the historical best position of the particles. Thus, the movement of each particle naturally results to an optimal or near-optimal solution. The particle has memory, and every particle keeps track of its previous finest position and the comparable fitness value. The fitness value is also stored and this value is termed as P_{best}. When a particle captures all the population as its topological neighbors, the best value is a global best and is termed as G_{best}. After determining the two best values, both velocity and positions of the particle are updated according to Eqs. (1) and (2). Figure 6 shows the basic flowchart of the PSO technique [64–69]. Figures 6 and 7 shows the basic MATLAB® implementation of PSO algorithm used for wind power maximization technique in microgrid (Fig. 8).

$$V_{k+1}^{i} = V_{k}^{i} + C_1 R_1 \left(P_{\text{best}} - X_{k}^{i}\right) + C_2 R_2 \left(G_{\text{best}} - X_{k}^{i}\right) \tag{1}$$

$$X_{k+1}^{i} = X_{k}^{i} + V_{k+1}^{i} \tag{2}$$

3.2 Genetic Algorithm (GA)

A genetic algorithm (GA) is a search and enhancement strategy which works by imitating the evolutionary standards and chromosomal handling in common hereditary qualities. GA starts its search in a random manner as a rule coded in

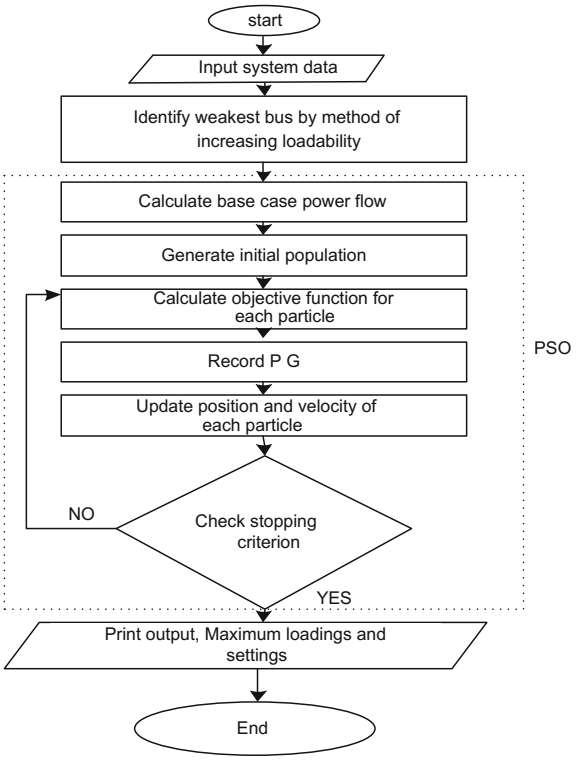

Fig. 6 PSO flowchart

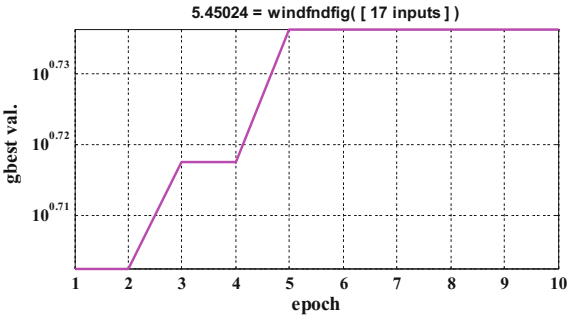

Fig. 7 PSO running optimization

double strings. Each iteration is relegated a fitness which is straightforwardly identified with the target dimensions of the search. From there on, the number of inhabitants in arrangements is altered to another population by applying three operators like to normal hereditary operator reproduction, crossover, and mutation. It works iteratively by progressively applying these three operators in every generation till an end paradigm is fulfilled. GAs has been effectively applied to various optimization problems due to their straightforwardness and global approach. (Fig. 9)

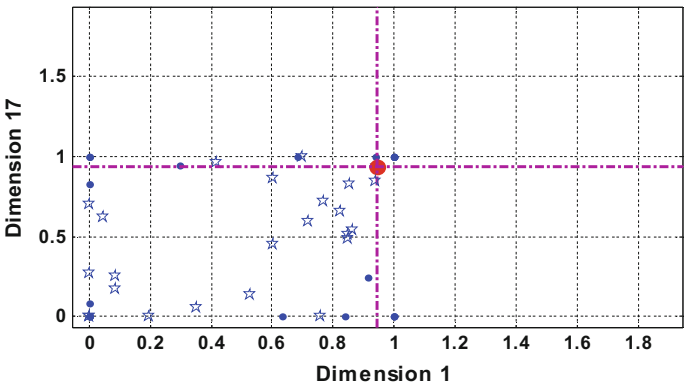

Fig. 8 PSO converging

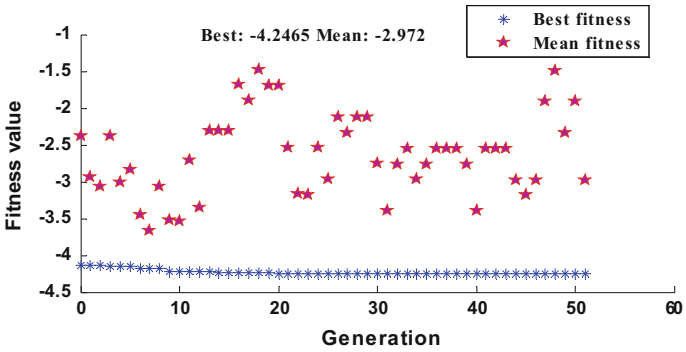

Fig. 9 MATLAB® implementation of Genetic Algorithm

(i) Basic Concepts and working principle

The GA is an iterative technique and works with a self-contained arrangement in iteration. GA works with various solutions (known as population) in the every iteration. A flowchart of the working standard of a basic GA is depicted in Fig. 10. Without any knowledge of the problem, GA starts its search from a random population of solutions. If a termination criterion is not satisfied, three different operators—reproduction, crossover and mutation—are applied to update the population of strings. One iteration of these three operators is known as a generation in the case GAs. Since the representation of a solution in a GA is like a characteristic chromosome and GA operators are like genetic operators, the above method is known as a GA. Figure 11 shows the basic working principle and steps involved in GA.

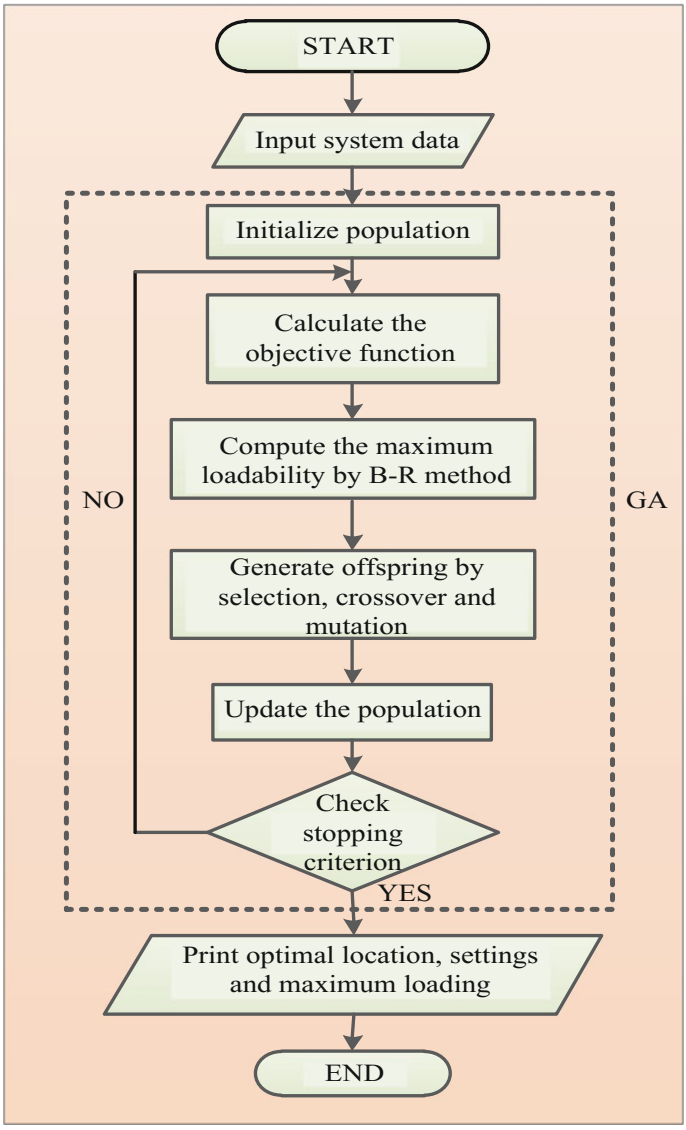

Fig. 10 GA flowchart

(ii) Various Steps involved in GA Procedure

The various steps that are included in the GA process are representation, reproduction, crossover and mutation [70–74].

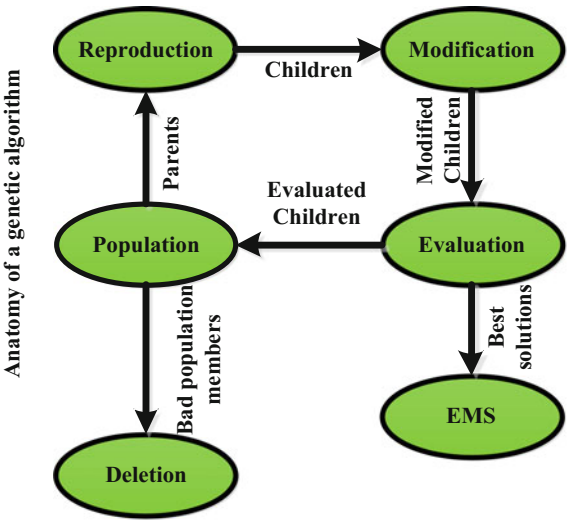

Fig. 11 Anatomy of GA

(a) ***Representation***

The first step in the GA is the represent the codes in the form of binary string as given in the example below.

$$\underbrace{11010}_{x_1}\underbrace{1001001}_{x_2}\underbrace{010}_{x_3}\ldots\underbrace{0010}_{x_N} \tag{3}$$

The *i*th problem variable is coded in a binary substring of length l_i, the total number of alternatives allowed in that variable is 2^{l_i}. The lower bound solution $x_i^{\min}$ is represented by solution (0, 0, 0 … 0) and the upper bound solution $x_i^{\max}$ is represented by the solution (1, 1, 1 … 1). The other substring s_i decodes to a solution x_i as follows:

$$x_i = x_i^{\min} + \frac{x_i^{\max} - x_i^{\min}}{2^{l_i} - 1}\mathrm{DV}(s_i) \tag{4}$$

where, DV (s_i) is the decoded value of string s_i. The decoded value of the binary substring $s \equiv (s_{l-1}s_{l-2}\ldots s_2 s_1 s_0)$ is calculated by $\sum_{j=0}^{l-1} 2^j$, where $s_j \in \{0, 1\}$. The length of substring is usually decided by precision needed in a variable. For example if three decimal places of accuracy are needed in the *i*th variable, total number of alternatives in the variable must be set equal to 2^{l_i} and l_i can be computed as follows:

$$l_i = \log_2\left\{\frac{x_i^{\max} - x_i^{\min}}{\varepsilon_i}\right\} \tag{5}$$

$$\begin{array}{lll} \text{Parrent 1} & 0\,0 & \\ \text{Parrent 1} & 0\,0 & \text{Parrent 1} \quad 0\,0 \\ \text{Parrent 2} & 1\,1 & \text{Parrent 2} \quad 1\,1 \\ 0\,0\,0\,0\,0 \rightarrow 0 & 0\,1\,0\,0 & \\ \text{Parrent 2} & 1\,1 & \end{array} \left| \begin{array}{ll} 0\,0\,0 & 1\,1\,1 \\ 1\,1\,1 & 0\,0\,0 \end{array} \right| \begin{array}{l} \text{Child 1} \\ \text{Child 2} \end{array} \quad (6)$$

Here, the parameter ε_i is desired precision in ith variable. The total string length of a N variable solution is then $l = \sum_{i=1}^{N} l_i$. In the population of, 1 bit strings are made indiscriminately (at each of positions, there is an equivalent likelihood of making a 0 or 1). Once such string is made, the principal l_i bits can be extricated from the complete string and relating estimation of the variable x_i can be figured utilizing Eq. 4 and utilizing the lowerpicked and maximum breaking points of variable x_1. This procedure is preceded until all N-variables are gotten from complete string. Consequently, a 1-bit string speaks to a complete arrangement indicating all N variables particularly. Once these qualities are known, the objective function $f(x_1, x_2, x_N)$, can be registered.

In a GA, every string made either in the initial population or in the resulting generation must be allotted a fitness value which is identified with objective function value. For maximization problems, a string's fitness can be equivalent to string's objective function value. In minimization problem, the objective is to discover an answer having least objective function value. In this way, the fitness can be figured as the negative of the goal work with comparable objective function value get larger fitness.

There are number of advantages for utilizing a string representation to code variables. In the first place, this permits a protecting between working of GA and actual problem. The same GA code can be utilized for various problems by just changing meaning of coding a string. This permits a GA to have broad pertinence. Second, a GA can exploit the likenesses in string coding to make its search quicker, a matter which is vital in working of a GA.

(b) ***Reproduction***

Reproduction (or selection) is typically the principal operator connected to a population. Reproduction chooses best strings in a population and structures a mating pool. The crucial thought is that above-normal strings are picked from the present population and copies of them are embedded in the mating pool. The normally utilized reproduction operator is the proportionate determination operator, where a string in the present population is chosen with likelihood relative to the string's fitness. That is the ith population is generated based on a probability function f_i. One approach to accomplish this proportionate choice is to utilize a roulette-wheel with the boundary set apart for every string proportionate to the string's fitness.

(c) ***Crossover***

The crossover operator is an operator in GA which is applied next to the string in the mating pool. In this operation two strings are selected from the mating pool randomly and some portion of the strings will get exchanged to produce the new offspring. In a single crossover operation each string will cut at arbitrary points and right side of each string swaps each other as shown below:

$$\begin{array}{llll} \text{Parrent 1} & 00 \mid 000 & 00 \mid 111 & \text{Child 1} \\ \text{Parrent 2} & 11 \mid 111 & 11 \mid 000 & \text{Child 2} \end{array} \tag{7}$$

It is fascinating to note from the development that good substrings from either parent string can be joined to frame better kid string if a fitting site is picked. Since the information of a suitable site is normally not known, an arbitrary site is generally picked. In any case, understand that the decision of an arbitrary site does not make this search operation irregular. With a random point the crossover on two 1—bit parent strings, the search can just find at most $2(i - 1)$ distinctive strings in the search space, while there are a sum of $2i$ strings in the search space. With an arbitrary space, the kids strings delivered could conceivably have a blend of good substrings from parent strings relying upon whether the intersection site falls in the proper site or not. If great strings are made by crossover; there will be more duplicates of them in the following mating pool produced by the generation operation. If great strings are not made by crossover; they won't get by past people to come, since reproduction won't choose poor strings for the following mating pool. In a two-point crossover operation, two irregular locales are picked. This thought can be reached out to make multi-point crossover operator and the

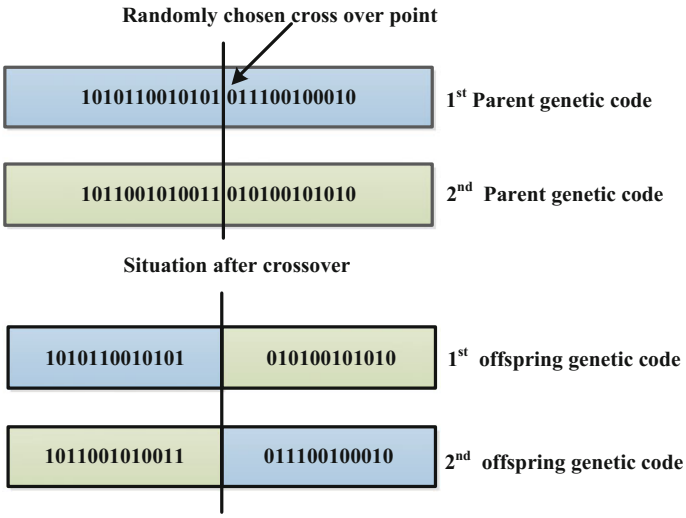

Fig. 12 Crossover mechanism of a genetic algorithm

compelling of this augmentation is known as a uniform crossover operator. In a uniform crossover for paired strings, every piece from either parent is chosen with a probability of 0.5. The fundamental motivation behind the crossover operator is to seek the parameter space. Other perspective is that the search should be performed in an approach to safeguard the data put away in the parent string maximally, on the grounds that these parent strings are occurrences of good strings chose utilizing the reproduction operator. In the single-point crossover operator search is not broad, but rather the most extreme data is saved from parent to offspring. In another ways, in the uniform crossover, the search is exceptionally broad however least data is saved amongst parent and offspring strings. On other hand the crossover probability is utilized as a part of the population. In the event that a crossover probability of p_c is utilized then 100 p_c % strings in the population are utilized as a part of the crossover operation and $100(1 - p_c)$ of the population are basically duplicated to the new population. Figure 12 shows the crossover mechanism of a GA.

(d) ***Mutation***

Crossover operator is fundamentally in charge of the search part of GA, even in spite of the fact that the mutation operator is likewise utilized for this reason sparingly. The mutation operator changes $a1$ to $a0$ and the other way around with a little mutation probability p_m:

$$00000 \rightarrow 00\,100 \tag{8}$$

In the above given example the third bit is changed from 0 to 1. This transformation will affect in the new generation and the mutation operator is used to give best fitness value for the newly generated offspring.

After reproduction, crossover and mutation are applied to entire population, one generation of GA is finished. These three operators are basic and direct. The reproduction operator chooses great strings and the crossover operator recombines good substrings from two good strings together to ideally frame a superior substring. The mutation operator adjusts a string locally to ideally make a superior string. Despite the fact that none of these cases ensured and/or tried while making another population strings, it is normal that if poor strings are made they will be dispensed with by the reproduction operator in next generation to come and if good strings are made, they will be stressed. To make a speedier meeting of a GA to real problems, particular operator are frequently created and utilized, yet the above three operators depict basic operations of a GA and encourage a relatively simpler numerical treatment.

3.3 Non Dominated Sorting Genetic Algorithm II (NSGAII)

The major drawback of the PSO and GA explained in the previous sections are they are applicable to only for single objective optimization problems. As we are

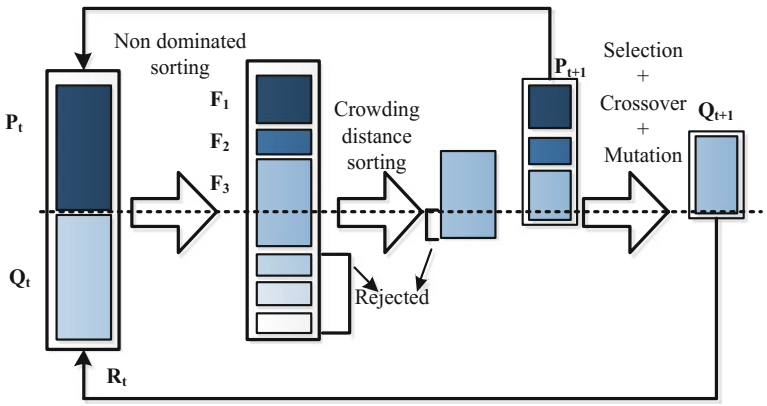

Fig. 13 NSGAII operation modes

considering the microgrid the optimization problem will be multi objective function based. In this case the non-dominated sorting genetic algorithm ii (NSGAII) is the suitable option [75].

Basic operation

Figure 13 shows the basic operation modes of the NSGAII. The population is initialized randomly as in the case of GA. Once the population in initialized the population is sorted in light of non-domination into every front. The primary front being totally non-dominating set in the present population and the second front being ruled by the individuals in the primary front just and the front goes so on. Each individual in the every front are appointed rank (fitness) values or taking into account front in which they belongs to. Individual in primary front are given a fitness value of 1 and people in second are relegated fitness value as 2 and so on [76].

A crowding distance also calculated for each individual in order to make the iterative process fast. The crowding distance gives the idea about how far an individual each other. The large average crowding distance is the best indication of diversity of the search space. Based on the rank and the crowding distance the parents are selected and from these parents the offspring are produced by crossover and mutation. The newly generated population is again sorted on non-dominated manner and best individuals will select from this sorting. The basic steps involved in NSGAII is explained [77].

(i) ***Population Initialization***

The population is initialized based on the problem range and constraints if any.

(ii) ***Non-Dominated sort***

The second step is to sort the population initialized based on the rank for better population by a non-dominated sorting method. The steps involved in non-dominated sorting are described below:

- Initialize $S_p = \phi$. This set of individuals that are being dominated by p.
- Initialize $n_p = 0$. The number of individuals that dominate p.
- for each individual q in P
  - if p dominated q then
    add q to the set S_p i.e. $S_p = S_p \cup \{q\}$
  - else if q dominates p then
    increment the domination counter for p i.e. $n_p = n_p + 1$
- if $n_p = 0$ i.e. no individuals dominate p then p belongs to the first front; Set rank of individual p to one i.e. $p_{\text{rank}} = 1$. Update the first front set by adding p to front one i.e. $F1 = F1 \cup \{p\}$
- This is carried out for all the individuals in main population P.
- Initialize the front counter to one. $i = 1$
- Following is carried out while the ith front is nonempty i.e. $Fi \neq \phi$.
  - Q = $\varnothing$. The set for storing the individuals for $(i + 1)$th front.
  - for each individual p in front Fi

    for each individual q in Sp (Sp is the set of individuals dominated by p)
    - $nq = nq - 1$, decrement the domination count for individual q.
    - If $nq = 0$ then none of the individuals in the subsequent fronts would dominate q. Hence set $q_{\text{rank}} = i + 1$. Update the set Q with individual q i.e. $Q = Q \cup q$.
  - Increment the front counter by one.
  - Now the set Q is the next front and hence $Fi = Q$.

(iii) ***Crowding Distance***

Once the non-dominated sort is finished the crowding distance is allotted. Since the individuals are chosen taking into account rank and crowding distance every one of the people in the population are relegated a crowding distance value. Crowding distance is relegated front wise and looking at the crowding distance between two individuals in various fronts is meaningless. The crowing separation is ascertained as below:

- For each front Fi, n is the number of individuals.
  - Initialize the distance to be zero for all the individuals i.e. $Fi\,(dj) = 0$, where j corresponds to the jth individual in front Fi.
  - for each objective function m

    Sort the individuals in front Fi based on objective m i.e. $I = \text{sort}(Fi, m)$.
    Assign infinite distance to boundary values for each individual in Fi i.e. $I\,(d1) = \infty$ and $I\,(dn) = \infty$
    for $k = 2$ to $(n - 1)$

$$I(d_k) = I(d_k) + \frac{I(k+1)m - I(k-1)m}{f_m^{\max} - f_m^{\min}} \tag{9}$$

- $I(k).m$ is the value of the mth objective function of the kth individual in I

The basic idea behind the crowding distance is to find out the Euclidian distance between the two individual in the same front.

(iv) ***Selection***

After initialization, non-dominated sorting and assigning crowding distance, next stage is selection using a crowding distance comparison operator (n) and the comparison process is as explained below:

(a) Non-domination rank p_{rank} i.e. individuals in front F_i will have their rank as $p_{\text{rank}} = i$.
(b) Crowding distance $Fi(dj)$

- $p \prec_n q$ if
  - $p_{\text{rank}} < q_{\text{rank}}$ or
  - if p and q belong to the same front Fi then $Fi(d_p) > Fi(d_q)$ i.e. the crowing distance should be more.

The individuals are selected by binary tournament selection procedure using the crowd selection operator.

(v) ***Genetic Operators***

The genetic operation is carried out by simulated binary crossover and polynomial mutation.

(a) **Simulated binary crossover**

The simulated binary crossover is inspired from nature and is mathematically given as follows.

$$c_{1,k} = \frac{1}{2}\left[(1-\beta_k)p_{1,k} + (1+\beta_k)p_{2,k}\right] \tag{10}$$

$$c_{2,k} = \frac{1}{2}\left[(1+\beta_k)p_{1,k} + (1-\beta_k)p_{2,k}\right] \tag{11}$$

Here, $c_{i,k}$ is the ith offspring with kth component, $p_{i,k}$ is the selected parent and $\beta_k(\geq 0)$ is a sample from, a random number generated with the probability density,

$$p(\beta) = \frac{1}{2}(\eta_c + 1)\beta^{\eta_c}, \quad \text{if } 0 \le \beta \le 1 \tag{12}$$

$$p(\beta) = \frac{1}{2}(\eta_c + 1)\frac{1}{\beta^{\eta_c + 2}}, \quad \text{if } \beta > 1 \tag{13}$$

This distribution can be obtained from a uniformly sampled random number u between (0, 1). η_c is the distribution index for crossover. That is

$$\beta(u) = 2u^{\frac{1}{\eta+1}} \tag{14}$$

$$\beta(u) = \frac{1}{[2(1-u)]^{\frac{1}{(\eta+1)}}} \tag{15}$$

(b) **Polynomial Mutation**

The polynomial mutation can be given mathematically as,

$$c_k = p_k + (p_k^u - p_k^l)\delta_k \tag{16}$$

where, c_k and p_k are the offspring and parent respectively with upper bound p_u^k and lower bound p_u^l on the parent component. δ_k is the small deviation as given below,

$$\delta_k = (2r_k)^{\frac{1}{\eta_m+1}} - 1 \quad \text{if } r_k < 0.5 \tag{17}$$

$$\delta_k = [2(1-r_k)]^{\frac{1}{\eta_m+1}} \quad \text{if } r_k \ge 0.5 \tag{18}$$

where η_m is the mutation distribution index and r_k is the random space between (0, 1)

(vi) ***Recombination and Selection***

The last stage of iteration is to combine the offspring with the current generation to obtain the best fitness individuals. In this process the superiority is ensured due to the involvement of all the current and previous best solutions. The new generation is filled by every front in this manner until the population size surpasses the present population size. If by including every one of the individual in front *Fj* the population surpasses *N* then individual in front *Fj* are chosen based on their crowding distance in the descending manner until the population size is *N*. By this method the process repeats generates the new generations.

This chapter explained the most efficient optimization tools that can be used for microgrid optimization purpose. Besides this a lot of tools are available in the literature (refer Table 4).

4 Illustration of NSGAII in Microgrid Application

This section illustrates the simulation of the above explained three optimization tool in modified IEEE 14 bus test system.

4.1 Microgrid Modeling

Figure 15 shows the test system used for analyzing the proposed NSGAII optimization algorithm (Fig. 14). The microgrid under the analysis consists of solar PV, fuel cell distributed generation sources and the loads under consideration are

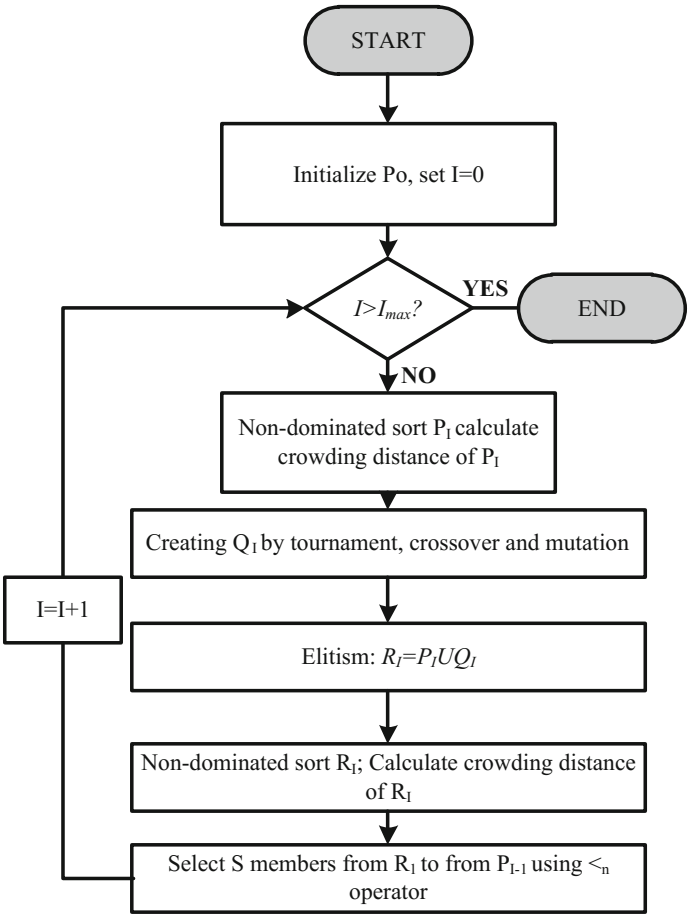

Fig. 14 NSGAII flowchart

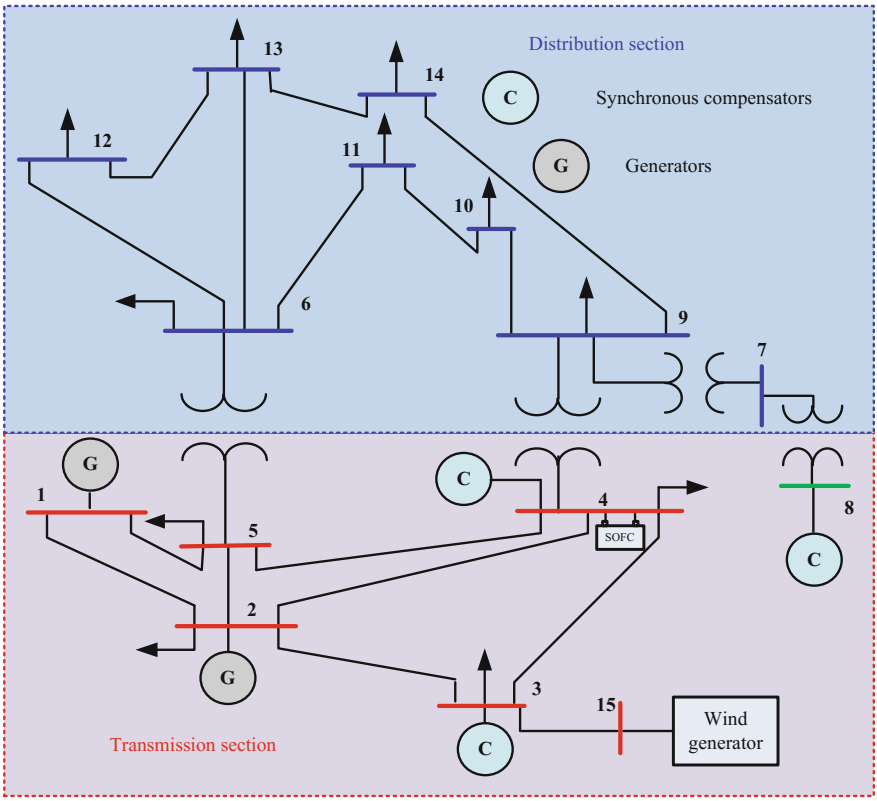

Fig. 15 Proposed microgrid

frequency dependent load, voltage dependent loads, MIX loads and PQ loads. The goal of the optimization problem is to maximize the safe instantaneous system loadability, minimize the total losses, and the total grid emission. Voltage and angle instability are the main limiting factors for synchronous operation of distributed generators hence grid control authorities are limiting the distributed generator penetration level for maintaining grid stability. Optimal DG placement methodology for maximizing the system loadability has been suggested by taking into account, small signal stability, voltage sensitivity index and line stability index.

The proposed algorithm for finding the optimal location of distributed generator for maximizing the system loadability has been implemented using MATLAB®. The performance of the algorithm is studied on IEEE 14 bus standard test system. The power flow analysis is carried out using Newton Raphson method. The test system used in this work is shown in Fig. 15. All per-unit quantities used in this study are on a 100-MVA base. Wind farm consisting of 300 wind turbines and 600 MVA/69 kV capacity has been connected to bus 3 as identified using wind farm placement index by creating another bus (bus 15) through a transformer of tap ratio unity. Maximum penetration of wind power can be achieved by connecting wind

turbine generator at bus 3, solid oxide fuel cell (SOFC) generator is connected at bus 10 and Solar PV generator (Spv) is connected as a static generator at bus 14. Loads were modeled as static loads (constant PQ) with constant power factor, and increased according to Eqs. (1) and (2). The decision variables considered are the locations of fuel cell, voltage and angle settings of the slack buses, and voltage settings of the PV buses. All the buses of the system except the voltage controlled bus and the bus with generators are selected to be the optimal location of the fuel cell. In this case, buses 4, 5, 7, 9, 10, 11, 12 and 13 are suitable for DG placement as they already has generators on them.

4.2 Modelling of the Robust Controller

With the knowledge of the maximum loading condition the system operator can take corrective actions to provide a maximum security margin. The load is increased in the system by:

$$P_{D_i}(\lambda) = \lambda P_{D_i}; \quad i = m+1, \ldots N_b \tag{18}$$

$$Q_{D_i}(\lambda) = \lambda Q_{D_i}; \quad i = m+1, \ldots N_b \tag{19}$$

where P_{Di} is the base case total active loads at bus i and N_b is the total number of buses in the system, $\lambda \in R$ is a loading parameter, i.e., a scalar independent parameter that multiplies all generator and load powers.

(i) **Objective Function and Constraints**

The optimal location and settings of SOFC is formulated as a real constrained mixed integer non-linear multi-objective optimization problem. The combined objective function is defined as

$$\text{Minimize } F(x,u) = [F_1(x,u), F_2(x,u), F_3(x,u)] \tag{20}$$

F_1 represents the objective function to maximize the system load ability given by,

$$\text{Maximize } F_1(x,u) = \sum_{i=1}^{N_b} P_{D_i}(\lambda) \tag{21}$$

F_2 represents the function to minimize the system losses given by,

$$\text{Minimize } F_2(x,u) = \sum_{i=1}^{N_b} P_{G_i} - \sum_{i=1}^{N_b} P_{D_i} \tag{22}$$

F_3 represents the function to minimize the fuel cell generator and substation bus emissions [99].

$$\text{Minimize } F_3(x,u) = \sum E_{\text{FC}} + \sum E_{\text{Grid}} \tag{23}$$

The load factor λ represents the variation of system real and reactive loads P_{Di} and Q_{Di}, defined as in Eqs. (21) and (22) where, m is the total number of generator buses, $\lambda = 1$ indicates the base load case. The fuel cell generator and the substation bus emissions are given by [75].

$$\left.\begin{aligned} E_{\text{FC}} &= \text{NO}_{x\text{FC}} + \text{SO}_{2\text{FC}} = (0.03 + 0.006)^{\text{lb/MWh}} \times \sum P_{\text{FC}} \\ E_{\text{Grid}} &= \text{NO}_{x\text{Grid}} + \text{SO}_{2\text{Grid}} = (5.06 + 7.9)^{\text{lb/MWh}} \times \sum P_{\text{sub}} \end{aligned}\right\} \tag{24}$$

where E_{FC} is the emission of SOFC, E_{Grid} is emission of large-scale sources (substation bus that connects to grid), NO_{xFC} is nitrogen oxide pollutants of SOFC, $\text{SO}_{2\text{FC}}$ is sulphur oxide pollutants of SOFC, $\text{NO}_{x\text{Grid}}$ is nitrogen oxide pollutants of grid and $\text{SO}_{2\text{Grid}}$ is sulphur oxide pollutants of grid.

Objective function should be optimal, considering technical constraints. Figure 16 show the basic block diagram of the control strategy implemented in this work. The data from the IEEE 14 bus test system is fetched by the NSGAII controller and after manipulating the data the NSGAII is fed back the control signals to the DFIG based wind generating system to maximize the penetration.

(ii) **Equality Constraints**

The optimization problem is subjected to the equality constraints as given in Eq. (25). Total real and reactive power of the system is taken as inequality constraints. The total real and reactive power generation by each generator should be maintaining the load-generation profile.

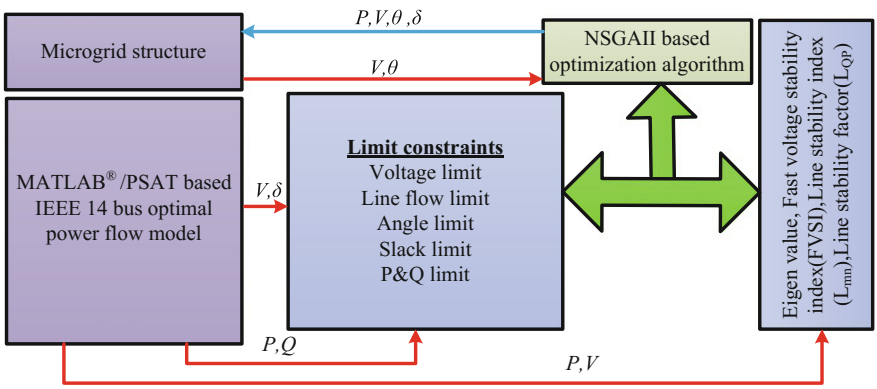

Fig. 16 Block diagram of the proposed control strategy

$$P_i = P_{G_i} - P_{D_i} - |V_i| \sum_{j=1}^{N_b} |V_j||Y_{ij}| \cos(\delta_i - \delta_j - \theta_{ij})$$
$$Q_i = Q_{G_i} - Q_{D_i} - |V_i| \sum_{j=1}^{N_b} |V_j||Y_{ij}| \sin(\delta_i - \delta_j - \theta_{ij}) \quad (25)$$

Here P_i and Q_i are the injected real and reactive power to the system, P_{G_i} and Q_{G_i} are the real and reactive power generation, P_{D_i} and Q_{D_i} are the real and reactive power demanded by the load and N_b is the total number of buses.

(iii) **Inequality constraints**

They are the limits of maximum and minimum allowable operating values of different power system parameters for stable grid operation. They include generator active power (P_{G_i}) limit, reactive power (Q_{G_i}) limit, voltage (V_i) limit, and phase angle (δ_i) limit which are restricted as follows.

$$\left.\begin{array}{l} P_{G_i}^{\min} \le P_{G_i} \le P_{G_i}^{\max} \\ Q_{G_i}^{\min} \le Q_{G_i} \le Q_{G_i}^{\max} \\ V_i^{\min} \le V_i \le V_i^{\max} \\ \delta_i^{\min} \le \delta_i \le \delta_i^{\min} \end{array}\right\} \quad (26)$$

The constraint of transmission loading (P_{ij}) i.e., line flow limit is represented as

$$|P_{ij}| \le P_{ij}^{\max} \quad (27)$$

The loading factor of each bus also consider as an inequality constrain and its limit is given by,

$$1 \le \lambda \le \lambda^{\max} \quad (28)$$

The loading factor should me maintain with in the safe limit in order to load the bus safely.

(iv) **Power System Stability Constraints**

The optimization problem here is carried out by considering the stability of the entire power system. To enhance and ensure the stability of the system after implementing the control algorithm some power system constraints and indices are also incorporated with the control system.

(v) **Small signal stability**

Small signal stability ensures the stability of the power system in S domain (Eigen value stability) [78]. For the small signal stability analysis, the power system with distributed generators is modelled as a set of differential equations and a set of algebraic equations as given below:

$$\begin{aligned} \dot{x} &= f(x, y) \\ 0 &= g(x, y) \end{aligned} \tag{29}$$

Here x, y represents the vector of the state variables and the vector of the algebraic variables respectively. f, g are the vector of differential equations and the vector of algebraic equations.

The Eigen value analysis is carried out by the analysis of the state matrix A_s. The state matrix A_s is obtained by manipulating the complete Jacobian matrix A_c that is defined by the linearization of the DAE system equations Eq. (19) at the equilibrium point.

$$\begin{bmatrix} \Delta\dot{x} \\ 0 \end{bmatrix} = \begin{bmatrix} f_x & f_y \\ g_x & g_y \end{bmatrix} \begin{bmatrix} \Delta x \\ \Delta y \end{bmatrix} = A_c \begin{bmatrix} \Delta x \\ \Delta y \end{bmatrix} \tag{30}$$

The state matrix A_s is obtained by eliminating the algebraic variables and, thus, it is implicitly assumed that g_y is not singular (i.e., absence of singularity-induced bifurcations):

$$A_s = f_x - f_y g_y^{-1} g_x \tag{31}$$

(vi) **Fast voltage stability indices (FVSI)**

Fast voltage stability index (FVSI) is utilized in this paper to assure the safe bus loading [79]. The FVSI is given in Eq. (32).

$$\mathrm{FVSI}_{i,j} = \frac{4Z^2 Q_j}{V_i^2 X} \tag{32}$$

Here Z represents the impedance of the system, Q_j represents the reactive power and V_i is the voltage at ith bus. The line that exhibits FVSI close to 1.00 implies that it is approaching its instability point. If FVSI goes beyond 1.00, one of the buses connected to the line will experience a sudden voltage drop leading to the collapse of the system. FVSI index incorporation in the controller assures that no bus will collapse due to overloading.

(vii) **Line stability index**

The line stability index symbolized by L_{mn} is formulated based on a power transmission concept in a single line. The line stability index L_{mn} is given by [80],

$$L_{mn} = \frac{4Q_r X}{\left[|V_s| \sin(\theta - \delta)\right]^2} \tag{33}$$

Here X is the line reactance, Q_r is the reactive power at the receiving end, V_s is the sending end voltage, θ is the line impedance angle, and δ is the angle difference between the supply voltage and the receiving voltage. The value of L_{mn} must be less than 1.00 to maintain a stable system.

(viii) **Line stability factor**

System Stability is also assured by Line Stability Factor (L_{QP}) as given in (24). The LQP should be less than 1.00 to maintain a stable system [81].

$$L_{QP} = \left(\frac{X}{V_i^2}\right)\left(\frac{XP_i^2}{V_i^2} + Q_j\right) \tag{34}$$

4.3 Analysis of NSGAII Optimization Method in Microgrid

Maximum load ability analysis discussed in previous section has been applied to modified IEEE 14-bus standard test system. The optimization result recorded the maximum instantaneous safe bus loading, when fuel cell was placed at bus 4. Total generation and load at maximum system loading is given in Table 1.

From the table it is obvious that with optimal placement and setting of SOFC, more load demand can be met. In the present work, for IEEE 14 bus test system 1.46 p.u additional active load i.e. an increase of 56.37% loading could be handled without driving the system into instability. Accordingly the line limit settings and slack limit settings are considered in the control algorithm.

The system active power losses for the three case studies analyzed viz. base case, base case with DG, and at maximum loading condition, is shown in Table 2. From the table it can be seen that as the system is integrated with DG, the losses are significantly reduced.

Table 1 Generation and load at maximum system loading

System loadability	P_G (pu)	Q_G (pu)	P_L (pu)	Q_L (pu)
Base loading	2.73	1.09	2.59	0.81
At maximum loading	4.21	1.52	4.05	1.28
Difference (max load-Base load)	1.48	0.43	1.46	0.47

Table 2 System losses

P_{lossbase} (pu)	P_{loss} (pu) with controller	P_{lossbase} (pu) without controller
0.066053284	0.106365669	0.164010957

Table 3 Grid emission comparison

Grid emission (lb)			SOFC emission (lb)		
E_{Grid}			E_{FC}		
Base case loading	Without NSGAII	With NSGAII	Base case loading	Without NSGAII	With NSGAII
30.43561	29.64276	9.84164	0	0.124312	0.011075

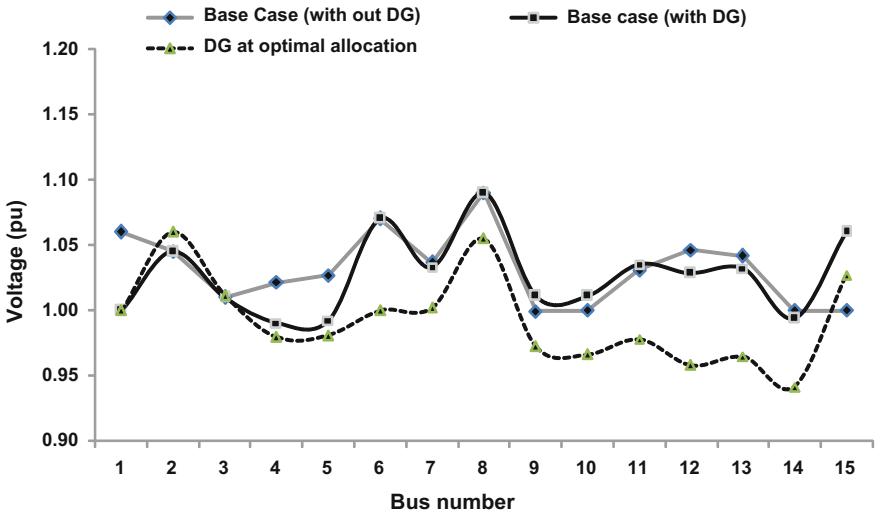

Fig. 17 Voltage profile

Table 3 shows the fuel cell and grid emissions for the three cases considered. The proposed robust controller is efficient to obtain an optimal solution where the emissions are the least. Voltage profile of power system with DG at bus 4 and without DG is compared in Fig. 17. The variation of voltage at each bus is studied to analyze the impact of loadability enhancement through fuel cell DG placement. The *x* axis indicates the bus numbers 1 through 15 and *y* axis represents the voltage magnitude in per unit. It can be seen that at maximum system loading the voltages are maintained within the stipulated limits of 0.9 and 1.1 p.u. Here base case indicates without any microgrid integration. Without controller indicate the operation of grid with microgrid without the proposed controller. The third case is the operation of the microgrid with the integration of proposed NSGAII controller.

Figure 18 shows the generations at different buses. It can be seen that with optimal placement and setting of fuel cell at bus 4, the conventional generations can be reduced and the whole load disturbance is absorbed by the fuel cell. Bus 3 has the largest load share and the robust controller is able to accurately locate the best suitable location for placement of fuel cell at bus 4. During the maximum loading the fuel cell share 2.32 pu, from the base case value of 0.30 pu.

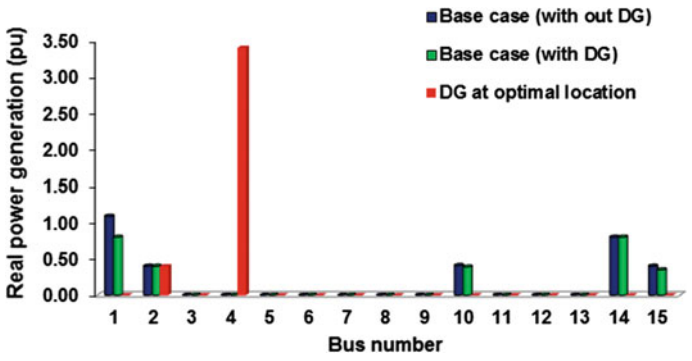

Fig. 18 Generation scheduling

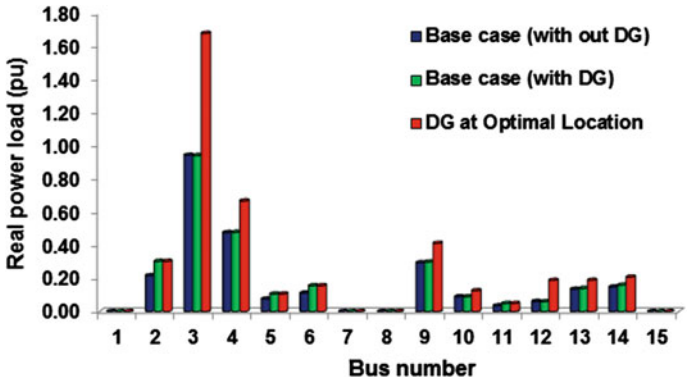

Fig. 19 Load scheduling

Figure 19 shows the maximum loadability at different buses with and without DG. It can be seen that bus 3 has the largest load share. The loading of the IEEE 14 bus test system without integration of DG can only be increased up to 1.2 times. With the optimal placement and setting of SOFC at bus 4 the loadability was able to be increased from the base case loading of 2.59 p.u to 4.9 p.u.

In Fig. 20 line power flows with and without DG is shown. The line active power flows increases as the system loading is increased. The stability constraints assure that the increase in line flows are within the permissible limits as per the standards of IEEE 14-bus system.

The stability constraints at the best compromise solution represented by their eigenvalue, FVSI, LSI and LQP are shown in Figs. 21 and 22. It is evident that the incorporation of small signal stability constraint into the robust controller assures grid stability. Also it can be seen that voltage and line stability indices (FVSI and LQP) are well within acceptable limits.

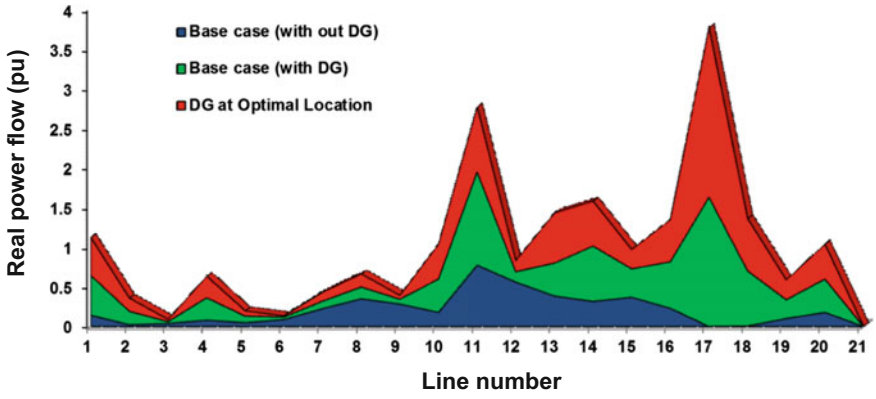

Fig. 20 Line flows

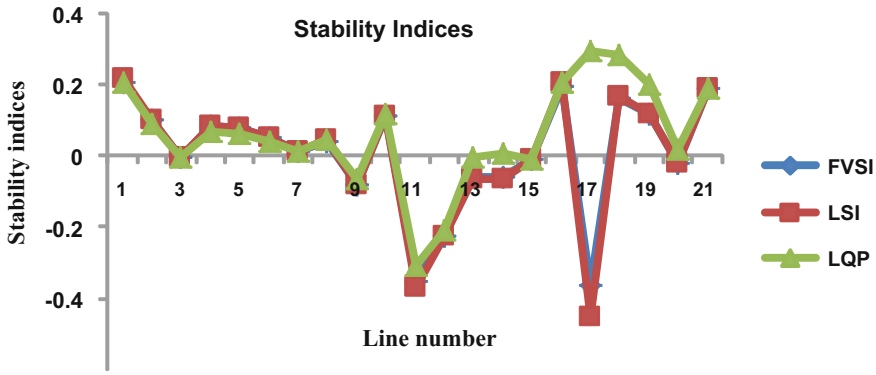

Fig. 21 Power system stability indices

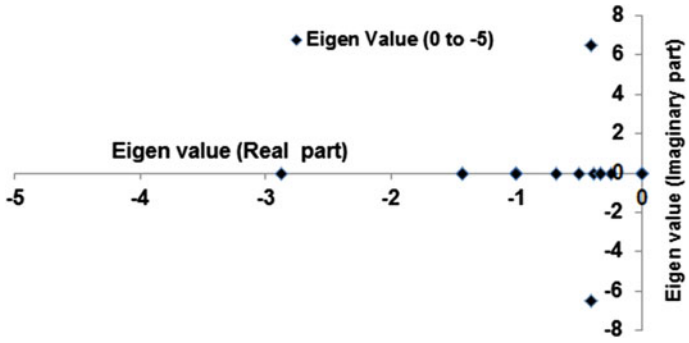

Fig. 22 Eigen value plot

Table 4 Different heuristic and meta-heuristic optimization algorithm and their applications in microgrid

Optimization strategy	Algorithm	Application	References
Heuristic and metaheuristicoptimization	Evolutionary Algorithm (EA)	Power generation optimization, selection and DG sizing	[82]
	Genetic Algorithm (GA)	Power generation optimization, selection and DG sizing	[82]
		DG placement	[83]
		Scheduling of operation	[83]
	Simulated Annealing (SA)	Power generation optimization and sizing	[84]
		DG placement	[85]
	Particle Swarm Optimization (PSO)	Sizing of DG and ES	[86]
		DG placement	[87]
		Scheduling of operation	[88]
	Artificial Immune System (AIS)	DG placement	[89]
	VACCINE-AIS	DG placement	[90]
		Scheduling of operation	[91]
	Multi-Dimensional PSO (MDPSO)	DG placement	[92]
	Mesh Adaptive Direct Search (MADS)	Scheduling of operation	[93]
	Modified Gravitational Search Algorithm (MGSA)	Scheduling of operation	[94]
	Adaptive Modified Firefly Algorithm (AMFA)	Scheduling of operation	[95]
	Gravitational Search Algorithm (GSA)	Scheduling of operation	[96]
	Self-Adaptive GSA (SGSA)	Scheduling of operation	[97]
	Bacterial Foraging Algorithm (BFA)	Scheduling of operation	[98]
	Competitive Heuristic Algorithm for Scheduling Energy-Generation (CHASE)	Scheduling of operation	[99]

5 Summary

In this chapter, a comprehensive analysis of artificial intelligence optimization methods are used for microgrid technologies and described in details. The different challenges and steps involved in the microgrid energy management system have been reviewed. Artificial intelligence based optimization techniques such as GA, PSO and NSGAII have been studied and analyzed for the microgrid application. Among these, NSGAII algorithm is found to be suitable for the microgrid optimization due to its fast operation, which is the desirable quality for a real time controller. The NSGAII algorithm is applied to the microgrid for solving the MOOM. Power system security and stability are considered as the constraints for the optimization problem. The control algorithm maximizes the system loadability to a safe limit without violating any power system security constraint. The best location for the placement of fuel cell has been identified through the static voltage study and the grid settings by the controller. The proposed control algorithm was tested and verified on IEEE 14-bus standard test system using Newton Raphson power flow method and modal analysis. Total system losses and grid emissions are significantly reduced by the NSGAII. The voltage profile, real power flow and stability indices are plotted for stability analysis purpose. The different heuristic and meta-heuristic algorithms that can be used for the microgrid planning, optimization and management are given in Table 4.

References

1. Ramakumar R (2001) Role of distributed generation in reinforcing the critical electric power infrastructure. Paper presented at power engineering society winter meeting, vol 1. IEEE. pp 139–139
2. Lasseter RH, Paolo P (2004) Microgrid: a conceptual solution. Paper presented in power electronics specialists conference, 20 Jun 2004
3. Lasseter R et al (2002) The CERTS microgrid concept. White paper for Transmission Reliability Program, Office of Power Technologies, US Department of Energy, vol 2, p 30
4. Lasseter, Robert H (2002) Microgrids. In: Power engineering society winter meeting, Vol 1, pp 305–308
5. Chowdhury S, Crossley P (2009) Microgrids and active distribution networks. The Institution of Engineering and Technology
6. Jiayi H, Chuanwen J, Rong X (2008) A review on distributed energy resources and MicroGrid. Renew Sustain Energy Rev 12:2472–2483
7. Lasseter R et al (2002) The CERTS microgrid concept, white paper on integration of distributed energy resources. California Energy Commission, Office of Power Technologies-US Department of Energy, Available via, http://certs.lbl.Gov. Accessed 10 June 2016
8. Biczel P (2007) Power electronic converters in DC microgrid. In: IEEE proceedings of the compatibility in power electronics, 29 May 2007
9. Ito Y, Zhongqing Y, Akagi H (2004) DC microgrid based distribution power generation system. In: IPEMC'04: topics in power electronics. 4th International conference on power electronics and motion control, vol 3. IEEE, pp 1740–1745, Aug 2004

10. Arulampalam A et al (2004) Control of power electronic interfaces in distributed generation microgrids. Int J Electron 91:503–523
11. Momoh J (2012) Smart grid: fundamentals of design and analysis. Wiley, New York
12. Jiang Z, Dougal RA (2008) Hierarchical microgrid paradigm for integration of distributed energy resources. In: Power and Energy Society general meeting. Conversion and delivery of electrical energy in the 21st century
13. Perea E, Oyarzabal JM, Rodríguez R (2008) Definition, evolution, applications and barriers for deployment of microgrids in the energy sector. E&I Elektrotechnik and Informationstechnik 125(12):432–437
14. Marzband M et al (2013) Experimental evaluation of a real time energy management system for stand-alone microgrids in day-ahead markets. Appl Energy 106:365–376
15. Colson CM, Nehrir MH (2009) A review of challenges to real-time power management of microgrids. In: IEEE Power and Energy Society general meeting
16. Khodaei A, Bahramirad S, Shahidehpour M (2015) Microgrid planning under uncertainty. IEEE Trans Power Syst 30(5):2417–2425
17. Marzband M et al (2014) Experimental validation of a real-time energy management system using multi-period gravitational search algorithm for microgrids in islanded mode. Appl Energy 128:164–174
18. Narayanaswamy B, Garg VK, Jayram TS (2012) Online optimization for the smart (micro) grid. In: Proceedings of the 3rd international conference on future energy systems: where energy, computing and communication meet, May 2012
19. Mehrizi-Sani A, Iravani R (2010) Potential-function based control of a microgrid in islanded and grid-connected modes. IEEE Trans Power Syst 25:1883–1891
20. Katiraei F et al (2008) Microgrids management. IEEE Power Energ Mag 6:54–65
21. Katiraei F, Iravani MR, Lehn PW (2005) Micro-grid autonomous operation during and subsequent to islanding process. IEEE Trans Power Delivery 20:248–257
22. Hatziargyriou N (ed) (2013) Microgrids: architectures and control. Wiley, New York
23. Tsikalakis AG, Hatziargyriou ND (2011) Centralized control for optimizing microgrids operation. In: IEEE power and energy society general meeting
24. Lopes JAP, Moreira CL, Madureira AG (2006) Defining control strategies for microgrids islanded operation. IEEE Trans Power Syst 21:916–924
25. Dimeas AL, Hatziargyriou ND (2005) Operation of a multiagent system for microgrid control. IEEE Trans Power Syst 20:1447–1455
26. Sanseverino ER et al (2011) An execution, monitoring and re-planning approach for optimal energy management in microgrid. Energy 36:3429–3436
27. Katiraei F et al (2008) Microgrids management. IEEE Power Energy Mag 6:54–65
28. Vaccaro A et al (2011) An integrated framework for smart microgrids modeling, monitoring, control, communication, and verification. Proc IEEE 99:119–132
29. Logenthiran T et al (2010) Multi-agent system (MAS) for short-term generation scheduling of a microgrid. In: ICSET'10. IEEE international conference on sustainable energy technologies, 6 Dec
30. Logenthiran T et al (2012) Multiagent system for real-time operation of a microgrid in real-time digital simulator. IEEE Trans Smart Grid 3:925–933
31. Jian F, Li J-Q, Wu X-Y (2012) Microgrid monitoring system based on IEC 61850. High Power Converter Technol 2:008
32. Kanchev H et al (2010) Smart monitoring of a microgrid including gas turbines and a dispatched PV-based active generator for energy management and emissions reduction. Paper presented in IEEE PES innovative smart grid technologies conference Europe, 11 Oct 2010
33. Shamshiri M, Gan CK, Tan CW (2012) A review of recent development in smart grid and micro-grid laboratories. Paper presented in IEEE power engineering and optimization conference Melaka, Malaysia, 6 June 2012
34. Yoo B-K et al (2011) Communication architecture of the IEC 61850-based micro grid system. J Electr Eng Technol 6:605–612

35. Liang H et al (2012) Multiagent coordination in microgrids via wireless networks. IEEE Wirel Commun 19:14–22
36. Jingding R, Yanbo C, Lihua Z (2011) Discussion on monitoring scheme of distributed generation and micro-grid system. Paper presented in IEEE 4th international conference on power electronics systems and applications, 8 June 2011
37. Vaccaro A et al (2005) A self-organizing architecture for decentralized smart microgrids synchronization, control, and monitoring. IEEE Trans Ind Inf 11:289–298
38. Özdemir MT, Sönmez M, Akbal A (2014) Development of FPGA based power flow monitoring system in a microgrid. Int J Hydrogen Energy 39:8596–8603
39. Aung HN et al (2010) Agent-based intelligent control for real-time operation of a microgrid. Paper presented in power electronics, drives and energy systems (PEDES), 20 Dec 2010
40. Islam FR, Gabbar HA, Pots HR (2014) Power quality improvement of distribution network using V2G. Paper presented in international conference on smart energy grid engineering (SEGE), Canada, 27 Aug 2014
41. Farhangi Hassan (2010) The path of the smart grid. IEEE Power Energy Mag 8:18–28
42. Wilshaw AR, Pearsall NM, Hill R (1997) Installation and operation of the first city centre PV monitoring station in the United Kingdom. Sol Energy 59:19–26
43. Finkelstein PL et al (1986) Comparison of wind monitoring systems. Pad II: Doppley. Sodars. J Atmospheric Oceanic Technol 3:594–604
44. Ebrahim M, Lakov G, Oliver S (2006) Microturbine engine system having stand-alone and grid-parallel operating modes. U.S. Patent No. 7,078,825. 18 Jul 2006
45. Fu Q et al (2012) Microgrid generation capacity design with renewables and energy storage addressing power quality and surety. IEEE Trans Smart Grid 3:2019–2027
46. Zaidi AA et al (2010) Load recognition for automated demand response in microgrids. Paper presented in 36th annual conference on IEEE industrial electronics, 7 Nov 2010
47. Shi W et al (2014) Evaluating microgrid management and control with an implementable energy management system. Paper presented in IEEE international conference on smart grid communications (SmartGridComm), 3 Nov 2014
48. Katiraei Farid et al (2008) Microgrids management. IEEE Power Energ Mag 6:54–65
49. Molderink A et al (2010) Management and control of domestic smart grid technology. IEEE Trans Smart Grid 1:109–119
50. Tsikalakis AG, Hatziargyriou ND (2011) Centralized control for optimizing microgrids operation. Paper presented in IEEE power and energy society general meeting, 3 Nov 2011
51. Wang R-Q, Li Ke, Zhang C-H (2011) Optimization allocation of microgrid capacity based on chaotic multi-objective genetic algorithm. Power Syst Protect Control 39:16–22
52. Russell SJ et al (2003) Artificial intelligence: a modern approach. Prentice Hall, Upper Saddle River
53. Pearl J (1984) Heuristics: intelligent search strategies for computer problem solving. Addison-Wesley Publication, Boston
54. Schwefel H-PP (1993) Evolution and optimum seeking: the sixth generation. Wiley, New York
55. Lai LL et al (1997) Improved genetic algorithms for optimal power flow under both normal and contingent operation states. Int J Electr Power Energy Syst 19:287–292
56. Somasundaram P, Kuppusamy K, Kumudini Devi RP (2004) Evolutionary programming based security constrained optimal power flow. Electr Power Syst Res 72:137–145
57. Li Fu-Dong et al (2012) Optimal control in microgrid using multi-agent reinforcement learning. ISA Trans 51:743–751
58. Bhuvaneswari R et al (2010) Intelligent agent based auction by economic generation scheduling for microgrid operation. Paper presented in IEEE innovative smart grid technologies, 19 Jan 2010
59. Leitão P, Barbosa J, Trentesaux D (2012) Bio-inspired multi-agent systems for reconfigurable manufacturing systems. Eng Appl Artif Intell 25:934–944
60. Yoshida H et al (2000) A particle swarm optimization for reactive power and voltage control considering voltage security assessment. IEEE Trans Power Syst 15:1232–1239

61. Park J-B et al (2005) A particle swarm optimization for economic dispatch with non-smooth cost functions. IEEE Trans Power Syst 20:34–42
62. Wang C-R et al (2005) A modified particle swarm optimization algorithm and its application in optimal power flow problem. Paper presented in IEEE international conference on machine learning and cybernetics, 18 Aug 2005
63. Vlachogiannis JG, Lee KY (2005) Determining generator contributions to transmission system using parallel vector evaluated particle swarm optimization. IEEE Trans Power Syst 20:1765–1774
64. Hassan MA, Abido MA (2011) Optimal design of microgrids in autonomous and grid-connected modes using particle swarm optimization. IEEE Trans Power Electron 26:755–769
65. Al-Saedi Waleed et al (2012) Power quality enhancement in autonomous microgrid operation using particle swarm optimization. Int J Electr Power Energy Syst 42:139–149
66. Wu Z et al (2011) Economic optimal schedule of CHP microgrid system using chance constrained programming and particle swarm optimization. Paper presented in IEEE power and energy society general meeting, 24 Jul 2011
67. Al-Saedi W et al (2013) Power flow control in grid-connected microgrid operation using particle swarm optimization under variable load conditions. Int J Electr Power Energy Syst 49:76–85
68. Walters DC, Sheble GB (1993) Genetic algorithm solution of economic dispatch with valve point loading. IEEE Trans Power Syst 8:1325–1332
69. Chen P-H, Chang H-C (1995) Large-scale economic dispatch by genetic algorithm. IEEE Trans Power Syst 10:1919–1926
70. Wang R-Q, Li Ke, Zhang C-H (2011) Optimization allocation of microgrid capacity based on chaotic multi-objective genetic algorithm. Power Syst Protect Control 39:16–22
71. Haesens E et al (2005) Optimal placement and sizing of distributed generator units using genetic optimization algorithms. Electr Power Qual Utilisation J 11:97–104
72. Mohamed FA, Koivo HN (2012) Online management genetic algorithms of microgrid for residential application. Energy Convers Manag 64:562–568
73. Liang HZ, Gooi HB (2010) Unit commitment in microgrids by improved genetic algorithm. Paper presented in IEEE conference proceedings IPEC'10, 27 Oct 2010
74. Ismail MS, Moghavvemi M, Mahlia TMI (2014) Genetic algorithm based optimization on modeling and design of hybrid renewable energy systems. Energy Convers Manag 85:120–130
75. Mohammadi M, Hosseinian SH, Gharehpetian GB (2012) GA-based optimal sizing of microgrid and DG units under pool and hybrid electricity markets. Int J Electr Power Energy Syst 35:83–92
76. Nagasaka K et al (2012) A research on operation planning of multi smart micro grid. Paper presented in IEEE international conference on advanced mechatronic systems, 18 Sep 2012
77. Yang X et al (2013) Optimization allocation of energy storage for microgrid based on economic dispatch. Power Syst Protect Control 41:53–60
78. Reeves CR (1995) A genetic algorithm for flowshop sequencing. Comput Oper Res 22:5–13
79. Beasley JE, Chu PC (1996) A genetic algorithm for the set covering problem. Eur J Oper Res 94:392–404
80. Whitley D (1994) A genetic algorithm tutorial. Stat Comput 4:65–85
81. Deb K et al (2002) A fast and elitist multiobjective genetic algorithm: NSGA-II. IEEE Trans Evol Comput 6:182–197
82. Buayai K, Ongsakul W, Mithulananthan N (2012) Multiobjective microgrid planning by NSGAII in primary distribution system. Eur Trans Electr Power 22:170–187
83. Hamdani TM et al (2007) Multi-objective feature selection with NSGAII. In: Proceedings of international conference on adaptive and natural computing algorithms. Springer Berlin, 11 April 2007

84. Michalak K (2015) Improving the NSGA-II performance with an external population. In: proceedings of international conference on intelligent data engineering and automated learning. Springer, Berlin, 14 Oct 2015
85. Kundur P (1994) Power system stability and control. McGraw-hill, New York
86. Musirin I, Abdul Rahman TK (2002) Novel fast voltage stability index (FVSI) for voltage stability analysis in power transmission system. Paper presented in IEEE students conference on research and development
87. Moghavvemi M, Omar FM (1998) Technique for contingency monitoring and voltage collapse prediction. IEE Proc Gener Trans Distrib 145:634–640
88. Mohamed A, Jasmon GB (1989) Voltage contingency selection technique for security assessment. IEE Proc C-Gener Trans Distrib 136:24–28
89. Logenthiran T et al (2010) Optimal sizing of an islanded microgrid using evolutionary strategy. Paper presented in IEEE 11th international conference on probabilistic methods applied to power systems (PMAPS), 14 June 2010
90. Kirthiga MV, Arul Daniel S, Gurunathan S (2013) A methodology for transforming an existing distribution network into a sustainable autonomous micro-grid. IEEE Trans Sustain Energy 4:31–41
91. Mohamed FA, Koivo HN (2008) Multiobjective genetic algorithms for online management problem of microgrid. Int Rev Electr Eng-IREE 3:46–54
92. Yang Y, Pei W, Qi Z (2012) Optimal sizing of renewable energy and CHP hybrid energy microgrid system. Paper presented in IEEE PES innovative smart grid technologies, 21 May 2012
93. Verda Vittorio, Ciano Chiara (2005) Procedures for the search of the optimal configuration of district heating networks. Int J Thermodyn 8:143–153
94. Basu AK, Chowdhury S, Chowdhury SP (2009) Strategic deployment of CHP-based distributed energy resources in microgrids. Paper presented in IEEE power & energy society general meeting, 26 July 2009
95. Mohamed FA, Koivo HN (2013) System modeling and online optimal management of microgrid using mesh adaptive direct search. Int J Electr Power Energy Syst 32:398–407
96. Tan S, Xu J, Kumar Panda S (2012) Optimization of distribution network incorporating microgrid using vaccine-AIS. Paper presented in IEEE 8th annual conference on Industrial Electronics Society, 25 Oct 2012
97. Mohamed FA, Koivo HN (2012) Multiobjective optimization using Mesh Adaptive Direct Search for power dispatch problem of microgrid. Int J Electr Power Energy Syst 42:728–735
98. Niknam T, Golestaneh F, Reza Malekpour A (2013) Probabilistic model of polymer exchange fuel cell power plants for hydrogen, thermal and electrical energy management. J Power Sources 229:285–298
99. Mohammadi S et al (2013) An adaptive modified firefly optimisation algorithm based on Hong's point estimate method to optimal operation management in a microgrid with consideration of uncertainties. Energy 51:339–348

Energy Management of AC-Isolated Microgrids Based on Distributed Storage Systems and Renewable Energy Sources

Andoni Urtasun, Pablo Sanchis and Luis Marroyo

Abstract This chapter presents the frequency and voltage regulation and the energy management strategy for an AC islanded microgrid based on distributed energy storage and Renewable Energy Sources (RES). The primary control in AC microgrids makes it possible to achieve real and reactive power sharing between the distributed inverters. This is usually performed through droop methods, thereby avoiding the need for high-bandwidth communication and rendering the system more cost-effective and reliable. In the first part of this chapter, the conventional droop method is discussed and modelled followed by an analysis of the effect of line impedance and the presence of nonlinear loads on this method. When using the conventional droop method, it is not possible to perform a secondary control or energy management of a distributed storage system. For this reason, local droop control is usually enhanced by an overall control through low-bandwidth communication. In order to completely avoid the need for any kind of communication system and to improve the reliability of an islanded grid, a frequency-based energy management strategy can be used. The first part of this energy management strategy is related to the regulation of the State-Of-Charge (SOC), in which the conventional power–frequency droop is modified as a function of the battery SOC in order to balance the SOCs of the distributed batteries. First, this method is described, and then guidelines to design the control parameters are given, followed by simulation and experimental validation. The second part of the frequency-based energy management strategy is related to the regulation of the battery voltage and current. In order to maintain these variables within acceptable limits while avoiding the use of a communication system, a number of power–frequency curves are programmed in the battery inverters, RES inverters and non-critical loads. This energy management strategy is described, then the subsequent operating modes are presented and, finally, the experimental validation is provided.

A. Urtasun (✉) · P. Sanchis · L. Marroyo
Department of Electrical and Electronic Engineering, Public University of Navarre (UPNa), Campus Arrosadía, 31006 Pamplona, Spain
e-mail: andoni.urtasun@unavarra.es

F.M.R. Islam et al. (eds.), *Smart Energy Grid Design for Island Countries*,
Green Energy and Technology, DOI 10.1007/978-3-319-50197-0_11

Keywords Energy management · AC isolated microgrids · Distributed storage systems · Renewable energy sources

1 Introduction

Nowadays most islanded power grids are powered by diesel generators. However, the use of fossil fuels contributes to climate change and increases the levelized cost of energy, especially in island countries, where diesel needs to be transported over long distances. Therefore, these isolated grids are ideally powered by renewable energy systems, thereby reducing energy costs, greenhouse gas emissions, and providing job opportunities for the local population [1].

Although a more widespread use of renewable energies in islanded countries is desirable, the integration of renewable-energy generators is not without its complications. In a power grid with high renewable penetration, renewable generators must participate in grid support. Some requirements, such as low current THD or reactive power support, can be obtained thanks to the interfacing inverter, while others, such as low-voltage ride-through, are more difficult to achieve and may require the use of additional hardware [2]. Furthermore, the energy produced by a renewable generator cannot generally be controlled since it is resource-dependent. High penetration of renewable energies decreases the ratio of dispatchable generators whilst it also adds an unpredictable factor to the power profile, thus making it more complicated to regulate the power grid.

In order to address these issues and to make a renewable energy-based grid possible, storage units or controllable generators need to be included close to the renewable distributed generators. Depending on the ratio between controllable and non-controllable elements, different power regulation levels can be achieved in this system. This combination of elements together with loads is termed a microgrid, and includes an energy management strategy which is fundamental in order to guarantee a reliable power supply.

Microgrids can be classified into three groups according to configuration. The first is the AC microgrid, whereby all elements are connected to the AC bus, which can either be connected or disconnected from the power grid through the point of common coupling. The main advantage of this topology is its versatility since most of the system elements are currently designed and prepared for AC grids. It permits the straightforward integration of distributed generators and system scalability following initial installation. The second configuration is the DC microgrid, in which all elements are connected to the DC bus, and this in turn is connected to the power grid through a DC/AC inverter. The main advantages of this topology in relation to the AC microgrid are that a lower number of electronic converters are required and the DC side is easier to manage. The third configuration is termed a hybrid microgrid due to the fact that it incorporates both DC and AC buses. This configuration offers the advantages of DC microgrids yet with greater versatility. However, the presence of two buses makes the system and the control more

complicated. The AC and DC buses are connected through a DC/AC inverter and the AC bus can be either connected or disconnected from the power grid.

This chapter addresses the energy management of an AC-isolated microgrid, based on distributed storage systems and renewable energy sources. This system is suitable for island networks given the fact that it makes it possible to have an AC network available at all points of consumption whilst it also permits the low-voltage connection of small distributed generation and storage elements close to consumption. The system to be examined in this chapter is shown in Fig. 1, including PV and wind-power generation as renewable sources and batteries as storage elements. In this configuration, wind turbines are connected to the grid through AC/AC converters, whilst batteries and PV generators are connected through DC/AC inverters.

In this system, the frequency and voltage regulation can be implemented in a number of ways. In the one hand, there is a central control or master–slave approach whereby the operating point of each device is set in real time by a manager. However, the drawback here is that there is a need for a rapid communication system between the master and microgrid devices. Distributed control is another possibility, with the battery inverters operating under voltage-control mode and using droop methods as a means of regulating the grid frequency and voltage. This system ensures that the inverters are independent with no need for inter-communication, leading to cost savings and greater reliability. Whereas current-controlled RES converters capture the solar/wind energy and deliver power to the grid.

Droop methods are used to regulate the frequency and voltage of inverter-based microgrids operating with distributed control, as only local measurements are necessary. For conventional droop control, each inverter is responsible for measuring its real and reactive powers and then a frequency–voltage droop is applied

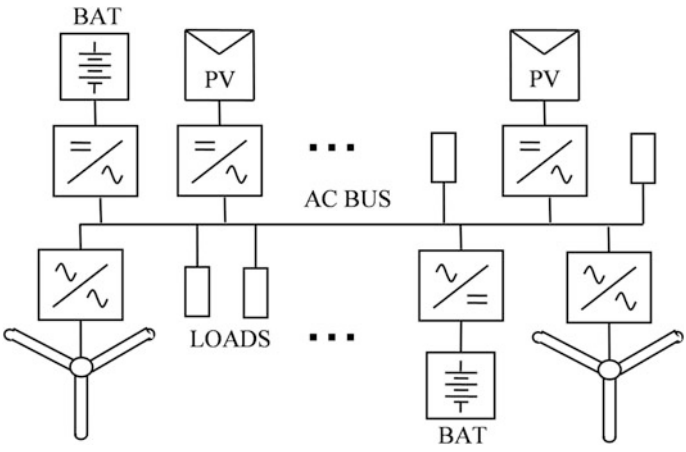

Fig. 1 Stand-alone system with distributed energy storage and generation

based on the real power–frequency (*P–f*) and reactive power–voltage (*Q–V*) droops. As a result of that, the power is equally shared between the inverters.

Section 2 first presents the calculation of the real and reactive powers, given the fact that it is important to make a rapid calculation of the power outputs for the correct operation of the droop control. The section then goes on to discuss the droop concept in order to understand how the power of each inverter can be shared with no need for communication between inverters and to present a system model that will make it possible to obtain the droop curve parameters. Finally, an analysis is made of how non-idealities can affect the conventional droop method, such as the presence of long lines between inverters or the presence of nonlinear loads.

Although the conventional droop method achieves power sharing, it is unable to perform a secondary control or energy management of a distributed storage system. For this reason, local droop control is usually enhanced by an overall control through low-bandwidth communication. In order to completely avoid the need for any kind of communication system and to improve the reliability of an islanded grid, frequency-based energy management can be used. This energy management scheme is carried out by modifying the conventional droop method and can be divided into two parts.

The first part deals with the regulation of the battery state-of-charge (SOC). In fact, small errors in the conventional droop control can accumulate over time, leading to an SOC imbalance. Likewise, differences not contemplated between the battery capacities will mean that the same power input or output could create different variations in the SOC. Section 3 therefore proposes the modification of the conventional droop method in order to maintain the SOC of all batteries at the same level, yet with no need for communication. Two techniques shall be proposed in order to achieve this objective; the first changes the slope of the curve whilst the other raises or lowers the whole curve. After showing the second method to be better, the section goes on to discuss how to obtain the curve parameters and the experimental and simulation results are presented.

The second part addresses the battery current and voltage regulation. In order to lengthen the useful life of a battery, it is essential to maintain its voltage between the maximum and minimum limits at all times, and also never to exceed the maximum charge or discharge current. However, when endeavouring to meet the power demand and also to harvest the maximum power from the RES, these restrictions may not be met. Therefore, an energy management strategy is required for all system elements, whereby a further modification of the conventional droop plays a key role. Section 4 describes this energy management strategy, permitting coordination between devices yet with no need for communication. The various system operating modes are explained below and, finally, some experimental results are given.

2 Conventional Droop Method

2.1 Power Calculation

Since the real and reactive powers are required as inputs for the droop control, an accurate and fast calculation is desirable. A number of methods can be used to obtain the real and reactive powers from the grid voltage and inverter current. The simplest one is presented here and is named the Product and Low-Pass Filter (P&LPF). The grid voltage and inverter current can be expressed using Eqs. (1) and (2).

$$v(t) = \sqrt{2}V \cdot \sin(\omega t) \tag{1}$$

$$\begin{aligned} i(t) = I_{\mathrm{dc}} &+ \sqrt{2}I_1 \cdot \sin(\omega t - \varphi_1) + \sqrt{2}I_3 \cdot \sin(3\omega t - \varphi_3) \\ &+ \sqrt{2}I_5 \cdot \sin(5\omega t - \varphi_5) + \cdots, \end{aligned} \tag{2}$$

where ω is the fundamental angular frequency, V is the RMS grid voltage, I_{dc} is the DC current, I_1 is the RMS fundamental current, I_3, I_5… are the RMS harmonic currents, and φ_1, φ_3, φ_5… are the angles between the grid voltage and currents. It is assumed that the inverters are feeding typical nonlinear loads, and the voltage harmonics are disregarded in order to simplify the derivation. The DC current can either be due to a nonlinear load such as a half-wave rectifier or can represent a low-frequency transient.

The instantaneous power can be obtained as the product of the grid voltage and inverter current as follows:

$$\begin{aligned} p(t) = v(t) \cdot i(t) = {} & V \cdot I_1 \cdot \cos\varphi_1 + \sqrt{2}V \cdot I_{\mathrm{dc}} \cdot \sin\omega t - V \cdot I_1 \cdot \cos(2\omega t - \varphi_1) \\ & + V \cdot I_3 \cdot \cos(2\omega t - \varphi_3) - V \cdot I_3 \cdot \cos(4\omega t - \varphi_3) \\ & + V \cdot I_5 \cdot \cos(4\omega t - \varphi_5) + \cdots \end{aligned} \tag{3}$$

The real power is defined as the average value of Eq. (3). It can be observed that the instantaneous power has many harmonic components, which should be filtered in order to determine the real power. The main harmonic is generally due to the fundamental current, with amplitude $V \cdot I_1$ and twice the grid frequency. In order to filter this harmonic, the low-pass filter cutoff frequency should be much lower that 2ω, which is usually below 10 rad/s (1.59 Hz), slowing down the dynamic performance.

To enhance dynamic performance, a power calculation based on p–q theory can be used [3]. According to the p–q theory, the real and reactive powers can be obtained using Eqs. (4) and (5).

$$p_{\alpha\beta}(t) = 1/2 \cdot \left(v_\alpha \cdot i_\alpha + v_\beta \cdot i_\beta\right) \tag{4}$$

$$q_{\alpha\beta}(t) = 1/2 \cdot \left(v_\beta \cdot i_\alpha - v_\alpha \cdot i_\beta\right), \tag{5}$$

where $v_\alpha = v(t)$, $i_\alpha = i(t)$, and the voltage v_β and current i_β are obtained by introducing a phase delay of $\pi/2$ to v_α and i_α by using a circular buffer.

If a digital microprocessor is used, it is then much simpler to delay the voltage and current for a given time $T_d = 2\pi/4\omega_0$, where ω_0 is the nominal frequency (for 50 Hz, $T_d = 5$ ms), preventing the use of extra hardware. As a result, the v_α and i_α expressions change because the fundamental component and harmonics 5, 9, 13… are delayed $\pi/2$ but harmonics 3, 7, 11… are delayed $3\pi/2$. The voltage v_β and current i_β can then be expressed in Eqs. (6) and (7).

$$v_\beta = \sqrt{2}V \cdot \sin\left(\omega t - \frac{\pi}{2}\right) \tag{6}$$

$$i_\beta = I_{dc} + \sqrt{2}I_1 \cdot \sin\left(\omega t - \varphi_1 - \frac{\pi}{2}\right) + \sqrt{2}I_3 \cdot \sin\left(3\omega t - \varphi_3 - \frac{3\pi}{2}\right) + \sqrt{2}I_5 \cdot \sin\left(5\omega t - \varphi_5 - \frac{\pi}{2}\right) + \cdots . \tag{7}$$

Using the expression for $p_{\alpha\beta}(t)$ and $q_{\alpha\beta}(t)$ presented in Eqs. (4) and (5), and considering Eqs. (1), (2), (6) and (7), one obtains

$$\begin{aligned} p_{\alpha\beta}(t) = {} & V \cdot I_1 \cdot \cos\varphi_1 + V \cdot I_{dc} \cdot \sin(\omega t - \pi/4) \\ & - V \cdot I_3 \cdot \cos(4\omega t - \varphi_3) + V \cdot I_5 \cdot \cos(4\omega t - \varphi_5) + \cdots \end{aligned} \tag{8}$$

$$q_{\alpha\beta}(t) = V \cdot I_1 \cdot \sin\varphi_1 - V \cdot I_{dc} \cdot \cos(\omega t - \pi/4) - V \cdot I_5 \cdot \sin(4\omega t - \varphi_5) + \cdots . \tag{9}$$

The real and reactive powers are defined as the average value of Eqs. (8) and (9), respectively. By comparing these expressions to Eq. (3), it can be observed that the most problematic harmonic, at a frequency of 2ω, has disappeared, and the harmonic due to the DC current has been reduced. As a result, the low-pass filter cutoff frequency can be higher than for the previous method, specifically about 60 rad/s (9.55 Hz). This makes it possible to improve the droop method dynamic performance.

Equations (6)–(9) are obtained for $\omega = \omega_0$. However, the frequency varies around its nominal value during operation due to the droop method. Because a fixed delay time T_d is used for v_β and i_β, the actual phase delay will be around $\pi/2$ or $3\pi/2$ when $\omega \neq \omega_0$. Although not shown here for reasons of space, the harmonics at ω, 2ω, 4ω… change slightly in relation to Eqs. (8) and (9) and the average value of $p_{\alpha\beta}(t)$ is still equal to real power P. However, the average value of $q_{\alpha\beta}(t)$ does change and is no longer equal to reactive power Q but to Eq. (10).

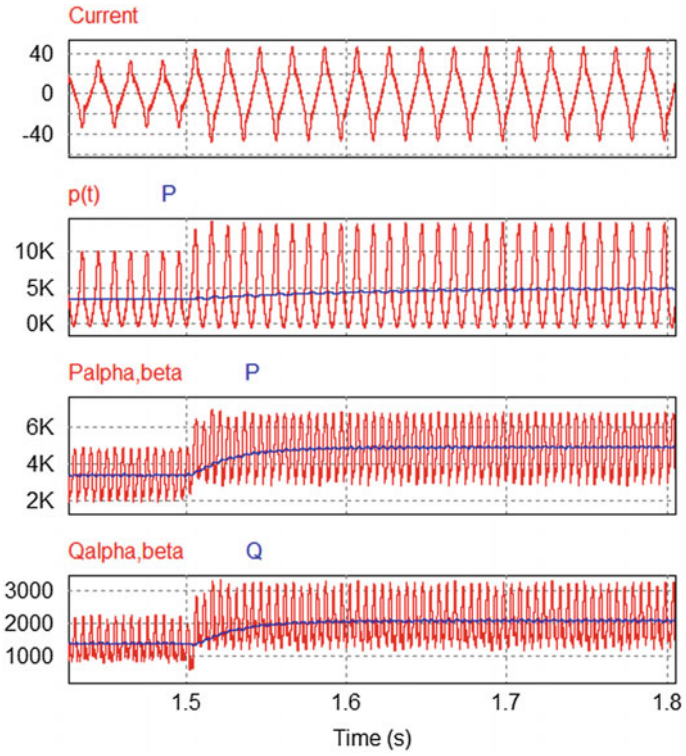

Fig. 2 Power calculation for product plus LPF (method 1) and for *p-q* theory and digital sampling plus LPF (method 2)

$$Q_{\alpha\beta,\mathrm{av}} = V \cdot I_1 \cdot \sin\varphi_1 \cdot \cos(\pi/2 \cdot (1 - \omega/\omega_0)) \tag{10}$$

This expression shows that, with this method, the calculated reactive power will be always lower than its actual value when $\omega \neq \omega_0$. However, since the frequency variation range must be between $\pm 2\%$ according to IEEE standards, the reactive power error is lower than 0.05%, and can be completely disregarded.

This method was validated and compared to the previous method by means of simulation results, shown in Fig. 2. At the start, the inverter is supplying both linear and nonlinear loads, with $P_{\mathrm{load}} = 3500$ W and $Q_{\mathrm{load}} = 1300$ VAr in total. Then, at second 1.5, other linear and nonlinear loads, with $P_{\mathrm{load}} = 1700$ W and $Q_{\mathrm{load}} = 600$ VAr in total, are connected. As a result of the power increase, the grid frequency changes from 49.63 to 49.53 Hz. The high value of the current harmonics can be observed in the first graph. The second graph represents the product and LPF method, both the instantaneous power $p(t)$ given by Eq. (3) and the real power P obtained after applying a LPF with cutoff frequency of 10 rad/s. The high value of the power harmonic at 2ω as well as the slow response of the calculation can be observed. The second method discussed in this section is shown in the third

and fourth graphs. It should be noted that the harmonics of $P_{\alpha\beta}$ and $Q_{\alpha\beta}$ both have lower amplitudes and higher frequencies, as predicted by Eqs. (8) and (9). As a result, real power P and reactive power Q are accurately obtained after applying an LPF with a cutoff frequency of 40 rad/s.

Thanks to its superior dynamic performance, the power calculation including the *p-q* theory, the fixed time delay and the low-pass filter will be used from here onwards.

2.2 Voltage and Frequency Droop Concept

Figure 3 shows an islanded microgrid with N single-phase parallel-connected inverters in voltage-control mode. The droop method allows the inverters to jointly regulate the voltage and frequency of the grid. Power sources $S1$ to SN are modelled as voltage sources, meaning that their power response is much faster than droop method dynamics. In order to be consistent with the energy management scheme proposed at the end of this chapter, batteries will be selected as the power source.

The inverters are connected to the AC bus through inductive filter L_{fi}. For the purpose of generalization, the inverters can be given different rated powers $S_{\text{bat},i}$, and also different per-unit output impedances. Linear loads and inverters operating under current-control mode are also connected to the AC bus, either absorbing (or delivering when negative) net real power P_T and net reactive power Q_T. Figure 3 also shows the instantaneous values for the voltages and currents.

Generic demonstrations shall be made throughout the chapter, which shall be particularized for specific cases. Also, at times, the design of the control parameters will be shown for a specific case. For these cases, the system data shown in Table 1 will be used.

Figure 4 shows the equivalent circuit for the N inverters connected to a common AC bus through their output impedances. These output impedances Z_i include the filter impedance and the line impedance, which can be either inductive or resistive

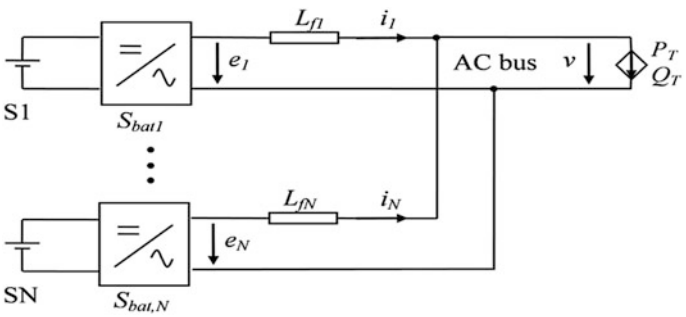

Fig. 3 Parallel-connected inverters under voltage-control mode

Table 1 System parameters

Non-load frequency f_0	50 Hz
Non-load voltage $V_0 = E_0$	230 V
Inverter 1 rated power S_{bat1}	6000 VA
Inverter 1 output inductance L_{f1}	3 mH
Battery 1 nominal capacity C_1	48 kWh
Battery 1 nominal voltage $V_{bat,nom1}$	240 V
Battery 1 absorption voltage $V_{bat,abs1}$	284 V
Inverter 2 rated power $S_{bat,i}$	3000 VA
Inverter 2 output inductance L_{f2}	4 mH
Battery 2 nominal capacity C_2	24 kWh
Battery 2 nominal voltage $V_{bat,nom2}$	120 V
Battery 2 absorption voltage $V_{bat,abs2}$	142 V
Inverter 3 rated power S_{bat3}	5000 VA
Inverter 3 output inductance L_{f3}	3 mH
Inverter 4 rated power S_{bat4}	4000 VA
Inverter 4 output inductance L_{f4}	4 mH
Power sampling time T_S	5 ms
Time constant of the real power filter τ_P	20 ms
Time constant of the reactive power filter τ_Q	50 ms
Time constant of the RMS voltage filter τ_V	40 ms
Time constant of the frequency filter τ_f	1 s

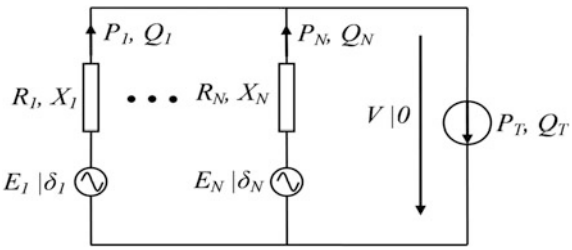

Fig. 4 Equivalent circuit of N inverters connected to an AC bus

depending on the type of grid. Their real part is the output resistance R_i and their imaginary part is the output reactance X_i. The real and reactive powers injected into the bus by every inverter can be expressed as shown in Eqs. (11) and (12) [4].

$$P_i = \frac{V \cdot E_i}{Z_i^2} \cdot X_i \cdot \sin\delta_i + \frac{V}{Z_i^2} \cdot R_i \cdot (E_i \cdot \cos\delta_i - V), \quad i = 1, \ldots, N \tag{11}$$

$$Q_i = -\frac{V \cdot E_i}{Z_i^2} \cdot R_i \cdot \sin\delta_i + \frac{V}{Z_i^2} \cdot X_i \cdot (E_i \cdot \cos\delta_i - V), \quad i = 1, \ldots, N, \tag{12}$$

where δ_i is the power angle (angle between e_i and v).

As will be shown later in Sect. 2.3, the output impedance can be considered to be inductive, regardless of the line impedance. Thanks to this assumption, and from Eqs. (11) and (12), the real power P_i and reactive power Q_i provided by each inverter can be expressed using Eqs. (13) and (14).

$$P_i = \frac{V \cdot E_i}{X_i} \cdot \sin \delta_i, \quad i = 1, \ldots, N \tag{13}$$

$$Q_i = \frac{V}{X_i}(E_i \cdot \cos \delta_i - V), \quad i = 1, \ldots, N. \tag{14}$$

In practical applications, power angle δ is small. Thus, Eqs. (13) and (14) can be rewritten using Eqs. (15) and (16).

$$P_i \approx \frac{V \cdot E_i}{X_i} \cdot \delta_i, \quad i = 1, \ldots, N \tag{15}$$

$$Q_i \approx \frac{V}{X_i}(E_i - V), \quad i = 1, \ldots, N. \tag{16}$$

Consequently, it can be observed that the real power mainly depends on power angle δ and the reactive power on output voltage E. Thus, power angle δ can be modified in order to control the real power and output voltage E can be changed to control the reactive power. This is how the conventional droop method operates, by imposing the following control on every inverter as shown in Eqs. (17) and (18).

$$f_i = f_0 - m_{Pi} \cdot P_i, \quad i = 1, \ldots, N \tag{17}$$

$$V_i^* = V_0 - m_{Qi} \cdot Q_i, \quad i = 1, \ldots, N, \tag{18}$$

where f_0 is the non-load frequency, m_{Pi} is the droop coefficient of the real power, V_i^* is the RMS grid voltage reference, V_0 is the non-load RMS grid voltage, and m_{Qi} is the droop coefficient of the reactive power.

The inverter rated power is normally used to set the P–f and Q–V slopes so as to share the real and reactive powers in proportion to the inverter ratings. Taking into account the fact that, when operating in steady-state every inverter has the same frequency and voltage reference, then this condition leads to the following Eqs. (19) and (20).

$$m_{Pi} = \frac{M_p}{S_{\text{bat},i}}, \quad i = 1, \ldots, N \tag{19}$$

$$m_{Qi} = \frac{M_q}{S_{bat,i}}, \quad i = 1, \ldots, N, \tag{20}$$

where M_p is the droop coefficient of the per-unit real power and M_q is the droop coefficient of the per-unit reactive power. Unlike m_P and m_Q, the values of M_p and M_q are the same for each inverter and represent the maximum frequency and voltage deviations.

By using Eqs. (19) and (20), the droop method can be expressed as a function of the per-unit power as follows:

$$f_i = f_0 - M_p \cdot p_i, \quad i = 1, \ldots, N \tag{21}$$

$$V_i^* = V_0 - M_q \cdot q_i, \quad i = 1, \ldots, N, \tag{22}$$

where p_i and q_i are the per-unit real and reactive powers provided by each inverter.

Figure 5 shows the P–f and Q–V droop curves. It can be observed how the maximum frequency and voltage deviation is related to per-unit droop coefficients M_p and M_q and that both the real and reactive powers can be either positive or negative. In the case of the real power, the reversibility is due to the presence of the battery (positive when delivering power and negative when absorbing power).

Let us intuitively see how the droop method functions with an example, in a system with two inverters connected in parallel to a linear load. At a given time, one

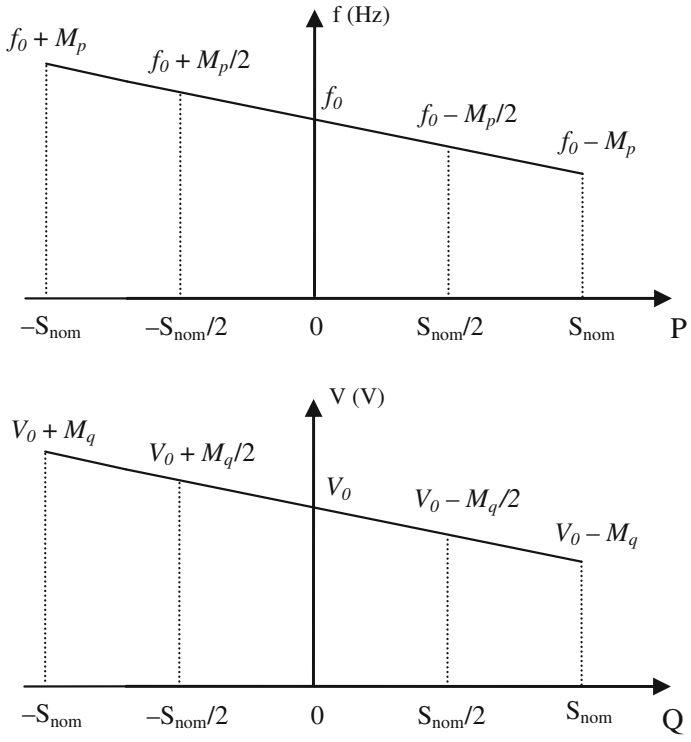

Fig. 5 *P–f* and *Q–V* droop curves for the conventional droop method

inverter is delivering a higher per-unit real power but a lower per-unit reactive power, for example $p_1 > p_2$ and $q_1 < q_2$. Both inverters continuously measure the real and reactive powers and set their frequency and voltage reference according to Fig. 5 or Eqs. (21) and (22). As a result of the power distribution and the droop curve, the frequency reference for the inverters is $f_1 < f_2$, resulting in a power angle decrease for inverter 1 ($\delta_1\downarrow$) and a power angle increase for inverter 2 ($\delta_2\uparrow$). Thus, according to Eq. (15), P_1 will decrease and P_2 will increase, helping balance the real powers. Similarly, the voltage references for the inverters become $V_1^* > V_2^*$, which leads to an output voltage increase for inverter 1 ($E_1\uparrow$) and an output voltage decrease for inverter 2 ($E_2\downarrow$) due to the voltage regulation. Therefore, according to Eq. (16), Q_1 will increase and Q_2 will decrease, helping balance the reactive powers. At the end of the transient both inverters will have the same frequency, voltage reference V^*, per-unit real power, and per-unit reactive power.

As shown above, the droop method obtains the frequency and grid voltage references for the inverter. Then, it is also important to perform a voltage regulation so that the frequency and grid voltage are actually equal to their references. In order to carry out this voltage regulation, there are primarily two options, namely RMS voltage regulation and instantaneous voltage regulation.

RMS Voltage Regulation

Figure 6 shows a block diagram of the droop method and the RMS voltage regulation. The droop method is used to obtain, for each inverter, the frequency and RMS grid voltage references, f and V^*, respectively, as a function of real and reactive powers, P and Q. By means of the RMS measured voltage V_m and a PI controller, the RMS output voltage E is obtained. Once the RMS output voltage E and frequency are known, then instantaneous voltage e can be obtained and modulated. As can be seen, this control includes a closed-loop RMS voltage-control and an open-loop frequency control. The latter presents no problem since the frequency is insensitive to plant variations or disturbances.

This regulation offers a number of advantages over instantaneous voltage control. Given the fact that the voltage regulation is implemented in DC, then a PI controller is sufficient for precise voltage tracking, whilst there is no need for the inner current loop. Although current protection is still required, it is far easier to implement this system. Furthermore, as shown in the sections below, the filter inductance is also included in the output impedance for the droop method. As a result, it is possible to ensure that an inductive grid is present and to reduce the impact of the line impedance on reactive power sharing.

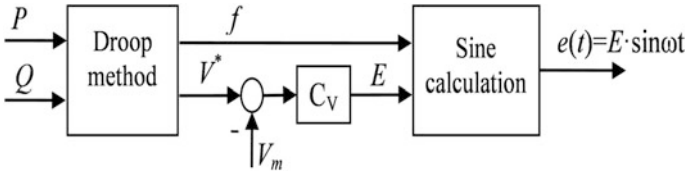

Fig. 6 Block diagram of the droop method and RMS voltage regulation

However, this method also has its drawbacks. The RMS controller means longer transients for load connections. Furthermore, when powering nonlinear load, the voltage THD increases and the current harmonics are not equally distributed among the inverters. This latter issue has been resolved in the literature through the addition of more controls, as discussed in Sect. 5.

Unless indicated otherwise, the RMS voltage regulation will be used in all procedures described in this chapter, thanks to the fact that it is easy to implement and offers adequate results.

Instantaneous Voltage Regulation

A block diagram of the droop method with instantaneous voltage regulation is shown in Fig. 7. Instantaneous voltage reference v_0^* is obtained from the frequency and RMS grid voltage references provided by the droop method. Output impedance $Z_v(s)$ is then emulated by subtracting the voltage drop across the virtual impedance, $Z_v(s) \cdot i$, from the original voltage reference v_0^*, which gives final voltage reference v^*. Finally, a closed-loop instantaneous voltage regulation is carried out by using voltage feedback v_m, and voltage controller C_v obtains the instantaneous voltage e to be modulated. As can be seen, this control performs a closed-loop instantaneous voltage regulation so that both the RMS voltage and the frequency are controlled in a closed-loop.

In this case, when operating solely with linear loads, the voltage reference has a fundamental component at grid frequency ω. Furthermore, as will be shown in Sect. 5, this voltage reference has other components at 3ω, 5ω… in the presence of typical nonlinear loads. As a result, a very fast voltage control is required, making it difficult to implement an inner current loop and to ensure stability. For this reason, no inner current loop is generally adopted, and therefore this fast voltage control can cause dangerous current transients.

Another important issue with this regulation is the output impedance. As a fast voltage regulation is implemented, it almost completely rejects the output current disturbance effect. As a result, the filter inductance is removed from the plant, causing the output impedance for the droop control to become the line impedance, which can be resistive in low-voltage grids and is not accurately known. Thus, in order to avoid this uncertainty, output impedance Z_v is emulated by modifying the voltage reference. This virtual impedance is usually inductive and much higher than the line impedance so that is it possible to make the inductive grid assumption.

Although the instantaneous voltage regulation will not be examined in detail in this chapter, information about the voltage closed-loop design, the output current rejection, and the output impedance Z_v design can be consulted in [5].

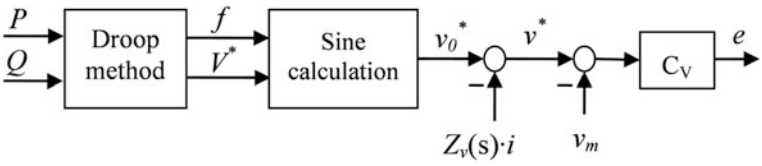

Fig. 7 Block diagram of the droop method and instantaneous voltage regulation

2.3 Modelling of a Droop-Controlled AC Microgrid

A model to assess the power response and to design the control parameters is developed in this section. This model is intended for a system in which the droop method and RMS voltage regulation are implemented (refer to Fig. 6) and with N parallel-connected inverters as can be seen in Fig. 3. The following assumptions are made:

- The output impedance is purely inductive.
- The power angle is very small. These two assumptions make it possible to use Eqs. (15) and (16).
- There is little voltage variation in relation to the rated value. Therefore, the following is obtained from Eqs. (15) and (16):

$$P_i \approx \frac{V_0 \cdot E_0}{X_i} \cdot \delta_i, \quad i = 1, \ldots, N \tag{23}$$

$$Q_i \approx \frac{V_0}{X_i} \cdot (E_i - V), \quad i = 1, \ldots, N \tag{24}$$

  where $E_0 = V_0$ is the non-load RMS output voltage.
- Net powers P_T and Q_T are independent of the grid voltage.

Based on these assumptions, P and Q linearly depend on δ and E–V, respectively, making the system linear and offering the possibility of applying linear modelling techniques. Moreover, since P is not dependent on the voltage and Q is not dependent on the power angle, then these approximations decouple the real and reactive power responses, which can therefore be examined independently.

Despite the fact that many assumptions have been considered, this linear model is sufficiently accurate for low-voltage grids. Its accuracy has been assessed by comparing it with a small-signal model with a non-stiff AC grid, in which the only assumption made is that the output impedance is purely inductive. The results are available for consultation in [6].

This model aims to find the transfer function poles so as to predict the transient response. The expression for the characteristic equation are thus determined, which makes it possible to overlook the independent terms such as net power P_T, net reactive power Q_T, and the initial values. Given the fact that the real and reactive power responses are decoupled, the real power response is first presented.

Based on its definition, it is possible to obtain the power angle using Eq. (25).

$$\delta_i = (\phi_{\mathrm{i}}(0) + I \cdot f_1) - \phi_v, \quad i = 1, \ldots, N \tag{25}$$

where ϕ_v is the angle position of v, $\phi_{\mathrm{i}}(0)$ is the initial angle position of e_{i}, and $I = 2\pi/\mathrm{s}$ is the Laplace integrator.

The balance of power at the point of common coupling is shown in Eq. (26).

$$\sum_{j=1}^{N} P_j = P_T \tag{26}$$

Simplified equation for the system plant can be obtained from Eqs. (23) and (25) which is shown in Eq. (27).

$$P_1 \cdot X_1 - P_i \cdot X_i = V_0 E_0 \cdot I \cdot (f_1 - f_i), \quad i = 2, \ldots, N \tag{27}$$

The conventional droop method modifies the frequency in order to share the real power. Therefore, Eq. (17) is changed to Eq. (28) in order to take account of the real power measurement, to give

$$f_i = f_0 - m_{Pi} \cdot H_P \cdot P_i, \quad i = 1, \ldots, N \tag{28}$$

where H_P represents the sampling and measurement of the real power, which can be modelled using Eq. (29).

$$H_{\mathrm{P}} = \frac{1}{1 + \tau_{\mathrm{P}} s} \cdot \frac{1}{1 + 1.5 \cdot T_{\mathrm{S}} \cdot s} \tag{29}$$

where τ_{P} is the power measurement time constant and T_{S} is the power sampling time.

From Eqs. (27) and (28), it is possible to express each power output using Eq. (30) as a function of P_1, i.e.

$$P_i = \frac{X_1 + V_0 E_0 \cdot m_{P1} \cdot I \cdot H_P}{X_i + V_0 E_0 \cdot m_{Pi} \cdot I \cdot H_P} \cdot P_1, \quad i = 2, \ldots, N \tag{30}$$

Then, by introducing Eq. (30) into Eq. (26) and operating, the following characteristic equation can be obtained using Eq. (31).

$$\mathrm{den}_P = \sum_{j=1}^{N} \frac{1}{X_j + V_0 E_0 \cdot m_{Pj} \cdot I \cdot H_P} \tag{31}$$

This equation is valid for a system with an arbitrary number of N parallel-connected inverters. For the specific case whereby $N = 2$, Eq. (31) becomes

$$\mathrm{den}_P = V_0 E_0 \cdot (m_{P1} + m_{P2}) \cdot I \cdot H_P + X_1 + X_2 \tag{32}$$

The transfer function poles, that is the roots of den_P, determine the closed-loop stability and power transient. Hence, for certain given system parameters, the choice of M_p is important for the design of the power response (see Eq. 19). Through Eq. (32), the root locus diagram for parameter M_p is shown in Fig. 8 for

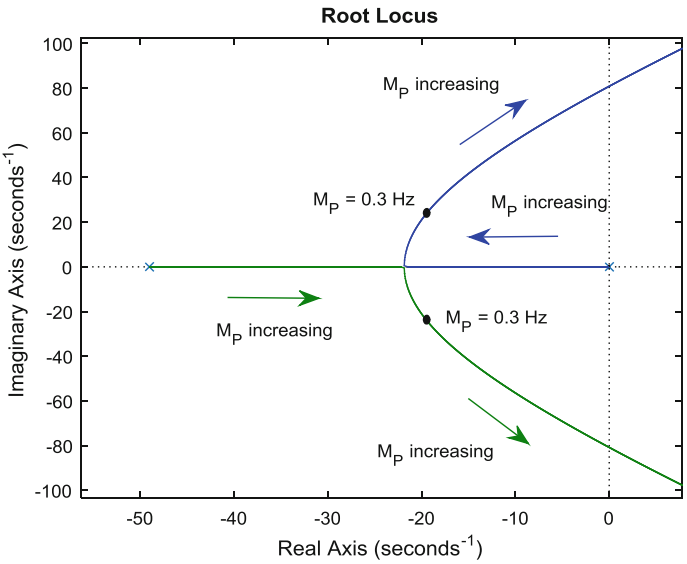

Fig. 8 Root locus diagram for the parameter M_p [7]

the system with inverter 1 and inverter 2 connected in parallel (see Table 1). Although the system actually has three poles, only the two dominant poles are shown in the figure. The system can be seen to have first-order dynamics for low M_p values, whilst it becomes less damped if M_p is increased. Finally, from a given M_p value onwards, the system becomes unstable. In this case, 0.3 Hz represents an appropriate solution for parameter M_p, being selected as a trade-off between fast dynamics and a high stability margin. Consequently, the operating frequency will vary between $f_0 - M_p = 49.7$ Hz and $f_0 + M_p = 50.3$ Hz, which is within the acceptable variation limits. It is also possible to design the droop coefficient based on the frequency domain analysis whereby crossover frequency $f_{cP} = 3.2$ Hz, and phase margin $PM_P = 63°$ are obtained for $M_p = 0.3$ Hz.

The root locus diagram, as shown in Fig. 8 and the droop coefficient M_p design were carried out for two inverters. Now, Table 2 shows the poles for various inverter configurations, based on Eq. (31) and the system characteristics of Table 1. As it can be observed, the system has $N - 1$ pairs of conjugate poles (dominant poles). Moreover, configurations with equal inverters have extreme poles whilst the poles for configurations with different inverters are in between.

After obtaining the real power response for N inverters, the next step is to determine the reactive power and voltage responses as indicated below. At the point of common coupling, the reactive power balance is shown in Eq. (33).

$$\sum_{j=1}^{N} Q_j = Q_T \tag{33}$$

Table 2 Closed-loop poles for the real power response [7]

Configuration	Poles
N times Inv1	$N-1$ times $-20.0 \pm 17.5j$ ($\xi = 0.75$)
N times Inv2	$N-1$ times $-20.0 \pm 25.7j$ ($\xi = 0.62$)
N times Inv3	$N-1$ times $-20.0 \pm 21.1j$ ($\xi = 0.69$)
N times Inv4	$N-1$ times $-20.0 \pm 19.8j$ ($\xi = 0.71$)
Inv1, Inv2	$-20.0 \pm 22.5j$ ($\xi = 0.66$)
Inv1, Inv2, Inv3, Inv4	$-20.0 \pm 24.5j$ ($\xi = 0.63$) $-20.0 \pm 20.5j$ ($\xi = 0.70$) $-20.0 \pm 18.5j$ ($\xi = 0.73$)

Simplified expressions for the system plant can be obtained from Eq. (24), as:

$$Q_1 \cdot X_1 - Q_i \cdot X_i = V_0 \cdot (E_1 - E_i), \quad i = 2, \ldots, N \tag{34}$$

The droop method changes V_i^* in order to equally share power Q_T. In order to follow this voltage reference, the voltage regulation changes E_i. Taking Eq. (18) and Fig. 6, it is possible to model the transfer functions of the voltage droop together with the voltage regulation as

$$\begin{aligned} E_i - E_i(0) &= C_V \cdot (V_i^* - H_V \cdot V) \\ &= C_V \cdot (V_0 - m_{Qi} \cdot H_Q \cdot Q_i - H_V \cdot V), \quad i = 1, \ldots, N \end{aligned} \tag{35}$$

where $E_i(0)$ is the initial controller output, H_Q is a low-pass filter with time constant τ_Q, to model the reactive power measurement, H_V is a low-pass filter with time constant τ_V, to model the RMS grid voltage measurement, and C_V represents the PI voltage controller. H_Q, H_V and C_V are assumed to be the same for each inverter.

Taking Eqs. (34) and (35), each reactive power output can be expressed as a function of Q_1, that is:

$$Q_i = \frac{X_1 + V_0 \cdot m_{Q1} \cdot C_V \cdot H_Q}{X_i + V_0 \cdot m_{Qi} \cdot C_V \cdot H_Q} \cdot Q_1, \quad i = 2, \ldots, N \tag{36}$$

By introducing Eq. (36) into Eq. (33) and operating, the characteristic equation can be obtained as

$$\text{den}_Q = \sum_{j=1}^{N} \frac{1}{X_j + V_0 \cdot m_{Qj} \cdot C_V \cdot H_Q} \tag{37}$$

Finally, the voltage response is obtained. Introducing (35) into (24) gives:

$$V = -\frac{X_i + V_0 \cdot m_{Qi} \cdot C_V \cdot H_Q}{V_0 \cdot \text{den}_V} \cdot Q_i, \quad i = 1, \ldots, N \tag{38}$$

$$\text{den}_V = C_V \cdot H_V + 1 \tag{39}$$

As can be observed in the equations above, two different expressions, den_Q and den_V, determine the transfer function poles for the voltage and reactive power responses. The reactive power response is dependent on den_Q, while the voltage response is primarily dependent on den_V, but also on den_Q through Q_i. The design of C_V is important for both responses, given the fact that it appears in both den_Q and den_V, while M_q only appears in den_Q and its design is, therefore, important for the reactive power response (see Eq. 20). Furthermore, it is possible to observe that the voltage response does not depend on the number of parallel-connected inverters. Based on Eq. (39), the PI controller is designed to obtain a voltage response with crossover frequency f_{cV} = 1 Hz and phase margin PM_V = 80°. The low f_{cV} value prevents dangerous load transients, such as when operating with motors or transformers, while the high PM_V value prevents voltage overshoots.

Once voltage controller C_V is designed, the next step is to select parameter M_q. For the case in question with N = 2, Eq. (37) becomes

$$den_Q = V_0 \cdot (m_{Q1} + m_{Q2}) \cdot C_V \cdot H_Q + X_1 + X_2 \tag{40}$$

As the reactive power dynamics are determined from Eq. (40), the selection of M_q is important for the reactive power response. In this case, 20 V is selected for parameter M_q, which from Eq. (40) gives reactive power crossover frequency f_{cQ} = 1 Hz and phase margin PM_Q = 76°. This high M_q value causes the voltage to vary between $V_0 - M_q$ = 210 V and $V_0 + M_q$ = 250 V, which is within the acceptable variation limits. It also helps reduce the inaccuracy of the reactive power control caused by line impedance, as discussed later on. Although a higher M_q value would improve the steady-state and transient responses still further, it would also mean that the voltage variation range would be out of limit.

Table 3 Closed-loop poles for the reactive power response

Configuration	Poles
N times Inv1	$N - 1$ times -7.91, -13.3 (ξ = 1)
N times Inv2	$N - 1$ times $-10.9 \pm 6.23j$ (ξ = 0.87)
N times Inv3	$N - 1$ times $-10.7 \pm 3.35j$ (ξ = 0.96)
N times Inv4	$N - 1$ times $-10.7 \pm 2.07j$ (ξ = 0.98)
Inv1, Inv2	$-10.8 \pm 4.37j$ (ξ = 0.93)
Inv1, Inv2, Inv3, Inv4	$-10.9 \pm 5.62j$ (ξ = 0.89) $-10.7 \pm 2.75j$ (ξ = 0.97) -9.10, -12.2 (ξ = 1)

After designing droop coefficient M_q for two inverters, the system poles for $M_q = 20$ V are then evaluated using Eq. (37) for N inverters. Table 3 shows the results for a number of inverter configurations, whose system parameters were presented in Table 1. In the same way as for the real power, it can be seen that the system has $N - 1$ pairs of poles and that configurations with equal inverters have extreme poles whilst the poles for configurations with different inverters are in between.

The system presented in Fig. 3, including inverter 1, inverter 2, and some linear loads, was modelled using the software PSIM. The droop method and voltage regulation shown in Fig. 6 were used for the control. The system parameters were presented in Table 1.

The simulation results are plotted in Fig. 9, the first graph shows the per-unit real powers, the second graph the per-unit reactive power, and the third graph shows reference voltages V_{ref1} and V_{ref2}, measured voltage V, and output voltages E_1 and E_2. Only inverter 1 is operating at the start, supplying an RL load with rated values $P_{\text{load}} = 4$ kW and $Q_{\text{load}} = 2.5$ kVAr. At start-up, from second 0.05, the voltage response is clear to see. The rise time and the lack of overshoot tally with crossover frequency $f_{cV} = 1$ Hz and $\text{PM}_V = 80°$ obtained in the voltage design. Inverter 2 is connected just after second 1, with the real power, reactive power, and voltage responses shown in Fig. 9. Again, the obtained crossover frequencies $f_{cV} = 1$ Hz, $f_{cQ} = 1$ Hz, and $f_{cP} = 3.2$ Hz, and phase margins $\text{PM}_V = 80°$, $\text{PM}_Q = 76°$, and $\text{PM}_P = 63°$, tally with the corresponding responses. Moreover, the power outputs are shared equally between the inverters. Finally, at second 1.6, an identical RL load is connected. In this case, the power outputs are also perfectly distributed at steady state.

The same system was tested in the laboratory. In this case, the system parameters are also the ones presented in Table 1 but taking account of the fact that both inverters have the same characteristics, corresponding to inverter 1.

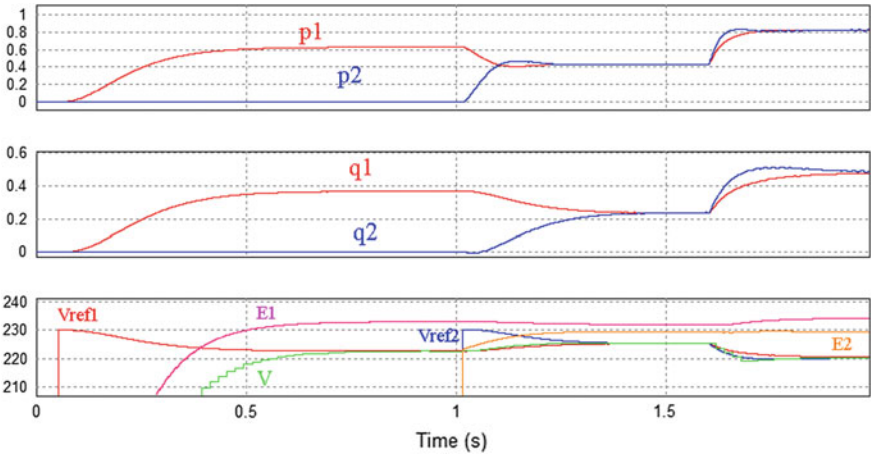

Fig. 9 Simulation results for the droop method with RMS voltage regulation [6]

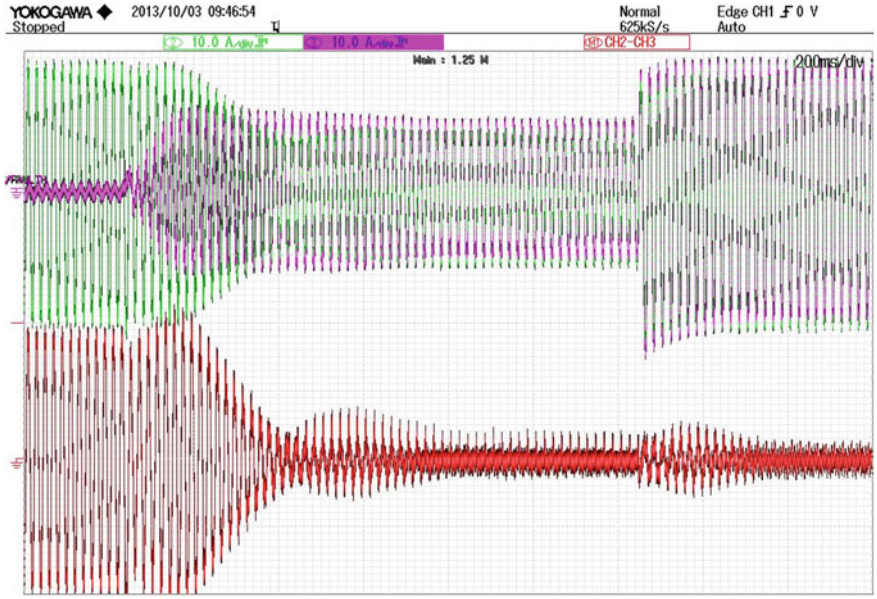

Fig. 10 Experimental results for the droop method

The experimental results are shown in Fig. 10, where i_1, i_2, and $i_1 - i_2$ are represented in green, purple, and red respectively. The transient responses for the second inverter and load connections are augmented in Fig. 11. At first, only inverter 1 is operating, supplying a linear load with $S_{\text{load}} = 3300$ VA. Then, when inverter 2 is connected, the current is well distributed thanks to the droop method. The currents are completely established after about 0.5 s, which is fast enough for this application. Finally, when an identical linear load is connected, the powers also remain perfectly distributed after a short transient.

2.4 Line Impedance Influence on Reactive Power Sharing

This section discusses the steady-state inaccuracy of the reactive power control due to line impedance, a factor which has not yet been considered. In contrast, the real power control is not affected by the line impedance since the steady-state frequency is the same at all grid points.

Once the droop method has been implemented, the equivalent circuit of Fig. 4 can be replaced by the one shown in Fig. 12. The differences between these two equivalent circuits are the voltage sources and impedances. In Fig. 4, voltage source $E_i|\delta_i$ represents the inverter output voltage before the filter impedance while here voltage source $V_i|\theta_i$ represents the voltage after the filter impedance, which is controlled by

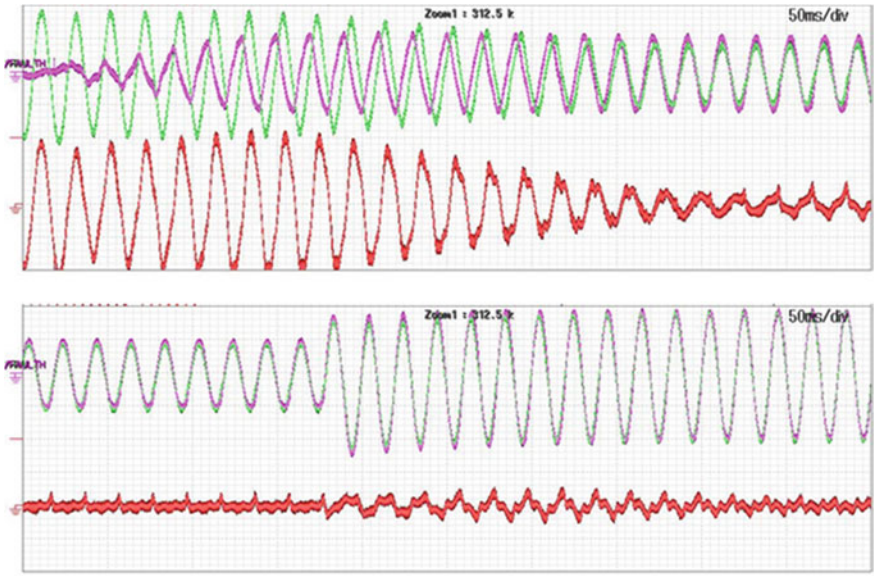

Fig. 11 Detail of the transients for the droop method

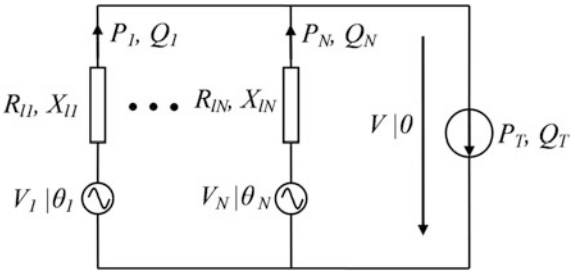

Fig. 12 Equivalent circuit of N droop-controlled inverters connected to an AC bus through line impedances

means of the droop method and the voltage regulation. As a result, impedance $R_i + X_i \cdot j$ shown in Fig. 4 includes the filter and line impedances while here impedance $R_{li} + X_{li} \cdot j$ only includes the line impedance.

In the system shown in Fig. 4, the real and reactive powers injected into the bus by every inverter were determined as Eqs. (11) and (12). These expressions can be readily adapted for the system of Fig. 12. Assuming that the voltage variation is very small in relation to the rated value and the power angle is very small, then the following expressions are obtained from Eqs. (11) and (12):

$$P_i = \frac{V_0^2}{Z_{li}^2} \cdot X_{li} \cdot \theta_i + \frac{V_0}{Z_{li}^2} \cdot R_{li} \cdot (V_i - V), \quad i = 1, \ldots, N \tag{41}$$

$$Q_i = -\frac{V_0^2}{Z_{\mathrm{l}i}^2} \cdot R_{\mathrm{l}i} \cdot \theta_i + \frac{V_0}{Z_{\mathrm{l}i}^2} \cdot X_{\mathrm{l}i} \cdot (V_i - V), \quad i = 1, \ldots, N \tag{42}$$

As can be observed, the real and reactive powers are now linearly dependent on θ_i, V_i, and V. From Eqs. (41) and (42), power angle θ_i and output voltage V_i can then be calculated as a linear function of P_i, Q_i and V:

$$\theta_i = \frac{X_{\mathrm{l}i}}{V_0^2} \cdot P_i - \frac{R_{\mathrm{l}i}}{V_0^2} \cdot Q_i, \quad i = 1, \ldots, N \tag{43}$$

$$V_i = V + \frac{R_{\mathrm{l}i}}{V_0} \cdot P_i + \frac{X_{\mathrm{l}i}}{V_0} \cdot Q_i, \quad i = 1, \ldots, N \tag{44}$$

Equation (44) shows that the real power causes a voltage drop when it flows through a resistance while the reactive power causes a voltage drop when it flows through an inductance.

Due to the droop method and the voltage regulation, the voltage droop curve, Eq. (18), can be expressed at steady state as

$$V_i = V_0 - m_{Qi} \cdot Q_i, \quad i = 1, \ldots, N \tag{45}$$

By means of Eqs. (44) and (45), an expression for the grid voltage can be obtained for every inverter as

$$V = V_0 - m_{Qi} \cdot Q_i - \frac{X_{\mathrm{l}i}}{V_0} \cdot Q_i - \frac{R_{li}}{V_0} \cdot P_i, \quad i = 1, \ldots, N \tag{46}$$

It can be observed that, with regard to the voltage drop, the droop method performs like a constant voltage source with an output inductance. As a result, Eq. (46) can be modified and expressed as

$$V = V_0 - \frac{X_{\mathrm{d}i} + X_{\mathrm{l}i}}{V_0} \cdot Q_i - \frac{R_{\mathrm{l}i}}{V_0} \cdot P_i, \quad i = 1, \ldots, N \tag{47}$$

$$X_{\mathrm{d}i} = m_{Qi} \cdot V_0 = \frac{M_q}{S_{\mathrm{bat},i}} \cdot V_0, \quad i = 1, \ldots, N \tag{48}$$

where $X_{\mathrm{d}i}$ is the equivalent droop reactance.

Taking these considerations into account, the equivalent circuit of Fig. 12 can be substituted by the equivalent circuit presented in Fig. 13, where the circuit is now only valid for the voltage drop but not for the phase calculation. Because droop reactances $X_{\mathrm{d}i}$ have the same per-unit value, the reactive power will be equally distributed if the line impedances are low in relation to the droop reactances. For this reason, a high droop coefficient M_q is desirable for the power sharing.

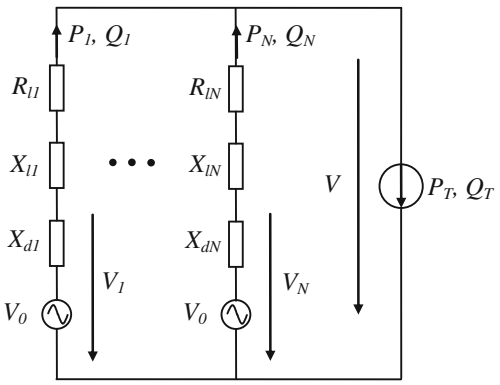

Fig. 13 Equivalent circuit of N droop-controlled inverters connected to an AC bus through line impedances, valid for the RMS voltage calculation

However, since a too high value would cause an excessive voltage deviation in steady state, a trade-off must be reached.

By means of the equivalent circuit of Fig. 13, the expressions for the reactive power distribution are derived below. Considering that the real power is perfectly distributed because it is not affected by the line, Eq. (47) becomes

$$V = V_0 - \frac{X_{\mathrm{d}i} + X_{\mathrm{l}i}}{V_0} \cdot Q_i - \frac{R_{\mathrm{l}i}}{V_0} \cdot \frac{S_{\mathrm{bat},i}}{S_{\mathrm{bat,tot}}} \cdot P_T, \quad i = 1, \ldots, N, \tag{49}$$

where $S_{\mathrm{bat,tot}}$ is the rated power of all inverters.

By equalizing Eq. (49) for $i = 1$ and $i \neq 1$, each reactive power can be expressed as a function of Q_1 and P_T, i.e.

$$Q_i = \frac{X_{\mathrm{d}1} + X_{\mathrm{l}1}}{X_{\mathrm{d}i} + X_{\mathrm{l}i}} \cdot Q_1 + \frac{R_{l1} \cdot S_{\mathrm{bat}1} - R_{\mathrm{l}i} \cdot S_{\mathrm{bat},i}}{(X_{\mathrm{d}i} + X_{\mathrm{l}i}) \cdot S_{\mathrm{bat,tot}}} \cdot P_T, \quad i = 2, \ldots, N. \tag{50}$$

Introducing Eq. (50) into Eq. (33) and operating makes it possible to obtain the expression for Q_1 as a function of Q_T and P_T. Proceeding in a similar manner for the other inverters, an expression for Q_i is obtained as

$$Q_i = \frac{\frac{1}{X_{\mathrm{d}i} + X_{\mathrm{l}i}}}{\sum_{j=1}^{N} \frac{1}{X_{\mathrm{d}j} + X_{\mathrm{l}j}}} \cdot \left[Q_T + \sum_{\substack{j=1 \\ j \neq i}}^{N} \frac{R_{\mathrm{l}j} \cdot S_{\mathrm{bat},j} - R_{\mathrm{l}i} \cdot S_{\mathrm{bat},i}}{\left(X_{\mathrm{d}j} + X_{\mathrm{l}j}\right) \cdot S_{\mathrm{bat,tot}}} \cdot P_T \right], \quad i = 1, \ldots, N. \tag{51}$$

As an example, Eq. (51) particularized for two inverters becomes

$$Q_1 = \frac{X_{d2} + X_{l2}}{X_{d1} + X_{l1} + X_{d2} + X_{l2}} \cdot Q_T + \frac{R_{l2} \cdot S_{bat2} - R_{l1} \cdot S_{bat1}}{(X_{d1} + X_{l1} + X_{d2} + X_{l2}) \cdot S_{bat,tot}} \cdot P_T \quad (52)$$

$$Q_2 = \frac{X_{d1} + X_{l1}}{X_{d1} + X_{l1} + X_{d2} + X_{l2}} \cdot Q_T + \frac{R_{l1} \cdot S_{bat1} - R_{l2} \cdot S_{bat2}}{(X_{d1} + X_{l1} + X_{d2} + X_{l2}) \cdot S_{bat,tot}} \cdot P_T. \quad (53)$$

In order to better understand how the reactive power is distributed in a real case, an example is provided for two inverters connected in parallel in a low-voltage grid with long lines. The inverters are inverter 1 and inverter 2, previously presented in Table 1, and the line cables are selected from recent regulations [8]. The line for inverter 1 is chosen with a cross-sectional area of 6 mm^2, which leads to a resistance of 3.56 Ω/km and a reactance of 2.06 Ω/km, and the line for inverter 2 is selected with a cross-sectional area of 2.5 mm^2, which leads to a resistance of 8.57 Ω/km and a reactance of 4.93 Ω/km, both at a 60 °C copper operation temperature [9]. It is worth noting that the cable lengths correspond to the distance before both inverters are connected in parallel because the line after this point can be considered as part of the load and does not thus cause power inaccuracy.

Figure 14 shows the per-unit reactive power provided by each inverter with a cable length equal to 100 m for inverter 1 and a cable length varying from 0 to 200 m for inverter 2. The first graph is obtained for a situation with more consumption than generation, with P_T = 7 kW and Q_T = 5 kVAr, while the second graph is determined for higher generation, with P_T = –7 kW and Q_T = 5 kVAr. Although S_T = 8.6 kVA is lower than the rated power $S_{bat,tot}$ = 9 kVA, one inverter is overloaded in many situations, specifically when $q_i > 0.63$. It can be observed that the line influence is very important in this system and that the real power also has a significant effect on low-voltage grids due to ratio $R/X > 1$. In conclusion, in a low-voltage system with very long lines, the inverters should be placed at a similar distance from the loads. If this is not possible, a more complicated reactive power droop method should be applied, where some examples can be consulted in [10, 11].

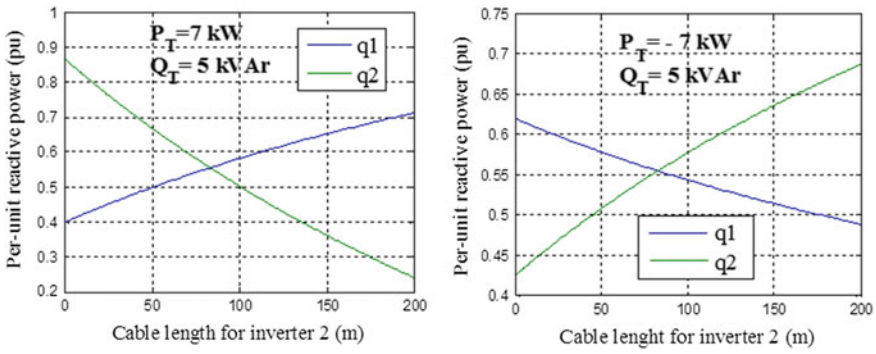

Fig. 14 Reactive power inaccuracy due to line impedance in a low-voltage grid with long lines, cable length for inverter 1 is 100 m

2.5 Droop Method for Nonlinear Loads

This section provides a brief introduction to the modifications that need to be made to the droop control in the presence of nonlinear loads. Strictly speaking, it cannot be affirmed that the changes are made to the droop control, given the fact that the droop method uses the real and reactive powers as inputs, and it can therefore only act on the fundamental voltage component. In contrast, the modifications are made by adding harmonic components to the fundamental grid voltage reference. Since these modifications are different depending on whether it is an RMS voltage regulation or an instantaneous voltage regulation, a separate analysis shall be made for each.

RMS Voltage Regulation

A block diagram of the droop method together with RMS voltage regulation and harmonic compensation is shown in Fig. 15. It can be seen that fundamental voltage component e_{fund}, is obtained in exactly the same way as for the linear load scheme shown in Fig. 6. At the same time, the harmonic components of voltage e_{harm}, are calculated in order to emulate an impedance for each grid harmonic. In order to obtain this voltage, Band-Pass Filters (BPF) are first used to separately extract the current harmonics from the output current and, then, the voltage drop is calculated for each harmonic and the emulated impedance. Output voltage e is finally obtained as the sum of the fundamental and harmonic components.

In the presence of nonlinear loads, if the inverter were to generate a harmonic-free voltage e, then the voltage drop at the filter inductance would create a considerable disturbance in the grid and, moreover, the current harmonics would not be shared between the various inverters. In order to reduce the grid harmonic distortion and to share the harmonic current in proportion to the rated power of each inverter, different virtual impedances can be emulated. One option is to emulate a negative virtual inductance, to reduce the filter inductance and also to impose the same per-unit inductance for all inverters. Further details of this method are available in [12]. Another option is to emulate a virtual impedance formed by a capacitor that is series-connected to a resistor, so that the capacitor cancels the effect

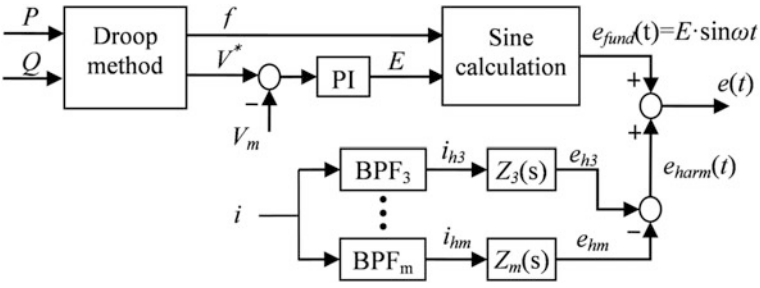

Fig. 15 Block diagram of the droop method and voltage regulation with harmonic compensation

of the filter inductance and the resistor takes the same per-unit value for all inverters in order to share the harmonics.

One drawback of the methods indicated above is that, as can be seen in Fig. 15, virtual impedance is emulated in open-loop. This means that it is difficult to completely eliminate the effect of the filter inductance, given the fact that its value may change in line with the operating point. Therefore, some methods propose a closed-loop control by monitoring the RMS value of each harmonic. These methods require high computational complexity and will not be discussed herein, however an example can be found in [13].

Instantaneous Voltage Regulation

The block diagram for the instantaneous voltage regulation is the same as shown in Fig. 7, where the only change is the emulated impedance expression $Z_v(s)$. With linear loads, the emulated impedance was an inductance in order to achieve an inductive-type grid. For nonlinear loads, this virtual impedance $Z_v(s)$ continues to be an inductance for the grid fundamental frequency but performs as a resistance for the current harmonics. In this way, the performance of an inductive grid is achieved for the active and reactive power response whilst, at the same time, the current harmonics are shared between the various inverters and the harmonic distortion in the grid voltage is reduced.

Instantaneous voltage regulation allows for closed-loop control and, therefore, a more accurate emulation of the virtual impedance. However, an extremely quick response is required in order to follow the reference voltage harmonic components. Therefore, it is normal to use resonant controllers that are able to perfectly follow these components. Further details about this method can be consulted in [14].

3 Battery State-of-Charge (SOC) Regulation

3.1 Introduction to SOC Regulation

The droop control system used makes it possible to share the real power, reactive power, and harmonic currents equally between a number of battery inverters. Yet, the conventional droop method does not allow for the secondary control or energy management of a distributed storage system. Despite the fact that, in an ideal situation, the ratios between the battery capacity and the inverter rated power (C/S_{bat}) should be the same for all battery inverters, so that all battery state-of-charges change simultaneously, this is not the case in real-life applications. Due to different manufacturing designs or to incorrect system sizing, the initial C/S_{bat} ratio will never be identical for all battery inverters. Furthermore, the battery ageing process results in a gradual reduction in capacity, which is more marked in some battery banks than in others. The considerable variations in the initial SOC, from one battery to another may also mean that each battery will operate with a different SOC, so that operation is less than optimal. Therefore, SOC management is

necessary. This is normally performed through an overall control based on low-bandwidth communication, intended to complement the local droop control system. In an endeavour to avoid any type of communication system whatsoever and to improve the reliability of a stand-alone grid, frequency-based SOC management is presented. This section discusses how this SOC management can be achieved, by making changes to the traditional droop method.

3.2 Description of the Two Potential Techniques

In order to balance the battery SOCs, without the need for a communication system, there is a need to change the *P–f* curve as a function of each battery SOC. Based on the *P–f* curve expression shown in Eq. (21), either the M_p parameter or f_0 parameter can be used for this purpose, which determines the two techniques available.

The first technique is termed the slope changing method, based on modifying the slope of the *P–f* curve, M_p. Although there are a number of manners to modify this slope, here we have considered the method proposed in [15], as this represents a more general approach. This curve is based on the following expression:

$$f_i = f_0 - M_p \cdot p_i = f_0 - \frac{M_0}{\mathrm{SOC}_i^n} \cdot p_i, \quad p_i > 0, \quad i = 1, \ldots, N \tag{54}$$

$$f_i = f_0 - M_p \cdot p_i = f_0 - M_0 \cdot \mathrm{SOC}_i^n \cdot p_i, \quad p_i < 0, \quad i = 1, \ldots, N, \tag{55}$$

whereby M_0 is the droop coefficient for $\mathrm{SOC}_i = 1$, and n is the SOC exponent ($n > 0$). Low n values cause slight variations in slope M_p and, as a result, M_p always stays similar to M_0. On the other hand, high n values cause significant variations in slope M_p for low SOCs, resulting in M_p attaining higher values than M_0 for $p > 0$ and lower values than M_0 for $p < 0$. Other slope modification methods are also based on the expression shown in Eqs. (54) and (55) but for $n = 1$ [16].

As an example, the *P–f* curve is shown in Fig. 16 for $f_0 = 50$ Hz, $M_0 = 0.1$ Hz, $n = 1$ and two batteries ($\mathrm{SOC}_1 = 1$ and $\mathrm{SOC}_2 = 0.5$). It can be observed that for

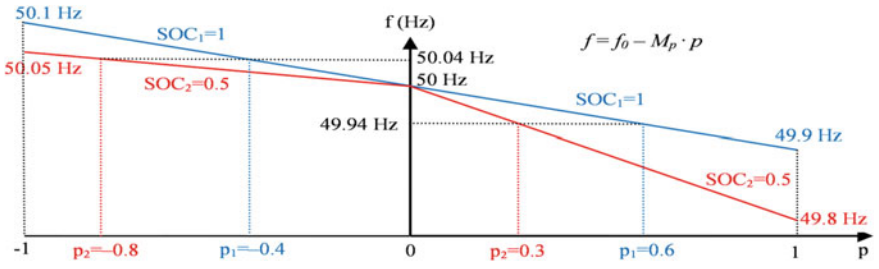

Fig. 16 *P–f* curve for the slope modification method

battery inverter 1, since $SOC_1 = 1$, then $M_p = M_0 = 0.1$ Hz whenever it is supplying or absorbing power. However, for battery inverter 2, $M_p = 0.2$ Hz $> M_0$ for discharging $M_p = 0.05$ Hz $< M_0$ for charging. The figure also shows two steady-state operating points for two frequencies (49.94 and 50.04 Hz). When load demand exceeds generation capacity ($P_T > 0$), then both batteries discharge. Inverter 1 can be seen to supply more per-unit power than inverter 2, thereby helping balance the SOCs. On the other hand, when generation exceeds the load demand ($P_T < 0$), then both batteries charge. In this case, more per-unit power is absorbed by inverter 2, in relation to inverter 1, which also helps to balance the SOC.

It is easy to obtain a steady-state operating point if it is considered that all inverters have the same frequency after the power transient. Equations (26) and (54) can be used to obtain, for $P_T > 0$,

$$\frac{p_i}{p_j} = \left(\frac{\mathrm{SOC}_i}{\mathrm{SOC}_j}\right)^n, \quad p_i, p_j > 0, \quad i = 1, \ldots, N, \quad j = 1, \ldots, N \tag{56}$$

$$P_i = \frac{S_{\mathrm{bat},i} \cdot \mathrm{SOC}_i^n}{\sum_{j=1}^{N} S_{\mathrm{bat},j} \cdot \mathrm{SOC}_j^n} \cdot P_T, \quad i = 1, \ldots, N \tag{57}$$

Equation (56) shows that, when this method is used, the real power ratio is dependent on the ratio between the SOCs. Parameter n either increases ($n > 1$) or decreases ($n < 1$) the power ratio for the same SOC ratio.

The grid frequency value will vary according to the inverter power and the battery SOC. The frequency will be less than f_0 when the battery is delivering power whilst it will be greater than f_0 when the battery is absorbing power. The minimum frequency $f_{\min}$ is given for $\mathrm{SOC} = \mathrm{SOC}_{\min}$ and $p = 1$, whereas the maximum frequency $f_{\max}$ is determined for $\mathrm{SOC} = \mathrm{SOC}_{\max} = 1$ and $p = -1$. The SOC is saturated to $\mathrm{SOC}_{\min} = 0.1$ to prevent M_P from considerably increasing its value. Based on Eqs. (54) and (55), the limit frequency values are thus determined as

$$f_{\min} = f_0 - \frac{M_0}{0.1^n}, \quad f_{\max} = f_0 + M_0 \tag{58}$$

There are two degrees of freedom for the design of the slope modification method: M_0 and n. These parameters should be selected with care since they affect the frequency deviation, the power response, and the SOC response. With regard to the frequency deviation, $f_{\min}$ can drop to exceedingly low values, as shown in Eq. (58). However, this problem has already been resolved in the literature through a secondary control, thereby restoring the frequency to its rated value [15]. Conversely, as shown in Sect. 2, droop method dynamics are extremely dependent on droop coefficient M_p. The slope modification method is based on changing this coefficient so as to balance the SOCs. Therefore, this method offers a variable power response. It is then necessary to limit the slope variation range so as to

prevent the system from offering a poor power response (low M_p) or instability (high M_p), which would limit the battery SOC convergence. Therefore, the preferred method is to modify parameter f_0, as it will be presented below, and the slope changing method will be discussed no further. An in-depth study of the performance of this method is provided in [7].

The second potential technique is termed the curve shifting method, proposing the modification of the independent parameter. This method moves the *P–f* curve either upwards or downwards based on the battery SOC. The *P–f* curve has the following expression:

$$f_i = f_0 - M_p \cdot p_i + M_S \cdot (\mathrm{SOC}_i - \mathrm{SOC}_{i0}), \quad i = 1, \ldots, N \tag{59}$$

where M_S is the SOC coefficient, being the same for all inverters. Term SOC_{i0} can be used to define the desired SOC distribution between the batteries. Usually, the control objective is to maintain the same SOC level for all the batteries and, for this purpose, $\mathrm{SOC}_{10} = \mathrm{SOC}_{20} = \mathrm{SOC}_0$ is imposed (for two batteries). However, in some situations, an unequal SOC distribution may be desirable; this can be easily achieved by setting different values for SOC_{10} and SOC_{20}. As a result, the control objective will become $\mathrm{SOC}_1 = \mathrm{SOC}_2 + \mathrm{SOC}_{10} - \mathrm{SOC}_{20}$. Furthermore, there will be no change to the power and SOC dynamic responses due to the fact that term $M_S \cdot \mathrm{SOC}_0$ is constant during operation.

The *P–f* curve is shown in Fig. 17 for $f_i = 50$ Hz, $M_p = 0.3$ Hz, $M_S = 0.3$ Hz, $\mathrm{SOC}_0 = 0.8$ and two batteries ($\mathrm{SOC}_1 = 1$ and $\mathrm{SOC}_2 = 0.5$). The curve for battery inverter 1 has moved upwards in relation to the curve for battery inverter 2, although slope M_p remains constant. Two operating points are plotted in Fig. 17, corresponding to $P_T > 0$ and $P_T < 0$. In both cases, p_1 is greater than p_2, making it possible to balance the SOCs.

It is possible to determine the steady-state power distribution by taking into account the fact that all inverters have the same frequency after the power transient. Equations (26) and (59) result in

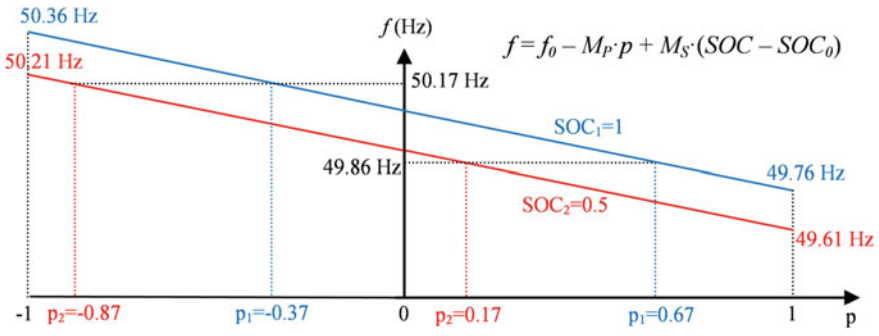

Fig. 17 *P–f* curve for the curve shifting method

$$p_i - p_j = \frac{M_S}{M_P} \cdot \left(\mathrm{SOC}_i - \mathrm{SOC}_j\right), \quad i = 1, \ldots, N, \quad j = 1, \ldots, N \tag{60}$$

$$P_i = \frac{S_{\mathrm{bat},i}}{S_{\mathrm{bat,tot}}} \cdot P_T + \frac{S_{\mathrm{bat},i}}{S_{\mathrm{bat,tot}}} \cdot \frac{M_S}{M_P} \cdot \sum_{\substack{j=1 \\ j \neq i}}^{N} S_{\mathrm{bat},j} \cdot (\mathrm{SOC}_i - \mathrm{SOC}_j), \quad i = 1, \ldots, N \tag{61}$$

Equation (60) shows that the real power difference is proportional to the SOC difference, with the proportionality constant being quotient M_S/M_p.

The grid frequency also varies with this method, as a function of the inverter power and the battery SOC. The frequency reaches its minimum $f_{\min}$ value for $\mathrm{SOC} = \mathrm{SOC}_{\min} = 0.1$ and $p = 1$, and its maximum value $f_{\max}$ for $\mathrm{SOC} = \mathrm{SOC}_{\max} = 1$ and $p = -1$.

$$f_{\min} = f_0 - M_P - M_S \cdot (\mathrm{SOC}_0 - 0.1) \tag{62}$$

$$f_{\max} = f_0 + M_P + M_S \cdot (1 - \mathrm{SOC}_0) \tag{63}$$

The curve shifting method offers two degrees of freedom for the design: M_p and M_S. It is important to select these parameters carefully, as they have a considerable influence on the frequency deviation, the power response and the SOC response. Therefore, an analysis will be made of the power and SOC responses in this section, so that the right choice can be made. As far as the frequency deviation is concerned, the frequency variation obtained is low for a stand-alone system, except for very high M_p and M_S values. Taking for example the parameters chosen for Fig. 17, $f_{\min} = 49.49$ Hz and $f_{\max} = 50.36$ Hz, which are acceptable.

3.3 Parameter Design for the Curve Shifting Method

Looking at the expression for the curve shifting method, Eq. (59), parameters M_p and M_S are the two degrees of freedom for the design. In order to make a correct selection, it is important to analyze the effect of these parameters on the power response and SOC response.

With regard to the power response, Eq. (31) shows that the characteristic equation depends solely on slope M_p and not on independent term f_0. Given the fact that parameter M_S does not change the curve slope, it has no impact on the power response. As a result, the system poles are the same as for the conventional droop method and the power response can be analyzed as indicated in Sect. 2.3 through the M_p root locus diagram shown in Fig. 8. This parameter can therefore be selected in order to optimize the power response, and based on the analysis above, it is chosen as $M_p = 0.3$ Hz in this case.

The next step is to analyze the influence of parameters M_p and M_S on the SOC. To this effect, for the purpose of simplicity, a simple model of the SOC response for a two-battery system is developed, although a general model for an N-battery system can also be consulted in [7]. With this model, it is possible to determine the SOC balancing time constant τ_{SOC}, which is related to the SOC transient after an initial SOC difference, as well as the SOC imbalance, which is related to the SOC difference after net power variations and is only present for different C/S_{bat} ratios. Here the battery discharging situation will be discussed, since the battery charging analysis is similar and reaches the same conclusions.

The battery state-of-charge can be determined as follows

$$\mathrm{SOC}_i = \mathrm{SOC}_i(0) - \frac{1}{C_{\mathrm{Ah}}} \cdot \int i_{\mathrm{bat},i} \cdot \mathrm{d}t, \quad i = 1, \ldots, N, \tag{64}$$

where SOC(0) is the initial SOC, initial SOC, C_{Ah} is the battery capacity in Ah, and i_{bat} is the battery current (supplied). To better estimate the SOC, an enhanced coulomb counting method has been used here [17]. Moreover, so as to avoid long-term errors, the SOC is reset to 100% when the lead–acid battery is operating at a float voltage for a given time, as indicated by the manufacturer. This situation often occurs in stand-alone systems with non-dispatchable units, given the fact that the renewable generators must be oversized in order to lessen the loss of load probability [18].

Disregarding conversion losses, whilst considering the battery voltage to be constant and applying the Laplace transform, Eq. (64) for two batteries becomes

$$\mathrm{SOC}_1 = \mathrm{SOC}_1(0) - \frac{P_1}{C_1 \cdot s}, \quad \mathrm{SOC}_2 = \mathrm{SOC}_2(0) - \frac{P_2}{C_2 \cdot s} \tag{65}$$

where C_1 and C_2 correspond to the battery capacities in Wh.

Considering that the SOC variation is far slower than that of the power response, it can be considered that the power steady state has been achieved and that Eqs. (60) and (61) are valid. Equations (26), (60) and (65) are used to obtain the expression for the SOC difference:

$$\begin{aligned} \mathrm{SOC}_1 - \mathrm{SOC}_2 = {} & \frac{M_P}{M_S} \frac{1}{C_1 + C_2} \left(\frac{C_1}{S_{\mathrm{bat1}}} - \frac{C_2}{S_{\mathrm{bat2}}} \right) \\ & \cdot \frac{P_T}{\tau_{\mathrm{SOC}} \cdot s + 1} + \frac{\tau_{\mathrm{SOC}} \cdot s}{\tau_{\mathrm{SOC}} \cdot s + 1} (\mathrm{SOC}_1(0) - \mathrm{SOC}_2(0)) \end{aligned} \tag{66}$$

$$\tau_{\mathrm{SOC}} = \frac{M_P}{M_S} \cdot \frac{1/S_{\mathrm{bat1}} + 1/S_{\mathrm{bat2}}}{1/C_1 + 1/C_2} \tag{67}$$

As shown in the two equations above, the transfer function has just one pole, which has associated time constant τ_{SOC}. This parameter τ_{SOC} is dependent on the battery capacity, the inverter rated power and parameters M_p and M_S. It can be set to

the required value through parameter M_S once parameter M_p has been selected to optimize the power response. Increasing M_S and therefore the M_S/M_p ratio makes the response faster. For example, for the batteries and inverters 1 and 2 presented in Table 1, with M_p = 0.3 Hz and M_S = 0.3 Hz, τ_{SOC} = 8 h is obtained.

Equations (66) and (67) also serve to determine the influence of the net power on the SOC imbalance for different C/S_{bat} ratios. It should be noted that net power P_T is best rejected for a low C/S_{bat} ratio difference and a high M_S/M_p ratio. Figure 18 shows the bode diagram for the SOC imbalance as a function of the net power, plotted for the batteries and inverters 1 and 2 shown in Table 1. The curves are obtained for M_p = 0.3 Hz, three different M_S values (M_S = 0.1 Hz, M_S = 0.3 Hz and M_S = 0.5 Hz) and assuming a partial loss of the capacity of battery 2 through ageing. More specifically, there are two families of curves: one for C_2 = 18 kWh (25% of capacity loss) and the other for C_2 = 12 kWh (50% of capacity loss). From the figure, it can be concluded that it is possible to reduce the SOC imbalance caused by the net power through high M_S values. Therefore the SOC imbalance can be limited by increasing M_S, since this parameter exerts no influence on the power response. In this case, M_S = 0.3 Hz is chosen since this value is high enough to reduce the SOC difference and causes an acceptable frequency deviation.

A 1-year simulation is carried out for the batteries and inverters 1 and 2 presented in Table 1, but with C_2 = 18 kWh (25% of capacity loss due to ageing). The simulation is conducted with Simulink, based on the model developed above, using Eqs. (61) and (65). When a battery is fully charged (SOC = 1) and $P_T < 0$, the generation is limited in order to ensure that the battery does not absorb any more power. Power profile P_T is shown in Fig. 19 with values obtained at 15-min intervals and corresponding to consumption and generation data measured from

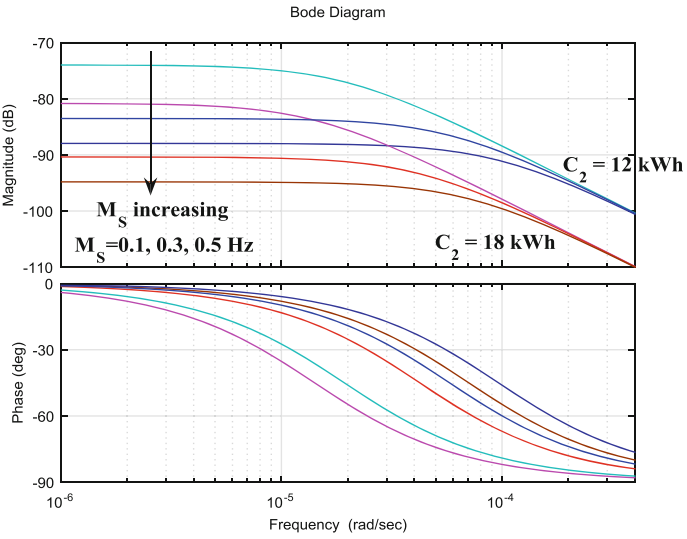

Fig. 18 Bode diagram of the SOC imbalance in relation to net power [7]

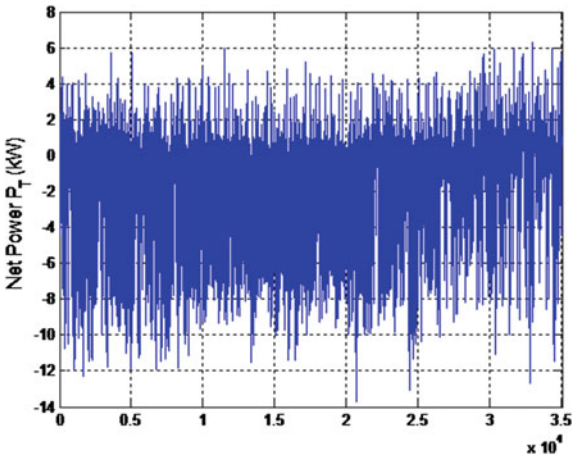

Fig. 19 One year net power profile PT [7]

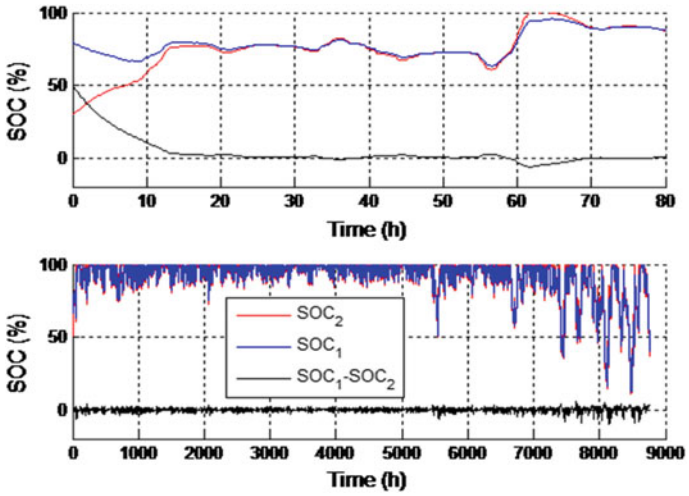

Fig. 20 SOC evolution for a stand-alone system for the curve shifting method [7]

1st February 2009 to 31th January 2010. The load profile was taken from two homes in Pamplona, Spain, occupied by a total number of nine people. The PV and wind generation profiles were adapted from irradiance, cell temperature and wind speed data taken from the Public University of Navarra, in Pamplona, Spain, for a 10 kWp PV generator and a 5 kWp wind turbine. The generation and battery sizing for the stand-alone system was based on [18].

Figure 20 shows the results, whereby $SOC_1(0) = 80\%$ and $SOC_2(0) = 30\%$. The SOC transient response is shown in the first graph. As a result of this control,

both SOCs tend to reach the same value following a different initial status. The SOC response can be seen to be fast enough, with a rise time that tallies with the time constant obtained from Eq. (67), $\tau_{SOC} = 6.6$ h. The second graph plots the complete 1-year simulation, showing a low SOC imbalance. After the initial transient, the net power causes the SOC difference to change due to the fact that $C_1/S_{bat1} = 8\ \text{h} \neq C_2/S_{bat2} = 6\ \text{h}$, as predicted by Eq. (66). In the course of the 1-year period, and disregarding the initial transient, the SOC_1–SOC_2 difference reached a peak value of −9.9%, an RMS value of 1.35% and an average value of −0.02%. These values are acceptable and can be reduced still further if desired by increasing M_S yet without interacting with the power response dynamics.

3.4 Experimental Results

The next step is to validate the SOC-based droop scheme through experimental tests. Two batteries with their inverters were parallel-connected to create the AC grid. Their technical details are shown in Table 1. The Ingecon Hybrid AC Link 3TL and Ingecon Hybrid AC Link 6TL were selected as the battery inverter models, yet with a modified configuration so as to implement the curve shifting method. The *P–f* curve employed is Eq. (59) for $f_0 = 50$ Hz, $M_P = 0.3$ Hz, $M_S = 0.3$ Hz, $SOC_0 = 0.8$, as designed above and indicated in Fig. 17. This curve was programmed in the inverter microprocessors. Each inverter measures its output power and then changes the output voltage frequency accordingly. The battery banks comprise series-connected vented lead–acid batteries, model 6 PVS 660. In the course of the experiments, battery 1 had a greater charge than battery 2, with $SOC_1 = 0.8$ and $SOC_2 = 0.4$. A load bank and a PV emulator with its inverter was connected to the grid, making it possible to change the real and reactive powers as desired and, therefore, to set the desired operating point. The data was obtained with precision power analyser WT1800, recording power outputs and frequencies every 50 ms. Figure 21 shows the battery inverters, battery banks, PV emulator and load bank.

The first test was conducted for the battery inverters in discharging mode. The per-unit real powers and the filtered grid frequency are shown in Fig. 22. Inverter 1 initially operated alone, supplying a 4 kW load. Therefore, $P_1 = 4$ kW, $p_1 = 0.67$, $P_2 = 0$ and $p_2 = 0$. Then, at second 2, inverter 2 was connected in order to help power the load. It was then possible to obtain the power distribution through Eq. (61) as $P_1 = 3.47$ kW, $p_1 = 0.58$, $P_2 = 0.53$ kW and $p_2 = 0.18$. Then, a 2.7 kW load was added to the AC bus. The net power reached $P_T = 6.7$ kW and the power distribution reached $P_1 = 5.27$ kW, $p_1 = 0.88$, $P_2 = 1.43$ kW, and $p_2 = 0.48$. Finally, at second 7.5, the 2.7 kW load was disconnected, and the system returned to the previous operating point. The figure shows how p_1 is always higher than p_2 thanks to the control. Since $SOC_1 = 0.8$ and $SOC_2 = 0.4$, this helps balance the SOCs. As far as the grid frequency is concerned, this changes in line with the

Fig. 21 Experimental setup, showing the PV emulator, battery and load banks [7]

net power variations based on Eq. (59). The figure shows this frequency variation to be moderate and completely acceptable for a stand-alone system.

The second test was carried out for the battery inverters in charging mode. The per-unit powers and the filtered grid frequency are shown in Fig. 23. In the course of the entire experiment, the PV inverter operated under MPPT and supplied 6 kW to the AC grid. Inverter 1 was initially connected with no load and, therefore, $P_1 = -6$ kW, $p_1 = -1$, $P_2 = 0$, and $p_2 = 0$. Shortly afterwards, inverter 2 was connected, changing the power distribution to $P_1 = -3.2$ kW, $p_1 = -0.53$, $P_2 = -2.8$ kW, and $p_2 = -0.93$. Then, at around second 5.5, a 2.7 kW load was connected, leading to net power $P_T = -3.3$ kW. The power distribution was then $P_1 = -1.4$ kW, $p_1 = -0.23$, $P_2 = -1.9$ kW and $p_2 = -0.63$. As can be seen in the figure, when both inverters are connected, p_1 is always greater than p_2.

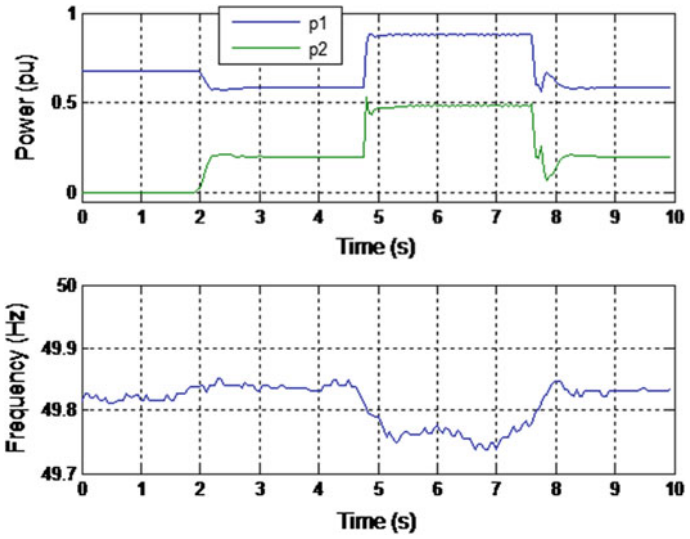

Fig. 22 Experimental results for two-battery inverters in discharging mode [7]

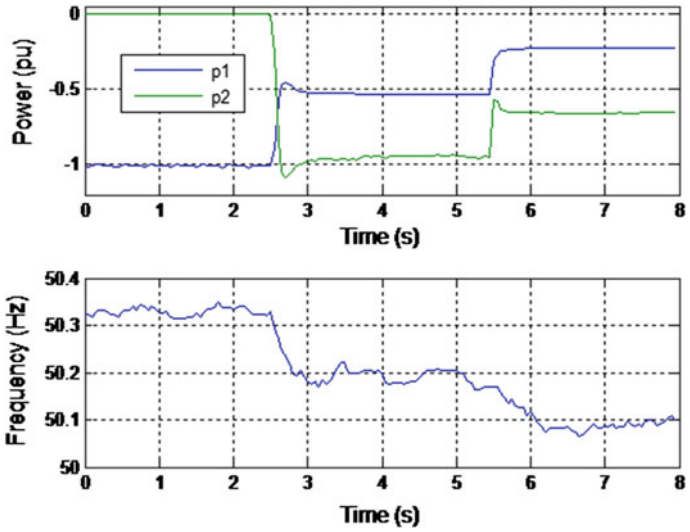

Fig. 23 Experimental results for two-battery inverters in charging mode [7]

Thus, battery 2 is charged with more per-unit power, helping balance the SOCs. Figure 23 also shows the grid frequency, which is in line with net power variations and its variation range is between acceptable limits for a stand-alone system.

4 Battery Current and Voltage Control

4.1 Introduction to Current and Voltage Control

Provided that the battery SOC has been correctly estimated then it is possible to maintain the same SOC level for all batteries, yet with no need for a communication system, based on the SOC regulation detailed in the section above. Nonetheless, this regulation fails to completely cover the secondary control, given the fact that it is unable to guarantee that the battery voltage and current remain within the rated values at all times. Therefore, in order to complement the secondary control whilst avoiding the need for low-bandwidth communication, this section discusses a further modification to the traditional droop method. The scheme indicated here is, therefore, compatible and complementary to the one discussed in the section above, making it possible to control the battery voltage and current, ensuring that these remain within their maximum permitted values.

This energy management scheme functions as follows. Whenever the batteries are fully charged or receiving too much current, the battery inverters increase the grid frequency. This is detected by the RES inverters, which reduce their power in order to regulate the battery voltages or currents. In addition, the control coordinates the various batteries. If some of the batteries are not at their maximum voltage or current, then the excess power is transferred from the charged batteries to the non-charged ones, yet without curtailing the RES power, taking full advantage of the solar/wind energy. This section also deals with protection during the battery discharging process. In the same way as for battery charging, whenever the batteries are either completely discharged or delivering too much current, then the grid frequency is lowered. The power is first transferred from some battery to the others. However, if all the batteries are at the minimum voltage or maximum discharge current, then the reduction in frequency is detected by the non-critical loads, which are either regulated or disconnected. If this is not possible, then the system is shutdown in order to prevent irrevocable damage to the batteries.

4.2 Description of the Energy Management Strategy

Figure 24 shows the stand-alone system shown in Fig. 3, yet now with N battery inverters, M PV inverters and with a number of loads connected to the common AC bus. The battery inverters are parallel-connected through the output impedance, comprising the filter inductance and line impedance. Given the fact that the line impedance is much lower than the filter impedance, the output impedance can be considered to be the same as filter inductance, L_{fi}. The figure also shows the battery inverter rated powers $S_{\text{bat},i}$, battery capacities C_i, battery real powers P_i, battery reactive powers Q_i, net real power P_T, net reactive power Q_T, PV inverter rated powers $S_{\text{pv},i}$ and instantaneous value of voltages and currents v, e_i and i_i.

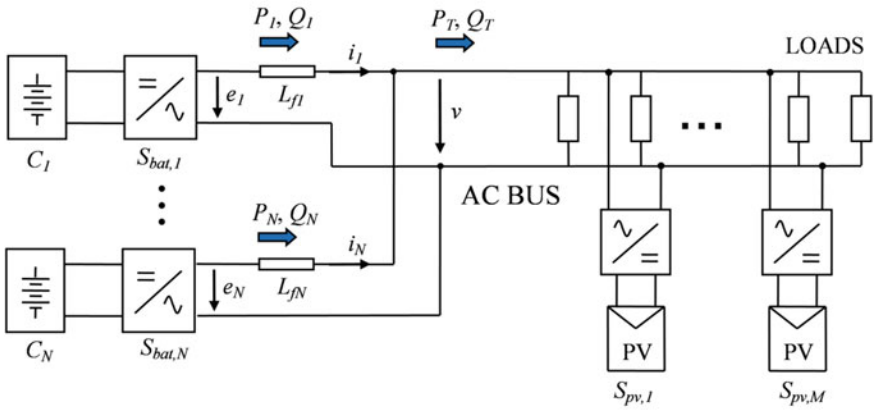

Fig. 24 Battery inverters, PV inverters and parallel-connected loads [19]

The battery inverters in this system always operate under voltage-control mode using droop methods in order to generate the grid power. Whilst the RES converters operate under current-control mode, delivering to the grid either the maximum power available or a power below the MPP. Given the fact that we are concerned with energy management and, therefore, real power, the reactive power sharing is not discussed here. The operation of the battery inverters, RES converters and non-critical loads is detailed below.

With regard to the battery inverters, the traditional droop method is used to distribute the real power in proportion to their ratings. For simplicity, two-battery inverters are used for the real power analysis, however this can easily be generalized for N inverters. For the sake of convenience, the droop method expression is recalled below:

$$f = f_0 - M_p \cdot p \tag{68}$$

When operating at steady state, all the inverters have the same frequency. Thus, from Eq. (68), and bearing in mind that the f_0 and M_p values are the same for all inverters, this gives the following:

$$f_1 = f_2 \Rightarrow p_1 = p_2 \tag{69}$$

With this energy control strategy, Eq. (68) is used in normal operating conditions and, as a result, the power is shared between the inverters. However, in some situations equal power sharing is undesirable. The energy control strategy then changes Eq. (68) as shown below:

$$f = f_0 - M_p \cdot p + \delta f \tag{70}$$

where δf is the shifting frequency to be changed by the control.

In steady-state operation, from Eq. (70), condition $f_1 = f_2$ leads to

$$f_1 = f_2 \Rightarrow p_1 - p_2 = \frac{\delta f_1 - \delta f_2}{M_p} \tag{71}$$

This equation shows that adding the term δf results in an unequal power distribution. From Eq. (71), if δf_2 and the load are maintained constant and δf_1 is increased, then this leads to an increase in p_1 and a decrease in p_2 whilst a reduction in δf_1 leads to a decrease in p_1 and an increase in p_2. Taking this into account, if battery 1 reaches its minimum voltage or its maximum discharge current, then battery inverter 1 will lower δf_1 and its power will decrease, thereby avoiding over-discharge. On the other hand, if battery 1 is fully charged or absorbs too much current, then the battery inverter will increase δf_1 and its power will increase. When in charging mode, the power is negative thereby resulting in a reduction in the battery current and voltage and impeding overcharging.

This can be observed in Fig. 25, where three different *P–f* curves are shown. The parameters are f_0 = 50 Hz, M_p = 0.3 Hz for all curves. The curve for inverter 2 remains unchanged ($\delta f_2 = 0$) whilst two modified curves are plotted for inverter 1 ($\delta f_1 = -0.1$ Hz and $\delta f_1 = 0.1$ Hz). Operating points for $P_T > 0$ and for $P_T < 0$ are plotted in the figure. In discharge mode ($P_T > 0$), the shifting frequency of battery 1 has been decreased to $\delta f_1 = -0.1$ Hz. As a result, inverter 1 injects less power than inverter 2. Whilst, in charging mode ($P_T < 0$), the shifting frequency of battery 1 has been increased to $\delta f_1 = 0.1$ Hz. In this situation, inverter 1 absorbs less power than inverter 2.

Although parameters f_0 and M_p are identical for all battery inverters so as to share the per-unit power during normal operation, parameter δf varies in line with the operating point and is determined for each battery inverter as:

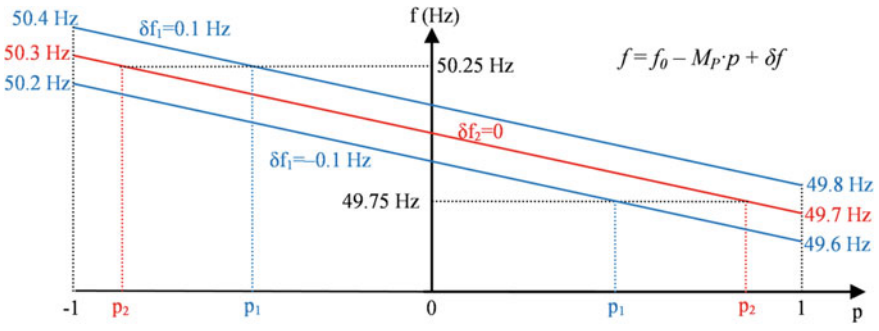

Fig. 25 *P–f* curve for the energy management strategy

$$\delta f = \delta f_c - \delta f_d \tag{72}$$

where δf_c ($\delta f_c \geq 0$) is the charge changing frequency and δf_d ($\delta f_d \geq 0$) is the discharge changing frequency.

Figure 26 shows how δf_c and δf_d are calculated. In charging mode, $\delta f_d = 0$, and $\delta f_c \geq 0$. The first step is to enter the difference between measured battery voltage, $v_{bat,m}$, and maximum battery voltage, $v_{bat,max}$, in the controller $C_{c,v}$, which then determines $\delta f_{c,v}$, with a limit from 0 to $\delta f_{c,max}$. Second, controller $C_{c,i}$ uses the difference between the measured battery current, $i_{bat,m}$ (negative for charging mode), and the maximum battery charging current, $i_{bat,c,max}$, to determine $\delta f_{c,i}$, which also has a limit from 0 to $\delta f_{c,max}$. Then, the highest δf_c value is chosen, since this value is more restrictive. During discharging mode, $\delta f_c = 0$, and $\delta f_d \geq 0$. In this case, the calculations are comparable to those for the charging mode, but the references are the minimum battery voltage, $v_{bat,min}$, and the maximum battery discharging current, $i_{bat,d,max}$. In this case, the outputs are $\delta f_{d,v}$, and $\delta f_{d,i}$, the threshold value is $\delta f_{d,max}$, and the highest value δf_d is selected as being the most restrictive.

In normal operation, the battery currents and voltages are within range, in other words $v_{bat,min} < v_{bat} < v_{bat,max}$ for the voltage and—$i_{bat,c,max} < i_{bat} < i_{bat,d,max}$ for

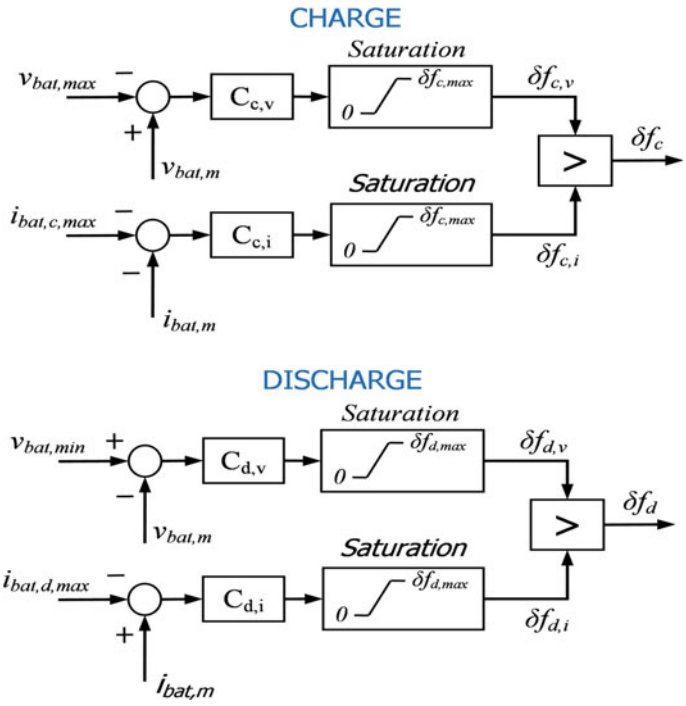

Fig. 26 Calculation of δf_c and δf_d [19]

the current. Therefore, the controller outputs are saturated to zero, $\delta f_c = 0$, $\delta f_d = 0$, $\delta f = 0$, and Eqs. (68) and (69) are valid, resulting in an equal power distribution. When a battery is fully charged and its voltage is greater than $v_{bat,max}$ ($v_{bat} > v_{bat,max}$), or its charging current is greater than $i_{bat,c,max}$ ($i_{bat} < -i_{bat,c,max}$), then δf is increased, making it possible to reduce the power input of that battery. On the other hand, when the battery is fully discharged and its voltage falls below $v_{bat,min}$ ($v_{bat} < v_{bat,min}$), or its discharge current is greater than $i_{bat,d,max}$ ($i_{bat} > i_{bat,d,max}$), then δf is decreased, leading to a decrease in the power output of that battery.

When there is no variation in generation and consumption, in other words, net power P_T is constant, then the decrease in the power absorbed (delivered) by one battery leads to an increase in the power absorbed (delivered) by the other battery. Therefore, the control strategy proposed will remain stable if the complete storage system is able to support the net power. However, if all batteries are fully charged or if they are drawing too much current, then all batteries will increase the frequency together. It is then necessary to reduce the RES power, as discussed below. On the other hand, if all batteries are at their minimum voltage or maximum discharge current, then they will all decrease the frequency together. In these circumstances, non-critical loads then need to be regulated, as also discussed below.

RES converters operate in current-control mode, delivering power to the grid. Their control strategy is generally based on MPPT, yet they can decrease the power in line with the grid frequency deviation Δf, which is defined as

$$\Delta f = f - f_0 \tag{73}$$

Each RES converter measures the frequency in order to obtain the measured frequency deviation Δf_m. There is no extra cost involved in the frequency measurement, given the fact that the RES inverters already include this feature for grid synchronization and islanding detection. The next stage is to filter the frequency obtained by the phase-locked loop (PPL) so as to avoid noise, transients and external interferences. A high value is preferable for the filter time constant, τ_f, in order to prevent any transient frequency oscillations from reducing the RES power when not required. However, an extremely high value would have a negative impact on the control stability margin, and a trade-off must be balanced. If the measured frequency deviation Δf_m is greater than a minimum value Δf_{min}, then the RES converter stores the MPP power, termed $P_{mpp,fr}$, and continuously reduces the power generated up to frequency deviation Δf_{max}, where the power is zero. The value of Δf_{min} should be greater than M_p so as to prevent interaction with the battery inverter droop and to limit the power when not required. Given the fact that the value of $P_{mpp,fr}$ is considered instead of rated power S_{pv}, then the RES power starts to be reduced when $\Delta f_m > \Delta f_{min}$, leading to a faster control. The frequency sensing and filtering H_f, and the ratio between the frequency deviation and RES power reference P^*_{RES} are shown in Fig. 27.

Although the RES power control implementation is not shown here, it is available for consultation in [20] for a PV system and in [21] for a wind-energy conversion system.

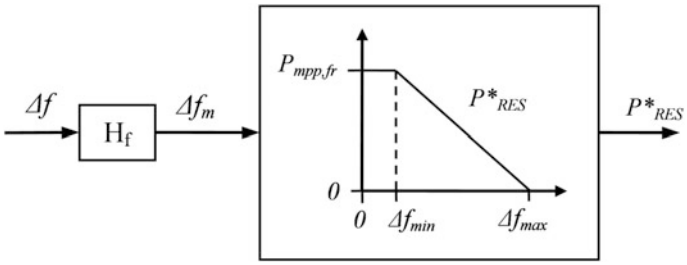

Fig. 27 Determination of RES power reference P * RES [19]

With regard to the loads, if the system has non-critical controllable loads, then their power can be regulated as a function of the grid frequency. In a similar manner to the RES inverters (see Fig. 27), a P–f curve can also be programmed to reduce the power consumed in low-frequency situations. Although it is possible to set the frequency deviation limits independently of the RES control, in this case, they will be considered to be the opposite of the RES control limits, namely $-\Delta f_{\min}$ and $-\Delta f_{\max}$. Typical programmable loads include thermal loads such as water heaters, refrigerators and air conditioning units.

If it is not possible to regulate the load, or whenever all non-critical loads have already been disconnected, then the system should be shutdown in low-frequency situations in order to prevent irrevocable damage to the batteries. The shutdown frequency deviation value is defined as $-\Delta f_{\text{stop}}$. If it is possible to control the load, then the shutdown frequency deviation should be $\Delta f_{\text{stop}} > \Delta f_{\min}$ so that the system does not shutdown when the load control is active. However, if it is not possible to regulate the loads, then it should simply be $\Delta f_{\text{stop}} > M_p$ in order to avoid interaction with the battery inverter droop.

4.3 Operating Modes

There are five operating modes, which are dependent on the values of δf and Δf. Each operating mode is defined in Table 4, and the shift from one mode to another is shown in Fig. 28 and explained below for a two-battery situation. Figure 29 shows the frequency deviation for the various operating modes.

Mode I applies during normal operation, when the battery voltages and currents are within the set limits. In Mode II, one battery is fully charged whilst, in Mode III, both batteries are fully charged and a PV power limitation is necessary. On the other hand, in Mode IV, one battery is discharged while, in Mode V, both batteries are fully discharged and load regulation is necessary.

Table 4 Energy management operating modes [19]

Operating mode	Frequencies Δf, δf_1, and δf_2	Battery voltages and currents v_{bat1}, v_{bat2}, i_{bat1}, and i_{bat2}	PV inverters	Non-critical loads
Mode I: normal operation	$\delta f = 0$ for both batteries $-\Delta f_{min} < -M_p < \Delta f$ $\Delta f < M_p < \Delta f_{min}$	v_{bat} within limits for both batteries i_{bat} within limits for both batteries	MPPT	As required
Mode II: one battery charged	$\delta f > 0$ for one battery $\delta f = 0$ for the other $-\Delta f_{min} < -M_p < \Delta f$ $\Delta f < M_p < \Delta f_{min}$	$v_{bat} = v_{bat,max}$ or $i_{bat} = -i_{bat,c,max}$ for one battery v_{bat} and i_{bat} within range for the other battery	MPPT	As required
Mode III: PV power limitation	$\delta f > 0$ for both batteries $\Delta f_{min} < \Delta f < \Delta f_{max}$	$v_{bat} = v_{bat,max}$ or $i_{bat} = -i_{bat,c,max}$ for one battery $v_{bat} = v_{bat,max}$ or $i_{bat} = -i_{bat,c,max}$ for the other battery	Power limitation	As required
Mode IV: one battery discharged	$\delta f < 0$ for one battery $\delta f = 0$ for the other $-\Delta f_{min} < -M_p < \Delta f$ $\Delta f < M_p < \Delta f_{min}$	$v_{bat} = v_{bat,min}$ or $i_{bat} = i_{bat,d,max}$ for one battery v_{bat} and i_{bat} within limits for the other battery	MPPT	As required
Mode V: load regulation	$\delta f < 0$ for both batteries $-\Delta f_{max} < \Delta f < -\Delta f_{min}$	$v_{bat} = v_{bat,min}$ or $i_{bat} = i_{bat,d,max}$ for one battery $v_{bat} = v_{bat,min}$ or $i_{bat} = i_{bat,d,max}$ for the other batery	MPPT	Load regulation

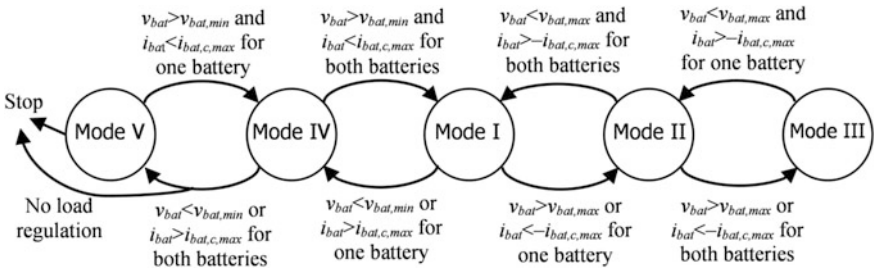

Fig. 28 Transitions between operating modes [19]

Mode I: Normal Operation

In Mode I, the battery voltages and currents are within the set limits and, as a result, based on Fig. 26, $\delta f = 0$ for both batteries. Based on Eqs. (68) and (69), the per-unit power is identical for both batteries, which either absorb or supply the

difference between generation and consumption, leading to the corresponding variation in their SOC. Given the fact that $\delta f = 0$, from Eq. (68), frequency deviation Δf is between $\pm M_p$. Since it was established that $\Delta f_{\min} > M_p$, the PV inverters operate under MPPT and the loads are not controlled (see Fig. 27).

When the voltage for one battery is greater than $v_{\text{bat,max}}$ ($v_{\text{bat}} > v_{\text{bat,max}}$), or the charging current is greater than $i_{\text{bat,c,max}}$ ($i_{\text{bat}} < -i_{\text{bat,c,max}}$), then the control increases δf, the power absorbed by that battery is reduced and the system changes to Mode II.

On the other hand, if the voltage for one battery drops to under $v_{\text{bat,min}}$ ($v_{\text{bat}} < v_{\text{bat,min}}$), or the discharge current is greater than $i_{\text{bat,d,max}}$ ($i_{\text{bat}} > i_{\text{bat,d,max}}$), then the control reduces δf, the power delivered by that battery decreases and the system changes to Mode IV.

Mode II: One Battery Charged

In Mode II, the voltage or current of one battery is controlled to its maximum value, $v_{\text{bat}} = v_{\text{bat,max}}$ or $i_{\text{bat}} = -i_{\text{bat,c,max}}$, whilst the voltage and current for the other battery are within the set limits. As a result of this control, $\delta f = 0$ for the second battery, and $\delta f > 0$ for the first battery. Therefore, from Eq. (71), the second battery absorbs a higher power than the first battery. Also in this case, since $\delta f = 0$ for one battery inverter, then frequency deviation Δf is between $\pm M_p$ and there is no change to the net power.

In this mode, the voltage and current of one battery are within the set limits, and with $\delta f = 0$. If the voltage or current of this battery is also greater than its maximum value, then it is impossible that the complete storage system absorbs the net power. In this situation, it is not possible to reorganize the power between the batteries, as this is carried out in this mode. According to the control, both batteries increase δf. At first, this has no effect on the net power. However, once the grid frequency deviation becomes greater than $\Delta f_{\min}$, then the PV power starts to be limited and the system changes to Mode III.

On the other hand, in Mode II, the voltage or current of one of the batteries is controlled to its maximum value. When this voltage or current decreases, the battery inverter reduces δf and the system changes to Mode I.

Mode III: RES Power Limitation

In Mode III, the voltage or current of all the batteries is adjusted to its maximum value, $v_{\text{bat}} = v_{\text{bat,max}}$ or $i_{\text{bat}} = -i_{\text{bat,c,max}}$. The control establishes $\delta f > 0$ for both batteries, resulting in frequency deviation $\Delta f > \Delta f_{\min}$. As a result, the PV power is decreased as shown in Fig. 27. This operating point requires a specific net power, which is obtained thanks to the control-imposed frequency.

In this mode, if the net power increases (for example due to a decrease in irradiance), and the system is unable to maintain the voltage or current reference for one battery, then the regulation reduces the frequency deviation to under $\Delta f_{\min}$, and the system changes to Mode II.

Various simulations were made, so as to validate the strategy in different operating modes. The PSIM software was used to develop an accurate model of the system shown in Fig. 24, consisting of two PV inverters, two-battery inverters and

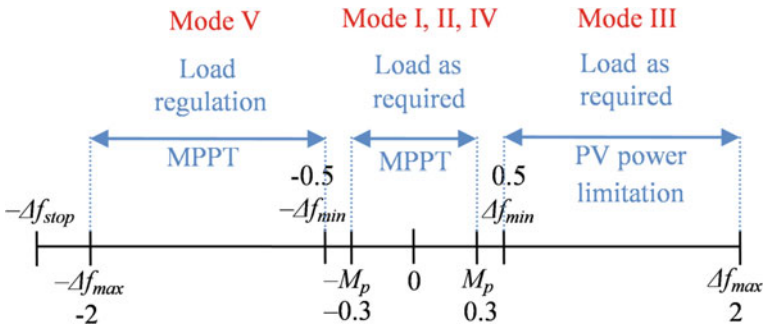

Fig. 29 Frequency deviation (Hz) and operating modes [19]

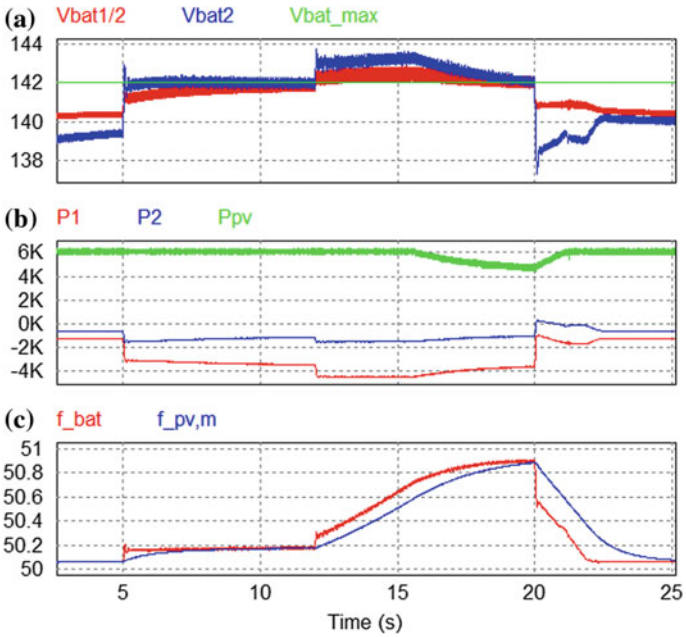

Fig. 30 Voltage regulation for the change from Mode I–Mode II–Mode III–Mode I [19]

various resistive loads. Some of the system features were presented in Table 1, where the two-battery inverters correspond to the battery and inverters 1 and 2, the two PV inverters have a rated power of 5 kW each and the parameters M_p, Δf_{min} and Δf_{max} are 0.3, 0.5 and 2 Hz, as shown in Fig. 29. The first simulation considers the voltage regulation during the change from Mode I–Mode II–Mode III–Mode I. This is shown in Fig. 30 and represents the battery 1 voltage divided by two, the battery 2 voltage, the maximum voltage for both batteries (Fig. 30a), the total PV power, the battery powers (Fig. 30b), the frequency imposed by the battery

inverters and the frequency measured by the PV inverters (Fig. 30c). During the simulation, the MPP power remains constant at 6 kW, whilst various resistive loads are disconnected and connected.

At first, the load consumes 4 kW, therefore the net power is $P_T = -2$ kW. Given the fact that the battery voltages are lower than the power input values, $\delta f = 0$ for both batteries (see Fig. 26), the system is in Mode I, both batteries have the same per-unit power ($P_1 = 2 \cdot P_2$) and the grid frequency is under $f_0 + \Delta f_{\min} = 50.5$ Hz.

Then, at second 5, a 2.7 kW load is disconnected, leading to net power $P_T = -4.7$ kW. The voltage of battery 2 is greater than its maximum value and, therefore, $\delta f_2 > 0$. According to Eq. (71), the absorbed power then moves from battery 2 to battery 1 so that the battery 2 voltage is controlled and the system operates in Mode II. Since $\delta f_i = 0$, the frequency is also lower than $f_i + \Delta f_{\min}$ in this case, and no limitation is required for the PV power.

Then, at second 12, a 1.3 kW load is disconnected, leading to net power $P_T = -6$ kW. The voltages of both batteries are above their input values, meaning that the storage system is unable to absorb this power and it is therefore necessary to reduce the PV power. δf_1, δf_2 and the grid frequency are all increased as a result of the control. Then, when the frequency measured by the PV inverters is greater than $f_0 + \Delta f_{\min} = 50.5$ Hz, the PV power is limited so that both battery voltages are adjusted. Therefore, the system is operating in Mode III, with $P_{\text{pv}} = 4.5$ kW and $f = 50.87$ Hz.

Finally, at second 20, the connection of a 4 kW load leads to net power $P_T = -0.5$ kW. This causes both battery voltages to decrease to below their maximum values, and δf_1 and δf_2 to decrease to $\delta f_1 = \delta f_i = 0$. The grid frequency also drops, the PV inverters operate at MPPT and the system changes to Mode I.

Mode IV: One Battery Discharged

In this mode, the voltage or current of one battery is regulated to its reference value, $v_{\text{bat}} = v_{\text{bat,min}}$ or $i_{\text{bat}} = i_{\text{bat,d,max}}$, whilst the other voltage and current of the other battery are within the set limits. The control establishes $\delta f < 0$ for the first battery and $\delta f = 0$ for the second battery. Based on Eq. (71), less power is therefore supplied from the first battery than from the second. Since $\delta f = 0$ for one battery inverter, frequency deviation Δf is between $\pm M_p$ with no modification to the net power.

In this mode, the voltage and current of one battery are within limits, and with $\delta f = 0$. When, for this battery, the voltage drops to under $v_{\text{bat,min}}$ or the discharge current is greater than $i_{\text{bat,d,max}}$, then the storage system as a whole is unable to deliver the net power. In this situation, it is not possible to reorganize the power between the batteries, as was the case for this mode. According to the control, both batteries decrease the δf value. The net power is not affected at first. However, when the grid frequency deviation drops to below $-\Delta f_{\min}$, then this marks the start of the adjustment of the load power and the system changes to Mode V. If the system does not permit non-critical load control, then the frequency will continue to decrease until $\Delta f < -\Delta f_{\text{stop}}$, at which point the system shuts down in order to avoid irrevocable battery damage.

Furthermore, in Mode IV, the voltage or current of one of the batteries is controlled to its reference value, $v_{bat} = v_{bat,min}$ or $i_{bat} = i_{bat,d,max}$, When either this voltage increases or this current decreases, then the battery inverter increases δf and the system changes to Mode I.

Mode V: Load Regulation

In Mode V, all the battery voltages and currents are controlled to their reference value, $v_{bat} = v_{bat,min}$ or $i_{bat} = i_{bat,d,max}$. Due to the control, $\delta f < 0$ for both batteries, resulting in a frequency deviation $\Delta f < -\Delta f_{min}$. As a result, the load power is regulated, making it possible to establish the required net power so that either the voltage or current is maintained at its reference value.

In this mode, if there is a drop in the net power to be delivered (due to a rise in irradiance for example), then the control increases the frequency deviation to more than $-\Delta f_{min}$, and the system changes to Mode IV.

On the other hand, if all non-critical loads have already been disconnected and the storage system is unable to supply the net power demanded, then $v_{bat} < v_{bat,min}$ or $i_{bat} > i_{bat,d,max}$ for both batteries, and the control continues to lower the value of δf until $\Delta f < -\Delta f_{stop}$, whereby the system is shutdown so as to avoid irrevocable battery damage.

Another simulation was conducted for the system proposed above, examining the current control during the change from Mode I–Mode IV–Mode V–Mode I. The simulation results plotted in Fig. 31 show the battery currents, the maximum discharge current for both batteries (Fig. 31a), the load power, the battery powers

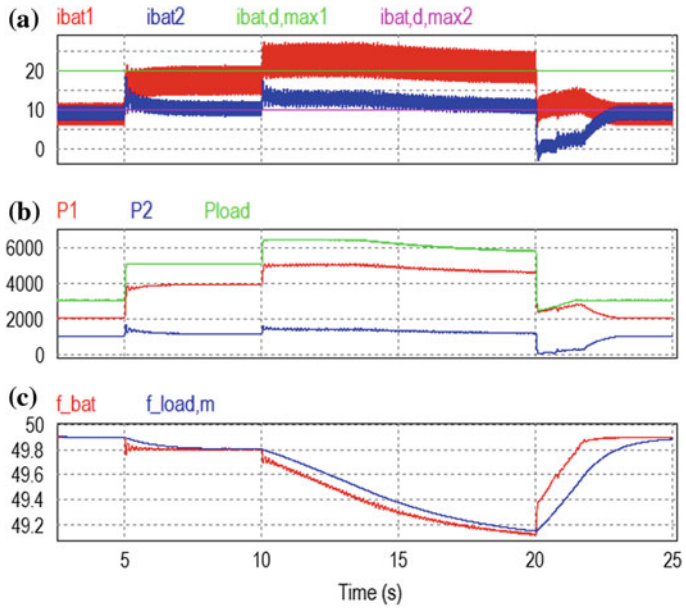

Fig. 31 Current control during the change from Mode I–Mode IV–Mode V–Mode I [19]

(Fig. 31b), the frequency imposed by the battery inverters and the frequency measured by the controllable load (Fig. 31c). Both batteries are assumed to be exceedingly hot, due to unfavourable conditions. To protect the batteries, their maximum current is decreased to $i_{\text{bat,d,max1}} = 20$ A and $i_{\text{bat,d,max2}} = 10$ A. Throughout the simulation, the PV power stays at 0, whilst various resistive loads are disconnected and connected, including a 2.7 kW controllable load.

A 3 kW load is initially connected to the grid. Given the fact that the battery currents are below their maximum values, $\delta f = 0$ for both batteries (see Fig. 26), and the system is in Mode I, the per-unit power is identical for both batteries ($P_1 = 2 \cdot P_2$) and the grid frequency is greater than $f_0 - \Delta f_{\text{min}} = 49.5$ Hz.

A 2 kW load is then connected at second 5. The current for battery 2 goes above the maximum value, which leads to $\delta f_2 < 0$. The power delivered then switches from battery 2 to battery 1 so that the current for battery 2 is controlled, causing the system to operate in Mode IV. Given the fact that $\delta f_1 = 0$, the frequency is also greater than $f_0 - \Delta f_{\text{min}}$ in this case, and no load management is required.

A 1.4 kW load is then connected at second 10. At that point in time, the currents for both batteries are greater than their maximum values, meaning that the storage system is unable to deliver the power demanded, making it necessary to reduce the load. δf_1, δf_2 and the grid frequency all decrease as a result of the control. When the frequency measured by the controllable load falls below $f_0 - \Delta f_{\text{min}} = 49.5$ Hz, then the power of the load is adjusted in such a manner that both battery currents are regulated. The system then switches to operation in Mode V, with $P_{\text{load}} = 5.8$ kW, $P_{\text{load,cont}} = 2.1$ kW and $f = 49.15$ Hz.

Finally, at second 20, a 3.4 kW load is disconnected. This causes the battery currents to decrease to less than their maximum values, and δf_1 and δf_i to increase up to $\delta f_1 = \delta f_2 = 0$. The grid frequency also rises, more power is consumed by the controllable load and the system changes to Mode I.

Control Parameter Design

The first step in the design of the control parameters is to derive a system model capable of describing the dynamic response. The main design parameters are the droop coefficient M_p and the controller parameters used for the voltage and current control (see Fig. 26). Secondary design parameters include the filter constants for the real power and grid frequency (τ_P and τ_f for first-order filters). For reasons of space, this is not addressed herein. However, a detailed small-signal model is available for reference in [19] whilst a flexible parameter design can be consulted in [22].

4.4 Experimental Results

The frequency-based energy management strategy discussed herein was validated through experimental results. Two batteries with their inverters were parallel-connected to generate the AC grid. A load bank and two PV emulators with

their inverters were connected to the grid. The battery and PV inverters are standard off-the-shelf equipment, yet with changes to their configurations in order to make it possible to implement the energy management strategy. Specifically, the droop method put forward by Eq. (70), where δf is obtained from Eq. (72) and Fig. 26, was programmed in the battery inverters whilst the PV power management, represented by Fig. 27, was programmed in the PV inverters. The system features are set out in Table 1 and the parameters M_p, $\Delta f_{\min}$ and $\Delta f_{\max}$ are 0.3, 0.5 and 2 Hz, as shown in Fig. 29. As can be seen, each battery system has different characteristics. Precision power analyser WT1800 was used to obtain the data, recording voltages, currents, powers and frequencies every 50 ms.

The first test conducted aimed to validate the battery voltage control during the change from Mode I–Mode II–Mode III, in a similar fashion to the simulation shown in Fig. 30. Figure 32 presents the experimental results, showing the voltage of battery 1 divided by two, the voltage of battery 2, the maximum voltage for both batteries (Fig. 32a), the battery powers, the load power, the total PV power (Fig. 32b), and the grid frequency (Fig. 32c). The initial battery voltages are lower than their maximum values. Therefore, the battery inverters share the power in line with their ratings ($P_1 = 2 \cdot P_2$), the frequency is close to 50 Hz and the system operates in Mode I. At around second 8, a 2.6 kW load is then disconnected. When

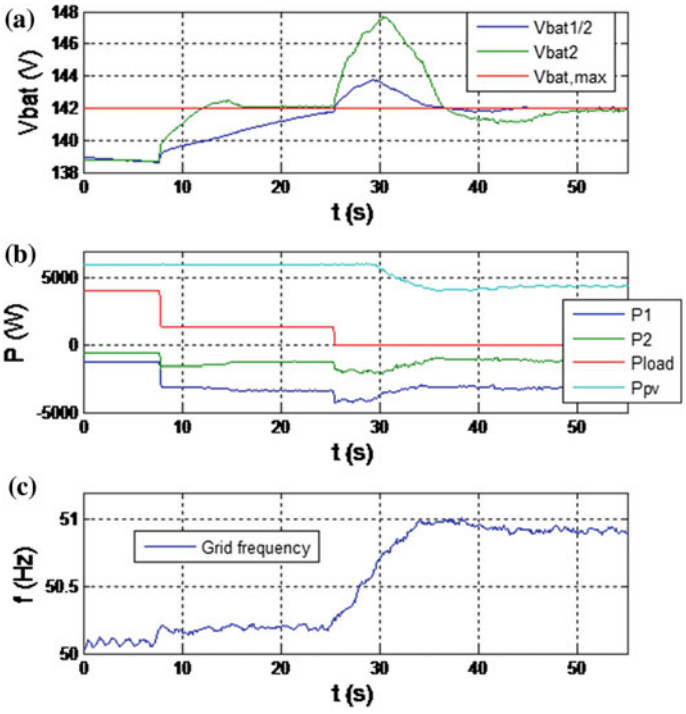

Fig. 32 Voltage control during the change from Mode I–Mode II–Mode III [19]

the voltage of battery 2 goes above its maximum value, the control ensures that the absorbed power shifts from battery 2 to battery 1, so that the voltage of battery 2 is controlled, making the system operate in Mode II. When in this mode, although the grid frequency increases, it does stay below $f_0 + \Delta f_{\min} = 50.5$ Hz due to the fact that there is no need to limit the PV power. Then, at around second 25, a 1.3 kW load is also disconnected, with the subsequent rise in the voltage of both batteries, to above their maximum value. The control therefore increases the grid frequency. Then, once the frequency measured by the PV inverters exceeds 50.5 Hz, the PV power is lowered so that both battery voltages are controlled, causing the system to operate in Mode III. The figure shows how the energy management strategy described succeeds in controlling the input voltage of either one or two batteries as required whilst taking full advantage of the solar energy, yet without the need for communication cables.

The second test aimed to validate the battery current control during the change from Mode I–Mode IV–Stop, in a similar manner to the simulation presented in Fig. 31. Figure 33 show the experimental results for the battery currents, the maximum discharge current for both batteries (Fig. 33a), the load power, the battery powers (Fig. 33b), and the grid frequency (Fig. 33c). Both batteries are assumed to be exceedingly hot, due to unfavourable conditions. To protect the batteries, their maximum current is reduced to $i_{\text{bat,d,max1}} = 20$ A and $i_{\text{bat,}}$

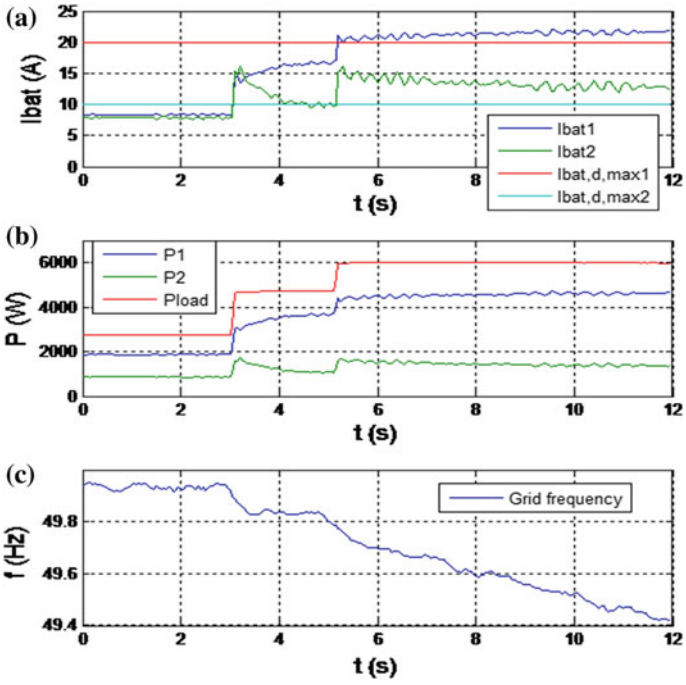

Fig. 33 Current control during the shift from Mode I–Mode IV–Stop [19]

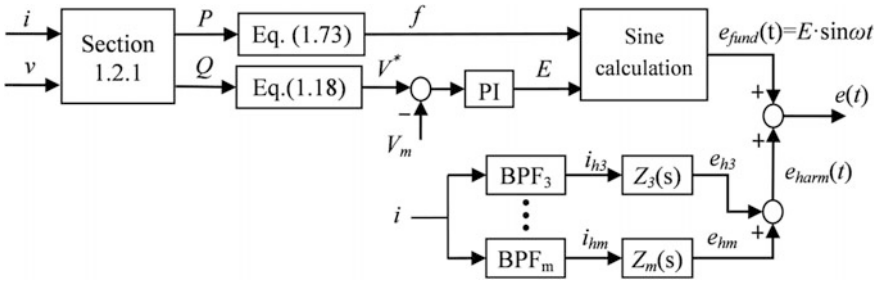

Fig. 34 Implementation of the battery inverter control

$_{d,max2}$ = 10 A. Throughout the test, the PV power stays at 0, and there are no controllable loads. The initial battery currents are under their maximum values. The system therefore operates in Mode 1, the inverters share the load power and the frequency is close to 50 Hz. A 2 kW load is then connected at second 3. The battery 2 current then exceeds 10 A, leading the control to make battery inverter 1 deliver more power so that the current of battery 2 is controlled, leading the system to operate in Mode II. Then, at around second 5, a 1.3 kW load is also connected, with the subsequent rise in the current of both batteries, to above their maximum value. The control therefore decreases the grid frequency. Since there are no controllable loads in this test, the frequency continues to fall until a value of $f_0 - \Delta f_{stop}$ = 49.4 Hz is reached, when the system shuts down in order to protect the batteries. The figure shows how the strategy proposed can either control the current of one battery or stop the system, as required, without the need for communication cables. In addition, it is also possible to configure the value of Δf_{stop} in order to control the overload time, depending on the thermal properties of the system.

5 Summary of the Control for Implementation in a Microgrid

In order to implement the overall energy management strategy in a real stand-alone microgrid, a summary of the different controls is provided in this section. The general scheme of the system was presented in Fig. 24. It is worth noting that each inverter only has information about local variables, on which the control is based.

The implementation of the strategy for the battery inverter is shown in Fig. 34. The real and reactive powers are obtained from the grid voltage and inverter current as described in Sect. 2.1. For the reactive power management, the conventional droop method is used, defined by Eq. (18), where the droop coefficient is obtained from Eq. (20). This control determines the RMS voltage reference V^*, which is in turn regulated by a PI controller, as shown in the figure. On the other hand, the

conventional droop method for real power control, defined by Eqs. (17) and (19), is modified in order to conduct the frequency-based energy management. The regulation of the battery voltage and current is carried out thanks to Eq. (70), where δf is obtained from Eq. (72) and Fig. 26. Equation (70) can be combined with Eq. (59) to balance the SOCs of the distributed battery systems. The combination of both methods represents the overall energy management strategy and can be expressed as

$$f = f_0 - M_p \cdot p + M_S \cdot (\mathrm{SOC} - \mathrm{SOC}_0) + \delta f \tag{73}$$

Since the RMS output voltage E and the frequency are now known, instantaneous voltage e can finally be obtained and modulated, as shown in Fig. 34. In this control there is no inner current loop, and a current protection system must also be implemented.

The regulation summarized so far deals with the fundamental components. However, some additional controls must be added in the presence of nonlinear loads. In this case, the inverter current harmonics are obtained by means of a BPF, and a harmonic voltage compensation is calculated as set out in Sect. 2.5. The harmonic voltage is then added to the fundamental voltage, as shown in Fig. 34.

With regard to the RES converters, these operate under MPPT as long as the frequency deviation is below $\Delta f_{\min}$. Once the frequency exceeds this value, then the renewable power is reduced following the curve shown in Fig. 27. In a similar way, the controllable loads can demand the power required, whenever the frequency deviation is over $-\Delta f_{\min}$, whilst the power consumed must be reduced, based on a similar curve whenever the frequency deviation is below this value.

Acknowledgements This work was supported in part by the Spanish Ministry of Economy and Competitiveness under Grant DPI2013-42853-R.

References

1. Franzitta V, Curto D, Rao D, Viola A. (2016) Renewable energy sources to fulfill the global energy needs of a country: the case study of Malta in Mediterranean Sea. Paper presented at the OCEANS 2016 symposium, pp 1–5, Shanghai, Apr 2016
2. Yang Y, Blaadjerg F (2012) Synchronization in single-phase grid-connected photovoltaic systems under grid faults. Paper presented at the 3rd IEEE international symposium on power electronics for distributed generation systems, pp 476–482, Aalborg, June 2012
3. Gao M, Yang S, Jin C, Ren Z, Chen M, Qian Z (2011) Analysis and experimental validation for power calculation based on p-q theory in single-phase wireless-parallel inverters. Paper presented at the 2011 twenty-sixth annual IEEE applied power electronics conference and exposition, pp 620–624, Fort Worth, Mar 2011
4. Bergen AR (1986) Power systems analysis. Prentice Hall, Englewood Cliffs
5. Guerrero JM, Vicuña LG, Matas J, Castilla M, Miret J (2005) Output impedance design for parallel-connected UPS inverters with wireless load-sharing control. IEEE Trans Industr Electron 52(4):1126–1135 (2005)

6. Urtasun A, Sanchis P, Marroyo L (2014) Comparison of linear and small-signal models for inverter-based microgrids. Paper presented at the 2014 Australasian Universities power engineering conference, pp 1–6, Perth, Sept 2014
7. Urtasun A, Sanchis P, Marroyo L (2015) State-of-charge-based droop control for stand-alone AC supply systems with distributed energy storage. Energy Convers Manage 106:709–720
8. ISO 13297 (2014)
9. Guide to the Wiring Regulations (2008) 17th edition IEE wiring regulations, BS: 7671
10. He J, Li YW, Guerrero JM, Blaadjerg F, Vasquez JC (2013) An islanding microgrid power sharing approach using enhanced virtual impedance control scheme. IEEE Trans Power Electron 28(11):5272–5282 (2013)
11. Ghzaiel W, Ghorbal MJB, Slama-Belkhodja I, Guerrero JM (2013) A novel grid impedance estimation technique based on adaptive virtual resistance control loop applied to distributed generation inverters. Paper presented at the 15th European conference on power electronics and applications, pp 1–10, Lille, Sept 2013
12. Urtasun A, Sanchis P, Marroyo L (2014) RMS voltage control with harmonic compensation for parallel-connected inverters feeding non-linear loads. Paper presented at the 2014 IEEE international symposium on circuits and systems, pp 1179–1182, Melbourne, June 2014
13. Patel H, Agarwal V (2008) Control of a stand-alone inverter-based distributed generation source for voltage regulation and harmonic compensation. IEEE Trans Power Deliv 23(2): 1113–1120 (2008)
14. Guerrero JM, Matas J, Vicuña LG, Castilla M, Miret J (2006) Wireless-control strategy for parallel operation of distributed-generation inverters. IEEE Trans Industr Electron 53(5): 1461–1470 (2006)
15. Lu X, Guerrero JM, Huang L (2012) SoC-based dynamic power sharing method with AC-bus voltage restoration for microgrid applications. Paper presented at the 38th annual conference on IEEE industrial electronics society, pp 5677–5682, Montreal, Oct 2012
16. Guerrero JM, Vasquez JC, Matas J, Vicuña LG, Castilla M (2011) Hierarchical control of droop-controlled ac and dc microgrids—a general approach toward standardization. IEEE Trans Industr Electron 58(1):158–172
17. Ng K, Huang Y, Moo C, Hsieh Y (2009) An enhanced coulomb counting method for estimating state-of-charge and state-of-health of lead-acid batteries. Paper presented at the 31st Telecommunications energy conference, pp 1–5, Incheon, Oct 2009
18. Markvart T, Fragaki A, Ross JN (2006) PV system sizing using observed time series of solar radiation. Sol Energy 80(1):46–50 (2006)
19. Urtasun A, Barrios EL, Sanchis P, Marroyo L (2015) Frequency-based energy-management strategy for stand-alone systems with distributed battery storage. IEEE Trans Power Electron 30(9):4794–4808 (2015)
20. Urtasun A, Sanchis P, Marroyo L (2013) Limiting the power generated by a photovoltaic system. Paper presented at the 10th multi-conference on systems, signals & devices, pp 1–6, Hammamet, Mar 2013
21. Dalala ZM, Zahid ZU, Lai J-S (2013) New overall control strategy for small-scale WECS in MPPT and stall regions with mode transfer control. IEEE Trans Energy Convers 28(4): 1082–1092 (2013)
22. Urtasun A, Barrios EL, Sanchis P, Marroyo L (2015) Frequency-based energy-management of stand-alone systems: design of the control parameters for high versatility. Paper presented at the 41st annual conference of the IEEE industrial electronics society, pp 3341–3346, Yokohama, Nov 2015

Optimal Design and Energy Management of a Hybrid Power Generation System Based on Wind/Tidal/PV Sources: Case Study for the Ouessant French Island

O.H. Mohammed, Y. Amirat, M.E.H. Benbouzid and G. Feld

Abstract Hybrid power generation systems have become a focal point to meet requirements of electric power demand. This kind of system combines several technologies and is considered as one of the appropriate options for supplying electricity in remote areas, such islands, where the electric utility is not available. It is one of the promising approaches due to its high flexibility, high reliability, higher efficiency, and lower costs for the same produced energy by traditional resources. Typically, hybrid power generation systems combine two or more conventional and renewable power sources. They will also incorporate a storage system. This chapter will focus on a typical hybrid power generation system using available renewables near the Ouessant French Island: wind energy, marine energy (tidal current), and PV. This hybrid system is intended to satisfy the island load demand. It will therefore explore optimal economical design and optimal power management of such kind of hybrid systems using different approaches: (1) Cascaded computation (linear programming approach); (2) Genetic algorithms-based approach; (3) Particle swarm optimization. In terms of economical optimization, different constraints (objective functions) will be explored for a given 25 years of lifetime; such as minimizing the Total Net Present Cost (TNPC), minimizing the Levelized Cost of

O.H. Mohammed (✉) · M.E.H. Benbouzid
University of Brest, Institut de Recherche Dupuy de Lôme (FRE CNRS 3744 IRDL),
3, Rue des Archives, 29238 Brest, France
e-mail: Omar-Hazem-Mohammed.Mohammed@univ-brest.fr

M.E.H. Benbouzid
e-mail: Mohamed.Benbouzid@univ-brest.fr

Y. Amirat · G. Feld
ISEN Brest, Institut de Recherche Dupuy de Lôme (FRE CNRS 3744 IRDL),
20, Rue Cuirassé Bretagne, 29200 Brest, France
e-mail: Yassine.Amirat@isen-bretagne.fr

G. Feld
e-mail: Gilles.Feld@isen-bretagne.fr

O.H. Mohammed
North Technical University, Technical College of Mosul, Mosul, Iraq

F.M.R. Islam et al. (eds.), *Smart Energy Grid Design for Island Countries*,
Green Energy and Technology, DOI 10.1007/978-3-319-50197-0_12

Energy (LCE). The concept of reliability will also be explored to evaluate the hybrid system based on renewables to satisfy the island load requirements. In this chapter, the Equivalent Loss Factor (ELF) is considered.

Keywords Hybrid power generation system · Renewable energy · Optimal sizing · Island

1 Introduction

Nowadays, the renewable energy is evolving in the same manner as expansion of energy demand. As conventional plants are reaching the end of their useful lives, they are expected to replace by renewable energy resources and cleaner technology such as wind, solar, tidal, gas, etc. Although renewable energy penetration in electricity is expected to have a spectacular growth in the forthcoming years, it still however has very low participation rate compared to other nonrenewable energies. In addition, it is necessary to integrate the renewable energy technologies into the power grid so as to support it, raising therefore reliability, improving power quality, increasing efficiency, and decreasing fluctuations [1]. Many studies have investigated the potential contribution of renewables to global energy supplies, indicating that in the second half of the twenty-first century their contribution might range from the present figure of nearly 20% to more than 50% with the right policies in place. About 30% contribution to world energy supply from renewable energy sources by year 2020 is reported in [2]. However, integrating those renewable energy resources into the grid is made more complex by a number of issues that are related to intermittent availability of those resources and to the electrical characteristics of the associated generators. To overcome these issues and to enhance the energy system reliability, these generation unit should be working together in two or more sources in the so-called hybrid system concept. Hybrid power station concept is not new, but has gained popularity and rapid development in the recent year. There are many types of hybrid energy systems including renewable and nonrenewable sources that have been considered. Figure 1 summarizes all the possible architectures and combinations including a grid connection. Nevertheless, it is essential that renewable energy hybrid systems to be cost-effective and achieve high reliability to meet the load requirements. Hence, designing a renewables-based hybrid energy system must fulfill different constraints. These constraints can be divided into two categories: The first category is a technical one and encompasses energy sources availability, generation components, battery systems state of charge, and electric load location. The second category is an economical one including reliability, flexibility, efficiency, and costs.

Various literature [3–5], has demonstrated that hybrid renewable electrical systems in off-grid applications are cheaply feasible in isolated areas. Moreover, environment can make a topology of hybrid system more efficient than another one.

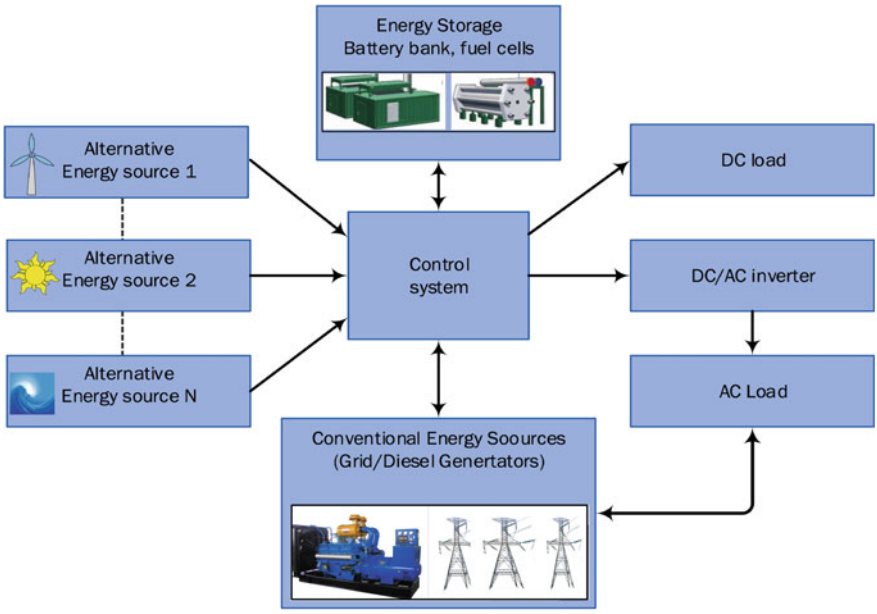

Fig. 1 Hybrid generation systems general architecture

For example, a hybrid system (Wind/Diesel/Battery) is ideal in areas where there are substantial wind resources rates all over the year [6]; since a photovoltaic hybrid system (Photovoltaic/Diesel/Battery) is perfect in areas with significant solar radiation. Hybrid renewable power generation systems optimal design is a very challenging task as far as most renewable energy resources are random and weather/climatic conditions-dependent. Figure 2 illustrates the general process of a hybrid generation system optimization. For that purpose, different techniques and various mathematical models have been used to design hybrid systems so as to reach various goals and get the optimization, such as particle swarm optimization technique (PSO), genetic algorithms (GA), fuzzy algorithms, cascade analysis, artificial neural network, etc. [7].

This chapter will focus on a typical hybrid power generation system using available renewables near the Ouessant French Island: wind energy, marine energy (tidal current), and PV as illustrated by Fig. 3. This hybrid power generation system is intended to satisfy the island load demand illustrated by Fig. 4. It will therefore explore optimal economical design and optimal power management of such kind of hybrid systems using different approaches: (1) Cascaded computation (linear programming approach); (2) Genetic algorithms-based approach; (3) Particle swarm optimization. In terms of economical optimization, different constraints (objective functions) will be explored for a given 25 years of lifetime; such as minimizing the Total Net Present Cost (TNPC), minimizing the Levelized Cost of Energy (LCE), etc. The concept of reliability will also be explored to evaluate the hybrid system ability to satisfy the island load requirements. In this chapter, the Equivalent Loss

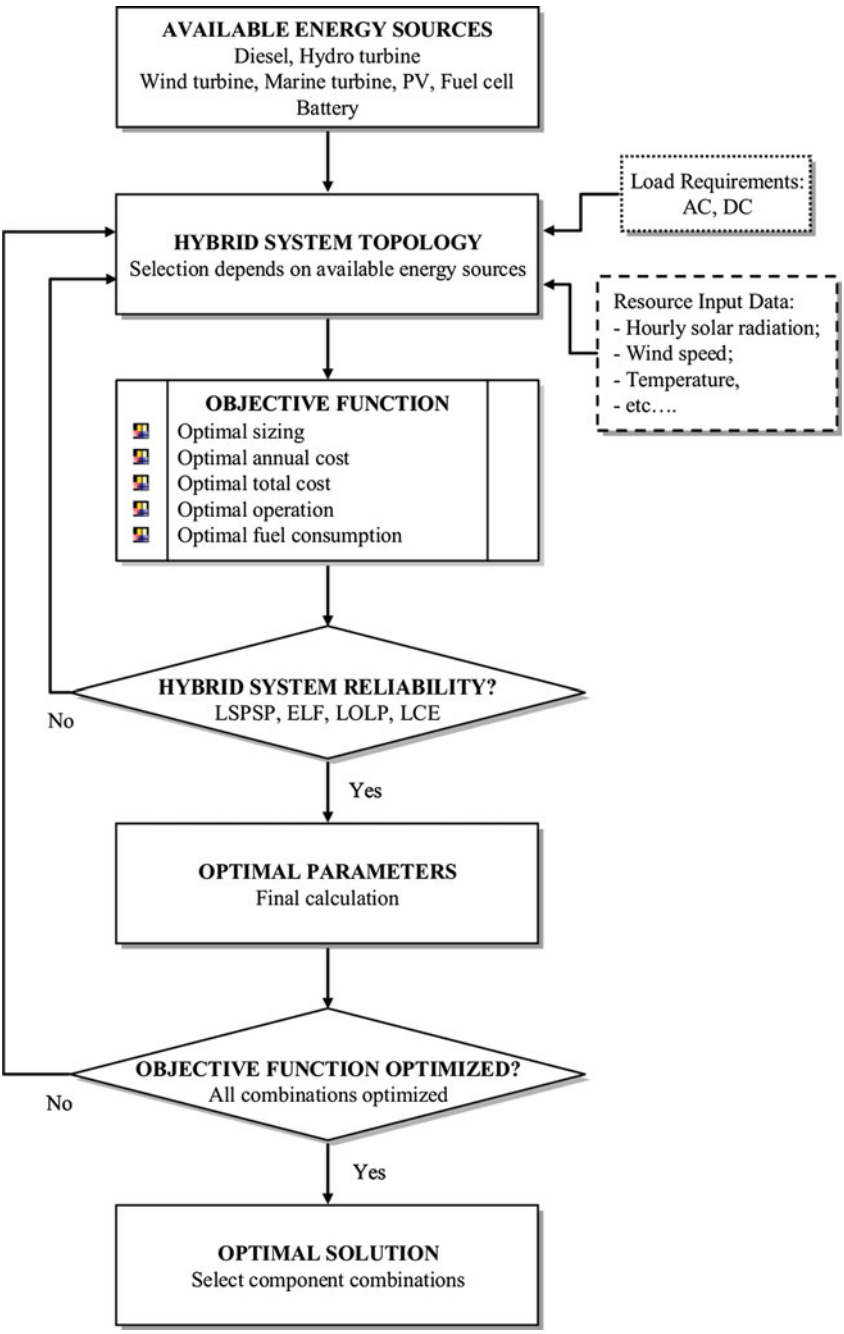

Fig. 2 Hybrid generation system optimization general model [10]

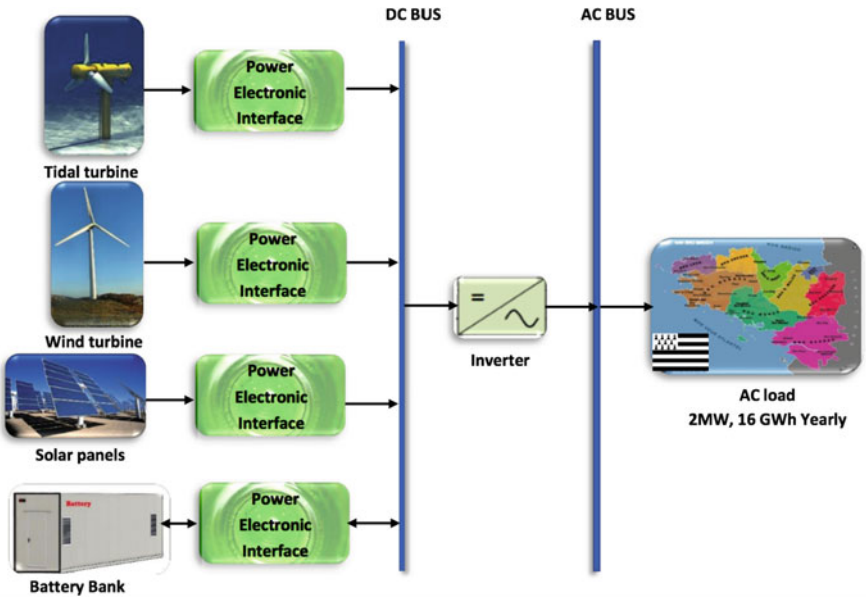

Fig. 3 Configuration of hybrid Wind/tidal/PV/battery stand-alone energy system

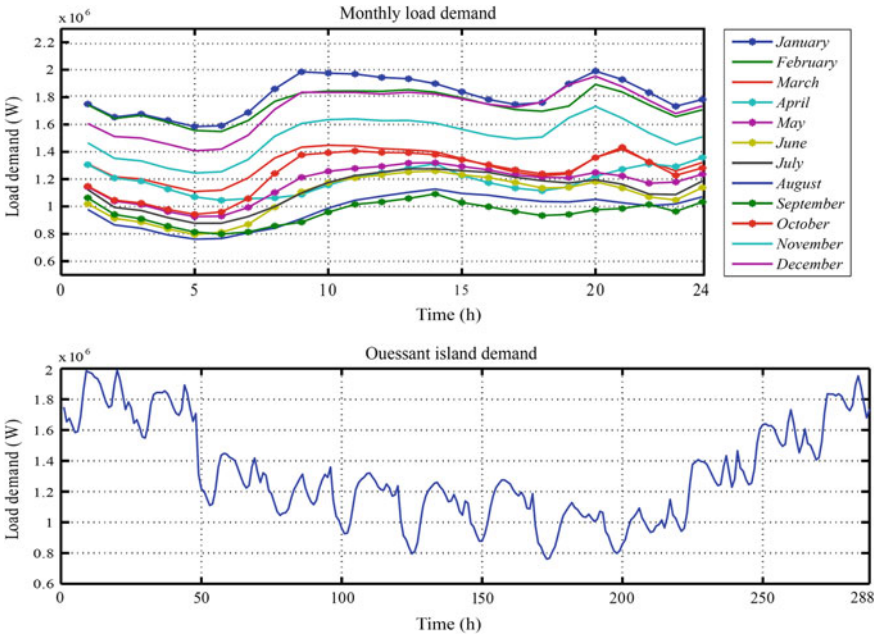

Fig. 4 Ouessant Island load demand

Factor (ELF) is considered. This approach can be extended with no a priori to any islanded or off-grid sites. It should be mentioned that previous studies have already attempted to address islands typical issue of energy management using marine renewable energies [8, 9].

2 Design, Analysis, and Optimization Software Tools for Hybrid Generation Systems

In the existing literature, there are various software and design tools to evaluate and to optimize hybrid energy systems. Each of these available softwares and tools has their specific advantages and drawbacks. This section is therefore is devoted to briefly present the most commonly used software for hybrid energy systems design and optimization.

2.1 RETScreen

RETScreen is a free clean energy management software system for co-generation project feasibility analysis, and energy performance evaluation. The Ministry of Environment of Canada has released it. The first version was introduced for on-grid applications, the RETScreen PV model was currently upgraded to deal with off-grid applications. These include stand-alone, hybrid and water pumping systems. The software guides the users in the design of their systems, by giving initial estimates of an array, battery, or pump size. By modifying few of the system parameters, users have the ability to quickly screen the most helpful technology and system size depending upon the load, weather conditions, and season of use. It has capabilities for evaluating both financial and environmental costs, assists in the decision, determine, and make the most of the advantages of renewable energy technologies for any location around the world [11–13]. RETScreen has several worksheet for carrying out detailed project analysis, including energy modeling, cost analysis, emission analysis, financial analysis and sensitivity and risk analyzes sheets. It has a global climate data database of over 6000 ground stations (month wise solar irradiation and temperature data for the year), hydrology data, energy resource maps (such as wind maps), product data like solar photovoltaic panel information and wind turbine power curves. It also offers a link to the climate database of NASA. it is used for the analysis of various types of energy-efficient and renewable technologies (RETS) dealing with mainly energy production, life-cycle costs, and greenhouse gas emission reduction. RETScreen Plus is based upon an energy management software tool to study the energy performance.

The main limitations of RETScreen are: it does not consider the effect of temperature on PV performance analysis, the data sharing problem, limited options for search and sensitivity analysis, no possibility of time series data files and import

retrieval, does not support more advanced estimations and visualization features [12, 14].

2.2 LEAP

LEAP (Long Range Energy Alternatives Planning) was developed at the Stockholm Environment Institute in 2008. It is a widely used software tool for the analysis of energy policy and evaluation of the impact of climate change. It includes a scenario manager that can be used to describe individual measures. It allows investigating the economic potential for energy performance and low emission development strategies to reduce gas emission as CO_2. It is mainly used to analyze national energy systems. It uses a yearly time step and time horizon may extend over a number of years (usually between 20 and 50 years). However, neither optimization nor controls are possible [15, 16].

2.3 HYSIM

HYSIM is a hybrid energy simulation model produced by Sandia National Laboratory of the US DOE. It is used for evaluating stand-alone off-grid hybrid systems consisting in PV panels, Diesel generators and battery storage combination with system reliability in 31 remote locations. The objective of this model was to look at increasing overall system reliability by adding PV and battery storage, in addition to financial analysis that LCOE, life-cycle, fuel cost, operation and maintenance costs. HYSIM appears to have been used up until 1996 [17, 18].

2.4 iHOGA

iHOGA (Improved Hybrid Optimization by Genetic Algorithms) is a software formerly known as HOGA (Hybrid Optimization by Genetic Algorithm), developed for the simulation and optimization of hybrid renewable energy systems. It has been developed at the University of Zaragoza (Spain) [19–21]. It is a single-purpose or multi-optimization software target hybrid renewable energy systems. It uses genetic algorithms to optimize the control strategies of hybrid systems consisting in PV panels, wind turbines, Diesel generators, batteries, hydraulic turbines, H_2 tanks, electrolyzers, fuel cells, rectifiers, and inverters. The simulation is performed using one-hour intervals, during which all parameters remain constant. Optimization is obtained by minimizing the total cost of the system throughout its lifetime. However, this software allows for multi-objective optimization, where additional variables can also be minimized, such as the equivalent CO_2 emissions or unmet load (energy not served). Since all these variables (costs, emissions or unmet load) are mutually against-productive in many cases,

more than one solution is provided. Some of these solutions show better performance when applied to emissions or unmet load while other solutions are better suited for costs. It is used for controlling system components. Indeed, the command with iHOGA is limited to energy flow management strategies [12, 21, 22].

2.5 ARES

ARES (Autonomous Renewable Energy Systems) is a software designed by the Cardiff school of engineering (UK). It is applied to simulate PV/Wind hybrid systems with battery storage [20, 23]. This software can calculate the system loss of load possibility and system autonomy by the prediction of the storage battery voltage if input load and essential weather profile are provided.

2.6 SOMES

The University of Utrecht (NL) developed SOMES (Simulation and Optimization Model for renewable Energy Systems). It is intended to simulate and to analyze the operation of a PV/Wind/Diesel hybrid system with batteries for storage. It allows economic analysis optimization of projects but it does not provide control systems. Optimal operating strategies and criteria for starting and stopping the Diesel generator are provided by the user [24, 25].

2.7 RAPSIM

RAPSIM (Remote Area Power Supply Simulator) is a windows-based software package developed by the Murdoch, University Energy Research Institute in Australia. It is intended to simulate PV arrays—wind turbines—Diesel generators with battery storage. It allows the user to select a hybrid system (PV and/or wind and/or Diesel), to simulate and calculate the total cost [12, 23, 26].

2.8 HOMER

HOMER (Hybrid Optimization Model for Electric Renewables) is the most commonly used software. It has developed by the National Renewable Energy Laboratory (USA). It is designed for both on- and off-grid systems and it is appropriate for carrying out fast pre-feasibility, optimization, and sensitivity analysis in multiple possible system configurations. HOMER has been used extensively

in the literature for hybrid renewable energy system optimization and different case studies [27, 28]. It will be particularly exploited in this study for comparative purposes.

3 Hybrid Power Generation System Model

The aim of modeling is to formulate a general model to evaluate the total investment depending on the location, renewable resources opportunities, and the load demand. For this purpose a macroscopic modeling of a stand-alone hybrid power generation system consisting of wind turbine generator (WTG), photovoltaic (PV) panels, tidal turbine generators (TTG) and storage batteries (SB) and other devices to feed a load demand is presented.

3.1 Wind Turbine Model

The wind turbine extracted obtained power depends on the power curve given by the manufacturer and also on the height of turbine h, and the roughness of the land surface. The available power at the front end of the wind energy conversion system is expressed by Eq. (1)

$$P_w = \frac{1}{2} \times \rho \times C_{\mathrm{p}} \times \pi \times R^2 \times v^3 \times \eta_w \tag{1}$$

where η_w is the wind turbine efficiency (assumed to be 90% in this study), R is the blades radius, ρ is the air density, C_{p} the power coefficient, and v is the wind speed. The relationship between available output power $P_w(t)$ and wind speed can be approximated by Eq. (2).

$$P_w = \begin{cases} 0; & v < v_{\mathrm{cutin}}, v > v_{\mathrm{cutout}} \\ P_{w\max} \times \frac{v - v_{\mathrm{cutin}}}{v_{\mathrm{rated}} - v_{\mathrm{cutin}}}; & v_{\mathrm{cutin}} < v < v_{\mathrm{rated}} \\ P_{w\max}; & v_{\mathrm{rated}} \leq v \leq v_{\mathrm{cutout}} \end{cases} \tag{2}$$

Table 1 Wind turbine parameters

Cut-in speed, v_{cutin}	5 m/s
Cut-out speed, v_{cutout}	25 m/s
Rated speed, v	15 m/s
The maximum output power, $P_{w\max}$	2300 kW
Swept area	3959 m^2
Number of blades	3
Rotor diameter	71 m
Hub height	57/64/85/98/113 m

where P_{wmax} is the maximum output power. $v, v_{cutin}, v_{rated}, v_{cutout}$ are the wind turbine cut-in, cut-out, and rated speed, respectively. The ENERCON E-70 wind turbine is used. Some of its parameters are described in Table 1 [29–32].

The height of the wind turbine tower is a very important factor significantly influencing the operating performance of the turbine. It may also be more than half of the wind turbine system cost. To adjust the measured wind speed to the hub height, Eq. (3) is used.

$$v(t) = v_r(t).\left(\frac{h}{h_r}\right)^{\gamma} \tag{3}$$

where v is the wind speed at the desired height h, v_r is the wind speed measured at a known reference height h_r, the power law exponent γ is a factor that depends on the roughness of the terrain. For this study this factor is set 0.2 [27, 33].

Figure 5 illustrates wind speeds of the considered island and wind turbine power production at different hub heights.

3.2 Photovoltaic Array Model

The output power of a PV module depends on the surface of semiconductors exposed to solar radiation, the tiled surfaces of the PV module, the ambient temperature, and the characteristics of the PV cells under industrial standard test conditions of solar radiation [34]. The output power P_{pv} can therefore be calculated by Eq. (4) [35, 36].

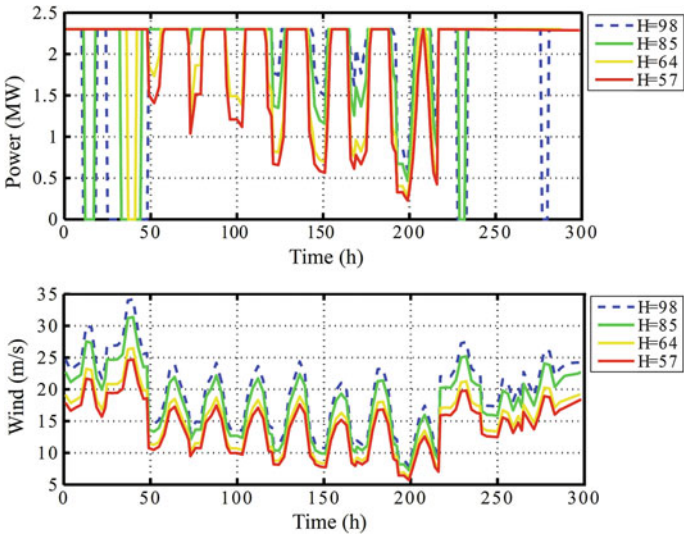

Fig. 5 Wind speed and power production at different hub heights

$$P_{\text{pv}} = N_{\text{pv}} \times \eta_{\text{pv}} \times A_m \times G_t \tag{4}$$

where η_{pv} is the instantaneous PV module generator efficiency, N_{pv} is the number of modules, A_m is the area of a single module used in a system and G_t is the global incident irradiance on the titled plane. In this analysis, each PV module has a rated power of 285 W.

Figure 6 illustrates monthly solar radiation close to the considered island and the generated power in one PV module.

3.3 Tidal Current Turbine Model

The output power of a tidal current turbine system P_{tid} has a similar dependence as a wind turbine and is expressed by Eq. (5).

$$P_{\text{tid}} = \frac{1}{2} \times N_{\text{tid}} \times \eta_{\text{tid}} \times C_{\text{p}}(\beta, \lambda) \times \rho_t \times A \times V^3 \tag{5}$$

where N_{tid} the total number of current turbines, η_{tid} is the efficiency of the tidal turbine is selected according to tidal current characteristics, ρ_t is the seawater density, A is the cross sectional area of the tidal turbine rotor, V is the tidal current velocity, C_{p} is the turbine power coefficient and is estimated to be in the range of (0.35–0.5) [37, 38]. For the considered system, the pitch has a fixed value, thus, the power coefficient depends only on the tip speed ratio λ, defined by Eq. (6).

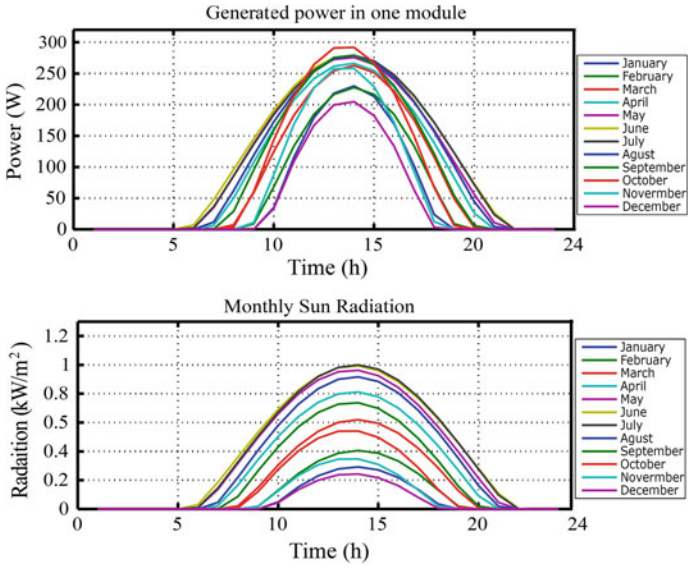

Fig. 6 Monthly solar radiation input data with power production

$$\begin{cases} \lambda = \frac{R_h \times \omega_h}{v_h} \\ \lambda_{ih} = \frac{1}{\frac{1}{\lambda} - 0.003} \\ C_{\mathrm{p}}(\lambda) = 0.73 \times \left(\frac{151}{\lambda_{ih}} - 13.2\right) \times \mathrm{e}^{-\frac{18.4}{\lambda_{ih}}} \end{cases} \tag{6}$$

where R_h is the tidal turbine rotor radius and ω_h is the rotor mechanical rotational speed. The maximum C_{p} value is 0.44, which corresponds to a tip speed ratio of 7.59. This value is considered as the optimal one (λ_{opt}) to achieve maximum power point tracking (MPPT) under rated tidal current speeds. The turbine maximum speed to follow (MPPT) is 25 rpm (2.1 rad/s) for a tidal current of 2.25 m/s. When the marine current exceeds 2.25 m/s, the extracted power will be limited by control strategies. The extracted power for different tidal current speeds is calculated by (5). A typical 500 kW direct-driven turbine is considered and the corresponding characteristics described in Table 2 [39]. Figure 7 illustrates typical tidal speed near the considered island and power generated by one marine turbine.

Table 2 Tidal turbine parameters

Cut-in tidal speed	v_{cutintid}	<1(m/s)
Rated tidal speed	v_{ratedtid}	2.25 m/s
Cross-sectional area of turbine	A	201.06 m^2
Power coefficient	C_{p}	0.44
Cut-out tidal speed	v_{cutoutid}	>5 m/s

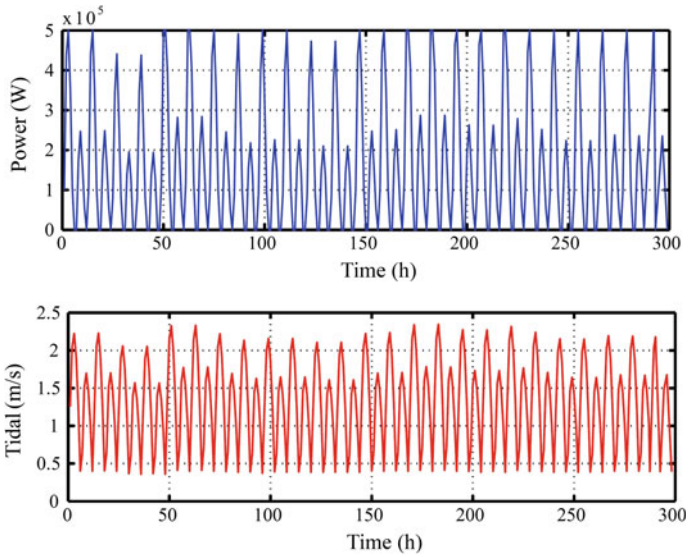

Fig. 7 Tidal speed and power production by one turbine

3.4 Storage Batteries Model

Storage batteries are used to store the energy surplus generated by the hybrid power generation system. They are also used to supply the load during low generation or deficit period. The battery state is related to the previous state of charge and to the system energy flow from $t - \Delta t$ to t. The battery capacity mainly depends on the load energy during the day and the period required for supplying the load from the battery bank in case of energy deficit. In all cases, the storage battery capacity (state of charge) is subject to the following constraint as shown in Eq. (7).

$$\mathrm{SOC}_{\min} \leq \mathrm{SOC}_t \leq \mathrm{SOC}_{\max} \tag{7}$$

where SOC(t) is the state of charge at time t, $\mathrm{SOC}_{\min}$ is the minimum value of battery state of charge, $\mathrm{SOC}_{\max}$ is the maximum value of battery state of charge. The battery SOC can be considered as the balance between the powers absorbed and generated every hour. The power generated by the hybrid power generation system PGH_t, at any time t, can be expressed using Eq. (8).

$$\mathrm{PGH}_t = P_{\mathrm{pv}_t} + P_{w_t} + P_{\mathrm{tid}_t} \tag{8}$$

Energy from batteries is required when the power generated by hybrid renewable system is unable to satisfy the load demand during time t. Furthermore, the energy is stored in the batteries whenever the supply from tidal turbine, wind turbines or *PV* panels exceeds the load demand. At any time, the state of charge of batteries SOC_t is related to the previous state of charge $\mathrm{SOC}_{t-\Delta t}$ and the energy flow between batteries and other sources during time lapse from $t - \Delta t$ to t. Therefore two cases are considered in expressing the energy stored in the batteries at time t.

- ***Case 1***: During charging, if the total output by other sources exceeds the load demand, the SOC_t is given by Eq. (9).

$$\mathrm{SOC}_t = \mathrm{SOC}_{t-\Delta t} + (\mathrm{PGH}_t - \mathrm{PL}_t) \tag{9}$$

- ***Case 2***: When the load demand is equal or greater than the available generated power, the batteries will then be discharged to cover this deficit, and the SOC_t will be given by Eq. (10).

$$\mathrm{SOC}_t = \mathrm{SOC}_{t-\Delta t} - (\mathrm{PGH}_t - \mathrm{PL}_t) \tag{10}$$

The $\mathrm{SOC}_{\max}$ is 1, and the $\mathrm{SOC}_{\min}$ is determined as expressed in Eq. (11).

$$\mathrm{SOC}_{\min} = 1 - \mathrm{DOD} \tag{11}$$

where DOD is the depth of discharge. As its maximum is considered 80%, $\mathrm{SOC}_{\min}$ is 20%.

3.5 Load Model

The number of electric power sources of the hybrid renewable system is determined by the electric load demand. The load profile of the considered island remote site is given in Fig. 4. The maximum load demand is 16 GWh/year with a pick demand of 2 MW, which usually happens in January.

3.6 Reliability Index

The concept of reliability index is extremely broad. It covers the system ability to satisfy the load requirement. There are several indicators in the reliability evaluation of a hybrid power generation system. Those indicators are the Loss of Load Expected (LOLE), the Loss of Energy Expected (LOEE) or the Expected Energy Not Supplied (EENS), the Loss of Power Supply Probability (LPSP), and the Equivalent Loss Factor (ELF). In this study, the ELF is considered in evaluating the proposed topology reliability. At each year time step, it should be calculated using Eq. (12).

$$\mathrm{ELF} = \frac{1}{H}\sum_{h=1}^{H}\frac{Q(h)}{D(h)} \tag{12}$$

where is H, is the total number of step time, $D(h)$ is the total energy demand, $Q(h)$ is the loss of load. The ELF contains information about both the number of outages and their magnitude, and in most cases it should be less than 0.01 [1].

4 Optimal Sizing Strategies

The most used strategies to size and design a hybrid power generation system based on renewable aim to select the optimal number of renewable energies converters, such as WTG, PV panels, TTG, and SB. Optimal sizing is achieved according to: (1) Renewables resources availability; (2) Equipment's costs and O&M services; (3) Maximum energy capacity for the load. It should be mentioned that a previous study has already dealt with a comparison of some optimal sizing approaches of hybrid renewable energy systems [10].

4.1 Cascade Algorithm

This algorithm is an optimized linear programming based on a cascade calculation. First, the main renewable energy source device feeds the main electric load, therefore calculating it optimal. After that, the energy shortfall is considered as a

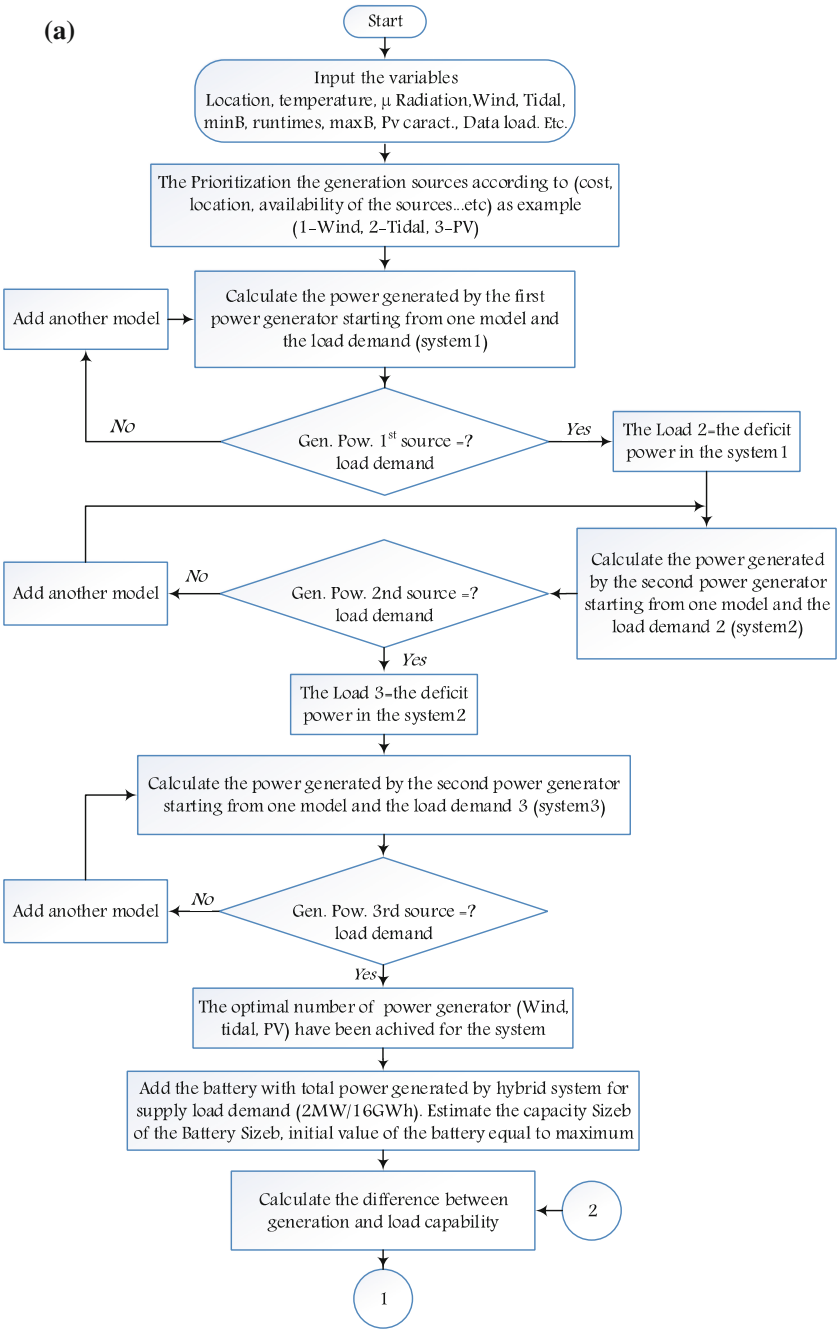

Fig. 8 Flowchart of the cascade algorithm

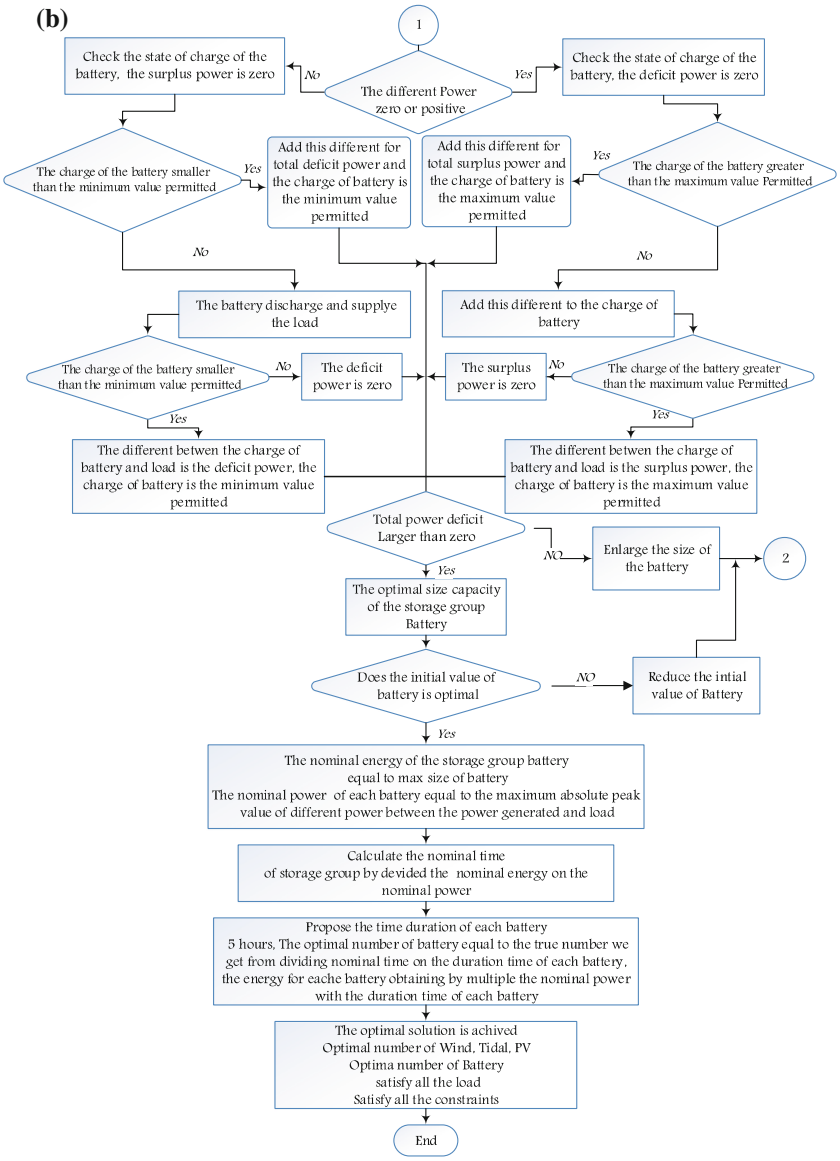

Fig. 8 (continued)

load demand for the consecutive renewable energy source (for optimal number of power generators devices), and so on for the next renewable energy source device as illustrated by the flowchart of Fig. 8.

Conducting energy balance calculations and ensuring high reliability of the system develop this approach. It also maintains the battery SOC between the minimum and

maximum values and ensures that this value remains equal or greater than the initial value of SOC the battery at the beginning of the year. It simulates different scenarios to obtain the optimal number of renewable sources available (wind, solar, tidal, and battery) for supplying the load considering a minimum cost, satisfying constraints such as the battery state of charge, limited operation times, and the assumption that no interruption in power supply occurs with a system reliability of 100%. To assess these algorithm different scenarios were carried out as follow.

- ***Scenario 1***: One of the available sources, wind, tidal, or PV is considered with battery regardless the system operating hours.
- ***Scenario 2***: It is the same as scenario 1 except of taking into consideration the determinant daily WTG and TTG working times. This scenario is used in a case of presence of residential areas close to the hybrid power generation system. This allows reducing the noise caused by wind turbine blades rotation.
- ***Scenario 3***: In this case, more than one renewable resource is available. The daily working time is also considered. In this scenario, a particular attention is paid to the priority order of renewable resources. The user selects the first renewable resource, and the algorithm determines its optimal number and reuses it as an entry of the cascade calculation.

4.2 Cascade Algorithm Optimization Results

The cascaded algorithm is implemented and applied to design and to optimally size the hybrid power generation feeding Ouessant Island (AC load—2 MW, 16 GWh/year). Simulation input data consists in the annual wind speed profile, the annual tidal current speed profile, and the hourly data of the solar radiation. The estimated power production for each resource is illustrated in Figs. 5, 6, and 7 [40].

For ***scenario 1***, a stand-alone system is considered including only one renewable resource wind, or tidal, or PV with storage batteries system, and with full-time operating hours. Results of the sizing of each component are detailed in Table 3. For this case, Fig. 9a depicts the difference between the total generated power and the load demand, the total generated energy, and the storage batteries energy variations for one year. For ***scenario 2***, the stand-alone hybrid power generation system also includes only one renewable resource wind, or tidal, or PV with a storage batteries system, and a constraint of reduced operation working time. Sizing results are presented in Table 3B. Figure 9b illustrates the difference between the generated power and load demand, the total generated energy, and the storage batteries energy variations for one year. For ***Scenario 3***, it is assumed that more than one renewable resource is available. The hybrid power generation system can be a collection of WTG, TTG, PV panels, and a storage batteries system. The constraints of renewable resource priority order and the reduced operation working time are also imposed. Sizing results are given in Table 3C, while the difference

Table 3 Optimal hybrid power generation system configurations

N_{wind}	N_{tidal}	N_{pv}	Number and sizes of batteries		Initial SOC%	Final SOC%
A: Scenario 1						
1	0	0	3	1.024 MW, 5.120 MWh	22	85
			9	340 kW, 1.71 MWh		
0	9	0	6	3 MW, 15 MWh	53	58
			18	1.0 MW, 5.0 MWh		
0	0	16,743	10	3.35 MW, 16.7 MWh	53.8	55
			30	1.12 MW, 5.58 MWh		
B: Scenario 2						
3	0	0	3	4.92 MW, 24.6 MWh	51	55
			9	1.64 MW, 8.2 MWh		
0	10	0	4	3.44 MW, 17.2 MWh	53	58
			12	1.15 MW, 5.73 MWh		
C: Scenario 3						
3	4	5829	1	9.3 MW, 46.5 MWh	40	42
			3	3.1 MW, 15.5 MWh		

between the total generated power and load demand, the total generated energy, and the storage batteries energy variations are illustrated in Fig. 9c for one year.

4.3 Genetic Algorithm

A genetic algorithm (GA) represents a heuristic search strategy based on the evolutionary ideas of natural selection, and genetics as crossing and mutation. GAs are usually used to solve optimization problems by exploitation random searches with many possible solutions in parallel and uses GA operators instead of deterministic ones. A GA does not need other auxiliary knowledge, except fitness functions or objective function. It is being able to find the global optimal solution that is difficult to approach with other techniques in multidimensional search area [41]. In this study, GAs are applied to searches for configurations of wind turbines, tidal turbines, PV panels, and storages batteries that minimize the hybrid system TNPC with respect to all constraints. Figure 10 depicts the flowchart of genetic algorithm-based optimization.

In this algorithm, in the first step, a set of initial populations (chromosomes) is randomly generated from the ranges of possible solutions. Each chromosome is configured and controlled in order to be an optimal solution for the hybrid power system. The choice of the best chromosome representation in genetic algorithms depends upon the variables of the optimization problem being solved, where the chromosome is a combination of vector of variables and each gene represents one component parameters of the renewable system and must be an optimum number as shown in Fig. 11. Then the fitness function is evaluated for each chromosome,

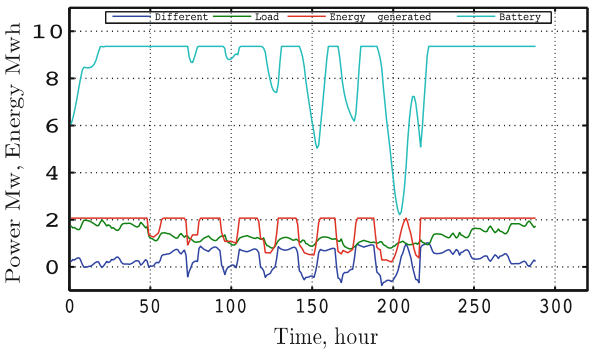

(a) Scenario 1.

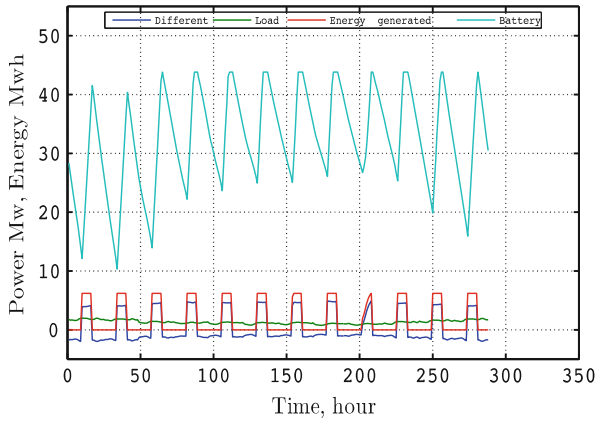

(b) Scenario 2.

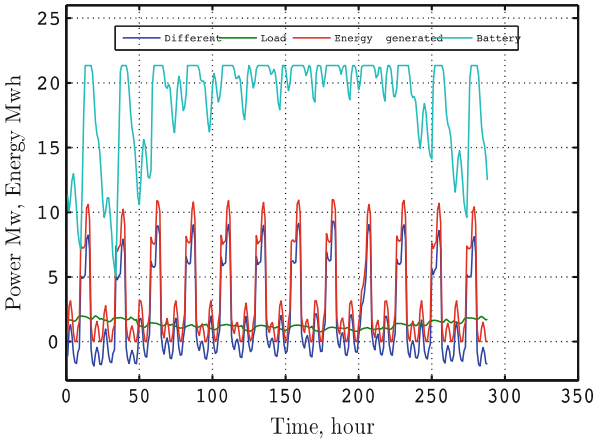

(c) Scenario 3.

Fig. 9 Optimal sizing results of the hybrid power generation systems

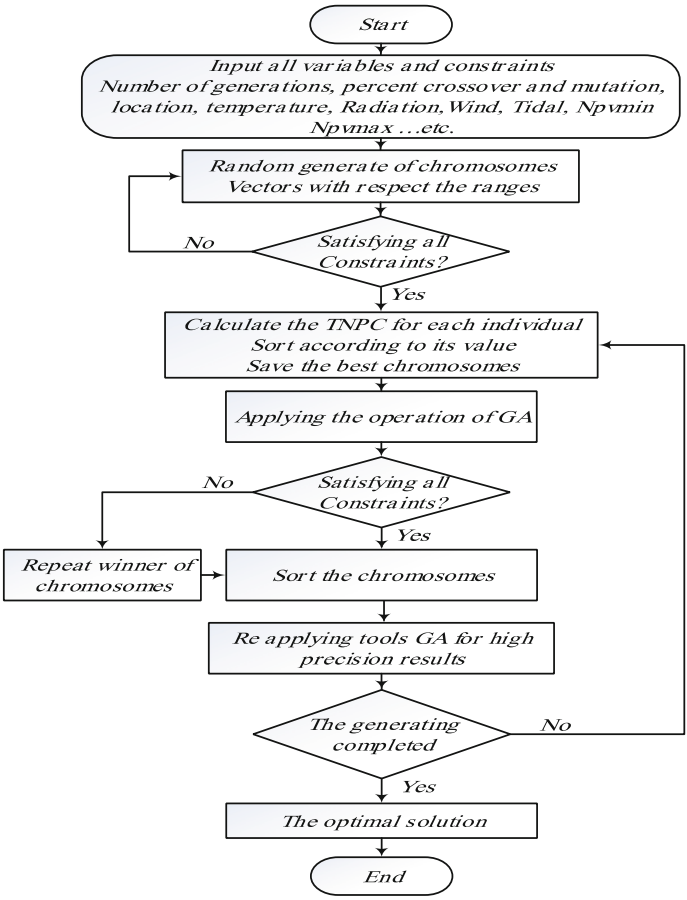

Fig. 10 Flowchart of genetic algorithm-based optimization

where chromosomes that meet all the constraints are selected and arranged according to values from the best to the worst, while others are ignored, as they do not meet constraints. After that, main operations of the genetic algorithms are applied to chromosomes. They consist in selection, crossover, and mutation, at each time. New generations are evaluated and sorted in order of preference, ensuring that restrictions were investigated, keeping best chromosomes in every generation.

In this work, at the first generation, random 100 chromosomes were generated according to ranges of each component. Dividing the chromosomes equally into two groups of parents in each time performs the crossover operation. Application of the crossover process between 1st parent (n) with 2nd parent ($n + 50$) is random and depends on the probability of crossover P_c. Before performing crossover, a single random crossover point on both parents chromosome strings (hybrid components) is selected.

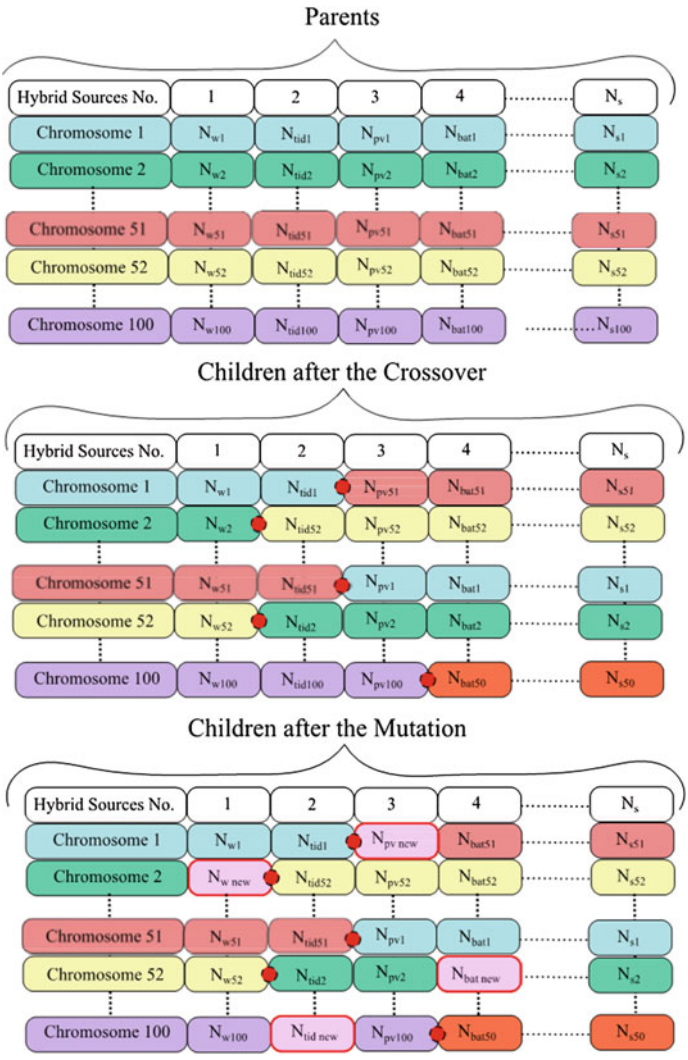

Fig. 11 Hybrid energy systems codification in chromosomes for one generation

All data beyond that point in either chromosome string is swapped between the two parent chromosomes. The resulting chromosome represents new children. As example, for a crossover between two parents when the randomized crossover point is 2, we can see the following new children.

Parent1	N_{wind1}	N_{tid1}	N_{pv1}	N_{bat1}
Parent2	N_{wind51}	N_{tid51}	N_{pv51}	N_{bat51}

Child1	N_{wind1}	N_{tid1}	N_{pv51}	N_{bat51}
Child2	N_{wind51}	N_{tid51}	N_{pv1}	N_{bat1}

The mutation operation depends on the probability called the probability of mutation P_{m}. There are several methods of mutation as the Flip Bit method, the boundary method, the non-uniform method, the uniform method, and finally the Gaussian method. In this work, the uniform mutation operation method has been applied, where the operator replaces the value of the chosen gene to a uniform random value chosen between the user-defined upper and lower bounds for that gene as the following example: The boundary of the components for the new genes are defined as follows:

Wind turbines numbers:

$$N_{\text{wind}_{\text{min}}} \leq N_{\text{wind}_{\text{new}}} \leq N_{\text{wind}_{\text{max}}}$$

Tidal turbine numbers:

$$N_{\text{tid}_{\text{min}}} \leq N_{\text{tid}_{\text{new}}} \leq N_{\text{tid}_{\text{max}}}$$

PV panels numbers:

$$N_{\text{pv}_{\text{min}}} \leq N_{\text{pv}_{\text{new}}} \leq N_{\text{pv}_{\text{max}}}$$

Batteries numbers:

$$N_{\text{bat}_{\text{min}}} \leq N_{\text{bat}_{\text{new}}} \leq N_{\text{bat}_{\text{max}}}$$

When mutation is applied in this chromosome in random gene as gene 3, we can see the new children as follows:

Parent1	N_{wind1}	N_{tid1}	N_{pv1}	N_{bat1}

Child1	N_{wind1}	N_{tid1}	N_{pvn}	N_{bat1}

Crossover and mutation processes can also be seen in Fig. 11. It is important to mention that to get to the optimal result, there are 1000 created generations. In each generation there are 100 generated chromosomes. The scattered crossover function is 80% of the total crossover operation, while the probability proportion of mutation function is 20% of the mutation operation. The initial applied classical GA algorithm has been improved considering genes within winner chromosomes to accelerate the convergence process to the optimal result. The proposed strategy is able to frequently modify chromosomes, where, over subsequent generations, the population develops toward the optimal solution. While giving flexibility in the

choice of system components, the economic issue has been taken into account considering the TNPC minimization.

4.4 Genetic Algorithm Optimization Results

The classical then the enhanced genetic algorithms have been applied to design and to optimally size the hybrid power generation feeding Ouessant Island (AC load—2 MW, 16 GWh/year). Table 4 summarizes the optimal sizing results (most recommended chromosomes). The main conclusion that could be drawn from these results is that a hybrid system based on wind and battery seems to be the best compromise in terms of cost (TNPC). Indeed, Bretagne region in France has favorable wind conditions. Conversely, a hybrid system based on PV and battery is clearly not an interesting solution mainly due to the region low temperatures and solar radiation. It is important to mention that the achieved results are almost specific the studied Ouessant Island and could not be generalized. Figures 12 and 13 illustrate the energy management balance in the proposed hybrid power generation for two scenarios.

Table 4 Optimization results using GA algorithm

N_{wind}	N_{tidal}	N_{pv}	Battery size (MWh)	TNPC (M$)	COE ($/MWh)
2	0	0	0.59	3.48	94.2
1	1	0	7.57	4.52	122.1
1	1	459	7.22	4.71	127.2
0	6	0	8.94	9.80	264.7
0	5	6819	11.17	12.33	333.1
0	0	19,998	12.94	28.27	763.7

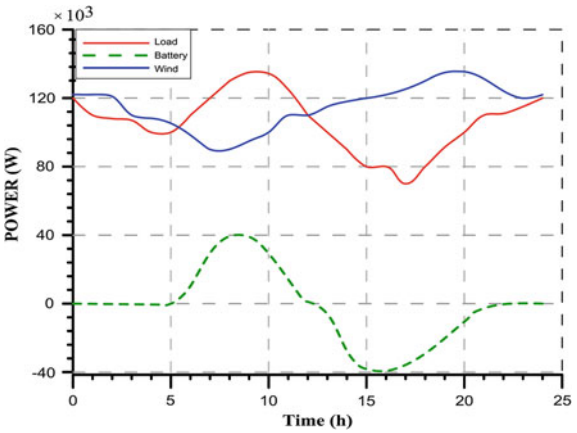

Fig. 12 Hybrid system powers variation in a day (scenario 1)

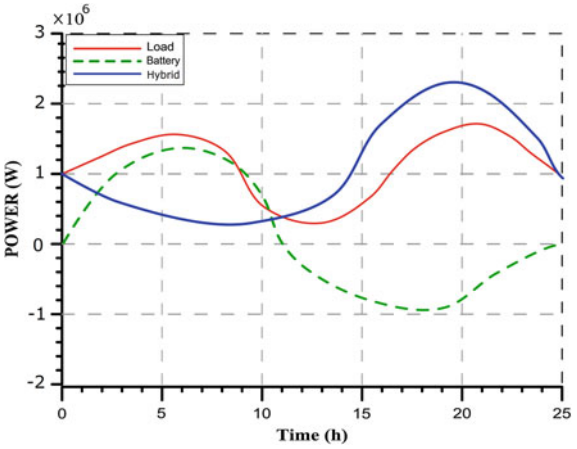

Fig. 13 Hybrid system powers variation in a day (scenario 2)

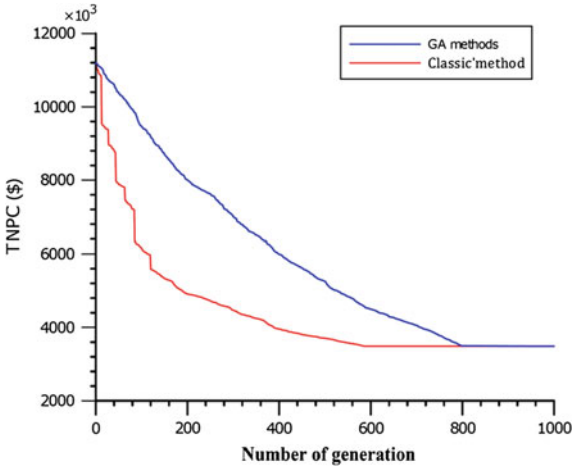

Fig. 14 Genetic algorithm methods convergence

Scenario 1: It represents the optimal system.

Scenario 2: It represents the system that considers all possible components with minimum cost.

It can be observed that the load demand is fully satisfied by the hybrid system in the optimal composition. Figure 14 illustrates the performance of developed enhanced genetic algorithm-based method. The brought convergence improvements are obvious, when achieving the optimal hybrid power generation system.

4.5 Particle Swarm Algorithm

Particle swarm optimization (PSO) is one of the recent techniques based on stochastic optimization [42]. The particle swarm optimization (PSO) algorithm is a member of the wide variety of swarm intelligence methods for solving global optimization issues. PSO is an evolutionary algorithm technique using individual improvement called particles, flying through the problem space plus population cooperation, and competition by following the current optimum particles [43]. In PSO, each individual, referred as a particle, represents a potential solution presumed to have two properties: a position and a velocity. Each particle wanders surrounding in the problem space and remembers the best position (objective function value), which has been already discovered. The fitness value is saved and called P_{best}. The particle swarm optimizer is tracking another best values obtained so far by any particle in the population. The position and velocity of each particle are adjusted according to its own experience and that of its neighbors. When a particle captures all the population as its topological neighbors, the best value is a global best and it is called G_{best}. Let x_i denote the position of particle i in the search space as expressed in Eq. (13).

$$x_i = [x_{i1}, x_{i1}, x_{i2}, \ldots, x_{id}, \ldots, x_{iN}] \tag{13}$$

In the N-dimensional space, each particle continuously records the best solution it has reached during its flight (best fitness value P_{best}). The best previous position of the ith particle is memorized under a vector expressed in Eq. (14).

$$P_{\text{best}i} = [P_{\text{best}i1}, P_{\text{best}i2}, \ldots, P_{\text{best}id}, \ldots, P_{\text{best}iN}] \tag{14}$$

where i = 1, 2, 3,…, N. The global best G_{best} refers to the best position, which is ever realized by all the population individuals. The best particle of all the swarm particles is denoted $G_{\text{best}d}$.

The velocity for particle i is represented in Eq. (15).

$$v_i = [v_{i1}, v_{i1}, v_{i2}, \ldots, v_{id}, \ldots, v_{iN}] \tag{15}$$

The velocity and position of each particle can be continuously adjusted based on the current velocity and the distance from $P_{\text{best}id}$ to $G_{\text{best}d}$ using Eqs. (6) and (17).

$$v_i(t+1) = w(t)v_i(t) + c_1 r_1(P_i(t) - X_i(t)) + c_2 r_2(G(t) - X(t)) \tag{16}$$

$$X_i(t+1) = X_i(t) + \chi v_i(t+1) \tag{17}$$

In the above equations c_1 and c_2 are acceleration constants that pulls each particle towards P_{best} and G_{best} positions and each equal to 1.0 for almost all applications. r_1 and r_2 are random real numbers drawn from [0, 1]. Thus, the particle flies through potential solutions toward $P_i(t)$ and $G(t)$ in a navigated way

Table 5 Some of PSO parameters

c_1 and c_2	1
r_1 and r_2	Randomly
w	Randomly (18)
Number of iteration	100
Number of population	10

while still exploring new areas by a stochastic mechanism to escape from local optima. Since there was no actual mechanism for controlling the velocity of a particle, it was necessary to impose a maximum value V_{max}, which controls the maximum travel distance in each iteration to avoid this particle flying past good solutions. After updating positions, it must be checked that no particle violates the boundaries of search space. If a particle has violated the boundaries, it will be set at the boundary of search space. χ is constriction factor, which is used to limit velocity, here $\chi = 0.7$ [44–47].

In (16), $w(t)$ refers to inertia coefficient, which indicates the impact of the previous history of velocities on the current iteration one and is extremely important to ensure convergent behavior. There are different strategies to calculate the inertia weight. These calculations depend on the designer that can assume it as fixes or variable [48, 49]. In this work we have considered the inertia weight as random and it is given by Eq. (18). All the PSO algorithm parameters are summarized in Table 5.

$$w(t) = 0.5 + \frac{\text{rand}()}{2} \tag{18}$$

4.6 Particle Swarm Optimization Results

The hybrid power generation system economic optimization is based on an objective function minimizing the COE and the TNPC, besides taking into account other constraints as meet the load demand with high reliability, system optimal sizing, battery SOC, and planning expansion for future development. In this context, Fig. 15 illustrates the flowchart of the proposed PSO optimization methodology.

One of the extremely important tasks in PSO algorithm application is how to design the objective function and the considered constraints in each individual particle.

Initially, random values for position and velocity are created for 10 individual particles in each swarm with respect to the PSO characteristics and all constraints (minimum and maximum of hybrid components, reliability etc.). The maximum iteration number is 100. Then, (16) and position are carried out with other parameters values as data in Table 5. Position and velocity will therefore be updated at each time, safeguarding best values and neglecting the worst ones. The

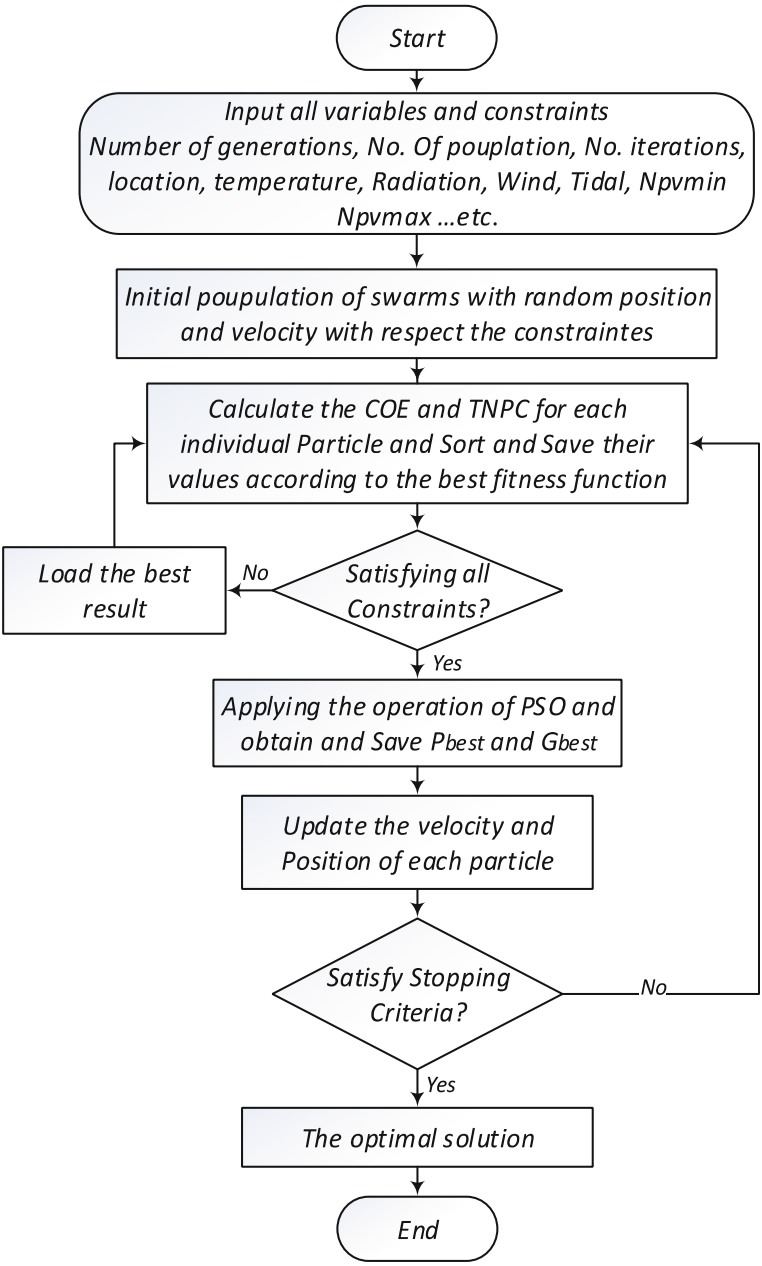

Fig. 15 PSO algorithm flowchart

search process will be terminated if the number of iterations reaches a final value or if the value of optimal solution reaches the tolerance value, which was considered in this paper equal to 0.0001. The final optimum solution is delegated to the system designer depending on its experience, development and expansion of a pre-existing system, or creating a new system hybrid system. In this study, The PSO algorithm is implemented to achieve the optimal solution for the different following scenarios and constraints.

Scenario 1: This scenario considers a hybrid renewable system including all the available renewable sources and the batteries to obtain the minimum COE and the lowest TNPC. The achieved optimal result is given in Table 6. The PSO algorithm convergence curve for this scenario is shown in Fig. 16.

Scenario 2: This scenario considers a hybrid renewable system including two renewable sources (wind turbines and PV panels, tidal turbines and PV panels, wind and tidal turbines) with batteries. The achieved optimal results are given in Table 7.

Table 6 Optimization results using PSO algorithm scenario 1

N_{wind}	N_{tidal}	N_{pv}	Battery size (MWh)	TNPC (M$)	COE ($/MWh)
2	0	0	5.9	3.48	94.2

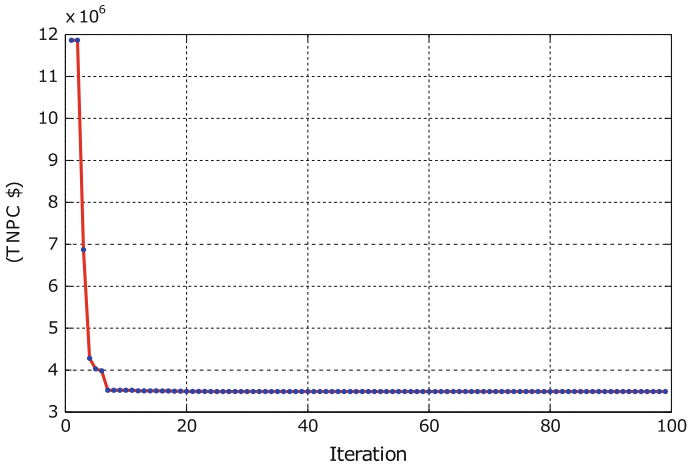

Fig. 16 PSO algorithm convergence for scenario 1

Table 7 Optimization results using PSO algorithm for scenario 2

N_{wind}	N_{tidal}	N_{pv}	Battery size (MWh)	TNPC (M$)	COE ($/MWh)
1	0	11	10.9	3.71	100.3
1	1	0	7.5	4.52	122.1
0	6	1	8.94	9.81	264.7

Scenario 3: This scenario considers a hybrid renewable system including one renewable source energy sources (among wind turbines, tidal turbines, and PV panels) with batteries. The achieved optimal results are given in Table 8.

Scenario 4: This scenario takes into consideration development and expansion of an existing system that has one tidal turbine with possible contribution of all the above-mentioned renewable sources with batteries. The achieved optimal result is given in Table 9.

Scenario 5: This scenario considers a hybrid renewable system including all the available renewable sources and the batteries to obtain the minimum surplus power, the minimum COE, and the lowest TNPC. The achieved optimal result is given in Table 10. The PSO algorithm convergence curve for this scenario is shown in Fig. 17.

Table 8 Optimization results using PSO algorithm for scenario 3

N_{wind}	N_{tidal}	N_{pv}	Battery size (MWh)	TNPC (M$)	COE ($/MWh)
0	6	0	8.94	9.80	264.6
0	0	21,862	114.5	27.28	736.8

Table 9 Optimization results using PSO algorithm for scenario 4

N_{wind}	N_{tidal}	N_{pv}	Battery size (MWh)	TNPC (M$)	COE ($/MWh)
1	1	1	7.57	4.52	122.2

Table 10 Optimization results using PSO algorithm for scenario 5

N_{wind}	N_{tidal}	N_{pv}	Battery size (MWh)	TNPC (M$)	COE ($/MWh)
1	0	1313	10.17	4.27	115.4

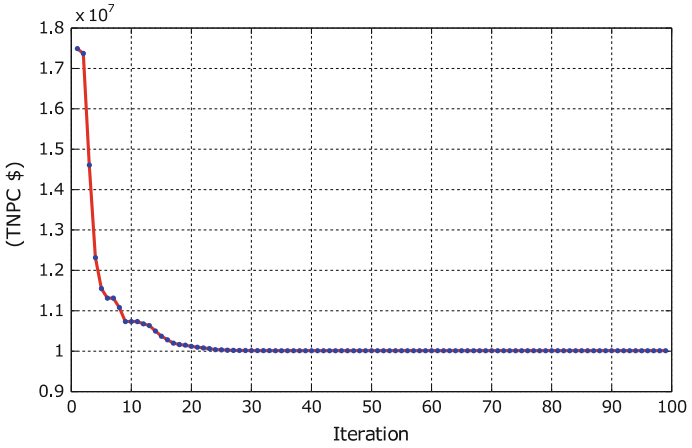

Fig. 17 PSO algorithm convergence for scenario 5

From all above presented scenarios and achieved results, it can be observed that load demand has been fully satisfied by the hybrid power generation system in the optimal composition. For illustration, Fig. 18 shows the optimal energy management balance in one day for scenario 1, while, Fig. 19 illustrates batteries SOC variation.

As for GAs and for the purpose of accelerating the PSO convergence to the optimal results, the initial classical PSO algorithm has been improved treating now each component size inside one particle.

The same conclusions as for GAs could be drawn from the achieved results illustrated by the above-presented tables. Indeed, a hybrid power generation system based on wind and battery seems to be the best compromise in terms of cost (TNPC).

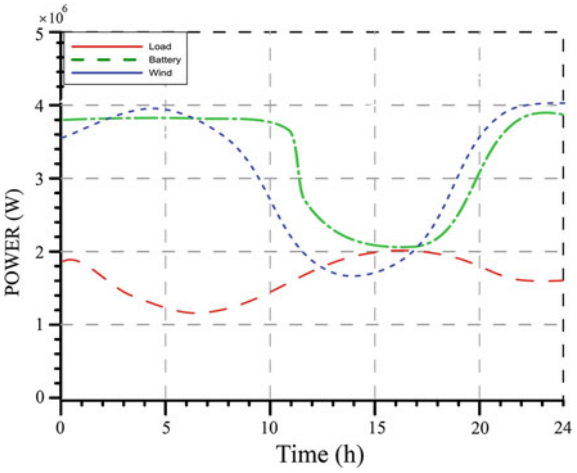

Fig. 18 Hybrid system powers variation in a day (scenario 1)

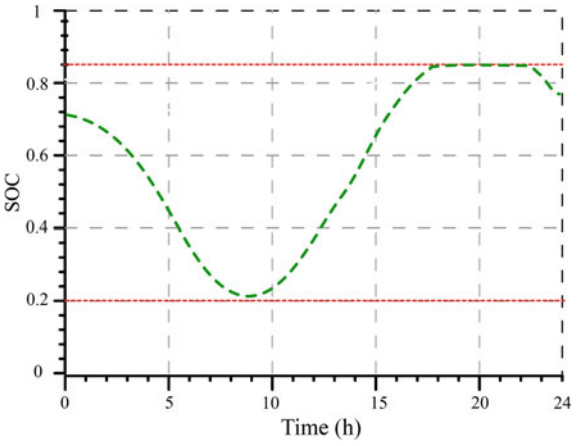

Fig. 19 battery SOC variation in a day (scenario 1)

Table 11 Comparison of the proposed optimization approaches

	Linear approaches		Artificial intelligence approaches			
Optimization tools/techniques	HOMER	Cascade	Classical GA	Enhanced GA	Classical PSO	Enhanced PSO
Accuracy	+	+	+	++	++	++++
Calculation time	8–10 min	1–2 min	4–6 h	2–3 h	30–45 min	2–3 min
Control optimization	Black Box	Full control	Full control	Full control	Full control	Full control
Number of iterations	Not available	1	800–1000	400–500	200–250	5–25
COE ($/MWh)	151	149	96.2	94.2	94.2	94.2

5 Summary and Conclusion

This chapter dealt with a comparative study of three approaches devoted to the optimal sizing of a hybrid power generation system full based on renewables and storage batteries to fulfill the load demand of a remote area in a specific marine context, which the Ouessant Island in the Bretagne region (France). The hybrid system uses the available renewables resources around the island: wind energy, marine energy (tidal current), and PV. The hybrid system has been designed and optimally sized based on economical targets, for different scenarios, that minimizes the COE and the TNPC, in addition to specific constraints.

Three specific optimization approaches have been investigated: (1) Cascaded computation (linear programming approach); (2) Genetic algorithms-based approach; (3) Particle swarm optimization. The achieved optimal results have been also compared to those achieved the well-known commercial software HOMER. Table 11 illustrates this comparison. This table clearly highlights the improvements brought by the proposed and enhanced optimization approaches

References

1. Mohammed OH, Amirat Y, Benbouzid MEH, Tang T (2013) Hybrid generation systems planning expansion forecast: a critical state of the art review. In: Proceedings of the 39th annual conference of the Industrial Electronics Society, Austria, 10–13 Nov 2013
2. Akella A, Saini R, Sharma MP (2009) Social, economical and environmental impacts of renewable energy systems. Renew Energy 34(2):390–396
3. Erdinc O, Uzunoglu M (2012) Optimum design of hybrid renewable energy systems: overview of different approaches. Renew Sustain Energy Rev 16(3):1412–1425
4. Addo EOK, Asumadu J, Okyere PY (2014) Optimal design of renewable hybrid energy system for a village in Ghana. In: Proceedings of the 9th conference on industrial electronics and applications, Hangzhou, China, 09–11 June 2014
5. Bhandari B et al (2015) Optimization of hybrid renewable energy power systems: A review. Precision Eng Manuf Green Technol 2(1):99–112

6. Safari M, Sarvi M (2014) Optimal load sharing strategy for a wind/diesel/battery hybrid power system based on imperialist competitive neural network algorithm. IET Renew Power Gener 8(8):937–946
7. Zahboune H et al (2014) The new electricity system cascade analysis method for optimal sizing of an autonomous hybrid PV/Wind energy system with battery storage. In: 5th IEEE international renewable energy congress, Hammamet, Tunisia, 25–27 Mar 2014
8. Sheng L, Zhou Z, Charpentier JF, Benbouzid MEH (2015) Island power management using a marine current turbine farm and an ocean compressed air energy storage system. In: Proceedings of the European wave and tidal energy conference, Nantes, France, 6–9 Sept 2015
9. Zhou Z, Scuiller F, Charpentier JF, Benbouzid MEH, Tang T (2014) Application of flow battery in marine current turbine system for daily power management. In: Proceedings of the international conference on green energy, Sfax, Tunisia, 25–27 Mar 2014
10. Mohammed OH, Amirat Y, Feld G, Benbouzid MEH (2016) Hybrid generation systems planning expansion forecast state of the art review: optimal design vs technical and economical constraints. Electr Syst (12). http://journal.esrgroups.org/jes/papers/1212:pdf
11. RETScreen: International Empowering Cleaner Energy Decisions (2016). http://www.retscreen.net/ang/home.php
12. Sinha S, Chandel S (2014) Review of software tools for hybrid renewable energy systems. Renew Sustain Energy Rev 32:192–205
13. Islam FR, Mamun KA (2016) Opportunities and challenges of implementing renewable energy in Fiji Islands. In: Australasian Universities power engineering conference (AUPEC-2016), Brisbane, Australia, 25–28 Sept 2016
14. Adhikary P, Roy PK, Mazumdar A (2014) Multidimensional feasibility analysis of small hydropower project in India: a case study. Eng Appl Sci 9(1):80–84
15. LEAP:An Introduction to LEAP (2016)
16. Ates SA (2015) Energy efficiency and CO2 mitigation potential of the Turkish iron and steel industry using the leap (long-range energy alternatives planning) system. Energy 90:417–428
17. Klise GT, Stein JS (2009) Models used to assess the performance of photovoltaic systems. Sandia National Laboratories
18. Chapman RN (1996) Hybrid power technology for remote military facilities, Technical report, Sandia National Labs., Albuquerque, NM
19. iHOGA: General Information SOFTWARE iHOGA (2016)
20. Morgan T, Marshall R, Brinkworth B (1997) Aresa refined simulation program for the sizing and optimisation of autonomous hybrid energy systems. Sol Energy 59(4):205–215
21. Dufo-Lopez R, Bernal-Agustın JL, Contreras J (2007) Optimization of control strategies for stand-alone renewable energy systems with hydrogen storage. Renew Energy 32(7):1102–1126
22. iHOGA V2.2 User Manual (2016) http://personal.unizar.es/rdufo/images/ihoga/UserManual:pdf
23. Bernal-Agustın JL, Dufo-Lopez R (2009) Simulation and optimization of stand-alone hybrid renewable energy systems. Renew Sustain Energy Rev 13(8):2111–2118
24. Turcotte D, Ross M, Sheriff F (2001) Photovoltaic hybrid system sizing and simulation tools: status and needs. In: PV horizon, workshop on photovoltaic hybrid systems, Montreal, pp 2–5
25. SOMES 3.2: A Simulation and Optimization Model for renewable Energy Systems (2016). http://www.web.co.bw/sib/somes32description:pdf
26. Patel M, Pryor T (2001) Monitored performance data from a hybrid raps system and the determination of control set points for simulation studies. In: Proceedings of International Solar Energy Society: solar world congress, Adelaide, Australia, 25–30 Nov 2001
27. HOMER—Hybrid Renewable and Distributed Generation System Design Software (2015) http://www.homerenergy.com/
28. Mohammed OH, Amirat Y, Benbouzid MEH, Feld G, Tang T, Elbaset AA (2014) Optimal design of a stand-alone hybrid PV/fuel cell power system for the city of Brest in France. Energy Convers 1(2):1–7

29. Normales et records des stations météo de France - Infoclimat. (2015)
30. ENERCON, energy for the world, Sept 2015. http://www.enercon.de/de-de/
31. Bashir M, Sadeh J (2012) Size optimization of new hybrid stand-alone renewable energy system considering a reliability index. In: Proceedings of the 11th international conference on environment and electrical engineering, May 2012
32. Johnson GL (2006) Wind energy systems. Gary L. Johnson
33. Amirat Y, Benbouzid MEH, Bensaker B, Wamkeue R (2007) Generators for wind energy conversion systems: state of the art and coming attractions. J Electr Syst 1(3):26–38
34. Kalogirou SA (2014) Photovoltaic systems. In: Kalogirou SA (ed) Solar energy engineering, 2nd edn. Academic Press, Cambridge, pp 481–540
35. Kusakana K, Vermaak HJ (2014) Hybrid diesel generator/renewable energy system performance modeling. Renew Energy 67:97–102
36. Skoplaki E, Palyvos J (2009) On the temperature dependence of photovoltaic module electrical performance: a review of efficiency/power correlations. Sol Energy 83(5):614–624
37. Benbouzid et al (2011) Concepts, modeling and control of tidal turbines. Marine renewable energy handbook. Wiley, ISTE, Paris
38. Benelghali S, Mekri F, Benbouzid MEH, Charpentier JF (2011) Performance comparison of three-and five-phase permanent magnet generators for marine current turbine applications under open-circuit faults. In: Proceedings of international conference on power engineering, energy and electrical drives, Malaga, Spain, 11–13 May 2011
39. Slootweg J, De Haan S, Polinder H, Kling W (2003) General model for representing variable speed wind turbines in power system dynamics simulations. IEEE Trans Power Syst 18(1): 144–151
40. Mohammed OH, Amirat Y, Benbouzid MEH, Haddad S, Feld G (2016) Optimal sizing and energy management of hybrid wind/tidal/PV power generation system for remote areas: application to the Ouessant French Island. In: Proceedings of the 42th annual conference of the Industrial Electronics Society, IECON 2016, Florence, Italy, 24–27 Oct 2016
41. Haupt RL, Haupt SE (2004) Practical genetic algorithms. Wiley, New York
42. Kennedy J, Eberhart R (1995) Particle swarm optimization. In: Proceedings of the IEEE international conference on neural networks, Perth, Australia, no 4, pp 1942–1948
43. Poli R, Kennedy J, Blackwell T (2007) Particle swarm optimization. Swarm Intell 1(1):33–57
44. Yin PY, Wang JY (2006) A particle swarm optimization approach to the nonlinear resource allocation problem. Appl Math Comput 183(1):232–242
45. Lu Y, Liang M, Ye Z, Cao L (2015) Improved particle swarm optimization algorithm and its application in text feature selection. Appl Soft Comput 35:629–636
46. Rasoulzadeh-akhijahani A, Mohammadi-ivatloo B (2015) Short-term hydrothermal generation scheduling by a modified dynamic neighborhood learning based particle swarm optimization. Int J Electr Power Energy Syst 67:350–367
47. Parsopoulos KE, Vrahatis MN (2004) On the computation of all global minimizers through particle swarm optimization. IEEE Trans Evol Comput 8(3):211–224
48. Bansal J, Singh P, Saraswat M, Verma A, Jadon SS, Abraham A (2011) Inertia weight strategies in particle swarm optimization. In: Proceedings of the 3rd world congress on nature and biologically inspired computing, Salamanca, Spain, 19–21 Oct 2011
49. Sun J, Lai CH, Wu XJ (2011) Particle swarm optimisation: classical and quantum perspectives, 1st edn. CRC Press, Boca Raton

Hybrid Diesel/MCT/Battery Electricity Power Supply System for Power Management in Small Islanded Sites: Case Study for the Ouessant French Island

Z. Zhou, M.E.H. Benbouzid, J.F. Charpentier and F. Scuiller

Abstract In this chapter, a hybrid Diesel/MCT/Battery system for power supply and power management on a small island is studied. The power variation of marine current turbine (MCT) related to the tidal phenomenon is considered. A semidiurnal tide causes the seawater to rise and fall with a period about 12 h, thus resulting large variations of the MCT output power on a daily basis. On the other hand, the electricity demand from the grid side (or load side) has its own pattern during each day. Large differences between the power produced from the renewable sources and the power demanded from the grid/load side could cause power unbalance problem. This chapter proposes using Vanadium Redox flow Battery (VRB) energy storage system to manage the total available power of the hybrid MCT/battery/diesel system and to follow the grid/load demand on a daily basis. The MCT-dominated power supply case and the case when diesel generators as the main supply source are investigated, respectively. The battery modeling and control with appropriate activating rules of the diesel generator are presented in this chapter. At the end of this chapter, some insights for future MCT farm operation for hybrid island power supply will be discussed.

Keywords Marine current turbine · Power fluctuation · Flow battery · Hybrid power supply system · Diesel-fuel reduction

Z. Zhou (✉) · J.F. Charpentier · F. Scuiller
French Naval Academy, Research Institute of Naval Academy (IRENav EA3634),
BCRM Brest, Brest 29240, France
e-mail: zhibin.zhou@ecole-navale.fr

J.F. Charpentier
e-mail: jean-frederic.charpentier@ecole-navale.fr

F. Scuiller
e-mail: franck.scuiller@ecole-navale.fr

M.E.H. Benbouzid
Institut de Recherche Dupuy de Lôme (FRE CNRS 3744 IRDL),
University of Brest, 3 Rue Des Archives, Brest 29238, France
e-mail: Mohamed.Benbouzid@univ-brest.fr

F.M.R. Islam et al. (eds.), *Smart Energy Grid Design for Island Countries*,
Green Energy and Technology, DOI 10.1007/978-3-319-50197-0_13

1 Introduction

Intense energy density and high predictability of tidal current resources make marine current turbine (MCT) a promising technology for generating electricity from the oceans. Industrial and academic research progresses on the MCT turbine designs are presented in [1]. Several megawatt level systems are currently under test and planned to be installed in pilot MCT farms in the coming years [2]. However, the power variation is still a problem for MCTs. For a daily-time scale, the astronomic nature of tides causes seawater to flow regularly each day (flood and ebb tides). For a longer time scale, the amplitude of the tide varies with the relative position of earth, moon and sun (spring and neap tides). On the other hand, an island grid load has its own variation pattern each day, which is related to the consumer's behavior. Therefore, energy storage system (ESS) is essential to solve the unbalances between the MCT generated power and the local load demand. A detailed comparison and evaluation of different ESS technologies for MCT application can be found in [3]. Daily power management for a single megawatt MCT-based on battery storage system has been studied in [4].

In this chapter, two different cases based on the power supply specifications for the Ouessant Island (off the Brittany coast, France) will be discussed. The Ouessant Island has a surface of 15.6 km^2 and residential population about 900. In the first case, the MCT is considered as the main power supply source and the Diesel generators (DG) serve only as backup sources. In the second case, the DGs serve as the main power supply source and the MCT is supposed to provide about 20–30% of the island load.

2 MCT-Based Hybrid Power Supply System

Tidal movements cause regular variations of tide current speed and MCT output power for each day. In this section, one hybrid MCT generation system with battery energy storage system (BESS) and diesel generator (DG) is studied to follow a given power demand profile on a daily basis. Figure 1 shows the general hybrid system structure.

The BESS is connected to the DC bus of a back-to-back PWM-controlled converter, which interfaces the permanent magnet synchronous generator (PMSG) and the grid/load. The Diesel Generator in Fig. 1 serves as an important power supply source for enhancing the grid/load demand following ability. It should be noted that the BESS in this hybrid system aims to facilitate the power management of the MCT and to reduce the fuel consumption of the Diesel Generator (DG). Supposing that the MCT produced power can be smoothed by MCT farm effects or fast energy storage technologies (such as supercapacitors or flywheels) in the first place, the short-time scale power fluctuation is then not very notable on a daily basis. Therefore, the MCT output power can be calculated by

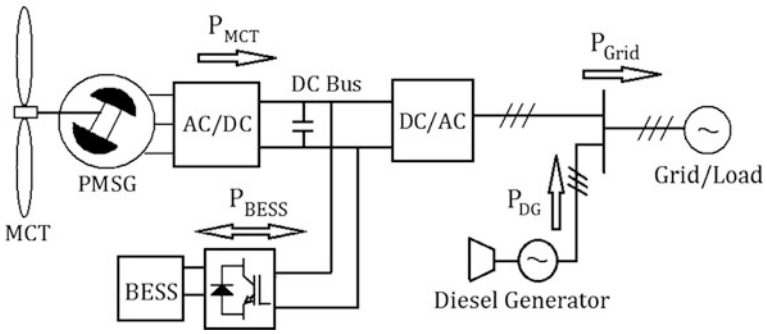

Fig. 1 General schema for a hybrid MCT/BESS/DG system

$$P_{\mathrm{MCT}} = \frac{1}{2}\rho C_{\mathrm{p,max}} \pi R^2 V_{\mathrm{tide}}^3. \tag{1}$$

In this work, one 1.5 MW MCT described in [5] is considered. Typical turbine power coefficient C_{p} values for a MCT under MPPT (maximum power point tracking) are in the range of 0.35–0.5 [6]. Different from wind turbines, MCT works in the seawater being more corrosive than air. Therefore, decreasing maintenances of MCTs as low as possible is naturally required. Eliminating pitch control can be an interesting design option for MCTs [7]. In this work, the MCT is considered as a nonpitchable turbine and this MCT is supposed to operate under MPPT with $C_{\mathrm{p,max}} = 0.45$ when the tidal current speed is under the rated value of 3.2 m/s. When the tidal current exceeds 3.2 m/s, the MCT harnessed power can be limited to its rated value by power limitation strategies. The detailed power control strategies under and over the rated marine current speeds have been proposed in [5, 8].

Figure 2 shows an example for the tidal current speed, the corresponding MCT harnessed power and the grid load power demand profile (assigned for the MCT) on 1-day period. The cubic relationship between the tidal current velocity and the turbine power makes the MCT produce high power at both flood tide and ebb tide crests. In the middle of these tide crests, especially during the transition between flood and ebb tides, the tidal current velocity would be very low.

The cut-in current velocity for MCTs should be over 0.7 m/s [9] and usually it can be considered that MCTs able to produce power efficiently for a current speed over 1 m/s due to the system inertia and mechanical losses [10]. The supposed grid/load demanded power profile (P_{Grid} in Fig. 2b) is calculated based on typical daily load curves (per unit values can be found in [11]) and the average MCT power during 1 day. From Fig. 2b, it can be seen that during the peak load periods (10–12 h and 18–20 h) the MCT produces low powers or it is unable to produce power due to low tidal current velocity. In this case, large-capacity ESS can be used to store the excessive energy during MCT peak power periods and then to inject the stored energy to the grid/load side during peak load periods.

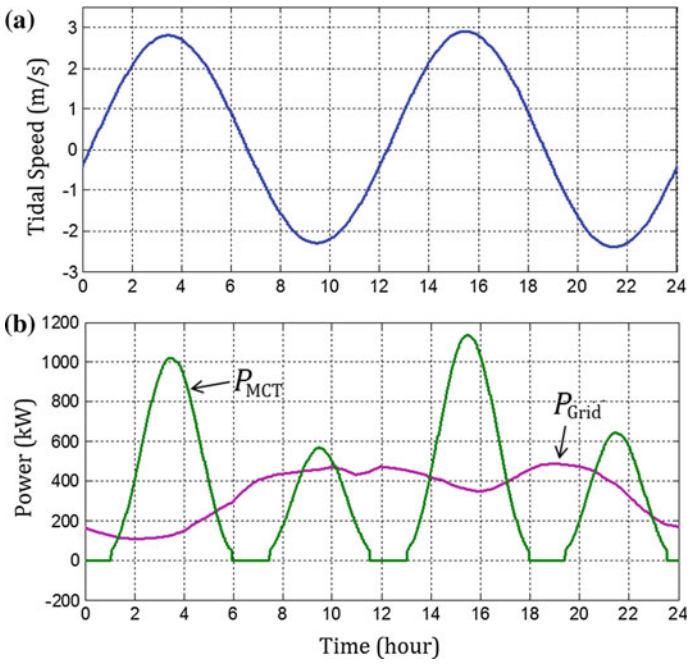

Fig. 2 Daily profile example: **a** tidal current speed, **b** MCT produced power and the assigned grid demand power

This example implies that if the MCT output power has a very high penetration level (accounts for a high percentage of the load) to maximally reduce the use and fuel consumption of the DG units, a large-capacity ESS is indispensable for storing and restoring the MCT produced energy to follow the load demand profile.

3 Flow Battery Technologies

Flow batteries are relatively new battery technology dedicated for large energy capacity applications. This technology uses two external tanks to reserve liquid electrolytes and uses pump system for circulating the electrolytes to the battery cell stack (consisting of the two electrodes and the ion exchange membrane). Figure 3 illustrates the structure of a vanadium redox flow battery (VRB) system. The charging and discharging processes are realized by means of a reversible electrochemical reaction between two liquid electrolyte reservoirs. Flow batteries are often called as redox flow batteries (RFB), because this technology is based on the redox (reduction-oxidation) reaction between the two electrolytes in the battery.

The most distinguished advantage of flow battery technologies is that the power and energy ratings can be flexibly sized [13–15]. The power rating is determined by

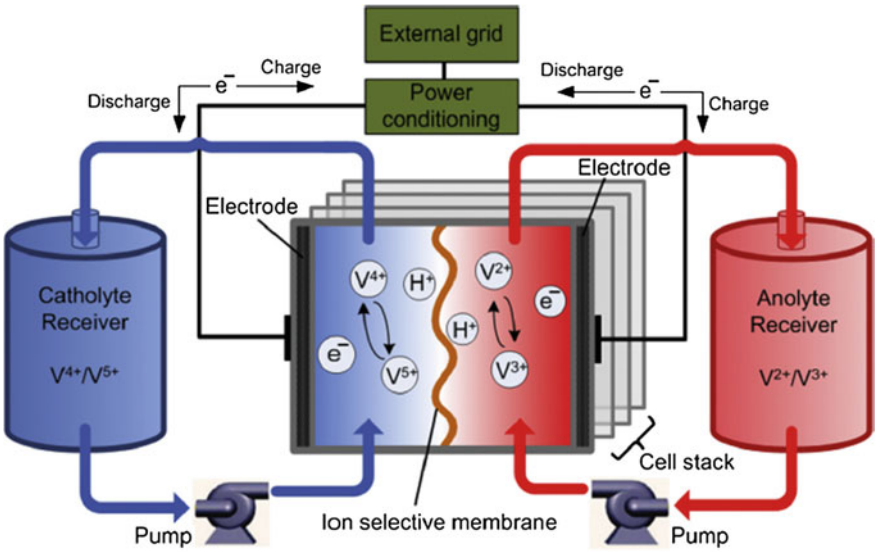

Fig. 3 Structure of a vanadium redox flow battery [12]

electrode cells design and the energy capacity depends on the volume of the electrolytes, which are separated from the cell stack and can be designed independently. Therefore, flow battery can be easily designed to meet specific energy capacity or power rating requirements. These characteristics make them suitable for a wider range of applications than conventional batteries. Another significant advantage is their long service life over 10,000 cycles at 75% depth of discharge. Other advantages include high safety, negligible degradation for deep discharge, and negligible self-discharge. The major disadvantages of flow batteries are that the power/energy density is relative low compared to other technologies and that the extra pumps systems are needed for electrolytes circulation.

Over the past 20 years, four designs of flow batteries have been demonstrated: vanadium redox (VRB), zinc bromine (ZnBr), polysulphide bromide (PSB), and cerium zinc (CeZn). Major installations are in Japan and North American, using the vanadium redox and zinc bromine designs. Energy efficiency is about 85% for VRB system and 75% for ZnBr system. 5 kW/20 kWh Community Energy Storage units based on ZnBr batteries are now being tested. Integrated ZnBr energy storage systems have been tested on transportable trailers (1 MW/3 MWh), and these systems could be connected in parallel for more powerful applications [16]. VRB system of 500 kW, 10 h (5 MWh) was installed by Sumitomo Electric Industries (SEI) in Japan for peak shaving and UPS applications in 2001. The largest VRB plant so far is the 4 MW/6 MWh plant in Hokkaido, Japan [15]. This VRB plant can provide a temporary overload up to 6 MW, and it is intended for smoothing output power fluctuations of a nearby 30.6 MW wind power plant.

Flexibility of energy and power sizing, long lifetime, low cost, and low maintenance make flow battery a very promising technology to be used for integrating fluctuant and intermittent renewable energies to the power grid. For marine current energy, flow batteries can be designed differently for compensation short- and long-time fluctuations, and more favorably they are suitable for hours energy storage for smoothing the fluctuation due to tidal phenomenon or realizing some energy management strategies.

4 Flow Battery Modeling

4.1 Battery Equivalent Circuit Model

The VRB represents the most mature flow battery technologies and the flow battery modeling is based on the literature of VRB batteries. Figure 4 shows the flow battery equivalent circuit model used in this work [4]. The equivalent circuit model was based on the models previously proposed in [17–19]; however, some parameter calculations are not detailed and the battery standby mode is not considered in these literatures.

In Fig. 4, the stack current (I_{stack}) and stack voltage (V_{stack}) represent the battery cell-stack internal current and electromotive force; and these two terms will be used to calculate the battery state of charge (SoC). The battery terminal voltage and current are expressed as V_{battery} and I_{battery}. The internal resistances (R_{reaction} and $R_{\text{resistive}}$) are modeled for reaction kinetics loss, mass transport resistance, membrane resistance, electrode resistance, and bipolar plate resistance. The transient component associated with the electrode capacitance is modeled by $C_{\text{eletrodes}}$. The parasitic resistance R_{fixed} allows modeling the stack-by-pass current. The power losses due to the circulation pump and the system controller are represented by the losses current I_{pump}. The switch on the parasitic branch of the equivalent circuit will be turned on when the battery is in operation (charge or discharge) and turned off when the battery is in standby mode.

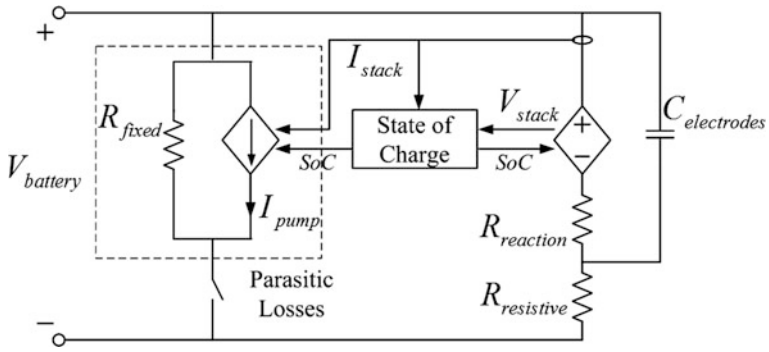

Fig. 4 VRB equivalent circuit model [4]

4.2 Battery Model Parameter Estimation Process

The battery stack voltage represents the internal battery electromotive force. The value is directly related to the battery SoC and can be empirically estimated by

$$V_{\text{stack}} = n \cdot \left(1.4 + k \ln\left(\frac{\text{SoC}}{1 - \text{SoC}}\right)\right). \tag{2}$$

In (2), n is number of cells in series in the battery stack; 1.4 V corresponds to the nominal battery electromotive force for one cell; k is a coefficient relating to the temperature and can take a value of 0.0514 V at 25 °C. The terminal battery voltage can be calculated from Fig. 4 as

$$V_{\text{battery}} = V_{\text{stack}} + I_{\text{stack}}(R_{\text{reaction}} + R_{\text{resistive}}), \tag{3}$$

where I_{stack} takes positive values for the charge mode and negative values for the discharge mode in this paper. The battery terminal current has the same direction as the I_{stack} and can be obtained considering the parasitic losses as

$$I_{\text{battery}} = I_{\text{stack}} + \left(\frac{V_{\text{battery}}}{R_{\text{fixed}}} + I_{\text{pump}}\right). \tag{4}$$

The internal resistances (R_{reaction} and $R_{\text{resistive}}$) and the parasitic resistance R_{fixed} can be estimated by the power losses at the rated battery discharge current and their values are generally constant during battery operational range.

The flow battery is supposed to have a 79% efficiency at the operating point of rated discharge current I_{bmax} and 20% SoC. It can then be estimated that the nominal power losses are ξ_N = 21%, with 15% accounts for internal losses (ξ_1 and ξ_2 for losses on R_{reaction} and $R_{\text{resistive}}$, respectively) and 6% accounts for parasitic losses (ξ_3 and ξ_4 for losses on R_{fixed} and I_{pump} respectively) [17].

In order to enable the battery to provide the rated power P_N with a nominal losses level of ξ_N (in pu.), the rated stack output power should be calculated by

$$P_{\text{stackN}} = \frac{P_N}{1 - \xi_N}. \tag{5}$$

For the fixed parasitic loss, the value of R_{fixed} can be calculated by

$$R_{\text{fixed}} = \frac{V_{\text{bmin}}^2}{\xi_3 \cdot P_{\text{stackN}}}, \tag{6}$$

where V_{bmin} is the minimum battery voltage defined at the rated discharge current I_{bmax} (considering as the rated battery current). The relationship with the battery rated power can be expressed by $P_N = V_{\text{bmin}} \times I_{\text{bmax}}$.

For the parasitic pump loss, it is related to the stack current and SoC as shown in the following equation.

$$P_{\text{pump}} = V_{\text{battery}} \times I_{\text{pump}} = k' \left(\frac{|I_{\text{stack}}|}{\text{SoC}} \right) \tag{7}$$

The constant k' can be estimated at the rated operating point (with $I_{\text{battery}} = I_{\text{bmax}}$ and $V_{\text{battery}} = V_{\text{bmin}}$). If the pump loss is estimated as two times as the fixed parasitic resistance loss at I_{bmax} and at 20% of the SoC, then the k' can be calculated by

$$k' = \frac{0.2\xi_4 P_{\text{stackN}}}{I_{\text{bmax}} + 3I'} \tag{8}$$

where I' is the current through the fixed parasitic resistance at the rated operating point (with $I_{\text{battery}} = I_{\text{bmax}}$ and $V_{\text{battery}} = V_{\text{bmin}}$) and can be calculated by $I' = V_{\text{bmin}}/R_{\text{fixed}}$. Then the pump current I_{pump} can be calculated as follows.

$$I_{\text{pump}} = \frac{k'}{V_{\text{bmin}}} \left(\frac{|I_{\text{stack}}|}{\text{SoC}} \right) = \frac{0.2\xi_4 P_{\text{stackN}}}{P_{\text{N}} + 3\xi_3 P_{\text{stackN}}} \left(\frac{|I_{\text{stack}}|}{\text{SoC}} \right) \tag{9}$$

The internal resistances R_{reaction} and $R_{\text{resistive}}$ can be calculated according to their losses by (10) and (11), respectively

$$R_{\text{reaction}} = \xi_1 P_{\text{stackN}} / (I_{\text{bmax}} + 3I')^2 \tag{10}$$

$$R_{\text{resistive}} = \xi_2 P_{\text{stackN}} / (I_{\text{bmax}} + 3I')^2. \tag{11}$$

The SoC of the battery is calculated as follows:

$$\text{SoC}_t = \text{SoC}_{t-1} + \Delta_t \text{SoC} \tag{12}$$

$$\Delta_t \text{SoC} = \frac{\Delta_t E}{E_{\text{N}}} = \frac{V_{\text{stack}} I_{\text{stack}} \Delta t}{P_{\text{N}} T_{\text{N}}}, \tag{13}$$

where Δt is the calculation step; E_{N} is the energy capacity of the battery, and T_{N} is the time duration for which the battery can provide P_{N}.

4.3 Battery Sizing and Basic Charge-Discharge Characteristic

In this section, an example of battery sizing and the simulation of a basic charge-discharge cycle are given. The required battery power/energy ratings depend strongly on the power profiles of the MCT and the grid/load demand.

In the first step, the daily profile shown in Fig. 2 is used to estimate the required battery capacity. It should be noted that in this case, the assigned load power is supposed to be supplied by the hybrid MCT/Battery system and in this case the DG is only considered as an auxiliary source. The power rating of the battery can be estimated from the maximum difference of P_{MCT} and the assigned P_{Grid} (in Fig. 2b) as

$$P_{\mathrm{N}} = \max(P_{\mathrm{MCT}}(t) - P_{\mathrm{Grid}}(t)) \approx 1000\,\mathrm{kW}. \tag{14}$$

By integrating the power difference of P_{MCT} and P_{Grid} (in Fig. 2), an energy level change profile can be obtained as shown in Fig. 5. From this figure, the maximum energy change is $\Delta E_{\max}$ = 2040 kW. Considering that the battery efficiency is about 80% and a possible initial SoC of 0.4, the required battery energy capacity can then be calculated by Eq. (15)

$$E_{\mathrm{N}} = \frac{\Delta E_{\max} \times 80\%}{1 - 0.4} = 2720\,\mathrm{kWh} \approx 3\,\mathrm{MWh}. \tag{15}$$

In this case, the BESS can be sized with a power rating of P_{N} = 1 MW and energy capacity of E_{N} = 3 MWh. The open-circuit battery voltage at 50% SoC is set as V_{b0} = 1500 V. It needs n = 1072 cells in series to make up the battery stack. The VRB has a usual operational voltage range about 0.78–1.2 $V_{\mathrm{b0.}}$ Therefore, the minimum battery terminal voltage is limited at V_{bmin} = 1170 V and the rated discharge current is set as I_{bmax} = 855 A.

The power losses (in pu.) used to calculate the resistance and parameters in the battery model are set as: ξ_1 = 9%, ξ_2 = 6%, ξ_3 = 2% and ξ_4 = 4%. Each battery cell capacitance is about 6 F, then the equivalent electrode capacitance for 1072 cells in series is calculated by $C_{\mathrm{eletrodes}}$ = 6 F/1072. The parameters for the VRB circuit model can be found in Appendix.

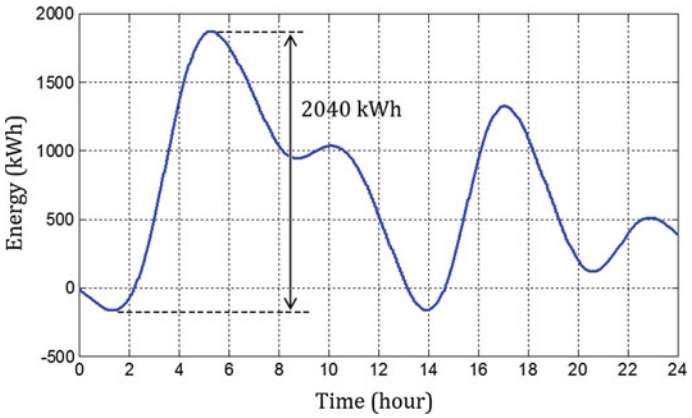

Fig. 5 The energy level change profile for battery capacity estimation

Figures 6 and 7 show the simulation results for the 3 MWh VRB on an elementary charge-discharge cycle.

This basic charge-discharge simulation is to test the feasibility of the flow battery model. In this simulation, the battery is charged during 3 h with a constant current

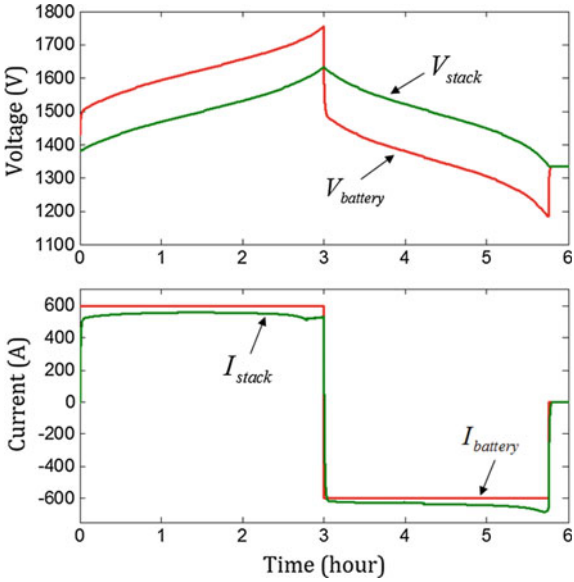

Fig. 6 VRB voltage and current variations during a charge-discharge cycle

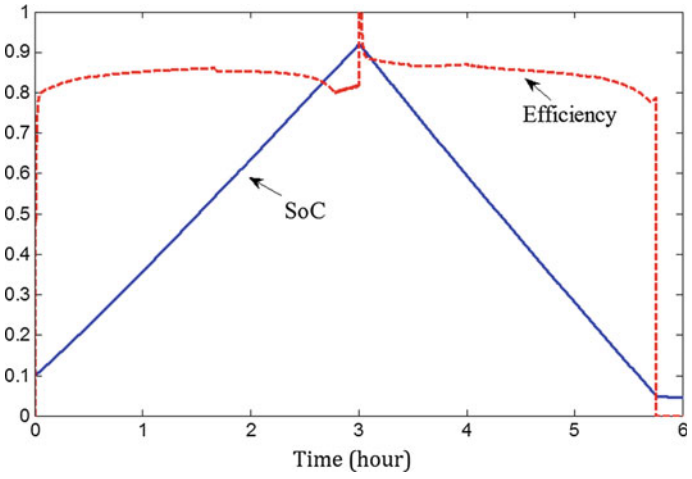

Fig. 7 SoC and efficiency variation during a charge-discharge cycle

of 600 A and an initial SoC of 0.1, and then discharged during 3 h with the same absolute current value. From Fig. 6, it can be seen that at the switching instant from charge mode to discharge mode, V_{battery} is discontinuous due to the sudden voltage polarity change on the internal resistances. The difference between I_{battery} and I_{stack} is caused by the parasitic current losses.

In this constant current charge-discharge cycle, the discharge mode cannot last up to the end of the 3 h because of the battery losses. The battery should be turned off when the SoC is too low (at 5% SoC in Fig. 7). Once the battery is turned off, the battery currents will return to zero and V_{battery} will be equal to the battery internal electromotive force V_{stack} as shown in Fig. 6. The battery efficiency is also illustrated in Fig. 7. It is calculated by $P_{\text{stack}}/P_{\text{battery}}$ in the charge mode and $P_{\text{battery}}/P_{\text{stack}}$ in the discharge mode. From Fig. 7, it shows that the battery efficiency varies mainly between 80 and 90%. This is reasonable because the nominal power losses $\xi_{\text{N}} = 21\%$ (maximum power losses) are considered in the VRB model.

5 Power Management of the Hybrid System—MCT Dominating Case

5.1 System Configuration and BESS Control Scheme

In this section, we focus on the BESS control for enabling the MCT-based hybrid system to follow a required load power profile. In this MCT dominating case, it should be noted that the assigned island load for the MCT is mainly supplied by MCT and the battery.

The general system structure of the MCT with BESS was shown in Fig. 1. The MCT has a rated power of 1.5 MW and the DC bus voltage is set to $V_{\text{dc}} = 1500$ V. The diesel generator shown in this section serves only as a backup power source. For simplicity, the diesel generator is modeled by a controlled current source (connected to the DC bus) to provide powers when the battery SoC is too low. The DG power rating is set as 500 kW in order to cover the maximum load demand shown in Fig. 2b.

The BESS is connected through a bi-directional DC/DC converter to the DC bus of the back-to-back converter as shown in Fig. 1. In the case where the battery maximum operational voltage is higher than V_{dc}, a bi-directional cascaded DC/DC converter can be used. Based on the principle of a cascaded DC/DC converter [20], the battery voltage can be controlled as

$$\frac{V_{\text{battery}}}{V_{\text{dc}}} = \frac{D_{\text{d}}}{1 - D_{\text{u}}} = D, \tag{16}$$

where D is the voltage ratio decided by the step-down duty ratio D_{d} and the step-up duty ratio D_{u}. In the step-down mode, $D_{\text{u}} = 0$ and D_{d} is controlled between 0 and 1; while in the step-up mode, $D_{\text{d}} = 1$ and D_{u} is controlled between 0 and 1. The

corresponding switches triggered to realize the duty ratios should be determined by converter topology and power flow direction. In this work, the power converter is modeled by average-value method for facilitating long-time period simulation. Therefore, the voltage ratio D serves as the control reference for the average-value converter model [21].

The battery reference power (positive for charge mode) is set to compensate the difference between the available power supply and grid/load power demand as follows:

$$P^*_{\mathrm{BESS}} = P_{\mathrm{MCT}} + P_{\mathrm{DG}} - P^*_{\mathrm{Grid}}. \tag{17}$$

Figure 8 shows the BESS side DC/DC converter control scheme. In this control scheme, the voltage ratio D is limited in the range of 0.78 and 1.2 indicating the battery voltage is limited from 1170 to 1790 V.

The "Battery limits" module in Fig. 8 is used to hold the value of D when the battery is turned off at standby stage. The battery is supposed to turn off once the SoC tends to exceed the range of 0.1 and 1, or the absolute value of P_{BESS} reaches the rated battery power P_{N}.

5.2 Simulation Without the DG

It should be noted that the tidal current speed and the corresponding average MCT produced power during 1-day period are predictable. In this simulation, the assigned load demand energy is set to have an average value which equals 90% of the daily MCT produced energy; and this allows the system losses to be considered. The load demand power profile (as shown in Fig. 2b) reflects the load variation during the 1-day period. In this section, only MCT and BESS are considered to provide grid demand power during the day. The 3 MWh VRB model and the control scheme described in the previous section are integrated into the 1.5 MW MCT system.

Figure 9 shows the MCT produced power, the power injected into the island grid, and the BESS power during this day. Positive BESS power indicates the battery is being charged and negative BESS power indicates battery is discharging.

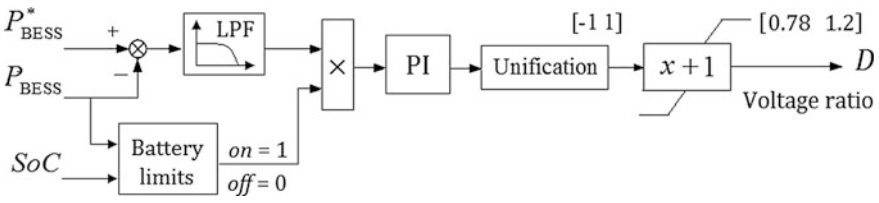

Fig. 8 Control scheme of the BESS side DC/DC converter

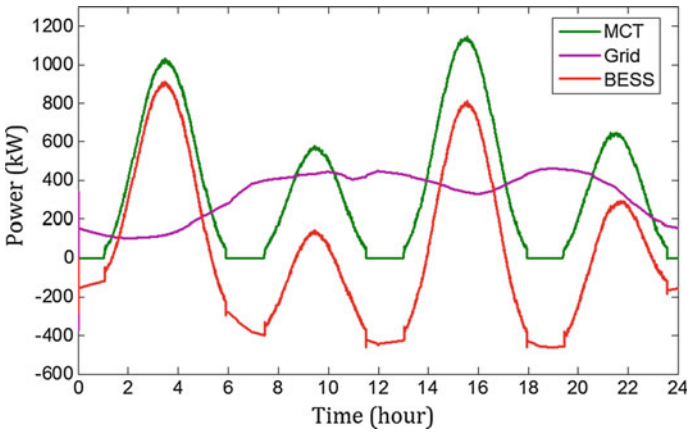

Fig. 9 Powers of the MCT system with BESS during 1 day

Figures 10 and 11 illustrate the battery voltage/current and SoC variation curves. The initial battery SoC is set at 0.4.

From Fig. 11 it can be seen that the battery SoC varies in the range of 0.11 and 0.91. At the end of the day, the SoC will decrease below 0.2. This SoC decreasing phenomenon is mainly caused by the battery losses during the 24 h continuous operation. This phenomenon shows that in the MCT-dominated power supply case, the burden of battery is heavy because the battery should be continuously operated in charge or discharge mode to insure the balance between the power supply and the power demand. In this case, the battery losses cannot be neglected and these losses may cause a very low SoC at the end of the day. The following figures show a lower initial SoC case.

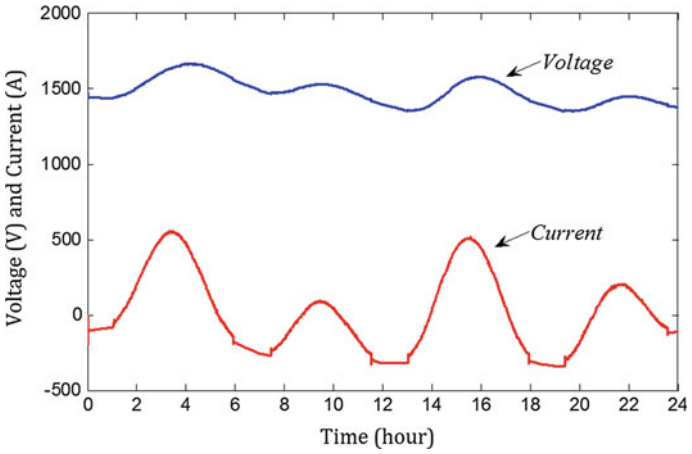

Fig. 10 Voltage and current of the BESS

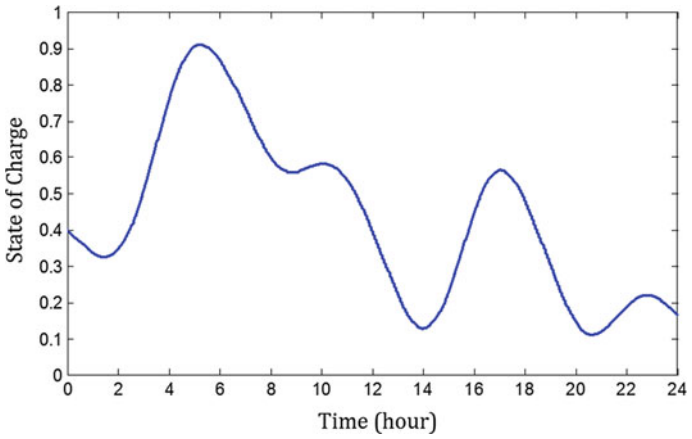

Fig. 11 SoC of the BESS

Figures 12, 13, and 14 show the case when the initial SoC is set at 0.3. It can be seen that during 13:05–14:00 and 20:10–20:50, the battery SoC will reach its low limitation of 0.1 and the battery will be turned off.

When the battery is turned off, the P_{Grid} will drop to the P_{MCT} (shown in Fig. 12) and that means the grid power demand cannot be satisfied under such situation. The battery voltage and current responses during the battery off time are highlighted in Fig. 13.

If the load assign requirement cannot be assured, there could be a problem on the stability of the stand-alone island grid. This indicates that the DG is necessarily needed in the hybrid power supply system.

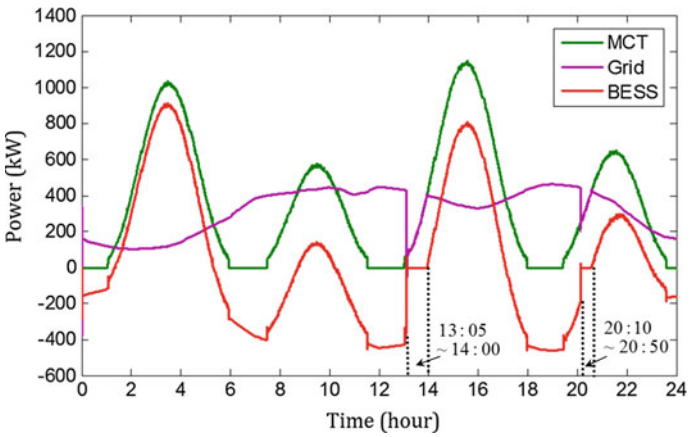

Fig. 12 Powers of the MCT system with BESS (initial SoC = 0.3)

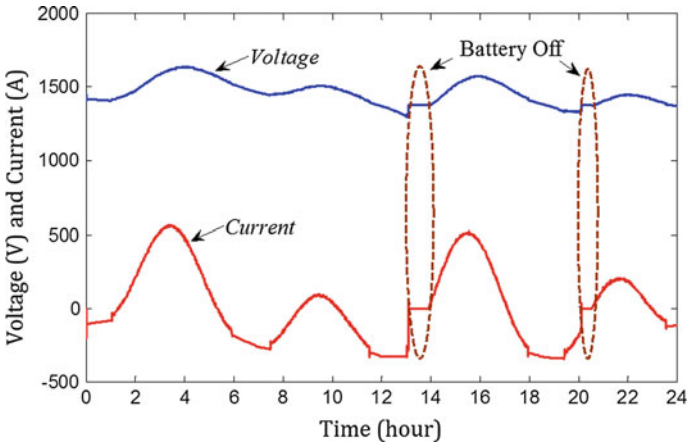

Fig. 13 Voltage and current of the BESS (initial SoC = 0.3)

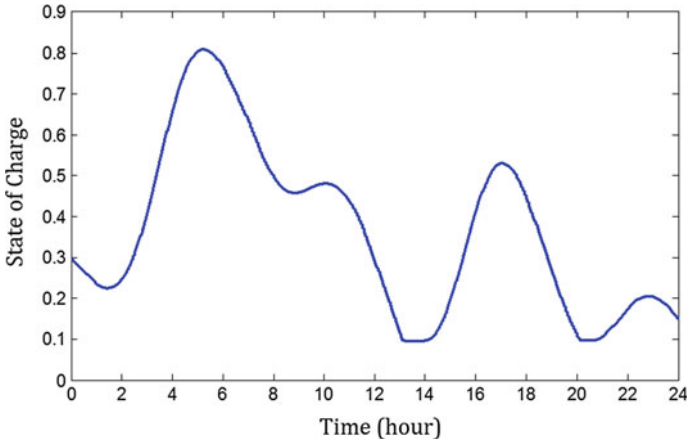

Fig. 14 SoC of the BESS (initial SoC = 0.3)

5.3 Simulation with the DG

It is reasonable to think that diesel generators are indispensible for a remote island even when renewable sources are the dominant power sources. As a backup source in this case, the DGs will operate just during small periods for insuring the load demand when the combination output of MCT and BESS is unable to supply the required load. This situation usually happens when MCT output is low (due to low tidal speed periods) and BESS SoC level is too low; and in this case the BESS cannot provide enough power to eliminate the deficiency between MCT output and load demand.

In order to avoid battery SoC reaching the low limitation and to insure the island grid demand power requirement to be satisfied at any time, the diesel generator is added to the simulation system in this section. The DG unit will be triggered when the battery SoC is near the low limitation. The DG is supposed to provide a constant power of 500 kW during the operation time. This power level is enough to cover the peak load demand (about 480 kW in the simulation).

Figure 15 compares the powers in the different parts of the MCT-based hybrid system. Figures 16 and 17 show the corresponding battery voltage/current and SoC variations.

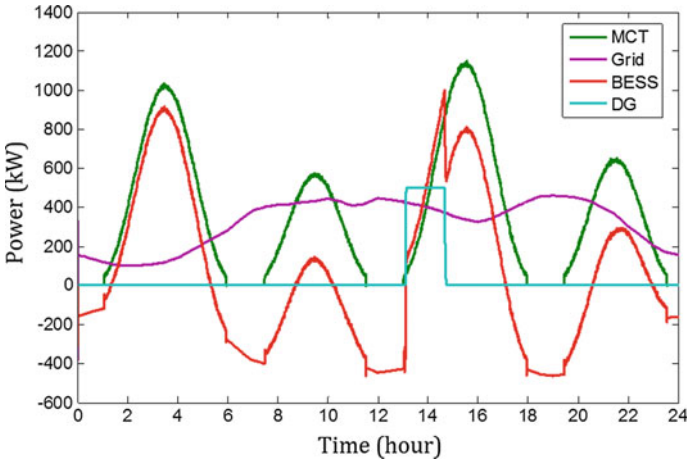

Fig. 15 Powers of the MCT system with BESS and DG

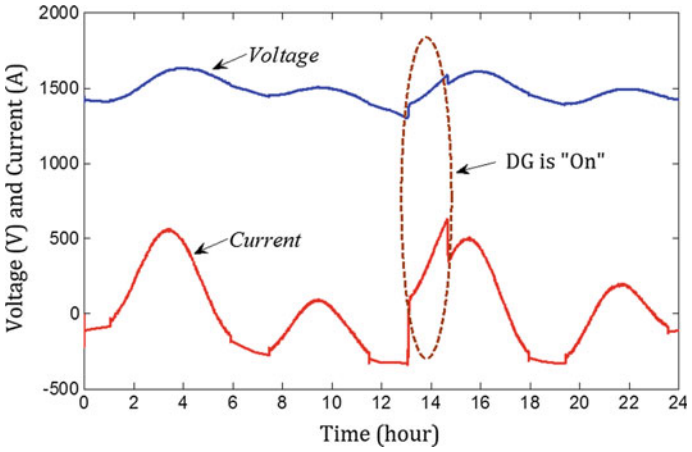

Fig. 16 Voltage and current of the BESS

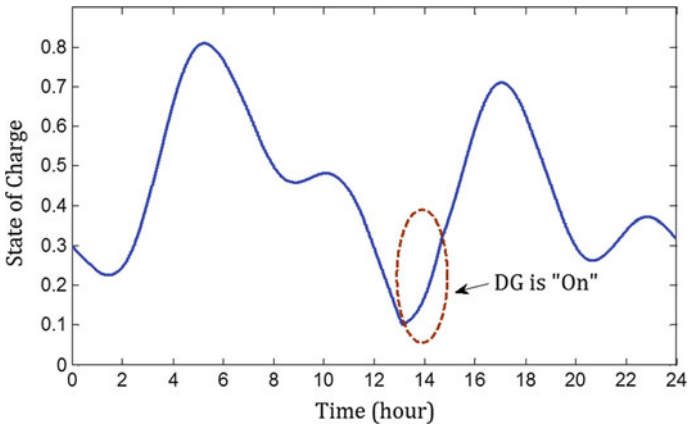

Fig. 17 SoC of the BESS

It can be seen that the DG is triggered at about 13:00 when the battery SoC is close to the low limitation 0.1. Then DG will provide power to maintain the grid demand and the battery is charged by both DG and MCT powers. The DG is turned off when the battery power reaches the rated value at 14:40; after this point the available MCT power is high enough to charge the battery and to provide grid demand power in the same time. In the simulation, another condition for turning off the DG is when the battery SoC reaches 0.4 during the charge mode. The reasons for setting these DG turnoff rules are to avoid overcharging the battery and to limit the fuel consumption of the DG.

5.4 A Small DG Case

In the previous case, the required DG power level (500 kW) is set to cover the maximum assigned load power (about 480 kW). However, when the DG is considered as a backup power source only to restore the battery at low SoC, a smaller DG might further reduce the system cost and the DG's fuel consumption. In this part, the simulation of a 250 kW DG case is carried out. Figure 18 shows the system power performance; the period of 12:00–16:00 is zoomed in Fig. 19. The corresponding battery SoC is illustrated in Fig. 20. In this smaller DG case, the battery SoC cannot be restored immediately when the DG is turned on. As shown in Fig. 19: the battery continues to provide power (periods T_1 and T_2) for maintaining the grid demand when the smaller DG is trigged; and the battery is charged (period T_3) when the available power produced by the MCT and DG is higher than the grid demand.

In the previous 500 kW DG case, the DG is in operation from 13:05 to 14:40 (Fig. 15) and provides 790 kWh. In the 250 kW DG case, the DG is in operation from 12:26 to 15:13 and provides 695 kWh. This implies that the smaller DG case

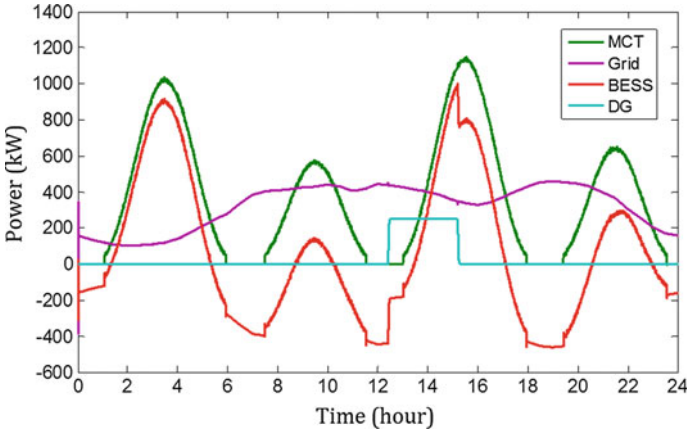

Fig. 18 Powers of the MCT-based hybrid system with small DG

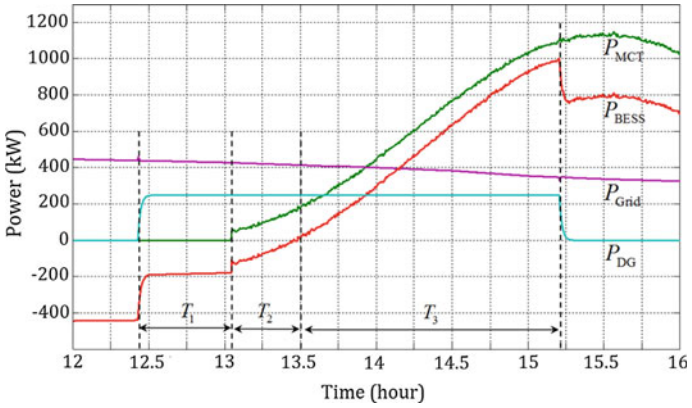

Fig. 19 Zoom of power profiles between 12:00 and 16:00

can have a possibility to further reduce diesel-fuel consumption. However, it should be noted that the small DG is incapable to cover the peak load demand; and therefore the small DG should be triggered more early than the previous case to ensure that the BESS still has a discharge margin to maintain the grid/load demand follow ability for the MCT-based hybrid system. From stability point of view for the hybrid power system, it is better to size the DG power rating enough to cover the peak load demand. This point is essentially important for the case at neap tides when the average current speed is very low and the MCT cannot produce enough powers during several days.

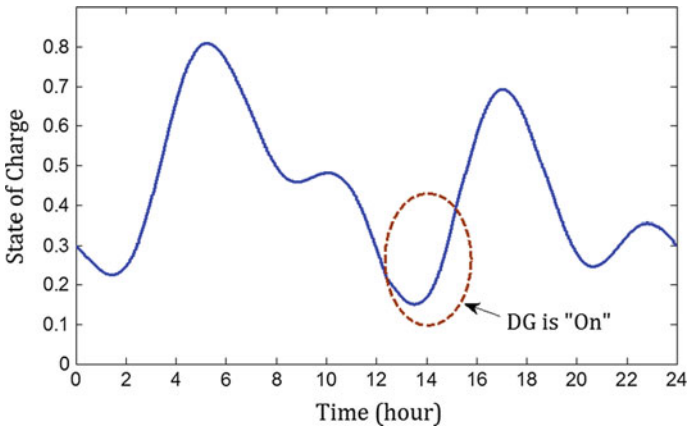

Fig. 20 SoC of the BESS

6 Power Management of the Hybrid System—DG Dominating Case

In the previous section, a large BESS is sized to shift large quantity of the MCT produced energy for compensating the large difference between the MCT output and grid/load demand. It can be seen that large ESS is indispensable when the MCT system is supposed to be the dominant power supply source (supplying almost 100% of the load demand). It means that if we want to maximally substitute the traditional fossil fuel generation units by MCT-based renewable source, it would require a very high capacity and cost of the ESS to obtain a satisfactory load following ability. This solution could be economically unrealizable if the total island load requirement is high.

Therefore, using MCT and BESS to cover a certain part of total load demand of remote stand-alone islands would be more realizable in the near future. For example, in the near future, several MCTs are planned to be installed in the Fromveur passage (near Brest, France) to supply 15–20% load demand of Ouessant Island [22]. Nowadays, most off-grid islands and remote area are strongly dependent on the DG sets for power supply [23]. However, considering the CO_2 emission issue and high fuel logistics cost, renewable energies will provide potential alternatives for reducing the diesel-fuel consumption. In the follows, Ouessant Island will be considered as a DG-dominated power supply example for the MCT-based hybrid system application.

6.1 Island Load Requirement

Ouessant Island is located 20 km off west shore of Brest, France. It has a surface of 15.6 km^2 and residential population about 900. During the summer, the population

would be over 2000 due to a large number of tourists. The daily electric power demand peak can be estimated by the national electricity consumption data. Based on [24], the daily average peak consumption in France is about 0.86 kW per capita for summers and 1.26 kW per capita for winters.

In the case of Ouessant Island, there are very few tourists on the island in winters and the winter electricity load can be estimated around 1134 kW (= 1.26 × 900). For summers, if we consider a larger population of 2500, then the estimated peak load will be about 2150 kW (= 0.86 × 2500). In fact, the island is power supplied by 4 groups of diesel generator sets with a total capacity of 5300 kVA [25]. The DG systems are usually designed with a normal power factor of 0.8, and the power ratings of the four DG sets are listed as follows.

Although there are 4 DG groups on Ouessant Island, during most time only 2 groups are in service and the other 2 groups are out of service or for maintenance [26]. That means half of the installed DG capacity enables to serve the load demand and the other half serves as a 100% backup source. It is quite reasonable to oversize the DG capacity for the off-grid island to ensure the power supply in case of emergency or DG unit's maintenance. Based on the peak load estimation, it implies that one DG of 960 kW and one DG of 1160 kW are enough for most load demands during the year on this island.

6.2 *System Configuration and Power Control Rules*

For the island case simulation, the DG system will be the main power supply source and the MCT is supposed to supply about 20–30% of the load. Figure 21 shows the daily MCT power profile and the load demands (high frequency components are neglected) used for the island case. The same current velocity and MCT power

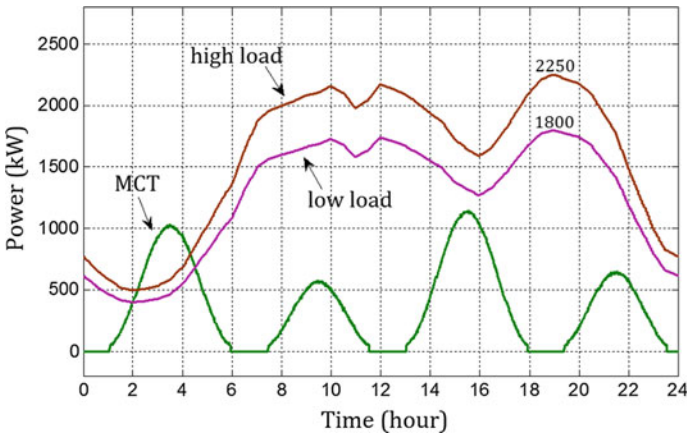

Fig. 21 Daily power profiles of the island case

profile are used, but the load demands are different from the previous MCT dominating supply case. In Fig. 21, the low load curve (range 400–1800 kW) and high load curve (range 500–2250 kW) represent two different load cases for the island. These two load curves can also be considered as examples of the island daily load in winter and summer respectively.

It should be noted that since for the island case the MCT is not supposed to provide 100% of the required load power, therefore the BESS size can be reduced compared with the cases in the MCT-dominated case. Based on the power profiles shown in Fig. 21, it can be seen that the energy needs to be stored by the BESS is greatly reduced; and it also means that the BESS is no longer required to operate continuously during the 24 h of the day. In this DG-dominated case, the BESS burden is reduced and it can be sized smaller. Therefore, for this DG-dominated case, the BESS is sized as 1.25 MWh (= 500 kW × 2.5 h). The BESS control strategy will not be changed.

For the DG system, the total available capacity is quite enough (in Table 1). However, by using MCT and BESS, it leads to possibilities for limiting the DG utilization. In this case, we consider using two DG sets: DG_1 and DG_3. The DGs should be operated over 30% of rated power for avoiding low fuel efficiency and engine damage [27]. In this DG-dominated case, the low power limitation of the DG system is set to 40% of rated power of DG_1. Therefore, the DG operational limits are given by

$$\begin{cases} P_{\mathrm{DG}_{\max}} = P_{\mathrm{DG}_1} + P_{\mathrm{DG}_3} = 2120\ \mathrm{kW} \\ P_{\mathrm{DG}_{\min}} = 40\% \times P_{\mathrm{DG}_1} = 400\ \mathrm{kW} \end{cases}. \tag{18}$$

The battery charge/discharge strategy is the same as presented in the previous section. However, for the island case, the DG output power roles are given as follows:

$$P^*_{\mathrm{DG}} = P^*_{\mathrm{DG}_{\mathrm{load}}} + P^*_{\mathrm{DG}_{\mathrm{b}}}, \tag{19}$$

with

$$P^*_{\mathrm{DG}_{\mathrm{load}}} = \begin{cases} P_{\mathrm{load}} - P_{\mathrm{MCT}}, & \Delta P_1 \geq P_{\mathrm{DG}_{\min}} \\ 0, & \Delta P_1 < P_{\mathrm{DG}_{\min}} \end{cases}.$$

$$P^*_{\mathrm{DG}_{\mathrm{b}}} = \begin{cases} P_{\mathrm{DG}_{\min}}, & \text{turn on} \\ 0, & \text{turn off} \end{cases}$$

Table 1 Diesel generators on Ouessant Island

	Apparent power (kVA)	Active power (kW)
DG_1	1200	960
DG_2	1200	960
DG_3	1450	1160
DG_4	1450	1160
Total	5300	4240

Equation (19) shows that the required DG output can be represented by two main elements: $P^*_{DG_{load}}$ represents the demanded DG power for supplying the island load, and the DG low load limitation should be considered in this part ($\Delta P_1 = |P_{load} - P_{MCT}|$ is used to avoid the DG low load operation); and $P^*_{DG_b}$ represents the needed DG power for charging the battery system. The power rule for $P^*_{DG_b}$ is designed in this way: when the battery SoC reaches the low limitation of 0.11, the term $P^*_{DG_b}$ will be turned on and fixed to the $P_{DG_{min}}$; the term $P^*_{DG_b}$ will be turned off $\left(P^*_{DG_b} = 0\right)$ when battery SoC is restored to 0.5 or when the total available battery charging power (from MCT and DG) reaches the battery rated power of 500 kW. Finally, the total P^*_{DG} will be limited by the $P_{DG_{max}}$ described in Eq. (18).

6.3 High Load Demand Case

Figure 22 shows the system power responses for the high load case with an initial battery SoC of 0.5. The BESS voltage/current and SoC variations are shown in Figs. 23 and 24. The BESS works well to store the excessive MCT produced power (2:10–4:20) and provide the power during the peak load around 12:00 and 19:00 as shown in Fig. 22.

It can be imagined that if there were no BESS, a third DG would be used in these peak load periods. This illustrates the load-leveling benefit brought by the BESS in the hybrid power supply system. It should be noted that the BESS also helps to avoid the DG low power operation when the MCT power is close to the load demand. In fact, the MCT produced power is seen as a negative load for the DGs; if there were no BESS, the MCT power would cause low load DG operation in some

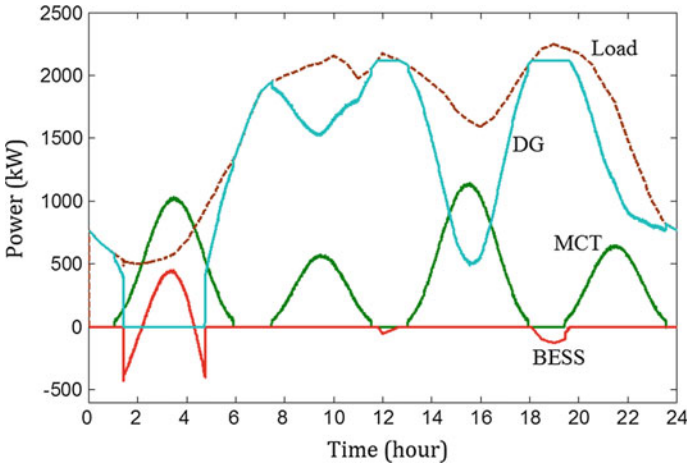

Fig. 22 Powers of the high load demand case (initial SoC = 0.5)

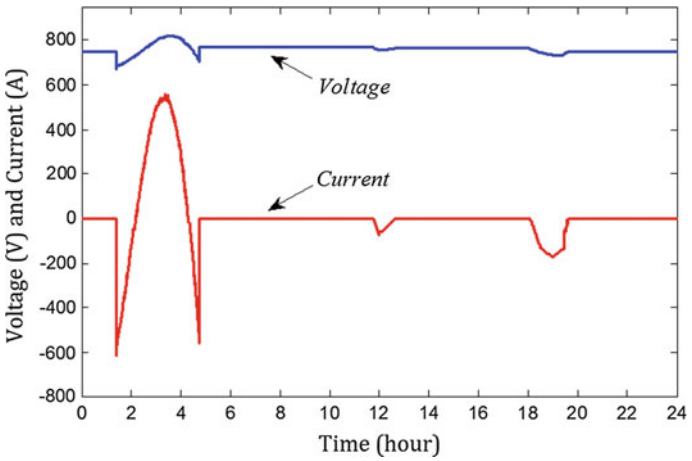

Fig. 23 Voltage and current of the BESS (initial SoC = 0.5)

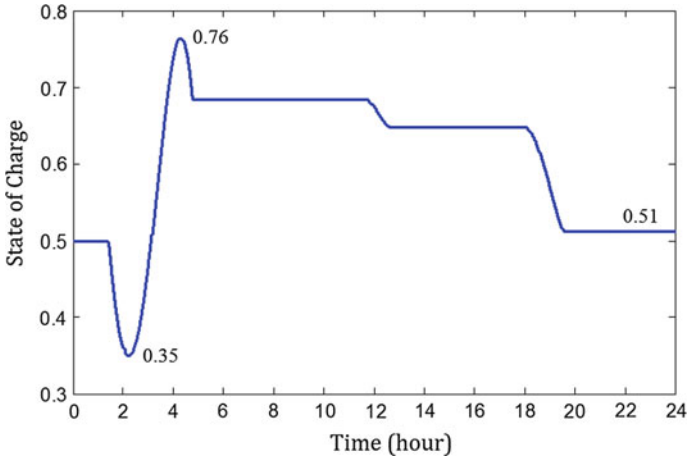

Fig. 24 SoC of the BESS (initial SoC = 0.5)

cases. This problem is successfully handled by the BESS in the proposed power management strategy.

In case of low battery SoC, the DG will be used to charge the battery. Figure 25 shows the system power profiles and Fig. 26 shows the battery SoC variation for the case of low BESS initial SoC. The zoomed curves on the period of 0:00–6:00 are illustrated in Figs. 27 and 28. From Fig. 27, it can be seen that the BESS is discharged during 1:25–2:00 and 4:20–4:46 for avoiding the DG low load operation and saving diesel-fuel consumption. When the battery SoC reaches 0.11, the DG provides power and the BESS is charged by the DG and MCT during 2:00–2:22

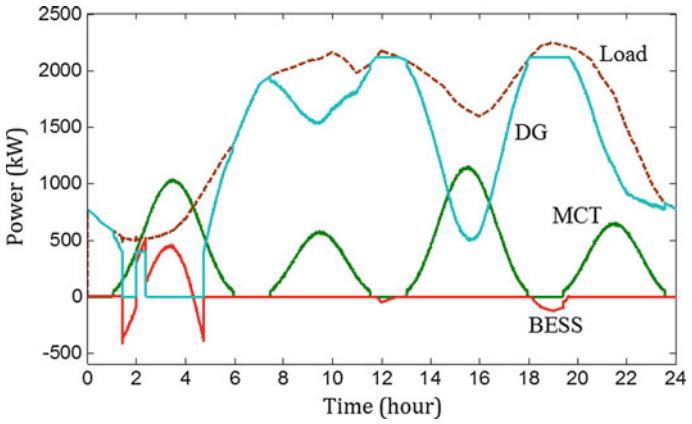

Fig. 25 Powers of the high load demand case (initial SoC = 0.25)

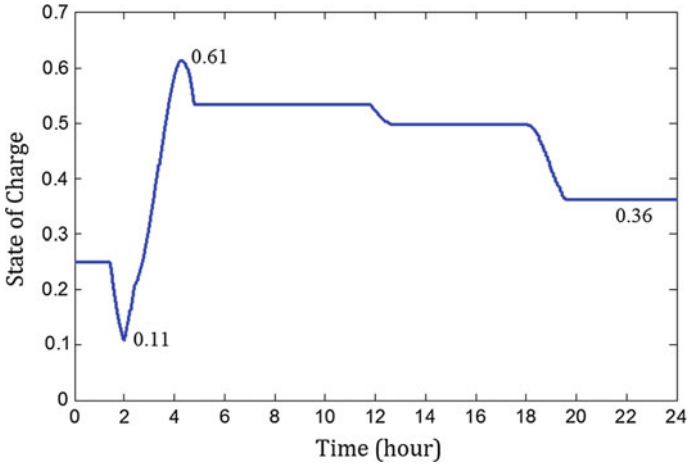

Fig. 26 SoC of the BESS (initial SoC = 0.25)

until the battery attends its rated power. After this point, the DG is turned off and the BESS is charged by excessive MCT power during 2:22–4:20.

6.4 Low Load Demand Case

In the previous section, the high load demand case may also happen during neap tides when tidal current speed is very low. In this section, the opposite case called low load demand case will be studied. The low load case will happen at low load periods (winter case in Ouessant Island) or spring tides when MCT output is high

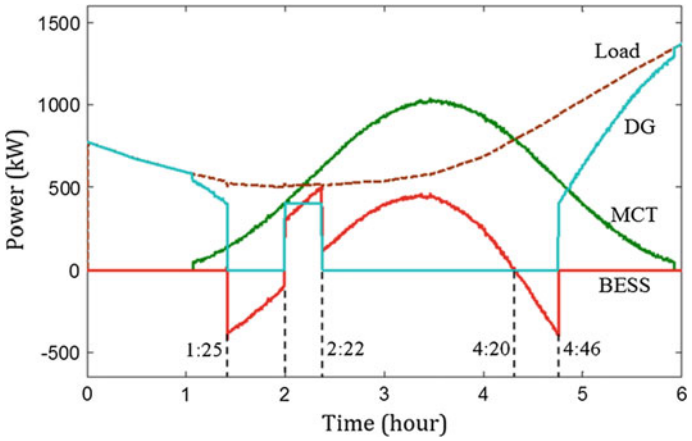

Fig. 27 Zoomed power curves (initial SoC = 0.25)

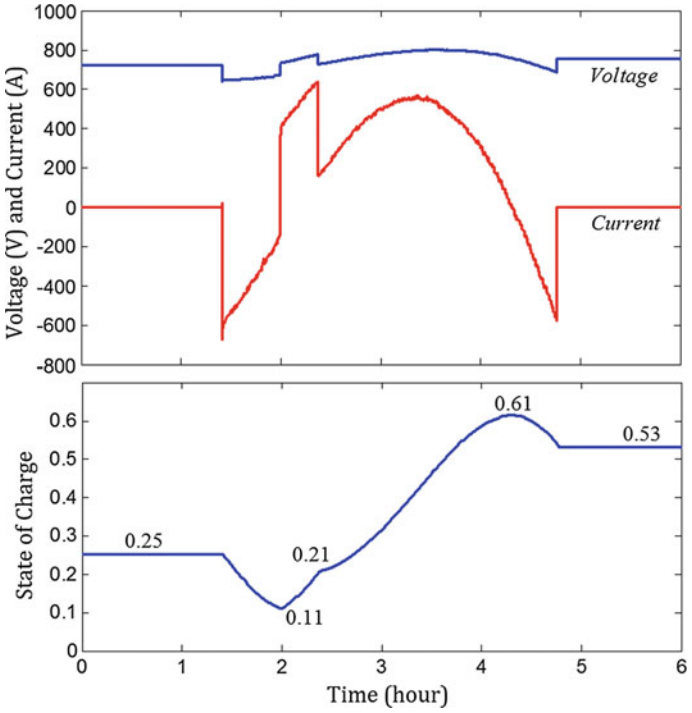

Fig. 28 Zoomed BESS curves (initial SoC = 0.25)

due to high tidal current speed. In the low load demand case, the DG can easily handle the peak load but the new constrain is that the MCT power will need to be limited when the MCT power is too high.

In the simulation, the same MCT power profile is used while the low load demand (in Fig. 21) is applied. As shown in Fig. 29, the MCT power has to be controlled to deviate from MPPT during 3:00–3:35 for limiting the BESS charging power at its rated value of 500 kW. Although the BESS is charged by the MCT to a high SoC value (Fig. 30), the BESS will be discharged during 14:55–16:15 to avoid DG low load operation and the battery output power is added to the MCT one for supplying the load requirement. It can be seen that, the DG utilization can be reduced and the battery SoC enables to maintain at a same level with the initial value at the end of day by the proposed power management strategy.

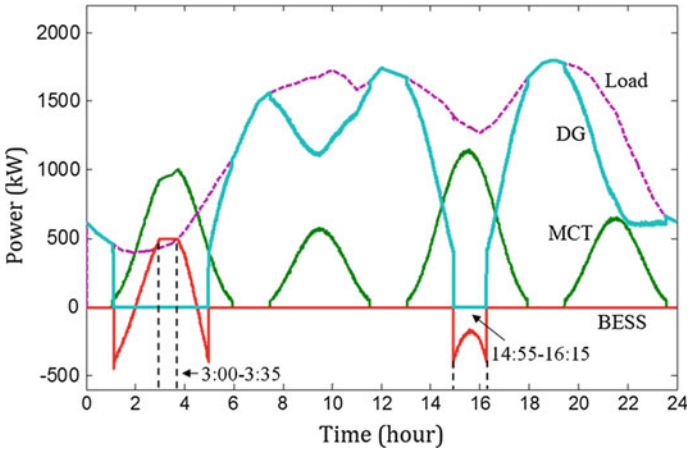

Fig. 29 Powers of the low load demand case

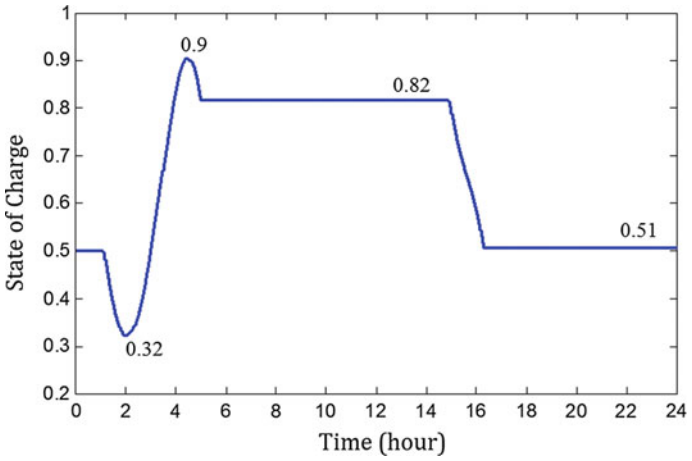

Fig. 30 SoC of the BESS

6.5 Without BESS

It is also interesting to show what would happen if there is no ESS. That means only MCT and DG are used to supply the load demand. In this case, the rules are given in Table 2. The load demand should be satisfied at all moments $\left(P^*_{\mathrm{MCT}} + P^*_{\mathrm{DG}} = P_{\mathrm{load}}\right)$; and the required MCT output power P^*_{MCT} should deviate from $P_{\mathrm{MCT_{MPPT}}}$ (maximum available MCT power) during some periods according to the power balance situation.

Figure 31 shows the power curves when there is no available ESS in the hybrid power supply system. In this figure, the dotted green curve shows the MCT power under MPPT strategy and the solid green curve shows the real MCT output power based on the proposed rules. It can be seen that during 2:00–4:30 and 14:55–16:15, the MCT is unable to follow the MPPT strategy due to the low load demand and the DG low load power limit respectively. This result indicates that, in this case, MCT output power potential cannot be fully utilized, and the complexity of the MCT power control will be increased.

Table 2 Power rules without the BESS $(\Delta P_2 = P_{\mathrm{load}} - P_{\mathrm{MCT_{MPPT}}})$

	$\Delta P_2 \leq 0$	$0 < \Delta P_2 \leq P_{\mathrm{DG_{min}}}$	$\Delta P_2 > P_{\mathrm{DG_{min}}}$
P^*_{MCT}	P_{load}	$P_{\mathrm{load}} - P_{\mathrm{DG_{min}}}$	$P_{\mathrm{MCT_{MPPT}}}$
P^*_{DG}	0	$P_{\mathrm{DG_{min}}}$	$P_{\mathrm{load}} - P_{\mathrm{MCT_{MPPT}}}$

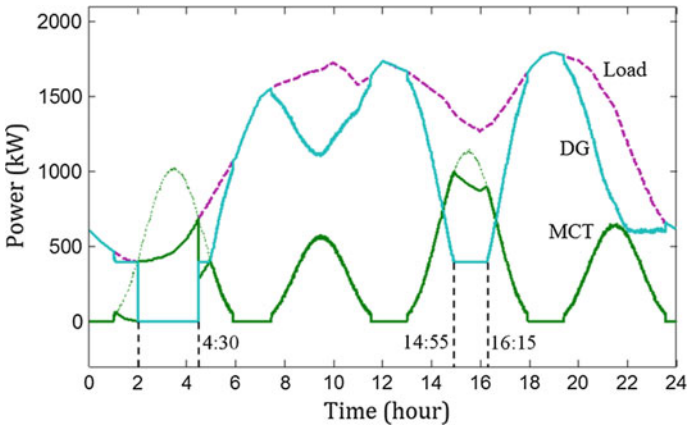

Fig. 31 Powers curves without the BESS

Table 3 DG consumption saving during 1 day

		E_{load} (MWh)	E_{MCT} (MWh)	E_{DG} (MWh)	Consumption saving (%)
High load	With BESS	37.9	8.6	29.5	22.2
	No BESS	37.9	7.8	30.1	20.6
Low load	With BESS	30.3	8.57	21.95	27.6
	No BESS	30.3	7.26	23.04	24.0

6.6 Diesel-Fuel Consumption Reduction

Table 3 summarizes the energy performance for comparing the DG consumption with and without the BESS in both high load and low load cases. The daily load demand energy E_{load}, the MCT produced energy E_{MCT} and the DG-provided energy E_{DG} are calculated by integration the corresponding power curves. The "with BESS" cases are based on the simulation results for the battery initial SoC of 0.5. The DG consumption saving is then calculated by Eq. (20); it indicates that how much DG consumption can be saved with the MCT and BESS.

$$E_{DG_{saving}} = \frac{E_{load} - E_{DG}}{E_{load}} \tag{20}$$

It can be seen from Table 3 that, in both high load demand and low load demand cases, the BESS enables to increase the MCT output energy. This is because that the BESS greatly facilitates to keep the MCT in maximal power extraction mode, especially in low load demand cases (3.6% increase of the DG consumption saving compared with the case without BESS).

It also indicates that when the MCT penetration increases (about 22% in the high load case and 27.6% in the low load case), the importance and requirements of the BESS will increase simultaneously. From the obtained simulation results (Figs. 24 and 30), it can be found that the battery SoC variation is much larger in the high penetration case (the low load demand case). Therefore, the conclusion is that larger BESS is required for higher MCT penetration. Although higher MCT penetration can result lower diesel-fuel consumption, the increasing ESS need would be considered as a constraint for optimizing the total system cost.

7 Conclusions and Perspectives

In this chapter, the hybrid power system of MCT/BESS/DG is studied for daily power management on a small stand-alone island. The VRB is chosen as the BESS type due to its high-energy capacity and relative flexible energy/power sizing. The flow battery is modeled by an equivalent circuit method, and the empirical model parameter

estimation based on battery nominal power and nominal losses are given. One 1.5 MW fixed-pitch MCT is chosen to represent the MCT output power (this may also be considered as a small MCT farm with three identical 500 kW MCTs). The MCT is supposed to operate under MPPT for capturing maximal power from the tidal current flow during most cases. Two different power supply configurations are studied: the MCT-dominated supply case (MCT power covers about 100% of the load) and the Diesel-dominated supply case (MCT power covers about 20–30% of the load).

For the MCT-dominated supply case, the DG consumption is maximally limited by serving as a backup source only for charging the BESS at low SoC. The load following ability is then totally realized by the BESS and this leads to a large battery system of 3 MWh for the one 1.5 MW MCT-based hybrid system. Obviously, the daily load energy assignment for this MCT/BESS system can hardly excess the daily energy production of the MCT. Therefore, if the MCT-dominated supply case is applied to meet the electricity needs of a remote island like Ouessant Island, the studied unit (1.5 MW MCT, 3 MWh BESS, and 500 kW DG) should be multiplied to 4 times for covering the total island load demand. High cost of megawatt MCTs and large BESS can make this solution economically nonattractable in the now stage.

For the Diesel-dominated supply case, load requirements based on the configuration of Ouessant Island and the existing DG capacity of this island are considered as the studied cases. The high load demand and low load demand cases are studied and compared. In this case, the DG groups serve as the main power supply source and a 1.25 MWh BESS is carried out in the simulation. Simulation results show that the BESS enables to facilitate the maximal power extraction operation of the MCT and contributes to reduce the diesel-fuel consumption.

Concerning future MCT farm applications for stand-alone islands, the MCT penetration would be increased to further reduce the local DG consumptions. In most cases, cost-benefit assessments are major concerns before the final commercialization. The configuration of the hybrid system (power rating of single MCT and the total number of MCTs, BESS sizing, DG ratings and numbers) depends highly on the specific site conditions, load demand profile, the costs (short term and long term) and the diesel-fuel consumption's reduction objective. In any way, the trend of applying the hybrid MCT/BESS/Diesel supply system for remote islands is strong due to the world common need of replacing fossil fuel-based power supply systems by renewable-energy based hybrid systems.

Other renewable sources, such as wave energy, solar energy and wind energy, can also be integrated in MCT-based hybrid island power supply scheme. In this trend, the ESS energy capacity requirement may also be increased to insure the power balance between produced power and demand. Higher energy capacity technologies such as ocean-based or underwater-compressed air energy storage (OCAES or UWCAES) [28, 29] could be interesting due to their applicable ranges and the economic feasibility.

Appendix: Flow Battery Equivalent Circuit Parameters

See Tables 4, and 5

Table 4 Parameters of the VRB equivalent circuit

3 MWh (= 1 MW × 3 h) Battery for the MCT-dominated supply case	
R_{fixed}	54.071 Ω
$R_{reaction}$	0.135 Ω
$R_{resistive}$	0.09 Ω
$C_{electrodes}$	0.0056 F
I_{pump} coefficient	0.0094

Table 5 Parameters of the VRB equivalent circuit

1.25 MWh (= 0.5 MW × 2.5 h) Battery for DG-dominated supply case	
R_{fixed}	27.036 Ω
$R_{reaction}$	0.067 Ω
$R_{resistive}$	0.045 Ω
$C_{electrodes}$	0.0011 F
I_{pump} coefficient	0.0094

References

1. Ng KW, Lam WH, Ng KC (2013) 2002–2012: 10 years of research progress in horizontal-axis marine current turbines. Energies 6(3):1497–1526
2. Zhou Z, Scuiller F, Charpentier JF et al (2014) An up-to-date review of large marine current turbine technologies. In: IEEE international power electronics and application conference and exposition, Shanghai, November 2014. IEEE, New York, pp 480–484
3. Zhou Z, Benbouzid MEH, Charpentier JF et al (2013) A review of energy storage technologies for marine current energy systems. Renew Sustain Energy Rev 18:390–400
4. Zhou Z, Scuiller F, Charpentier JF et al (2014) Application of flow battery in marine current turbine system for daily power management. In: IEEE international conference on green energy Sfax, March 2014. IEEE, New York, pp 8–13
5. Zhou Z, Scuiller F, Charpentier JF et al (2013) Power smoothing control in a grid-connected marine current turbine system for compensating swell effect. IEEE Trans Sustain Energy 4 (3):816–826
6. Batten WMJ, Bahaj AS, Molland AF et al (2008) The prediction of the hydrodynamic performance of marine current turbines. Renew Energy 33(5):1085–1096
7. Chiang MH (2011) A novel pitch control system for a wind turbine driven by a variable-speed pump-controlled hydraulic servo system. Mechatronics 21(4):753–761
8. Zhou Z, Scuiller F, Charpentier JF et al (2015) Power control of a non-pitchable PMSG-based marine current turbine at over-rated current speed with flux-weakening strategy. IEEE J Oceanic Eng 40(3):536–545
9. Pham CT, Martin VA (2009) Tidal current turbine demonstration farm in Paimpol-Bréhat (Brittany): tidal characterization and energy yield evaluation with Telemac. In: 8th European wave and tidal energy conference, Uppsala, September 2009. IEEE, New York, pp 181–188
10. KHPS (2016) Kinetic hydropower system—Verdant power. http://www.verdantpower.com/kinetic-hydropower-system.html. Accessed 30 Oct 2016
11. Wu B, Zhang B, Wang J et al (2010) Theoretical research for the application of flow storage battery in demand side management. In: IEEE POWERCON conference, Hangzhou, October 2010. IEEE, New York, pp 1–7

12. Luo X, Wang J, Dooner M et al (2015) Overview of current development in electrical energy storage technologies and the application potential in power system operation. Appl Energy 137:511–536
13. Hall PJ, Bain EJ (2008) Energy-storage technologies and electricity generation. Energy Policy 36:4352–4355
14. Muhando BE, Wies RW, Johnson TH et al (2012) Grid-scale rampable dispatchable storage: cascaded use of advanced battery technology to increase energy security in Alaska. In: IEEE power and energy society general meeting, San Diego, July 2012. IEEE, New York, pp 1–8
15. Alotto P, Guarnieri M, Moro F (2014) Redox flow batteries for the storage of renewable energy: a review. Renew Sustain Energy Rev 29:325–335
16. ESA (2016) Energy storage technologies. http://energystorage.org/energy-storage/energy-storage-technologies. Accessed 30 Oct 2016
17. Chahwan J, Abbey C, Joos G (2007) VRB modeling for the study of output terminal voltages, internal losses and performance. In: IEEE electrical power conference (EPC), Montreal, October 2007. IEEE, New York, pp 387–392
18. Li W, Joos G, Bélanger J (2010) Real-time simulation of a wind turbine generator coupled with a battery supercapacitor energy storage system. IEEE Trans Ind Electron 57(4):1137–1145
19. Wang W, Ge B et al (2010) Grid-connect wind farm power control using VRB-based energy storage system. In: IEEE energy conversion congress and exposition, Atlanta, September 2010. IEEE, New York, pp 3772–3777
20. Caricchi F, Crescimbini F et al (1998) Study of bi-directional buck-boost converter topologies for application in electrical vehicle motor drives. In: 13th annual applied power electronics conference and exposition, Anaheim, February 1998, vol 1. IEEE, New York, pp 287–293
21. Tara E, Filizadeh S et al (2012) Dynamic average-value modeling of hybrid-electric vehicular power systems. IEEE Trans Power Deliv 27(1):430–438
22. Hamard J (2013) Hydrolien Sabella prête pour l'immersion dans le Fromveur. http://www.letelegramme.fr/local/finistere-nord/brest/ville/hydrolien-sabella-prete-pour-l-immersion-05-04-2013-2059467.php. Accessed 30 Oct 2016
23. Arriaga M, Canizares CA, Kazerani M (2013) Renewable energy alternatives for remote communities in northern Ontario, Canada. IEEE Trans Sustain Energy 4(3):661–669
24. RTE-France (2015) Consommation d'électricité. http://www.rte-france.com/fr/eco2mix/eco2mix-consommation. Accessed 30 Oct 2016
25. Sys ENR (2016) Maîtrise de l'énergie et production d'énergies renouvelables sur les îles d'Ouessant et Molène. http://www.sysenr.com/actualites/maitrise-energie-production-energies-renouvelables-ouessant-molene.html. Accessed 30 Oct 2016
26. AFP (2013) Panne d'électricité à Ouessant. http://www.lefigaro.fr/flash-actu/2013/01/13/97001-20130113FILWWW00152-panne-d-electricite-a-ouessant.php. Accessed 30 Oct 2016
27. Kusakana K, Vermaak HJ (2013) Hybrid diesel generator—battery systems for off-grid rural applications. In: IEEE international conference on industrial technology, Cape Town, February 2013. IEEE, New York, pp 839–844
28. Sheng L, Zhou Z, Charpentier JF et al (2015) Island power management using a marine current turbine farm and an ocean compressed air energy storage system. In: Proceedings of the 11th European wave and tidal energy conference, Nantes, September 2015
29. Rogers A, Henderson A et al (2014) Compressed air energy storage: thermodynamic and economic review. In: IEEE PES general meeting, Washington, July 2014. IEEE, New York, pp 1–5

Optimal Power Flow of a Battery/Wind/PV/Grid Hybrid System: Case of South Africa

K. Kusakana

Abstract Photovoltaic and wind systems have been demonstrated to be sustainable alternatives of producing electricity in rural electrification, particularly in islanded applications. Currently, the advancement of research in the area of power electronics has allowed the connection of these renewable resources to the grid with bidirectional power flow. In this work, the optimal power scheduling for a grid-connected photovoltaic–wind–battery hybrid system is proposed to maximize the use of solar and wind resources to assist customers at demand side. The developed model for the hybrid system's optimal power flow management aims to minimize electricity purchased from the grid while maximizing the energy sold to the grid as well as the production of the renewable sources subject to the power balance, photovoltaic, wind, and battery storage outputs as well as other operational constraints. Relating to demand-side management, a control technique is developed to optimally schedule the power flow from the different components of the hybrid system over 24-h horizon. Simulations are performed using MATLAB, and the results demonstrate that operating the proposed hybrid system under the developed optimal energy management model can reduce the operation cost and allow consumers to generate substantial income by selling power to the grid.

Keywords Photovoltaic energy · Wind · Hybrid system · Optimal scheduling

1 Introduction

Renewable energy (RE) sources have become attractive choices of generating electricity in comparison to traditional fossil fuels due to different characteristics such as low cost, no pollutant emission, energy security as well as their modularity [1].

K. Kusakana (✉)
Department of Electrical, Electronic and Computer Engineering,
Central University of Technology, Bloemfontein, Free State, South Africa
e-mail: kkusakana@cut.ac.za

F.M.R. Islam et al. (eds.), *Smart Energy Grid Design for Island Countries*,
Green Energy and Technology, DOI 10.1007/978-3-319-50197-0_14

Renewable energy sources can be used in islanded or as grid-connected mode where bidirectional power flow can be implemented to buy or sell power to the utility company [2]. Because of the intermittent nature of their resources, renewable power systems are regularly coupled with storage systems such as batteries [3]. Energy storage systems can be used to ensure that the variable load demand is continuously met irrespective of the intermittency of the renewable resources [4].

Generally, grid-connected renewable systems do not necessitate battery storage systems. Therefore, advanced energy management systems are also not needed [5]. Maximizing the use of the power from the renewable sources is the only operation strategy implemented when the power generated is less than the instantaneous load power demand [6]. For grid-connected renewable with battery storage systems, the energy management becomes more difficult, as more complicated operation strategies must be taken into account, such as charging the battery from the grid or renewable source and discharging into the grid or to the load when necessary [7]. As a result, controllers are required for hybrid renewable-battery systems, such that the use of the renewable system can be considerably improved and the grid regulation can be enhanced in terms of safety, reliability, and efficiency [8].

For grid-connected hybrid renewable-battery systems, the changing electricity price imposed by the utility, the period of power transaction, and the balance between the instantaneous renewable power produced and the instantaneous load demand are main challenges encountered while implementing any suitable energy management strategy [9]. Several demand-side management (DSM) programs can be implemented when renewable energy systems are connected to the grid:

- Peak shaving: Where consumers can shift the usage of their electrical appliances to reduce the peak power demand [10].
- Direct load control: In which a utility operator remotely shuts down or cycles a customer's electrical equipment at short notice to address system or local reliability [11].
- Capacity market programs: In which customers commit to respond pre-specified load reduction when system contingencies arise and are subject to penalties if they do not curtail power consumption when directed [12].
- Time-of-use (TOU): Where the electricity price is high in the peak load time and low in the off-peak time [13].

From DSM approach, the energy from the renewable sources or from the grid can be stored when the generation is higher than the demand or when the electricity price from the grid is very low. The stored energy can then be used to supply the load during peak power demand; to be sold to the grid when the electricity price from the utility is high or even when the power from the renewable resources is unavailable [14]. Well-managed grid-connected hybrid system with DSM program can assist customers in substantially reducing their electricity cost, and also can assist utility companies to control the grid in terms of security and efficiency issues while increasing the reliability.

Therefore, at both supply and demand side, grid-connected systems can bring in new opportunities to smart grid but also induce several challenges in the following DSM programs. For the specific case of grid-connected renewable sources with battery storage systems operation under TOU scheme, challenges such as determining how to optimally schedule the hybrid system in peak, standard and off-peak periods with the aim of minimizing the total electricity cost and satisfying the consumer demand as well.

Research works have already been conducted on grid-connected renewable systems. However, most of these studies have focused on energy management for large-scale integration of renewable energy at the utility side [15, 16]. Currently, there are very few studies reporting on the optimal energy management and DSM for small-scale grid-connected hybrid systems at the demand side, because hybrid systems are installed for stand-alone or backup usage without any contribution of DSM program.

Wolisz et al. [17] have analyzed the feasibility and the resulting potential of coupling the electricity grid with the thermal supply of residential buildings. In this paper the technical and economical key impact factors for such thermal DSM approach are elaborated. The practicability and possible magnitude of the intended DSM is then analyzed based on the identified scenarios. It is found that especially the strong dissemination of smart metering and smart control infrastructure is crucial to incorporate these capacities into DSM activities.

Dufo-Lopez and Bernal-Agustin [18] have presented a methodology to evaluate the technical and economic performance of a grid-connected system with storage under a time-of-use electricity tariff. The storage can help smooth demand, reducing peak demand from the grid and, in some cases, also reducing the electricity bill for the consumer.

Dufo-Lopez [19] has considered a storage system to be added to a private electricity facility in order to reduce the electricity bill. This kind of system could make sense with a time-of-use tariff (with two or three periods of different electricity price) or a real-time pricing tariff, where each day, electricity is bought from the AC grid during off-peak hours to store energy, and during on-peak hours, the storage supplies the whole load or a part, avoiding the purchase of expensive electricity from the AC grid.

Sichilalu and Xia [20] have developed an optimal scheduling strategy model for a grid-tied photovoltaic (PV) system to power a heat pump water heater (HPWH). The system is composed of PV modules that are grid-tied and a backup battery. The PV is capable of supplying power simultaneously to the HPWH and domestic load, while the grid and the battery are complementary sources. The objective function of this model is energy cost. The time-of-use (TOU) electricity tariff is taken into account in the optimal scheduling model. The control variables are the power flows within the branches of the system. This model has shown to have more economic benefits than solar thermal heaters, because of the possibility to turn the dwelling into net-zero energy or positive-energy buildings with the attractiveness of the feed-in tariff.

Unlike the above-mentioned papers, the focus of this chapter will be on analyzing a more comprehensive grid-connected PV-WT-battery system under the Time-of-Use (TOU) program with contracted selling as an example using the specific South African context. An optimal power flow management algorithm of the proposed hybrid system is developed aiming to minimize the electricity purchased from the grid, maximize the energy sold to the grid as well as the renewable production within the DSM framework while satisfying the load demand. It will be shown how the developed system can assist consumers to optimally schedule the system's operation to earn cost savings with changing prices in the TOU program, and how they can manage their generation, consumption, and storage to sell surplus power to the grid over peak period.

2 Description of Hybrid System and Proposed Methodology

The hybrid system analyzed in this work is composed of a PV system, wind system, and battery bank that are connected to the grid. The output power of the renewable systems feeds the load demand directly. If the demand is less than the renewable output, the surplus power will be stored into the battery bank. If the load power requirement is larger than the renewable output, the deficit of power will be supplied by the battery or the grid. The grid plays a preponderant role in the hybrid system for charging the battery and directly supplying the load demand depending on the price of electricity in the considered time interval. The battery can be charged by the grid in the off-peak period, and then discharged in the peak period either to the load or to the grid to save electricity cost. The grid provides electricity directly when the load cannot be entirely met by the renewable sources and the battery storage system. The schematic of this hybrid system is shown in Fig. 1, in which arrows represent directions of power flows in the hybrid system. $P_{\text{PV-B}}$ and $P_{\text{WT-B}}$ are the renewable powers used for charging the battery; $P_{\text{B-L}}$ is the discharging power of battery for load demand; $P_{\text{G-B}}$ is the grid power for charging the battery; $P_{\text{G-L}}$ is the grid power for load demand; $P_{\text{PV-L}}$ and $P_{\text{WT-L}}$ are the renewable powers directly supplying load demand; P_{SOLD} is the battery discharge for selling power to the grid.

2.1 Photovoltaic System

When light strikes a silicon, gallium arsenide, or cadmium sulfide cell, an electric current is generated through the photovoltaic effect. The power rating of a PV panel is expressed in peak Watts (Wp) indicated at "standard test conditions" conducted

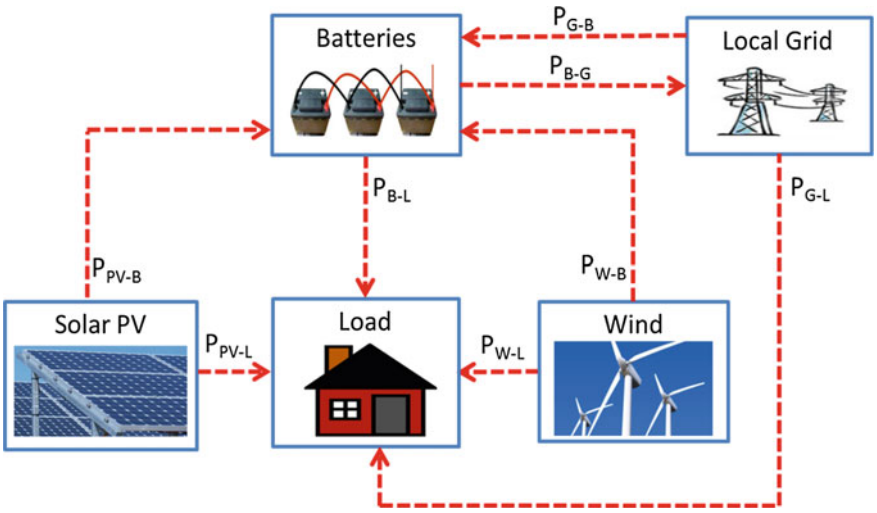

Fig. 1 Hybrid system layout (power flow)

at a temperature of 25 °C and irradiance of 1000 W/m^2. The output power of the solar PV system can be expressed as follows [21]:

$$P_{\mathrm{PV}} = A_{\mathrm{PV}} \times \eta_{\mathrm{PV}} \times I(t) \times f(t) \times \mathrm{d}t \tag{1}$$

where A_{PV} is the total area of the photovoltaic generator (m^2); η_{PV} is the module efficiency; I is the hourly irradiance (kWh/m^2); and $f(t)$ is the radiance density.

2.2 Wind Energy System

Wind energy systems convert the kinetic energy of moving air into mechanical and then electrical energy [21]. The power output (P_{WT}) of the wind system within a sampling time interval can be expressed as

$$P_{\mathrm{WT}} = \frac{1}{2} \times \rho_{\mathrm{a}} \times A_{\mathrm{WT}} \times C_{\mathrm{p,WT}} \times \eta_{\mathrm{WT}} \times v_a^3(t) \times f(t) \times \mathrm{d}t \tag{2}$$

where ρ_{a} is the air of water (1225 kg/m^3); $C_{\mathrm{p,WT}}$ is the coefficient of the wind turbine performance; η_{WT} is the combined efficiency of the wind turbine and the generator; A_{WT} is the wind turbine swept area (m^2); v_a is the wind velocity (m/s); and $f(t)$ is the wind probability density function.

2.3 Battery Storage System

The power flows from the PV, the grid, and the load demand at any given sampling interval j, determine whether the battery is charging or discharging. The dynamics of the battery state of charge (SOC) can be expressed in discrete-time domain by a first-order difference equation as follows [22, 23]:

$$\mathrm{SOC}_{(j+1)} = (1 - d_\mathrm{b}) \times \mathrm{SOC}_{(j)} + \frac{\Delta t \times \eta_\mathrm{C}}{E_\mathrm{nom}} \times (P_{\text{PV-B}(j)} + P_{\text{G-B}(j)} - \frac{\Delta t}{E_\mathrm{nom}\eta_\mathrm{D}} \times (P_{\text{B-L}(j)} + P_{\text{SOLD}(j)}) \quad (3)$$

where SOC is the state of charge of the battery; d_b is the self-discharging rate of the battery storage system; η_C is the battery charging efficiency; η_D is the battery discharging efficiency; and E_nom is the battery system nominal energy.

By induction reasoning, the dynamics of the battery state of charge at jth sampling interval can be expressed in terms of its initial value $\mathrm{SOC}_{(0)}$ of a day as follows:

$$\mathrm{SOC}_{(j)} = (1 - d_\mathrm{b}) \times \mathrm{SOC}_{(0)} + \frac{\Delta t \times \eta_\mathrm{C}}{E_\mathrm{nom}} \times \sum_{i=0}^{j-1} (P_{\text{PV-B}(j)} + P_{\text{G-B}(j)}) - \frac{\Delta t}{E_\mathrm{nom}\eta_\mathrm{D}} \times \sum_{i=0}^{j-1} (P_{\text{B-L}(j)} + P_{\text{SOLD}(j)}) \quad (4)$$

2.4 Flowchart of the Proposed Optimization Methodology

The simplified flowchart of the proposed methodology is presented in Fig. 2. The main optimization variables are described below:

- Independent variables: Load demand, solar and wind resources, Time-of-Use.
- Dependent variables are all variables which are affected by any change or variation in the input variables. In this case it is mainly the battery state of charge (SOC).
- Controlled variable: The powers related to the renewable sources, storage, and the grid are considered as controlled variables.

3 Optimization Model and Proposed Optimal Control Algorithm

As stated in the introduction, the optimization problem addressed in this work aims to minimize the electricity cost within the framework of TOU in which the electricity price changes over different time intervals according to cost imposed by the

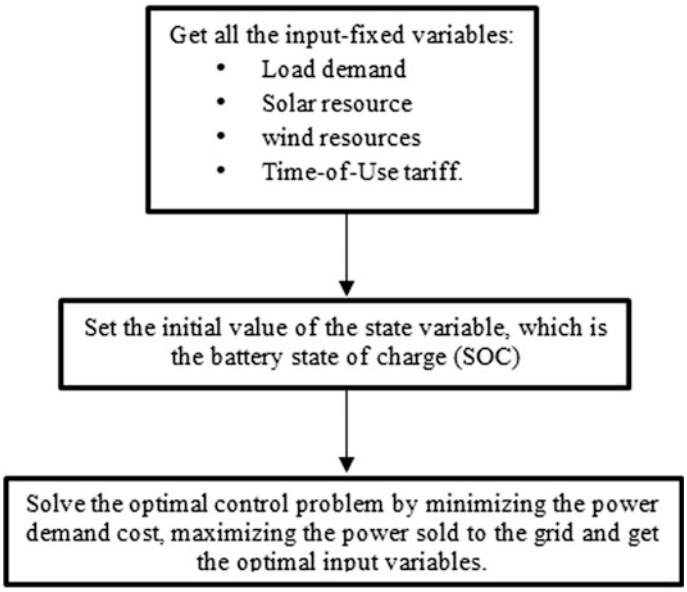

Fig. 2 Flowchart of the proposed optimization methodology

utility company, for instance a high price for peak load periods, medium price for standard periods, and low price for off-peak periods. In this study, the daily electricity price at the selected region of South Africa can be given as [24]

$$\rho(t) = \begin{cases} \rho_k; t \in T_k, T_k = [7,10) \cup [18,20) \\ \rho_0; t \in T_0, T_0 = [0,6) \cup [22,24) \\ \rho_s; t \in T_s, T_s = [6,7) \cup [10,18) \cup [20,22) \end{cases} \quad (5)$$

where

ρ_k 0.20538 $ = kWh is the price for the peak load period;
ρ_0 0.03558 $ = kWh is the price for the off-peak period;
ρ_s 0.05948 $ = kWh is the price for the standard period.

3.1 Objective Function

The proposed cost function has three main components. The first component is the cost of purchasing electricity from the grid, which is used to supply the load demand and charge the battery. The component is the revenue generated from selling electricity to the grid. The third part is the wearing cost of hybrid system. The total function can be expressed as

$$f = \sum_{j=1}^{N} \rho_j (P_{\text{G-B}(j)} + P_{\text{G-L}(j)}) \Delta t - r_k \rho_k \sum_{j=1}^{N} P_{\text{B-G}(j)} \Delta t + \sum_{j=1}^{N} a (P_{\text{B-L}(j)} + P_{\text{B-G}(j)}) \Delta t + 24b \quad (6)$$

where $r_k = 0.65$ is the contracted ratio of the peak price ρ_k for selling power during the peak load period; a is the coefficient of battery wearing cost; and b is the hourly wearing cost of other components [24].

3.2 Constraints

The control variables in the objective function above have to satisfy the following constraints:

- Renewable output constraints:

The sum of instantaneous PV or WT power for charging the battery and for supplying the load must be less than the PV or WT output power generated:

$$P_{\text{PV-B}(j)} + P_{\text{PV-L}(j)} \leq P_{\text{PV}(j)} \quad (7)$$

$$P_{\text{WT-B}(j)} + P_{\text{WT-L}(j)} \leq P_{\text{WT}(j)} \quad (8)$$

- Power balance constraint:

The required load demand must be exactly satisfied by the total power of PV, WT, grid, and the battery. This can be expressed as

$$P_{\text{B-L}(j)} + P_{\text{G-L}(j)} + P_{\text{PV-L}(j)} + P_{\text{WT}(j)} \leq P_{\text{L}(j)} \quad (9)$$

Each power source is modeled to be controllable in the range of zero to their rated power for the 24-h period. Therefore, the variable limits are the output limits of these different power sources at any sampling interval j. These can be expressed as

- Control variables limits:

$$0 \leq P_{\text{PV-B}(j)} \leq P_{\text{PV-B}}^{\max} (1 \leq j \leq N) \quad (10)$$

$$0 \leq P_{\text{WT-B}(j)} \leq P_{\text{WT-B}}^{\max} (1 \leq j \leq N) \quad (11)$$

$$0 \le P_{\text{B-L}(j)} \le P_{\text{B-L}}^{\max}(1 \le j \le N) \tag{12}$$

$$0 \le P_{\text{G-B}(j)} \le P_{\text{G-B}}^{\max}(1 \le j \le N) \tag{13}$$

$$0 \le P_{\text{G-L}(j)} \le P_{\text{G-L}}^{\max}(1 \le j \le N) \tag{14}$$

$$0 \le P_{\text{PV-L}(j)} \le P_{\text{PV-L}}^{\max}(1 \le j \le N) \tag{15}$$

$$0 \le P_{\text{WT-L}(j)} \le P_{\text{WT-L}}^{\max}(1 \le j \le N) \tag{16}$$

$$0 \le P_{\text{B-G}(j)} \le P_{\text{B-G}}^{\max}(1 \le j \le N) \tag{17}$$

The available battery bank state of charge in any sampling internal must not be less than the minimum allowable and must not be higher than the maximum allowable state of charge. This can be expressed as

$$\text{SOC}^{\min} \le \text{SOC}_{(j)} \le \text{SOC}^{\max} \tag{18}$$

3.3 Optimal Control Method

An optimal control method is used to manage the power flows P_i in all the sampling periods over a 24-h period to minimize the daily electricity cost, Eq. (4), subject to constraints, Eqs. (6)–(18). Because the objective function and constraints are linear, this power flow control problem can be expressed as a linear programming problem as [25]

$$\min f(x), \text{s.t.} \begin{cases} Ax \le b \\ A_{\text{eq}} X = b_{\text{eq}} \\ l_{\text{b}} \le x \le u_{\text{b}} \end{cases} \tag{19}$$

where $f(x)$ represents the objective function; A_{eq} and b_{eq} are the coefficients associated with equality constraints; A and b are the coefficients associated with inequality constraints; l_{b} and u_{b} are the lower and upper bounds of variables.

4 Case Studies

4.1 Control System Settings

In this work, real daily load data and water velocity have been used as input to evaluate the performance of the system submitted to the developed optimal energy management system. These hourly data are available from Ref. [21].

The sizing of PV, WT, and battery bank is based on a sizing model in [26]. The parameters (size, initial costs) of this hybrid system are available from Ref. [21]. The simulation results will be discussed and categorized according to the behavior of the proposed grid-connected hybrid system under the different pricing periods in South Africa.

4.2 Household's Results of Optimal Control

A 24-h detailed load data, given in Fig. 3, is obtained from a typical household situated in the KwaZulu Natal Province at 30.6° latitude south and 29.4° longitude east. The hybrid system is designed in such a way to provide electricity for low consumption electrical appliances such as lights, TV, radio, laptop, fridge, kettle, cell phone chargers, iron, toaster, etc. When scrutinizing this load profile, one can notice a general pattern arising from the daily activities of the users which changes depending on different seasons of the year. The selected load demand from Ref. [21] reaches a peak demand of 8 kW in winter; therefore, the hybrid system must be able to adequately respond to this demand.

4.2.1 Power Flow Under Off-Peak Load Period

Figure 3 shows the load profile for the selected winter day. It can be observed that the demand is highly nonlinear; low during the night with high peaks in the morning and in the evening. The power flow on the battery and load side are provided in Figs. 4 and 5 respectively.

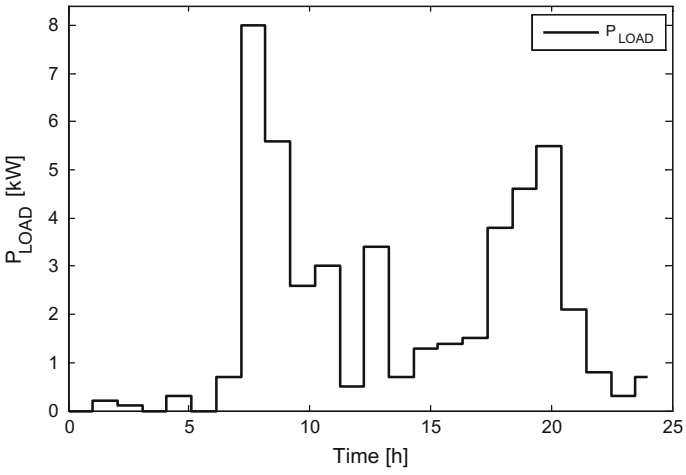

Fig. 3 Load profile (household case)

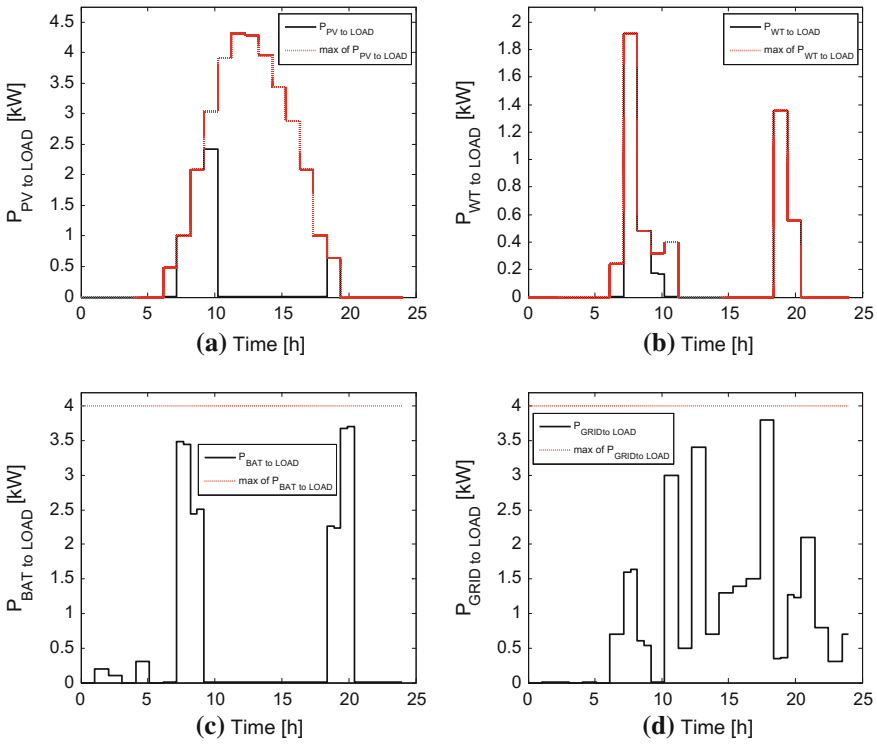

Fig. 4 Load-side power flow (household case)

The power provided to the load includes the batteries $P_{\text{B-L}}$, $P_{\text{G-L}}$, $P_{\text{PV-L}}$, and $P_{\text{WT-L}}$. During the off-peak period, only the battery system provides power to the load as illustrated in Fig. 4c; its corresponding state of charge decreases as shown in Fig. 5d. The PV, the WT, and the grid do not supply the load during that period as shown in Fig. 4a, b, d respectively.

There is enough power from the battery to supply the load and to be sold to the grid to generate revenue. Even if the price is low during this period, excess power not used to supply the load is sold to the grid as shown in Fig. 6.

4.2.2 Power Flow Under Standard Load Period

During the standard price period, although the battery system can fully satisfy the load demand, the grid power has been used as main supply to the load as well as to recharge the battery, which can be seen from Fig. 4c, d, respectively. There is a very small output from the PV and WT; these are used to recharge the battery as shown in Fig. 5a, b.

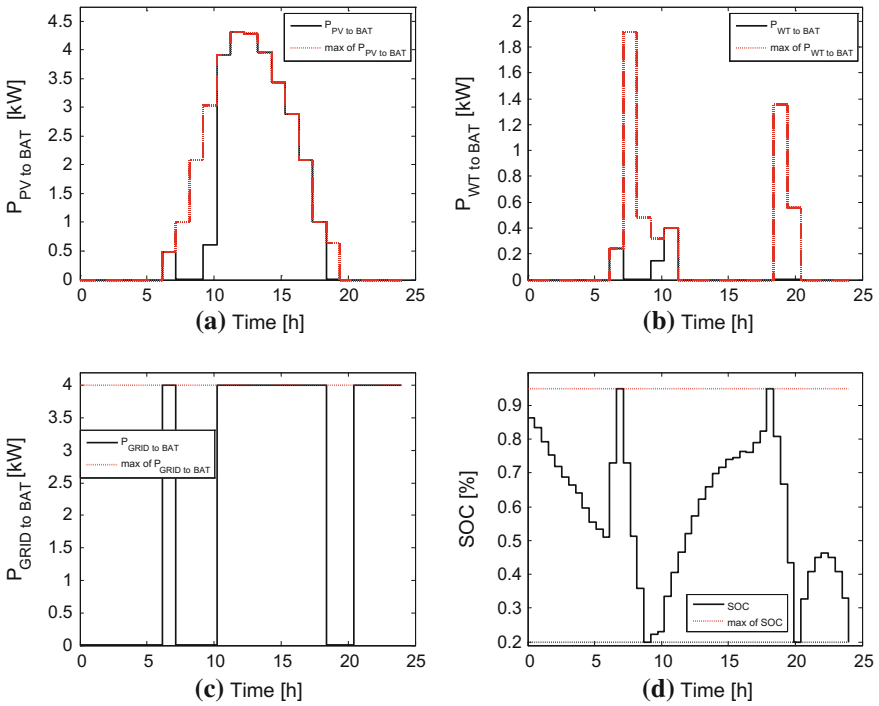

Fig. 5 Battery-side power flow (household case)

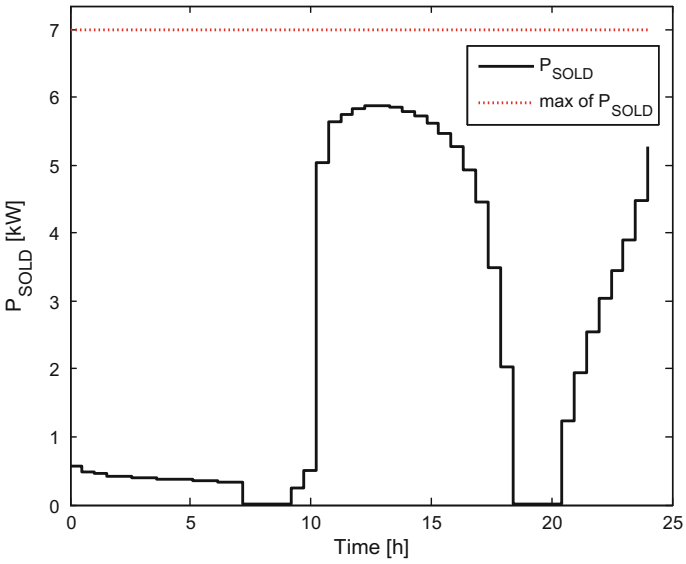

Fig. 6 Profile of power sold (household case)

4.2.3 Power Flow Under Peak Load Period

During the peak load period, the load is principally met by the power from the PV and WT, if there is any shortage in supply; the battery can be used in conjunction with the PV and WT (Fig. 4a–c). It can be seen from Fig. 5d how the state of charge decreases when the battery is giving power to the load. If the PV, WT, and battery cannot adequately respond to the demand, the grid can be used to balance the power needed to satisfy the load demand as shown in Fig. 4d. The power stored in the battery could have been sold to the grid during this period but because of the proposed hybrid system's size and the priority given to the load demand, there is almost no excess power to be sold during this peak power demand. Therefore, it can be seen from Fig. 6 that the power sold the grid at the end of this period is minimum.

4.2.4 Power Flow Under Off-Peak Load Period

During this off-peak load period, both the load demand and the price of electricity are low. Therefore, the power from the grid is used to principally supply the load and recharge the battery at the same time. This can be seen when looking at Fig. 4d and Fig. 5c respectively. Figure 4b, c confirms that no power from the PV or the battery is used to supply the load; this power is sold to the grid as illustrated in Fig. 5d.

4.2.5 Power Flow Under Peak Load Period

During this second peak load period, there is a very small amount of power generated by the PV. Most of the power consumed by the load is coming from the WT battery and the grid is shown in Fig. 5b–d. There is no power sold to the grid during this high-demand pricing period as illustrated in Fig. 6.

4.2.6 Daily Income Generated

On the selected day, if the load demand is supplied by the grid only without the PV, WT, and battery storage system, the daily electricity cost would be $4.32. When optimally operating the grid-connected hybrid system, the daily income generated by selling electricity to the grid is $20.79. In other words, when making the balance between what is purchased from the grid and what is sold to the grid, the customer can earn $16.47. This income is a function of the size of the hybrid system's components, the battery initial state of charge, as well as on the load profile.

4.3 Base Transceiver Station's Results of Optimal Control

The base transceiver station selected for this study is situated in the Western Cape region at 32.8° latitude south and 17.9° longitude east. The energies needed by the BTS communication equipment and the cooling system used to remove heat from the cabin are given in Ref. [27]. The load profile resulting from the daily power demand of the radio, power conversion, antenna, transmission, security lights, and cooling equipment at the base station site is given in [28]. It is noticeable from this table that except for the auxiliary equipment such as air conditioning which is running during the day for only 6 h (11:00–17:00 h), and the security lights for 11 h throughout the night (19:00–6:00 h), the rest of the BTS communication equipment is running for 24 h non-stop. However, during winter, the air conditioning is running for only 2 h (13:00–15:00 h) and the security lights for 13 h (18:00–7:00 h). This load (Fig. 7) has been selected because of its pattern which is different than the one from the household; this will induce a different response of the hybrid system operation energy scheduling. The power flows on the battery and load side are provided in Figs. 8 and 9, respectively.

4.3.1 Power Flow Under Off-Peak Load Period

During this off-peak period, the battery system and the grid provide power to the load as illustrated in Fig. 8c–d, respectively. Therefore, there is no excess of energy from the renewable components to be sold to the grid during this period as shown in

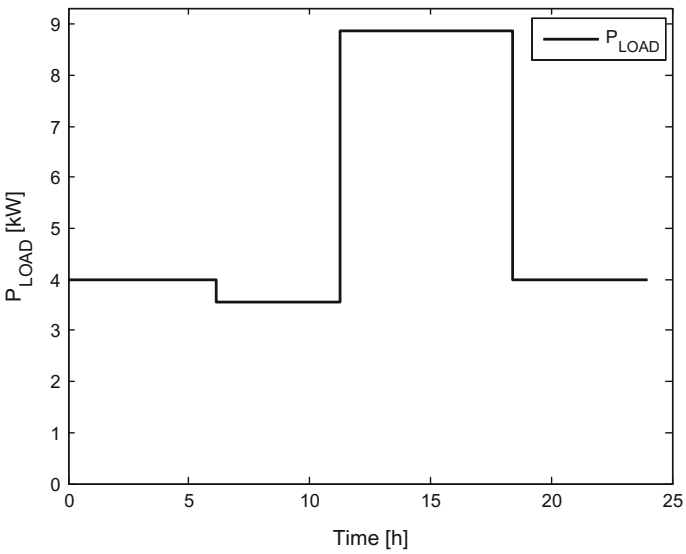

Fig. 7 Load profile (BTS case)

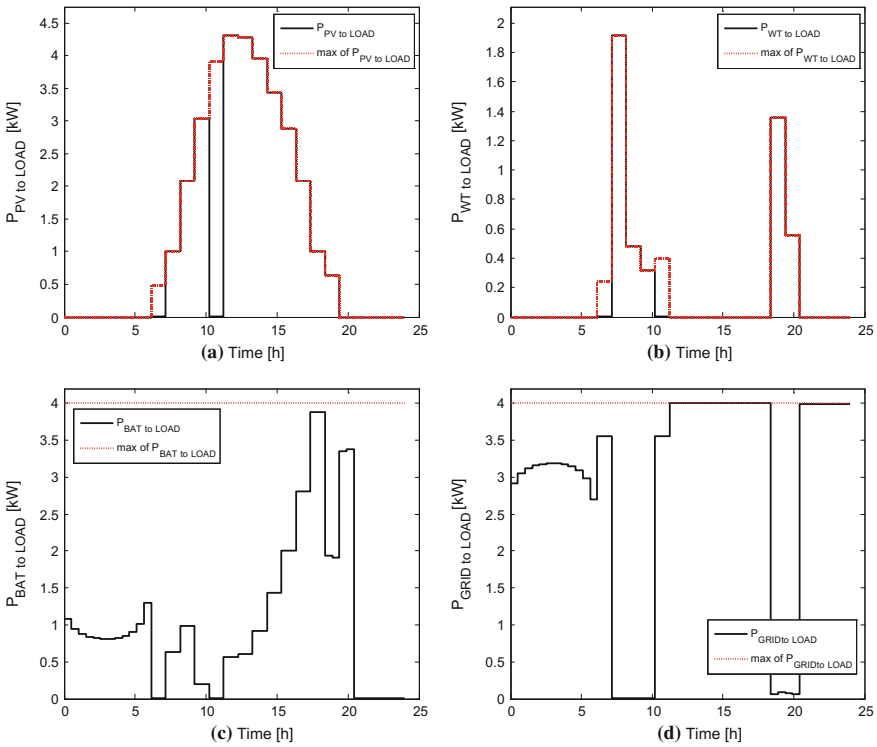

Fig. 8 Load-side power flow (BTS case)

Fig. 10. There is no power generated from the PV and WT because of the lack of resources as shown in Fig. 8a–b.

4.3.2 Power Flow Under Standard Load Period

During the standard price period, the powers from the PV, WT, and the grid are used to recharge the battery as shown in Fig. 9a–c; this is done so that there can be enough power stored to be for sold during the coming peak period. The load is exclusively supplied by the grid as shown in Fig. 8d.

4.3.3 Power Flow Under Peak Load Period

During the peak load period, the demand is primarily satisfied by the PV and WT as shown in Fig. 8a–b; any deficit of power demand is then balanced by the battery and the grid. There is no power sold to the grid because there is no excess of energy and because of the priority given to supply the load by the PV, WT, and the battery;

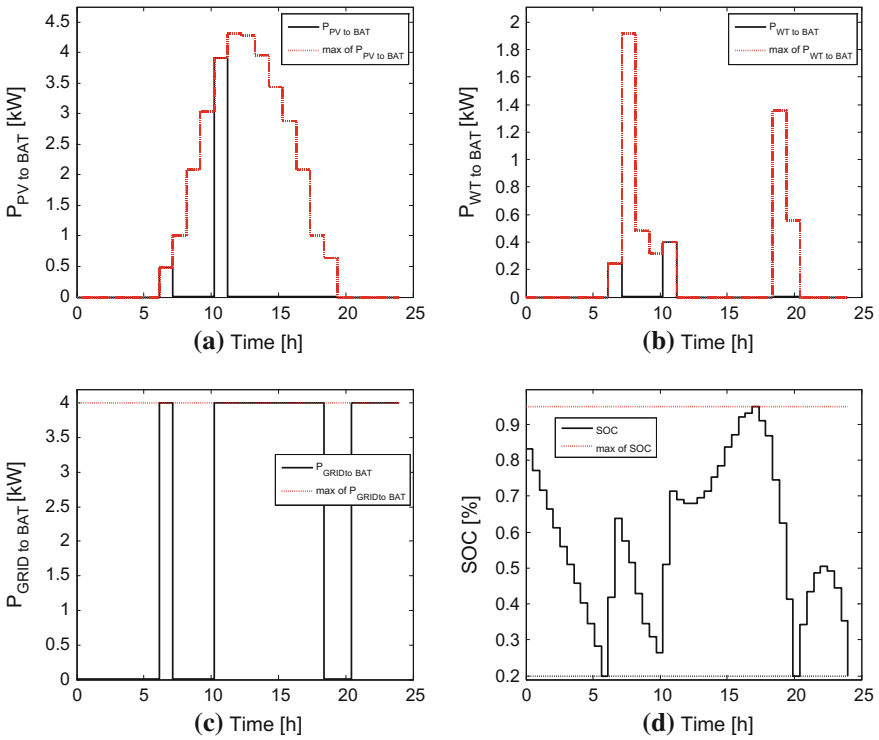

Fig. 9 Battery-side power flow (BTS case)

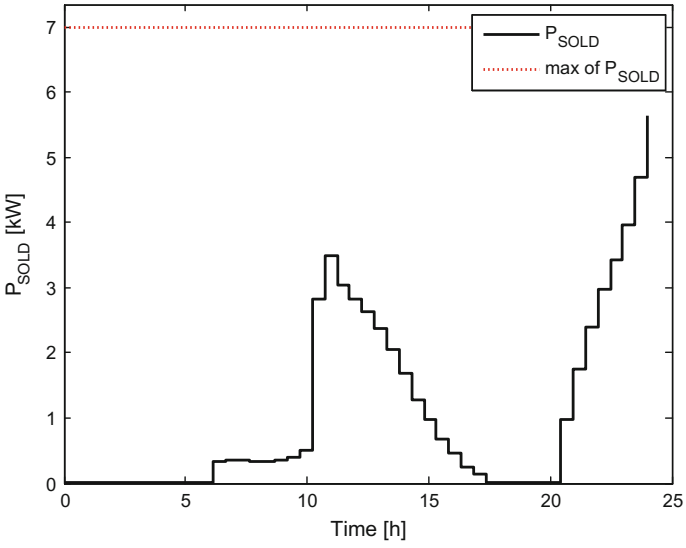

Fig. 10 Profile of power sold (BTS case)

the excess of energy from the hybrid system to be sold to the grid during this period is minimal as shown in Fig. 10.

4.3.4 Power Flow Under off-Peak Load Period

During this period the cost of electricity from the grid is low; therefore, the PV, WT, and the grid are used to supply the load demand as shown in Fig. 8a, b, d, respectively, and the excess of power from the PV and WT is sold to the grid through the battery as shown in Fig. 10. This load demand is supplemented by an increasing contribution from the battery in the afternoon toward the evening, due to the shortage of the output power of the PV and WT; this can be seen from Fig. 8a, b.

The battery is being recharged by the grid only and its corresponding state of charge increases as shown in Fig. 9c–d, respectively.

4.3.5 Power Flow Under Peak Load Period

During this second peak price period, all the power generated by the PV, WT system, and battery with as small contribution of the grid is used to supply the load as shown in Fig. 8a–d. There is no power used to either recharge the battery or supply the load as shown in Fig. 9a–c.

4.3.6 Daily Income Generated

If the BTS demand is supplied by the grid only without the PV, WT, and battery storage system, the daily electricity cost would be $12.69. When optimally operating the grid-connected PV, WT hybrid system, the daily electricity cost is reduced to 5.29$. In other words, when making the balance between what is purchased from the grid and what is sold to the grid, the income generated by selling electricity to the grid is $7.

5 Chapter Summary

In this chapter, demand-side management has been applied in the optimal energy management of grid-connected PV–WT–battery hybrid system. The Time-of-Use operating tariff with power selling to the grid has been studied for energy management in this work. A model for decreasing electricity charge at the consumer's side has been developed. The simulation results of two case studies in South Africa have demonstrated that the developed optimal operation model for the hybrid system results in the maximal use of PV, WT, and battery storage system. The simulation results highlight the important role played by the battery which is storing

power from the utility during off-peak periods and providing power to the load during peak periods. Consequently, by optimally operating the hybrid system, the load consumes nominal amount of power from the utility and the consumers can generate income by selling electricity to the grid. This income is a function of the size of the hybrid system's components, the battery initial state of charge, as well as on the load profile. It has also been demonstrated that optimal control is a powerful control method for power flow management in DSM.

For future work, Model Predictive Control will be developed to handle the control when the hybrid system experiences disturbances in PV output and load demand. Also different load patterns as well as different renewable energy sources will be considered.

References

1. Goedeckeb M, Therdthianwong S, Gheewala SH (2007) Life cycle cost analysis of alternative vehicles and fuels in Thailand. Energy Policy 35(6):3236–3246
2. Kusakana K, Vermaak HJ (2013) Hybrid renewable power systems for mobile telephony base station in developing countries. Renew Energy 51(419):425
3. Kusakana K (2014) Optimal operation control of hybrid renewable energy systems. Thesis, Central University of Technology
4. Jain S, Agarwal V (2008) An integrated hybrid power supply for distributed generation applications fed by nonconventional energy sources. IEEE Trans Energy Convers 23(2): 622–631
5. García-Triviño P, José Gil-Mena A, Llorens-Iborra F et al (2015) Power control based on particle swarm optimization of grid-connected inverter for hybrid renewable energy system. Energy Convers Manag 91:83–92
6. Aghajani GR, Shayanfar H, Shayeghi H (2015) Presenting a multi-objective generation scheduling model for pricing demand response rate in micro-grid energy management. Energy Convers Manag 106:308–321
7. Chen C, Duan S, Cai T et al (2011) Smart energy management system for optimal microgrid economic operation. IET Renew Power Gener 5(3):258–267
8. Kusakana K (2016) Energy management of a grid-connected hydrokinetic system under time of use tariff. Renew Energy. doi:10.1016/j.renene.2016.10.019
9. Riffonneau Y, Bacha S, Barruel F et al (2011) Optimal power flow management for grid connected PV systems with batteries. IEEE Trans Sustain Energy 2(3):309–320
10. Li L, Gong C, Tian S et al (2016) The peak-shaving efficiency analysis of natural gas time-of-use pricing: evidence from multi-agent simulation. Energy 96:48–58
11. Wu Z, Tazvinga H, Xia X (2015) Demand side management of photovoltaic-battery hybrid system. Appl Energy 148:294–304
12. Ottesen S, Tomasgard A, Fleten S (2016) Prosumer bidding and scheduling in electricity markets. Energy 94:828–843
13. Hedarian-Forushani E, Gloshan MEH, Shafie-khah M (2015) Flexible security-constrained scheduling of wind power enabling time of use price scheme. Energy 90(2):1887–1900
14. Logenthiran T, Srinivasan D, Shun TZ (2012) Demand side management in smart grid using heuristic optimization. IEEE Trans Smart Grid 3(3):1244–1252
15. Brando B, Dannier A, Del Pizzo A et al (2016) Grid connection of wave energy converter in heaving mode operation by supercapacitor storage technology. IET Renew Power Gener 10(1):88–97

16. Hu J, Zhu J, Dorrell DG (2014) Model predictive control of inverters for both islanded and grid-connected operations in renewable power generations. IET Renew Power Gener 8(3): 240–248
17. Wolisz H, Punkenburg C, Streblow R et al (2016) Feasibility and potential of thermal demand side management in residential buildings considering different developments in the German energy market. Energy Convers Manag 107:86–95
18. Dufo-Lopez R, Bernal-Agustin JL (2015) Techno-economic analysis of grid-connected battery storage. Energy Convers Manage 91:394–404
19. Dufo-Lopez R (2015) Optimization of size and control of grid-connected storage under real time electricity pricing conditions. Appl Energy 140:395–408
20. Sichilalu SM, Xia X (2015) Optimal power dispatch of a grid tied-battery-photovoltaic system supplying heat pump water heaters. Energy Convers Manag 102:81–91
21. Kusakana K (2015) Optimal scheduled power flow for distributed photovoltaic/wind/diesel generators with battery storage system. IET Renew Power Gener 8(8):916–924
22. Kusakana K (2015) Optimisation of battery-integrated diesel generator hybrid systems using an ON/OFF operating strategy. Paper presented at the international conference on the domestic use of energy, Cape Town, 30 Mar–1 Apr 2015
23. Bokopane L, Kusakana K, Vermaak HJ (2015) Optimal energy management of an isolated electric Tuk-Tuk charging station powered by hybrid renewable systems. Paper presented at the international conference on the domestic use of energy, Cape Town, 30 Mar–1 Apr 2015
24. Wu Z, Tazvinga H, Xia X (2015) Demand side management of photovoltaic-battery hybrid system. Appl Energy 148:294–304
25. Kusakana K, Vermaak HJ, Numbi BP (2012) Optimal sizing of a hybrid renewable energy plant using linear programming. Paper presented at the IEEE power engineering society conference and exposition in Africa, Johannesburg, 9–12 July 2012
26. Kusakana K, Vermaak HJ, Numbi BP (2015) Optimal operation control of hydrokinetic based hybrid systems. In: Sayigh A (ed) Renewable energy in the service of mankind, vol 1. Springer, Heidelberg, pp 291–303
27. Kusakana K (2015) Minimum cost solution of isolated battery-integrated diesel generator hybrid systems. Paper presented at the South African University power and energy conference, Johannesburg, 28–30 Jan 2015
28. Kusakana K, Vermaak HJ (2014) Cost and performance evaluation of hydrokinetic-diesel hybrid systems. Energy Procedia 61:2439–2442